



Annual Progress Report: ONR Short Pulse Research, Evaluation and non-SWaP (OSPRES) Demonstration for c-sUAV Study

OSPRES Grant: N00014-17-1-3016
Period of Performance: 01 OCT 2018 – 29 SEPT 2019

OSPRES Project Description:

Develop tunable High Power Microwave (HPM) sources and electronically steerable radiators whose waveform(s) enable control over all levels-of-lethality on cUAV and similar targets, with the least power density.

Distribution Statement A: Approved for public release: distribution unlimited.

REPORT DOCUMENTATION PAGE	Form Approved OMB No. 0704-0188

The public reporting burden for this collection of information is estimated to average 1 hour per response, including the time for reviewing instructions, searching existing data sources, gathering and maintaining the data needed, and completing and reviewing the collection of information. Send comments regarding this burden estimate or any other aspect of this collection of information, including suggestions for reducing the burden, to Department of Defense, Washington Headquarters Services, Directorate for Information Operations and Reports (0704-0188), 1215 Jefferson Davis Highway, Suite 1204, Arlington, VA 22202-4302. Respondents should be aware that notwithstanding any other provision of law, no person shall be subject to any penalty for failing to comply with a collection of information if it does not display a currently valid OMB control number.
PLEASE DO NOT RETURN YOUR FORM TO THE ABOVE ADDRESS.

1. REPORT DATE *(DD-MM-YYYY)*	2. REPORT TYPE	3. DATES COVERED *(From - To)*
15 - 10 - 2021	Annual Technical Report	Oct 2018- Sept 2019

4. TITLE AND SUBTITLE
OSPRES Grant Annual Technical Report FY2019

5a. CONTRACT NUMBER

5b. GRANT NUMBER
N00014 - 17 - 1 - 3016

5c. PROGRAM ELEMENT NUMBER

6. AUTHOR(S)
E. Myers, T. Fields, J. Currie, J. Smith, J. Crow, D. Chatterjee, P. Rulis, P. Doynov, A. Hassan, J. Lancaster, J. Verzella, F. Khan, L. Moler, A. Caruso

5d. PROJECT NUMBER

5e. TASK NUMBER

5f. WORK UNIT NUMBER

7. PERFORMING ORGANIZATION NAME(S) AND ADDRESS(ES)
University of Missouri- Kansas City
5110 Rockhilll Rd
Kansas City, MO 64110

8. PERFORMING ORGANIZATION REPORT NUMBER
OSPRES Grant Annual 2019

9. SPONSORING/MONITORING AGENCY NAME(S) AND ADDRESS(ES)
Office of Naval Research
One Liberty Center, 875 N Randolph
Arlington, VA 22203

10. SPONSOR/MONITOR'S ACRONYM(S)
ONR

11. SPONSOR/MONITOR'S REPORT NUMBER(S)

12. DISTRIBUTION/AVAILABILITY STATEMENT
Distribution A: Distribution Unlimited

13. SUPPLEMENTARY NOTES

14. ABSTRACT
This report summarizes the progress of year two of fundamental research in the areas of RF propagation, RF coupling, HPM system designs, electrically small antennas and multiple sub-areas of those listed above. Technical achievements and findings from Oct 2018 - September 2019 are presented.

15. SUBJECT TERMS
Antenna, RF, High power microwave, pulsed power, photoconductive switches, gallium nitride

16. SECURITY CLASSIFICATION OF:			17. LIMITATION OF ABSTRACT	18. NUMBER OF PAGES	19a. NAME OF RESPONSIBLE PERSON
a. REPORT	b. ABSTRACT	c. THIS PAGE			Anthony Caruso
U	U	U	SAR	353	19b. TELEPHONE NUMBER *(Include area code)* 816-235-2505

Reset

Standard Form 298 (Rev. 8/98)
Prescribed by ANSI Std. Z39.18

Distribution List

ADDRESSEE	DODAAD CODE	QUANTITY
Office of Naval Research ATTN: Ryan Hoffman ONR, 351 875 North Randolph St. Arlington, VA 22203-1995	N00014	1
Administrative Contracting Officer* *Transmittal letter only Fax: 312-353-6089	S1403A	1
DEFENSE TECHNICAL INFORMATION CENTER 8725 JOHN J. KINGMAN RD SUITE 0944 FORT BELVOIR, VA 22060-6218 E-mail: TR@dtic.mil	HJ4701	2
DIRECTOR, NAVAL RESEARCH LAB ATTN: CODE 5596 4555 OVERLOOK AVENUE, SW WASHINGTON, D.C. 20375-5320 E-mail: reports@library.nrl.navy.mil	N00173	1

Additional Distribution

Air Force Research Laboratory
ASR Corporation
Atlas Team
BAE Systems – New Hampshire
BAE Systems – Minnesota
Booz Allen Hamilton
Department of Energy's Kansas City National Security Campus, Managed by Honeywell
Eagle Harbor Technologies, Inc.
Georgia Tech Research Institute
KalScott Engineering, Inc.
Lawrence Livermore National Laboratory
Lockheed Martin Missiles and Fire Control
Metamagnetics
Missouri University of Science & Technology
Naval Air Systems Command
Naval Research Laboratory
Naval Surface Warfare Center, Dahlgren Division
Preston Grounds Consulting
Radiation Detection Technologies, Inc.
Raytheon Integrated Defense Systems
Scientific Applications & Research Associates, Inc.
Thomas Hussey
University of Missouri – Columbia
University of Missouri – Kansas City
Verus Research

OSPRES Grant Effort – YR 2 Executive Summary:

The OSPRES grant is represented by three categories: 1) Source development; 2) RF coupling; and, 3) RF transmission. Source development captures advances to silicon based photoconductive switches (SiPCSS) and power semiconductor alternatives to silicon PCSS. The effort is captured through results of modeling, simulation, and characterization including the required pulse charging, transmission line topology, and any power or transmission conditioning necessary based on the specific RF waveform to be generated. Antenna designs for RF propagation focuses on generating novel electrically small antennas to propagate RF waveforms and investigates the trade space of the ESA's in terms of bandwidth, VSWR, gain, input power, steerable angle, highlighting their tradeoffs. This report summarizes year two (YR2) of the OSPRES grant research and accomplishments during Oct. 2018 through Sept. 2019.

SiPCSS Evaluation and Development:

The majority of the Si-PCSS effort is now limited distribution; a summary of that work is presented here with details reported under N00014-18-C-1017 and N68335-17-C-0041.

By accurately modeling SiPCSS reverse recovery and controlling defect states and concentrations, we have enabled design feedback for selecting the electron dose and energy for optimal recovery. Prior art has demonstrated faster and more efficient recovery by targeting the junction with lower energy (550-keV) electrons, which we will explore in FY2020.

UMKC has generated time-dependent TCAD models of the Si-PCSS recovery process during both reverse recovery (i.e., carriers injected by an electronic forward bias), and photo-illuminated recovery (i.e., carrier generation via stimulation with laser pulse). These models have been extended to incorporate defect profiles within the bulk of the SiPCSS, indicating that a trade-space exists between not only the energy and concentration of the defect states, but also the concentration profile throughout the device. Experimental data validates the models with near-perfect agreement, but additional experimental and analytical studies are needed to rigorously connect specific defect states with the irradiating electron energy and fluence.

While simulations of device hold-off voltage were conducted, we have deprioritized this effort due to the complex nature of the Si-PCSS surface states and their interaction with passivants. Simulations have continued to over-estimate measured voltage hold-off, and it remains unclear if simulation can sufficiently model these complex interactions.

Continuing with the work from the previous year to improve SiPCSS design, device recovery time was measured as a function of 3-MeV electron dose, which indicate an increase in efficiency by a factor of two-to-five, even with minimal dose (i.e., 1.0-MR) at charge voltages up to 2-kV.

While the critical field of Si is low relative to UWBG materials, we were able to demonstrate a nearly two-fold increase in pulse hold-off voltage, bringing the maximum

pulsed charge voltage up from 5.5-kV in 2018, to 10-kV in 2019. This was achieved by improving passivation techniques, starting with materials with less impurities, and more reliable manufacturing methods developed by Bellinger and co-workers at Radiation Detection Technologies.

In 2018, we determined that Si-PCSS unique long recovery time, while enabling higher pulse energy gain (i.e. electrical power delivered per Joule of incident optical energy), makes Si particularly sensitive to charging. The long recovery time can lead to substantial losses (i.e., heat) in the device at the onset of pulse charging, and even greater leakage following each switching event when required to hold a charged DC line. Moreover, there is limited availability of pulse chargers tuned specifically to the demands of SiPCSS.

To overcome limited availability of optimized pulse chargers, effort toward developing HV-switch topologies combined with inductive output conditioning for optimally charging SiPCSS-based pulsers was initiated. Initially, a Behlke Si-based HV switch was acquired and integrated with a gate driver and output conditioning circuitry, but the limits of the Si-Behlke switch were quickly realized. The next generation currently under development incorporates a SiC-Behlke switch, whose specifications should enable charging to 10-kV at tens-to-hundreds of kHz for hundreds of shots. In parallel, the Khan group is evaluating novel HV switch topologies for further improving the performance and reliability of the pulse charger.

GaN:C-PCSS Evaluation and Development:

Although the GaN:C-PCSS characterization and development effort has been out-paced by SiPCSS, we have demonstrated 1-kV pulses (~2-ns pulse widths) with incident pulse energies of less than 30-µJ. Substantial room for improvement remains to bring the GaN:C-PCSS effort to greater power and efficiency, and optimized recovery time. Currently the GaN:C-PCSS recovery time is slightly longer (~2-ns) than necessary for direct RF generation via laser modulation, but too short for incorporation into high energy gain pulse forming networks similar to Si-PCSS. That said, the limitations of GaN:C-PCSS are far from realized, as (unlike Si) no current saturation has been detected even at 1-kV; the relationship between on-state resistance and illumination energy are thus far independent of current density.

An additional challenge with GaN:C-PCSS is the limited availability of accurate models for GaN:C which can be/have been validated/verified by experiment. Without a wealth of validated models, simulation and modeling efforts have the unique challenge of modeling a moving target (i.e., a material undergoing continuous change). For comparison, Si has been widely studied and characterized with a wealth of computational and experimental data available for reference and to inform computational studies. Efforts by the Rulis group have focused on resolving this issue by merging functional models (e.g., TCAD) with electronic-structure models to enable prediction of bulk material properties without the need for manufacturing and characterizing novel material configurations. The

framework of this approach has been drafted and, while the approach is still under development, initial validation is focused on replicating results from spectroscopic techniques.

Despite the promises of virtually zero current -saturation, the maturity and cost of manufacturing methods require a renaissance to make GaN:C PCSS competitive and viable for SWaP-C^2 conscious high power RF generation. We are currently conducting a review of GaN manufacturing processes and costs to establish the tradeoffs and recommend external commercial manufacturing paths forward, while modestly continuing research efforts to push the limits of GaN:C PCSS.

Electrically Small Antennas (ESA)

To reduce the overall size and cost of an array of antenna elements, efforts in developing electrically small antennas has focused on microstrip patch antennas. Microstrip patch antennas have shown to be capable of gain in excess of 5-dB and greater than 30% bandwidth when designed around center frequencies between 400- and 1200-MHz. Currently the microstrip patch antenna designs have an electrical length (kα) of approximately 0.6, which is larger than the electrical length of 0.5 or less that defines an “electrically small antenna’. Although the kα is above 0.5, the antenna designs are still small relative to the most common wideband antenna designs typically used to achieve performance and high power handling capabilities.

Simulations and modelling throughout the year have varied the substrate material, substrate geometry, and overall antenna geometry. The simulations focused on maximizing the gain, bandwidth, and VSWR, while keeping the kα as low as possible. From this work two antenna geometries were selected for prototyping and testing. The chosen designs have electrical lengths of 0.67 and 0.8 based on two different substrates with dielectric constants of 9.8 and 6.0 respectively. Experimental testing of the prototypes resulted in measured gains and VSWR’s that were in relatively good agreement with simulated data. The smaller electrical length of the antenna with a substrate dielectric constant of 9.8, has been used to feed the trade space analysis of arrays.

The end of the performance period of 2019 saw the beginnings of array simulations with the chosen antenna design. Preliminary calculations have shown that, in order to have above X-W/cm^2 at a minimum distance of Y-km, the ideal single element for an array would need to have greater than 35dB gain in order to keep the power input in to the antenna below 200-MW. These are starting points for the array trade space analysis and help to inform the requirements on a PCSS based system capable of feeding the antennas. Further work on the trade space and array designs are ongoing and will continue through FY20.

RF Coupling

Reported in the FY19 OSPRES contract report for N00014-18-C-1017.

SUMMARY OF RESEARCH EFFORTS

Specific Areas of Research:

1. Designing a Positive Feedback NLTL Based Soliton Generator
2. Development of a Power Conditioning Circuit for PCSS
3. Trade Space Analysis of a Phased Array of Electrically Small Antennas
4. UAV Asset Development and Experimental Design
5. RF Coupling Modeling and Experimental Measurements
6. GaN:C Electrical Carrier Transport Properties Simulations
7. High Power Ultrafast Switching Fundamentals, Materials and Figure of Merit
8. GaN:C Photoconductive Solid-state Switches (PCSS)

Objectives:

1. *Positive Feedback NLTL Based Soliton Generator*

Nonlinear transmission lines (NLTL) are used to generate high-power radio frequency (RF) signals using passive elements, and are primarily used for pulse sharpening. Traditionally, a continuous signal stream is required to generate sharpened RF signals at NLTL output. The objective of our research was to develop a compact high power RF signal generator using the combination of a laterally-diffused metal-oxide semiconductor (LDMOS) based push-pull power amplifier (PA) with a Schottky diode-based NLTL while a single pulse is used as a source. This compact self-sustaining soliton (high-frequency RF signal) generator can be used for low to medium power RF signal generation.

2. *Development of PCSS Power Conditioning Circuit*

Photoconductive semiconductor switches (PCSS) are promising devices for compact, repetitive pulsed power generation due to their fast response time, negligible time jitter, precise synchronization, high repetition rate and optical electrical isolation. One of the methods to generate a high-power RF signal is charging a transmission line from a high-voltage (HV) DC power supply, and subsequent discharge through another transmission line by a rapid triggering of the PCSS. Traditional methods of charging (e.g., Direct DC charging, low-pass filter based charging) may cause the PCSS to experience high voltage and temperature stress during the entire period of operation. This phenomenon adversely affects the lifetime of the PCSS, therefore, the reliability of the overall system. In addition, high voltage stress across the PCSS and leakage current through it during the OFF-state leads to excessive power loss, thereby reducing system efficiency. The objective of our research is to design a solid-state switch-based power conditioning circuit that can efficiently keep the voltage across the PCSS close to zero during its OFF-state leading to mitigation of excess voltage and temperature stress across it.

3. *Trade Space Analysis of a Phased Array of Electrically Small Antennas.*

The main objective of this project is to design a phased array composed of electrically small antennas. There are two distinct efforts involved: (a) investigations into electrically small antenna (ESA) characterization and (b) trade space studies/parametric analysis on down selecting a *phased array*. The ultimate goal is to explore options on how to finally integrate an ESA as an element in a phased array for realizing a desired performance between 400 MHz and 1200 MHz.

4. *UAV Asset Development and Experimental Design*

The focus of this aspect of the OSPRES program is on the continual improvement and innovation with regards to UAV platforms and diagnostics for both indoor and outdoor testing. The inclusion of UAV diagnostics is intended to provide detailed data from sensors, filters, and commands during and after testing. Additionally, the focus of this effort is on the experimental design that maximizes understanding while attempting to minimize the number of experiments required. Several different aspects within this regime have been considered and explored including automated testing and analysis as well as adaptive experiment design.

5. *RF Coupling Modeling and Experimental Measurements*

To be reported in contract report for N00014-18-C-1017

6. *GaN:C Theoretical Simulations*

To understand the operation of carbon doped gallium nitride as a photoconductive switch in pulsed power applications, it is necessary to combine theoretical models with experimental and characterization data to further understand how to maximize GaN:C for pulsed power applications. Based on this need, there is ongoing work to establish an understanding of all the computational concepts and explicit program codes that are needed in the long tool chain for computing high-level engineering quantities (breakdown voltages, thermal conductivities, macroscopic optical response) from basic *ab initio* methods. Build points of connectivity between well-developed tool chain (fig. 1) components and develop components where no tool currently exists but where it is required.

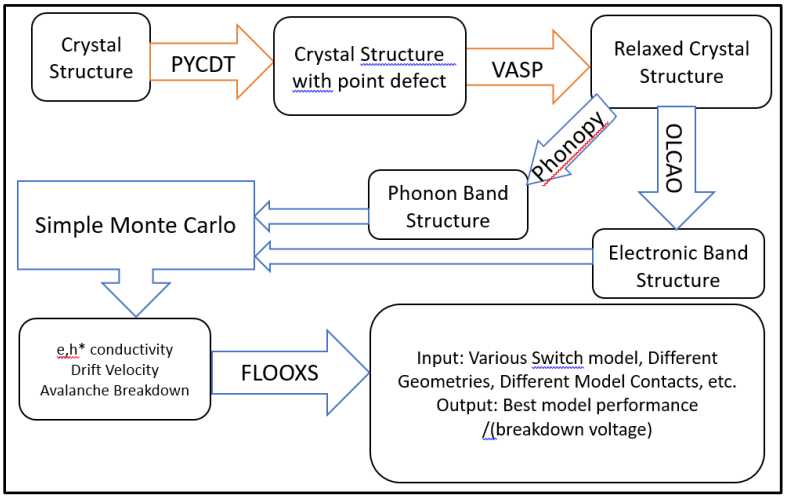


***Figure 1**: Basic outline of code and data tool chain to be used to produce engineering predictors.*

7. *High Power Ultrafast Switching Fundamentals, Materials and Figure of Merit*

To quantitatively evaluate the properties of semiconducting/semi-insulating materials and device topologies in the context of high power, fast-rise, high PRF capable switching to implement optimal source driver for HPM generation.

8. *GaN:C Photoconductive Solid-state Switches (PCSS)*

The purpose of the GaN:C PCSS project is to characterize and evaluate the performance and cost effectiveness of using GaN:C switches in pulsed power and HPM applications.

Summary of Progress:

1. *Positive Feedback NLTL Based Soliton Generator*

We constructed a compact 16-section NLTL from reverse-biased 1200 V rated Schottky diodes featuring nonlinear capacitance, and 100 nH fixed inductors. An LDMOS (BLF188XR) based power amplifier (PA) was constructed with suitable matching networks to match the impedance of the NLTL and to sustain the generated RF signal in the NLTL by compensating for the signal attenuation. Broadband RF transformers with type-61 (NiZn) ferrite toroid core were built for the input and output matching sections of the PA. A high voltage (650 V) compact pulse generator was constructed from 650 V rated GaN FETs (TPH3206PSB) made by Transphorm and an isolated universal half-bridge gate driver (UCC21520) from Texas Instruments. The rationale for fabricating this high voltage pulse generator was to replace the commercially available bulky pulse generator with this GaN FET based compact system. We obtained pulses with rise and fall times close to 20 ns and minimum width at full width at half maximum (FWHM) close to 100 ns using the fabricated pulse generator prototype. An external trapezoidal pulse

with 250 mV amplitude (peak-peak), 50 ns width, and rise and fall times of 8.9 ns generated by a function generator was used as the input pulse to the in-house pulse generator. A 50 V DC power supply was used at the FET side of the pulse generator, and the amplified output pulse (peak amplitude [40 V], and a width close to 200 ns, and rise and fall times close to 20 ns) generated from the pulse generator was applied to the NLTL. The output of the PA was connected to the NLTL, and the output of the NLTL was connected to the input of the PA, thereby forming a closed-loop configuration. As shown in Figure 2, continuous RF signals were observed across a 50 Ω resistive load connected to the 11th section of the NLTL.

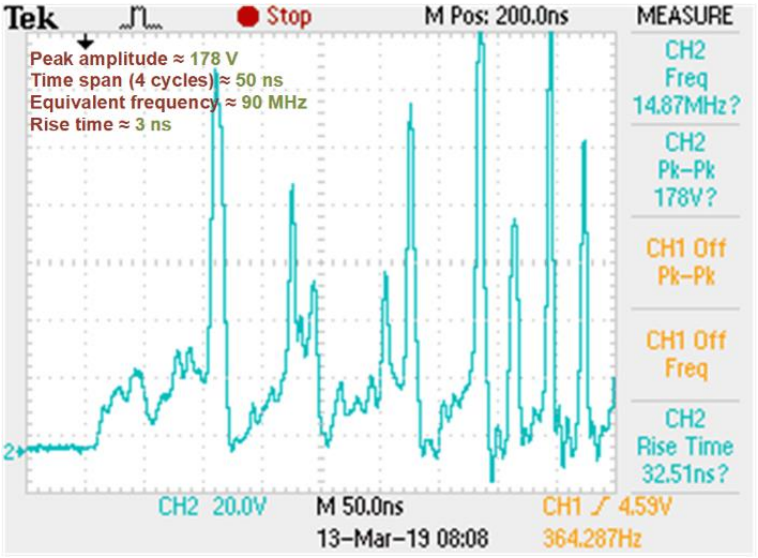


Figure 2: *Output across the 11th section of the 1200 V rated Schottky diode based NLTL coupled with UCC21520 based in-house pulse generator (V_{HVLINK}= 35 V, V_{DD} = 25 V, f = 2 MHz).*

The peak amplitude of the RF signal was about 178 V with a width and rise time close to 6 ns at full width at half maximum (FWHM) and 2 ns respectively. The corresponding peak power of the output RF pulse was about 2.1 kW across the 50 Ω resistive load. The experimental setup is shown in Figure 3.

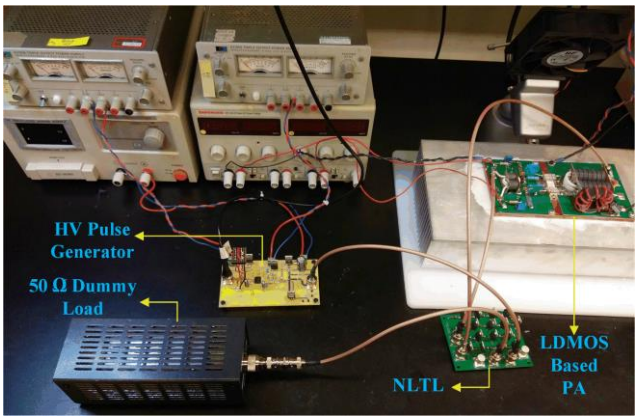


***Figure 3**: Experimental setup of an NLTL-PA closed loop configuration.*

2. *Development of PCSS Power Conditioning Circuit*

We have tested different techniques to charge a transmission line connected to a PCSS. A MOSFET with low input capacitance and an IGBT have been alternatively used as the charge controller of the transmission line. Both series and shunt configurations of the solid-state switches have been interchangeably used to evaluate their impact on the charging and discharging profiles. The solid-state switch-based charging method was able to reduce the power loss across the PCSS compared to the traditional charging methods e.g., direct DC charging, low-pass filter based charging. At an input voltage of 40 V and a repetition frequency of 2 kHz, the energy loss across the PCSS over a full cycle has been reduced from 101 mJ (direct DC charging) to 18 mJ (MOSFET based charging). However, high *di/dt* occurring from the rapid switching of the PCSS (<10 ns) interacts with the stray inductance of the circuit and causes ringing in the transmission line. The ringing in the transmission line results in an unintended secondary pulse at the output. To minimize this undesirable effect, we have developed a commercial 14 kV rated Si HV switch-based power conditioning circuit connected in series with the PCSS. We have evaluated the board by triggering the PCSS at a supply voltage up to 2 kV and at a repetition frequency of 2 kHz. Using this board, we have been able to generate output pulses with a peak amplitude close to the theoretical value (half of the supply voltage) and minimal ringing in the charging transmission line after PCSS triggering. The experimental result at a supply voltage of 1 kV and at a repetition frequency of 1 kHz is shown in Figure 4.

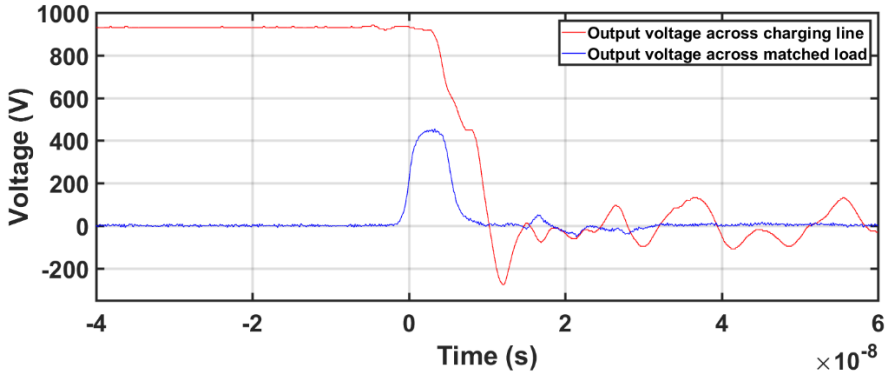


Figure 4: *Experimental result using a power conditioning board for a supply voltage of 1000 V, a repetition frequency of 1 kHz.*

We have tested the board using both positive and negative power supply. In both cases, we have obtained expected results, which confirmed that the board is suitable for different configurations of the transmission line. Using the power conditioning board, we were able to further reduce the energy loss across the PCSS to a value of 9.5 mJ. We conducted experiments using the board at a repetition frequency of 50 kHz up to a supply voltage of 2 kV. At 50 kHz, the HV Si switch operates in a burst mode to minimize excessive switching loss and protect the switch from physical damage due to thermal stress. We have been able to obtain up to 28 output pulses in a single burst at a repetition frequency of 50 kHz at a voltage up to 2 kV. The experimental result (supply voltage 700 V, repetition frequency 50 kHz) is shown in Figure 5.

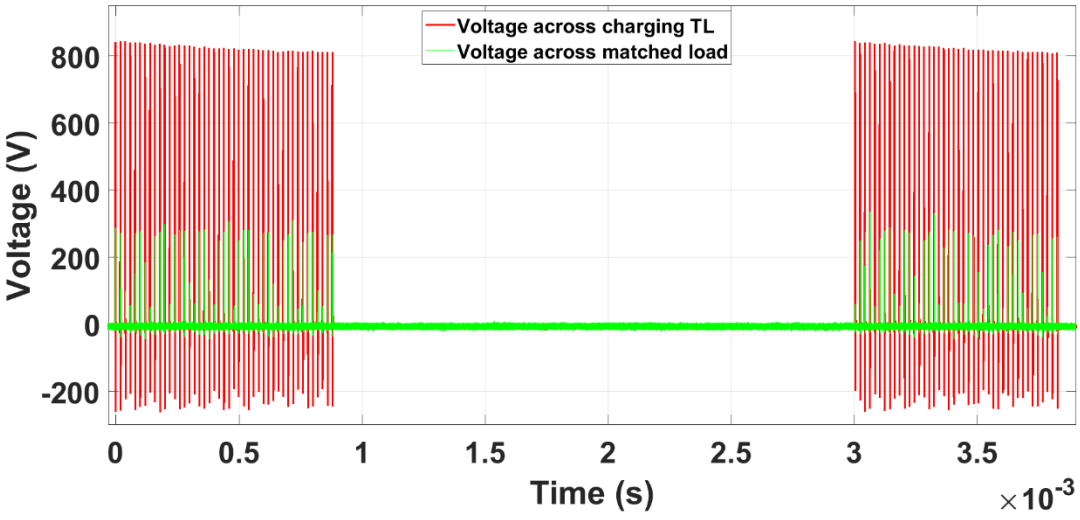


Figure 5: *Experimental results using HV switch for a supply voltage of 700 V at a repetition frequency of 50 kHz (zoomed out).*

At a voltage level close to 2 kV, the EMI induced from the rapid triggering of the PCSS is significant. We have constructed a Faraday cage from copper foil and wrapped it around the power conditioning board to prevent malfunctioning caused by the EMI.

3. *Trade Space Analysis of a Phased Array of Electrically Small Antennas.*

Element Design

Owing to their simple design, light weight, small size and tractable performance, coaxially fed microstrip patch antennas have been considered for the array element design. Contrary to common perception [1], it is possible to obtain >30% 2:1 VSWR bandwidth by strategically placing the probe at 2/3rd distance along the diagonal of a rectangular patch as shown in Figure 6.

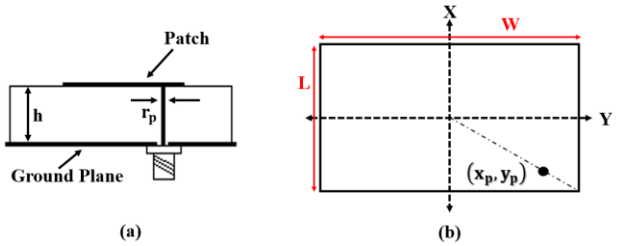


Figure 6: (a) Side view and (b) Top view of the designed coaxial probe fed microstrip patch antenna.

However, in UHF range, the 30% 2:1 VSWR bandwidth obtained using a single patch translates to be around 300 MHz. Hence, to cover the entire frequency range from 400 MHz to 1200 MHz, three separate antennas have been designed with center frequencies at 0.6 GHz, 0.8 GHz and 1 GHz. This is illustrated in figure 7.

Element Optimization

A new multi-parameter element optimization technique, also known as the D/Q method [2], is currently being used for the performance optimization of the antennas. Here D is the Directivity (far field parameter) and Q is the Quality Factor (near field parameter). Using this technique it is possible to optimize both the far field as well as the near field parameters simultaneously. A comparison between the performance optimization of the

designed antennas using the D/Q method and the well-known Characteristic Mode Analysis technique will be carried out in the future.

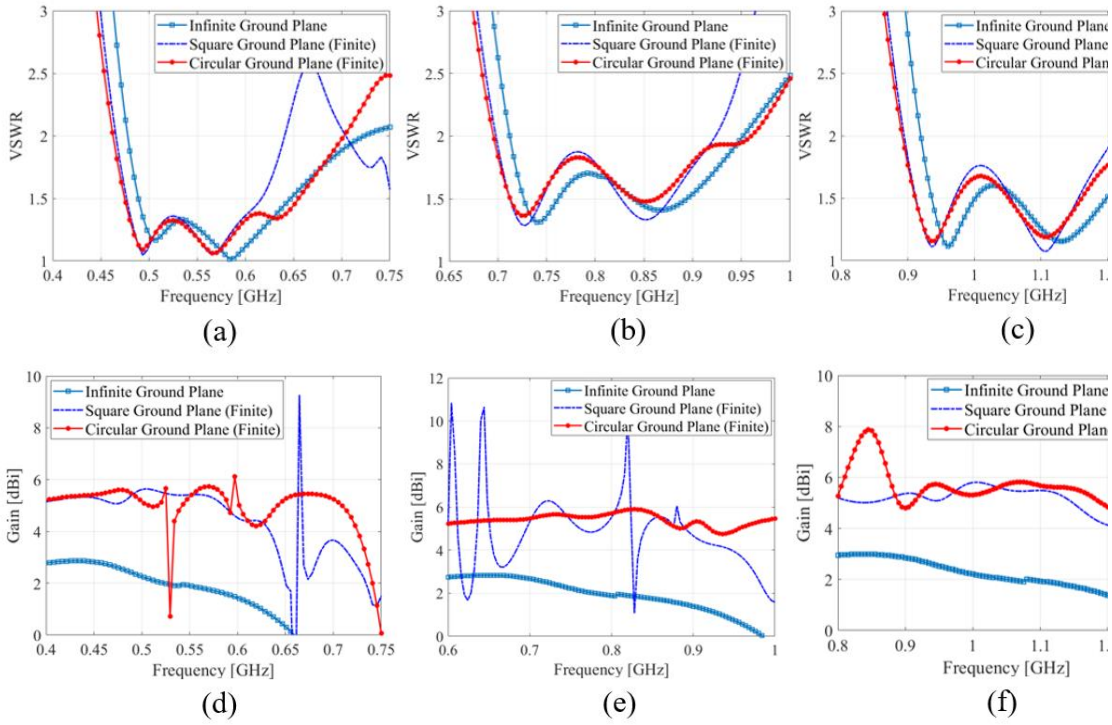


Figure 7: VSWR of (a) Antenna 1, (b) Antenna 2, (c) Antenna 3 and Gain of (d) Antenna 1, (e) Antenna 2, (f) Antenna 3 for different ground plane shapes.

Array Trade Space Analysis

The main aim of the phased array design is to achieve the desired power density at a distance of 1 km with $\pm 45°$ scan. The array power density, $S(\theta, \phi)$, can be related to the total realized gain $G^R(\theta, \phi)$ at a distance R as [3]:

$$S(\theta, \phi) = \frac{1}{4\pi} \frac{P_{in}}{R^2} G^R(\theta, \phi) \qquad (1)$$

Where P_{in} is the total input peak power, the far field power density at a certain distance can be controlled by either the input power P_{in} or the array realized gain $G^R(\theta, \phi)$.

Figure 8 shows the input peak power and the total array gain required to obtain the desired power density at a distance of 1 km. It can be noted that a high gain array requires less input peak power which not only helps to reduce power consumption but also takes care of the power handling capacities of the individual array elements.

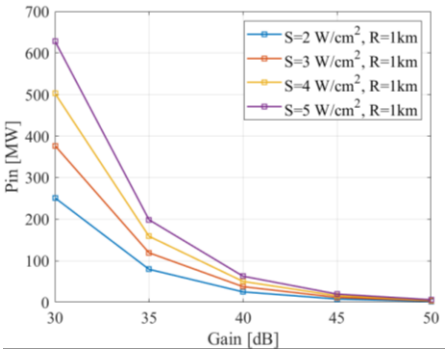


***Figure 8:**. Input power as a function of gain for selected antenna designs.*

(a) Investigations into Sidelobe Level (SLL) Reduction: An array designed for directed applications should have low SLL and narrow beamwidth. Two SLL reduction techniques have been investigated, viz. Non-uniform amplitude distribution and Non-Uniform inter-element spacing. Figure 9 shows the effect of different sidelobe level reduction techniques on a 25 element linear array. Among the different amplitude distributions, Bickmore-Spellmire leads to the maximum sidelobe level reduction and hence proves to be useful for high power applications due to reduced wide-angle radiations. Also, for uniform distribution, ≈ 7.5 dB of SLL reduction has been achieved with non-uniform inter-element spacing.

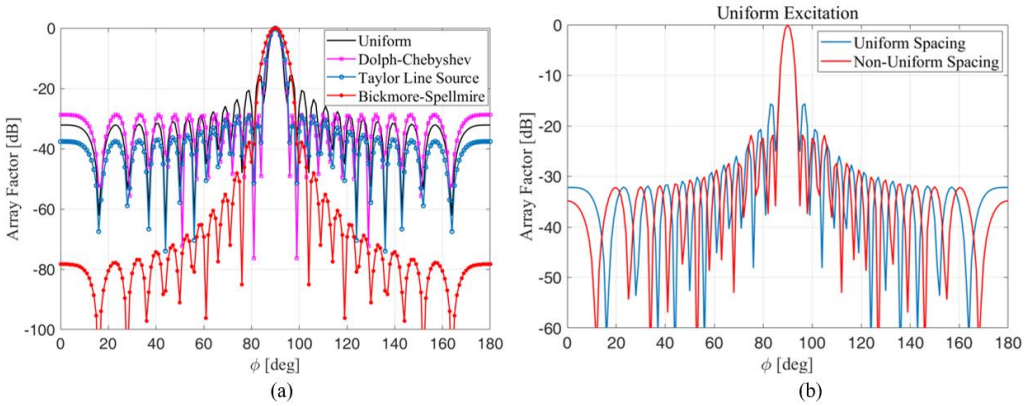


***Figure 9**: Reduction of sidelobe levels using (a) Non-uniform amplitude distribution and (b) Non-uniform element spacing.*

(b) Calculation of Directivity: Full-wave simulations of large arrays on finite ground planes using commercially available EM solvers (such as FEKO, HFSS, etc.) are computational bottlenecks. Hence, a closed form expression to calculate the directivity has been derived as given below:

$$D = \frac{\left|\sum_{n=1}^{N}\sum_{m=1}^{N} w_m^* w_n e^{jkd(n-m)[\cos\phi-\cos\phi_s]}\right|^2}{\sum_{n=1}^{N}\sum_{m=1}^{N} w_n w_m^* e^{jkd(n-m)\cos\phi_s} J_0[kd(n-m)]} \qquad (2)$$

The results obtained using eq. (2) do not involve the effect of mutual coupling or the element pattern but helps to quickly anticipate the full wave results. Compared to the closed form directivity expression given by R. C. Hansen [4], the derived expression shows better agreement with the full wave simulated results obtained using FEKO.

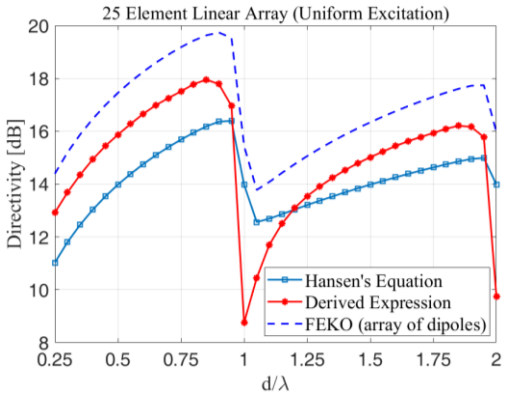


***Figure 10**: Comparison of the derived directivity with existing and FEKO generated results.*

Reference:

[1] R. Garg, P. Bhartia, I. Bahl, and A. Ittipibon, Microstrip Antenna Design Handbook, Boston, USA: Artech House, 2001.

[2] M. Gustafsson, *et al*, "Physical limitations on antennas of arbitrary shape," *Proceedings of the Royal Society A: Mathematical, Physical and Engineering Sciences*, vol. 463, issue 2086, 2007, pp. 2589-2607.

[3] R. J. Mailloux, *Phased Array Antenna Handbook,* 3rd ed. Boston, USA: Artech House, 2018.

[4] R. C. Hansen, *Phased Array Antennas,* USA: John Wiley & Sons, 1998.

4. UAV Asset Development and Experimental Design

Over the past 12 months the cUAV grant team has developed several different UAV assets for both indoor and outdoor testing. The multirotor platforms developed are: 1) DJI Phantom 4 Pro (V1.0 & V2.0), 2) Pixhawk 2.1 (Cube) PX4 quadcopter, Pixhawk 2.1 (Cube) hexcopter, and Navio quadcopter (Figure 11). These systems all collect and store onboard diagnostics information including inertial measurement unit sensors, GPS, input commands (R/C input), motor commands, and attitude state estimates.

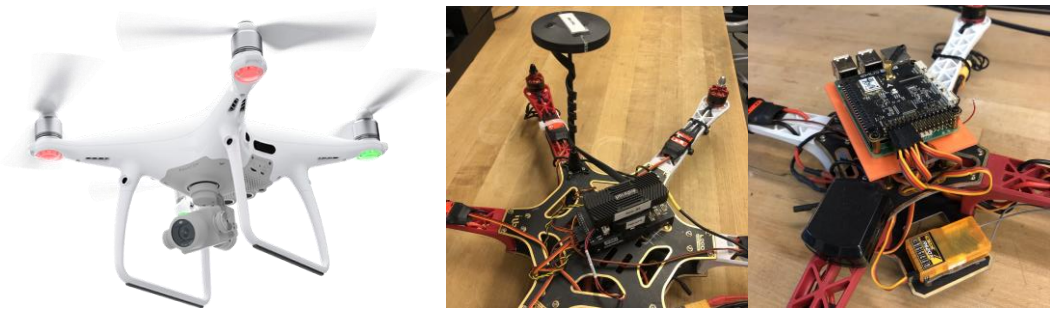


***Figure 11**: DJI Phantom 4 (left), Cube Hexcopter (center), Navio Quadcopter (right).*

In addition to the multirotor platforms integrated into the UMKC diagnostics space, a fixed-wing platform was developed utilizing the same internal hardware as the multirotor. The fixed-wing (Skywalker X8) shown in Figure 12 also incorporates the Cube flight control system.



***Figure 12:** Skywalker X8 Fixed-Wing UAV.*

To increase the diagnostic capability of these platforms, particularly in outdoor testing, a self-contained RF measurement system was developed and tested. The system utilizes a dual polarization UWB antenna and RMS detector connected to a Raspberry Pi Zero coupled with a small IMU (Figure 13). The system was calibrated within the GTEM, and provides some indication of source illumination but does not provide accurate power estimates across the frequency ranges of interest within the program.

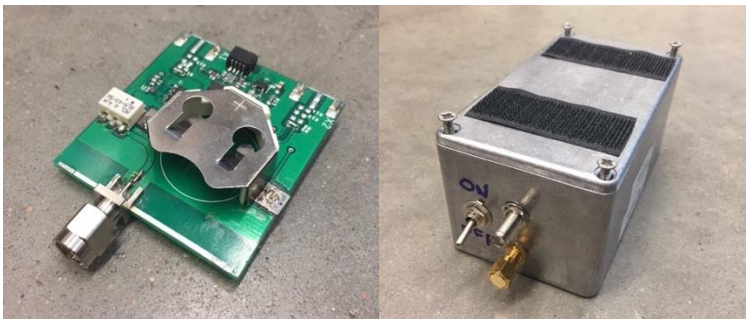


Figure 13: *UMKC-Developed RF Sensor.*

5. *RF Coupling Modeling and Experimental Measurements*

To be reported in contract report for N00014-18-C-1017

6. *GaN:C Theoretical Simulations*

As suggested at the end of last year, we achieved the ability to get the FLOOXS program for technical computer aided design to work in a production environment. In particular, we completed a review of the FLOOXS simple Alagator language tutorial, the complex system language tutorial, a reading of the Alagator language reference, and Training Course PowerPoint presentations. There are a number of differences between the documentation given in those resources and the 2011 implementation of the FLOOXS code. We now have finer-grained familiarity with the basic trial FLOOXS scripts that come with the code and were delivered to use through NRL collaborators. We are able to run and debug pre-made demonstration models of resistors, P- and N-MOS, etc. We produced elementary 1-D and 2-D models of electronic components that include variable concentrations of electrons and holes in doped regions (see Figure 40 example of a 2-D silicon PN diode with computation and subsequent fitting of the I-V curve).

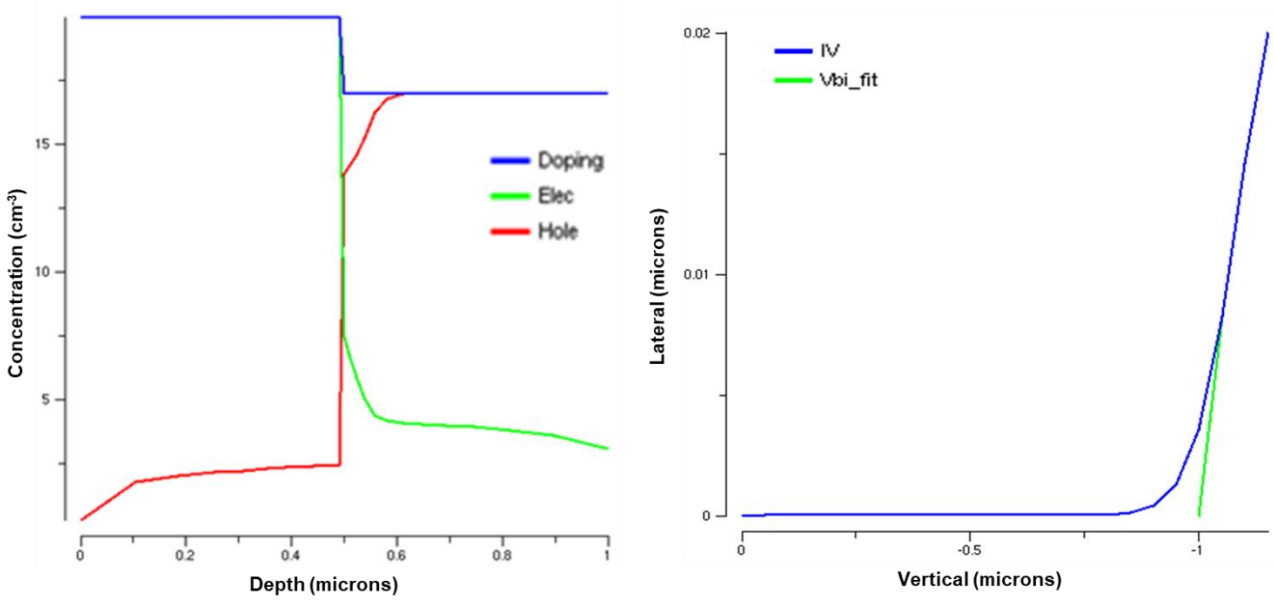


Figure 40: *Two dimensional silicon PN diode: LEFT: Blue – Dopant profile; Green – Electron concentration; Red – Hole concentration. RIGHT: Blue - I-V curve; Green – Linearly extrapolated fit to the I-V curve to obtain built-in voltage at the x-intercept.*

We created 2-D models (Figure 40) of the target PCSS with metal contacts, interfaces, and all regions defined. This will become the basis for future work once we have understood and feel confident with our abilities to simulate more well-documented Si-based systems. The exact nature of the material regions will need to be defined in future work, but this will serve as the skeleton for that effort.

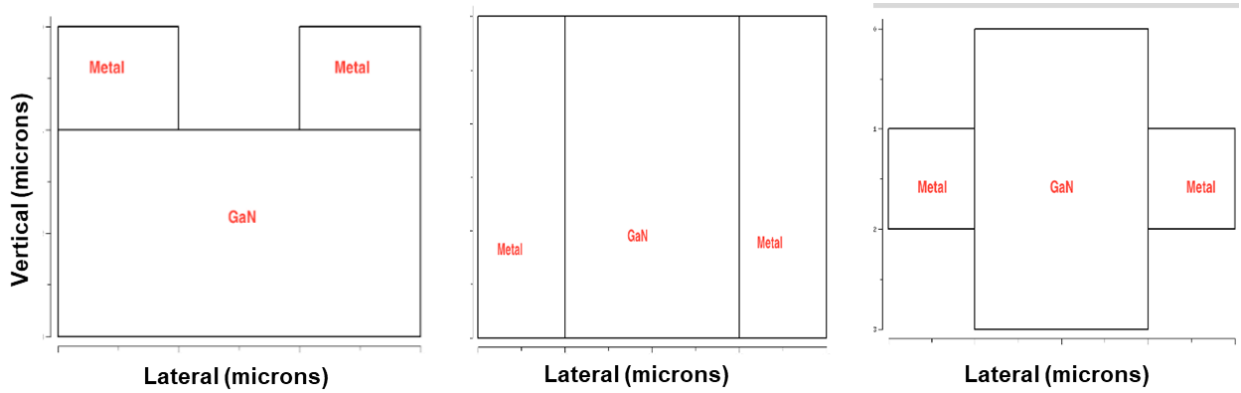


Figure 41: *Test geometries for device configurations created without relying on geometries created by others. This demonstrates the ability to specify specific desired geometries and types of contact interfaces of our own creation.*

It is necessary to establish definitions within the FLOOXS script for how the interfaces should be treated. For example, determining what width, depth, and mesh density is needed for the contact regions so that the continuity equations, electric potentials, etc. will act across the interfaces between materials as a real system should operate. This process is still being completed.

We plan to add more programs to the developing tool chain and over the next year we will seek out and evaluate additional full-band Monte Carlo simulators that may be used to link *ab initio* electronic band and phonon band structures to FLOOXS simulations. The first code we will evaluate is MOCA from the University of Illinois.

As with the last year, the longer term critical task is to test our ability to direct FLOOXS to correctly model the simple electronic systems we have created so far when fundamental parameters are modified according to known empirical trends). That process is still ongoing but is moving closer to completion. Several Si-based simulations have been demonstrated but some of the underlying aspects (as mentioned above) still need refinement before we will be able to integrate with computed ab initio input data, hence the investment in time proposed for seeking out Monte Carlo codes.

In particular in the past year we have found and started working with a 1D code called Simple Monte Carlo which has been shown to work successfully for Si, GaAs, and InGaP. We are still mastering this software and will begin developing the necessary input files for GaN during the upcoming year. Based upon preliminary results, it appears to be a promising approach to connect our *ab initio* calculations to the FLOOX TCAD simulations.

The Simple Monte Carlo (SMC) program can compute material properties such as electron/hole drift velocity and ionization coefficients relevant for avalanche breakdown. In the past year we fixed a few small operational (machine dependent) bugs that the program had in it. The bugs had no impact on computed results but they prevented the code from working on the machines that were accessible to us. These issues have been resolved now. We ran the program to reproduce Si and other material results as published in the paper of record for the method (Zhou X, Ng JS, Tan CH, “A simple Monte Carlo model for prediction of avalanche multiplication process in Silicon” J Inst, 2012 7(08), P08006–P08006 (2012). Available from: https://doi.org/10.1088/1748-0221/7/08/P08006). Preliminary results are shown in Figure 42 below.

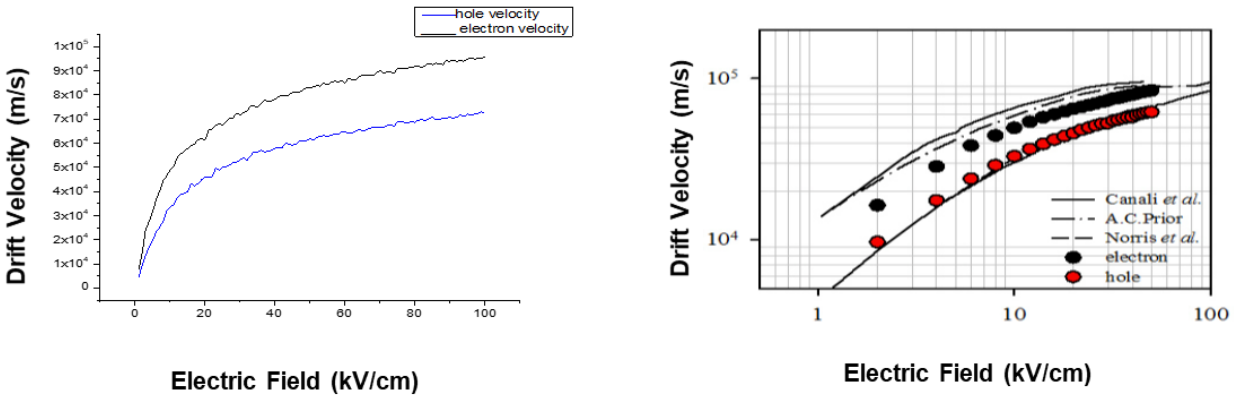


Figure 42: *Newly computed (left) vs. previously published Si drift velocities from SMC (right). Publication source is the same as that listed in the text.*

We also ran a basic simulation for GaN where some parameters were obtained from literature and others were guessed at or adapted from other materials. Results are shown in Figure 42.

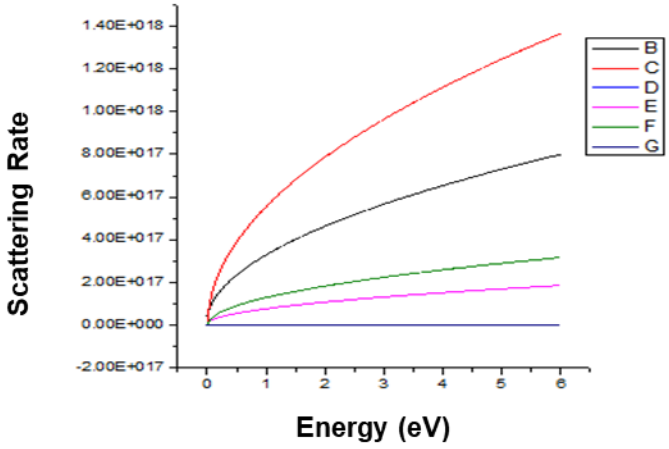


Figure 43: *Scattering rates computed using SMC for different electric field strengths B-G ranging from 0 to 10000 kV/cm.*

Finally, as shown in Figure 44, we are nearing establishment of an understanding of all the computational concepts and explicit program codes that are needed in the long tool chain for computing high level engineering quantities (breakdown voltages, thermal conductivities, macroscopic optical response) from basic *ab initio* methods.

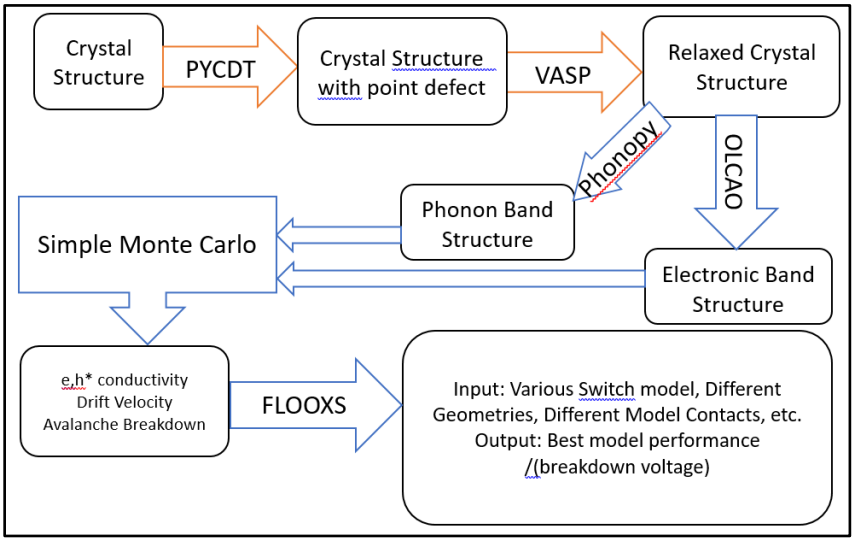


Figure 44: *Basic outline of code and data to be used to produce engineering predictors*.

Additional activity to report over the past year is the further development of our tool-chain in concert with discussion with Jay Eifler and his work on Silvaco TCAD. We identified appropriate areas to focus our efforts. Of key interest is the determination of certain material dependent parameters for Monte Carlo simulation. In the Simple Monte Carlo code the parameters needed are given in Table 1. The list of parameters needed in Silvaco TCAD is being compared to this list.

Table 1: *Parameters and data required by SMC for GaN.*

Our capability / Parameters	Can	Cannot
Phonon energy (meV)	Yes (Phonopy)	
Threshold energy Eth (eV)	Full band Monte Carlo (FBMC)	----------
Impact ionization rate coefficient C_{ii} (s^{-1})	Simple Monte Carlo Device Simulator (SMCS)	Required Full Band Monte Carlo
Softness factor γ	Required Experiment	----------
Effective mass m ∗ (kg)	Yes (VASP), OLCAO	
Free path length λ (A)	Yes (Phonopy-vasp)	
X-ray spectroscopy	Possible	
XANES/ELNES calculation	Yes (OLCAO)	

The PyCDT and PyMatGen codes were installed and made operational on Lewis. The PyCDT code is crucial for helping establish working models of carbon doped GaN. We do not yet know where in the lattice the carbon goes and we are planning to predict sites using PyCDT. This is ongoing. We have also spent time this past year identifying user

facilities that can assist with XANES or ELNES based core-level spectral measurements of samples so that we could compare modeled results with experimental data to confirm any predictions from the OLCAO + PyCDT combination.

The student was able to start using VASP+PyCDT to produce a range of GaN:C defect models that are more sophisticated than those produced previously. He tested possible combinations of substitutions, interstitials, different charge states, and vacancies in standard hexagonal but also in the similar energy cubic GaN.

For many of the models the student was able to compute core level spectra (ELNES spectra). The student also discussed with other students on the team to evaluate the suitability of existing samples for use in ELNES experimental measurements that could be conducted by a collaborator. The student now has a much better understanding of how to compute accurate spectra.

This activity will establish the model structures that serve as the base foundation of the tool chain shown in Figure 5. In the coming year, now that the tool chain has been mostly established we will endeavor to begin executing it.

7. *High Power Ultrafast Switching Fundamentals, Materials and Figure of Merit*

In the previous year, semiconducting/semi-insulating materials with photo- and electro-stimulated device topologies were studied to evaluate high-power, ultra-fast transient capabilities for source driver implementation alongside UMKC's active efforts with Si-DSRDs, Si-, SiC- and GaN:C- PCSS. A two-stage evaluation was implemented.

(1) Evaluate device topologies based on their transient response, jitter, pulse repetition rate (PRF), and power density for both modes of stimulation along with circuit level implementation.
(2) Evaluate semiconducting/semi-insulating materials optimal for the selected topologies by extending and tailoring figures of merit in prior art to specific topologies and application space.

The metrics required for each device technology to be an optimal source driver were laid out and carrier drift limiting factors (joule heating, carrier scattering) at high fields and current densities were studied. The critical phenomena for switches—both for general and optically actuated considered in this study are provided in Table 2.

Table 2: *Critical phenomena affecting properties of high power devices at a micro and macro levels.*

General Switches		PCSS-Specific	
Macro parameters	**Micro parameters**	**Macro parameters**	**Micro parameters**
-Rise-time	- Generation	-Incident energy	-Absorptivity
-Voltage hold-off	- Recombination	-Contact Pattern	-Direct/Indirect Abs.
-Recovery	-Defect States	-AR coatings	-State transitions
-Conductance	-Scattering		
-Impedance	-Dopants		
-Dark current	-Carrier transport		
-Contacts	-Drift and diffusion		
-Geometry	-Injection		

From the evaluation of device topologies, Gunn diodes, HEMTs, DSRDs, and linear mode PCSS were selected for further evaluation. From these, PCSS were chosen for an initial evaluation due to their relatively simple operation and our wealth of expertise with the technology.

Because device performance and losses are highly dependent on the circuits in which they are used, we selected a representative model of a class-E amplifier for initial modeling. In the circuit shown in Figure 44, a switch was driven by a 1.2-kV pulses with a 50% duty cycle. The rise and fall time of the pulse was 1-ns, and a constant 3-kV bias was applied to the circuit. In the on-state, the switch resistance (voltage controlled) was set to decrease to micro-Ohms. Because the class-E's zero voltage switching (ZVS) minimizes the power losses during turn-on, turn-off losses in the switch were readily isolated and evaluated. This behavior can be seen in Figure 45 in which the excitation pulse rise (green) initiates when the switch voltage reaches (blue) zero volts. However, due to the arbitrary voltage-control of this of this model, our focus shifted to generating a general FoM for high power switches.

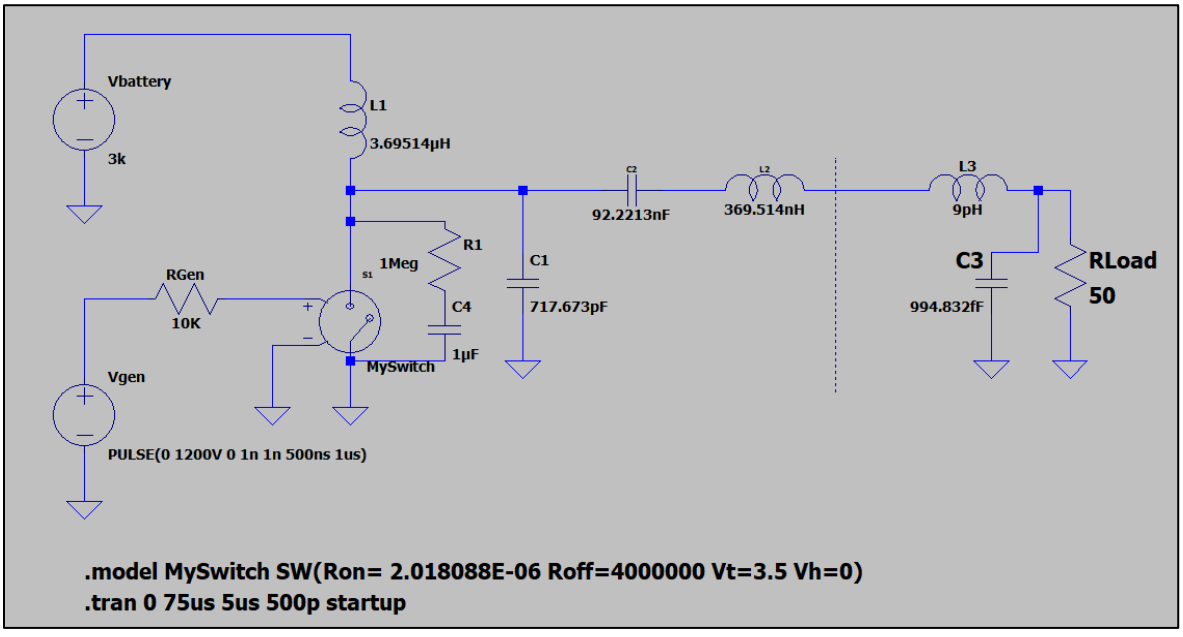


Figure 44: *Modelled class E amplifier with 50% duty ratio, tuned at 10 MHz.*

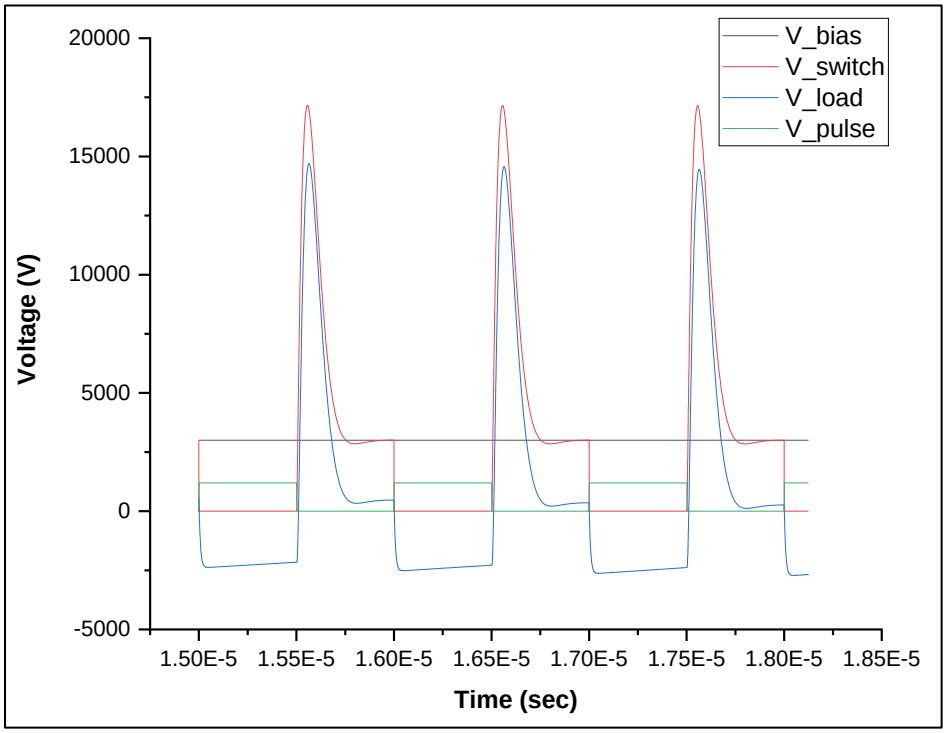


Figure 45. *The switching response of the class E amplifier; excitation pulse (green) of 50% duty cycle and the switch voltage (blue) waveform across the load.*

Focusing on a more applicable FoM, we reviewed efforts by Baliga, Johnson, Keyes, Kim, Shigekane, Wang, Huang and Shenai [1], and hierarchically classified the materials for electrically-actuated devices. A major issue with existing figures of merit is their basis on electrically-actuated devices; no such FoM existed for optically-actuated devices. To resolve this, we narrowed the power dissipation model to the on-off transition and on state—the switching state being of particular importance due losses peaking while switching under load, further exacerbated at high power and PRF—and derived a new FoM for linear PCSS, based on photo-generation and recombination.

Starting with Nunnally's equations for carrier generation and device resistance, we created MATLAB script considering the cases of Si, SiC and GaN, while varying their geometry and incident light intensity. Materials 500-μm thick were modeled when illuminated with a optical pulse energy of 600-mJ. All material recombination times were set to 1-μs, and the resulting carrier generation and resistance are shown in Figure 46. The resistance of each switch declined with carrier generation, but the 1-μs recombination time was not representative of SiC and GaN, as their recombination times are generally one-to-two orders of magnitude less. However, this represented an initial application of Nunnally's equations and laid the foundation for generating a PCSS-specific FoM.

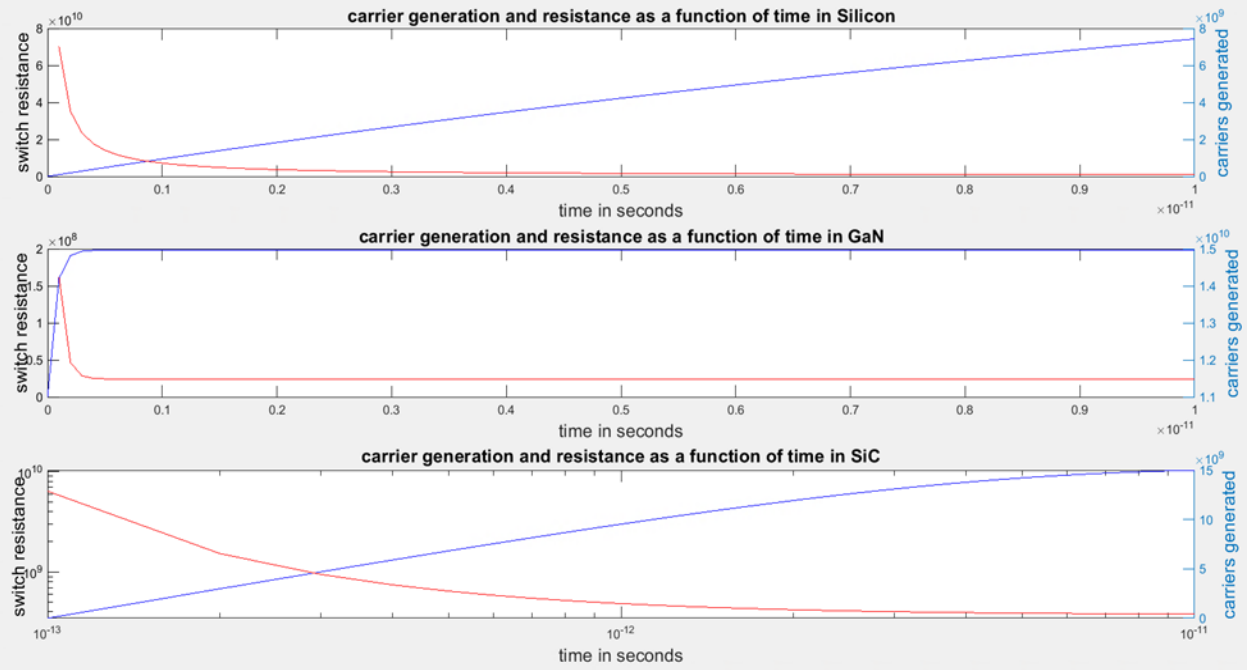


Figure 46: *Carrier generation (blue) and switch resistance (red) as a function of time for Si, GaN and SiC.*

Expanding on the carrier generation model, parameters from Table A1 were incorporated into a power loss equation including, but not limited to: breakdown field, saturation velocity, carrier- generation, transport and recombination, e-h mobility, geometry, incident energy, and thermal conductivity. During the on-state, the derived power loss is given by Equation 1.

$$P_{on} = \frac{E_c^2 L^4 h\vartheta}{(R_{on}+R_{Load})^2 q\mu_T t_\tau I_0} \qquad \text{Eq. (1)}$$

However, because the resistance is time dependent during the switching state, calculating the corresponding power losses is more complex, requiring the time-dependent device resistance (R_{device}), current (i), and net carriers generated (n), given by Equations 2, 3, and 4, respectively.

$$R_{device}(t) = \frac{L^2\, h\upsilon}{qIT_{net}\mu_T(1-e^{-\frac{t}{T_{net}}})} \qquad \text{Eq. (2)}$$

$$i(t) = \frac{E_c L dwq\, \mu_T n(t)}{R_L dwq\mu_T n(t)+L} \qquad \text{Eq. (3)}$$

$$n(t) = \frac{I}{h\upsilon\, dwL} T_{net} * [1 - e^{-\frac{t}{T_{net}}}] \qquad \text{Eq. (4)}$$

Where:

E_c – critical field
L – Thickness of the device (switch gap)
d,w – length and width of the device
hu – Energy carried in each photon
*$I – I_0$*exp (-2.77(t/T_{FWHM})^2)*

I_0 – peak optical intensity
R_{on} – On-state resistance
R_{Load} – load resistance
q – Charge of the electron
μ_T – Mobility of holes and electrons
t_r – inherent device recombination time
t_T – transit time of carriers
T_{net} – $t_r * t_T / (t_r + t_T)$

The incident optical pulse was modeled by a temporal Gaussian with a FWHM of 2-ns and wavelength equivalent to the material's bandgap. The resulting on-state losses (Eq. 1) for Si are shown in Figure 47 as a function of optical energy and device length (i.e., thickness). Those for SiC and GaN, were also calculated but are not included in this report. These plots show the on-state power loss accounting for mobility of the generated carriers and the recombination time into account as shown in Equation (1). The recombination time used was held constant for all materials. By comparing the plots for Si, GaN and SiC, we notice SiC has relatively higher on-state losses.

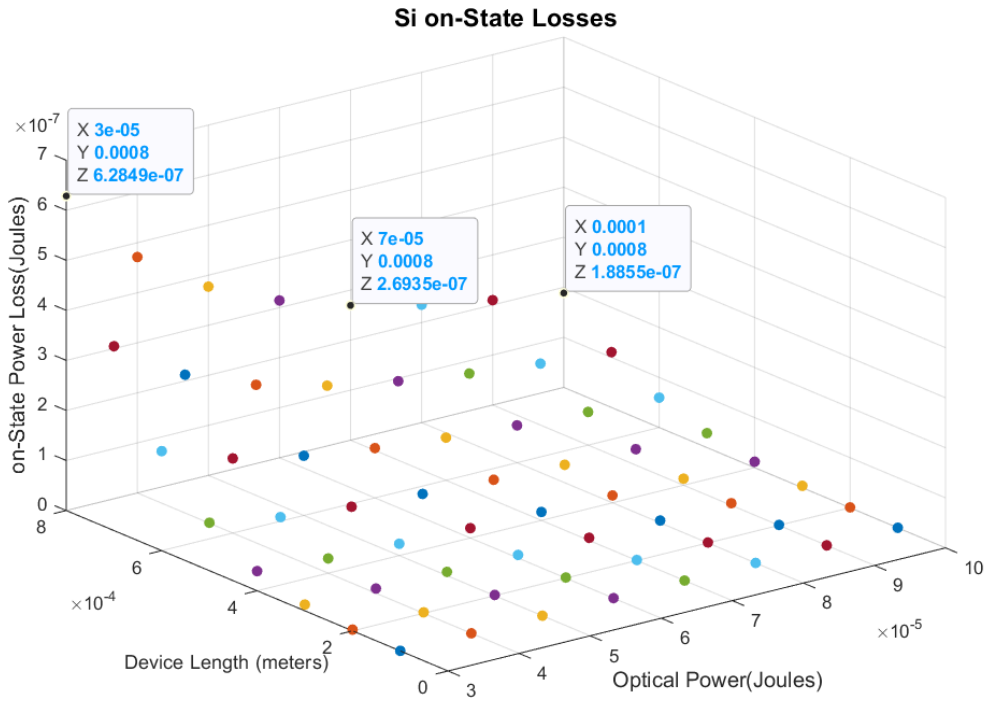


Figure 47: *Si on-state losses as a function of path length and optical power. GaN and SiC losses were calculated, but omitted from this report.*

For switching transition, we derived the power dissipation omitting size approximations as shown in equations (6) and (7), while equation (5) shows the time varying device resistance. The power dissipated in the device during these stages of operation adds heat to the lattice and drives device damage at high peak powers and repetition rates. Equations (6) and (7) will be quantitatively analyzed with time-varying Gaussian laser profiles, geometric variations, recombination, and dopant dependent mobility

$$R_{device}(t) = \frac{\frac{E_\lambda L}{w}}{q\mu_T(t)(1-r)I_0T_{net}[1-e^{-\frac{t}{Tnet}}]} \quad \text{Eq. (5)}$$

$$P_{turn\text{-}on} = \frac{E_c^2L^3}{R_{Load}I_0}\int_{t_1}^{t_2} \frac{\left(1-exp\left(-\frac{t}{Tnet}\right)\right)}{\exp\left(-2.77\left(\frac{t}{t_p}\right)^2\right)\left[2+\frac{R_{Load}\,q\,\mu_T I0 T_{net}}{h\upsilon\ L}\right]-2R_{Load}\,q\,\mu_T I_0 T_{net}\left[\exp\left(-5.54\left(\frac{t}{t_p}\right)^2-\left(\frac{t}{T_{net}}\right)\right)\right]/(h\upsilon\ L)}\ dt \quad \text{Eq. (6)}$$

$$P_{turn\text{-}off} = I_0T_{net}q\mu_TE_c^2L^3\int_{t_3}^{t_4} \frac{\left[\exp\left(-2.77\left(\frac{t}{t_p}\right)^2-\frac{t}{T_{net}}\right)\right]}{h\upsilon L^3+2R_{Load}\,q\mu_T\,I_0T_{net}\,exp\left(-2.77\left(\frac{t}{tp}\right)^2-\frac{t}{T_{net}}\right)}\ dt \quad \text{Eq. (7)}$$

Where:

- *E_c – critical field*
- *L – Thickness of the device (switch gap)*
- *d, w – length and width of the device*
- *hv – the energy carried in each photon*
- *R_{Load} – load resistance*
- *q – Charge of the electron*
- *μ_T – mobility of holes and electrons*
- *t_r – inherent device recombination time*
- *t_T – transit time of carriers*
- *t_p – FWHM duration of the laser pulse*
- *Tnet – tr*tT/ (tr+tT)*
- *I_0 – peak optical intensity*

Considering only the power dissipation calculations, the FoM is inconclusive. For example, although SiC showed the greatest power losses, in reality this may be overcome by its higher thermal conductivity, allowing for greater dissipation of losses. Therefore, the materials' specific heat and thermal conductivities necessary for a realistic FoM.

Another caveat to this FoM arises from the demands of specific applications. While some applications require maximum power or pulse energy at low repetition rates, others require less at greater repetition rates. Thus, depending on application, power losses may not be the most critical factor in performance. To compensate for these difference, future analysis will be conducted through the lens of SWaP-C^2 to provide cost-effective, application-specific solution(s) for high power switches.

References

[1] Baliga, B J. 1989. "Power Semiconductor Device Figure of Merit." *IEEE Electron Device Letters* 10 (10): 455–57.

[2] W. C. Nunnally and R. B. Hammond, "Optoelectronic switch for pulsed power", *edited by Chi. H. Lee, Orlando, Florida: Academic Press, Inc., 1984.*

8. GaN:C Photoconductive Solid-state Switches (PCSS)

Early in the reporting year, GaN: PCSS testing was delayed due to challenges in obtaining lasers delivering 355-nm pulses with the appropriate pulse width (~1-ns) and energy (tens of µs. Previously, testing was conducted using a N_2 gas laser with a pulse width of approximately 10-ns and the GaN:C PCSS were used to trigger simple 10-ns pulse forming transmission lines—both greater than the expected recovery time of the switch. However, the use of transmission-line based PFNs resulted in a time-dependent bias on the PCSS, obscuring measurements needed for recovery time and time-dependent on-state resistance. Since then, we have (1) acquired a 1064-nm Wedge-HB laser system delivering a 1-ns pulse width and a triple harmonic generation (THG) system for converting the 1064-nm pulse to 355 nm, (2) conducted a series of characterization studies using new pulse forming networks, and (3) began a manuscript for evaluating the cost-effectiveness of GaN manufacturing for high power applications.

GaN:C PCSS switching was characterized on two different test fixtures: (1) a parallel plate transmission line, shown in Figure 48, designed for the 70-ps pulse width of the NeoLASE 1064-nm laser with the THG setup, and, (2) a more compact PCB-based pulse forming network (PFN) (Figure 49) to allow for a more compact fixture and ease in switching out circuit components.

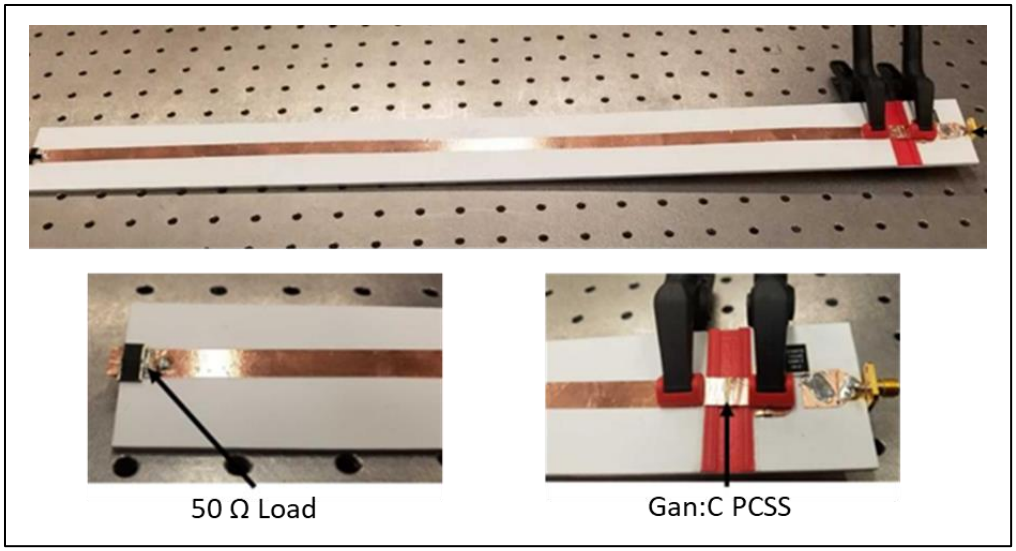


Figure 48: *Strip line transmission line fixture for GaN:C PCSS pulse testing for more accurate characterization of GaN:C PCSS recovery time.*

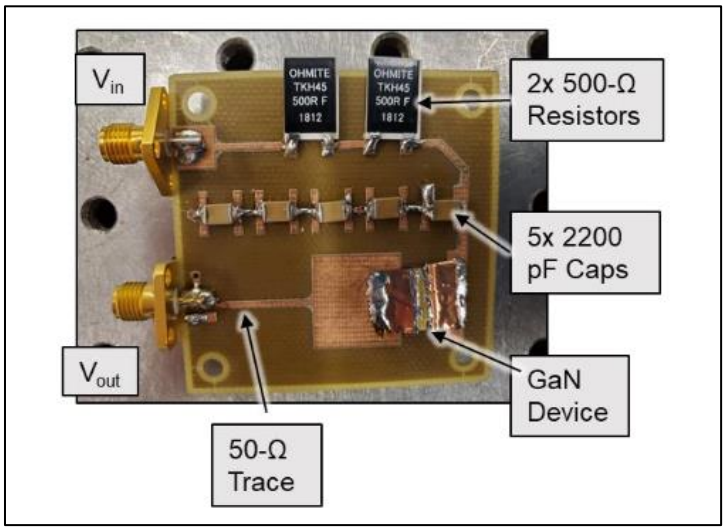


Figure 49. *PCB test fixture for GaN:C PCSS for ease of testing, switching out circuit elements and device characterization.*

Both setups allowed for the output voltage to equal the charge voltage on the line and more accurate characterization of time-dependent on-state resistance. While originally designed for the 70-ps pulse width of the NeoLASE laser, the pulse width was too short GaN:C devices were not able to be fully activated (in part due to the THG system), and continued characterization was conducted using the 1-ns pulse width Wedge-HB with the THG system.

To understand the trade-space between low on-state resistance, breakdown, and laser energy cost, we measured the on-state resistance as a function of gap length (distance between the contacts) and incident energy. Initial measurements swept through a range of charge voltage while increasing the incident laser energy. The laser energy was measured using an Ophir energy meter, but ultimately the energy was limited by the damage threshold of the THG system and beam shaping optics. The on-state resistances calculated from the output pulse voltage, charge voltage, load resistance are shown in Figure 50. However, some error exists due to inaccuracies in the charge voltage used in the calculations, but the trends extrapolated from the data hold.

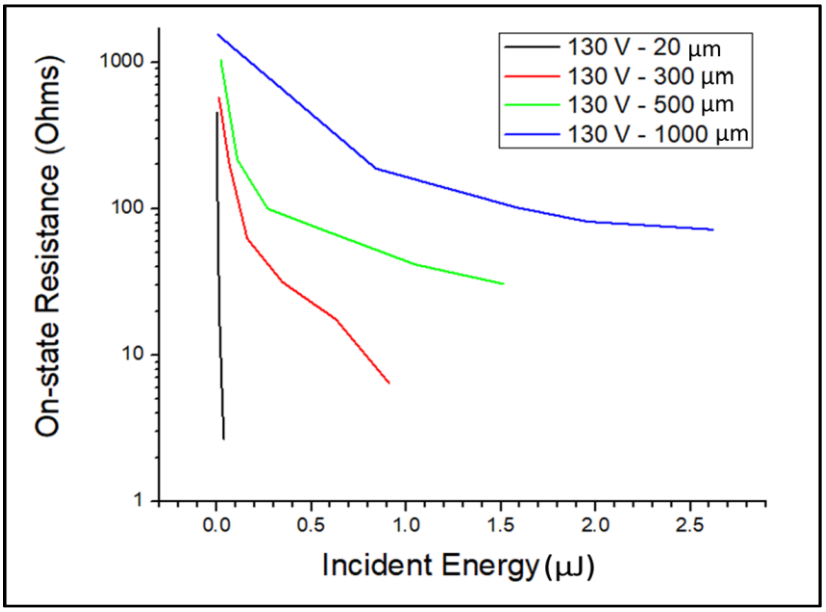


Figure 50. *On-state resistance as a function of incident energy for various gap lengths of GaN:C devices. Minimum on-state resistance was not achieved due to limited laser energy.*

As shown in Figure 50, the trend follows the expectation of larger gap lengths requiring more incident energy to reduce on-state resistance than smaller gap lengths. The plot is shown using a log y-axis to show that on-state resistance can be further minimized by using higher incident energies.

To minimize the on-state resistance, new optics were purchased and installed. To measure the incident energy, the laser pulse was expanded to an area greater than the active switch before measuring the energy density. The energy density was then multiplied by the device area to calculate the total incident energy. The error in the charge voltage was corrected by directly measuring with the oscilloscope instead of using the DC supply reading. Pulse waveforms were collected on a 500 μm GaN:C PCSS, and the peak voltage and on-state resistance were calculated, shown in Figure 51, at a charge voltage ranging from 100–800 V. At 900 V, the charge resistors failed, ending the study.

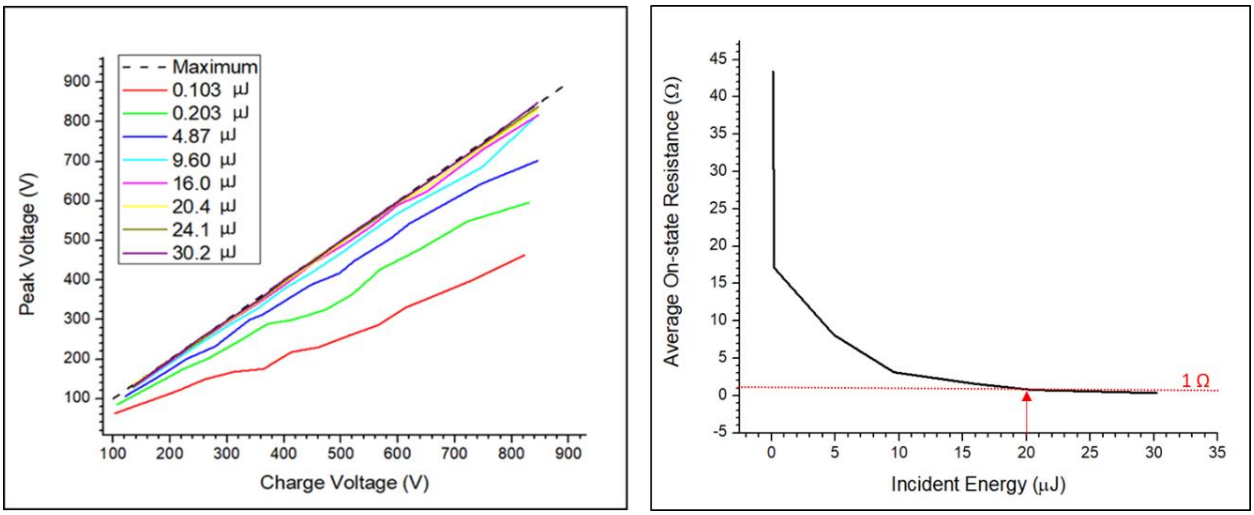


Figure 51: *(left) Peak output voltage as a function of charge voltage for different incident energies on a 500 µm GaN:C PCSS showing the approximately linear relationship between charge voltage and peak output voltage across a range of incident energies. (right) Average (over all charge voltages tested) on-state resistance as a function of incident energy for a 500 µm GaN:C PCSS with maximum output ($V_{out} \approx V_{in}$) occurring with ~20 µJ of incident energy.*

The expected relationship between incident energy and lower on-state resistances was confirmed, as shown in Figure 51 (a) and (b). The gain (V_{out}/V_{charge}) was constant over charge voltage and increased with incident energy increases to a maximum of 1 (occurring at approximately 20 µJ), indicating a switch resistance of much less than 50 Ohms (the load resistance). The linear gain lends itself for extrapolation of expected device behavior at voltages outside of those measured. Further studies are needed to determine the incident energy required for sub-Ohm on-state resistance at additional gap lengths.

To push the performance of GaN:C PCSS, a second study was conducted using 1000-µm gap length devices, encapsulated in Sylgard 184. The charge voltage range was extended from 400–1900 V, at which point failure occurred, likely due to insufficient encapsulation, as shown in Figure 52. To overcome this failure, we are revisiting the

methods for applying the Sylgard 184 to ensure complete and uniform encapsulation. Waveforms measured up to the failure are shown in Figure 53.

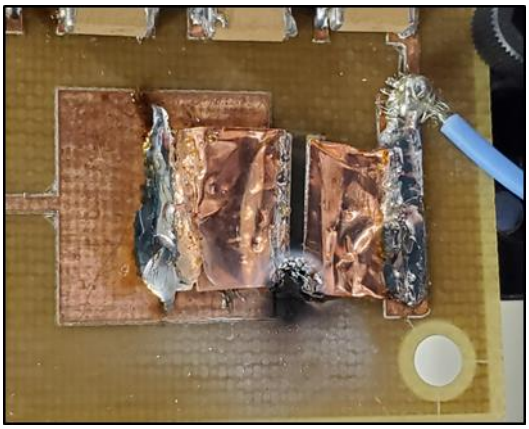


Figure 52. *Resultant damage to GaN:C device and PCB due to failure at 1900 V. Damage due to arcing between the copper tabs used for mounting and the PCB copper.*

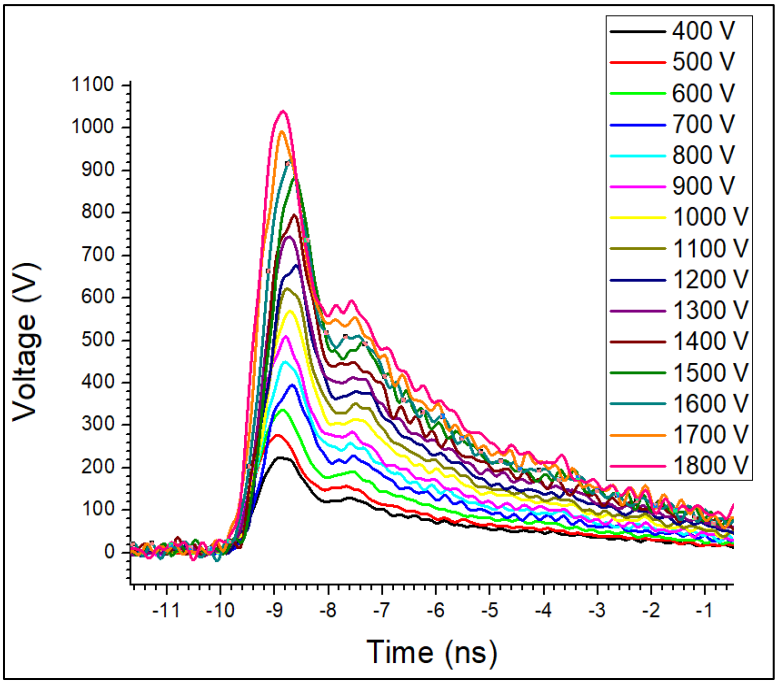


Figure 53. *Waveforms from 1000 µm gap length device using a charge voltage of 400 V - 1800 V. Failure occurred at 1900 V.*

The peak output measured at 1800 V charge voltage was 1040 V, giving an on-state resistance of approximately 36 Ω and a peak power (V^2/R_{load}) of approximately 21.6 kW (50 Ω load). The on-state resistance was relatively constant at all charge voltages, leading to the output peak power to also be around 33% of the theoretical maximum at sub-ohm on-state resistance. Had sufficient laser energy been used to achieve sub-ohm

on-state resistances been achieved, peak power would have been upwards of 65 kW. The consistency of on-state resistance demonstrates that even at 1800 V, pulse power is not limited by current saturation within the material. If this holds at greater voltages, (e.g., 4 kV), a peak power of 300 kW could be achieved on a 50 Ohm impedance. Further testing and improved encapsulation are needed to evaluate GaN at higher voltages.

Technical Highlights:

1. *Positive Feedback NLTL Based Soliton Generator*
   - *i.* Developed a self-sustaining positive feedback soliton generator.
   - *ii.* Using the soliton generator, produced RF output pulse with a peak power of 2.1 kW across a 50 Ω resistive load with a width and rise time close to 6 ns at full width at half maximum (FWHM) and 2 ns respectively.

2. *Development of PCSS Power Conditioning Circuit*
   - *i.* Developed an HV Si switch-based power conditioning circuit.
   - *ii.* Reduced the energy loss across the PCSS by close to 90% (using the power conditioning board) compared to the traditional methods.

3. *Tradespace Analysis*
   - *i.* Finding the new technique to obtain > 30% 2:1 VSWR bandwidth using a simple probe fed rectangular patch antenna.
   - *ii.* Derivation of a closed form expression to calculate array directivity for speedier calculations.

4. *UAV Asset Development and Experimental Design*
   - *i.* Developed PX4-based UAV platforms capable of untethered, outdoor flight while collecting diagnostic data (fixed-wing and multirotor).
   - *ii.* Developed experimental testing plan for broad spectrum indoor evaluation.

5. *RF Coupling Modeling and Experimental Measurements*

To be reported in contract report for N00014-18-C-1017

6. *GaN:C Theoretical Simulations*
   - *i.* None Submitted

7. *High Power Ultrafast Switching Fundamentals, Materials and Figure of Merit*
   - i. Evaluation of high power switching technologies and pulse forming networks has been done and viable candidates have been identified for further evaluation with materials.

ii. Theoretical equations for power dissipation at on- and switching stages of linear mode PCSS have been derived; initial calculations and analysis were done towards material evaluation and circuit level analysis.
iii. Efforts for a potential publication “PCSS Figures of Merit” are underway, at 70% completion.

8. *GaN:C Photoconductive Solid-state Switches (PCSS)*
   i. New 50 Ω strip line transmission line test fixture designed, fabricated, and tested showing proof of concept of achieving $V_{out} = V_{charge}$.
   ii. PCB test fixture designed, fabricated, and tested to allow for a compact test fixture, easy swapping of circuit components, and device characterization.
   iii. Achieved 1.8kV, X-ns FWHM pulses using a on a 1000-μm gap GaN:C PCSS
   iv. Achieved 900 V output with sub-ohm resistance using a 500 μm GaN:C PCSS

Next 12 months:

1. *Positive Feedback NLTL Based Soliton Generator*

   Effort terminated in March of 2019. Resources transitioned to power conditioning and other source development support.

2. *Development of PCSS Power Conditioning Circuit*

Our objective is to operate the PCSS continuously at a repetition frequency greater than 50 kHz. The ON-resistance of the HV Si switch is in the range of tens of ohms. Therefore, at this high frequency, switching loss of the HV switch increases significantly leading to high switching loss and potential switch damage. We are planning to design a power conditioning board based on an HV SiC MOSFET. Because SiC MOSFETs have lower ON-resistance compared to Si MOSFETs, the new solution can reduce the switching loss in the system compared to Si MOSFET based solutions. We are working on improving the thermal management of the HV switch and the PCSS to perform the continuous operation at a high voltage (≥ 10 kV) and high repetition frequency (≥ 50 kHz). In addition, we are exploring alternative HV switch designs to increase the average power handling capability of the power conditioning board. The research goals are summarized as follows.

i. Designing an HV SiC switch-based power conditioning board (February 2020).
ii. Designing a thermal management system for the power conditioning board (February 2020).
iii. Testing the power conditioning board at a voltage close to 10 kV, and repetition frequency 100 kHz (April 2020).

iv. Developing improved EMI mitigation system for the power conditioning board (April 2020).
v. Designing a single gate driver-based HV switch constructed from stacked series MOSFETs (July 2020).
vi. Fabricating an in-house HV switch based on the single gate driver-based switch design (August 2020).
vii. Designing a power conditioning board based on the in-house HV switch and testing the power conditioning board at a voltage close to 10 kV, and repetition frequency 100 kHz (October 2020).

3. *Tradespace Analysis*
   i. Performance optimization of the individual antennas using the D/Q optimization technique and validating with the commonly used Characteristic Mode optimization method.
   ii. Measurement of antenna parameters of single elements in GTEM and validation of simulated results.
   iii. Using the designed elements to obtain a planar array and study its characteristics.
   iv. Investigation into the scan blindness of the array.
   v. Fabrication and measurement of a smaller array (3×3) and its characterization in GTEM.
   vi. Application of the optimization technique to optimize the overall array performance.

4. *UAV Asset Development and Experimental Design*
   i. Developed PX4-based UAV platforms capable of untethered, outdoor flight while collecting diagnostic data (fixed-wing and multirotor).
   ii. Developed experimental testing plan for broad spectrum indoor evaluation.

5. *RF Coupling Modeling and Experimental Measurements*

To be reported in contract report for N00014-18-C-1017

6. *GaN:C Theoretical Simulations*
   i. With the development of the individual simulation and modelling tools, the tool chain will now be executed to perform calculations on GaN:C over the next 12 months

7. *High power ultrafast switching fundamentals, materials and figure of merit*

In the first quarter of 2020, power dissipation equations revisited through the lens of temperature rise and cooling requirements, cost-effectiveness, application-specific

SWaP-C^2 requirements. We will continue our work on the “PCSS Figures of Merit” manuscript. In the second quarter, we will expand the the FoM for linear PCSS to include additional modes of operation (e.g. lock-on and avalanche), and incorporate electrically actuated switches, including but not limited to DSRDs. This effort will include device modelling in TCAD, circuit level modeling, and device characterization, to determine the optimal source driver.

8. GaN:C Photoconductive Solid-state Switches (PCSS)

Beginning in 2020, a cost analysis of GaN:C will be completed to determine commercialization routes for semi-insulating GaN. This will include analyzing manufacturing methods for semi-insulating GaN to determine the most efficient and cost effective methods of producing GaN while maintaining crystal quality sufficient for high power applications. The study will also consider expanding the applications of GaN to drive down the cost of manufacturing. This analysis will be compiled in a manuscript: *Can Semi-insulating GaN be Cost Competitive?*.

Further experimental evaluation of GaN:C PCSS will also be conducted over the next 12 months to evaluate switching efficiency and rise time of GaN:C PCSS. High voltage testing will be performed with improved encapsulation to achieve higher voltage holding and thus peak power, and these results will be combined with TCAD simulation to improve the device design.

Acknowledgments:

This work is supported in full by the Office of Naval Research under grant number N00014-17-1-3016.

The Missouri Institute of Defense and Energy would like to acknowledge and thank multiple members of their staff for their constant support of all operations

1) Leta Moler for business support
2) Mallory Snyder for business support
3) Lauren Dorsett for laboratory management
4) James Verzella, Steve Siegel, Allen Dale, and Jeffrey Newhook for their work in fabrication and equipment support

The institute would also like to acknowledge members of the project who departed over the last year for their work and efforts on this project. Sean Ahern and John Lancaster's work was vital to the success of the project and we are happy to announce that they have both moved on to new things.

ONR HPM 2018 Program - Monthly Status Report (MSR) – OCT 2018
Anthony Caruso – Univ. Missouri – Kansas City
N00014-17-1-3016 [OSPRES Grant]
ONR Short Pulse Research, Evaluation and non-SWaP Demonstration for C-sUAV Study

11/15/2018

Distribution Statement ~A: Distribution authorized to all OSPRES Grant and Contract Participants, and any uncompensated collaborators. Further dissemination per Ryan Hoffman (ryan.hoffman@navy.mil).

OSPRES Project Description: Develop tunable High Power Microwave (HPM) sources and electronically steerable radiators whose waveform(s) enable control over all levels-of-lethality on cUAV and similar targets, with the least power density.

Executive Summary

I. Overview

In the month of October, the Effects team began to present analyzed data from >1500 tests/experiments performed over the last 4 months. This data summarizes the effects to UAV across various source parameters and groups the effects into levels of lethality. Due to the sensitive nature of the data, plots and analyzed data can be found in the October 2018 monthly status report for the OSPRES cUAV Contract. The Si-PCSS subgroup continues to make progress in switch development showing 6-kV holdoff consistently. Thermal management designs are continuing to advance weekly toward their goal of 500-W/cm^2 cooling power. After discussion with Randy Curry, an in-line V-dot probe for the PCSS transmission lines has been designed and fabricated for testing. Allowing for more accurate voltage measurements over the previous SMA based probe connected to an oscilloscope. The RF coupling group continues to improve their UAV frame models and investigate coupling currents in ranges of interest to the cUAV project.

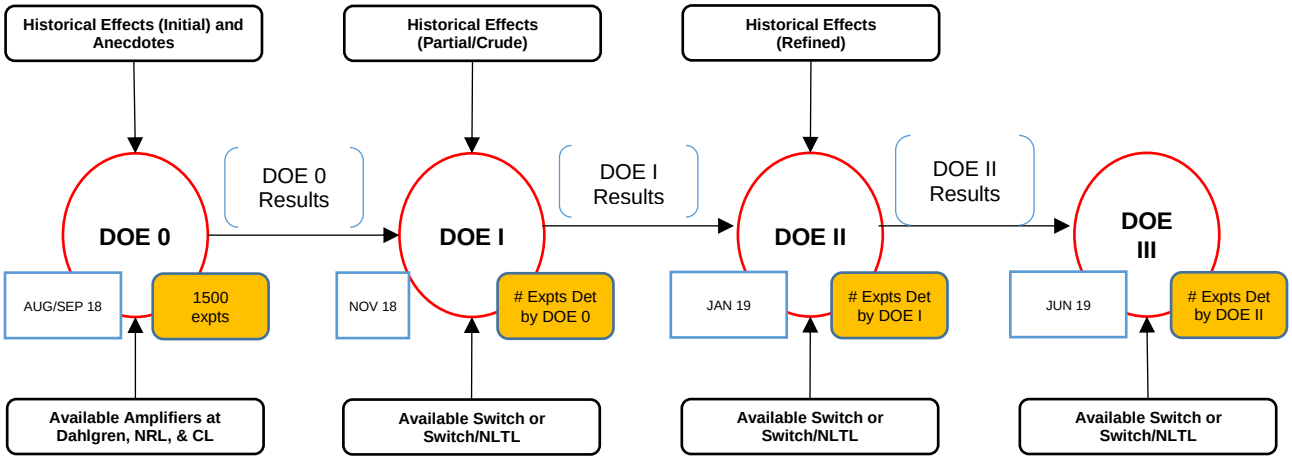
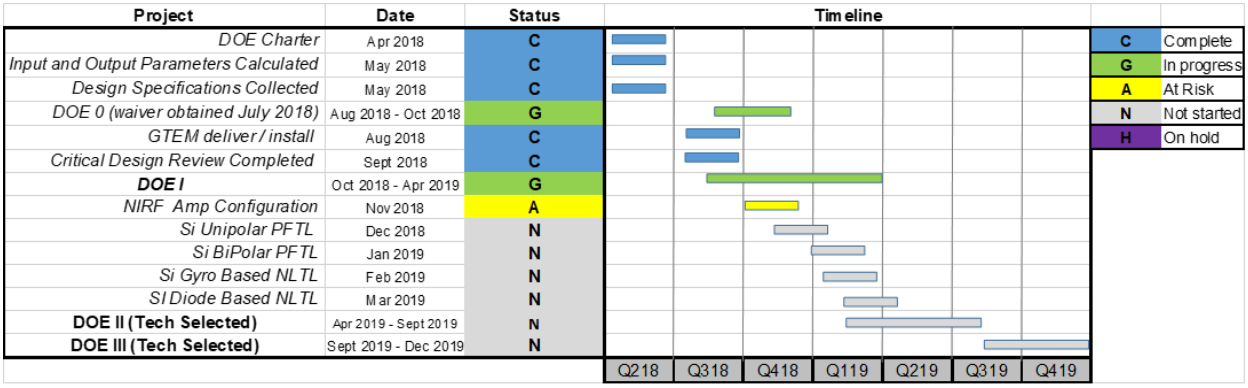


Figure ES1. Design of Experiments

- **DoE 0: (Previously Postponed)** Data analysis ongoing. See OSPRES Contract report for the month of October to see data analysis.
- **DoE I:** Data will be collected at UMKC, MS&T, NAWCWDCL, and LLNL with their respective technologies and equipment identified below. The government performers are waiting for new budgets to turn on before restarting work.
- **DoE II:** TBD based on refined historical effects and available technology.
- **DoE III:** TBD based on available technology.

***Table ES1**. OSPRES Timeline (Updated).*



Project	Date	Status
DOE Charter	Apr 2018	C
Input and Output Parameters Calculated	May 2018	C
Design Specifications Collected	May 2018	C
DOE 0 (waiver obtained July 2018)	Aug 2018 - Oct 2018	G
GTEM deliver / install	Aug 2018	C
Critical Design Review Completed	Sept 2018	C
DOE I	Oct 2018 - Apr 2019	G
NIRF Amp Configuration	Nov 2018	A
Si Unipolar PFTL	Dec 2018	N
Si BiPolar PFTL	Jan 2019	N
Si Gyro Based NLTL	Feb 2019	N
SI Diode Based NLTL	Mar 2019	N
DOE II (Tech Selected)	Apr 2019 - Sept 2019	N
DOE III (Tech Selected)	Sept 2019 - Dec 2019	N

DoE I Preparations OCT – NOV 2018 (OSPRES Team)

- Refine and perform a test-readiness-review for source and effects testing with the NIRF amps in the UMKC GTEM.

Critical Tasks

- Finish DOE 0 data analysis/identify remaining parameter spaces for testing in light of the adaptive DoE recommendation.
- Begin high power/field characterization of GTEM using arbitrary waveform generator and NIRF Amp at UMKC.
- Develop an efficient thermal mitigation system for Si-PCSS.

II. Current Month Progress

A. Photoconductive Solid-State Switches (Myers/Crow)

i. Fundamental Si-PCSS Development

Critical Efforts Si-PCSS

The following table outlines the efforts of UMKC for fundamental PCSS development.

Table A1. *Progress tracker for identified critical tasks and statuses. Color indicates the criticality of each task with respect to its current status and the objectives of the program: (GREEN) low-risk and/or no major delays, (YELLOW) medium risk and/or minor delays, (RED) major risk and/or delays.*

Critical Effort		Critical Task		Status
Simulation and Modeling	Si	Optoelectrical and thermal modeling		Efforts to develop a model for the transient optoelectrical performance. Students have taken over this effort and are currently building a foundation for improving the models.

Simulation and Modeling	Si	TCAD Simulation		Students have focused on understanding the fundamental behavior of the Si-PCSS system in lieu of TCAD simulations. Update will be provided in the subsequent reporting period.
Device Characterization	Si	Recovery Time Measurements		We have conducted reverse recovery time tests on a set of devices both before and after irradiation with an electron beam. Initial results show a 50-80% reduction in the recovery time. Effort is underway to determine the effect of bias voltage on recovery time.

UMKC spent much of the reporting period making improvements to the PCSS experimental process, including improvements in waveform measurement, creating 50-Ohm transmission lines for reverse recovery time measurements of SiPCSSs and fixturing for both Si and GaN PCSS testing, and exploring DC biasing for operationally improving switching efficiency of Si based devices. Some of these developments will not be covered in this report. Additionally, transmission lines are being prototyped for testing the 7-cm Si-PCSS which have been received from RDT.

Simulation and Modeling

Optoelectrical and Thermal Modeling: Si-PCSS

Developments in optoelectrical and thermal modeling have been limited as we continue to incorporate the fundamental carrier generation, recombination, and transport physics. A Python model of the transient photocarrier generation and recombination was generated using a Gaussian light pulse and assuming a uniform semiconductor material, shown in Figure A1.

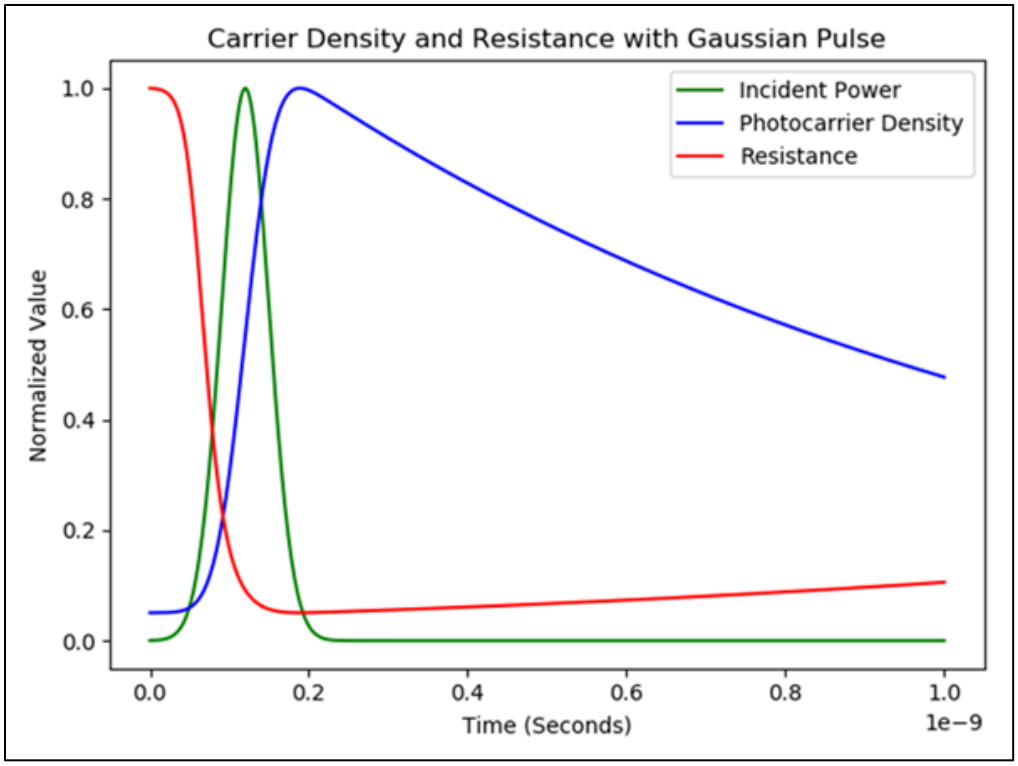


Figure A1. *Normalized time dependent model of bulk silicon photocarrier generation and recombination: (Green) incident time-dependent incident light pulse, (blue) photocarrier density, and (red) bulk resistivity. No bias nor meshing were included in the transient model.*

The time-dependent carrier generation and recombination rate model will be extended to the one dimensional models of free- and phonon-assisted carrier absorption covered in previous reports. In addition, built-in electric fields and applied bias voltage will be incorporated into the model. The objective is to characterize the effects of reverse bias, doping concentration and profile, bulk-resistivity, and device geometry on the R_{on}, rise time, recovery time, and switching efficiency. Ultimately, the outputs of the model will be fed into pulse forming network circuit models and device simulations.

Device Characterization

Effort in device characterization was focused on improving the device recovery time while maintaining adequate hold-off voltage and sufficiently low on-state resistance (R_{on}). Additionally, steps were taken to improve test and measurement systems and methods.

Test and Measurement

To support the needs of Si-PCSS experiments, specifically for the 7-cm devices recently received by RDT, we have begun prototyping and evaluating the S-parameters of transmission lines suitable for Si-PCSS testing. The first prototype used an approximately 3-mm thick PTFE dielectric, a wide ground plane, and a 1-cm wide copper strip for mounting the switch, with a designed characteristic impedance of 50 Ω. The S_{11} and S_{22}

of the transmission were measured using a vector network analyzer. The results of the S-parameters measures are shown in Figure A2. The next prototype will be a 7-cm wide transmission line with a target impedance of approximately 1 Ω. The reflection coefficient (S_{11}) was less than -10dB up to about 2.7 GHz. However the transmission coefficient (S_{21}) exceeded -3dB at 1 GHz.

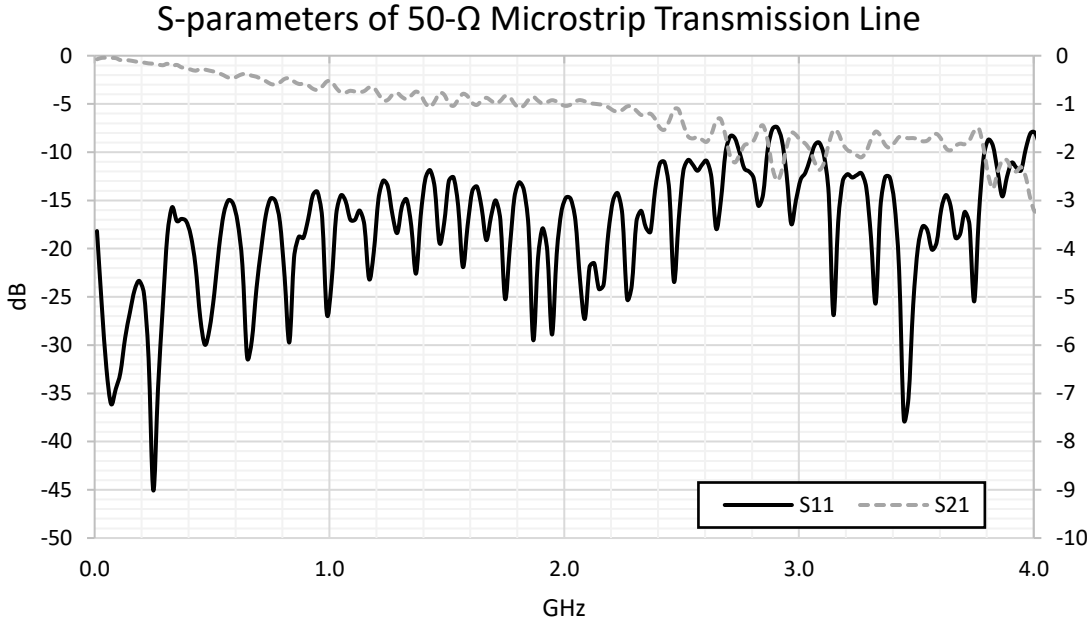


Figure A2. *S-parameters of 50-Ohm microstrip transmission line taken using a vector network analyzer.*

In addition to prototyping transmission lines, we are currently prototyping and evaluating a built-in V-dot probe to the transmission line to measure the pulse in lieu of the power dividing SMA connector used currently. The pulse measurement approach used at present is a 50-Ω SMA soldered to the transmission line. In theory this pulls approximately 10% of the pulse power off, which is attenuated before being captured by the oscilloscope. We are currently evaluating an alternative imbedded V-dot probe. A prototype of the V-dot has been assembled on a 1-cm wide, 50-Ohm micro-strip transmission line where part of the conductor has been removed and replaced with an SMA that has had its pin cut flush with the surface of the transmission line. The prototype and concept illustration are shown in Figure A3. Note that the photo was taken before the second SMA was soldered to the transmission line.

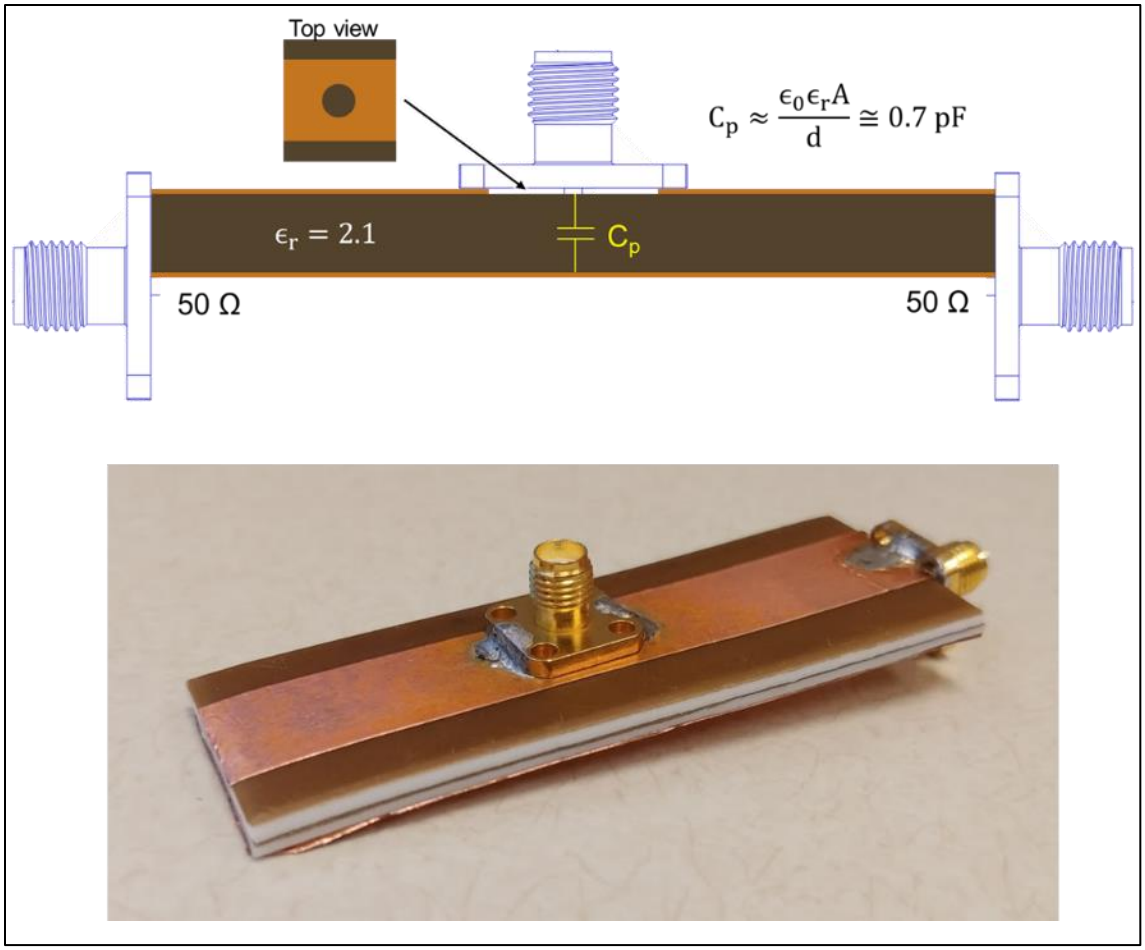


Figure A3*. Prototype of integrated SMA-based V-dot probe. (Top) Cross sectional illustration of V-dot concept and (bottom) photo of V-dot probe prototype prior to attaching the second SMA connector.*

The V-dot probe will be tested with the VNA to collect S-parameters of the probe. To simplify these measurements, the V-dot probe was prototyped on a 50-Ω transmission line in lieu of the 4.4-Ω transmission used in testing the Si-PCSSs. The S-parameters and phase information will be used to improve the design, and eventually improve the rise time measurements of the Si-PCSS output waveform.

Hold-off Voltage

In early September, devices were pulse tested up to 6-kV, meeting the near term objectives of device passivation for increased hold-off. The primary contribution to this success appears to be in the secondary passivation of the devices (i.e. the dielectric epoxy applied on top of the Shin-etsu polyimide and between the copper contacts). Due to this success, UMKC has deprioritized our efforts on further improving the device hold-off. Radiation Detection Technologies (RDT) will continue to push the hold-off voltage higher via device beveling, device surface passivation, adhesion treatments, and improvements in the application process.

Recovery Time

A set of Si-PCSS devices were evaluated using a reverse recovery test before and after irradiation with an electron beam. Devices were manufactured by RDT and tested by UMKC before and after irradiation with an electron beam. The test fixture used a function generator to apply a forward bias to the Si-PCSS, injecting carriers into the depletion region. The forward bias was then quickly reversed causing charge to flow in the reverse direction until the free carriers have recombined and the diode returns to reverse-blocking state. Throughout the test, the output voltage on the cathode was measured using an oscilloscope. A photo and circuit diagram of the test is shown below in Figure A4.

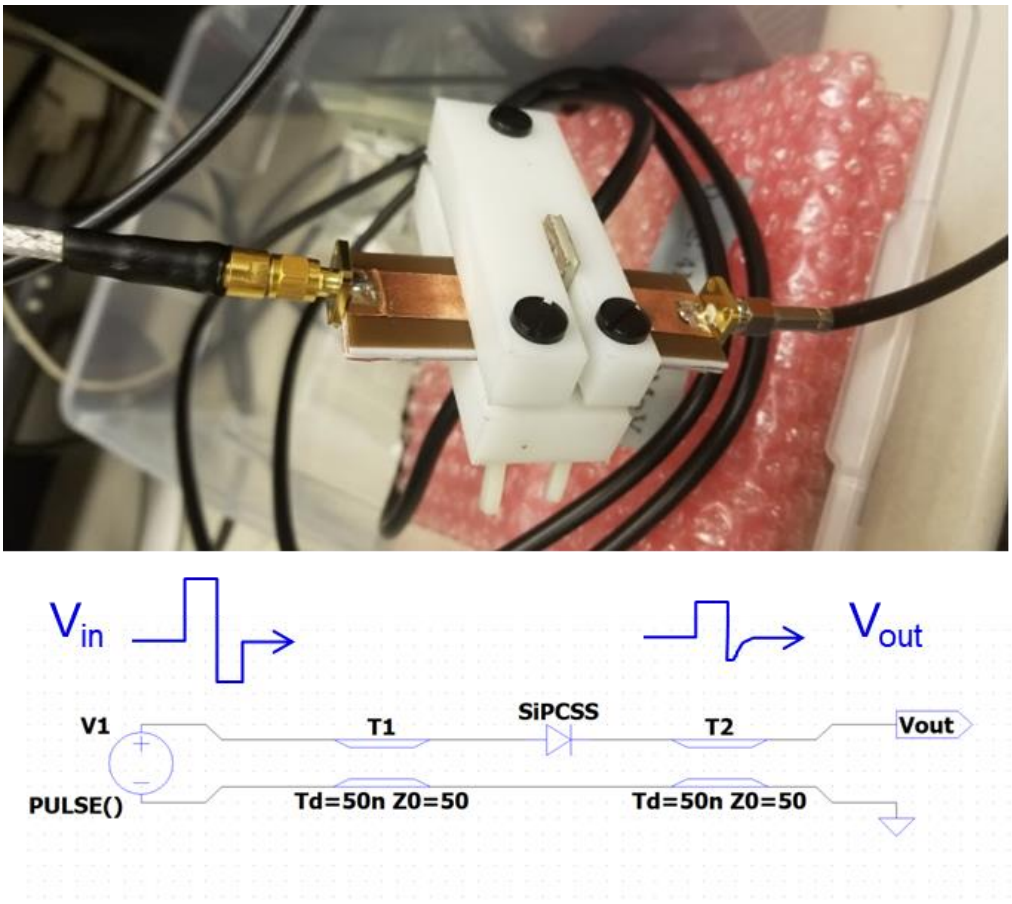


Figure A4. *(Top) photo of the SiPCSS reverse recovery test fixture. (Bottom) LTSpice model of the reverse recovery test circuit. A forward bias is applied to the device, followed by a reverse bias.*

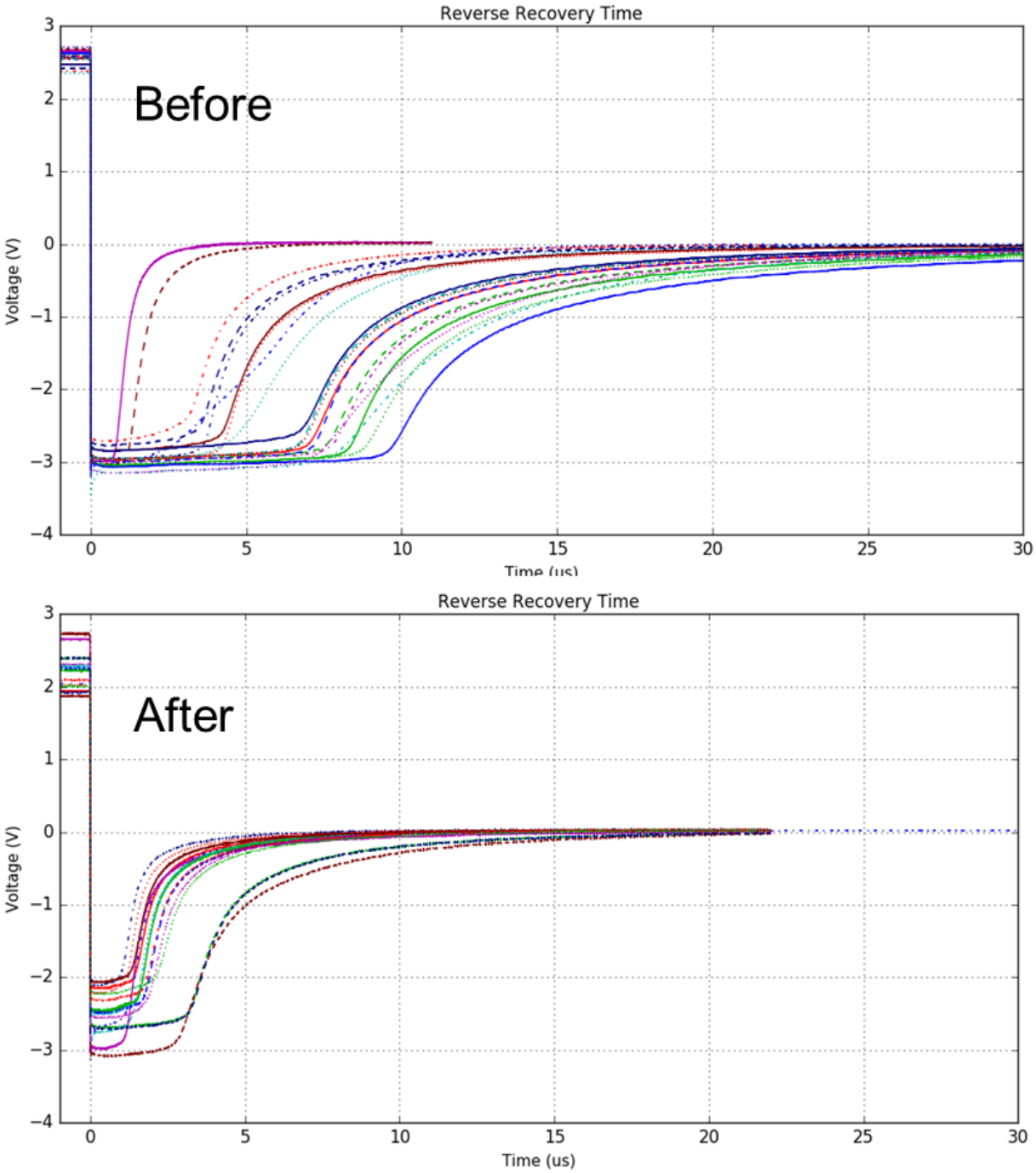


***Figure A5**. Reverse recovery waveforms collected before (top) and after (bottom) irradiation with an electron beam. The reverse recovery time was measured at the point where the reverse voltage have fallen to 10% of its peak value.*

Waveforms collected during the testing are shown in Figure A5. The recovery time was calculated by taking the time at which the reverse voltage returned to 10% of its peak value. Before irradiation, the devices showed reverse bias recovery of 9.0-21.4 µs with an average of 15.6 µs. After e-beam radiation with an absorbed radiation dose of 2-10

Megarad (MRad), the measured reverse recovery times were 2.6-9.5 µs, with an average of 5.1 µs. This corresponded to reduction in the average recovery time of 10.6 µs (67% reduction). Moreover, the majority of the reduction held even at the lowest dose (2 MR), shown in Figure A6. The lifetime was reduced by nearly 50% with a dose of 2 MR, which increased nearly linearly with dose to about 77% at 10 MR.

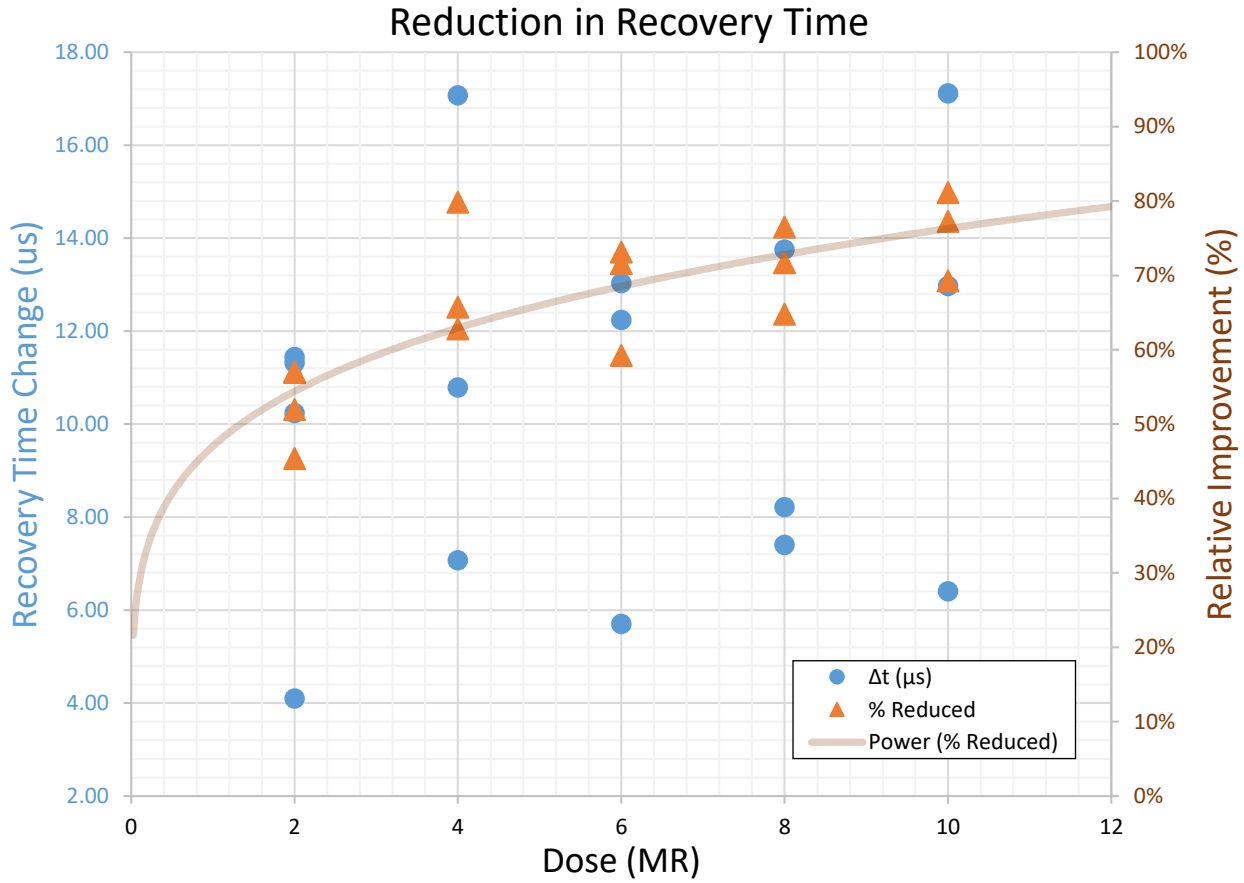


Figure A6. *Results from reverse recovery testing of SiPCSS devices before and after electron-beam irradiation. (Blue) absolute reduction of recovery time as a function of absorbed radiation dose. (Green) percent improvement in recovery time with respect to recovery time measured prior to irradiation. (Green line) trendline of percent reduction in recovery time assuming power function.*

These results are promising in terms of reducing recovery time with E-beam irradiation, but the effect on voltage hold-off must be measured before committing to this approach. It is expected that some reduction in hold-off voltage and R_{on} will result from this process. Over the coming month, we will be conducting high-voltage tests and pulse-testing to determine the extent of these anticipated effects. It is expected that the irradiation dose has a lot more space to optimize before it will be acceptable.

Critical Tasks of Si PCSS Subgroup

The Si-PCSS sub-group has identified the following critical tasks to enable further development of the PCSS and supporting subsystems:

i. Improve models for transient opto-electric device behavior as a function of bias voltage, incident light, and electrical pulse characteristics.
ii. Evaluate the effect of electron beam irradiation on the voltage hold-off and R_{on}
iii. Evlaute beveled 7-cm devices received from RDT.

Expected Products of Si PCSS Subgroup

The Si-PCSS sub-group has identified the following products/outputs to be generated in subsequent reporting period(s):

i. Transient models and simulations of the Si-PCSS system.
ii. V-dot probe for improved rise time measurement accuracy.
iii. Transmission line for testing the beveled 7-cm switches.

ii. Fundamental GaN-PCSS Development

For the reporting period of October, the GaN-PCSS subgroup was focused on efforts to identify the optimum wavelength for operation of GaN devices. A demo unit laser from Opotek was loaned to UMKC for 2 weeks at the end of September and beginning of October. The laser in question was an Opolette 355 variable wavelength laser with the UV option installed capable of operating from 220nm up to 2100nm. Pulse testing with the laser and various geometry GaN devices was performed. Unfortunately, the UMKC GaN subgroup was not aware of off wavelength laser light leakage into the main beam. This resulted in the existence of 1064nm and 532nm within the target wavelengths between 330nm and 380nm. Upon calling the manufacturer this was expected at UV wavelengths and was expected to be less than 1mJ of power. We were unable to verify the power of the residual beam and deemed the loaner laser unsuccessful. We are anticipating a return of the demo unit in early December with filters to block the residual beams so that we can ensure only the wavelengths of interest are incident on the sample.

Critical Tasks of GaN PCSS subgroup

The GaN-PCSS sub-group has identified the following critical tasks to enable further development of the PCSS:

i. Perform testing with the 355nm triple harmonic of the 1064nm NeoLase.
ii. Determine if the output of the triple harmonic generator can be modified by changing the set point of the heater.

iii. Repeat onstate resistance measurement with GaN using the 355nm wavelength.

Expected Products of GaN PCSS Subgroup

The GaN-PCSS sub-group has identified the following products/outputs to be generated in subsequent reporting period(s):

i. On state resistance as a function of sample mount
ii. Low voltage pulse measurements using picosecond 355nm
iii. Identify the sample mount configuration for future testing

B. GaN:C Calculations Subgroup (Rulis)

During the month of October the calculations subgroup was focused on the installation of Singularity and to get it running on production level computer systems. Through one-on-one interactions with system administrators and support staff for the UM-System Lewis computer cluster we have directed the installation of the Singularity package. It has been installed and tested with non-customized Singularity images such that the program is working and we are able to use it. The next step is to create a customized Singularity image that contains all of the necessary components for running FLOOXS. Once this process is complete we will be able to share the image on Singularity-HUB so that any future researcher that wants to use FLOOXS will be able to do so with minimal technical effort. Two possible routes for the process are essentially understood, but they need to be implemented and tested. The first approach makes use of a round-about image conversion process. Starting from a VirtualBox (.ova) image it is converted into a Docker image, and then a singularity image. Certain debugging efforts need to be done so that the image size is optimized for Singularity-HUB distribution. The second approach uses a default Ubuntu installation and would make use of a script to extract the relevant environmental components of the working FLOOXS image and inserting them into the default Ubuntu Singularity image.

Over the past month some time has been spent developing an understanding of the Alagator language for specifying both device structure and the types of solutions that should be computed. In the report from the previous month, demonstration-level examples of the FLOOXS software were run. We have also obtained some basic GaN device decks from previous work that had been done by Erin Patrick (a collaborator of Andy Koehler (NRL) who is at University of Florida) and have started to work on understanding their contents. Not all of the decks are functioning, but most basic elements are and that is what we are working to learn from.

C. Small Unmanned Aerial Vehicle Diagnostics and Design of Experiments (Fields)

DOE-0 experiments were conducted at NRL to further explore areas of interest from tests conducted there in May. Approximately 150 tests were conducted over 4 days of testing. The lower number of tests was due to technical difficulties with target acquisition hardware and source amplifier difficulties. The amplifier that was needed to conduct replication experiments on areas of interest suffered a failure and we were only able to obtain 24 tests in this region.

Sensor Propagation for Free-Flight Response

A more rigorous analysis of sensor effects data from NRL, Dahlgren and China Lake is underway with the results to be fed into the free-flight response of the UAV programmatically. The fault injection software (PX4 Autopilot) was further refined to inject noise in terms of bias, type and duration on multiple sensors and hardware points for testing conducted in free-flight at Camp Roberts, CA during the month of November. The PX4 autopilot will be used to close the control loop and bridge the knowledge gap that exists between sensor effects seen in the GTEM to the free-flight response of the UAV. For instance, in the figure below a bias is induced on multiple axes of a sensor from tests conducted at NRL. The same bias will be artificially injected on the same sensor at the same levels in free-flight to determine if the autopilot of the UAV can compensate for the sensor perturbation and to classify the level of effects thereof. Work is underway to determine how the state estimator (Extended Kalman filter) is affected by varying levels of sensor bias, failure and/or noise. State estimator effects are being tested in flight and will be compared to simulations in Simulink. A MATLAB script is also being developed to parse the greater than 20 log files created from the PX4 autopilot for each flight. Initial effort is being made to classify levels of effects based on sensor disruptions to build a classification model of the feedback controller as a whole.

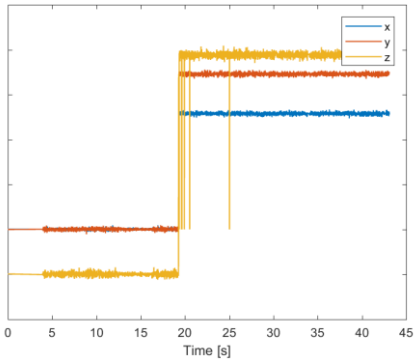


Figure C1: *Sensor bias induced by HPM interrogation*

Design of Experiments

Analysis of the data from DOE-0 is ongoing and being used to inform upcoming study with NIRF amplifiers. Different plotting techniques are being looked into to make clear any trends in the data. A simulation to provide a proof of concept at using classification modeling to inform an adaptive design of experiments is still in development. The simulation takes a set of quantitative inputs sends then through a sensitive dynamic model and then produces a set of categorical outputs based on the response of the dynamic model. The quantitative inputs and categorical outputs are analogous to the cUAV DOE problem. A classification model has been setup to map the relationship of input to output. Stochastic search methods have been employed to find the lowest set of input parameters that will result in a given level of categorical output, informed from the classification model. This set of input parameters is then run through the dynamic model, simulating running an experiment, and then the result used to update the classification model.

DOE – 0 Results

Results/Data analysis from DOE 0 can be found in the OPRES contract report for October 2018.

Immediate Tasks for Diagnostics/DoE Subgroup

i. Analyze data from DOE 0 testing at all locations;
ii. Investigate individual sensor component propagation through a feedback control system;
iii. Demonstrate feasibility in adaptive experimental design for improved effects results confidence with minimal experiments.

Expected *Products of Diagnostics/DoE Subgroup*

i. Experimental design plan based on results from DOE-0.

D. Positive Feedback Non-Linear Transmission Line (Khan)

During October 2018, we have coupled a 9-section schottky-diode based NLTL with the output of the LDMOS based RF power amplifier (1.5kW continuous, over 10kW in burst mode) in open loop and closed loop configurations. We have obtained experimental data from the open loop and closed loop configurations with the NLTL included in the configuration. We have designed a 16-section NLTL PCB in Eagle CAD and are awaiting the fabricated PCB from Goldphoenix Ltd, a PCB manufacturer.

A trapezoidal pulse with 300mV amplitude (peak-peak), 1V DC offset, 50ns pulse width, rise and fall time of 9ns has been used as the input pulse in a closed loop formed by the NLTL and amplifier. The pulse is generated by a function generator in burst mode for one cycle. Two setups have been used in the experiments. In the first setup, the input pulse is applied to the amplifier, and the amplifier output is fed towards the NLTL through a full-bridge rectifier from Genesic Semiconductor (BR108). The full-bridge rectifier converts any bipolar signal at its input to a unipolar signal. This rectification stage is essential because a unipolar input pulse is essential for soliton generation through the NLTL. A feedback signal from the last stage of the 9-section NLTL is then applied at the input of the amplifier. Figure D1 shows a simplified block diagram of this setup. The output readings from different locations of the closed-loop configuration are illustrated in Figure D3. Channel-2 readings represent signal at the amplifier input and Channel-1 readings represent signals at different points of the closed-loop network. Figure D1 demonstrates the continuation of RF signal through the NLTL- amplifier feedback loop for a single pulse from the function generator.

In the second setup, we have applied the same input signal at the 5th section of the NLTL. Signal from the last stage of the NLTL is fed to the input transformer of the amplifier. The signal from the secondary side of the output transformer is then applied to the full-bridge rectifier. The unipolar output of the full-bridge rectifier is fed back to the first stage of the NLTL. Figure D2 shows a simplified block diagram of this setup. We have observed sustaining oscillations in response to a single input pulse. Figure D4 illustrates signals at different points of the closed loop. Channel-1 represents signals at different points of the closed-loop network, and channel-2 represents the signal at the input of the amplifier.

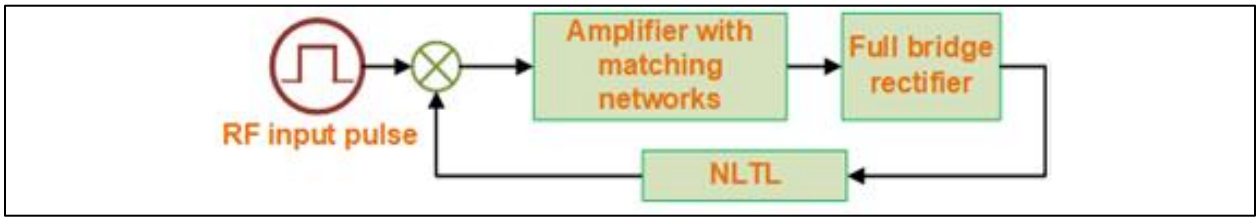


Figure D1. *Simplified block diagram of the first experimental setup.*

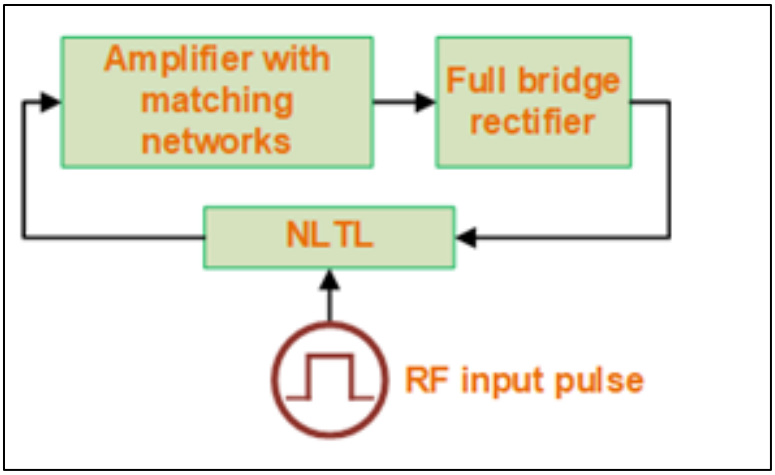


***Figure D2**. Simplified block diagram of the second experimental setup*

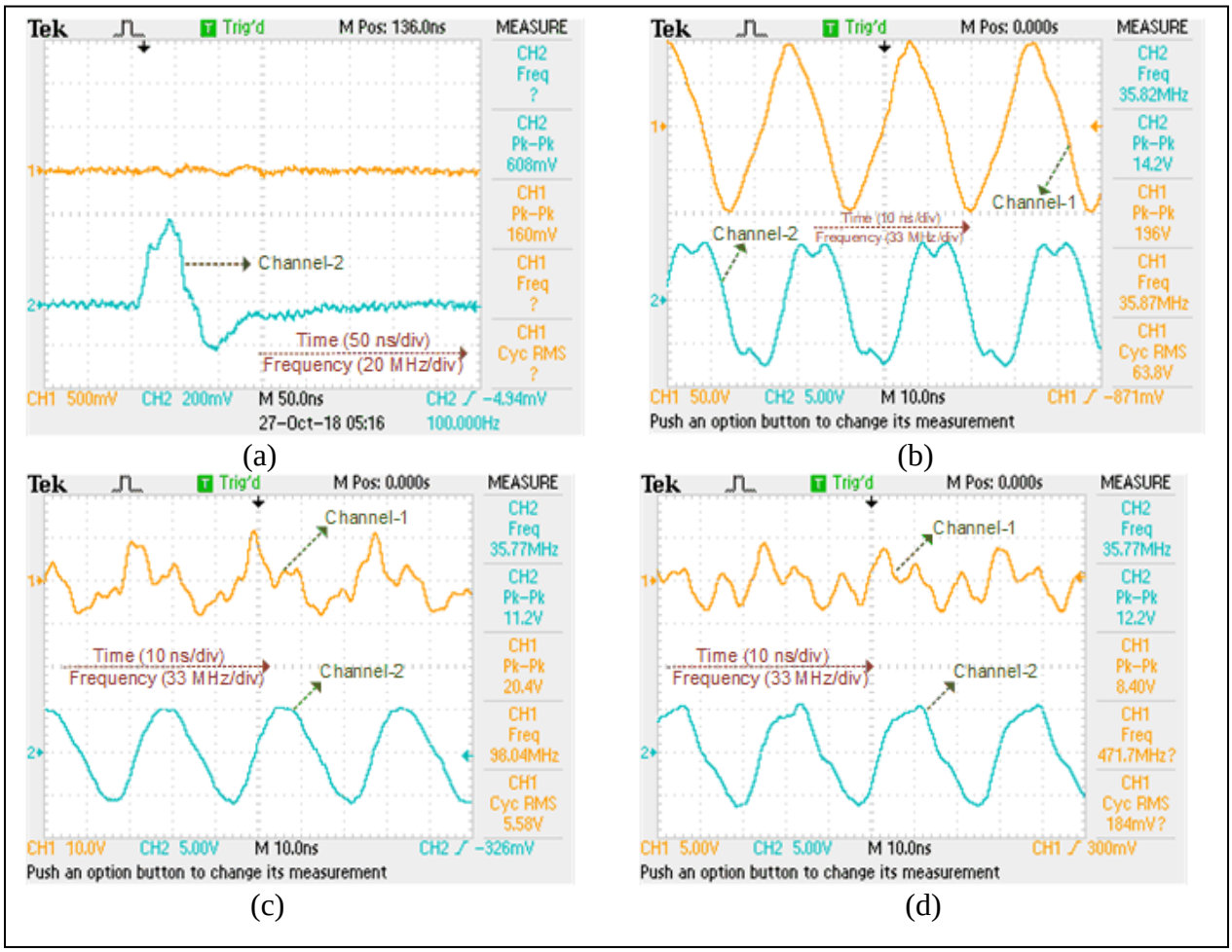


***Figure D3**. (a) Input pulse (CH2) (b) Signal at the secondary of the output transformer before full-bridge rectifier (c) Signal after the full-bridge rectifier (d) Signal at the 5th section of the NLTL.*

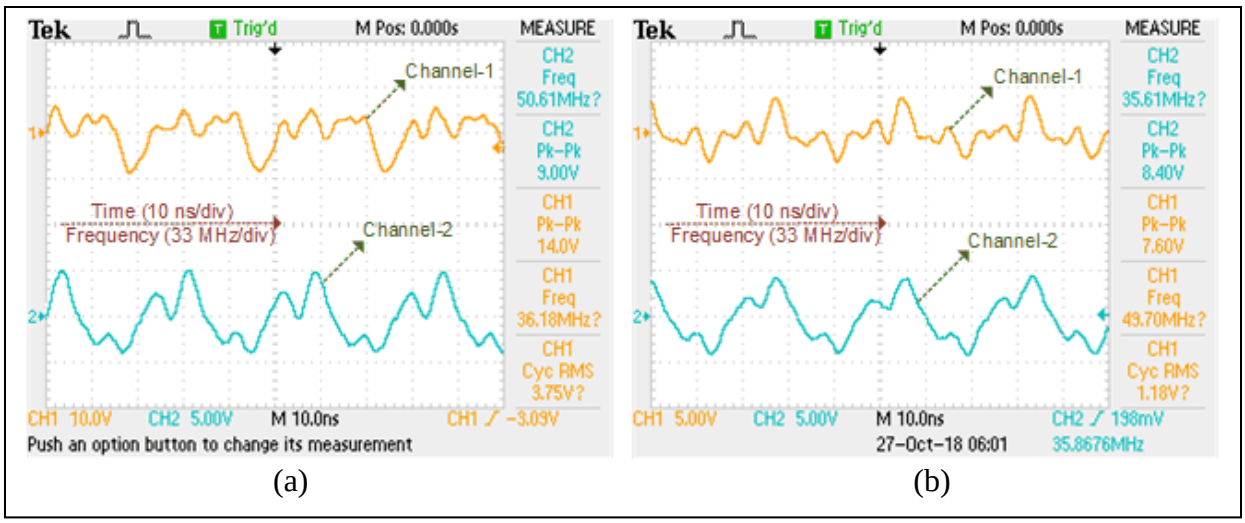


***Figure D4**. (a) Signal after the full-bridge rectifier (d) Signal at the 5th section of the NLTL. The NLTL-amplifier closed-loop configuration is illustrated in Figure D5.*

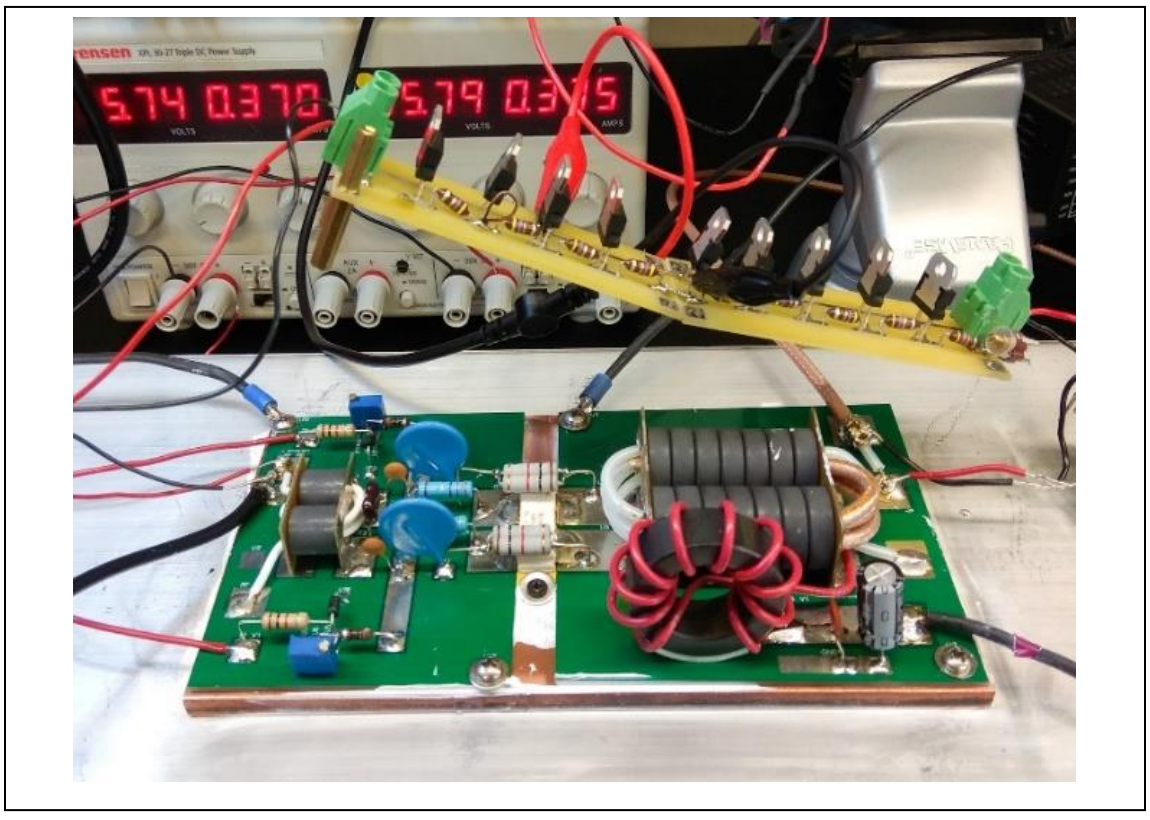


***Figure D5**. Experimental setup of the NLTL-amplifier closed-loop configuration.*

In addition, we are working on an alternative output-matching network using three 10-Ω 150 watt rated power resistors in parallel connection. The parallel resistor network is placed across the two drain terminals of the push-pull amplifier. We are doing

comparative performance analysis of the two output matching networks using transformer and power resistors.

We have designed a Schottky diode-based 16-section NLTL in Eagle Cad. Six right angle through-hole RF connector footprints are incorporated in the PCB design. The connectors are coupled with the 1st, 3rd, 6th, 9th, 12th, 15th and 16th section of the NLTL. This feature will enable us to connect the RF input signal and amplifier output signal at different locations of the NLTL. In addition, we will be able to get the output signal from different sections of the NLTL. These features will give a certain amount of control over the amplitude and frequency of the generated RF signal. We will use 600-volt rated through hole schottky diodes (C3D02060F) from Cree as the nonlinear capacitor and 100 nH fixed inductor from EPCOS in the PCB. We will fabricate another PCB using a 47-pF Y5R type ceramic capacitor from Vishay as the nonlinear element of the NLTL. The PCB layout of the 16-section NLTL is illustrated in Figure D6.

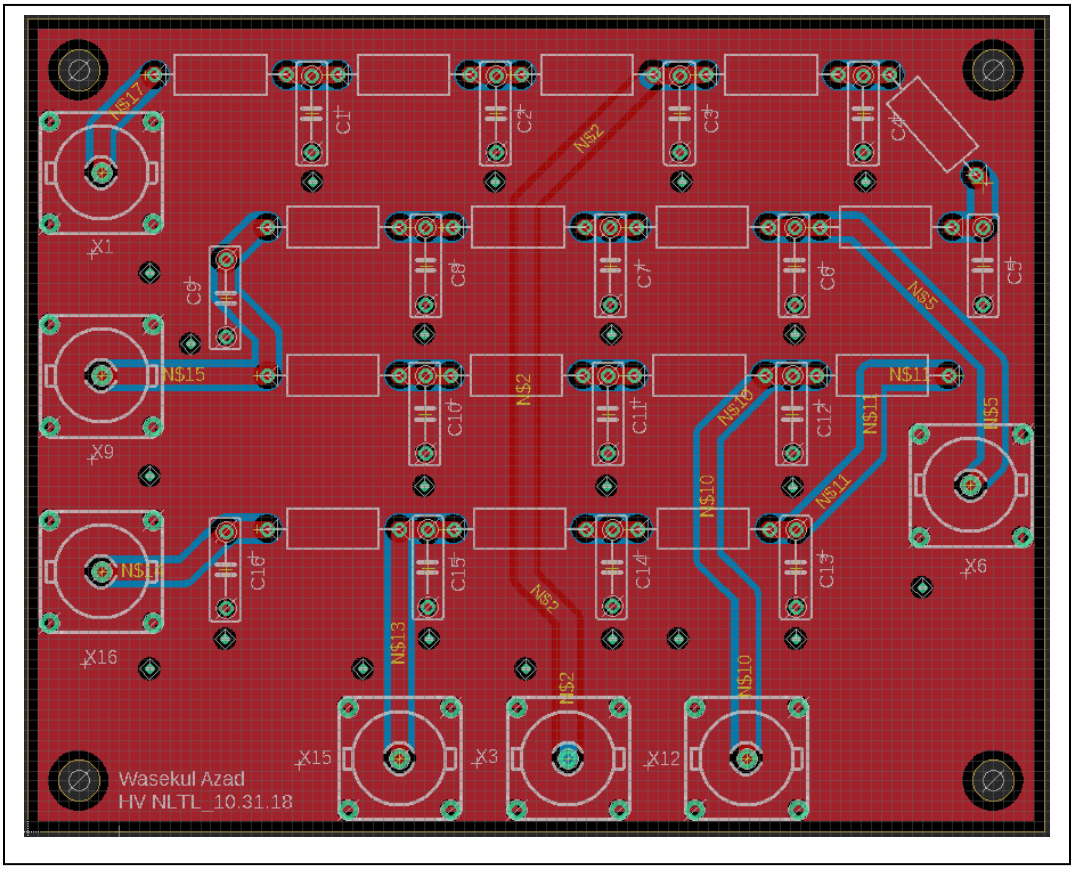


Figure D6*. PCB layout of the 16 section NLTL.*

Immediate *Tasks for the Positive Feedback NLTL Subgroup*

i. Incorporating the 16-section NLTL in the experimental closed-loop setup and obtaining experimental data.

ii. Obtaining experimental data from nonlinear ceramic capacitor based NLTL-amplifier feedback loop, and schottky diode based NLTL-amplifier feedback loop.

iii. Modifying matching network design of the power amplifier to be compatible in the range of 100 MHz – 200 MHz.

Expected Products of Positive Feedback NLTL Subgroup

i. Designing a RF amplifier with operating frequency in the range of 400 MHz - 600 MHz with 100 MHz bandwidth.

E. Applied RF Coupling Simulation and Modeling to/for sUAV (Hassan)

Characteristic Mode Analysis of UAVs

Characteristic Mode Analysis of Perfect Electric Conductor UAV frames

In the previous MSR, we showed how Characteristic Mode Analysis (CMA) could predict the exact modes that are excited and thereby contribute to the total current coupled to a UAV's frame similar to the one shown in Figure E1. The measurement results, conducted by Professor Beetner's group at MS&T, confirmed the CMA predictions. CMA provides the radiation characteristics of each mode. Therefore, by identifying at each frequency which modes are significant, as shown in Figure E2, we can predict the radiation characteristics of the entire UAV.

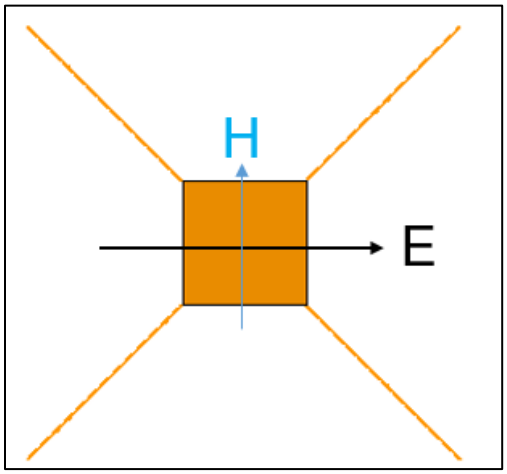


Figure E1*. PEC model of the UAV.*

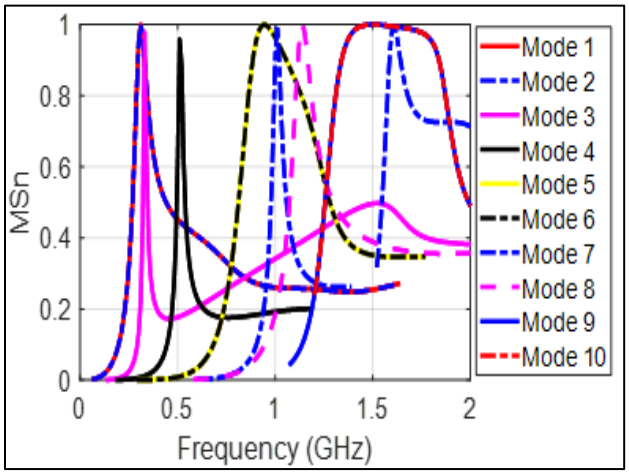


Figure E2. Modal significance of the UAV.

To further examine the CMA predictions, we simulated the UAV with an oblique incidence electric field shown in Figure E3a. Figure E3b shows the total coupled current to one arm at normal incidence and Figure E3c shows the same coupled current due to oblique incidence. By comparing Figure E3c with E3b, we noticed the emergence of a new peak in the coupled current at ~ 0.55 GHz, marked with an arrow, which was not there at normal

incidence. Revisiting the modal significance of the UAV, shown in Figure E2, we can see that Mode 4 resonates exactly at the same frequency of ~0.55 GHz. This indicates that Mode 4 is responsible for the emergence of the additional peak in the case of oblique incidence in Figure E3c. This peak occurs in the frequency range of interest of the project and it also occurs in the frequency range where the experimental setup provides the highest accuracy. Therefore, in this report we will use CMA to study this peak and Mode 4 extensively.

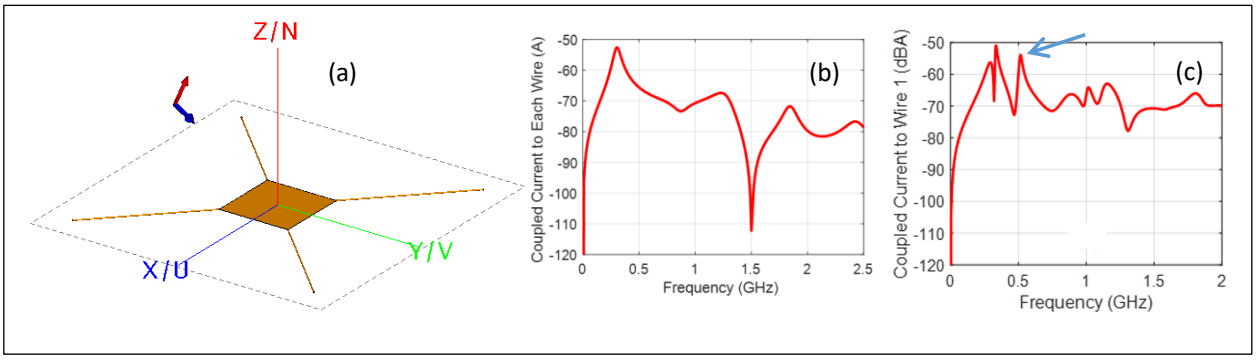


Figure E3. *(a) UAV frame at oblique incidence, (b) Coupled current at normal incidence, and (c) coupled current at oblique incidence (Azimuthal Angle θ = 45°).*

The modal excitation coefficient of Mode 4, V4, is shown in Figure E4 (Left) for several azimuthal angles of incidence. The modal excitation is a representation of the radiation characteristics of the mode. That is, it allows us to identify which angles of incidence will lead to strong coupling between the incident field and Mode 4, i.e., which angles will strongly excite Mode 4 leading to the maximum in the coupled current at 0.55 GHz. Figure E4 (Left) shows that the modal excitation coefficient of Mode 4 is zero for θ = 0 i.e. Mode 4 cannot be excited for normal incidence when $\theta = 0^{\circ}$. Figure E4 (Left) also illustrates that the modal excitation coefficient increases as the incidence angle increases until it reaches a maximum at $\theta = 40^{\circ} - 50^{\circ}$. This CMA analysis explains why a peak in the coupled current at 0.55 GHz is not achieved at normal incidence but it emerges at an angle of incidence $\theta = 45^{\circ}$ as shown in Figure E4 (Right). In fact at 0.55 GHz, the coupled current increases by ~500% at $\theta = 45^{\circ}$ in comparison to that at $\theta = 0^{\circ}$. This large variation makes it easy to verify it experimentally within anticipated experimental tolerances and noise. In the next MSR, these CMA predictions will be independently validated using experiments conducted by Dr. Beetner's group at MS&T to show the usefulness of the CMA in determining the optimum excitation to maximize/minimize the coupled current to an UAV.

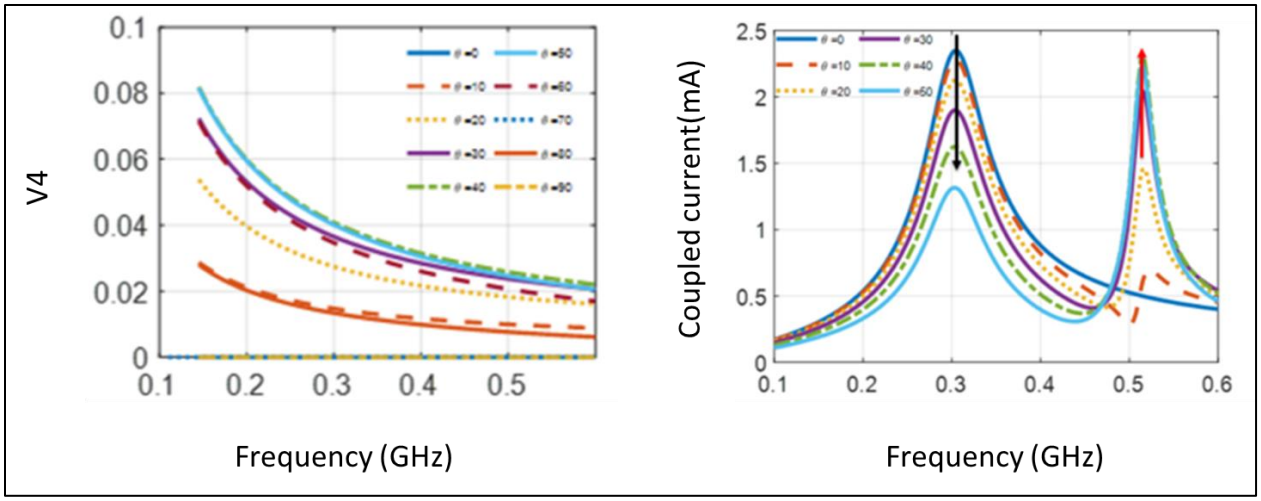


Figure E4. (Left) *Modal Excitation Coefficient of Mode 4.* ***(Right)*** *Total coupled current to the UAV frame at different electric field incidence angles.*

Characteristic Mode Analysis of Dielectric UAV frames

In the previous MSRs, we applied CMA to 3D scans of UAV frames with different resolutions as shown in Figure E5. In our previous simulations, we assumed that the scanned versions of the UAV model were composed of a perfect electric conductor (PEC). In this month, we performed CMA of the same structures in Figure E5 but we assigned realistic dielectric properties to the frame. Specifically, we assigned a relative dielectric permittivity, $\varepsilon_r \approx 3.3$, to the frames which matches that of the common plastic "Nylon 66". The Modal Significance figure of Version 1 and Version 2 of the frame is shown in Figure E6. The modal significance of both versions is identical while version 2 has extra pieces at the arms of the UAV which illustrates that, for the first 10 modes, the response of the dielectric UAV frame is less sensitive to the shape and dimensions of the arms of the frame. Moreover, the modal significance curve in Figure E6 show resonances with broader bandwidths and the modes are more clustered than the case of PEC frames (as shown for example in Figure E2).

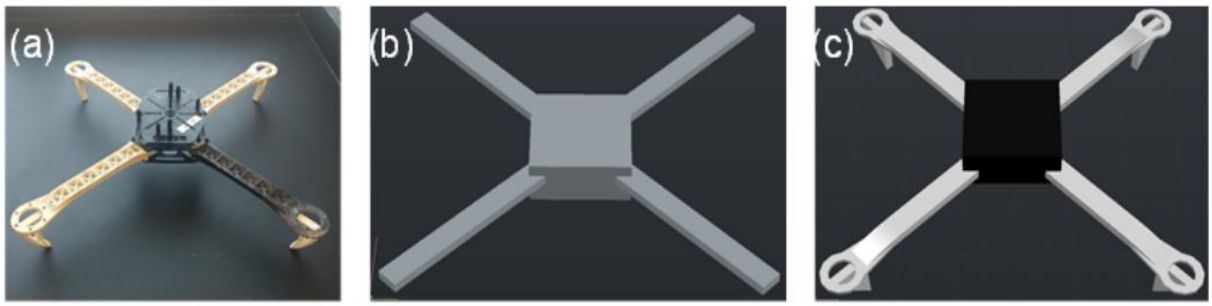


Figure E5. *(a) Picture of the actual UAV frame, (b) 3D scanned version 1 and, (c) 3D scanned version 2.*

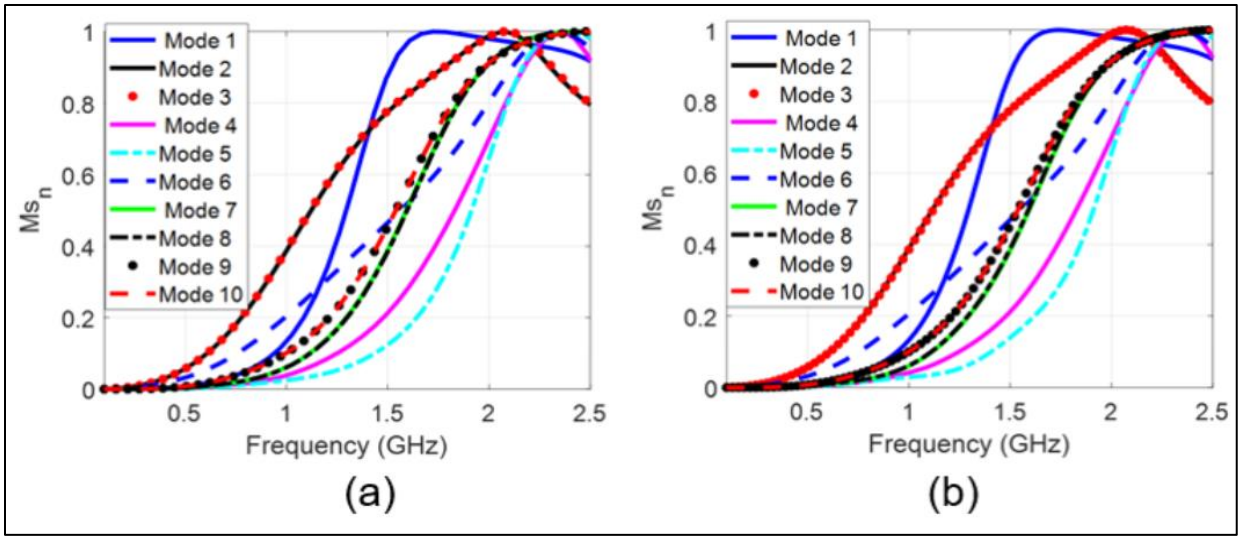


Figure E6. *Modal significance of a dielectric UAV frame (a) the 1st version, (b) the 2nd version.*

The current distribution of Mode 1 was studied for the two UAV versions and presented in Figure E7. The current distribution of the first mode is concentrated at the central part of the frame, not in the arms. Therefore, changing the length/width of the arm will have a minor effect on the overall electrical path of the current distribution of Mode 1. This behavior of Mode 1 of a dielectric frame is the complete opposite of the perfectly conducting frames where we showed that the central part of the frame will have a minor contribution to behavior of the first mode. The current distribution of modes 2, 3, and 4 is shown in Figure E8 for Versions 1 and 2. Again, the modes for the two different versions are very similar since the "hot spots" of the modes are in the central part. Due to the symmetry of the frame, the current distributions of Modes 2 and 3 are identical but they differ by a 90° rotation. The current distribution of Mode 4 is a hybridization of Modes 2 and 3.

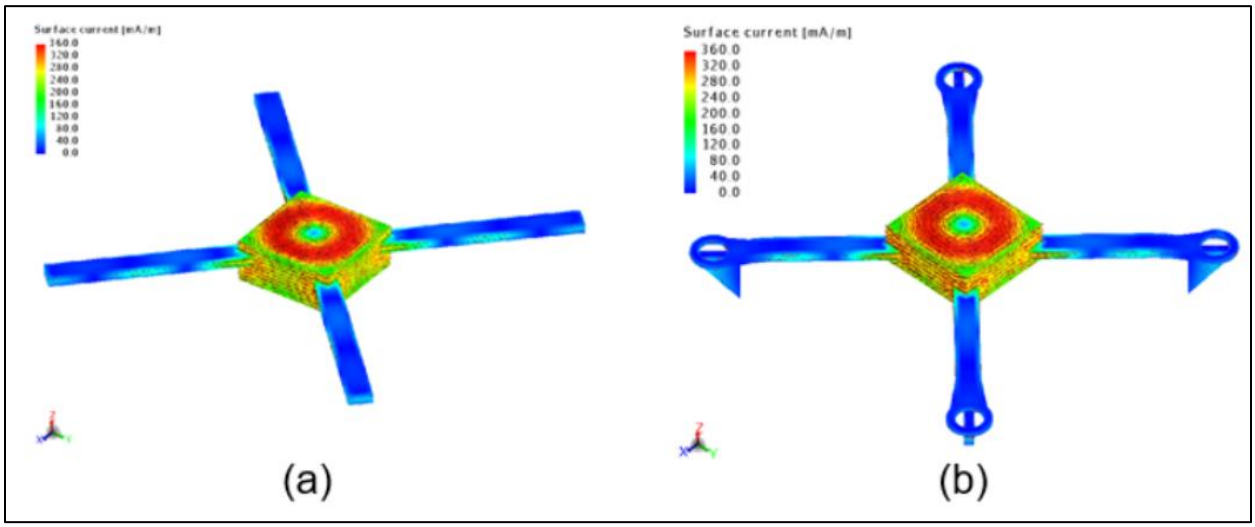


Figure E7. *Mode 1 current distribution over (a) the 1st version and (b) the 2nd version of the dielectric UAV*

The current distributions of Figure E7 and Figure E8, indicate that if electronic devices or wires are mounted on the central part of the UAV they will be in the vicinity of the hotspots and will be more prone to coupling and interference. To demonstrate how the relative location of the wire can affect the coupling current, we studied coupling to four identical wires, (wire length = 6.5 cm, wire radius= 0.25 mm, and wire height above the frame = 0.2 mm), at different locations above Version 1 of the UAV. The incident electric field is oriented parallel to the current of Mode 2 of the frame and parallel to all the wires as shown in Figure E9a. Figure E9b shows the coupled current at the center of each of the 3 wires. At 1.5 GHz, Wire 2 has the highest coupled current whereas in the case of PEC frames Wire 2 had the lowest coupled current as no hot spot existed at the central part of the PEC frame for the first few modes. To validate our conclusion, the same wires setup was simulated in free space and the comparison between the coupled current to wire 2 in free space and above the dielectric frame is shown in Figure E10. Therefore, at 1.5 GHz the UAV's frame increases the coupled current to Wire 2 which agrees with the CMA predictions.

Both Wire 1 and Wire 3 show a resonance at 2 GHz in spite of not being above the center part of the UAV. This frequency corresponds to the resonance frequency of the wire itself and this resonance will be exhibited even if the wire exists in free space far from the UAV. Wire 3 shows higher coupled current in Figure E9b since it is closer to the center part of the UAV's frames which is the location where the hot spots exist for the first few modes. Therefore, the results for Wire 1 and Wire 3 indicate to the importance of identifying the individual modes of the UAV frame, the individual modes of the wires, and how these modes couple/hybridize when they the wires are placed in the vicinity of the UAV frame. This topic will be expanded upon further in the following subsection.

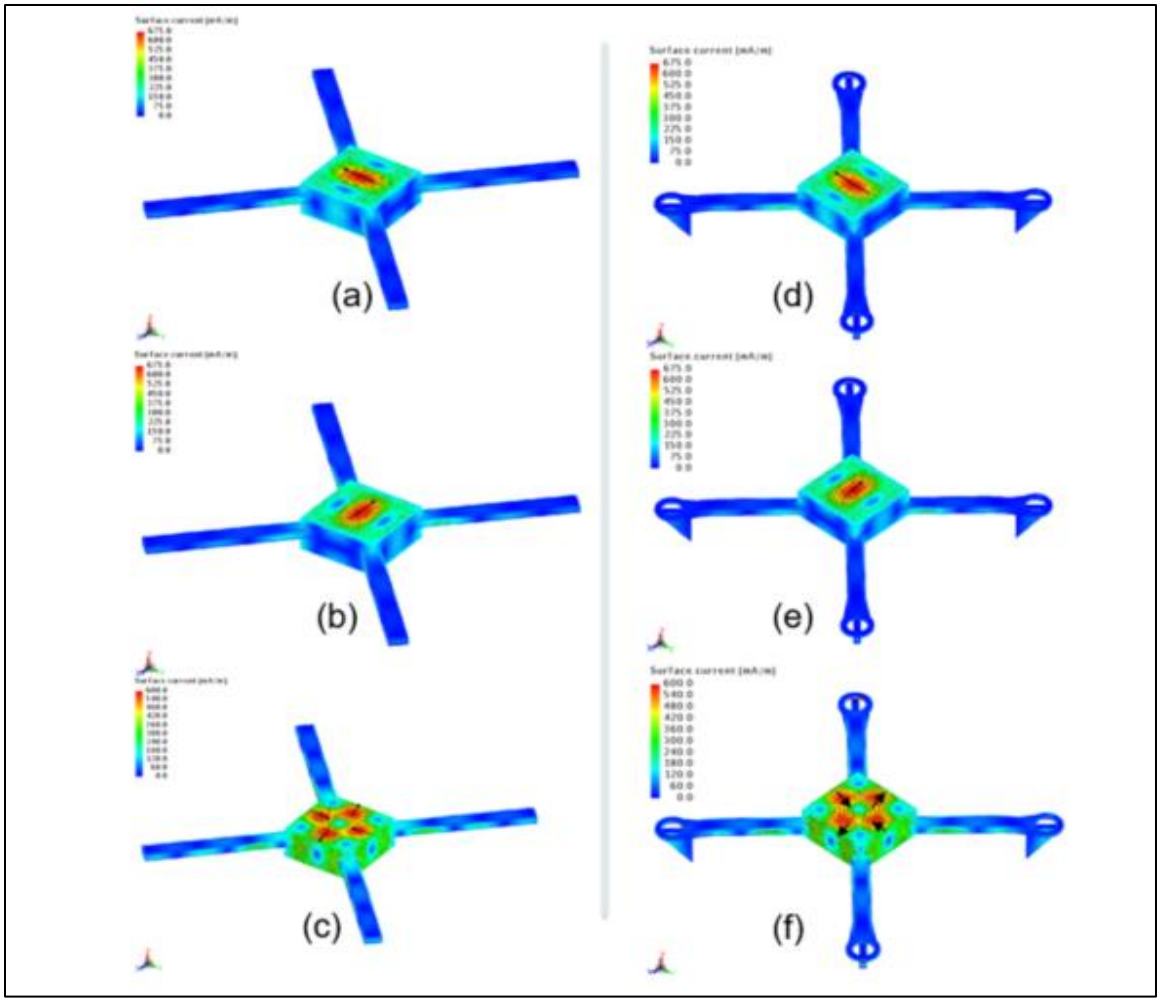


Figure E8. *Current distribution of (a) mode 2, (b) mode 3, (c) mode 4 for the 1st version of the dielectric UAV frame, (d) mode 2, (e) mode 3, (f) mode 4 for the 2nd version of the dielectric UAV frame.*

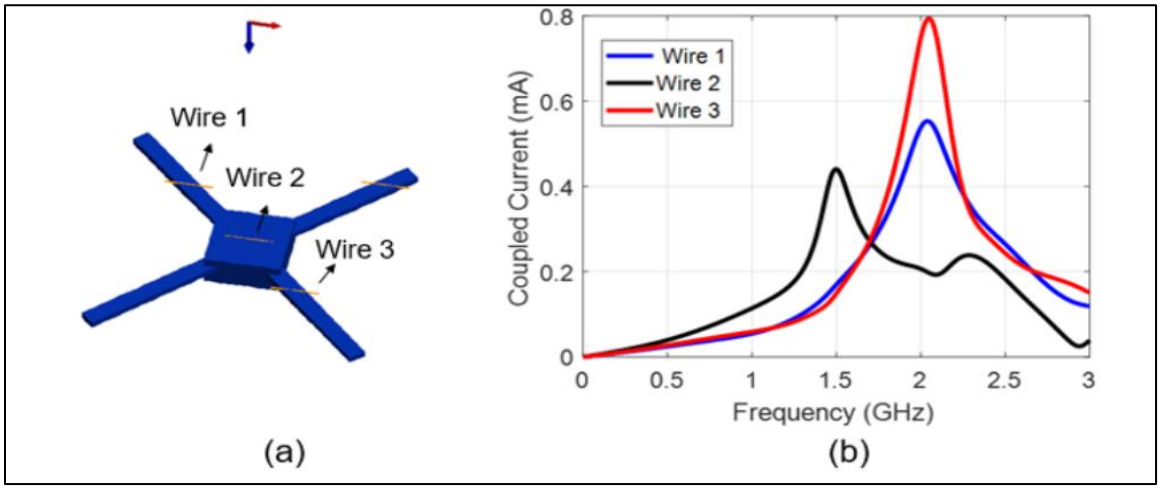


Figure E9. *(a) Wiring system above a dielectric frame (V1) and the applied electric field orientation, (b) Coupled current of the wires above the dielectric UAV frame.*

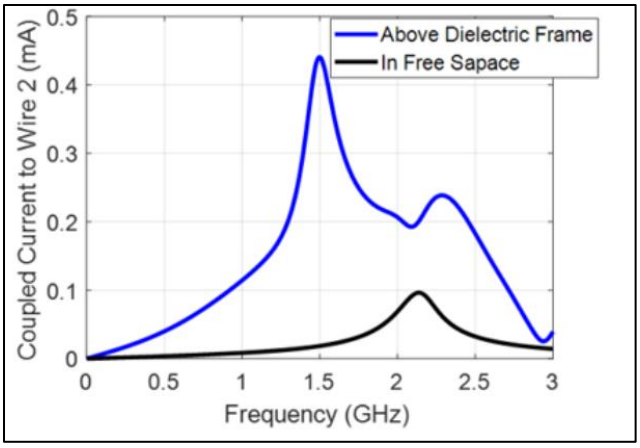


Figure E10. *Comparison between the total coupled current to wire 2 above the dielectric frame and in free space.*

Domain Decomposition Techniques and Innovative Numerical Approaches for CMA

Over the last month, we initiated collaboration with Dr. Zhen Peng at the University of New Mexico to explore utilizing different domain decomposition techniques to calculate the modes of the entire UAV based on the knowledge of the modes of its individual components. In addition to this, we also started to investigate the use of Multilevel Fast Multipole Algorithms (MLFMA) for the efficient CMA of densely meshed UAV with many fine components. Further updates on these two newly established directions will be reported in the following MSRs.

Immediate Tasks for RF Coupling Subgroup

i. Study different scanned UAV frames with different practical dielectric properties.
ii. Perform an exhaustive statistical analysis of coupling to wires with different length, different heights, and different locations above the UAV frames with realistic shapes and dielectric properties.
iii. Study the effect of mounting a Printed Circuit Board (PCB) above the scanned UAV versions.
iv. Collaborate with Dr. Zhen Peng on domain decomposition and Multilevel Fast Multipole Algorithms (MLFMA) for CMA.

F. Diode Based Non-Linear Transmission Line (Doynov)

Introduction and Problem Scope

Nonlinear Transmission lines (NLTL) are widely employed in a variety of engineering applications where compression (narrowing) of pulse width and edge sharpening is needed. In general, the change of the input signal is based on the balancing cancelation

of the nonlinear and dispersive effects of the transmission line structure. The nonlinearity could be based on the inductance and/or the capacitance of distributed material or lumped elements forming the network. A standard representation of a section of NLTL is presented in Figure F1 with lumped elements. As δ approaches 0, the ***L*** and ***C*** represent the characteristic inductance and capacitance per unit length of the TL with a length ℓ.

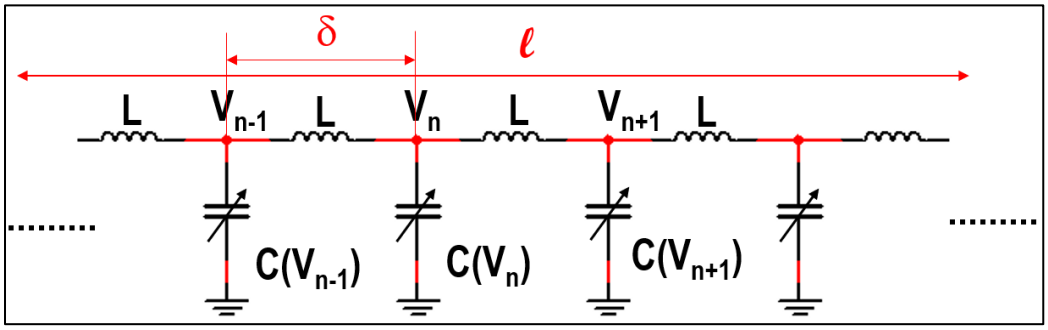


Figure F1. *Schematic presentation of lumped elements NLTL.*

When the nonlinear capacitance is based on a reversed biased diodes, the structure is referred to as a Diode-based NLTL or D-NLTL, as presented in Figure F2, left.

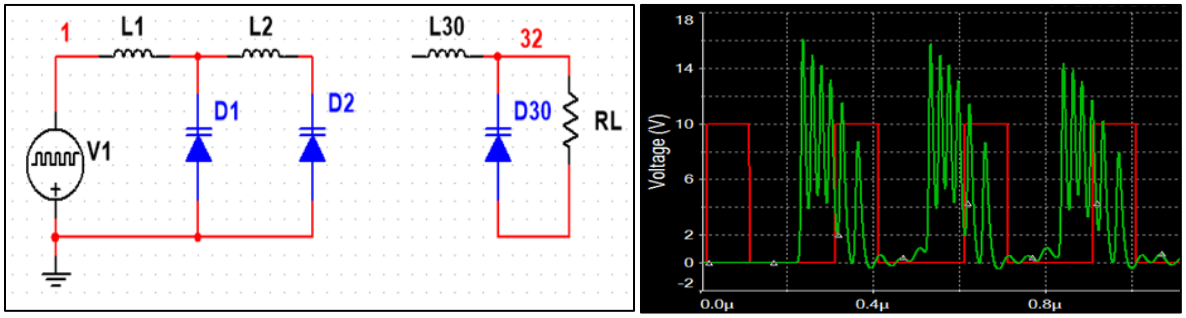


Figure F2*. Schematic presentation of lumped elements D-NLTL (left) and the voltage waveform at the output when a sequence of rectangular pulses is applied at the input (right).*

D-NLTL overview

The input signal change(s) in Figure F2 are based on non-linear dependence of the capacitance of the reverse-biased diode (i.e., varactor) with which the network is built. The capacitance of the diode elements is altered non-linearly when it is biased or poled with reverse polarity. The non-linear response of the capacitance with voltage, in concert with the inductive elements, results in different propagation speeds of the input signal, whose superposition yields pulse sharpening (decreased rise-time), damped oscillatory behavior, and soliton formation. In frequency space, the output is a superposition of the high-frequency content of interest (e.g., hundreds of MHz to ones of GHz) and a low frequency or direct current (DC) component.

Depending on the particular component, the nonlinear dependence of the capacitance may vary as can be seen from the manufacturer's C(V) curves for three different varactor families presented in Figure F3 (left), or available data in the literature (Figure F3, right).

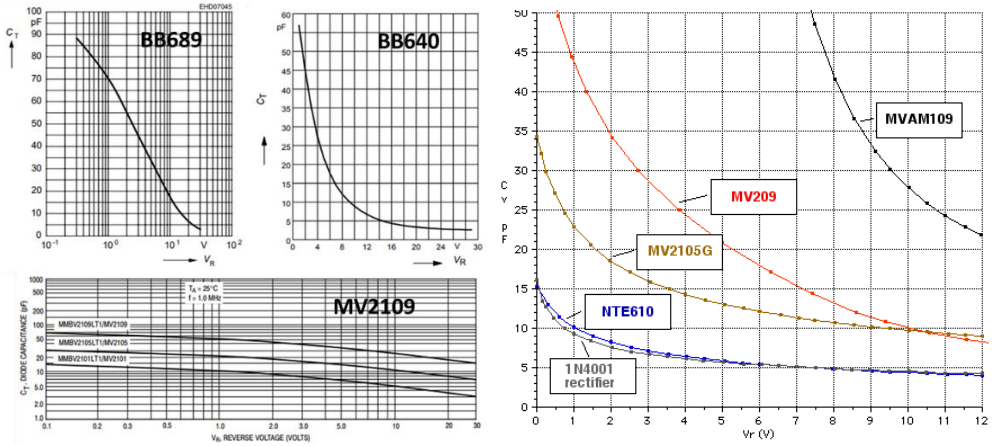


***Figure F3**. C(V) curves for different diode families.*

The different nonlinear behavior results in different changes to the input waveform. The output waveforms for networks with 30 cells and input rectangular pulse with 10 ns width and different amplitude are presented in Figure F4. For clarity of display, the input pulses have been intentionally delayed in time.

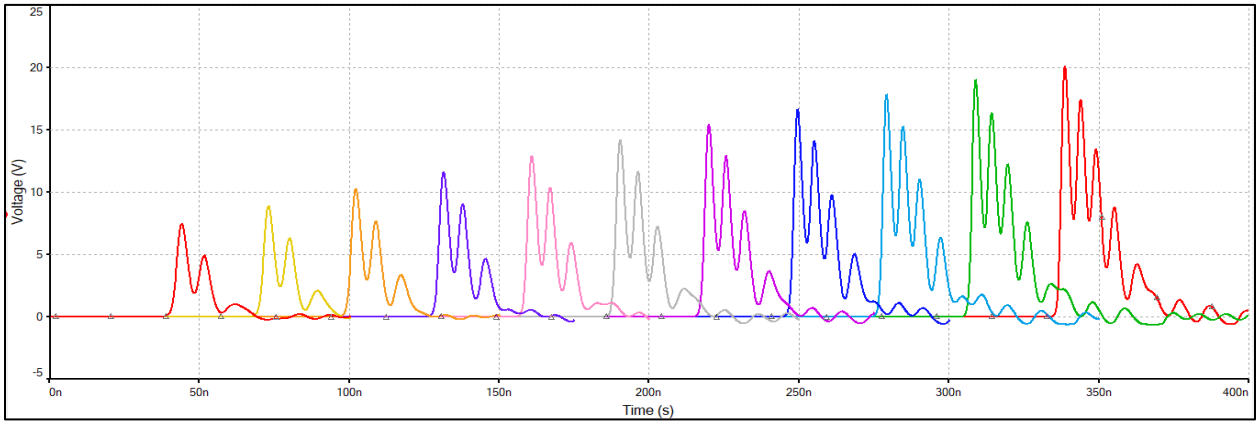


***Figure F4:** Output waveforms for various pulse amplitudes at a constant slew rate.*

<u>Considerations for D-NLTL design</u>

The exploration of design parameters was driven by the following factors:

- Excitation with currently available PCSS-based pulse sources;
- Ability to generate waveforms that will produce frequency in the desired bandwidth;
- Efficiency of the D-NLTL.

Based on the available PCSS pulse generators, the parameters of the excitation pulses were examined. Then, the parameters for a given optimized network were varied to evaluate the possibility of controlling the center frequency and bandwidth. The efficiency of the network was calculated as the ratio of the output RF-signal power and the network's input excitation power. One key consideration was to lower the width of the excitation pulse which minimizes the input power and also lowers the heat load of the PCSS. Additionally, the inherited D-NLTL problem of DC and low frequency content of the output waveform was addressed. The results of the conducted studies of design configurations and excitation pulse parameters are presented below. They address the improvement of efficiency, ability to control frequency and bandwidth (tuning ability), and interoperability with the available PCSS-based excitation sources.

When the rise time of the input pulse is kept constant (a variable slew rate), the resulting output waves are very similar but not identical (Figure F5). The shorter rise time of the input pulses results in higher frequency of the generated oscillations. This effect can be viewed in terms of network edge sharpening of already shorter rise time. Similar effect is achieved using a long NLTL to achieve accumulative edge sharpening in order to generate waveforms with higher frequency content.

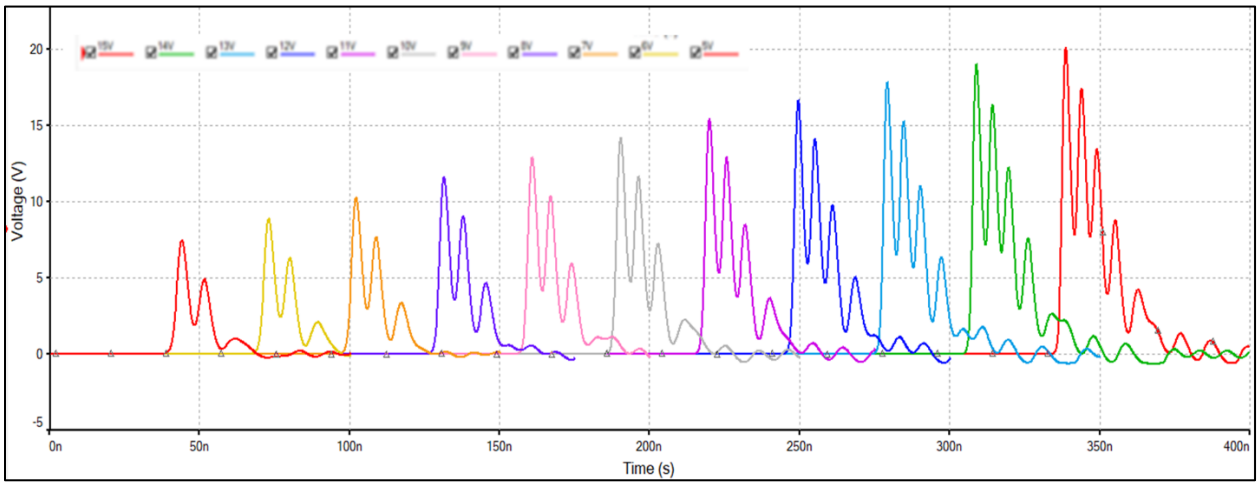


Figure F5: *Output waveforms for various pulse amplitudes at a constant rise time (variable slew rate). Input pulses are delayed for clarity.*

The length of the NLTL represented by the number of component cells (equally distributed pairs of an inductor and a capacitor) also plays an important role. However, the net effect of additional edge sharpening is offset by the additional losses in a longer NLTL.

The pulse width at a given amplitude is directly proportional to the amount of energy with which a NLTL is excited. In simulations of a network with 20 cells, output oscillations do not occur for pulses shorter than 5 ns. Figure F6 presents the results for using a 15-V amplitude input pulses with width varying from 6 ns to 15 ns and a constant rise and fall times.

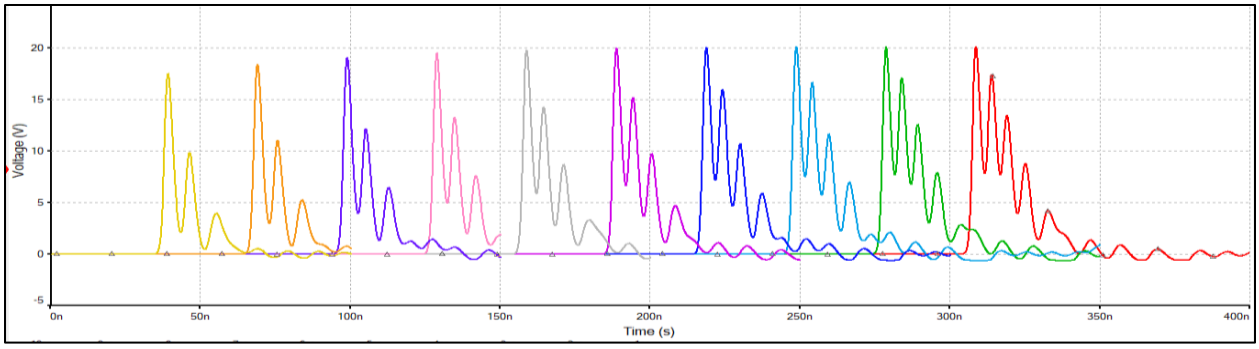


***Figure F6**: Output waveforms for various pulse width, constant rise time, and 15 V amplitudes.*

Exploring the parameter space and multivariable optimization may result in a design implementation which accounts for all factors. While many of the simulations are performed with available models of low voltage components, the understanding of the design parameters can be used for components with high reverse voltage ratings. As shown in Figure F7, for the same number of network cells, the response to the same input signal is very different and very dependent on the C(V) characteristic of the diodes. In this particular example, the excitation input pulses are the same for three D-NLTL with 30-cells each constructed using three different diode types.

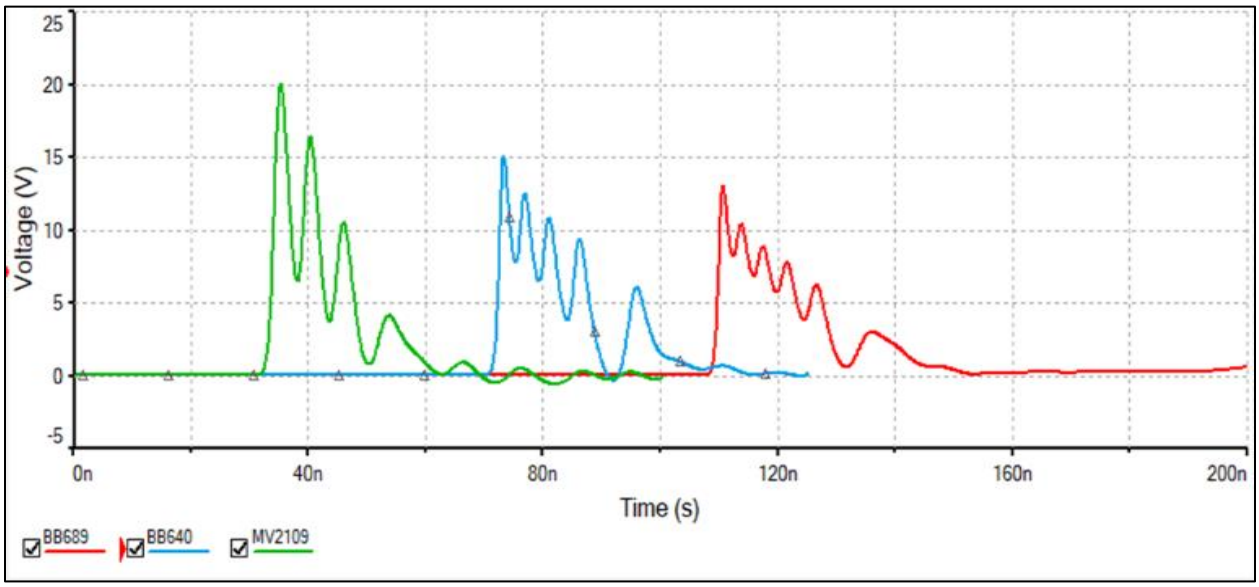


***Figure F7:** Output waveforms for input pulses with 14V amplitude, 8ns width and 5 ns rise and fall times.*

To eliminate the influence of the simulation tool, all D-NLTL have been studied in Multisim (NI) and LTspice (Linear Technology). The two environments use SPICE (Simulation Program with Integrated Circuit Emphasis) simulation models of electrical components. The different parameters were explored to understand how they affect the NLTL. The MV2109 and FMMV2109 diodes were compared to find out which parameters

are the reason for the differences in the output waveforms. The relevant diodes model parameters are presented in Table F1.

Table F1: *Model parameters and their values for FMMV2109 and MV2109 diodes.*

Parameters	Unit	FMMV2109	MV2109
Is (saturation current)	fA	42.92	1,365.0
Rs (Series Resistance)	Ω	0.152	1.0
N (Emission coefficient)	-	1.111	1.0
Cjo (Zero bias Junction Capacitance)	pF	70.85	82.03
M (Grading Coefficient)	-	0.4875	0.4933
Vj (Junction potential)	V	0.9663	0.75

The three parameters that determine the non-linear capacitance of the diodes [1] are:

- Cjo – zero bias junction capacitance
- M – Junction grading coefficient
- Vj – junction potential

Using the SPICE parameters [2], the capacitance of the diode as a function of voltage is formulated as

$$C = \frac{Cjo}{\left(1 + \frac{V}{Vj}\right)^{m}}$$

The (+) sign in the denominator is used due to the revers bias of the diodes. When ***m*** gets closer to 0.5, the capacitance becomes increasingly non-linear. As ***Vj*** decreases, the capacitance becomes increasingly non-linear. Using the SPICE model values the constructed C(V) curves for five different diodes are presented in Figure F8.

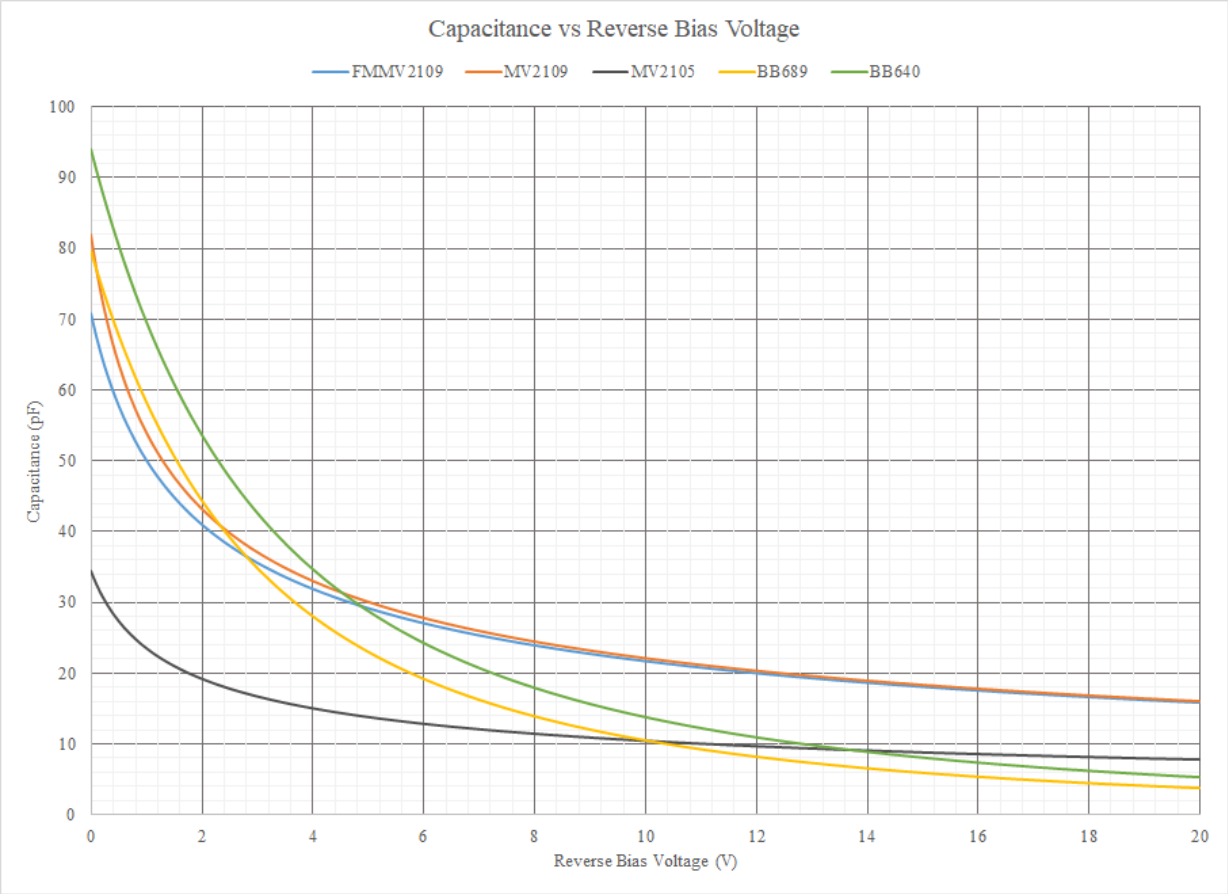


Figure F8: *C(V) curves of five diodes constructed from their SPICE model values.*

Efficiency of a D-NLTL can be defined in many different ways. Ultimately, it is the RF content generated at desired center frequency and bandwidth for given input energy. To evaluate the effect of different parameters, one option is to study the relation between excitation pulse and output waveform strictly in the time domain. The optimization parameter could be selected as depth of modulation of the output waveform or the peak-to-peak amplitude of the leading oscillation (which typically is the maximal). As shown in Figure F7, the diode parameters (the C-V curve) are critical. In order to understand the importance and interdependence of the multiple variables, a series of simulations were used in which a model parameter of a diode was substituted with the value of this parameter from a different diode. Table F2 presents the results for changes in relative efficiency for NLTL using model parameters' value replacement. D-NLTL based on FMMV2109 was evaluated for performance at different input signal. A peak performance was observed at 5V amplitude of the input pulse. An experimental evaluation was performed by replacing the value of each parameter of the FMMV2109 diode model with the MV2109 model value to observe the influence on the output waveform. As can be seen in Table F2, some parameters did influence slightly the reference output waveform labeled "Original" in the table. The only one that eliminated (substantially reduced) the peak at 5V input amplitude was the series resistor value Rs in the diode's model. This is an important observation. The design of D-NLTL should be based on components with

low Rs values. The design of new HV diode structures should target the development of components with a low Rs values.

Table F2. *D_NLTL performance with FMMV2109 model values replacement.*

Parameter	4V	5V	6V
Original	0.872	0.874	0.870
Is	0.872	0.874	0.870
Rs	0.771	0.769	0.763
N	0.872	0.847	0.870
Cjo	0.861	0.865	0.863
M	0.872	0.874	0.870
Vj	0.872	0.872	0.865

D-NLTL waveform in time and frequency domains

The presence of a DC content in the output waveform generated by a D-NLTL is unwanted as it cannot be radiated and requires filtering before the radiating element, or, reflection of that component will occur. The DC output of a non-linear network (NLN) also is a loss or a substantial efficiency reducer. UMKC has developed a D-NLTL, with EHT co-inventors and leveraging the prior-art, in which the DC content of the waveform was minimal or not present. An invention disclosure was filed with the UMKC Office of Technology Commercialization. The invention seeks to describe two methods that have not been reported in the prior-art and lead to an enhanced efficiency over the existing D-NLTL. The two methods may be categorized as unique electrical circuit topology designs: (1) a method of opposing diode elements with a bipolar wave input; and, (2) a design of staggered DC bias applied along a D-NLTL ladder. Both methods yield a reduced or zero DC component, which has been demonstrated by circuit simulation with pulse injection. Figure F9 displays the attachment that was included as Figure F1 in the invention disclosure and the provisional patent application and the provisional patent application.

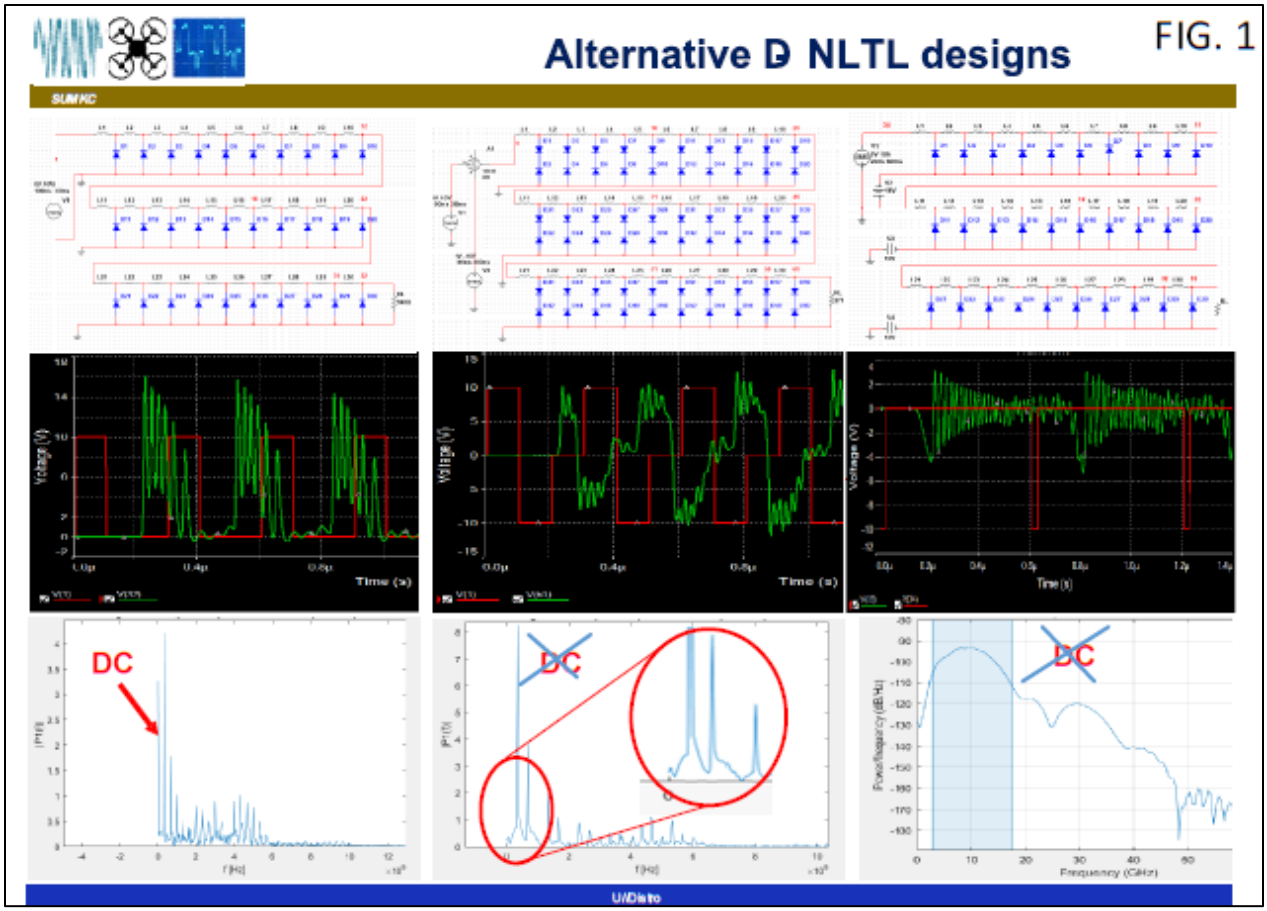


Figure F9: *Output waveforms for a standard D-NLTL (left) and the two novel designs: opposing in-series diodes (middle) and staggered DC-offset biased network.*

(1) Opposing Diode-based Unbiased Non-Linear Network:
The core of the proposed invention is the connection of two (or multiple) diode in series and in opposite direction forming an element that changes its capacitance with positive and negative polarity signals. When one of the diode (or a stack of multiple diodes connected in series) is in reverse bias, the other diode (or stack of diodes) is forward biased. An excitation with a symmetric, zero-integral in time-domain bi-polar input signal results in a generation of a waveform with high-frequency output signal with very minimal or without any DC content. The result is high efficiency (low-loss), high-frequency signal generation which can be applied directly to the input of an antenna element. This can be seen on the FFT graph of the output waveform signal in Figure F9, bottom row, center plot. The FFT of the output waveform of a standard D-NLTL has a very high DC content as pointed by the red arrow on the Figure F9. From the zoomed insert one can see that the DC spectral line is missing in the middle FFT plot. When the D-NLTL is constructed based on the proposed new design with HV components, it can generate waveforms which can be directly coupled to an antenna element for HPM generation.

(2) D-NLTL with staggered DC Bias:
The core of the proposed invention is the use of a DC offset for the entire D-NLTL. In general, the magnitude of the offset is the same as the amplitude of the excitation mono-polar input pulse or pulses and with the opposite polarity. In such configuration the net effect is that the generated high frequency waveform is at a zero offset level. For example, the D-NLTL is biased with a negative DC voltage V^- and it is excited with a mono-polar pulse with an amplitude V^+. The result is a high-frequency output signal oscillating about zero voltage with very small or without any integral DC content in the time domain, and with a zero low-frequency or DC content in the frequency domain. This can be seen on the single-side FFT graph of the output waveform in Figure F9, bottom row, right plot. Based on the network design and the commercially available high electrical power components (i.e., tens-of-kV and ones-to-tens-of-kA) the described approach can be used to generate high power radio frequency signals with improved efficiency from the elimination of a DC content. The result is high-efficiency (low-loss) high-frequency, high-power signal generation which can be apply directly to the input of a radiating antenna element.

Issues

During the reporting period, the input and output parameters of D-NLTL have been studied. The results are used for the design of optimized D-NLTLs. Many design issues and component specifications remain to be investigated. For example, some of the parameters cannot be defined precisely based on simulation only and will be available after the initial implementation and testing. A separate constraint is that most available models and components are low voltage and the purpose of the studies is HPM generation. Impedance matching is also an important aspect of investigation.

Immediate Tasks for D-NLTL Research

During the next reporting period, we plan to:

i. Continue parameter space investigation based on simulation;
ii. Simulate multiple designs including associated losses and parasitic effects considerations;
iii. Build, test and compare empirical to simulation based D-NLTL results;
iv. Develop multivariable optimization algorithms specific to the design and development of D-NLTL for HPM; and,
v. Collaborate with EHT for the simulation, evaluation and testing of HV D-NLTL.

Accomplishing these tasks will determine the feasibility of the design approaches. We will continue active communications and design documentation exchanges and updates.

Expected Products of D-NLTL Research

i. Comprehensive D-NLTL parameter space evaluation.

ii. Design and implementation of D-NLTL working prototypes.
iii. Conference and/or journal paper on the topic.

References

[1] Rustagi, S. C., & Leung, C. C. C. (2000). Accumulation mode MOS varactor SPICE model for RFIC applications. Electronics Letters, 36(20), 1735-1736. doi:10.1049/el:20001225.

[2] Van Halen, P. (1994). Physical charge-based model for the space charge region of abrupt and linear semiconductor junctions. Paper presented at the Proceedings - IEEE International Symposium on Circuits and Systems, 1 403-406. Retrieved from www.scopus.com on 10/27/2018.

G. Focus Wave Mode (Chatterjee)

The efforts in the two research directions are described below. It is noted that the efforts in the newly initiated Electrically Small Antennas (ESA) project had substantially more emphasis compared to Minimally Dispersive Waves (MDW).

Electrically Small Antennas (ESA)

ESA (beam steering array) studies were initiated for the following nominal set of specifications:

a) Frequency: UHF
b) VSWR: 2:1 or 1.5:1 – examine consequences
c) Power density: X Watts/cm^2 at X Km distance
d) Power per element (input): X MW/element (peak) at 5 ns pulse width & 100 (or 50) kHz p. r. f
e) Number of elements: 5×5 or 16×16
f) Polarization: Linear or Circular
g) A stipulation is to shrink the array form factor (size) by choosing electrically small elements

Element size and type plays an important role. The consideration of electrically small antenna elements implies that the electrical size of an element is such that it can be enclosed inside the smallest sphere of radius *a*. The definition [1, p. 2, Eq. (1.1)] of a ESA states that $ka \leq \frac{1}{2}$. Thus one can assume for the purpose of our calculations here, $ka = 0.5$.

In the following, first we consider the isolated gain and the maximum achievable bandwidth (upper limit) of a single ESA element. The assumption is that bandwidth of an array is also influenced by the element bandwidth. We omit the influence of the array mutual coupling on the array behavior. Thus the information here is of preliminary nature and further details on the array topology will be addressed in the subsequent investigations. The exact size of the antenna element shall depend on its type and its excitation. However, we start by choosing the smallest size to get ballpark estimates.

The ESA size $ka = 0.5$ is used to find the normal maximum gain (Harrington limit) that reads [2, Eq. (54)], [3, Eq. (23)] as:

$$G_m = 10\log_{10}([ka]^2 + 2ka) \quad \ldots. \ (1)$$

For ka =0.5, we find that for such a small element $G_m = 0.97 \cong 1$ dB. This is even *smaller* than a small Hertzian element whose maximum gain is 1.76 dB. The upper bound of the fractional bandwidth for such a ESA is given by [1, p. 75, Eq. (1.156)]:

$$B = \frac{(ka)^3}{1+(ka)^2} \times \frac{S-1}{\sqrt{S}} = \frac{1}{Q} \times \frac{S-1}{\sqrt{S}} \ldots\ldots. \ (2)$$

The above is valid for assuming either TM or TE mode of radiation. In the preceding, the (minimum) quality factor Q is calculated either TM or TE mode that reads [1, p. 103]:

$$Q = \frac{1}{ka} + \frac{1}{(ka)^3} \ldots\ldots. \ (3)$$

For $ka = 0.5$ and VSWR values given by S = 2 and 1.5, we can calculate the upper bound of the fractional bandwidth that is:

$$B = \frac{1}{10} \times \frac{2-1}{\sqrt{2}} = 7.07\%$$

For a VSWR defined by S=1.5 the upper bound of the fractional bandwidth of the single element is:

$$B = 4.08\%.$$

For a circular polarized antenna, these results change because the quality factor $Q = 18$. The results for the fractional bandwidth these are: $B = 3.93\%$ (VSWR=2) and $B = 2.26\%$ (VSWR=1.5).

Next, the array system parameters are investigated. The relationship between peak and average power is given by [5, p. 74, Eq. (2-50)]:

$$P_{av} = P_{peak}(\tau_p f_p) \quad \ldots\ldots. \quad (4)$$

The maximum (average) power density at a distance R from the array antenna can be found using the relation [4, p. 3, Eq. (1.8)]:

$$\mathcal{S}_m = \frac{P_{av}}{4\pi R^2} \mathcal{G}^R \ldots\ldots. \ (5)$$

From the specifications, $\mathcal{S}_m = X$ Watts/cm^2, R=X Km (1 x 10^5 cms). For $\tau_p = 5 \times 10^{-9}$ secs, $f_p = 100$ KHz, and $P_{peak} = X \times 10^6$ Watts/element, we can calculate the average

power radiated per element (assuming 100% efficiency) is $P_{av} = 2500$ Watts/element. If we have an array of 5 x 5 elements, we can assume that the total average power radiated by the array is $P_{av}^{25} = 25 \times 2500$ Watts. In that case the maximum realized gain can easily be calculated from (5) that gives an overall array gain

$$\mathcal{G}_{25}^{R} \cong 67.8 \text{ dB}.$$

If we choose a $16 \times 16 = 256$ element array, we find $P_{av}^{256} = 256 \times 2500$ Watts is the total average power radiated by the array. In that case array gain is

$$\mathcal{G}_{256}^{R} \cong 57.7 \text{ dB}.$$

Comments

1. The gain per element for the 25 element array is roughly 2.72 dB for realizing a power density of X Watts/cm^2
2. The gain per element for the 256 element array is roughly 0.22 dB for realizing a power density of X Watts/cm^2
3. From the results that have been detailed here, we conclude that application of the ESA element is appropriate for the 256 element case.
4. The average gain per element was determined from the total array gain/number of elements. (This is a *heuristic* assumption and may be only be regarded as a guideline. The actual gain can be dramatically different because we have not considered the full-wave analysis.)
5. However, the preceding heuristic approach (item 4 above) suggests that a 8 x 8 ESA element array can give a gain roughly of $8 \times 8 \times 0.97 = 62$ dB and perhaps this smaller size array may be appropriate for the application.
6. The bandwidth given by (2) gives zero bandwidth when VSWR $\rightarrow 1$. Its accuracy is reliable when VSWR$\cong 2$.

References

[1] John L. Volakis, Chi-Chih Chen and Kyohei Fujimoto, *Small Antennas: Miniaturization Techniques and Applications*. NY, USA: McGraw-Hill, 2010.

[2] R. F. Harrington, "Effect of Antenna Size on Gain, Bandwidth and Efficiency," *Jour. Res. Nat. Bureau of Standards*, vol. 64D, no.1, pp. 1-12, Jan.-Feb.1960.

[3] R. F. Harrington, "On the Gain and Beamwidth of Directional Antennas," *IRE Transactions on Antennas and Propagation*, pp. 219-225, July 1958.

[4] R. J. Mailloux, *Phased Array Antenna Handbook* (3rd ed.). Norwood, MA, USA: Artech-House, 2018.

[5] M.I. Skolnik, *Introduction to Radar Systems* (3rd ed.). NY, USA: McGraw-Hill, 2001.

Minimally Dispersive Waves (Electromagnetic Pulse Propagation)

Implementing the computer algorithm based on [1, Eqs. (53), (71), (72)]. Because the original paper [1] does not give any results for the Poynting vector, currently the numerical

algorithm is being debugged for any errors. Validation of the results from other appropriate sources are continuing.

References

[1] T. T. Wu and H. M. Shen, “Radiation of an Electromagnetic Pulse from an Open-ended Circular Waveguide,” Proc. SPIE, 1988, pp. 329-337.

III. Issues

A. Lack of key personnel for timely execution of the project has resulted in the need to hire more individuals at both management and technician levels. Financial burn rate across entire program will see marked increase.

IV. Interaction with Others

A. Verus
B. Various AFRL Entities
C. Lockheed Martin

V. Major Procurement Actions

A. Purchase of GTEM for UMKC source/effects testing
B. Funds spent on the modifications to building 71 including, demolition and restructuring of interior walls to generate a large enough room to house GTEM, electrical modifications, and security modifications.

VI. Travel

A. John Lancaster will be attending DEPS in January

VII. Pending or Upcoming Public Release Requests

A. Hassan and Chatterjee group abstracts forthcoming

VIII. Selected Highlights (texts and/or images)

A. Nothing outstanding this month

ONR HPM 2018 Program - Monthly Status Report (MSR) – NOVEMBER2018
Anthony Caruso – Univ. Missouri – Kansas City
N00014-17-1-3016 [OSPRES Grant]
ONR Short Pulse Research, Evaluation and non-SWaP Demonstration for C-sUAV Study

12/14/2018

Distribution Statement ~A: Distribution authorized to all OSPRES Grant and Contract Participants, and any uncompensated collaborators. Further dissemination per Ryan Hoffman (ryan.hoffman@navy.mil).

OSPRES Project Description: Develop tunable High Power Microwave (HPM) sources and electronically steerable radiators whose waveform(s) enable control over all levels-of-lethality on cUAV and similar targets, with the least power density.

Executive Summary

Overview:

November was heavy on report writing, as a full reporting month for the grant and the annual report for the grant overlapped and required more dedication from all involved. Also, November was cut a little short due to the holidays as many researchers/students were on travel for a portion of the holiday week. During this time, the Caruso group identified three positions that needed to be filled in order to relieve staff work-loads. These positions cover RF/effects, switch development/integration, and support services for the group. The Si-PCSS group performed pulse testing on irradiated Si switches to investigate the role of induced defects on device cooling and switch recovery time, which have led to significant thermal dissipation advatnages. They also continued to explore variations of the integrated V-dot probe (compared to the original in series oscilloscope method showing improved rise time measurement accuracy). UMKC's theoretical group obtained input cards for the FLOOXS software package from collaborators and are refining them for GaN calculations. The RF coupling group has expanded their models to include PCB's, moving beyond simulation of coupling with wires and frames.

Critical Tasks:

i. Identify and procure the remaining necessary resources to head GTEM testing and coordinate effects testing.
ii. Identify and procure a second picosecond to femtosecond laser to enable both continued Si and GaN switch development, while performing Si switch testing with the GTEM.

I. Current Month Progress:

I.A Photoconductive Solid-State Switches (Myers)

Si-PCSS Development

i. We continue to evaluate the performance of various Si-PCSS devices which have been subjected to varying levels of irradiation to understand the effects of irradiation on the recovery time. It appears an irradiation of less than 2 MegaRads is sufficient to reduce the recovery time by more than 50%, leading to a major reduction in heat dissipated in the switch during operation.

ii. Initial tests of the SMA-based V-dot for measuring the output pulse of the Si-PCSS module are promising. A qualitative assessment of rise times, with and without the V-dot, has shown some improvement in the accuracy of rise time measurement. We have not quantified the amount of improvement at this time.

iii. We are fabricating the transmission line and fixturing for the 7-cm Si-PCSS testing. We hope to have results from these devices in the subsequent reporting period.

GaN-PCSS Development

i. Purchased and received beam collimators for the triple harmonic generators and installed in beam path.

ii. Hecht analysis on variable wavelength pulse data from tunable laser, the results were not definitive due to saturation of switch. More results expected once new demo unit laser is obtained.

I.B GaN:C Subgroup (Rulis)

The main activities of the past month have been:

i. Get FLOOXS running in a Singularity environment on production computer systems.
   a. Through continued interaction with Singularity developers and the community of users, we understand how to go about taking the FLOOXS installation we have running in a Virtual Machine into a Singularity image.
   b. We have demonstrated how the process will work with a simple application and now we will have to implement it for FLOOXS, which is a more complicated software package than the simple test case we did this past month. However, the route is clear and we just need to execute it.

ii. Learn the FLOOXS application specific language (Alagator).
   a. We have completed review of the simple Alagator language tutorial, the complex system language tutorial, a reading of the Alagator language reference, and Training Course PowerPoint presentations.
   b. We now have finer-grained familiarity with the basic trial FLOOXS scripts that come with the code and that were delivered to use through NRL collaborators.
   c. We are now at the stage that we will be able to start making our own models.

I.C Small Unmanned Aerial Vehicle Diagnostics and Design-of-Experiments (Fields)

i. Developed and initially tested an adaptive design of experiments system on a simpler analogous platform. Results are currently being analyzed to make recommendations on the classification-based adaptive DOE approach.

ii. A gimbal mechanism was created to provide a safer platform for testing of the attitude stabilization controller when interrogated with noise injections.

iii. Conducted outdoor testing of our custom UAV using the PX4 autopilot. Direct injections of HPM-related effects were sent to a variety of sensors.

I.D Positive Feedback Non-Linear Transmission Line (Khan)

i. The 600V Schottky diode based NLTL provided results producing 100 MHz solitons from a single pulse.

ii. We identified four degrees of freedom in the closed loop system that can alter the soliton frequency, repetition rate, magnitude, and rise/fall time. The variables/degrees of freedom are (a) the Amplifier's bias, gain, and input/output network, (b) the total length of the soliton (number of sections), (c) the location where the pulse generator is connected, (d) the location where the load is connected.

I.E Applied RF Coupling Simulation and Modelling to/for sUAV (Hassan)

i. We continued our Characteristic Mode Analysis (CMA) of dielectric UAV frames. Specifically, we calculated the fundamental modes of the UAV frame and investigated placing wires of varying lengths near/far from the hotspots of these fundamental modes. The wires placed near the hotpots of the fundamental modes exhibited a larger coupling current than those positioned far from the hotspots regardless of the wire lengths and the direction of the incident waveform.

ii. In addition to wires above a UAV frame, we performed CMA of Printed Circuit Board (PCB) above a dielectric UAV frame and compared the ensuing fundamental modes with those of a PCB in free space. The fundamental modes of the PCB+frame can be used for more accurate coupling analysis to the PCB traces.

iii. So far, our approach has been to calculate the fundamental modes of the frame, whether it is dielectric or conducting, and use the current distribution of the modes to guide the wire placement. However, this month we found out that, for the dielectric frames, the modes of the wires+frame are similar to the modes of the wires in free space. That is, it can be efficient to calculate the modes of the wires in free space and use the dielectric frame as a "load" that marginally modifies the intrinsic modes of the wires and the other metallic components of the UAV. We will continue investigating this path over the next month as part of our goal of characterizing the overall electromagnetic response of an UAV based on the modes of its individual components.

I.F UMKC Diode NLTL (Doynov)

i. Continue to investigate the optimal load impedance matching for most efficient power transfer. The best matching load for optimal efficiency occurs at $1.28Z_0$, where $Z0 = \sqrt{L/C_{J0}}$ and using an inductor connected in series to the load with a value that is half the line inductance.

ii. Determined the minimum number of inductance-diode pairs for a given rise time of the input pulse. Preliminary results indicate that depending on the C(V) of the network diodes, between 50 and 100 number of cells are needed when excitation pulses with rise time between 1 to 5 ns are used.

iii. Explored the possible range of center frequency and bandwidth control given a fixed hardware implementation. Examples will be given in the monthly report for December 2018.

I.G Focus Wave Mode (FWM) Subgroup (Chatterjee)

Electrically Small Antennas (ESA)

i. Finishing some revision/corrections for some important analysis for electrically small antennas (ESA). The gain calculations and hence the choice of the element size are now based on PEAK power rather than the earlier ones with AVERAGE power. It was concluded that a 14 x 14 = 196 element planar array appears to be a viable choice. (The revised report will be submitted soon.)

ii. Next stage of the work related to planar array gain calculations using a two-dimensional Taylor amplitude taper is being explored. Tradeoff studies between beam width, gain and element spacing will be investigated. The frequencies chosen will be around 400 MHz and 800 MHz.

iii. The array bandwidth calculation is currently under investigation.

iv. The other continuing effort in seeking a suitable design of an electrically small antenna (which is not exactly small, but ka=0.72) is being pursued.

v. The Gustafsson limit is also under investigation because it provides antenna performance bounds based on different criterion/perspective than Chu-Harrington or McLean limits – that are based solely on quality factor of the antenna element.

II. Issues:

Research and research support requirements continue to push the staffing needs. Caruso group is hiring one more technician for PCSS and other lab related testing, one assistant director of research to head up RF and switch integration research, and one staff level engineer to help with designs, fabrication, and project management.

III. Interactions with Others:

None

IV. Major Procurement Actions:

None.

V. Travel:

Travel Plans

Please note that all papers or presentations on any aspect of the ONR HPM program must be reviewed by the ONR Program Officer (or in some cases ONR Public Release Process) regardless of classification level or audience.

Planned Travel Details	Purpose	Attendees	Estimated Costs
DEPS	Conference	Multiple	Not established yet
2019 IEEE	Antenna Conference	Chaterjee group	Not established yet

VI. Pending or Upcoming Public Release Requests:

None

VII. Selected Highlights (text and/or images):

None

ONR HPM 2018 Program - Monthly Status Report (MSR) – DECEMBER2018
Anthony Caruso – Univ. Missouri – Kansas City
N00014-17-1-3016 [OSPRES Grant]
ONR Short Pulse Research, Evaluation and non-SWaP Demonstration for C-sUAV Study

1/15/2019

Distribution Statement ~A: Distribution authorized to all OSPRES Grant and Contract Participants, and any uncompensated collaborators. Further dissemination per Ryan Hoffman (ryan.hoffman@navy.mil).

OSPRES Project Description: Develop tunable High Power Microwave (HPM) sources and electronically steerable radiators whose waveform(s) enable control over all levels-of-lethality on cUAV and similar targets, with the least power density.

Executive Summary

Overview:

Two new hires have been brought on board: John Lancaster to head up switch and GTEM integration efforts, Benjamin Bissen (new hire in January) will be working with John as an engineering tech supporting research efforts. The switch development team began working with 7-cm alongside of the 1-cm length Si devices. The move to 7-cm devices is expected to help mitigate heating dissipation limitations as measured with the 1-cm switches. Work with 7-cm devices has seen hold-off issues suspected to be the result of inadequate passivation. Calculations from the GaN electronic structure and modelling subgroup are beginning to make progress in simulating electronic devices moving them closer to realistic GaN PCSS devices; they have developed doping models in two-dimensional objects, which will facilitate simulation of carbon doped GaN switches. The effects team designed, built, and tested alternative gimbal designs for stable constrained flight during HPM testing within the GTEM. Hassan's RF coupling subgroup has shown a correlation between the measured current induced in wire and the height from the wire to the UAV frame. Increased distance between the wire and the frame show increasing coupling current at frequencies of interest to the cUAV project. They have also experimented with simple PCB geometries and shown lower frequency coupling trends based on the location of the PCB model relative to the frame of the UAV. The Positive feedback NLTL subgroup has started designing hybrid NLTL's utilizing Schottky diodes and ferrite beads. Their simulations on a 24 section hybrid NLTL has shown a center frequency of 800MHz and a correlation between the number of sections of the hybrid NLTL and the number of oscillations in the output. The Doynov subgroup implemented a cost estimation and engineering thrust focused on researching, forecasting, and budgeting the project from concept to field deployed units. A near term goal for the cost estimation subgroup/thrust is a cost analysis and budget development for the small scale demonstration.

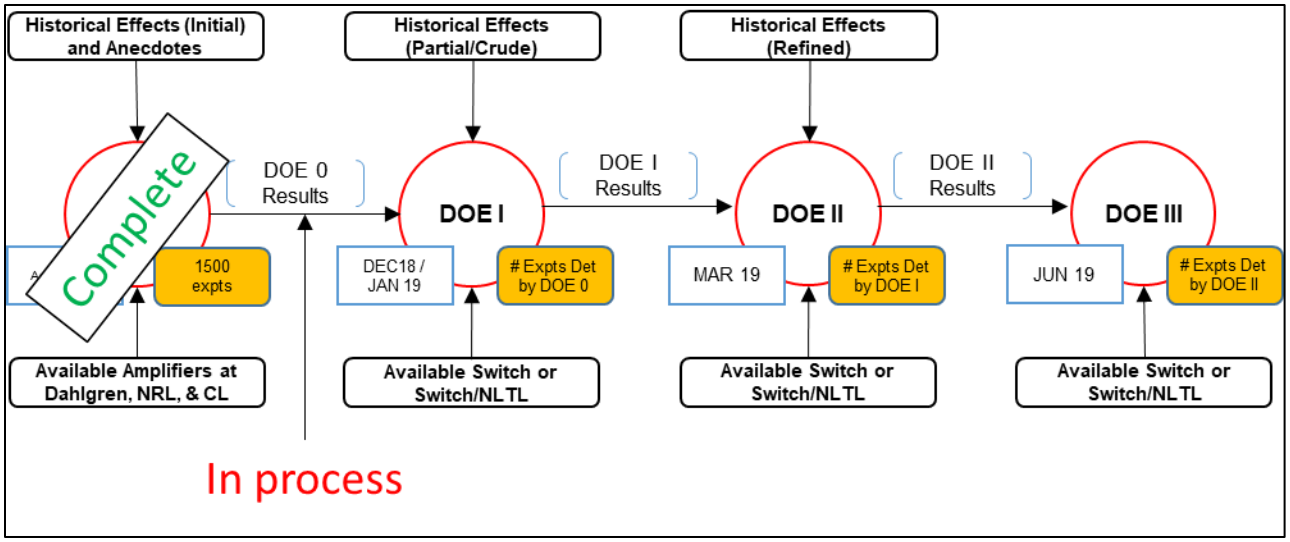


Figure ES1*. Design of Experiments (DoE High Level Plan-Updated).*

- **DoE 0:** Completed. Data analysis continues.
- **DoE I:** Data will be collected at UMKC, MS&T, NAWCWDCL, and LLNL with their respective technologies. UMKC to start with NIRF amps and refine the parameter space as needed.
- **DoE II:** TBD based on refined historical effects and available technology.
- **DoE III:** TBD based on available technology.

Critical Actions

- Identify and mitigate high voltage breakdown in 7-cm SiPCSS devices.
- Design and validate cooling on 7-cm SiPCSS devices.
- Obtain effects testing and validate results of inverted pendulum simulations to inform the design of experiments.
- Finalize effects testing from DOE 0 to determine parameter space of DOE I.

I. Current Month Progress:

I.A Photoconductive Solid-State Switches (Myers)

The following table outlines the efforts of UMKC for fundamental PCSS development.

Table A1. *Progress tracker for identified critical tasks and statuses. Color indicates the criticality of each task with respect to its current status and the objectives of the program: (GREEN) low-risk and/or no major delays, (YELLOW) medium risk and/or minor delays, (RED) major risk and/or delays.*

Critical Effort		Critical Task		Status
Device Characterization	Si	Recovery Time Measurements		We have recently conducted 4 sets of tests on new devices and shipped out for irradiation at doses of 0.5, 1.0, and 20 Mrad. Devices tests will be repeated after irradiation for a 1-to-1 comparison of recovery time and efficiency.
Simulation and Modeling	Si	TCAD Simulation		We have begun TCAD simulations of reverse recovery process as a means to build confidence in our PCSS model in TCAD via direct comparison to experimental results. Optically triggered pulsing will be added to the simulation next.
Device Characterization	Si	Electrolumine-scence Studies		7-cm devices have been experiencing hold-off issues. We have revisited electroluminescence studies on these devices to help identify cause of breakdown. We believe it is due to polyimide adhesion and/or uniformity.
Ultrafast Switching	TBD	Parameter Survey		We are exploring alternative approaches to high power, ultrafast rise-time switches, beginning with a survey of existing technologies and the fundamental properties critical to their performance.

SiPCSS Recovery Time Measurements (Fry)

In a continuing effort to improve the reverse recovery time, efficiency, and cooling demands of Si-based PCSS, a side by side analysis of different methods to improve recovery time have been conducted. Initially, we conducted high voltage pulse testing with an added DC-bias, this led to doubling the switching efficiency in some cases. In parallel, we began a study of electron-beam irradiated devices to further improve the recovery time and efficiency.

It was shown in the previous report that the recovery time of all devices receiving irradiation were reduced anywhere from 40% - 80% depending on the amount of irradiation. However, this initial testing was limited due to not conducting high voltage pulse testing before irradiating the devices to establish a baseline for comparison. In the previous report concerns from irradiation were hold-off voltage and R_{on} since no pre-irradiation pulse testing was completed, it is hard to say if these parameters were affected, leading us to conduct a second study. For the upcoming round of testing, 12 devices will receive 4 different tests before and after irradiation: (1) high voltage pulse testing with no bias, (2) high voltage pulse testing with DC-bias, (3) reverse recovery tests with a ±4 V bipolar pulse and (4) reverse recovery tests with a ±4 V bipolar pulse with a -1 V DC offset. The DC offset during the reverse recovery test is used to mimic the effect of a DC bias on recovery time during pulse testing. All the pre-irradiation recovery time testing has been completed and the results are shown in Figure A1.

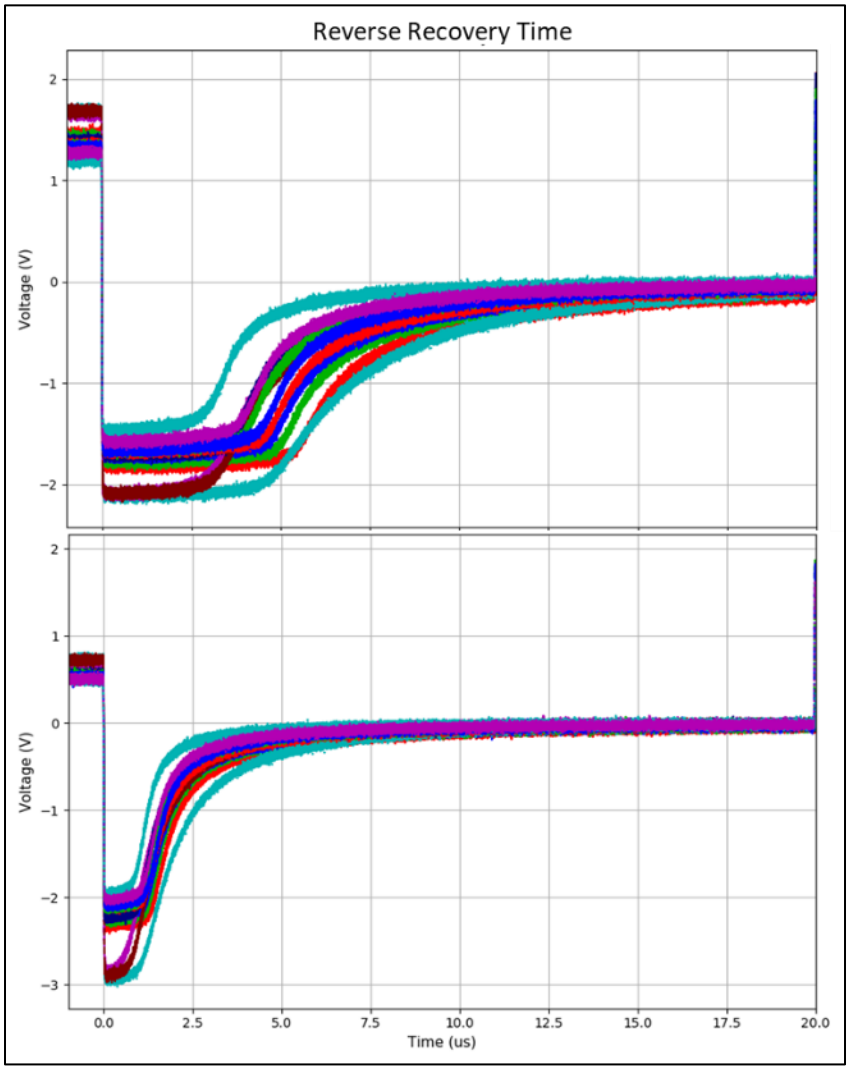


Figure A1. *Reverse recovery waveforms collected before irradiation with an electron beam without (top) and with (bottom) DC offset. The reverse recovery time was measured at the point where the reverse voltage has fallen to 10% of its peak value.*

Average recovery time for these devices with and without a DC offset was 3.7 µs and 9.8 µs, respectively, resulting in an improvement of 62% — even with an offset as small as a –1 V DC. The devices have been sent out for irradiation, but we are still processing the pre-irradiation results from pulse testing with and without a bias voltage and will report these results in the following period along with results from after irradiation. We have further refined our process for collecting and analyzing pulse testing data, and upon receipt of the irradiated devices, testing and analysis will be completed within a couple of weeks.

SiPCSS Simulation and Modeling (Hauptmann)

The Python model of carrier generation, covered in previous reports, were insufficient for characterizing pulse performance of SiPCSSs because it neglected to account for recombination and electric field considerations. To account for these effects, we have begun transient TCAD simulations of recovery tests being performed on the switches. Our first objective is to simulate the reverse recovery process in SiPCSS devices and compare to experimental data. In these experiments, the SiPCSS is subjected to a forward bias for a short duration, immediately followed by a reverse bias, at which point the device continues to conduct until the injected carriers have recombined. The circuit, as shown in the inset of Figure A2 uses a pulse generator which applies an 8 V peak-to-peak bipolar pulse to the PCSS and a 50-Ω oscilloscope is used to measure the output, represented by the 50-Ω Load. A preliminary simulation of the same parameters and setup has been simulated in TCAD, shown in Figure A2, in which V2 corresponds to the output of the switch. Despite differences, the basic recombination process is visible and the recovery time is of the same order of magnitude as that measured experimentally in Figure A1. It is important to note that in the recovery time experiments, the switch is not subjected to any pulses of light. The first simulations emulating the experiments also do not include a light pulse. However, 1064-nm light will be added to future simulations of optically triggered pulsing to compare to experimental pulse testing results.

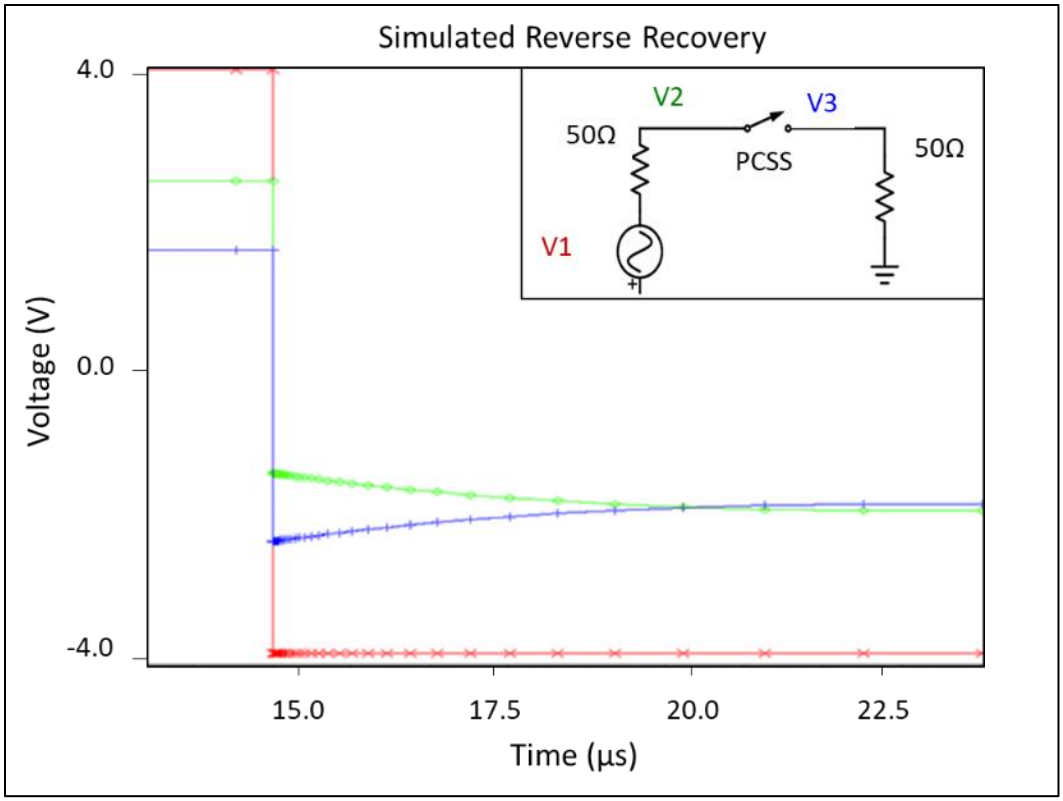


Figure A2. *Initial simulation of reverse recovery process in SiPCSS. The legend represents the circuit diagram and corresponding voltage probes in TCAD. V2 (blue) corresponds to the voltage measurement in experiment.*

We will be improving on this simulation to more accurately represent the reverse recovery profile measured in experiment, both validating assumptions made in the TCAD simulation and improving their agreement with observations. Silvaco's TCAD includes models to characterize carrier mobility under bias conditions, trap states introduced by defects, and recombination time. Through use of different combinations of models, we plan to explore which physical processes contribute most to the characteristics seen in experiment.

Identifying the physical processes that determine recovery time, rise time, etc… observed in the circuit will guide the design of future PCSS devices and experiments. These circuital simulations will provide an understanding of the switch's fundamental electrical behaviors such as recombination time, resistance, and other recovery characteristics of the output pulse provided by the switch. The simulations can then act as a precursor to pulse experiments for supplying expectations of the electrical results found in experiment. Future plans for simulations will include variations to the PCSS's shape and doping to find structures that produce the optimal pulse output for a given circuit.

SiPCSS Electroluminescence Studies (Landwehr)

Challenges with hold-off voltages have resurfaced on the 7-cm SiPCSS devices. We are currently determining if the breakdown in these devices is of the same origin as that in

the 1-cm devices, in addition to our continued effort to optimize edge and surface termination method(s). We have conducted electroluminescence (EL) imaging on the new PCSS design to determine high leakage points leading to device failure. Specifically, we are looking for points of breakdown, so improvements can be made to the PCSS hold-off voltage.

Electroluminescence is done by first taking a background image of the device, then subjecting the PCSS to progressively larger voltages until a “knee” in the reverse leakage current is measured. Breakdown, ideally non-destructive, is then confirmed by visible light emitted from the surface of the PCSS where radiative carrier recombination is occurring. Once the images of the experiment are captured, (1) the background image is subtracted, (2), the average intensity of the resulting image is subtracted, and (3) the data is filtered using a 2-D Gaussian filter in python to identify regions of recombination. The exact filter varies from test to test, but our most recent process uses the standard deviation of the image data (after 1) for defining the Gaussian distribution. Results from a 7-cm device are shown in Figures A3 and A4. The result in Figure A3 indicates that the sharp corner of the device exhibits the greatest leakage current, which corresponds to previous results on the 1-cm devices.

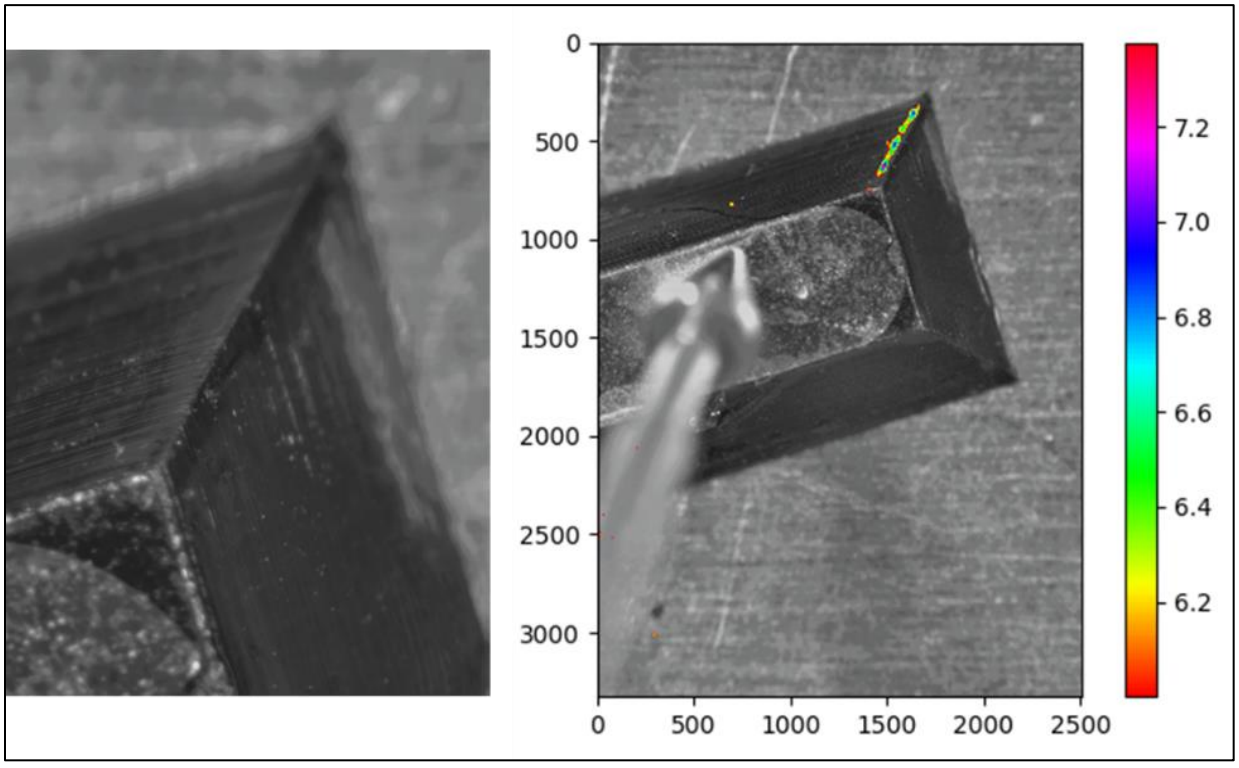


Figure A3. *Electroluminescence on beveled 7-cm SiPCSS. (Right) image of device with electroluminescence overlay. The intensity of light corresponds to the color legend, corresponding to greater leakage current. (Left) Close-up view of device corner where bulk of luminescence was detected along the slightly lighter region of the device edge. This breakdown was observed at 370V and the leakage current measured 370 μA.*

The test was repeated on the opposite end of the switch to determine what, if any, leakage could be identified and those results are shown in Figure A4. These images

indicate that in addition to leakage on the edge of the device, leakage current may be due to poor adhesion of the polyimide, due to the correlation between the lighter regions of the device and the leakage current.

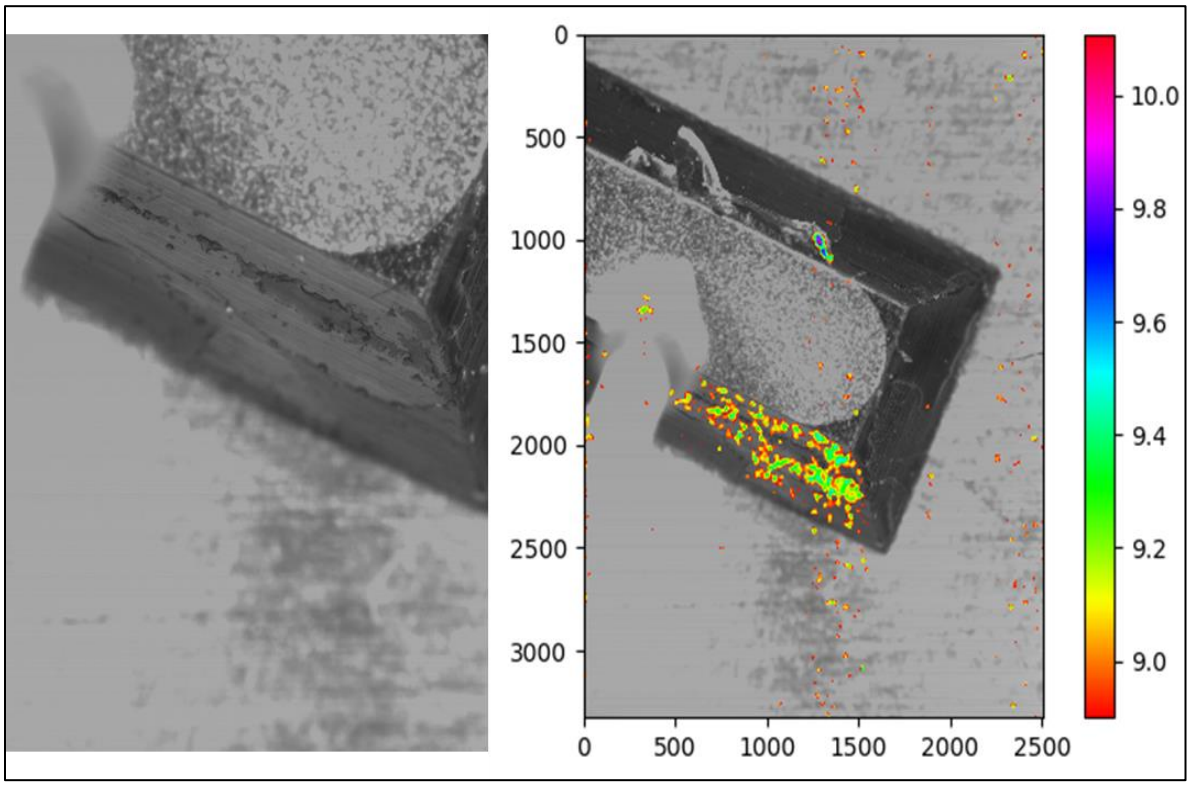


Figure A4. *EL on beveled 7-cm SiPCSS. (Right) image of device with electroluminescence overlay. The intensity of light corresponds to the color legend, corresponding to greater leakage current. (Left) Close-up view of the side of the device where the bulk of the luminescence was detected. This breakdown was observed at 350 V, the leakage current measured 0.33 mA.*

Because the breakdown regions correlate with the sharp edges of the device, and regions where the polyimide appears to be either too thin or having poor adhesion, we expect improvement in the adhesion and/or uniformity of the polyimide passivant to improve the hold-off of the device. The polyimide on these samples appears inconsistent, so it is challenging to confirm how much breakdown is caused by the sharp corner in Figure A3 versus poor polyimide adhesion. Additional EL tests will be conducted on this and similar samples received in order to verify these results. Moreover, devices without the polyamide applied may be useful for comparison, since the non-polyamide coated device will allow us to determine isolate breakdown caused by the bevel angle or sharpness of the edge. Once these devices have reached the same hold-off as the 1-cm devices, we will explore other bevel angles that can be compared to further improve hold-off. Another passivation method that could improve hold-off would be softening the sharp edge at the intersection of the bevels. For any of these examples, more testing is required.

High Power Ultrafast Switch Fundamentals (Bhamidipati)

In addition to continued development of SiPCSS devices, we are also conducting a survey of both optically stimulated (e.g. PCSS) and non-optically stimulated high power ultrafast switching technologies that may enable breakthroughs in microwave technologies. The priority of this effort is first exploring the factors inhibiting the transient response of both PCSS and non-optically stimulated devices to identify technologies with optimal performance (e.g. rise time, reverse recovery). Key properties that may limit the performance of high power devices are those associated with scattering due to high current densities, producing heat and limiting drift velocity. However, scattering phenomena are not the only device and material parameters critical to high power, ultrafast switching technologies. Many properties determine the performance of such devices, including but not limited to those listed in Table A2. These properties are universal to optically and non-optically stimulated technologies and will be further studied to narrow down and identify those most critical to performance.

Table A2. *Macro and micro properties influencing semiconductor switch performance.*

General Semiconductor Properties	
Macro properties	**Micro Properties**
Rise-time	Carrier Generation
Hold-off	Carrier Recombination
Heating	Traps/crystal defects
Recovery	Scattering
Conductance	Dopants
Impedance	Carrier transport
Dark current	Drift and diffusion
Contacts	Injection
Geometry	

In addition to these general parameters, Table A3 lists the parameters that exclusively influence optically-stimulated device performance, which will be studied in parallel with the PCSS-development effort at UMKC. This will include a deep dive into device modeling in TCAD to verify the formulated theory on scattering, parasitic effects in SiPCSS devices and continued literature review to determine the feasibility of implementing non-optically stimulated switching technologies.

Table A3. *Macro and micro properties affecting PCSS specifically.*

PCSS-Specific Properties	
Macro properties	**Micro properties**
Incident energy	Absorption
Wavelength	Phonon assist vs direct
Contact geometry	Sub-band gap states
AR coatings	

Some non-optically stimulated devices such as high electron mobility transistors (HEMTs), drift-step recovery diodes (DSRDs), and impact ionization avalanche transit-time (IMPATT) diodes, may exhibit better thermal properties and bypass the need for laser, reducing costs. In particular, HEMTs which implement 2-dimensional electron gas (2DEG) reduce electron-electron collisions and may further address thermal management challenges.

The goal of this effort is to identify and narrow the fundamental device parameters that enable high-power, ultrafast rise time pulses. The parameters in the above tables will be refined for general and optically stimulated devices, and the parameters specific to non-optically stimulated devices will be added and refined. Additionally, a long term objective is to survey the practical and economical boundaries of each technology including manufacturing processes and technological maturity.

GaN:C PCSS development and Testing

For GaN PCSS, a new test plan has been drafted. The focus of testing with GaN will be to determine the viability of GaN as a material for high-power PCSSs, and determine if the increased cost of this material outweighs the performances increases versus using Si. Considerations in cost-benefit analysis include the cost of manufacture, cost of operation, peak power, required laser costs, thermal requirements, and switch geometry (amount of material needed). Moving forward, a combination of simulations and pulse-testing will be used to determine GaN's viability as a PCSS HPM driver.

To work towards gaining insight on laser requirements and how wavelength of the incident laser affects the on-resistance of GaN, work has been done on setting up the optics of the THG system with the Neolase 1064 nm laser to ensure that the entire gap of the switch is hit with the incident beam. New test fixture designs are being explored and tested for use with the THG system. The fixture (figure A5), that was used with the demo laser is not compatible with the faster picosecond laser system, due to the fixture's contact impedance. Fixtures using PCB with a micro-strip design at 50 Ohm impedance and lower impedances are being made and will be tested with the THG set-up. Manufacturing of the fixture was held up due to the machine to customize the PCB to our needs being down. Once a working fixture is made, on-state resistance measurements will be done using the THG system to obtain measurements at 355 nm, so we can compare these results with previous testing done at 337 nm.

We are still waiting on the demo laser from Opotek, which is expected to arrive in February. We are also researching other laser options for the triggering of GaN devices.

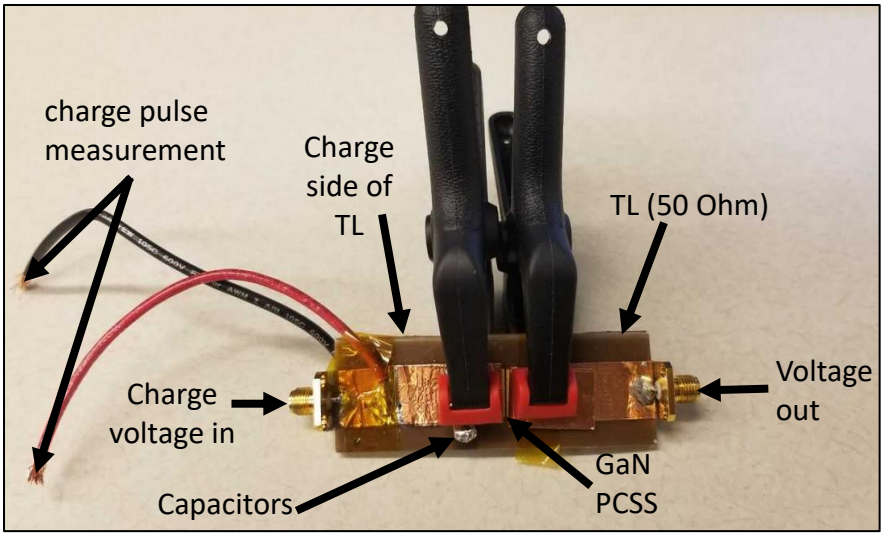


Figure A5*: Test fixture used with demo laser for GaN device testing*

I.A.1 Immediate Tasks of Fundamental PCSS Subgroup

i. Identify cause of 7-cm breakdown and resolve using electroluminescence and other characterization methods.
ii. Determine optimal irradiation dose for optimal recovery time, voltage hold-off, and R_{on}
iii. Improve TCAD model of transient recovery time in PCSS to agree with experimental results.

I.A.2 Expected Products of Fundamental PCSS Subgroup

i. Transmission line for testing the beveled 7-cm switches
ii. Attenuator network for continuous pulse-testing
iii. Student and staff abstracts for DEPS.

I.B GaN:C Subgroup (Rulis)

FLOOXS is now running in a production environment (the Joey computer cluster at UMKC) so that extended calculations (e.g. ones that require more than 1 GB of memory and more than just a few hundred MB of disk space in a virtual machine environment) can be performed fairly easily.

Over the previous two reporting periods we have been able to run and debug pre-made demonstration models of resistors, P- and N-MOS, etc. and we described efforts to gain traction in understanding the methods for specifying FLOOXS simulations. That includes definition of the component models themselves, definition of the interfaces, and how to specify the attributes of new materials that are not present in the material database (e.g. GaN, etc.)). This has been a significant challenge due to the academic nature of the code. Definitions of GaN, AlGaN, AlN, SiC, generic metals and nitrides are given in various definition files but they are not always consistent with each other and with

published literature. This situation has however helped us define a next critical step given below regarding verification of our modeling ability and our understanding of the FLOOXS simulation method.

We have now learned how to produce elementary 1-D and 2-D models of electronic components that include variable concentrations of electrons and holes in doped regions (see Figure 1 example of a 2-D silicon PN diode with computation and subsequent fitting of the I-V curve). This also leads to the next step which is to incorporate (and understand exactly) explicit metal contacts.

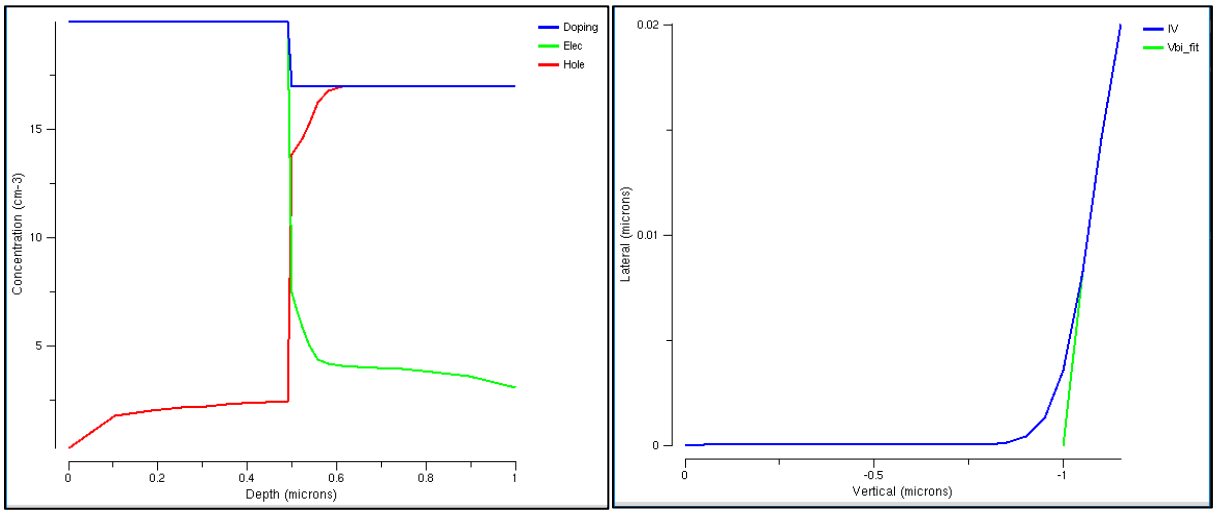


Figure B1*. Two dimensional silicon PN diode: LEFT: Blue – Dopant profile; Green – Electron concentration; Red – Hole concentration. RIGHT: Blue - I-V curve; Green – Linearly extrapolated fit to the I-V curve to obtain built-in voltage at the x-intercept.*

I.B.1 Immediate Tasks of GaN:C Calculations Subgroup

i. Test our ability to direct FLOOXS to correctly model the simple electronic systems we have created so far when fundamental parameters are modified according to known empirical trends (http://www.ioffe.ru/SVA/NSM/Semicond/Si/electric.html). That is, we will use the data given in the references listed in that URL to modify models of the diodes and resistors that we have created so far and compare the I-V curves to verify that the trends we compute are consistent with experimental evidence. This should tell us the degree to which we are really able to direct accurate simulations as we move from Si to GaN.

I.B.2 Expected Products of GaN:C Calculations Subgroup

i. Creation of 2-D models of the target PCSS with metal contacts, interfaces, and all regions defined. This will become the basis for future work once we have understood and feel confident with our abilities to simulate more well-documented Si-based systems. The exact nature of the material regions will need to be defined in future work, but this will serve as the skeleton for that effort.

ii. Si-based electronic models (basic 1-D and 2-D resistors, diodes, etc.) with variations in key parameters (e.g., hole and electron mobility, carrier concentration, all as a function of temperature).

I.C Small Unmanned Aerial Vehicle Diagnostics and Design-of-Experiments (Fields)

Sensor Propagation for Free-Flight Response

After the successful feasibility prototype gimbal mechanism developed in November, a series of alternative approaches were designed. The final platform consists of an aluminum tubing-based square ring system that provides substantially more rigidity in the rings over the initial wooden prototype. The platform has been tested initially, and provides a good environment for stable flight in a constrained environment (initial prototype design induced instability in the flight controller). Currently, the platform is being readied for data collection.

One challenge with the gimbal platform is quantifying the actual aircraft attitude during a noise injection, because the onboard sensors that provide attitude are exactly the ones being targeted. Therefore, a new UAV platform is being incorporated, the Intel Aerodrone, which has separate IMU systems for two onboard computing modules. This platform utilizes the same flight software architecture as the Navio platform currently in use by the cUAV team, but has additional camera capabilities in a low-cost platform.



Figure C2*. Intel AeroDrone UAV platform currently being integrated with existing cUAV architecture.*

Design of Experiments

The K-nearest classification method described previously has been shown on a controlled inverted pendulum simulation with similar performance classifications to the UAV HPM scenario. However, it is important to verify the initial feasibility findings on the UAV platform. In order to conduct these tests, the UMKC GTEM chamber is being readied with the Navio UAV system. Testing is anticipated for mid-January.

I.C.1 Immediate Tasks for Diagnostics/DoE Subgroup

i. Analyze data from DOE 0 testing at all locations;
ii. Investigate individual sensor component propagation through a feedback control system;
iii. Demonstrate feasibility in adaptive experimental design for improved effects results confidence with minimal experiments;
iv. Integrate Intel AeroDrone into cUAV architecture.

I.C.2 Expected Products of Diagnostics/DoE Subgroup

i. Further simulated evaluation of adaptive DOE methods to fully quantify potential benefits of the technique;
ii. Experimental design plan based on results from DOE-0;
iii. More powerful and cost-effective UAV platform for cUAV applications.

I.D Positive Feedback Non-Linear Transmission Line (Khan)

During December 2018, we focused on the development of high-speed NLTL design. Operating frequency of the commercial off-the-shelf (COTS) nonlinear ceramic capacitor based NLTL and schottky diode based NLTL is limited by the dielectric loss, stray inductance and ESR of the nonlinear lines constructed from lumped components. A hybrid NLTL constructed from nonlinear inductor and nonlinear capacitor has the potential of increasing the soliton frequency generated from the NLTL.

We have constructed a closed-loop experimental setup from a schottky diode-based NLTL and power amplifier coupled with BNC type coaxial connectors. In the closed-loop setup, a single trapezoidal pulse with 250 mV amplitude (peak-peak), 50 ns pulse width, rise and fall time of 9 ns is applied at the 4^{th} section (S-4) of a 16-section 1200 V rated schottky diode based NLTL. We have connected the output of the power amplifier to the first section (S-1) of the 16-section NLTL. The last section (S-16) of the NLTL is connected to the input transformer of the amplifier. The 50-Ω 1500 watt rated dummy load is connected to the 14^{th} section (S-14) of the NLTL through a BNC type coaxial connector. A schematic of the closed-loop setup is illustrated in Figure D1.

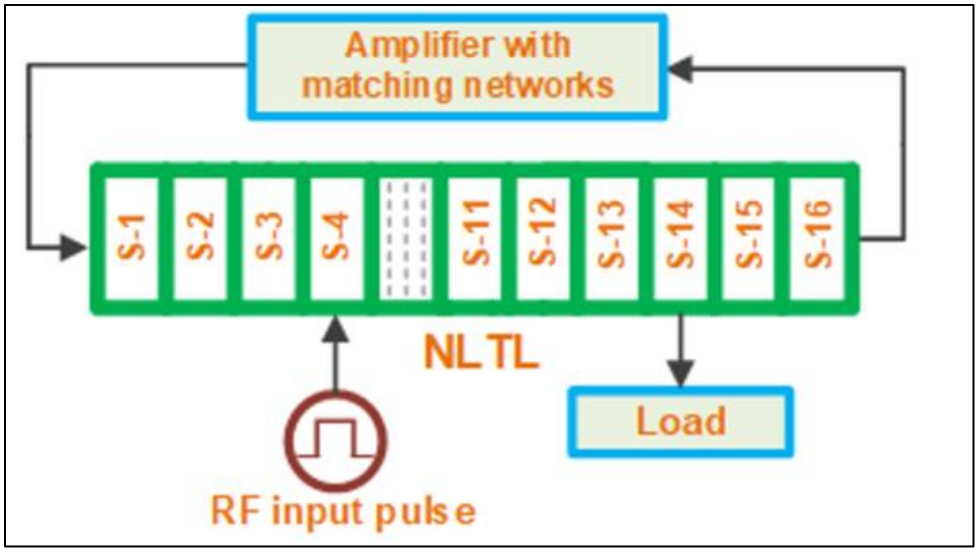


Figure D1*. Simplified block diagram of the closed-loop configuration of the NLTL and power amplifier with external excitation.*

We have obtained RF pulses with effective frequencies of around 120 MHz and 100 MHz from the 14th section and 11th section of the NLTL respectively. Figure D2 illustrates the output measured across the 50 Ω dummy load.

However, the Bragg frequency of the line and ESR of the lumped components limit the maximum achievable frequency from this NLTL. The Schottky diode exhibits decreasing junction capacitance with respect to increasing reverse voltage across it. The maximum and minimum junction capacitances of the selected diode are 180 pF and 12 pF respectively. The effective Bragg frequency of the constructed NLTL can be calculated as:

$$f_c = \frac{1}{\pi\sqrt{(L*C(V_{max}))}} \qquad (1)$$

The effective Bragg frequency of the line, if lossless, is around 225 MHz considering the lumped inductance is 100 nH. However, stray inductances, dielectric losses and ESR losses limit the effective frequency of the generated solitons.

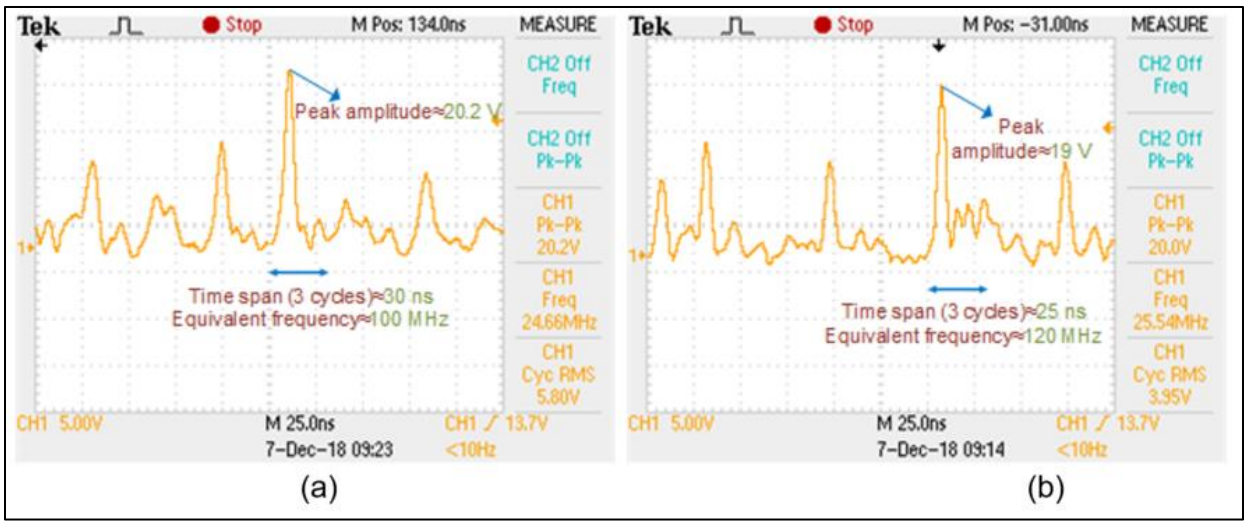


***Figure D2**. Output across a 50 Ω dummy load connected to the (a) 11th section of a 16-section NLTL (b) 14th section of the same 16-section NLTL.*

We are designing a hybrid NLTL constructed from ferrite beads and reverse-biased schottky diodes. The ferrite bead from Fair-rite shows strong nonlinearity in inductance as increasing current through it causes saturation resulting in diminished inductance. We have chosen a new schottky diode from CREE with stronger nonlinearity compared to the previously used ones. The maximum and minimum junction capacitance of the diode is about 750 pF and 30 pF respectively. We have modeled the nonlinear inductor in LTSpice with a flux equation as given by:

$$Flux = 150nH * 5 * \tanh(\frac{x}{5}) \qquad (2)$$

We have performed simulation on a 24-section hybrid NLTL in LTSpice. A pulse with 10 ns rise and fall time, 30 ns on time, and 2000 V peak amplitude is used as the excitation for the NLTL. The simulation result is illustrated in Figure D3.

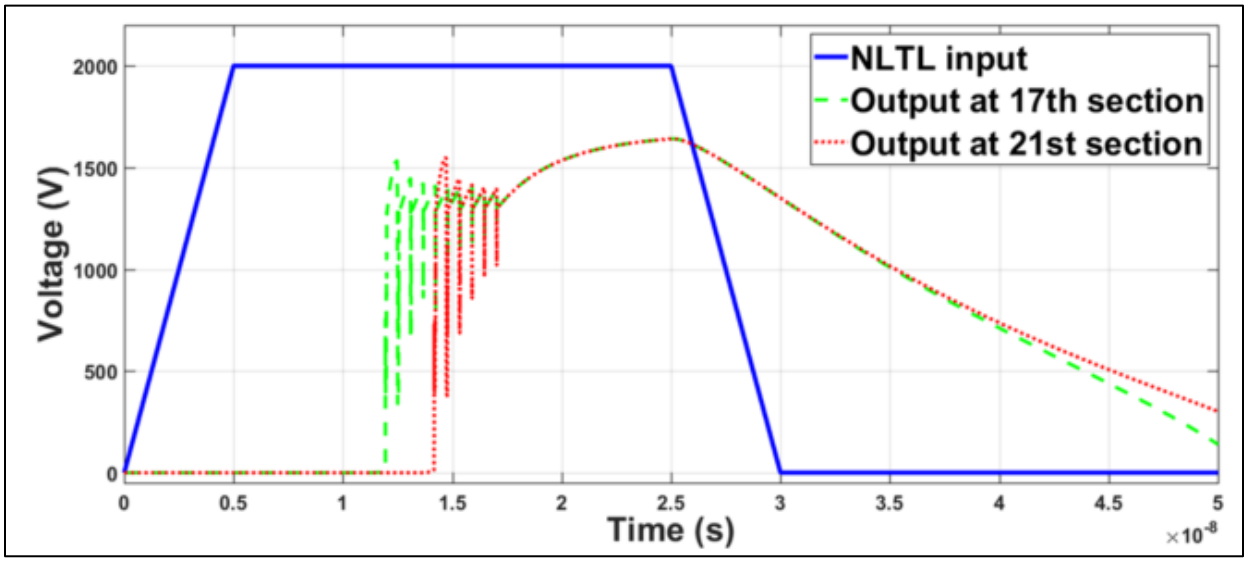


***Figure D3**. Simulation output from the 17th and 21st section of a 24-section hybrid NLTL.*

The simulated effective soliton frequency from the hybrid NLTL model is around 800 MHz. Another significant observation is that oscillation count increases with the number of sections in the NLTL, and soliton frequency increases with the increase of input pulse amplitude. Crosslink capacitor is another feature that can be incorporated in the NLTL design. They can increase the voltage modulation depth of the output RF pulse at the expense of the cutoff frequency of the line.

We are designing another NLTL without using a lumped inductance to increase the cutoff frequency of the line. We will use the self-inductance of 18 AWG wire in addition with the reverse-biased schottky diodes to construct the NLTL. The inductance of a cell constructed from the 18 AWG wire is given by [1]:

$$L = \frac{\mu_0}{\pi} * l * [ln\frac{d}{b} + 0.5 * \left(\frac{d}{b} + 1\right)^2 \ln(1 + \frac{d}{b}) + 0.5\left(\frac{d}{b} - 1\right)^2 \ln(1 - \frac{d}{b}) \ ] \qquad (3)$$

Here l is the length of a cell of the NLTL, d is the distance between the centers of conductors, b is the diameter of the conductor, μ_0 is magnetic constant. For the line that will be used in the experiment, b= 1.02 mm, d=1.9812 mm, and l= 12 mm, resulting in an inductance of about 26 nH. The effective Bragg frequency of this line if lossless is around 520 MHz calculated from (1).

We will fabricate another NLTL prototype with multiple series connected diodes to further decrease the effective capacitance of a cell of the NLTL to increase the cutoff frequency of the line.

In addition, we are working on the modification of the output-matching network of the power amplifier. At present, we are planning to replace the existing transformer with a different model, which can operate up to 300 MHz.

I.D.1 Immediate Tasks for the Positive Feedback NLTL Subgroup

i. Fabricating a hybrid NLTL and obtaining experimental results.
ii. Fabricating fixed inductor-less NLTL and obtaining experimental results.
iii. Fabricating and testing NLTL with multiple diode configurations.
iv. Performing high voltage tests on different NLTL prototypes.

I.D.2 Expected Products of Positive Feedback NLTL Subgroup

i. Designing an RF amplifier with operating frequency in the range of 400 MHz - 600 MHz with 100 MHz bandwidth.
ii. Optimizing NLTL design for high frequency and high power soliton generation.

References

[1] P. V. Priputnev, I. V. Romanchenko, V. V. Rostov, O. B. Kovalchuk and V. V. Barmin, "Nanosecond Front Dynamics and RF Oscillation Generation in a Transmission Line with Nonlinear Capacitors," 2018 20th International Symposium on High-Current Electronics (ISHCE), Tomsk, 2018, pp. 85-88.

I.E Applied RF Coupling Simulation and Modelling to/for sUAV (Hassan)

CMA of Wires Above a Dielectric UAV Frame

As we illustrated in the previous MSRs, the frame shape and material controls the resonance frequency, bandwidth, and the current distribution of the modes of the structure. Also, we showed that frame modes can affect the external electromagnetic coupling to the wires mounted to it. We have started using small wires as a very crude model of an electronic component to test the effect of the frame in such small components.

This month, to demonstrate how the relative location and height of the realistic wire can affect the EM coupling, we studied the coupling to three identical wires, wire length = 135 mm, wire radius= 0.25 mm, wire height above the frame is firstly fixed as 1 mm, at different locations above Version 1 of the UAV. These wires are longer than what we considered in the previous MSRs and are therefore more practical. Every MSR, we will progressively increase the complexity of the wiring system studied until eventually a realistic wiring system is considered. This report focusses on the case when the frame is composed of a dielectric medium with a relative permittivity of ~ 3.3 (corresponding to NAYLON66 as a practical material typically used for UAV frames).

In contrast to the PEC frame, the modes of a dielectric frame with PEC wires, similar to that shown in Figure E1a, is dominated by the modes of the wires. That is, the hotspots in the current distributions of the frame+wires will be located on the wires and not on the frame. If the wires in Figure E1a, are placed in free space (i.e. far away from the dielectric UAV frame) their Modal Significance Spectrum will be as shown in Figure E1b. In this case, the resonance frequency of Mode 1 will be approximately at ~ 1.1 GHz. However, adding the wires to the frame results in a red shift in the first resonance of the wire as illustrated in Figure E1c to 0.9 GHz.

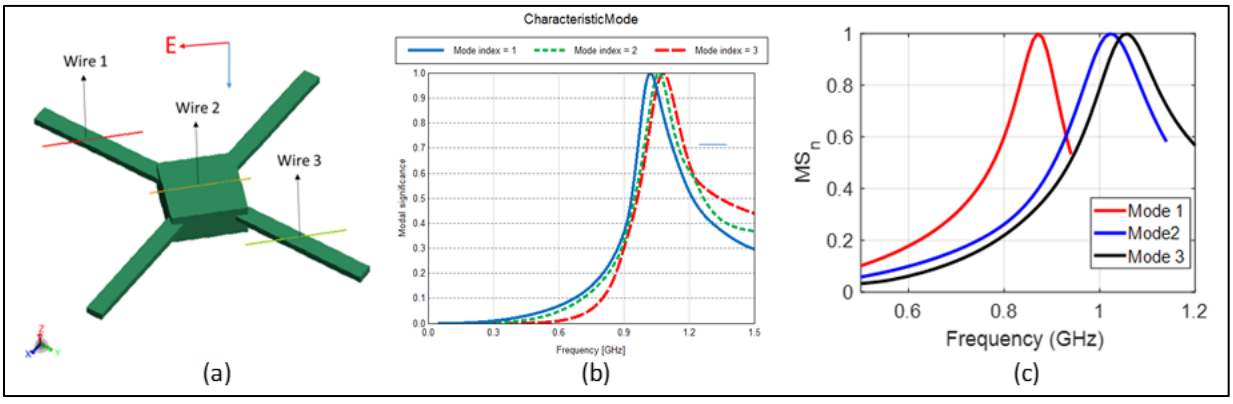


Figure E1. *(a) Frame model of the UAV and wire distribution, (b) Modal significance of the three wires in free space, (c) Modal significance of the three wires above dielectric UAV frame.*

In Figure E2, we further study the effect of the dielectric UAV frame on the modes of the wire by varying the height of the wire above the frame. Figure E2 shows the coupled current at the center point of Wire 2. For large heights above the frame, larger than 5 mm, Wire 2 acts as if it is in free-space exhibiting a resonance in the coupled current

around 1.1 GHz. As the height decreases below 5 mm, the maximum in the coupled current shifts to just below 0.9 GHz, and a less significant peak is still exhibited near 1.1 GHz which is the pristine resonance frequency of the wire in free-space. This study illustrates the effect of the wire separation and frame material on the coupling current. It also, illustrates how CMA can be used to identify the optimum coupling frequency of a wire system in a complex environment such as in the vicinity of a dielectric UAV frame.

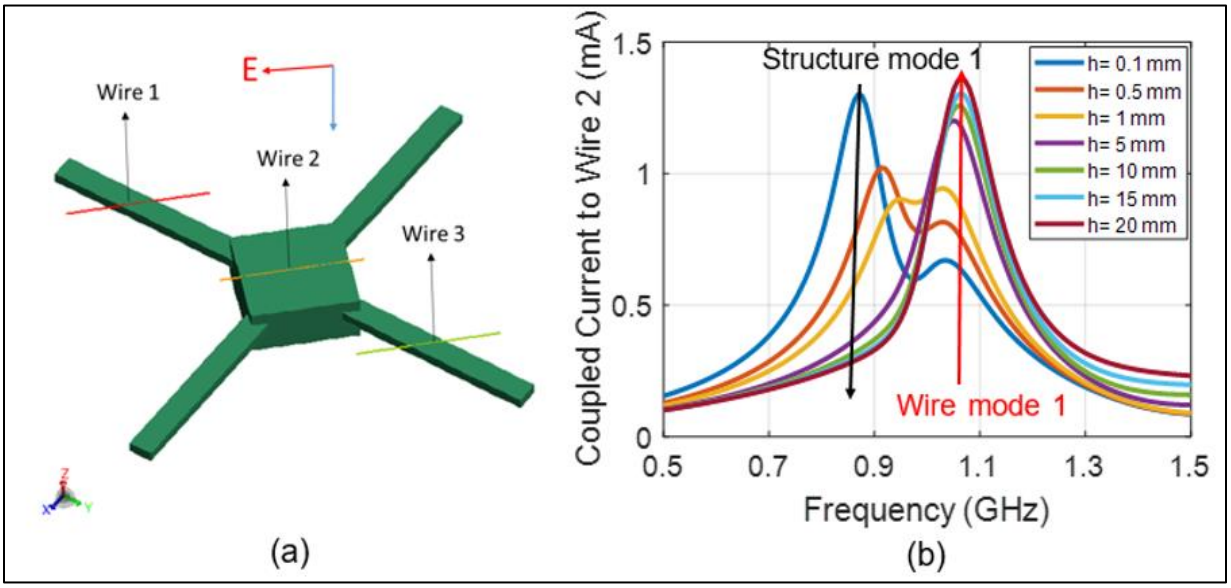


Figure E2. *(a) Frame model of the UAV and wire distribution (b) Total coupled current at the center of Wire 2 for different heights above the dielectric frame.*

CMA of a Printed Circuit Board (PCB) Above a Dielectric UAV Frame

The CMA of wires in the previous subsection, can also be utilized to quantify coupling to the PCBs typically found in UAVs. Simple PCB geometries will be evoked as a crude model of the flight controller kit on the frame. The board dimensions is composed of a perfect electric conductor (PEC) sheet with an FR4 substrate ($\varepsilon_r \sim 4.4$) on top. The lateral dimensions of the PCB model are set to 56 mm x 85.6 mm. We performed the CMA analysis of the board in free space and above the UAV dielectric frame ($\varepsilon_r \sim 3.3$) described in the previous Subsection. Figure E3 shows the Modal Significance of Mode 1 for 3 different configurations: (i) the UAV frame, (ii) the PCB in free space, (iii) the PCB above the UAV frames. Mode 1 of the frame by itself (purple curve) and the PCB by itself (dotted yellow curve) is broadband and resonate at a high frequency which means that the coupling path to each component individually is poor at lower frequencies. However, adding the PCB on top of the frame changes the behavior of Mode 1 completely. Mode 1 becomes narrower and its resonance frequency exhibits a redshift. This illustrates that the composite UAV+PCB structure has a good coupling path at lower frequencies relative to the individual components.

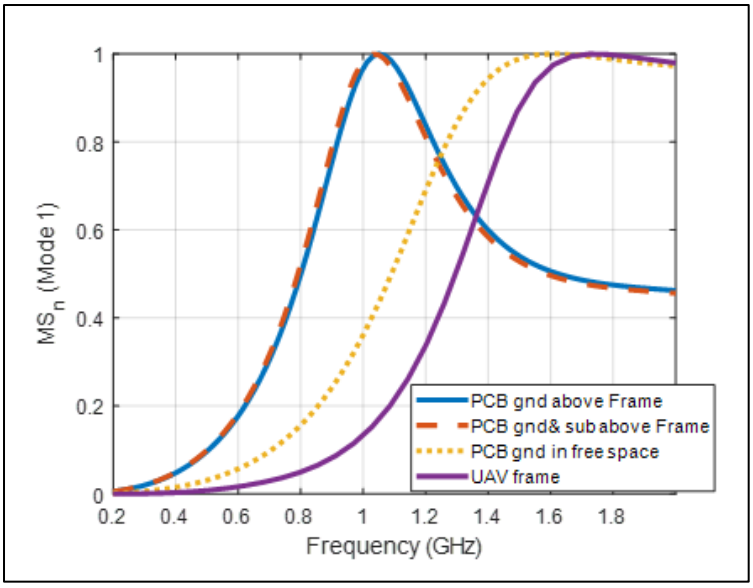


Figure E3. *Modal significance of various configurations of the PCB+UAV frame.*

To illustrate the usefulness of the modal analysis of this structure, a dielectric frame with PCB is studied in Figure E4. Figure E4a shows the Modal Significance of the first 4 modes of the PCB+UAV structure. The PCB is modeled as a PEC sheet mounted above the central part on the frame where the modes of the dielectric frame exhibit significant hot spots. Comparing Figure E4b and Figure E4c shows that the maximum coupled currents at 1 GHz, the resonance frequency of Mode 1 of the PCB+UAV, is 54 mA/m which is almost double that at 1.4 GHz, the resonance frequency of the PCB by itself. Therefore, the frame of the UAV can affect the optimum coupling frequencies of its individual electronic components.

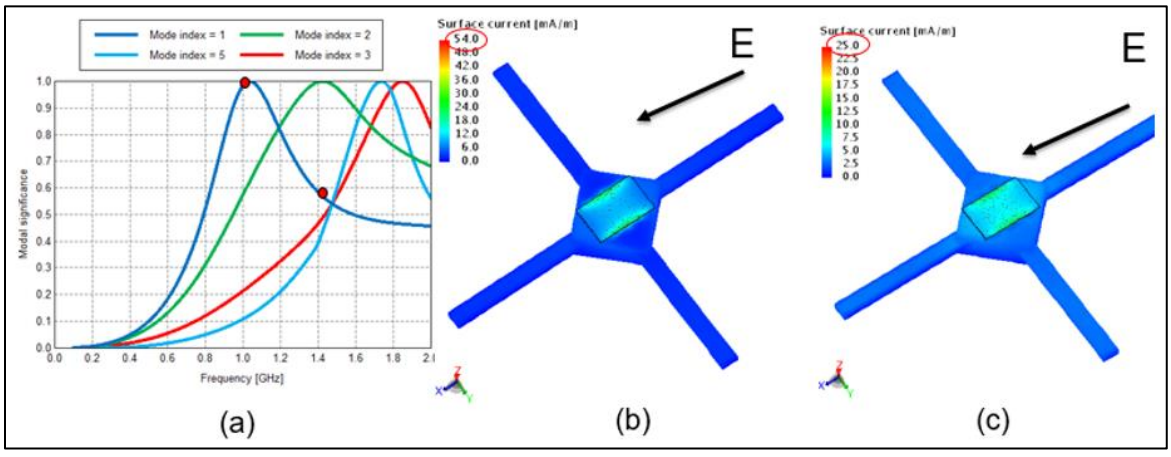


Figure E4. (a) Modal significance of the structure. (b) Total coupled current to the structure at 1GHz. (c) Total coupled current to the structure at 1.4 GHz.

The resonance frequency and bandwidth of Mode 1 were plotted versus the relative permittivity of the frame and presented in Figure E5a and E5b respectively. A fitting tool is used to obtain an expression that can be used to show the effect of the frame material on the resonance frequency and bandwidth of the first mode of PCB+UAV frame. For a

fixed PCB-frame separation, the resonance frequency of the first mode, which is the dominant mode at low frequencies, can be estimated as follows:

$$f(\text{GHz}) = 0.86 + 0.9/\varepsilon_r - 0.02*\varepsilon_r \quad (1)$$

The bandwidth of the mode can also be estimated using the following formula:

$$BW(\text{GHz}) = 1.6/\varepsilon_r - 0.073 \quad (2)$$

For example, if the UAV frame material is a dielectric with $\varepsilon_r = 4.4$, using (1) and (2) we expected that the resonance frequency of the first mode of the structure will be ~ 0.97 GHz and the bandwidth will be ~0.29 GHz.

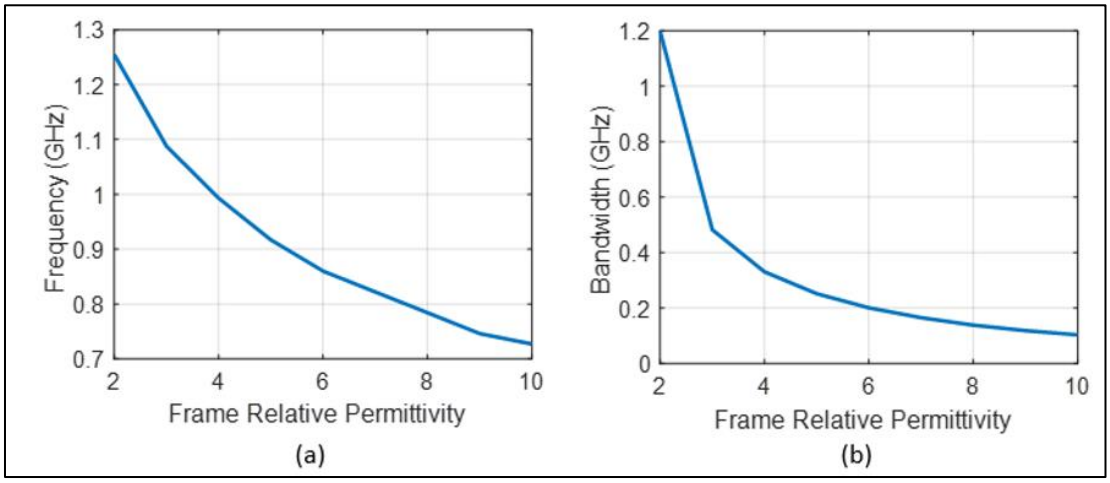


Figure E5. *(a) Resonance frequency of Mode 1 for different frame dielectric material. (b) Bandwidth of mode 1 for different frame dielectric material.1.4 GHz.*

I.E.1 Immediate Tasks for RF Coupling Subgroup

i. Apply CMA on the CAD model of the actual flight controller kit.
ii. Study more realistic wire and PCB systems above dielectric UAV frames

I.F UMKC Diode Network Based NLTL (Doynov)

Introduction and Problem Scope

For an introduction to the scope of work on Diode-based Non-linear Networks (D-NLN) transmission lines, please see previous reports (originally titled Diode NLTL and changed to avoid confusion with other diode based NLTL work). For a brief reference, Figure F1 illustrates the waveform generated using a D-NLN. UMKC efforts are focused on lumped elements networks, in general, and diode-based voltage dependent capacitance in particular. In all current designs we use reversely-biased diodes as a variable capacitance.

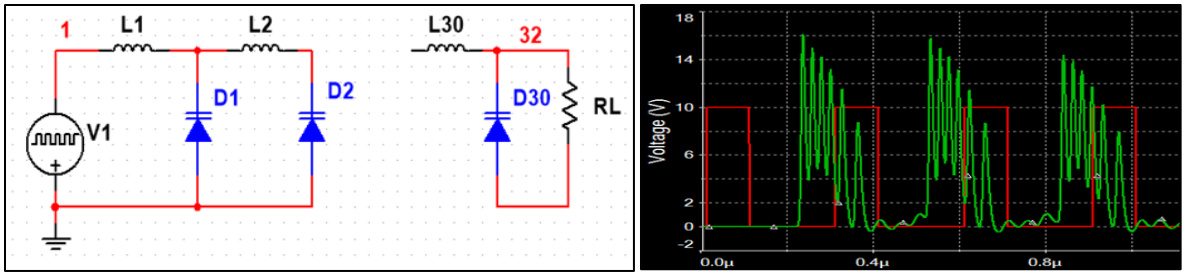


Figure F1*. Schematic presentation of lumped elements D-NLN (left) and the voltage waveform at the output when a sequence of rectangular pulses is applied at the input (right).*

D-NLN Design Considerations

We continue the exploration of design parameters primarily driven by the following factors:

i. Simulation validation of previously developed designs with commercial off the shelf parts;
ii. Ability to generate waveforms that will produce frequency in the desired bandwidth;
iii. Efficiency of the D-NLN transmission line;
iv. Excitation with currently available pulse sources.

These approaches are driven by the prototyping and design validating stage of our work. In this regard, we build and test the new designs with low-voltage, low-power parts (readily available components). The preliminary design validation verifies device operation and extends the ability to observe and understand the effects of a network's practical implementations in regards to: PCB layout, parasitic inductance, capacitance, impedance matching, and efficiency. The next step is implementation with high-voltage, high-power components. While theoretically the scalability is straightforward, in practice additional factors play roles. Some of those factors include high voltage standoff and the availability of high current inductors. High standoff voltage is achieved with a serial cascading of multiple diodes which presents additional constraints to PCB layout. High-current inductors, which are applicable to D-NLN are not readily available at the values required based on the design. To shorten the design to test cycle, designs need to be modified based on the available components.

Issues

As indicated in the previous reports, some of the D-NLN parameters cannot be defined precisely based on simulation only and will be available after the initial implementation and testing. Many design issues and component specifications remain to be investigated. A separate constraint is that most available models and components are low voltage and the purpose of the studies is HPM generation. Some of the relatively high-voltage COTS devices do not have publically available electrical characteristics and the C versus V responses must be measured prior to implementation. The same applies to the use of serially-stacked diodes, where proper practical impedance matching continues to be an important aspect of investigation.

I.F.1 Immediate Tasks for D-NLN Research

i. Continue parameter space investigation based on simulation;
ii. Build, test and compare empirical to simulation based D-NLN;
iii. Modify simulated designs to replicate the observed effects in the practical implementations;
iv. Focus on improving the network efficiency; and,
v. Collaborate with EHT for the simulation, evaluation and testing of HV D-NLTL.

I.F.2 Expected Products of D-NLN Research

i. Comprehensive D-NLN parameter space evaluation.
ii. Design and implementation of D-NLN working prototypes.
iii. IP and presentations/publications on the topic.

I.G Focus Wave Modes (FWM) and Electrically Small Antennas (ESA) (Chatterjee)

The efforts in the two research directions are described as below. As before (see October 2018 revised MSR), the major efforts are for parametric characterizing of a planar phased array. The previous report summarized the basic array parameters and element electrical size. The Taylor distribution was assumed to determine the appropriate array length for the specific beamwidth. However, the array excitation weights and beam steering phase shifts are not calculated; these will be determined for a full-wave simulation for future work. The main results of the previous effort that are used here are as below:

Electrically Small Antennas (ESA)

ESA (beam steering array) studies were initiated for the following nominal set of specifications:

a) Frequency: **400** MHz
b) Number of elements: $\mathbf{14} \times \mathbf{14}$ (square planar array)
c) Gain: (1) Electrically small element gain: **2.97** dB
(2) Array peak gain at boresight: **25.85** dB
d) Element size (ESA): $ka = 0.72$

The main objective is to find out the array size, but the other antenna parameters such as: 3 dB beamwidth, 1st sidelobe level and the interelement spacing in both planes are unknown. These parameters are needed in the array size characterization and hence will have to be chosen *a-priori.* Assuming a square planar array of 196 elements, suggests that a pencil beam can be realized with equal beamwidth in the orthogonal planes. For a small- to medium-sized phased array, one can assume some system loss and hence choose the aperture efficiency as $\epsilon_{ap} = 0.9$. The maximum value is obviously unity (no losses). The gain and directivity can be written as [2]-[4]:

$$G = \epsilon_{ap} D \qquad (1)$$

If the pencil beam is scanned to an angle θ_s from the boresight (zenith) then the directivity is given by [2, p. 24, Eq. (1.67)] as:

$$D = \frac{32400}{(\Theta_{3dB})^2} \cos\theta_s \qquad (2)$$

In (2) it is assumed that a pencil beam is generated that has equal 3 dB beamdwidths in the orthogonal planes. For a pencil beam pointing to the boresight ($\theta_s = 0^0$), the 3 dB beamwidth is thus given by:

$$\Theta_{3dB} = 8.7^0 \qquad (3)$$

Because we are assuming a square (14×14) array the remainder of the analysis simplifies to that of a linear array assuming the principle of separability of pattern distributions [2, p. 18, Eq. (1.60)]. We shall now look at Taylor distributions. The Taylor distribution is used to determine the amplitude excitation weights across the array. For beam steering, a linear progressive phase shift can be applied. The gain and the sidelobe levels are necessary to determine the amplitude excitation weights. However, in this MSR we shall be gainfully using the relationship between array length, 3 dB beamwidth and the 1st sidelobe level. From [4, pp. 453-459] the relationship between beamwidth, sidelobe level and array size (length L) reads:

$$\Theta_{3dB} = 2\sin^{-1}\left\{\frac{\lambda\sigma}{\pi \mathrm{L}}\left[(\cosh^{-1} R)^2 - \left(\cosh^{-1}\frac{R}{\sqrt{2}}\right)^2\right]^{\frac{1}{2}}\right\} \qquad (4)$$

Equation (4) can be used to determine the (linear) array length L for a specific sidelobe level, and a beamwidth, with the attendant assumption that the (excitation current) amplitude distribution across the array follows a Taylor form [4, p. 457, Eqs. (10-91, 92)]. However, we need to choose the beam *dilation* factor σ. The beam dilation factor is calculated from [4, p. 456, Eq. (10-81)] as:

$$\sigma = \frac{\bar{n}}{\sqrt{A^2 + \left(\bar{n} - \frac{1}{2}\right)^2}} \qquad (5)$$

In (5), for a specific sidelobe level, R, the quantity A is defined, $A = \frac{1}{\pi}\cosh^{-1} R$. Finally, the quantity $\bar{n}$ designates the equal number of sidelobe levels close to the main beam. Typically, $\bar{n} = 3$ for small and medium size arrays. Thus for a fixed beamwidth as given by (3), one can choose various sidelobe levels and determine the various array lengths $\frac{\mathrm{L}}{\lambda}$ and hence the array size. Equation (4) is used normally by assuming a fixed sidelobe level and an array length, to determine the 3 dB beamwidth. In our situation we are using it in an inverse manner. Whether the results are acceptable or not can be determined from the full-wave analysis.

***Table G1**. Array length for an array gain of 35.85 dB and beamwidth 8.7 degrees assuming Taylor distribution.*

Sidelobe Level R	$\bar{n} = 3$		$\bar{n} = 5$	
	Dilation Factor σ	Array Length $\frac{L}{\lambda}$ (linear)	Dilation Factor σ	Array Length $\frac{L}{\lambda}$ (linear)
316.228 (-25 dB)	0.92737	8.117467	1.010878	8.848433
1000.0 (-30 dB)	0.86238	8.212558	0.9786711	9.319125
3162.288 (-35 dB)	0.801446	8.201700	0.9447122	9.667833
10000.0 (-40 dB)	0.74565	8.126610	0.91003912	9.918237

The results indicate that the square planar array has a linear dimension between: $8.0 \leq \frac{L}{\lambda} \leq 10$. However for a frequency of 400 MHz this could imply a very large array. The interelement spacing for this array is given by $d = \frac{L}{(N-1)\lambda}$. This means for $\mathrm{N} = 14$, the interelement spacing $0.615\lambda \lesssim d \lesssim 0.769\lambda$. This result is way higher than the standard half wavelength spacing between adjacent elements to avoid the occurrence of grating lobes.

For a sidelobe level of -15 dB and the same values of gain and beamwidth the above procedure, when repeated, gives an interelement spacing of $d = 0.57\lambda$. This is close to the standard $\frac{\lambda}{2}$ spacing in an array.

Summary

The results obtained by assuming a peak array gain value of 25.85 dB obtained from the Harrington limits yields the linear dimension of a square planar array that subsequently yields an interelement spacing $\geq \frac{\lambda}{2}$.

The results suggest that substantially more parametric studies are necessary to define the array topology. This work is currently in progress.

References

[1] John L. Volakis, Chi-Chih Chen and Kyohei Fujimoto, *Small Antennas: Miniaturization Techniques and Applications*. NY, USA: McGraw-Hill, 2010.

[2] R. J. Mailloux, *Phased Array Antenna Handbook* (3rd ed.). Norwood, MA, USA: Artech-House, 2018.

[3] A. W. Rudge, K. Milne, A. D. Olver and P. Knight (eds.), *The Handbook of Antenna Design* (vol. 2). London, UK: Peter Peregrinus, 1983.

[4] W. L. Stutzman and G. A. Thiele, *Antenna Theory and Design* (3rd ed.) Hoboken, NJ, USA: John-Wiley & Sons, Inc., 2013.

Minimally Dispersive Waves (Electromagnetic Pulse Propagation)

The pulse radiation from a waveguide circular aperture excited in a TE_{11} mode is being analyzed differently than the Wiener-Hopf analysis in [1]. The equivalence principle and image theory concepts [2, ch. 3] are utilized to obtain the forward radiation from the pulsed waveguide aperture.

[1] T. T. Wu and H. M. Shen, "Radiation of an Electromagnetic Pulse from an Open-ended Circular Waveguide," Proc. SPIE, 1988, pp. 329-337.

[2] R. F. Harrington, *Time Harmonic Electromagnetic Fields*. NY, USA: McGraw-Hill, 1961.

I.H Cost Estimates and Engineering

Background and Task Justification

This section provides the initial overview of our attempt for cost estimation/engineering as they relate to the objectives of the OSPRES program (i.e., downselect and innovate to a transitionable system). The final capability or asset produced must depend on what can be *afforded* and *justified* by both the developer and a resource sponsor. We attempt to answer, "What can be done to make a field-able cUAV capability available within a given non-recurring engineering, innovation, and acquisition budget?"

Currently, the development of PCSS-based HPM sources is not a SWaP-C driven program. We have started the process of cost estimation to demonstrate the importance of cost in achieving the objective of the OSPRES program: development of a transitionable system. We describe how cost elements are structured within the various categories of materials, modules, labor, and other resources; state the purpose of cost accounting and its importance; and finally describe how these cost elements and cost structures can be used for the purpose of cost engineering and management.

As we approach the tasks associated with cost estimation, we are determined to embrace the recent developments in cost engineering processes [1]. These will involve the identification of all cost elements, their interdependence and limiting roles in order to provide alternatives. In other words, if a given cost element is outside of an acceptable cost range, we will utilize scientific, engineering, and management means to "engineer" the cost within an acceptable range.

In a series of reports by research laboratories and independent contractors, the issues associated with cost and the methods to improve the tools used to estimate the costs of future weapon systems have been addressed. Arena et al. [2] quantifies the magnitude of historical cost growth of weapon systems, and Younossi et al. [3] examines both completed and ongoing programs to determine whether a trend has developed since the 1970s. The RAND Corporation [4] presented a study that examines 35 weapon-system acquisition programs to determine the sources of cost growth. In 2014, the National Auditing Office published the "Forecasting in government to achieve value for money" document with the vision to help the nation spend wisely [5]. The U.S. Government

Accountability Office (GAO) published a report in 2015 on the “key factors that drive transition of technologies” as related to DARPA [6]. The document reviews the reasons why successfully completed technology projects failed to transition to a Program of Record (PoR). It also has a clear illustration of the DoD Technology Management Process which is presented in Figure H1.

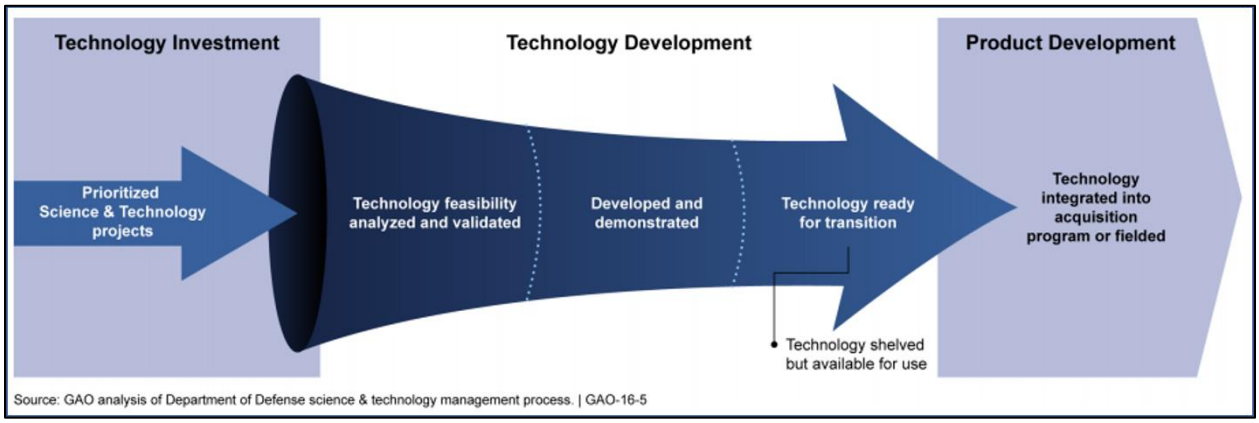


Figure H1*. DOD Technology Management Process.*

In its “Transition & Commercialization Strategy Development Guide,” DARPA Small Business Programs Office, lists the “best practices” for a successful transition and the “balance of the right level of cost vs, functionality” is toward the top of the list [7]. Other documents analyze the reasons for transition failures and provide an insight for the need of a clear plan for transition in addition to technological breakthroughs and demonstrated capabilities. The 2018 National Defense Strategy has placed an emphasis on a culture of performance and affordability that operates at the speed of relevance. This shift impacts how the Acquisition Workforce executes program objectives to enable them to remain relevant and maintain a competitive edge. It is our intention to address the importance of cost engineering on the OSPRES program HPM technology development for a successful transition to a PoR. We have identified that cost is a major factor for avoiding the scenario of “technology shelved but available for use” (Figure H1).

Objectives of Cost Engineering Task

After completing this task, we will be able to:

i. Understand what formulates all aspects of cost - i.e., the resources (materials, COTS, labor, etc.) and activities that are needed to accomplish the project’s goal;
ii. Understand the distinction between cost elements that are either directly or indirectly applied to an asset;
iii. Relate the cost elements to the life cycle of the produced asset: acquisition, use, and disposal;
iv. Use the understanding of cost elements to further understand how cost is measured, applied, and recorded to arrive at the total activity and/or asset cost;
v. Apply the knowledge gained to solve problems related to cost element source, definition and ability to re-engineer them.

There are several challenges that we foresee in the cost estimation process:

a. Level of accuracy (quality) – how to validate and ensure that we have fully comprehended the cost elements, cost drivers, constraints and limitations in order to derive best possible cost estimates;
b. Consistency – the efforts to provide valid cost estimates often lead to the use of different estimating methodology, which means that the granularity and the outcomes of cost forecasts change over time. Comparing a top-down parametric estimate to a bottom-up analytical forecast may be used and may lead to different results. The challenge is further problematic when the cost estimate needs to be compared to actuals or historical data of unknown or debatable origin;
c. Coordination of cost estimation – we cannot generate a cost estimate in isolation. Even a methodical, well-intended and rigorous cost forecast needs to engage the participation of all stakeholders. In this regard, we will work with all stakeholders to be able to receive and coordinate their inputs (involving the so called "negotiation" method);
d. Security and information access – for the current project we are very cautious with information and data. Classified or confidential information may prevent the collection of information and also limit the process of requests for information. This presents a challenge to develop a cost database;
e. Resource and schedule constraints – while the cost estimation task was not intended initially, its importance for achieving the project goals has been determined and we are allocating resources to work on the cost estimation and cost engineering task in parallel.

Cost Factors and Cost Estimation Methods

Cost is associated with one of the three fundamental attributes of a project activity for product development: (1) price (overall cost: direct and indirect cost, R&D, NRE, O&M); (2) features (performance – operational capabilities); and (3) availability (schedule – time to deliver). As related to the current program, Figure H2 illustrates the cost factor as one of the three success aspects of product development and adoption.

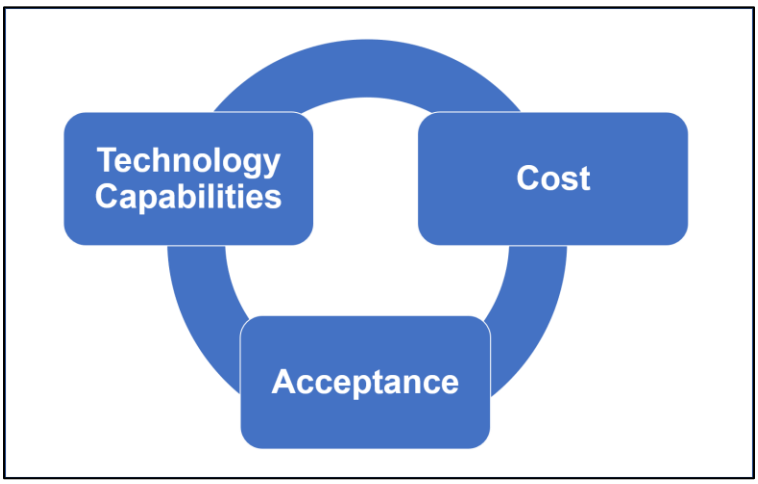


Figure H2. *Three main factors for technology adoption.*

The technology has to provide the expected counter-UAV capabilities (cUAV) with respect to frequency content and power density at the target for the intended level of effect and at the desired range of effectiveness. Scalability for different assets protection, robustness, ease of deployment, operation and maintenance with a sufficiently long time between failures are also key features. The acceptance of the technology is driven by the pressing need for a successful cUAV solution. However, additional social and political factors play important roles: ability for controlled operation as intended and a guaranteed level of confidence for unwanted and unexpected issues associated with the use of the technology. In summary, the developed technology has to provide the confidence to deliver effects as specified. Extended to socio-economic aspects, the cost to develop, deploy and operate is the third critical factor.

The goal to develop a transition capable system depends on proper cost considerations, including cost estimation and cost forecasting. While the cost estimations consider the costs associated with current immediate project activities, systems and services, the cost forecasting tends to consider the next generation of projects, systems and services, perhaps a decade into the future. Our goal is to successfully develop a transitionable system with a realistic and justifiable cost that will meet the mission requirements to provide the optimal cUAV services. Our initial task is understanding the cost estimation process, learn and apply the governing rules and best practices, and utilize available tools to develop a realistic view of the overall cost of our current projects. This approach evaluates the cost of system today, at its current level of maturity and at low volume. The next effort will be cost estimation of the next generation of system(s) with innovation-based value added in each subarea. This will produce a cost forecasting for 2020 – 2025 years and will include best-effort evaluation of enabling technological advancements, prediction of evolving needs and development of strategic counter-measure solutions.

Forecasts are very similar to estimates and are related to future activities and assets. Cost estimates involve establishing the budget at completion for a given performance baseline. Forecasts are predictions of the cost to complete or estimate to complete for cost elements that have not started. Therefore, a sound cost forecast will be based on cost element data from inception of the project work to the date of the forecast, the cost trend of that data compared to accomplishments, and a cost estimate of the work [1]. We are in the process of acquiring and reviewing available documents related to DoD cost estimation processes. The “Independent Government Cost Estimate (IGCE) “Handbook for Services Acquisition” [8] defines the 7-step Services Acquisition Process as shown in Figure H3.

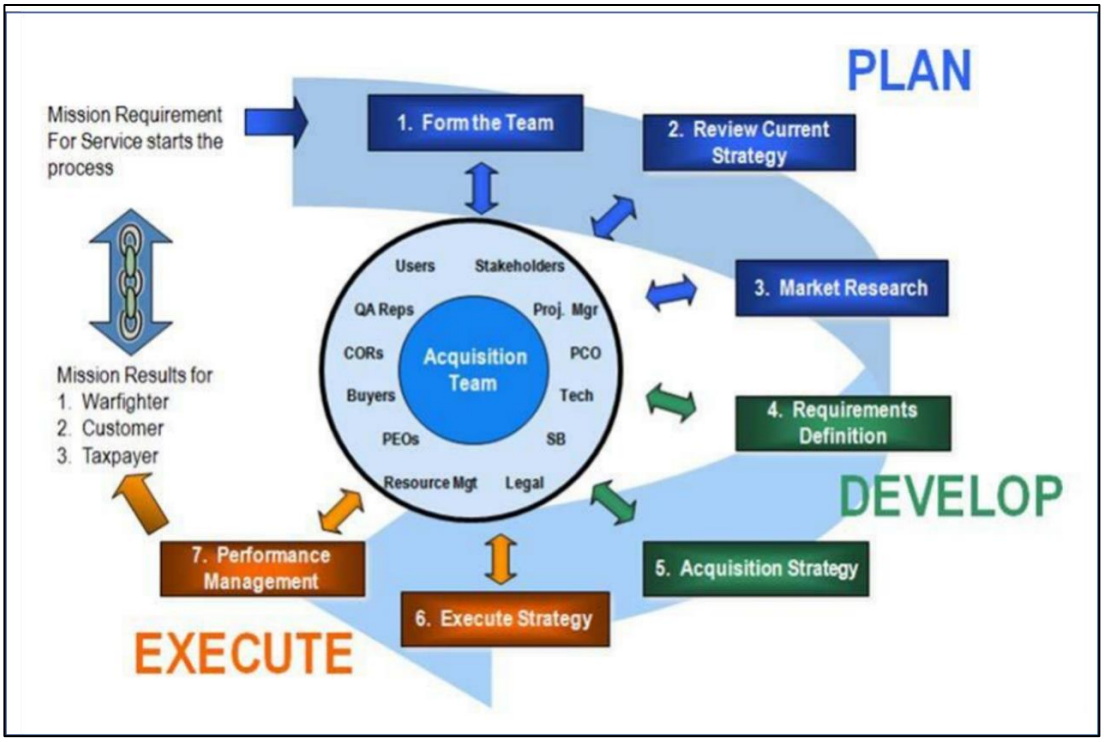


Figure H3*. 7-step Services Acquisition Process (adapted from [2]).*

The cost estimation and cost engineering are essential parts of developing an effective acquisition strategy (step 5) and influence the executive strategy (step 6) and the delivered technological capabilities (step 7). We view the cost engineering as an enabling tool in the maturity cycle of the currently developed technology.

The updated "Handbook for Services Acquisition" (February, 2018) includes many valuable resources for DoD cost estimation processes. It includes the principles for cost estimation and the four primary methods for cost estimation:

i. Analogous (Top-Down) - estimates are based on historical data of a similar system;
ii. Parametric (Statistical) - relies on statistical analysis to establish a relationship between a technical characteristic and the cost of the system;
iii. Engineering (Bottom-Up) - estimates are very detailed, separated into tasks/elements; the cost of individual tasks and elements are estimated to the greatest level of specified detail;
iv. Actual Costs (Extrapolation) - typically associated with tasks/elements in progress or material items when taking the actual cost of previous production sets.

Some of the strengths and weaknesses of Analogous (Top-Down), Engineering (Bottom-Up) and Parametric (Statistical) cost estimating are compared in Table H1.

***Table H1**. Strengths and Weaknesses of Analogous (Top-Down), Engineering (Bottom-Up) and Parametric (Statistical) cost estimating.*

Method	Strength	Weakness	Application
Analogous	Requires little data	Subjective adjustments	When little data is available
	Based on actual data	Accuracy depends on similarity of items	Rough order of magnitude estimate
	Reasonably quick	Difficult to assess effect of design change	Cross-check
	Good audit trail	Blind to cost drivers	
Bottom-Up	Easily audited	Requires detailed design	Production estimating
	Sensitive to labor rates	Slow and laborious	Software development
	Tracks vendor quotes	Cumbersome	Negotiations
	Time honored		
Parametric	Reasonably quick	Lacks detail	Budgetary estimates
	Encourages discipline	Model investment	Design-to-cost trade studies
	Good audit trail	Cultural barriers	Cross-check
	Objective, little bias	Need to understand model's behavior	Baseline estimate
	Cost driver visibility		Cost goal allocations
	Incorporates real-world effects (funding, technical, and risk)		

There are additional methods and techniques associated with cost estimation (i.e., three-point estimate, Delphi cost estimation, Expert judgment, Reserve analysis and others). We shall consider the methods typically used and referred to in the DoD processes. For example, **U.S. GAO** recommends a 12-step process for creating high-quality cost estimates [10]. Essentially a deterministic estimating technique, the 12-step process is a systematic approach where estimators select an appropriate estimating technique for each component of a work breakdown structure, fully identify the assumptions underlying estimates, and conduct risk and uncertainty analyses for estimates.

Current Goals of Cost Engineering

The short-term goal of cost estimation efforts is to:

i. Comprehend modern methods and tools used for cost estimation and especially the one applicable to the DoD acquisition process;

ii. Understand what makes up cost, i.e., the basic resources (material, labor, etc.) that are needed to perform an activity or create an asset;
iii. Use the understanding of cost elements to further understand how cost is measured, applied, and recorded to arrive at the total activity and/or asset cost;
iv. Understand the distinction between cost elements that are either directly or indirectly applied to an asset;
v. Relate the cost elements to the life cycle of the asset: acquisition, use, and disposal;
vi. Apply the knowledge gained to solve problems related to cost element – identify cost-limiting sources and define alternatives.

The accuracy of estimation is an important aspect, as project cost estimates are classified into categories based on how well the scope is defined at the time of estimation, on the types of estimation techniques used, and on the general accuracy of estimates. These categories are not standardized, but they are all based on the recognition that a cost estimate can only be as accurate as the project scope is detailed. In its estimating manual, the American Society of Professional Estimators (ASPE) classifies cost estimates in order of increasing accuracy on a five-level scale. Level 1 is an order of magnitude estimate and level 5 is a final bid. The U.S. DoE uses a similar five-class scale, but in the reverse accuracy order: class 5 as an order of magnitude estimate and class 1 as a definitive estimate.

The reviewed references indicate that estimate classifications are commonly used to indicate the overall maturity and quality for the various types of estimates that may be prepared [9]. In its "Recommended Practice for Cost Estimate Classification", the AACE International (formerly Association for the Advancement of Cost Engineering) provides generic guidelines for the general principles of estimate classification that may be applied across a wide variety of industries. We would like to illustrate the expected accuracy range of cost estimation on the maturity level of deliverables definition as illustrated in Table H2 (adapted from [3]). We need to point out that in some references the estimation classes and maturity levels are in reverse, comparing to one given in [9].

Table H2*. Cost Estimate Classification Matrix.*

Primary Characteristic		**Secondary Characteristic**		
ESTIMATE CLASS	MATURITY LEVEL OF DELIVERABLES DEFINITION Expressed as % of complete definition	END USAGE Typical purpose of the estimate	METHODOLOGY Typical estimating method	EXPECTED ACCURACY RANGE Typical variation in low and high ranges
Class 5	0% to 2%	Concept screening	Capacity factored, parametric models, judgment, or analogy	L: -20% to -50% H: +30% to +100%
Class 4	1% to 15%	Study or feasibility	Equipment factored or parametric models	L: -15% to -30% H: +20% to +50%

Class 3	10% to 40%	Budget authorization or control	Semi-detailed unit costs with assembly level line items	L: -10% to -20% H: +10% to +30%
Class 2	30% to 75%	Control or bid/tender	Detailed unit cost with forced detailed take-off	L: -5% to -15% H: +5% to +20%
Class 1	65% to 100%	Check estimate or bid/tender	Detailed unit cost with detailed take-off	L: -3% to -10% H: +3% to +15%

Cost engineering is the application of scientific principles and techniques to problems of estimation, cost control, business planning and management science, profitability analysis, project management, as well as planning and scheduling [1]. While this definition seemingly addresses non-cost areas, it lists key engineering activities that either incur cost when they are performed, or defines plans and processes that cause (or influence) cost to be generated in other activities and/or assets. The successful execution of the cost engineering task will position us to apply the cost elements and categories to the insight for managing activities and assets for the successful completion of the mission.

Keywords: Assets, Acquisition, Cost Accounting, Cost Elements, Cost Engineering, Cost Management, Cost Structure, Resources, and R&D.

References

[1] D. Shermon and M. Gilmour, *Cost Engineering Health Check - How Good are Those Numbers?* Routledge, London and New York, ISBN: 978-1-4724-8407-9, 2017.

[2] M. V. Arena, R. S. Leonard, S. E. Murray, and O. Younossi, “Historical Cost Growth of Completed Weapon System Programs”, TR-343-AF, (2006).

[3] O. Younossi, M. V. Arena, R. S. Leonard, C. Robert Roll, Jr., A. Jain, and J. M. Sollinger, “Is Weapon System Cost Growth Increasing? A Quantitative Assessment of Completed and Ongoing Programs”, MG-588-AF, 2007. Arena et al. (2007).

[4] Joseph G. Bolten, Robert S. Leonard, Mark V. Arena, Obaid Younossi, Jerry M. Sollinger, “Sources of Weapon System Cost Growth Analysis of 35 Major Defense Acquisition Programs”, (2014), The RAND Corporation, https://www.rand.org/content/dam/rand/pubs/monographs/2008/RAND_MG670.pdf

[5] National Accountability Office, “Forecasting in government to achieve value for money”, (2014), https://www.nao.org.uk/wp-content/uploads/2015/01/Forecasting-in-government-to-achieve-value-for-money.pdf

[6] GAO-16-5 DARPA Technology Transition, (2015), https://www.gao.gov/assets/680/673746.pdf

[7] DARPA Small Business Programs Office, “Transition & Commercialization Strategy Development Guide”, (2018), https://www.darpa.mil/attachments/Transition-and-Commercialization-Guide.pdf

[8] Independent Government Cost Estimate (IGCE) Handbook for Services Acquisition, https://www.acq.osd.mil/dpap/sa/Policies/docs/DoD_IGCE_for_SA_Handbook.pdf,
[9] M. Hastak, Editor, Skills and Knowledge of Cost Engineering - A continuing project of the AACE International Educational Board, AACE International, Sixth Edition, (2015).
[10] United States Government Accountability Office, "GAO Cost Estimating and Assessment Guide - Best Practices for Developing and Managing Capital Program Costs", GAO-09-3SP, (2009), https://www.gao.gov/new.items/d093sp.pdf

II. Issues:

III. Interactions with Others:

None

IV. Major Procurement Actions:

None

V. Travel:

Travel Plans

Please note that all papers or presentations on any aspect of the ONR HPM program must be reviewed by the ONR Program Officer (or in some cases ONR Public Release Process) regardless of classification level or audience.

Planned Travel Details	Purpose	Attendees	Estimated Costs
DEPS	Conference	Multiple	Not established yet
2019 IEEE	Antenna Conference	Chatterjee group	Not established yet

VI. Pending or Upcoming Public Release Requests:

None

VII. Selected Highlights (text and/or images):

None

ONR HPM 2018 Program - Monthly Status Report (MSR) – JANUARY2019
Anthony Caruso – Univ. Missouri – Kansas City
N00014-17-1-3016 [OSPRES Grant]
ONR Short Pulse Research, Evaluation and non-SWaP Demonstration for C-sUAV Study

2/13/2019

Distribution Statement ~A: Distribution authorized to all OSPRES Grant and Contract Participants, and any uncompensated collaborators. Further dissemination per Ryan Hoffman (ryan.hoffman@navy.mil).

OSPRES Project Description: Develop tunable High Power Microwave (HPM) sources and electronically steerable radiators whose waveform(s) enable control over all levels-of-lethality on cUAV and similar targets, with the least power density.

Executive Summary

Overview:

Coordination within and between performers, has cut turnaround time in half for design, prototype, and iterate of most HPM driver components. UMKC's PCSS team purchased a new laser to cover new Si and GaN switch testing, while the main laser is shifted to effects testing with the high maturity switches. The effects team, in coordination with the PCSS team, commissioned the TEM cell. Their focus is now parallel testing of the TEM cell and GTEM. GaN:C simulations have developed device models for simulation with user specified doping profiles with success. Characteristic Mode Analysis has shown that the UAV frame is a large factor in coupling to wires and PCB's within the UAV itself. The Electrically small antennas group has performed literature studies to determine down selection criteria for phased array systems and the study of ESA's used in phased arrays.

I. Current Month Progress:

I.A Photoconductive Solid-State Switches (Myers)

i. PCSS Modeling – We've made progress in modeling the reverse recovery testing of the SiPCSS, however, the recovery obtained is roughly one order of magnitude less than experiment. We are working to modify the material model for Si and device parameters to achieve agreement with experiment. Following reasonable agreement, we will introduce the laser pulse to the model to simulate switching parameters.
ii. Lasers – We have ordered a second laser system to continue testing at lower PRF. This laser will support SiPCSS and GaNPCSS testing. The laser is capable of single shot to 2-kHz PRF at pulse energies up to 2 mJ and pulse widths of ~1 ns.
iii. GaN Testing – Anticipated redelivery of demo laser expected in February-March. Efforts to improve fixturing for continued testing underway and an initial prototype has been fabricated.

I.B GaN:C Subgroup (Rulis)

i. The primary activity of the past month has been developing knowledge and ability to create our own device models with doping profiles of our choosing and material compositions.
ii. Illustrative elementary models are shown in Figure B1. We have also tested the creation of a variety of 1-D doping profiles with an example shown in Figure B2.

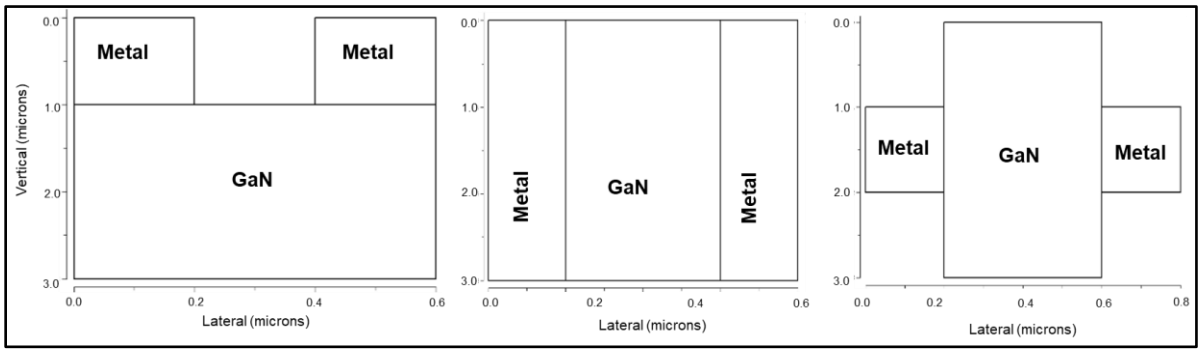


Figure B1*. Test geometries for device configurations created without relying on geometries created by others. This demonstrates the ability to specify specific desired geometries and types of contact interfaces of our own creation.*

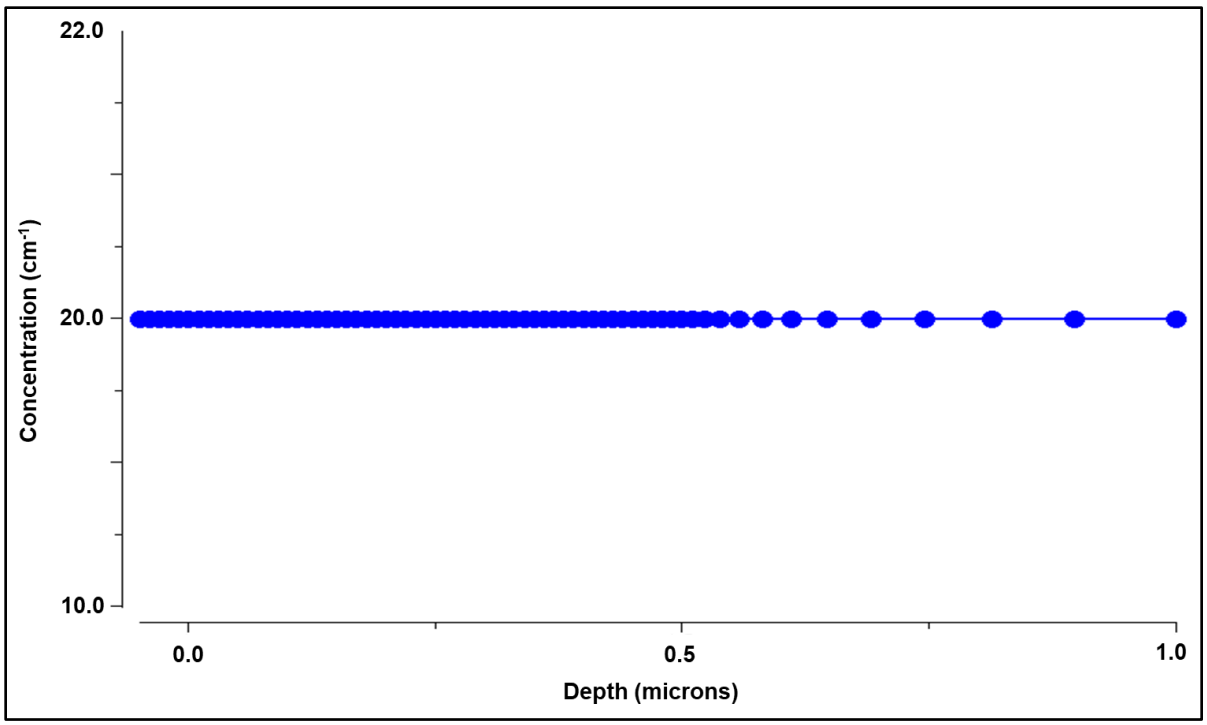


***Figure B2**. Test 1-D doping profile in an exponential decrease from 1e20 to 1e17. As with the geometries, we have a good understanding of how to generate our own doping profiles in the FLOOXS specification language (Alagator).*

I.B.1 Critical Tasks of GaN:C Calculations Subgroup

i. As with the last month, the longer term critical task is to test our ability to direct FLOOXS to correctly model the simple electronic systems we have created so far when fundamental parameters are modified according to known empirical trends (http://www.ioffe.ru/SVA/NSM/Semicond/Si/electric.html). That is, we will use the data given in the references listed in that URL to modify models of the diodes and resistors that we have created so far and compare the I-V curves to verify that the trends we compute are consistent with experimental evidence. This should tell us the degree to which we are really able to direct accurate simulations as we move from Si to GaN.

I.B.2 Expected Products of GaN:C Calculations Subgroup

i. Refine the model geometries to more exactly match physical specimens that have been or that are planned to be fabricated.
ii. Establish the equations that govern contact interfaces. We will focus initially on Si so that we can then compare with known examples.

I.C Small Unmanned Aerial Vehicle Diagnostics and Design-of-Experiments (Fields)

i. Conducted many experiments in gimbal platform with directly injected noise. Results are currently being analyzed for propagation modeling.
ii. Modified the software platform to facilitate automated testing at UMKC in GTEM, and finalized adaptive DOE architecture for evaluation in UMKC GTEM.

I.D Positive Feedback Non-Linear Transmission Line (Khan)

i. Modified the amplifier design to achieve a 64V pulse at 120 MHz. The rise time and fall times are 5 ns each. We are still pushing the frequency limit of the amplifier.
ii. Building a burst generator using RF MOSFETs.

I.E Applied RF Coupling Simulation and Modelling to/for sUAV (Hassan)

i. Continued Characteristic Mode Analysis (CMA) of dielectric UAV frames. Specifically, adding complexity to the frame shape and wire/PCB distributions. The goal is to progressively build up the complexity until a complete UAV is analyzed.
ii. CMA is showing that the dielectric frame can have significant effects on the coupling to the wire and PCBs mounted on the UAV. We are exploring multiple ways to validate these effects such as the use of independent electromagnetic solvers and designing new experimental setups.

I.F UMKC Diode Network Based NLTL (Doynov)

i. A low-voltage Diode-based Non-Linear Transmission Line (D-NLTL) was constructed based on simulation results and tested for validation. Results are in good agreement with the simulated design;
ii. A high-voltage D-NLTL has been designed and is being implemented;
iii. The efficiency of new D-NLTL topologies are being evaluated.

I.G Electrically Small Antennas (Chatterjee)

i. Initiated the studies on developing the criterion for down selecting a phased array topology (with graduate student Bidisha Barman).
ii. Initiated full-wave (FEKO) analysis for understanding the influence of mutual coupling in a linear array (Bidisha Barman).
iii. Initiated literature search on compiling information on Electrically Small Antennas for use as radiating elements in a phased array (Bidisha Barman and James Kovarik).

iv. Continuing on full-wave simulations for the phased array to develop a trade-space for parameters.

NOTE: December 2018 MSR revised to eliminate arithmetic errors. Revised MSR is attached in section VIII. Appendix

I.H Cost Estimates and Engineering (Doynov)

i. Continuing the resources search and building a collection of papers, books and DoD materials related to methods and tools for cost estimation and cost management;
ii. Reviewing several tools which are used by DoD and DoD contractors in order to select and use one (preferably free source).

II. Issues:
None

III. Interactions with Others:

None

IV. Major Procurement Actions:

None. (We could mention the Laser we put a req. in for?)

V. Travel:

Travel Plans

Please note that all papers or presentations on any aspect of the ONR HPM program must be reviewed by the ONR Program Officer (or in some cases ONR Public Release Process) regardless of classification level or audience.

Planned Travel Details	Purpose	Attendees	Estimated Costs
DEPS	Conference	Multiple	Not established yet
2019 IEEE	Antenna Conference	Chatterjee group	Not established yet
UMKC to MM and BAE	Design discussion Testing Demo	Myers, Lancaster, Fry, Bissen	~$3500

VI. Pending or Upcoming Public Release Requests:

i. M. Z. M. Hamdalla, A. N. Caruso, Ahmed M. Hassan, "Characteristic Mode Analysis of the Effect of the UAV Frame Material on Coupling and Interference," *Submitted to the IEEE International Symposium on Antennas and Propagation and USNC-URSI Radio Science Meeting at Atlanta, Georgia*, USA, 7-12 July 2019.

ii. M. Z. M. Hamdalla*, Ahmed M. Hassan, A. N. Caruso, J. D. Hunter, Y. Liu, V. Khilkevich, D. G. Beetner, "Electromagnetic Interference of Unmanned Aerial Vehicles: A Characteristic Mode Analysis Approach," *Submitted to the IEEE International Symposium on Antennas and Propagation and USNC-URSI Radio Science Meeting at Atlanta*, Georgia, USA, 7-12 July 2019.

VII. Selected Highlights (text and/or images):

None

VIII. Appendix

Revised report section for December 2018

Section: *I.G*
Title: *Focus Wave Modes (FWM) and Electrically Small Antennas (Chatterjee)*

ONR HPM 2018 Program - Monthly Status Report (MSR)

December 2018 (***revised/updated***)

Current Month Progress Summary: The efforts in the two research directions are described as below. As before (see October 2018 revised MSR), the major efforts are for parametric characterizing of a planar phased array. The previous report summarized the basic array parameters and element electrical size. The Taylor distribution was assumed to determine the appropriate array length for the specific beamwidth. However, the array excitation weights and beam steering phase shifts are not calculated; these will be determined for a full-wave simulation for future work. It is reported here that a mean interelement spacing of 0.57λ is adequate. However more investigations on reducing the overall array size are continuing. The main results of the previous effort that are used here are as below:

(a) Electrically Small Antennas (ESA) (*Deb Chatterjee*)

ESA (beam steering array) studies were initiated for the following nominal set of specifications:

a) Frequency: **400** MHz
b) Number of elements: 14 × 14 (square planar array)
c) Gain: (1) Electrically small element gain: **2.93** dB
(2) Array peak gain at boresight: **25.85** dB

d) Element size (ESA): $ka = 0.72$

The main objective is to find out the array size, but the other antenna parameters such as: 3 dB beamwidth, 1st sidelobe level and the interelement spacing in both planes are unknown. These parameters are needed in the array size characterization and hence will have to be chosen *a-priori.* Assuming a square planar array of 196 elements, suggests that a pencil beam can be realized with equal beamwidth in the orthogonal planes. For a small- to medium-sized phased array, one can assume some system loss and hence choose the aperture efficiency as $\epsilon_{ap} = 0.9$. The maximum value is obviously unity (no losses). The gain and directivity can be written as [2]-[4] as:

$$G = \epsilon_{ap} D \quad \text{..... (1)}$$

If the pencil beam is scanned to an angle θ_s from the boresight (zenith) then the directivity is given by [2, p. 24, Eq. (1.67)] as:

$$D = \frac{32400}{(\Theta_{3dB})^2} \cos\theta_s \quad \text{..... (2)}$$

In (2) it is assumed that a pencil beam is generated that has equal 3 dB beamdwidths in the orthogonal planes. For a pencil beam pointing to the boresight ($\theta_s = 0^0$), the 3 dB beamwidth is thus given by:

$$\Theta_{3dB} = 8.7^0 \quad \text{..... (3)}$$

Because we are assuming a square (14×14) array the remainder of the analysis simplifies to that of a linear array assuming the principle of separability of pattern distributions [2, p. 18, Eq. (1.60)]. We shall now look at Taylor distributions. The Taylor distribution is used to determine the amplitude excitation weights across the array. For beam steering, a linear progressive phase shift can be applied. The gain and the sidelobe levels are necessary to determine the amplitude excitation weights. However, in this MSR we shall be gainfully using the relationship between array length, 3 dB beamwidth and the 1st sidelobe level. From [4, pp. 453-459] the relationship between beamwidth, sidelobe level and array size (length L) reads:

$$\Theta_{3dB} = 2\sin^{-1}\left\{\frac{\lambda\sigma}{\pi \mathrm{L}}\left[(\cosh^{-1} R)^2 - \left(\cosh^{-1}\frac{R}{\sqrt{2}}\right)^2\right]^{\frac{1}{2}}\right\} \quad \text{..... (4)}$$

The preceding equation can easily be inverted for obtaining the linear electrical length of one side of the square planar array that reads as follows:

$$\frac{L}{\lambda} = \frac{\sigma\left[(\cosh^{-1} R)^2 - \left(\cosh^{-1}\frac{R}{\sqrt{2}}\right)^2\right]^{\frac{1}{2}}}{\pi \sin\left(\frac{1}{2}\Theta_{3dB}\right)} \quad \text{..... (5)}$$

Equation (5) can be used to determine the (linear) array length L for a specific sidelobe level, and a beamwidth, with the attendant assumption that the (excitation current) amplitude distribution across the array follows a Taylor form [4, p. 457, Eqs. (10-91, 92)]. However,

we need to choose the beam *dilation* factor σ. The beam dilation factor is calculated from [4, p. 456, Eq. (10-81)] as:

$$\sigma = \frac{\bar{n}}{\sqrt{A^2 + \left(\bar{n} - \frac{1}{2}\right)^2}} \quad \text{..... (6)}$$

In (6) the for a specific sidelobe level, R, the quantity $\mathrm{A} = \frac{1}{\pi}\cosh^{-1}\mathrm{R}$. The quantity R is connected to the actual voltage sidelobe level via the relation: $\mathrm{R} = 10^{\frac{-\mathrm{SLL}}{20}}$. Finally, the *positive integer* quantity $\bar{n}$ designates the equal number of sidelobe levels close to the main beam. Typically,$3 \leq \bar{n} \leq 5$, for small and medium size arrays. Therefore, for a fixed beamwidth as given by (3), one can choose various sidelobe levels and determine the various array lengths $\frac{\mathrm{L}}{\lambda}$ and hence the array size. Equation (5) is used normally by assuming a fixed sidelobe level and an array length, to determine the 3 dB beamwidth. In our situation we are using it in an inverse manner. Whether the results are acceptable or not can be determined from a detailed full-wave analysis reserved for future investigation. The summary of the results are shown in Table 1 below.

We illustrate one typical numerical calculation in detail; the others in the table below can easily be verified by following an identical procedure.

Consider the case for a SLL=-25 dB and the chosen integer value is given by $\bar{n} = 3$. The following simple steps are then executed in sequence.

Step 1: Calculate, $\mathrm{R} = 10^{\frac{25}{20}} = 10^{1.25} = 17.7827941$

Step2: Calculate, $\mathrm{A} = \frac{1}{\pi}\cosh^{-1}(17.7827941) = 1.136553154$

Step 3: Calculate, $\cosh^{-1}(17.7827941) = 3.580587$ and $\cosh^{-1}\left(\frac{17.7827941}{\sqrt{2}}\right) = 3.22322005$

Step 4: Calculate, $\left[(\cosh^{-1} R)^2 - \left(\cosh^{-1}\frac{R}{\sqrt{2}}\right)^2\right]^{\frac{1}{2}} = 1.536211014$

Step 5: Calculate the dilation factor, $\sigma = \frac{\bar{n}}{\sqrt{A^2+\left(\bar{n}-\frac{1}{2}\right)^2}} = 1.092408574$

Step 6: Calculate the quantity $\pi \sin\left(\frac{1}{2}\Theta_{3dB}\right) = 0.238286367$

Step 7: Calculate the electrical length $\frac{L}{\lambda} = \frac{1.092408574 \times 1.536211014}{0.238286367} \cong 7.04266$ from equation (5).

The other entries in Table 1 are thus obtained similarly.

Sidelobe Level R (-SLL)	$\bar{n} = 3$		$\bar{n} = 5$	
	Dilation Factor σ	Array Length $\frac{L}{\lambda}$ (linear)	Dilation Factor σ	Array Length $\frac{L}{\lambda}$ (linear)

17.7827941 (-25 dB)	1.092408574	**7.04266**	1.077282197	**6.94514**
31.6227766 (-30 dB)	1.061171462	**7.39325**	1.066190356	**7.42822**
56.234132 (-35 dB)	1.028401635	**7.66472**	1.053864153	**7.8545**
100.0 (-40 dB)	0.994803109	**7.86888**	1.040441835	**8.23**

Table 1: Array (linear) length for an array gain of 25.85 dB and beamwidth 8.7 degrees, assuming Taylor distribution. The (voltage) sidelobe level values are in parentheses in column 1 of the table. The beamwidth is assumed 8.7^0 fixed at boresight.

The results indicate that the square planar array has a linear dimension between: $7 \leq \frac{L}{\lambda} \leq 8$, but only approximately. However for a frequency of 400 MHz this still could imply a very large array. The interelement spacing for this array is given by $d = \frac{L}{(N-1)\lambda}$. This means for N = 14, the interelement spacing $\mathbf{0.53\lambda \lesssim d \lesssim 0.61\lambda}$. This result is *slightly* higher than the standard half wavelength spacing between adjacent elements to avoid the occurrence of grating lobes, and, can be further reduced at the expense of increased mutual coupling for smaller overall array form factor.

Other extensive parametric studies on the (graphical) relationship between boresight gain, beamwidth, sidelobe levels for various linear array lengths are under investigation. Full-wave simulation studies for obtaining results for element mutual coupling and radiation pattern for a

Summary

The results obtained by assuming a peak array gain value of 25.85 dB obtained from the Harrington limits yields the linear dimension of a square planar array with an interelement spacing $d \approx 0.57\lambda$. The results suggest that substantially more parametric studies are necessary to define the array topology. This work is currently in progress.

References

[1] John L. Volakis, Chi-Chih Chen and Kyohei Fujimoto, *Small Antennas: Miniaturization Techniques and Applications*. NY, USA: McGraw-Hill, 2010.

[2] R. J. Mailloux, *Phased Array Antenna Handbook* (3rd ed.). Norwood, MA, USA: Artech-House, 2018.

[3] A. W. Rudge, K. Milne, A. D. Olver and P. Knight (eds.), *The Handbook of Antenna Design* (vol. 2). London, UK: Peter Peregrinus, 1983.

[4] W. L. Stutzman and G. A. Thiele, *Antenna Theory and Design* (3rd ed.) Hoboken, NJ, USA: John-Wiley & Sons, Inc., 2013.

(b) Minimally Dispersive Waves (Electromagnetic Pulse Propagation) (*Deb Chatterjee*)

The pulse radiation from a waveguide circular aperture excited in a TE_{11} mode is being analyzed differently than the Wiener-Hopf analysis in [1]. The equivalence principle and

image theory concepts [2, ch. 3] are utilized to obtain the forward radiation from the pulsed waveguide aperture.

[1] T. T. Wu and H. M. Shen, "Radiation of an Electromagnetic Pulse from an Open-ended Circular Waveguide," Proc. SPIE, 1988, pp. 329-337.
[2] R. F. Harrington, *Time Harmonic Electromagnetic Fields*. NY, USA: McGraw-Hill, 1961.

ONR HPM 2018 Program - Monthly Status Report (MSR) – FEB2019
Anthony Caruso – Univ. Missouri – Kansas City
N00014-17-1-3016 [OSPRES Grant]
ONR Short Pulse Research, Evaluation and non-SWaP Demonstration for C-sUAV Study

3/12/2019

Distribution Statement ~A: Distribution authorized to all OSPRES Grant and Contract Participants, and any uncompensated collaborators. Further dissemination per Ryan Hoffman (ryan.hoffman@navy.mil).

OSPRES Project Description: Develop tunable High Power Microwave (HPM) sources and electronically steerable radiators whose waveform(s) enable control over all levels-of-lethality on cUAV and similar targets, with the least power density.

Executive Summary

Overview:

During the month of February, the PCSS development subgroup made substantial progress in GaN:C testing. Fixtures have been designed and constructed to normalize collected data between Silicon and GaN:C for comparison of switching behavior. Two parallel GaN:C research fronts are being pursued: 1) fundamental properties for more accurate modeling in TCAD and 2) continued pulse testing to identify optimum PCSS geometry, wavelength, and pulse energy.

The Positive Feedback Non-Linear Transmission Line (PF-NLTL) subgroup has designed and fabricated a custom pulse generator for testing the PF-NLTL and are iterating on the design to reduce pulse width from 750 ns.

UMKC's Electrically Small Antenna (ESA) subgroup have simulated a linear array of 25 elements using Taylor and Bickmore-Spellmire amplitude distributions, concluding that the Bickmore-Spellmire distribution is better suited to high power applications. They have also validated the use of Harrington's formulas for estimating the gain and bandwidth of the meandering dipole ESA's.

UMKC's RF coupling subgroup has confirmed Characteristic Modal Analysis predictions that incident angle affects the current generated at loads in specific models of UAV frames.

The Diode Non-Linear Network effort at UMKC has modeled 10-40 element networks and predicted maximum efficiency with 15-20 cells.

I. Current Month Progress:

I.A Photoconductive Solid-State Switches (Myers)

The following table outlines the efforts of UMKC for fundamental PCSS development.

Table A1. *Progress tracker for identified critical tasks and statuses. Color indicates the criticality of each task with respect to its current status and the objectives of the program: (GREEN) low-risk and/or no major delays, (YELLOW) medium risk and/or minor delays, (RED) major risk and/or delays.*

Critical Effort		Critical Task		Status
Device Characterization	Si	Recovery Time Measurements		Multiple devices have been tested up to 20MR with no indication of reduced voltage hold-off.
Simulation and Modeling	Si	TCAD Simulation		We are refining our SiPCSS model in TCAD to more closely represent the recovery times measured experimentally.
Device Characterization	Si	Electrolumine-scence Studies		Results of previous EL testing are no longer considered to be valid. Erroneous results caused by unquantified shot noise. Project refocused to shot noise characterization and how to reduce the noise.
Ultrafast Switching	TBD	Parameter Survey		We have listed out the parameters critical to the performance of ultrafast rise-time switches and have shortlisted some switching technologies and materials. Working towards eliminating non-viable technologies to narrow down possibilities for alternative source drivers
Device Characterization	GaN:C	Wavelength Dependence		UMKC will be repeating tests with the Opotek tunable laser system in early March in an effort to finalize wavelength selection.
Device Characterization	GaN:C	Lifetime Measurements		UMKC is evaluating methods for measuring GaN carrier lifetime measurements in addition to recovery time from pulsed testing.

SiPCSS Simulation and Modeling – SiPCSS Recovery (Hauptmann)

The reverse recovery time simulations reported previously were repeated using the measured doping profile, and the results now agree more closely with experimental recovery time. The simulated circuit, as shown in Figure A1, applies an 8-V (peak-to-peak) bipolar pulse to the Si-PCSS (through a 50 Ω source resistance) and the output voltage is measured with an oscilloscope, represented by the 50-Ω load. The simulated

PCSS is 1-cm x 1-cm x 500-µm with a doping profile shown in Figure A2. Results of the simulation yielded a recovery time of about 0.25-µs. Experiments show recovery times averaging around 8.5-µs (Figure A3). This difference in recovery times is attributed to defect and trap states not included in the simulated PCSS model: the model includes only the default carrier lifetime. Trap states within the bandgap capture an electron (or hole) and prevent it from recombining with a hole (or electron). In turn, the recovery time of a switch with more trap states is increased, and a switch without trap states, like the simulated PCSS, will have a faster recovery time.

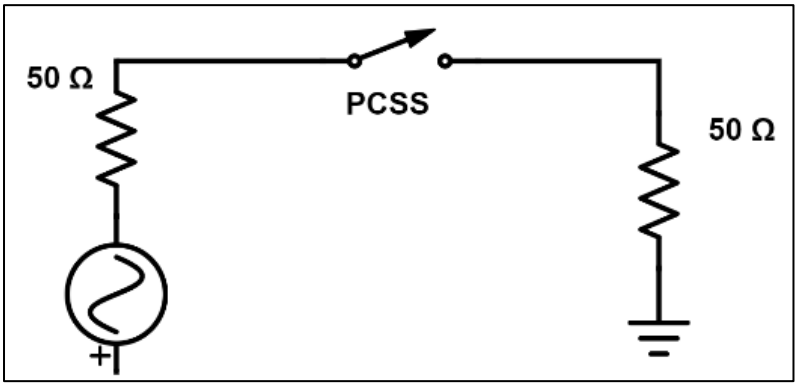


Figure A1*. Circuit diagram depicting the circuital simulations which will be ran to compare modelling results with experimental observations.*

As shown in Figure A2, the voltage of the simulated PCSS in forward bias is about 1.0 V; lower than the 1.5 V average for the real devices. Yet, the voltage in reverse bias of the simulation yielded a lower minimum than was observed in experiments, –2.5 V in simulation and about –1.7 V in experiment. This suggests that the simulated PCSS is exhibiting a lower resistance in forward bias than during the transition to reverse bias.

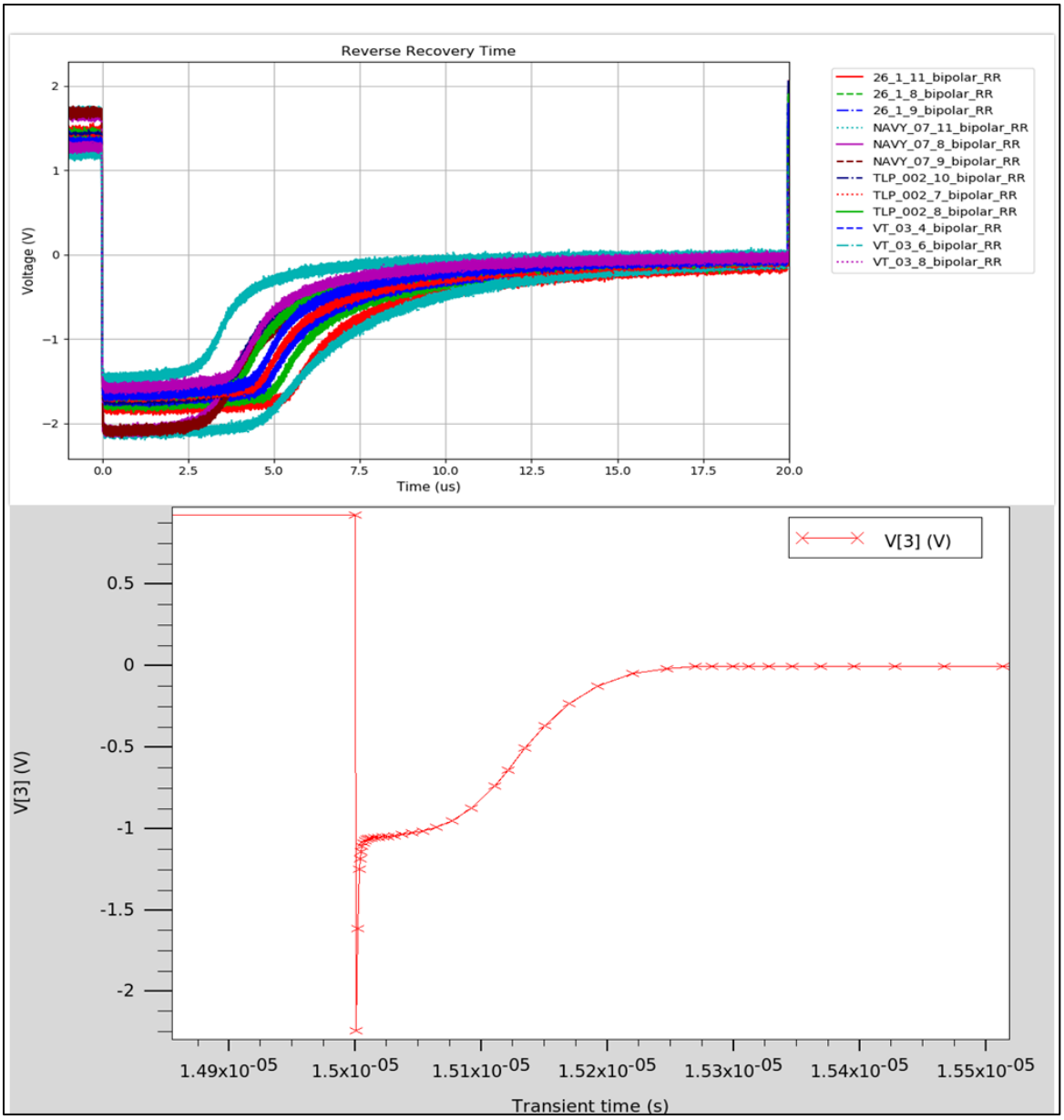


Figure A2. *Reverse recovery time results in experiment (top) reported previously and from TCAD simulation (bottom). The horizontal axis is time and voltage is plotted vertically.*

Further simulations were conducted to test the effects on reverse recovery caused by device thickness and intrinsic doping concentration. Two different PCSS thicknesses were simulated, 500-µm and 1300-µm, to replicate the two primary sizes of the devices tested in the reverse recovery experiment. As expected from experimental results, the thicker PCSS exhibited a greater forward voltage drop, reduced recovery charge, and longer recovery time of about 0.4-µs compared to 500-µm switch (0.25 µs) per Figure A3. A final set of simulations were conducted to evaluate the carrier lifetime dependence on intrinsic doping concentration. It was found that higher concentrations of phosphorus leads to longer recovery times. In forward bias, switches with higher intrinsic

concentrations exhibit lower resistance and will output pulses with higher voltages as illustrated in Figure A4.

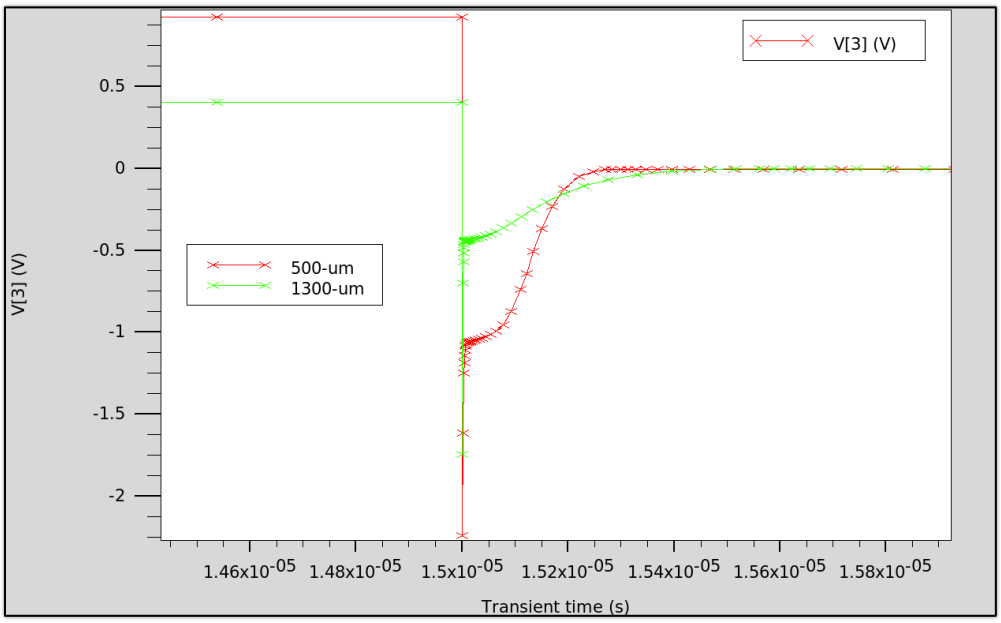


Figure A3. *Thickness-dependent reverse recovery profiles: (red) 500 µm and (green) 1300 µm.*

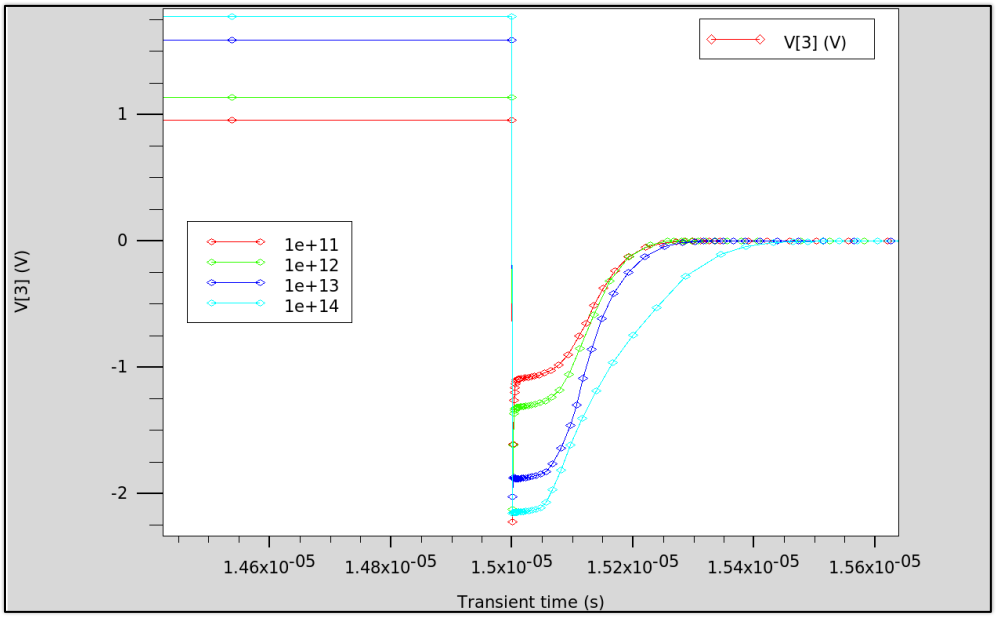


Figure A4. *Reverse recovery profiles of devices with an intrinsic doping concentration ranging from 1×10^{11} cm^{-3} to 1×10^{14} cm^{-3}.*

The reverse recovery simulations qualitatively agree with measured recovery time, and simulations, the magnitude of the simulated reverse recovery is a fraction of that measured experimentally. However, these results are still useful for exploring relative improvements in reverse recovery due to parameters that are far more time consuming

to manufacture or otherwise inefficient/impractical to measure experimentally. Therefore, TCAD can supply us with valuable information (i.e. recovery characteristics) about PCSS devices by simulating any experiments we want to perform on real switches. Our efforts moving forward will be focused on two things: (1) Improving the accuracy of the SiPCSS model in TCAD to more closely represent devices manufactured by RDT via inclusion of defect/trap states or the carrier mobility functions and (2) replicating the pulse forming network experimental circuit in TCAD including photo generation from the laser to enable transient simulation of SiPCSS switching phenomena.

SiPCSS Electroluminescence Studies (Landwehr)

Over the reporting period, we determined that the results reported previously did not correlate with actual device luminescence due to inadequate subtraction of the background signal and noise. To validate future EL data, we have temporarily refocused on quantifying the Apogee F8300 background and read noise, and the best methods for reducing and/or filtering such noise. The current and CCD counts from data reported previously is shown in Figure A5, indicating little-to-no coorelation between luminessence intensity and leakage current.

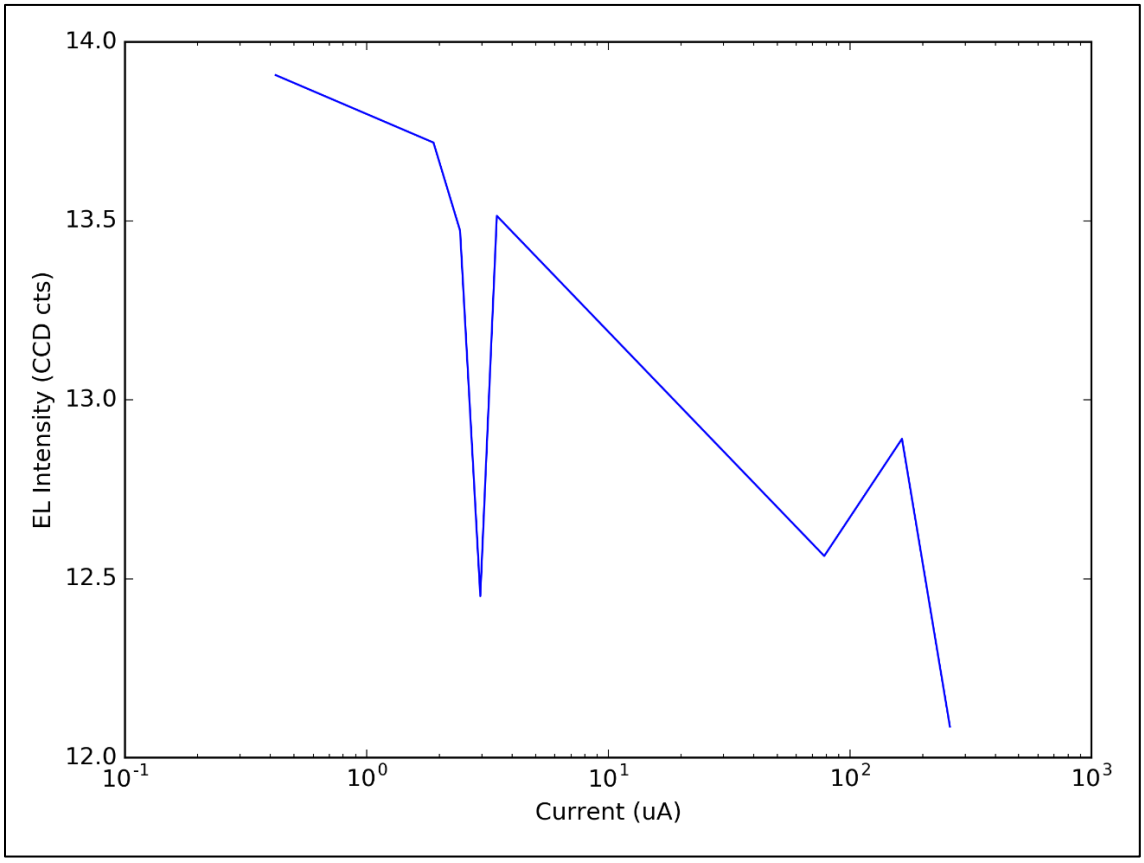


Figure A5. *CCD intensity as a function of leakage current during EL measurement.*

We are characterizing/quantifying three types of noise including read, periodic, and dead/hot pixel associated with the CCD and environment. While enviromental noise is caused by reflections and/or ambient light sources creating errouneous pixel values not

represenative of EL, read noise is a base per pixel value that is generated when the ADC reads each CCD pixel. To evaluate read noise, images were taken with a zero-exposure, and the read measured noise was approximately 1213 on average on a 12 bit ADC. Thiscan be subtracted from the EL images along with background noise for future EL studies. Unlike read noise, periodic noise a subset of read noise is generated by the CCD due to electrical interference or CCD damage. For the purposes of EL imaging, no measurebale perodicity was found in the noise signal. We are currently working on quantifying the number of dead and hot pixels.

Moving forward, the project's goal is to increase the measured luminescence from EL experiments by testing for longer exposures at increased reverse biases. We are designing and fixturing a vaccum chamber filled with sulfer hexaflouride (SF6) gas future testing which will enable higher reverse bias testing with reduced risk of breakdown in the air, giving greater insight as to the causes of device breakdown. Ideally this system will be constructed and in operation for data collection by the next report.

High Power Ultrafast Switch Fundamentals (Bhamidipati)

Along with the recent efforts on Si-PCSS and GaN:C-PCSS development, we continue to survey additional novel switching technologies for fast-rise pulsed power applications. This effort can be broken into two down-selection processes: (1) selecting the device topologies that are most promising in addition to PCSS, and (2) selecting the optimal materials for a given topology. Table A2 and Table A3 below show the device types and materials, respectively, currently included in the down-selection.

***Table A2**. Device topologies currently included in down-selection.*

Device Type	Sub-type
Diodes	PCSS Diode
	DSRD Diode
	Gunn diode
Transistors	MOSFET
	Controlled Rectifier
	Gate Commutated Thyristors (GCT)
	Phase controlled Thyristors
2DEG-based	HEMT
	Quantum well devices
	2D PCSS

Table A3. *Semiconductor materials and properties currently included in down-selection.*

Property	Si	GaAs	6H-SiC	4H-SiC	GaN	Diamond
Bandgap (eV)	1.12	1.43	3.02	3.23	3.4	5.46-5.6
Breakdown Field (MV/cm)	0.3	0.4	2.5	2.2	4	13
Saturated Electron Velocity (10^7 cm/s)	1	1	2	2	1.4	2.3
Hole Mobility (cm^2/V-s)	480	400	80	120	50	5300
Electron Mobility (cm^2/V-s)	1300	8500	415	1000	1600	7300
Direct or Indirect Bandgap	Indirect	Direct	Indirect	Indirect	Direct	Indirect
Thermal Conductivity (W/cm-K)	1.5	0.5	4	4.8	2.5	22.8

We continue to refine our metrics for down-selecting both devices and materials to achieve the greatest rise times, peak and average power, and jitter among other metrics reported previously. We have reviewing prior efforts to define figures of merit (FOMs) including those by Huang and Baliga [1]. Our approach will be to generate a new FOM for materials and devices emphasizing parameters relevant to PCSS and other, more recent technologies (e.g. 2DEGs).

Fundamental Properties of GaN (Kramer)

To accurately model GaN in carrier generation and charge transport simulations, it is important to verify that the values used in our analytical calculations, as well as simulations (via Silvaco TCAD) match what is measured for NRL's carbon doped GaN devices or are replaced with accurate values.

Measuring the mobility-lifetime product (μτ) of GaN:C will be performed by fitting the Hecht equation to responsivity measurements taken at varying wavelengths (300-400 nm). Knowing μτ then allows for the calculation of the material's external quantum efficiency (η_E). These measurements will be taken using the monochromator at UMKC.

$$J = J_0 \frac{\mu\tau E}{d}\left[1 - \frac{\mu\tau E}{d}\left(1 - \exp\left(-\frac{d}{\mu\tau E}\right)\right)\right] \qquad \text{(Hecht Equation)}$$

$$Responsivity\left(\frac{A}{W}\right) = \frac{I_{Photo}}{P_{Incident}} = \eta_E * \left(\frac{q\lambda}{hc}\right) * \frac{\mu\tau V}{Z^2} \qquad \text{(Responsivity)}$$

$$\eta_E = \frac{I_{Photo}}{P_{Incident}} * \left(\frac{hc}{q\lambda}\right) * \frac{Z^2}{\mu\tau V} \qquad \text{(External Quantum Efficiency)}$$

$$\eta_I = \frac{I_{Photo}}{P_{Incident} * (1 - e^{-\alpha d})} * \left(\frac{hc}{q\lambda}\right) * \frac{Z^2}{\mu\tau V} \qquad \text{(Internal Quantum Efficiency)}$$

Finding the device's internal quantum efficiency requires measuring the absorption coefficient (α) isolated from the SiC substrate. Surface absorption may be measured via ellipsometry, however the ellipsometer at UMKC does not reach the wavelengths of interest (<400 nm), thus these measurements are being conducted at NRL. To separate the mobility and lifetime, techniques such as photo-hall, photoconductance decay (PCD), and photoluminescence decay (PLD) are being considered. After these fundamental properties are measured, they will be incorporated into GaN model included in Silvaco TCAD, and simulations and analytical modeling will be performed to characterize the devices charge generation, carrier transport, and thermal transport phenomena.

Pulse Testing of GaN PCSS (Thompson)

A second effort on GaN:C development is focused on pulse testing to quantify the switching performance achievable with the present devices. To be competitive with Si, GaN:C must first achieve multiple kW of peak pulse power. To enable testing of GaN:C with the THG system on the neoLASE 1064 nm laser, a new test fixture was designed and a prototype was fabricated with the short pulse-width of the laser in mind. Initial testing using with a device with a gap length of 300 um was tested at a charge voltage of 20 V. The output pulse was just under 3 V, far less than the approximately 20-V pulse anticipated. We are currently testing with smaller gap lengths will be done to determine if the 70-ps pulse width was too short in duration preventing complete photoconductivity. A second prototype of the test fixture was also fabricated with a SMA V-dot setup, to allow for accurately measuring the pulse width of the devices on the picosecond laser. The design and prototype of the test fixture is shown in Figure A6 and A7.

The Opotek wavelength tunable laser arrived at UMKC the last week of February, and we are currently repeating testing on the wavelength- and beam energy-dependency of photoconductivity and recovery time in GaN devices. Below is a table of the tests that are being done using the demo laser. The top prioritized tests are highlighted in green, as the laser will only be at UMKC for one week.

Table A4. *Test parameters planned for GaN:C testing with the Optotek tunable lasers system. Top priority parameters are highlighted in green.*

Wavelengths (nm)	E_γ (mJ)	Gap Lengths (μm)
350	1.6	1000
355	1.2	500
360	1.1	300
365	1	200
370	0.8	50
380	0.5	30
400		20

A 1 ns pulse length, single-shot to 2 kHz laser has been purchased for UMKC. This longer pulse length (compared to the 70 ps neoLASE) will allow UMKC to perform

measurements of GaN:C's on-state resistance versus pulse energy as a function of active area to determine the minimum laser requirements for GaN:C.

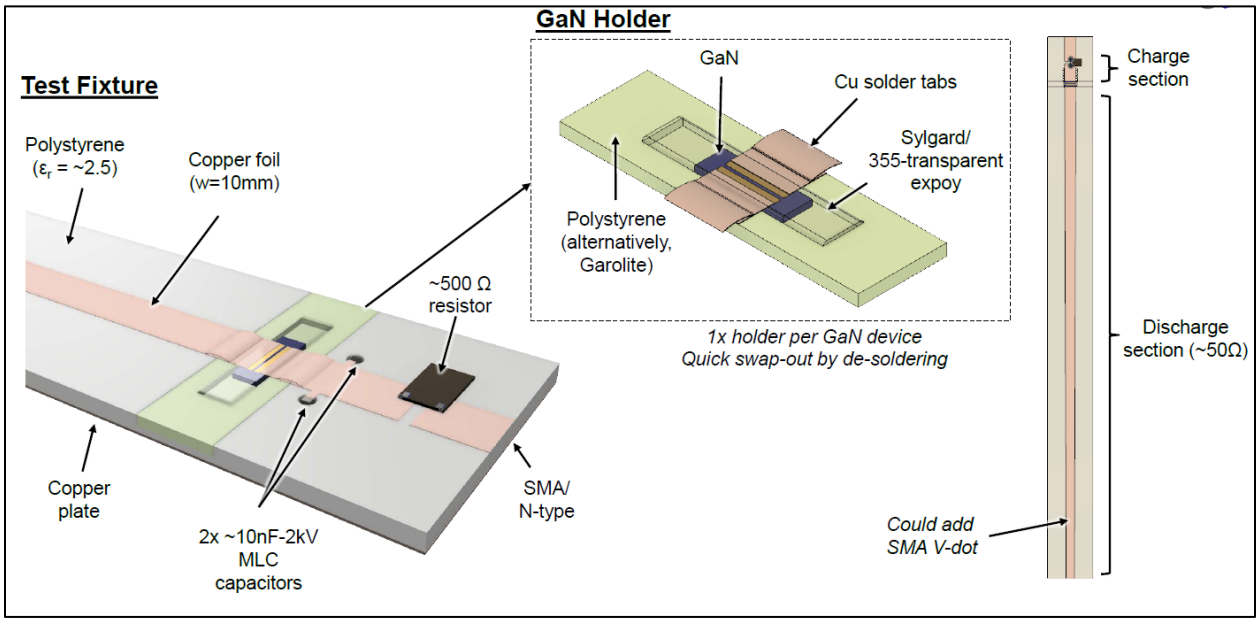


Figure A6. *Design of new GaN test fixture.*

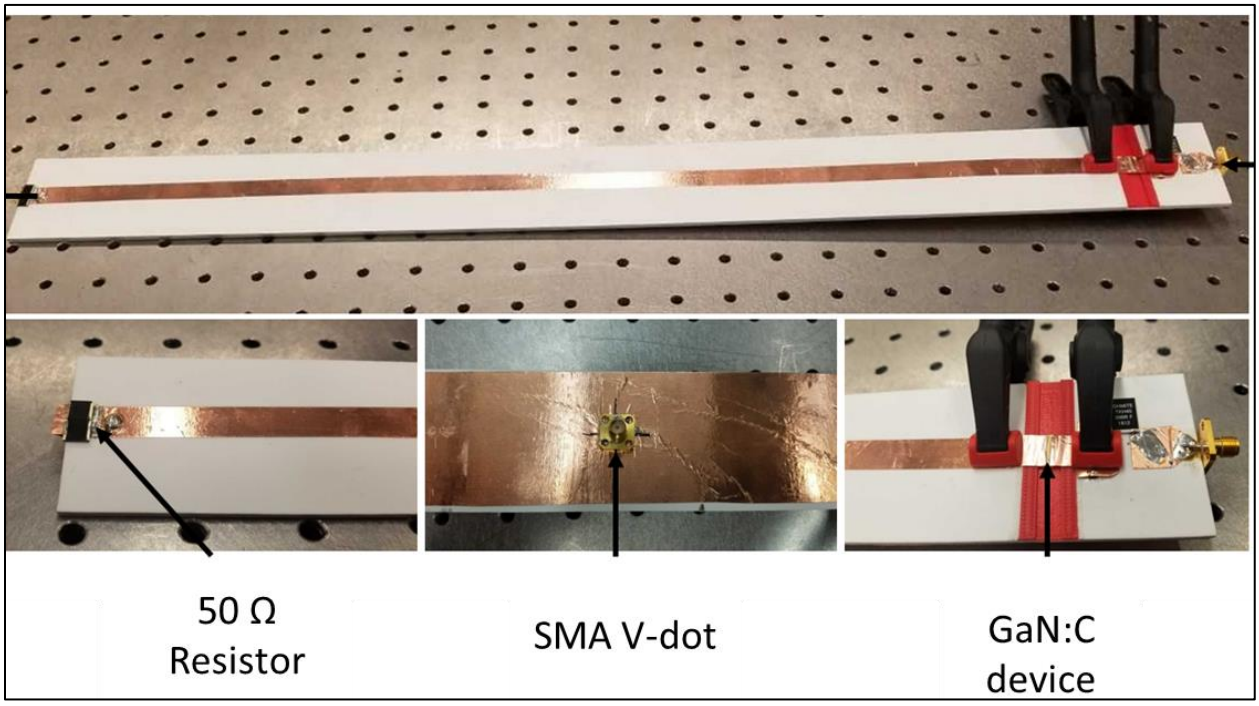


Figure A7. *Photos of GaN:C test fixture prototype.*

GaN Passivation with Epoxy (Utt)

Various epoxies are being considered for the GaN test fixture to prevent air breakdown at the surface and aid in device mounting. To determine the epoxy with the greatest transmittance at 355 nm, the THG system was used to illuminate epoxies pressed between two glass slides, and a power meter was used to measure the transmitted power. Two glass slides with no epoxy were used as a baseline. The samples and experimental block diagram are shown in Figure A8.

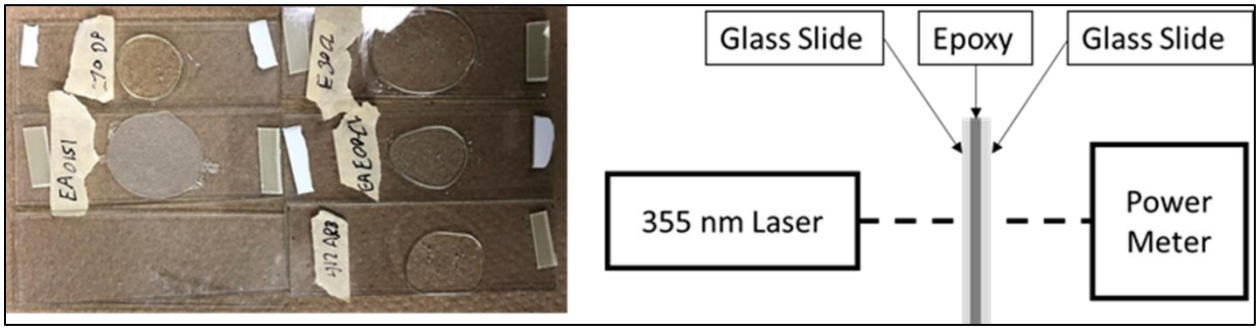


Figure A8. *(Left) Slides with transparent epoxy evaluated and (right) experimental block diagram of epoxy 355-nm transmittance measurement.*

The results shown in Figure A9 indicate that that the EA E-30CL, 412A&B, and the DP270 epoxies had the most transmittance at 355 nm. Moving forward, these two epoxies will be evaluated for hold-off on the GaN:C devices.

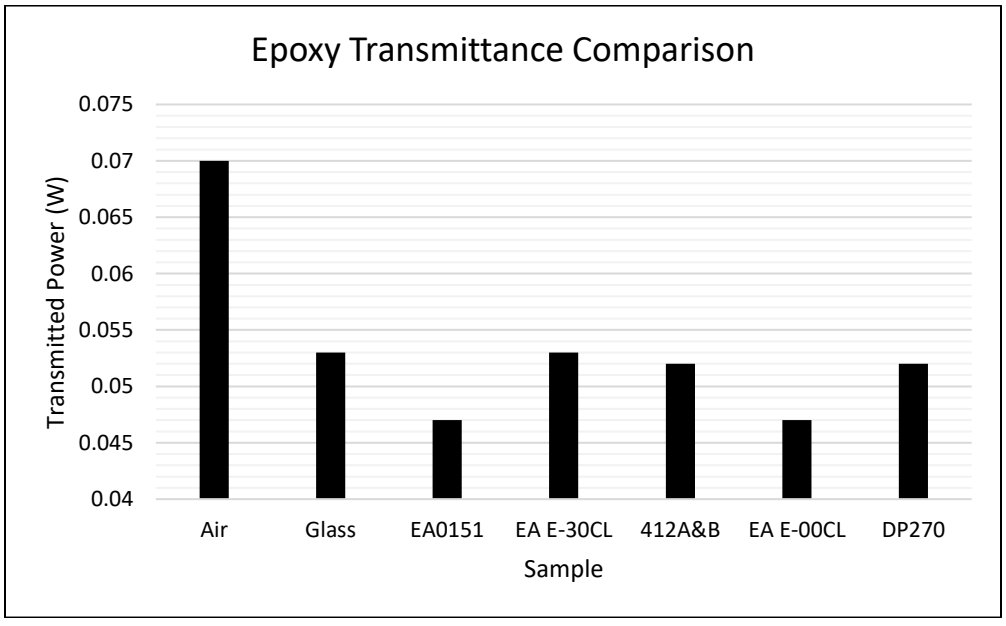


Figure A9. *Transmitted power through epoxy samples at 355-nm.*

I.A.1 Immediate Tasks of Fundamental PCSS Subgroup

i. Improve EL measurement process for characterization of PCSS breakdown.
ii. Improve TCAD model of transient recovery time in PCSS to agree with experimental results.
iii. Simulate SiPCSS pulsing via TCAD
iv. Narrow down the exploration to a specific material and switching technology.

I.A.2 Expected Products of Fundamental PCSS Subgroup

i. Student and staff posters and presentations for DEPS
ii. Epoxy selection for increasing GaN:C-PCSS hold-off

I.B GaN:C Subgroup (Rulis)

i. After the January activity of developing the ability to create device models, the past month refined that work to make the models align as needed with any designs that are produced or proposed by partners. Different material definitions and interfaces can be incorporated. Hence, the main activity of the past month has now moved to internal aspects of the device models.
ii. It is necessary to establish definitions within the FLOOXS script for how the interfaces should be treated. For example, what width, depth, and mesh density is needed for the contact regions so that the continuity equations, electric potentials, etc. will act across the interfaces between materials as a real system should. This process is still being completed.
iii. The current program code is shown illustratively in Figure B1 and over the past few weeks it has been developed and the correct expression of interface characteristics is still being debugged.

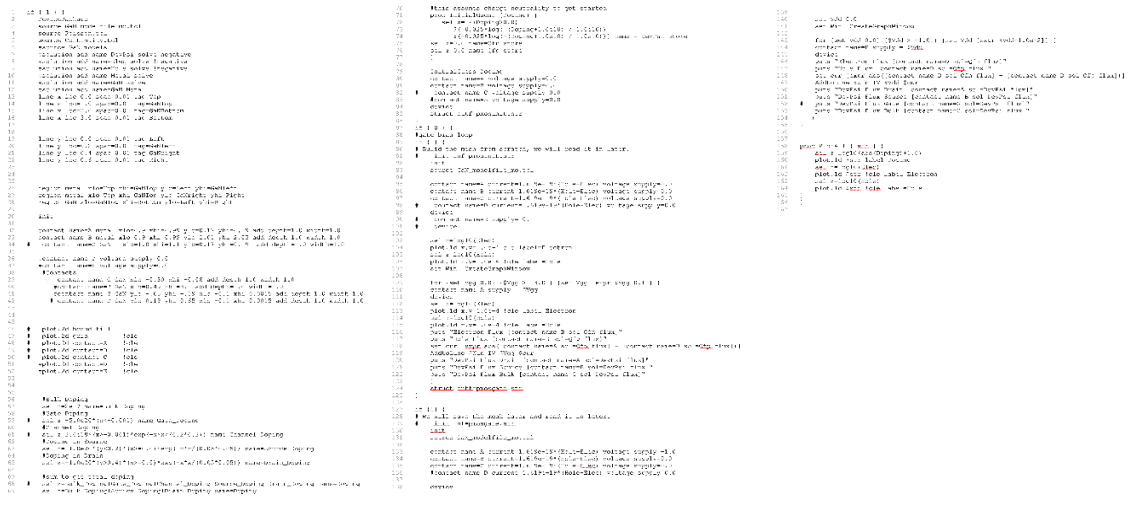


Figure B1*. Program code for GaN PCSS switch model.*

I.B.1 Critical Tasks of GaN:C Calculations Subgroup

i. We are looking to add more programs to the developing tool chain and over the next month we will seek out and evaluate additional full-band Monte Carlo simulators that may be used to link *ab initio* electronic band and phonon band structures to FLOOXS simulations. The first code we will evaluate is MOCA from the University of Illinois.
ii. As with the last month, the longer term critical task is to test our ability to direct FLOOXS to correctly model the simple electronic systems we have created so far when fundamental parameters are modified according to known empirical trends (http://www.ioffe.ru/SVA/NSM/Semicond/Si/electric.html). That process is still ongoing but is moving closer to completion. Several Si-based simulations have been demonstrated but some of the underlying aspects (as mentioned above) still need refinement before we will be able to integrate with computed ab initio input data. (Hence the investment in time proposed for seeking out Monte Carlo codes.)

I.B.2 Expected Products of GaN:C Calculations Subgroup

i. We have refined the basic models from last month and have made good progress in understanding how to correctly interface different materials "internally" in FLOOXS. In the coming month we will refine the internal interfaces in the models and to test the correctness of the simulations as described in the Critical Tasks above.
ii. We have started to more deeply understand the internals of the model interfaces. The next step will be to debug the programs and ensure via testing against Si models that the interface behavior is correct.

I.C Small Unmanned Aerial Vehicle Diagnostics and Design-of-Experiments (Fields)

aDOE/Testing

In preparation for testing at LLNL, the LabVIEW software for both the source control and UAV control were modified to accommodate the new LLNL platform while retaining as much automation as possible in the HPM-UAV testing environment. Additionally, another branch of the LabVIEW software was developed to integrate with the NIRF amplifiers and function generated (both housed at UMKC) in order to enable rapid source parameter exploration in the UMKC GTEM.

The adaptive DOE algorithm uses a K-nearest neighbor non-parametric model relating normalized source parameters to effects data as the basis for choosing the next set of source parameters to test. K-nearest neighbors is a form of non-parametric modeling that allows for variable flexibility in model structure. This feature allows the algorithm to "learn" and select its flexibility based on the level that best represents the data at that test cycle. After the algorithm spits out normalized test parameters, that test is conducted and the results analyzed and fed back into the original data set. This process is then looped until the relative error gets to a level deemed acceptable.

Using results from the GTEM testing at several facilities, an initial test regime was created using the adaptive DOE algorithm. Initial results indicate that there may be a problem with the way the algorithm prioritizes the normalized source parameters. Further vetting is required to give a complete assessment, and the data analysis is ongoing.

I.C.1 Immediate Tasks for sUAV Diagnostics and Design-of-Experiments Subgroup

i. Analyze data from DOE 0 testing at all locations;
ii. Investigate individual sensor component propagation through a feedback control system;
iii. Demonstrate feasibility in adaptive experimental design for improved effects results confidence with minimal experiments;

I.C.2 Expected Products of sUAV Diagnostics and Design-of-Experiments Subgroup

i. Experimental design plan based on results from DOE-0;
II. More powerful and cost-effective UAV platform.

I.D Positive Feedback Non-Linear Transmission Line (Khan)

During February 2019, we have initiated the design procedure of an in-house pulse generator to characterize the performance of fabricated NLTLs. Two pulse generator circuits have been fabricated based on half-bridge gate driver ICs. One of the initial prototypes is capable of generating pulses with minimum width of about 750 ns with a rise time of 50 ns. During the initial testing phase, we have used a 50V supply voltage to generate high voltage peaks. This design can be used with several hundred volts DC sources.

Input pulse amplitude applied to an NLTL directly affects the frequency of solitons generated in the NLTL. In general, the frequency of the soliton increases proportionately with bigger pulse amplitude. We have used a function generator to feed the NLTL in our previous experiments. The peak amplitude function generator output is limited to 10 V and the minimum rise and fall time of the pulse is limited to 8.9 ns. Commercial pulse generators can generate pulses with peak amplitude in the range of kilovolts and rise and fall time in the range of nanoseconds. However, the commercial pulse generators are expensive and occupy a significant amount of space, which could be problematic in our closed-loop NLTL setup. Our in-house generator can produce rectangular pulses with much higher peak amplitude (in the range of kilovolt) with adjustable pulse width in the range of hundreds of nanoseconds.

We have designed the first in-house pulse generator prototype using a half bridge gate driver IRS2104 from Infineon. This gate driver has two channels with the floating channel designed for bootstrap operation up to 600 V. The floating channel can be used to drive an N-channel power MOSFET or IGBT in the high-side configuration which operates from

10 V to 600 V. We have used a power MOSFET from Fairchild (Model-FQA8N100C) as the switching device of our pulse generator. This MOSFET has drain-source breakdown voltage of about 1000 V and a relatively low gate charge of around 53 nC. However, the MOSFET has a relatively large input capacitance (C_{iss}) of 2475 pF which affects the minimum achievable pulse width from the pulse generator circuit. The typical turn-ON and turn-OFF propagation delay time of the gate driver IRS2104 are about 680 ns and 150 ns. The typical turn-ON rise time and turn-OFF fall time of the driver are about 70 ns and 35 ns. The pulse generator circuit has been designed in Eagle CAD. The PCB board layout of the design and the fabricated prototype are demonstrated in Figure D1.

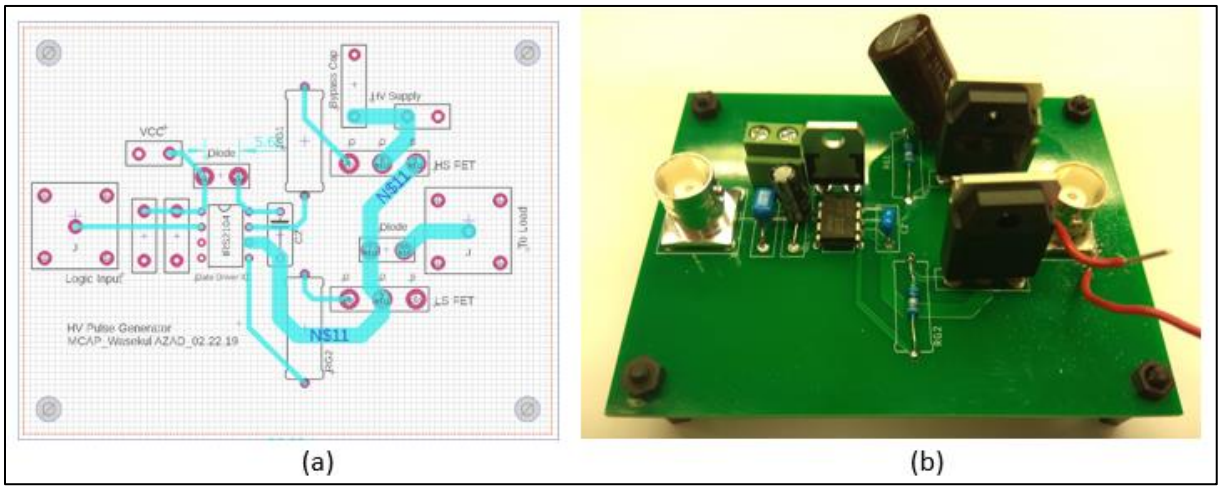


Figure D1*. (a) PCB board layout of IRS2104 based pulse generator (b) Fabricated prototype of the pulse generator.*

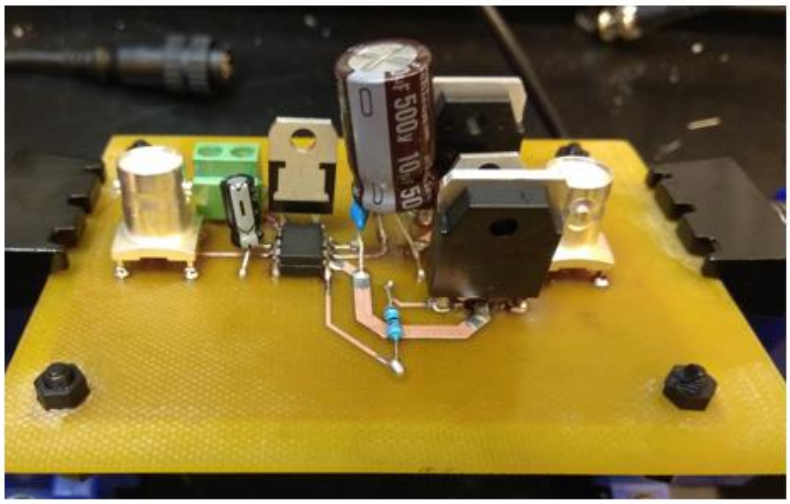


Figure D2*. In-house fabricated pulse generator prototype based on MIC4421.*

We have designed our second pulse generator prototype based on a 9A-Peak Low-Side MOSFET Driver MIC4421 from Microchip in an 8-pin DIP package. This gate driver has matched rise and fall times of 25 ns and typical turn-on and turn-off propagation delay times of about 15 ns and 35 ns. We have chosen the same power MOSFET FQA8N100C

in this pulse generator design. The PCB design has been done in Eagle Cad and the board has been fabricated in our in-house PCB milling machine LPKF ProtoMat. The fabricated prototype is shown in Figure D2.The output pulses across a 50 Ω resistive load corresponding to different switching frequencies are illustrated in Figure D3.

We are in the process of designing another pulse generator capable of producing pulses with narrower widths. We are considering silicon-carbide FETs like SCT10N120, C3M0120100J and GaN FET like TPH3206PSB with lower input capacitances as our switch options. SCT10N120 has input capacitance of about 290 pF which is significantly lower than FQA8N100C. TPH3206PSB has gate charge of about 6.2 nC and rise and fall times of about 4 ns which is considerably faster. We are planning to use a surface mount gate driver with lower propagation delay time and lower rise and fall times compared to the ones we have used so far. IXDD604 from IXYS, UCC27511A from Texas Instruments are two low side gate drivers which we are planning to use in our pulse generator design. In addition, we are considering a universal isolated gate driver UCC21520DWR from Texas Instruments as an alternative gate driver to use in half bridge configuration.

We will design the next pulse generator prototype in ExpressPCB. We will characterize the NLTLs with pulses with higher peak amplitude. We will incorporate the in-house pulse generator prototype in our closed-loop experimental setup constructed from NLTL and power amplifier and perform the closed-loop experiments.

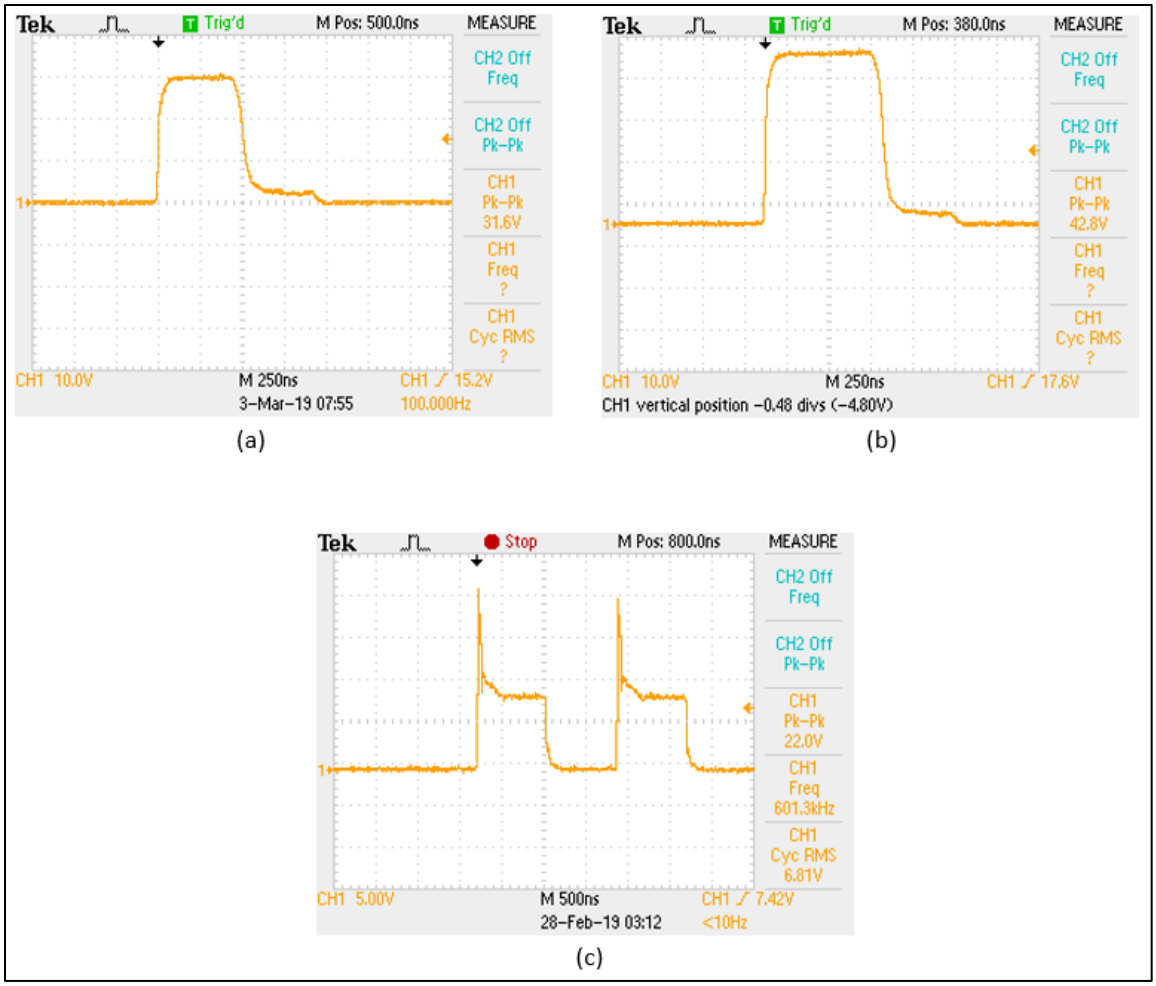


***Figure D3**. (a) A single pulse with 750 ns pulse width (b) A single pulse with 1000 ns pulse width (c) Two pulses with 750 ns pulse width generated by fabricated pulse generators.*

I.D.1 Immediate Tasks for the Positive Feedback NLTL Subgroup

i. Fabricating pulse generator capable of producing pulses in the range of hundred nanosecond and capable of handling high voltage in the range of kilovolts.
ii. Performing high voltage tests on different NLTL prototypes using excitation from the in-house high voltage pulse generator.

I.D.2 Expected Products of Positive Feedback NLTL Subgroup

i. Designing an RF amplifier with operating frequency in the range of 300 MHz - 800 MHz with around 300 MHz bandwidth.
ii. Power combining of multiple amplifier modules to scale up the power rating of the test setup.

I.E Applied RF Coupling Simulation and Modelling to/for sUAV (Hassan)

Characteristic Mode Analysis of Dielectric UAV frames

In the previous MSRs, we applied CMA to 3D scans of UAV frames with different resolutions as shown in Figure E1. In our previous simulations, we studied two materials for the UAV frame: (*i*) perfect electric conductor (PEC) and (*ii*) "Nylon 66" which has a relative dielectric permittivity, $\varepsilon_r \approx 3.3$. We focused on the first representation of the frame i.e. the one with the lowest resolution shown in Figure E1b. We showed that for the dielectric frame, the modal currents of the dominant modes at low frequencies exhibit maxima, hot spots, at the center part of the frame and minima at the arms. In this MSR, we move on to the 2nd representation of the UAV frame, Figure E1c, which has more features than the representation in Figure E1b and therefore is a more accurate representation of the actual geometry of the frame in Figure E1a. We hypothesized that the behavior of the characteristic modes of the representation in Figure E1c will be similar to that of the representation in Figure E1b since both representations have identical central parts and they differ only in the arms. Figure E2 shows that the current distributions of the first mode for both representations are very similar confirming this hypothesis. Therefore, Representation 1 is sufficient to quantify the coupling to the adjacent wires and electronics at a much lower computational cost than Representation 2.

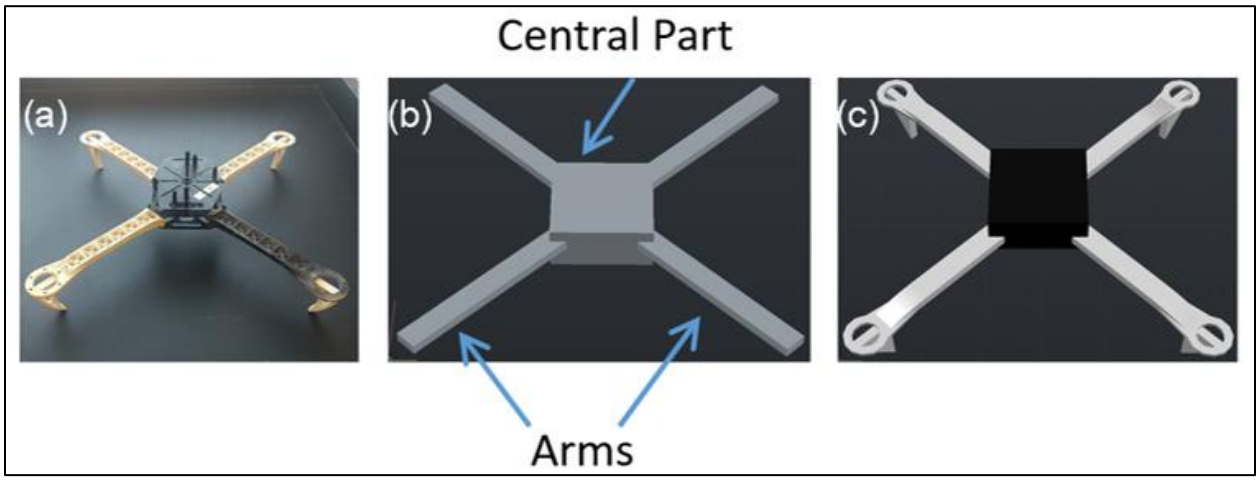


***Figure E1**. (a) Picture of the actual UAV, (b) 1st representation, and (c) 2nd representation.*

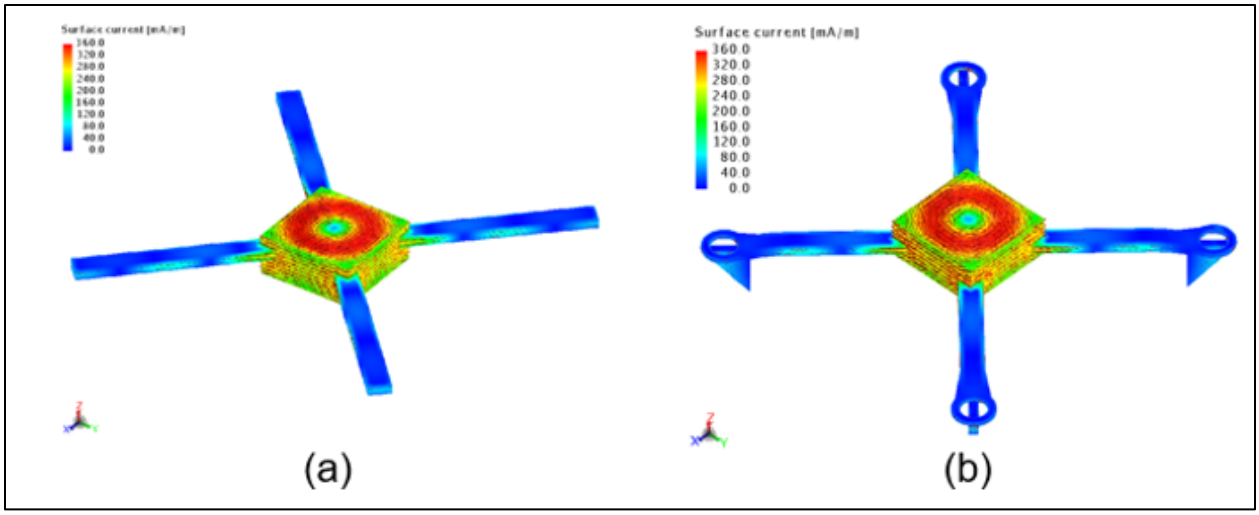


***Figure E2**. Mode 1 current distribution over (a) the 1st version, (b) the 2nd version of the dielectric UAV.*

In fact, Representation 1 can be simplified further by removing the arms and having only a dielectric block representing the central part of the frame to make the calculations even more efficient. Characteristic Mode Analysis (CMA) for both representations of the frame, shown in Figure E3 was performed. The two representations are assumed to have the same realistic dielectric properties as the common UAV frame plastics ($\varepsilon_r \approx 3.3$ "Nylon 66"). The Modal Significances of the first two modes for both representations are shown in Figure E4. The modal significances of both representations are identical. This analysis shows that the effect of the dielectric frame on the PCBs mounted on the center part of the UAV can be simplified and performed efficiently faster. Therefore, in addition to quantifying the response of a scatterer, CMA can also be leveraged to reduce the computational complexity of the coupling analysis.

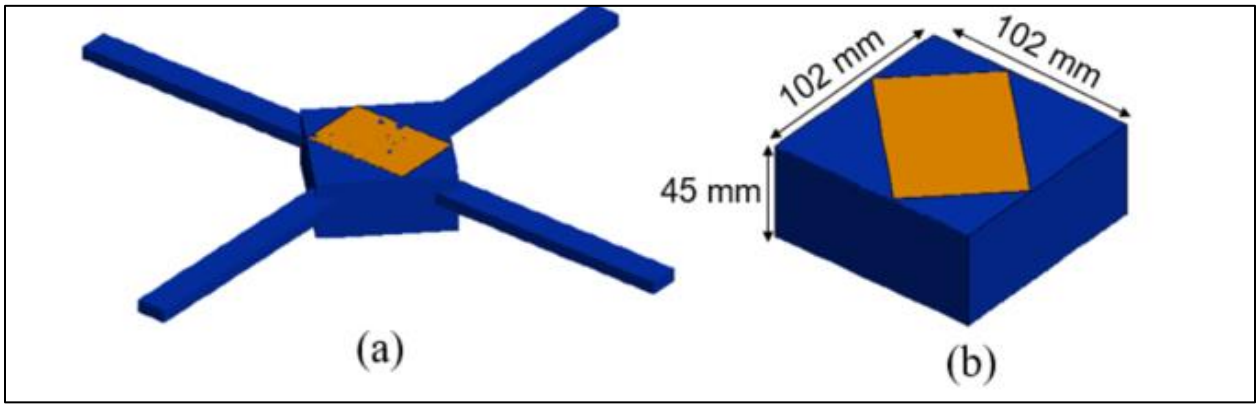


***Figure E3**. (a) The 1st version (b) Simplified representation of the dielectric UAV.*

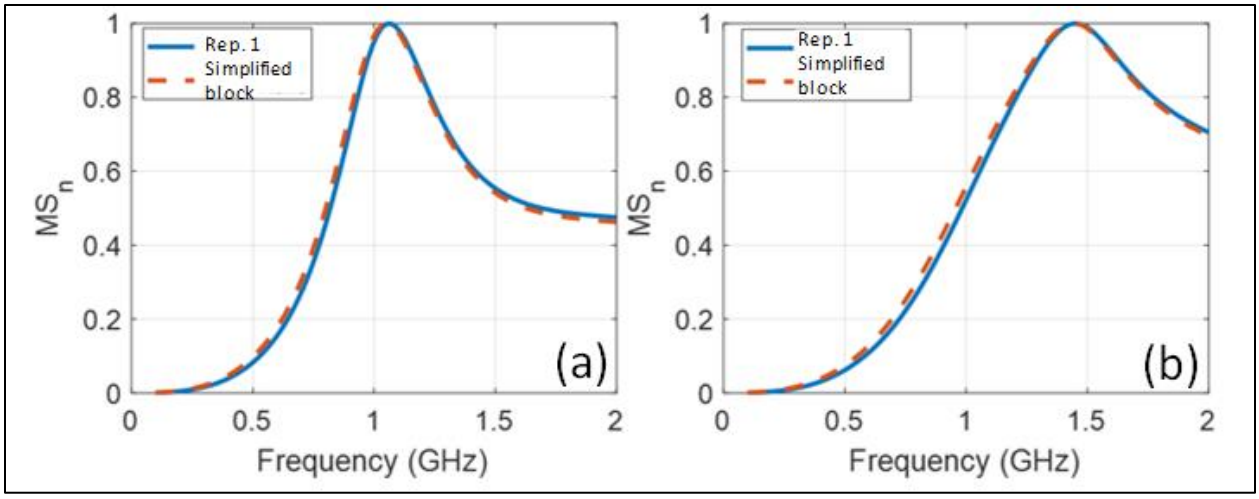


Figure E4*. The modal significance of the 1st Representation versus the simplified representation of the dielectric UAV (a) Mode 1 (b) Mode 2.*

CMA of Realistic Wire distribution of the UAV

In this section, we continue in our analysis of realistic UAV wire distributions. As shown in Figure E5, we simplified the wire distribution above the UAV and modeled the motors as 50 Ω resistors. We also started by modeling the PCBs as PEC sheets and the batteries as PEC boxes. The entire model is shown in Figure E5. The wire distributions in Figure E5 typically carry high currents since they are used to feed the motors. Therefore, an incident wave with significantly high power is needed to alter its nominal current flow significantly. However, we will focus on this wire configuration for the next few months because they are the larger features and they can also be used as secondary radiators to couple into the more relevant signal/microcontroller lines.

The length of one wire from one motor to the other motor in the opposite arm is 515 mm which is expected to resonate at around 0.3 GHz if the wire exists by itself in free space. However, the placement of the wires in the heterogeneous distribution in Figure E5, generates another mode at ~ 0.2 GHz. The modal significance of this mode has a complicated current distribution as shown in Figure E7. The maximum of the current distribution of Mode 1 is at two different positions. First, the battery lines exhibit maxima and this is clear in Figure E7 where these segments are shown in red. Second, the loads, which represent the motors, also have a high coupling which is not very clear in Figure E7 due to their small size. A parallel electric field is applied as shown in Figure E7 and the induced current at the load is calculated. Figure E8 shows the induced current at load 1. The induced currents resonance frequencies match these of the modal significance shown in Figure E6.

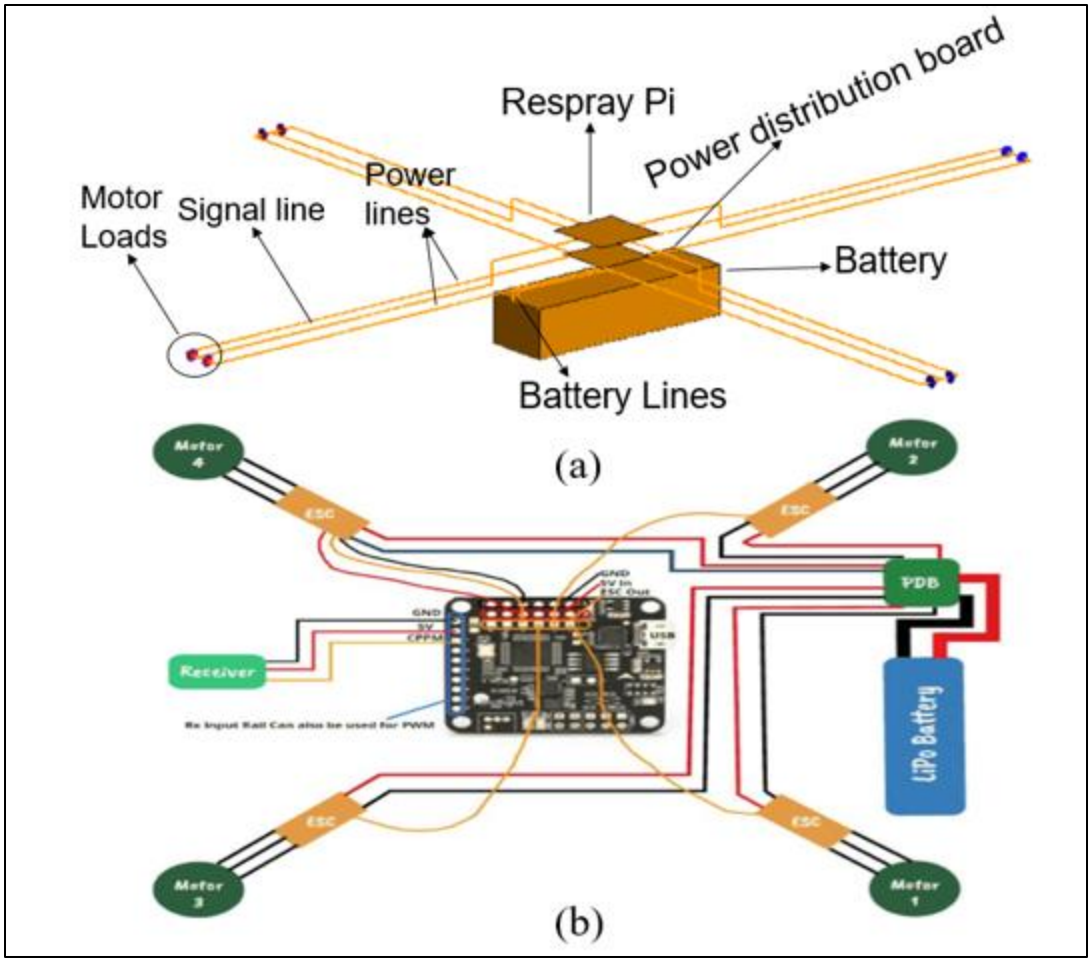


***Figure E5**. (a) Model of the wire distribution over the UAV, (b) the actual simple wire distribution of the UAV.*

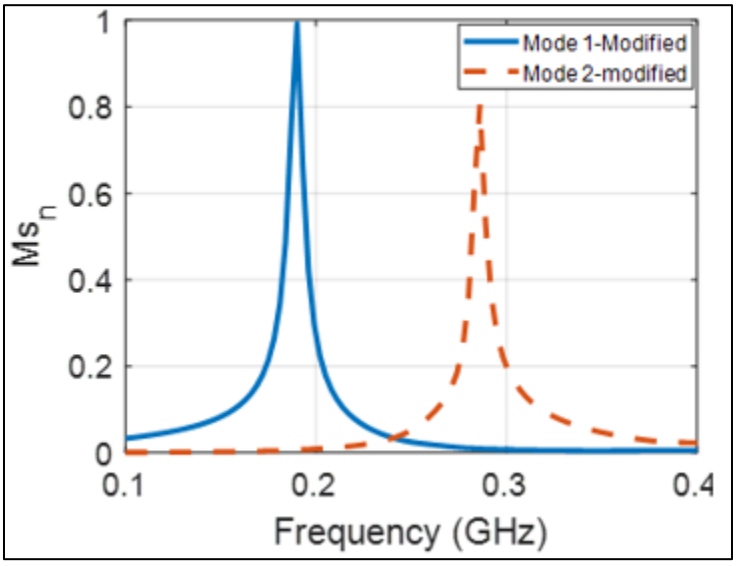


***Figure E6.** The modal significance of the wire distribution*.

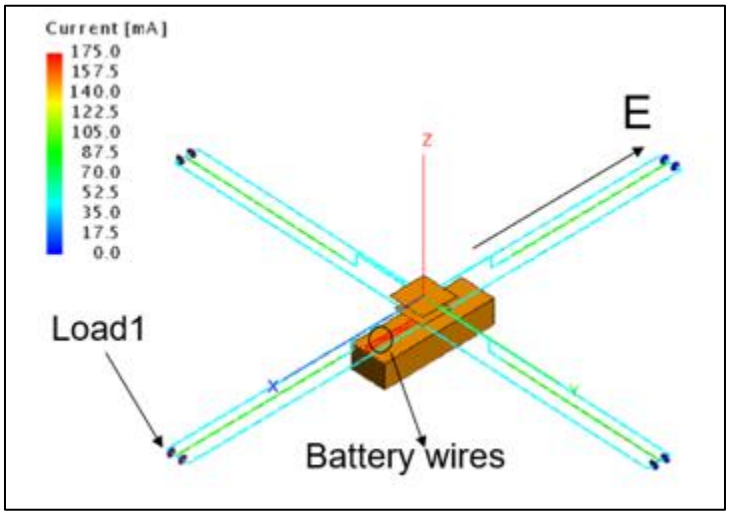


Figure E7*. The modal current of mode 1 of the wire distribution.*

The effectiveness of the modal analysis can be shown by maximizing/ minimizing the coupling to load 1. This can be guided using the radiation characteristics of Mode 1 of the structure. The radiation characteristics show how the excitation of the mode depends on the direction of the incident wave. That is the radiation characteristics indicate the optimum directions that can couple to each mode. The radiation characteristics of Mode 1 is shown in Figure E9 which shows that Mode 1 can be optimally excited by a ~ 90^o incident wave. In Figure E8, we plotted three different incidence angles to prove that a 90^o incident wave generates a larger current at the load than any other angle of incidence confirming the CMA predictions.

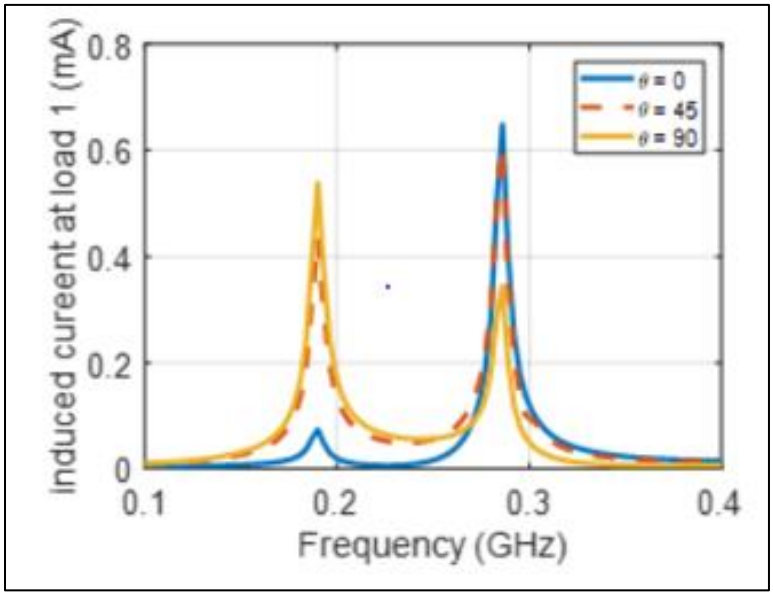


Figure E8*. Induced currents at the load at different angles of incidence.*

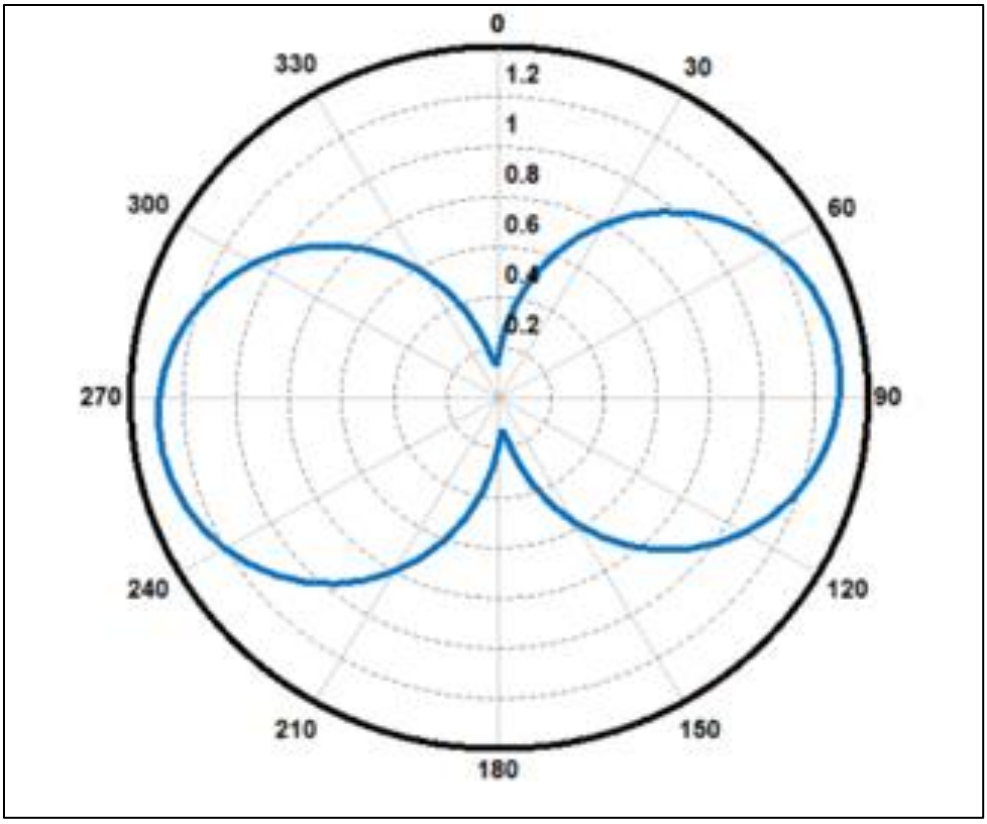


Figure E9*. Normalized Radiation Characteristics of Mode 1 of the configuration in Figure E5.*

I.E.1 Immediate Tasks for RF Coupling Subgroup

I. Study the effect of the geometrical features of the center part of the dielectric UAV on the coupling to the wires/PCB.
II. Study realistic wire distributions above the UAV frame to shows the effect of the frame on the modes of the wires.

I.F UMKC Diode Network Based NLTL (Doynov)

Introduction and Problem Scope

For an introduction to the scope of work on Diode-based Non-linear Networks (D-NLN), please see previous reports. For a brief reference, Figure F1 illustrates the waveform generated using a D-NLN. UMKC efforts are focused on lumped elements networks, in general, and diode-based voltage dependent capacitance in particular. In all current designs we use reversely-biased diodes as a variable capacitance.

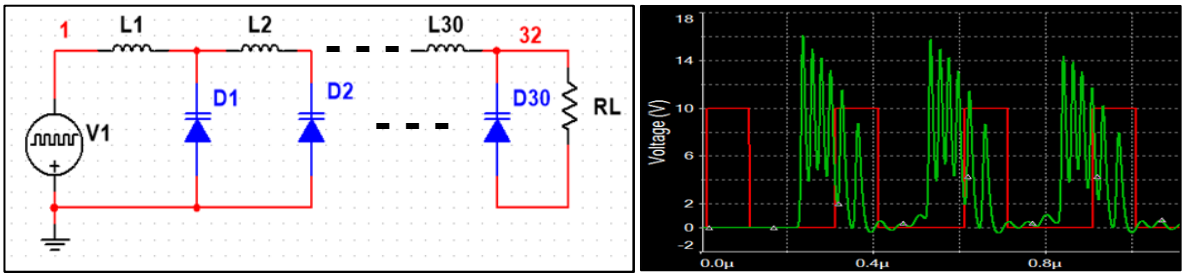


Figure F1*. Schematic presentation of lumped elements D-NLN (left) and the voltage waveform at the output when a sequence of rectangular pulses is applied at the input (right).*

D-NLN design considerations

We continue the exploration of design parameters primarily driven by the following factors:

- Ability to generate waveforms that will produce frequency in the desired bandwidth;
- Efficiency of the D-NLTL;
- Excitation with currently available pulse sources.

Graduate student, Nicholas Gardner, conducted an exhaustive exploratory investigation of the parameter space and made an internal presentation on the topic. The work continue to expand the study of the associated losses in a D-NLTL.

In our previous work, the parameter space of the input waveform was investigated. The focus of the investigation involved determining how the parameters of the input pulse would affect the output waveform. The primary pulse parameters of interest include; pulse width, pulse amplitude, and rise time. We have studied the input parameters with respect to the generated frequency and the generation efficiency. Trends of the dependencies are shown in Table F1.

Table F1*. Parameter space effects.*

Parameter	Effect on Frequency	Effect on RF efficiency
Pulse Amplitude [V]	Increased amplitude produces increased frequency	Increased amplitude produces increased RF generation efficiency
Rise Time [s]	Shorter rise times produce higher frequency.	Longer rise times decrease RF generation efficiency
Pulse Width [s]	Wider pulses produce higher frequency. Minimum width is needed	Unnecessary wide pulses decrease RF efficiency
Line Inductance [H]	Lower line inductance increases the Bragg and center frequencies	Lower line inductance decreases RF efficiency*

*Lower line inductance also decreased the amount of energy that could be injected into the line (it lowers the min/max values of the characteristic impedance range).

Multisim and LTspice are used to simulate D-NLNs with 10 to 40 inductor-capacitor cells. A pulsed voltage source is used to simulate the behavior of a PCSS. The input pulse parameters, the termination impedance and the C(V) characteristic are studied with respect to their effects on the output waveform. The effects of the amplitude and duration of the excitation pulse are shown in Figure F2. The wave-forms for each parameter are generated with delayed excitation pulses and superimposed on a single plot.

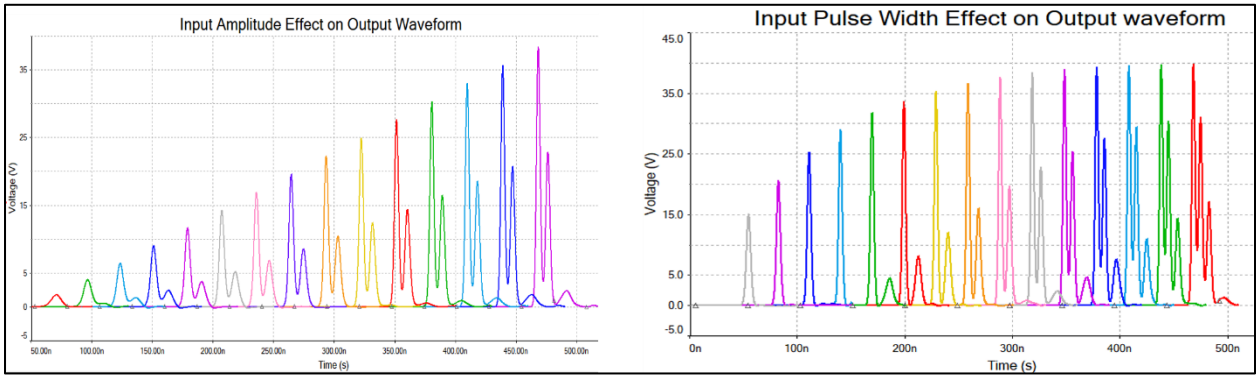
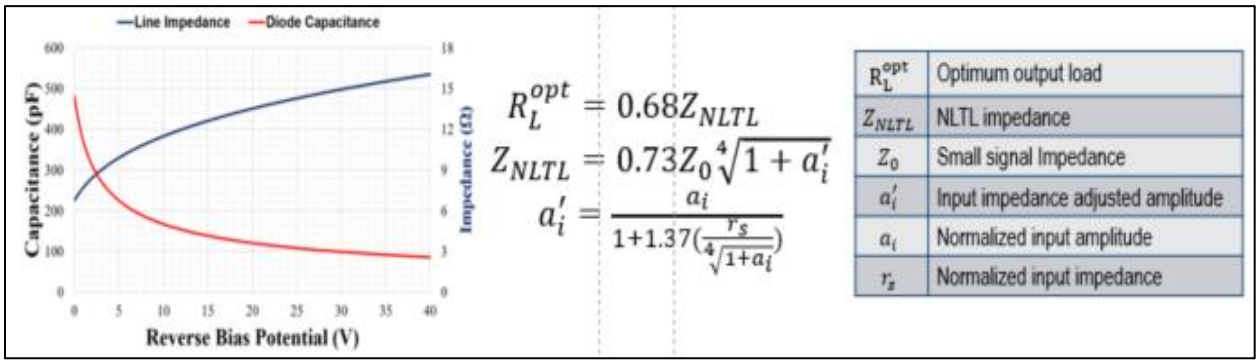


***Figure F2**. Examples of output wave-forms using input pulse with a different amplitude (left) and different pulse width (right).*

The additional parameters we have studied include the rise and fall time of the input pulse, the network cells' inductance and capacitance values, the number of LC-cells (line length), and the impedance matching with the load. Efficiency is calculated as the ratio of the output and input power. To block the DC and low-frequency content, a 3rd order Chebyshev filter is used at the end of the D-NLN.

With the rapid changes of the waveform, the impedance of the D-NLN sections changes rapidly and has a variable range of impedances due to the alteration of the instantaneous waveform amplitude by each cell. Examples for the C(V) characteristic of the 1N5822 diode and the characteristic impedance of a 20-cells network built with this diode is shown in Figure F3, left, with respect to the working voltage potential of the diodes. In [1,2], the authors defined a method for impedance matching and derived the formulas shown in Figure F3, center. The formula's notations are given in the table (Figure F3, right).



R_L^{opt}	Optimum output load
Z_{NLTL}	NLTL impedance
Z_0	Small signal Impedance
a_i'	Input impedance adjusted amplitude
a_i	Normalized input amplitude
r_s	Normalized input impedance

***Figure F3**. The range of diode capacitance and characteristic impedance (left); the derived empirical formulas (center) and parameters table (right).*

We conducted simulations to explore the generation efficiency using D-NLN with lengths ranging from 10 to 40 cells and using different load impedances. The results are shown in Figure F4. For the plots, the amplitude of the excitation pulse is normalized with respect to the diode junction potential. The input impedance is normalized with the small signal impedance. The red dot in the left plot indicates the calculated optimum impedance of 7.5Ω. For the simulated lumped-elements D-NLN, the efficiency peaks in the 15 to 20 number of cells range after which dispersive and losses decrease the overall efficiency (Figure F4, right).

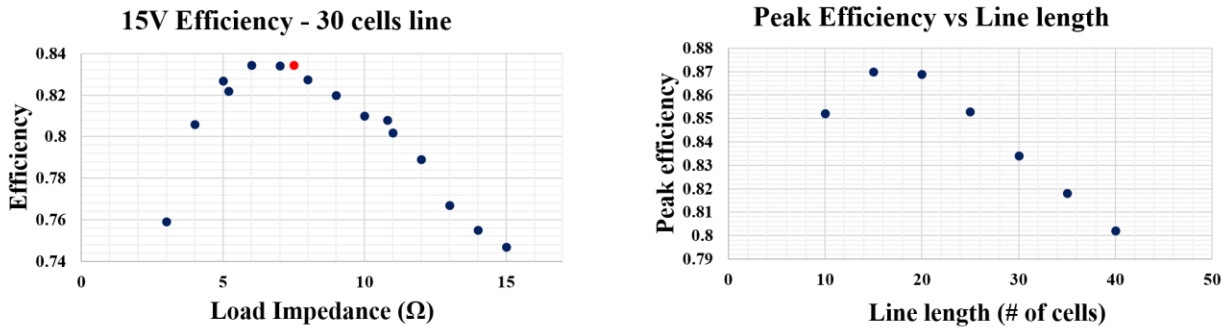
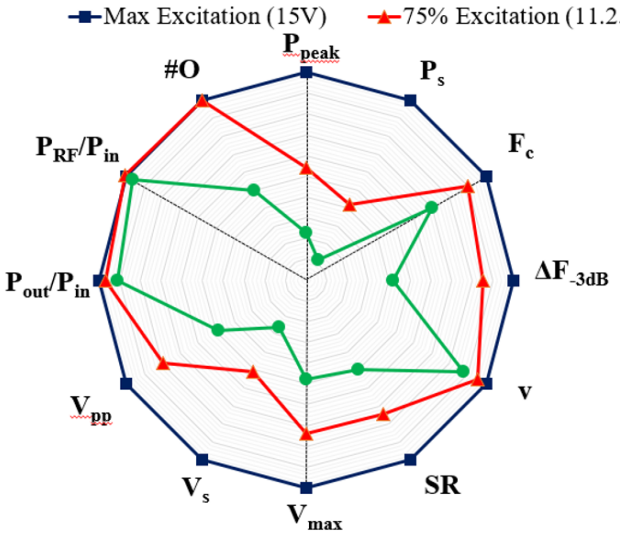


Figure F4*. The overall efficiency with different load impedance (left) and the peak efficiency for different number of cells (network length).*

We use a high-pass filter placed at the end of the line to deliver only the high-frequency content to the 50Ω load. We have developed a performance comparison graph that is used to display visually the input-output parameters for a given D-NLN topology. The performance comparison graph and a table with the associated values for each parameter are shown in Figure F5. In this example, the pulse width and rise time are kept constant and the amplitude of the input pulse is varied in the range from the maximum possible value (limited by the used diodes) down to 50% of the maximal value. Similar graphs are produced for varying the rise time or the pulse width.



Parameter	Symbol	Max	75%	50%
Peak Power (W)	P_{peak}	29.5	16	6.7
Second peak power (W)	P_s	10.5	4.4	1.2
Center Frequency (MHz)	F_c	100	90	70
-3dB bandwidth (MHz)	ΔF_{-3dB}	100	85	42
Per cell speed (cell/s)	v	0.41	0.39	0.36
Slew rate (V/ns)	SR	7.5	5.6	3.75
Peak voltage (V)	V_{max}	38.4	28.3	18.3
Second peak voltage (V)	V_s	29.4	14.9	7.7
Peak to peak voltage (V)	V_{pp}	27	21.5	13.2
Efficiency	P_{out}/P_{in}	0.482	0.465	0.439
RF efficiency	P_{RF}/P_{in}	0.148	0.149	0.143
# peaks above 50% Peak Power	#O	2	2	1

Figure F5*. Performance comparison. Max input corresponds to max excitation amplitude possible without exceeding the max reverse bias voltage of the diodes. The performance parameter values for the 75% Vmax and 50% Vmax input pulses are normalized with the Vmax values.*

The C(V) characteristic of the used diode effects the most performance characteristics of the D-NLN. SPICE simulation software typically models the characteristic curve using the parameters: zero bias junction capacitance *Cjo,* grading coefficient *m*, and junction potential of the diode *Vj*. The capacitance is given by

$$C = \frac{Cjo}{\left(1+\frac{V}{Vj}\right)^{m}}$$

We have evaluated the effects of the individual parameters of the model on the C(V) curve of the diode and on the output frequency of the line. The results are shown in Figure F6.

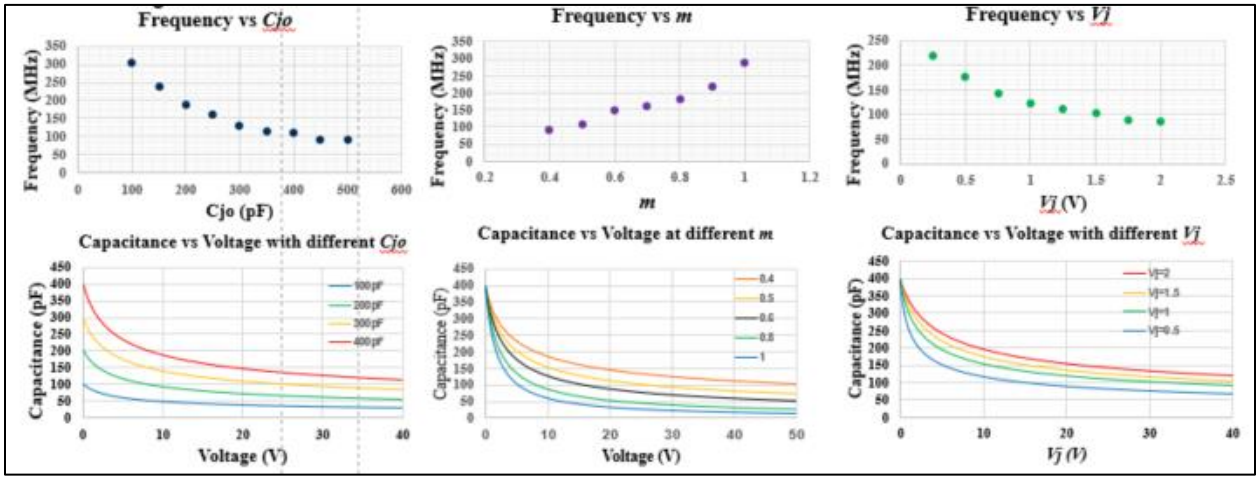


Figure F6*. Top row, left to right: Parameters' effects on the output waveform frequency. Bottom row: Series of C(V) curves for different values of each parameter: small signal capacitance (Cjo), junction grading coefficient (m), junction potential (Vj).*

To investigate the effects of losses on the line, the ideal inductor is replaced with a model which includes the resistance of the inductor. The value of the in-series resistor was varied from 1mΩ to 100mΩ and the results are shown in Figure F7. The center frequency remained unchanged at around 105MHz. Additional effects will be studied and will include parasitic capacitance and inductance and frequency dependence of the losses.

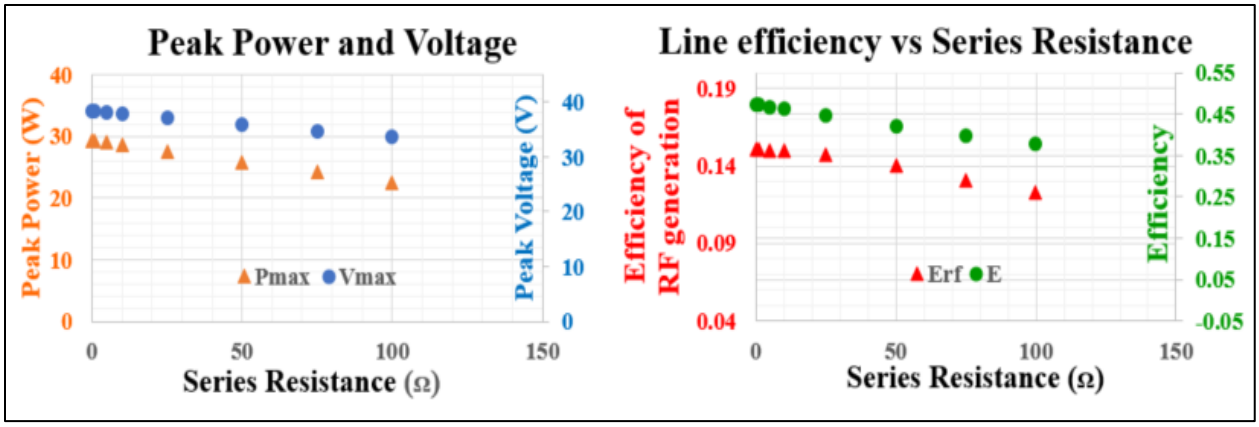


Figure F7*. Effect of inductor resistance on the peak power and voltage (left) and the RF efficiency generation and the total line efficiency (right).*

We have started to implement the simulated designs to test and compare the measured values with the simulated results. An image of 20-cell D-NLN is presented in Figure F8.

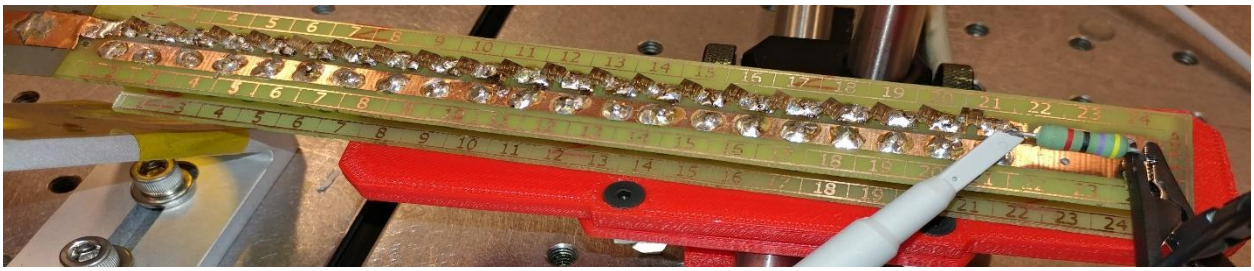


Figure F8*. 20-cell Diode NLN under test.*

Issues

As indicated in the previous reports, some of the D-NLN parameters cannot be defined precisely based on simulation only and will be available after implementation and testing. Many design issues and component specifications remain to be investigated using measurements. A separate constraint is that most available models and components are for low-voltage components and the purpose of the studies is HPM generation. Some of the relatively high-voltage devices do not have publically available C(V) characteristics and they have to be measured in order to be used in simulation. The same applies to the use of serially-stacked diodes. Proper practical impedance matching continues to be an important aspect of our investigation.

I.F.1 Immediate Tasks for UMKC Diode Network Based NLTL Subgroup

During the next reporting period, we plan to:

i. Implement additional D-NLN to generate different center frequencies and power;
ii. Test and compare measured to simulation results;
iii. Modify simulated designs to replicate the observed effects;

iv. Focus on improving the network efficiency; and,
v. Collaborate with EHT for the simulation, evaluation and testing of HV D-NLN.

Accomplishing these tasks will determine the success of the design approaches. We will continue active communications and design documentation exchanges and updates.

I.F.2 Expected Products of UMKC Diode Network Based NLTL Subgroup

i. Comprehensive D-NLN parameter space evaluation.
ii. Design and implementation of D-NLN working prototypes.
iii. IP and presentations/publications on the topic.

References

[1] Nikoo, M. S., & Hashemi, S. M., "Analysis of the power transfer to a nonlinear transmission line", IEEE Transactions on Microwave Theory and Techniques, 65(11), 4073-4083. doi:10.1109/TMTT.2017.2701366, (2017).
[2] Nikoo, M. S., Hashemi, S. M. and Farzaneh, F., "Theory of terminated nonlinear transmission lines", IEEE Transactions on Microwave Theory and Techniques, 66(1), 91-99. doi:10.1109/TMTT.2017.2731958, (2018).

I.G Electrically Small Antennas (Chatterjee)

The efforts in the two research directions are described as below. There are two distinct efforts: (a) trade space studies/parametric analysis on down selecting a *phased array* and (b) investigations into *electrically small antenna* (ESA) characterization. The ultimate goal is to explore options on how to finally integrate an ESA as an element in a phased array for realizing a desired performance at 400 MHz and 800 MHz. We have assumed the steady-state (or CW) behavior of transmission in our present studies. It is possible that pulse-modulated signals will be used. While the variety of options are indeed vast to determine the various important aspects of the trade space studies, in this present preliminary study we have limited the scope to the most important and fundamental aspect of phased arrays and investigated only one type of electrically small antenna – meandering dipole. For phased array characterization, we need to study both the planar and linear topologies. However, the present preliminary study focuses on results and analysis for the linear array. Similar issues are shared by a planar array, which shall specifically be addressed later. For the ESA, many topologies can be studied. However, for the current investigation of a preliminary nature, we present results for a meandering dipole. Aside from obtaining the results that characterize the antennas, reasonable background material has been included to present a comprehensive overview. The outline for future work in each category has been included. These efforts are described below.

Linear Phased Array (Bidisha Barman and Deb Chatterjee)

The phased array [1]-[4], in general, is distinct from any other antenna in the sense that the pattern is dynamic – moves in space. This is electronic scanning and is achieved by putting a progressive phase taper across the elements. Thus in a linear array of 7 elements the main beam can be moved by 15^0 from the boresight by putting progressive phase shifts: $0°$, $15°$, $30°$,$45°$, $60°$, $75°$ and $90°$ across each of the individual elements.

It is well known [4], the most important function of a phased array is *beam steering*. A topical question of interest in the phased array performance is: what are the most important parameters of importance that get affected by the beam steering, and how? This question is of paramount importance because these would assume significant importance in our trade space/parametric studies. The fundamental issue here is to seek what causes the degradation and/or enhancement of the antenna parameters as beam steering is affected. The results included here are focused on elaborating aspects that are of importance in the trade space analysis.

The ***primary*** quantities of interest in *any* antenna are: (a) directive gain, (b) beamwidth, (c) sidelobe levels, (d) polarization, and, (e) bandwidth. Each of these parameters are related to the scan or steering angle. The trade space study aims at studying the degradation of these parameters with scan angle. The issue here is that while some parameters may degrade more rapidly than the others, some may degrade only gracefully or not at all. This then becomes a tradeoff issue.

The array behavior is dictated by one very important physical phenomena: *mutual coupling.* The mutual coupling has been the subject of many investigations reported [1]-[10]. As shown in [1], [4], [5], [6], [10], the mutual coupling is contained within the vector (electromagnetic) nature of the array, while the beam forming aspect of the array is scalar and is contained in what is known as the array factor. Taken together, the overall array pattern can be written/derived as:

$$\text{Array Pattern} = \text{Element Pattern} \times \text{Array Factor}$$

The element pattern is the one that contains the mutual coupling effects, but it surely affects the overall array radiation behavior. This is the most crucial aspect in the trade space analysis. Since the gain, beamwidth and sidelobe levels are all dependent on the array radiation pattern, it follows that mutual coupling affects in all three important parameters. Thus, our radiation pattern results shall include both with and without mutual coupling at the boresight (no scan). At scan angles off the boresight the results shall include mutual coupling. Inclusion of mutual coupling in the results for the radiation patterns is accomplished with the full-wave EM solver FEKO. The use of FEKO for phased arrays has been advocated in [5], and this suggestion is followed here for obtaining the relevant results.

In general the array factor can be expressed as a sum that reads:

$$\mathrm{AF} = \sum_{n=0}^{N-1} w_n z^n$$

.....(1)

In (1), w_n array excitation weights, $z = e^{j(\beta d \sin\phi + \alpha)}$. Here the wavenumber is $\beta = \frac{2\pi}{\lambda}$ and *d* is the interelement spacing. The progressive phase shift between elements is α. The angle ϕ is measured from the x-axis for a linear array of dipoles oriented parallel to the z-axis and hence lying in the z-x plane. Note that $0^\circ \leq \phi \leq 360^\circ$. The dipole radiation is on both sides and is symmetrical about the x-axis. The beam forming with this linear array therefore happens in the x-y plane and the array boresight is along the y-axis ($\phi = 90^\circ$). The array radiation patterns are considered only in the x-y plane. Note that $|z| \leq 1$. Equation (1) is the fundamental basis of what is known as the *Schelkunoff's array polynomial method* (unit circle) and described variously in [3],[4],[5],[10].

To obtain an array factor, one needs to determine the (real) amplitude excitation weights, we have considered only two: (i) Taylor and (ii) Bickmore-Spellmire [5]. The details of the Taylor method for calculating the weights are given in [10], but the Bickmore-Spellmire has not been investigated as extensively in the published literature. However, both belong to the narrow main beam, low-sidelobe synthesis category. Thus we have included results for both for a preliminary comparative analysis.

The synthesis method for both cases begins by specifying the required sidelobe level. In comparison to the Taylor, the Bickmore-Spellmire offers more degrees of freedom but that was not very important for the cases examined here. Essentially, both methods actually sample a *continuous* current distribution. The forms of the current in the two cases are different. The Bickmore-Spellmire has the unique property that the current vanishes identically for the edge elements. This means that the edge elements are not excited, which means saving of energy.

The Taylor weights are given by [10]:

$$w_n = f(n, A, \bar{n}) = \frac{[(\bar{n}-1)!]^2}{(\bar{n}-1+n)!\,(\bar{n}-1-n)!} \prod_{m=1}^{\bar{n}-1} \left(1 - \frac{n^2}{x_m^2}\right); |n| < \bar{n}$$

..... (2)

$$w_n = 0; |\mathrm{n}| \geq \bar{n}$$

..... (3)

The array 3-dB beam width is given below for an array length L and sidelobe level R as:

$$\Theta_{3dB} = 2\sin^{-1}\left\{\frac{\lambda\sigma}{\pi \mathrm{L}}\left[(\cosh^{-1} R)^2 - \left(\cosh^{-1}\frac{R}{\sqrt{2}}\right)^2\right]^{\frac{1}{2}}\right\}$$

..... (4)

In (4) there is the term σ which is known as the *beam dilation factor.* This factor shows the amount by which the main beam gets enlarged because of the design requirement for a lower sidelobe level.

In much the same way, the amplitude weights for the Bickmore-Spellmire are given by:

$$w_n = \left[1 - \left(\frac{r_n}{r_{max}}\right)^2\right]^q \Gamma(q+1) \sum_{k=0}^{\infty} \frac{\left(\frac{y_n}{2}\right)^{2k}}{\Gamma(k+1)\Gamma(k+q+1)}$$

..... (5)

The expression in (5) is a simplified and computationally useful form of the original form available in [5]. The derivation of (5) is shown in Appendix I. The quantity r_n is the distance of the nth element from the array center. The edge element is located at r_{max}. When $r_n = r_{max}$, $w_n = 0$. The quantity y_n is defined in equation (9) in Appendix I. The $\Gamma(x)$ in (5) is the standard Gamma function.

Once the weights are known from (2), (3) (Taylor) or (5) (Bickmore-Spellmire), these are then used in FEKO, which is a full-wave EM solver, to get the radiation pattern that includes mutual coupling effects. The effects of beam scanning in presence of mutual coupling on the boresight gain and 3-dB beamwidth degradation are studied by comparing against the formula from [4] that reads:

$$\Theta_{3dB} = \frac{\Theta^{\circ}_{3dB}}{\cos\theta_{\circ}}$$

..... (6)

In (6) Θ°_{3dB} is the 3-dB beamwidth when there is no scan, or, $\theta_{\circ} = 0$. In (6) the scan angle $\theta_{\circ} \Rightarrow \alpha$ in (1), which is the progressive phase shift across the elements. The representative preliminary results are shown and discussed briefly.

Results

A linear array of 25 elements was considered with an interelement spacings of $\frac{\lambda}{4}$ and $\frac{\lambda}{2}$. For both Taylor and Bickmore-Spellmire synthesis, a design sidelobe level of -25 dB was chosen. The schematic of the array is shown below for visualization.

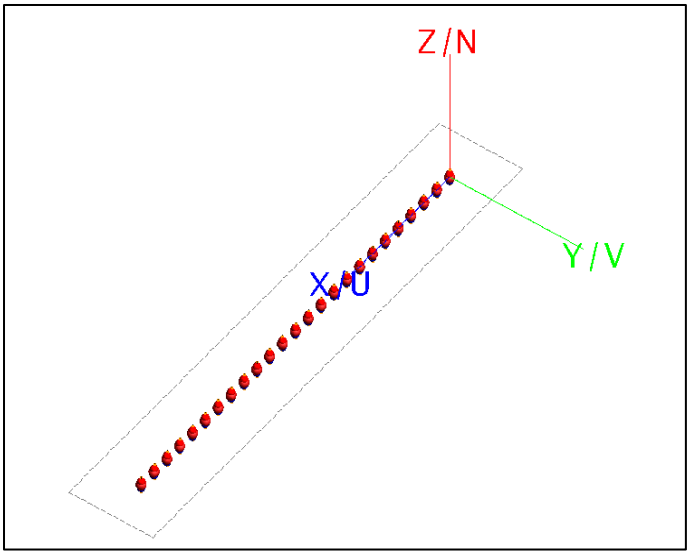


***Figure G1**. Linear array with elements along x-axis. The red blurbs are elements of the array.*

The current distribution across the array for the Taylor synthesis is shown in Figure G2, below and in Figure G3 the same result for Bickmore-Spellmire is included.

A comparative analysis of radiation pattern is shown in Figure G4 that shows the basic differences between Taylor and Bickmore-Spellmire synthesis. We can conclude that Bickmore-Spellmire is more suitable for high power applications because of the rapid decay of the far out sidelobes compared to Taylor. This means most of the power is concentrated in the main beam region in the Bickmore-Spellmire excitations than Taylor. However, the 3-dB beamwidth is narrower for the Taylor case and this accompanied by the much higher far-out sidelobes for the Taylor case. The narrower beamwidth in the Taylor case means that ½ the power is passing through a narrower angular zone in the Taylor synthesis, but the power in the sidelobe region is much less in the Bickmore-Spellmire case.

Figure G5 shows the effects of mutual coupling on the radiation pattern for the Taylor case. (The Bickmore-Spellmire was not explicitly computed for *without* mutual coupling because the array factor needed to be computed by the Schelkunoff's array polynomial method and this is deferred to for an immediate future work.) One can notice the effects of mutual coupling, which causes the sidelobe levels to rise. This is a distinctive feature of mutual coupling in general.

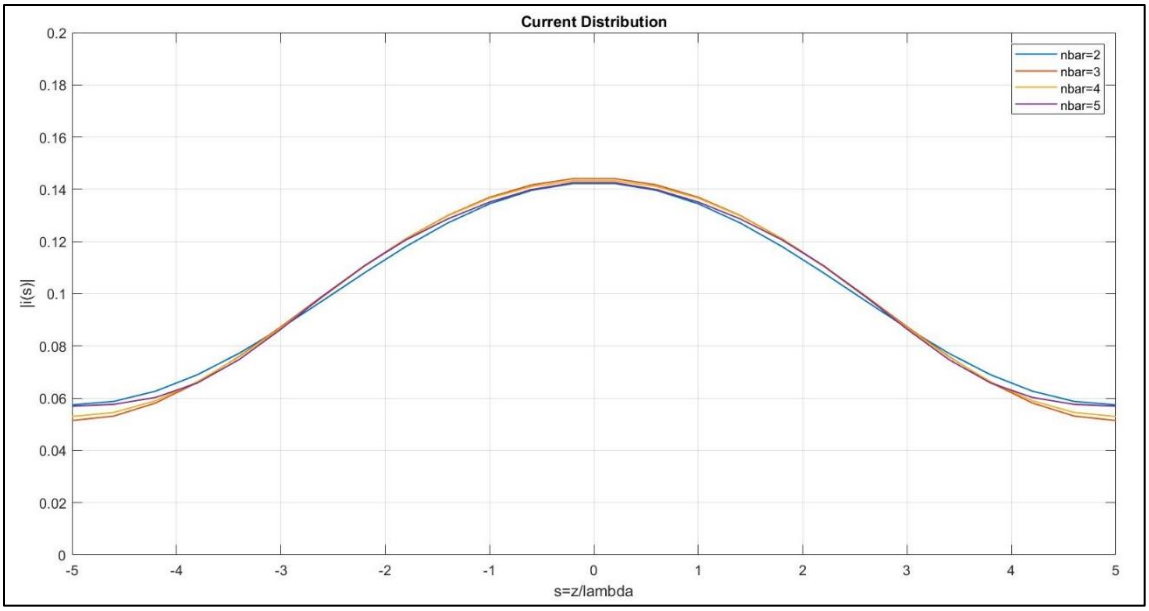


***Figure G2**. Current across the linear array for Taylor synthesis with $\frac{\lambda}{2}$ interelement spacing and $\bar{n} = 2, 3, 4, 5$*

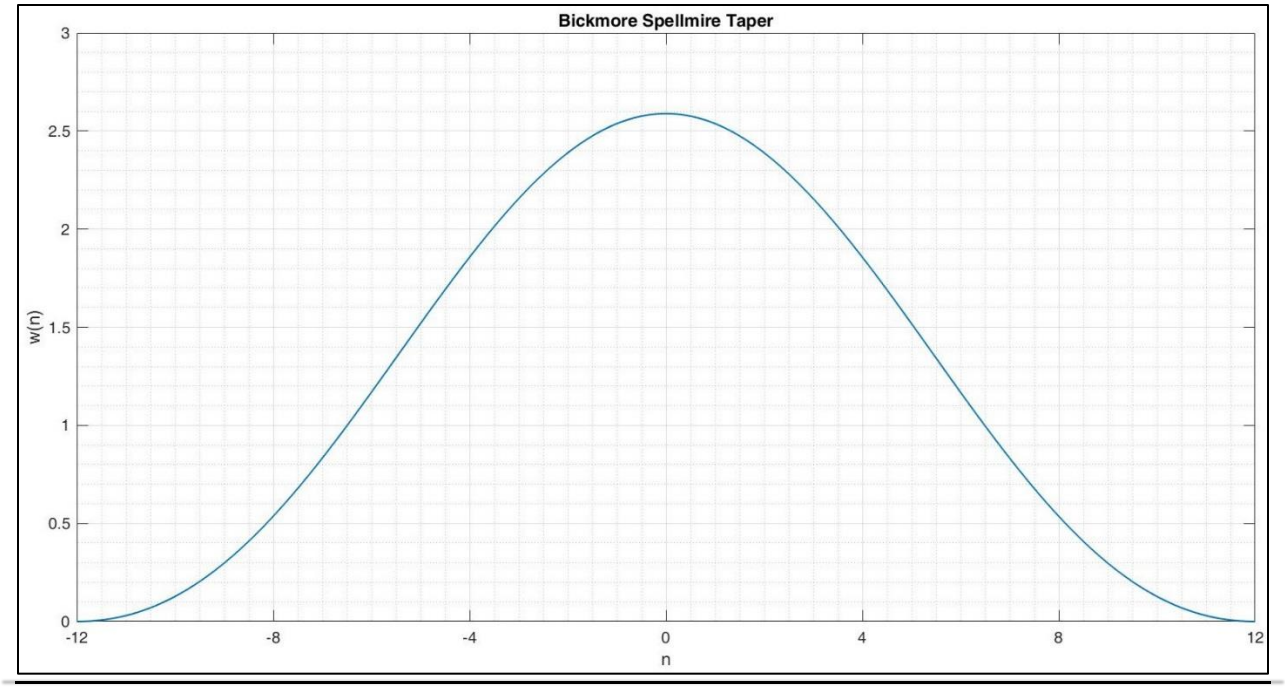


***Figure G3**. The current across a 25 element linear array of interelement spacing of $\frac{\lambda}{2}$ for Bickmore-Spellmire synthesis.*

Figures G6 and G7 show the beam steering in presence of mutual coupling (FEKO). In both Taylor and Bickmore-Spellmire cases one does not observe much noticeable degradation in radiation patterns. However, the beamwidth increases and that is demonstrated in the tables following Figures G6 and G7.

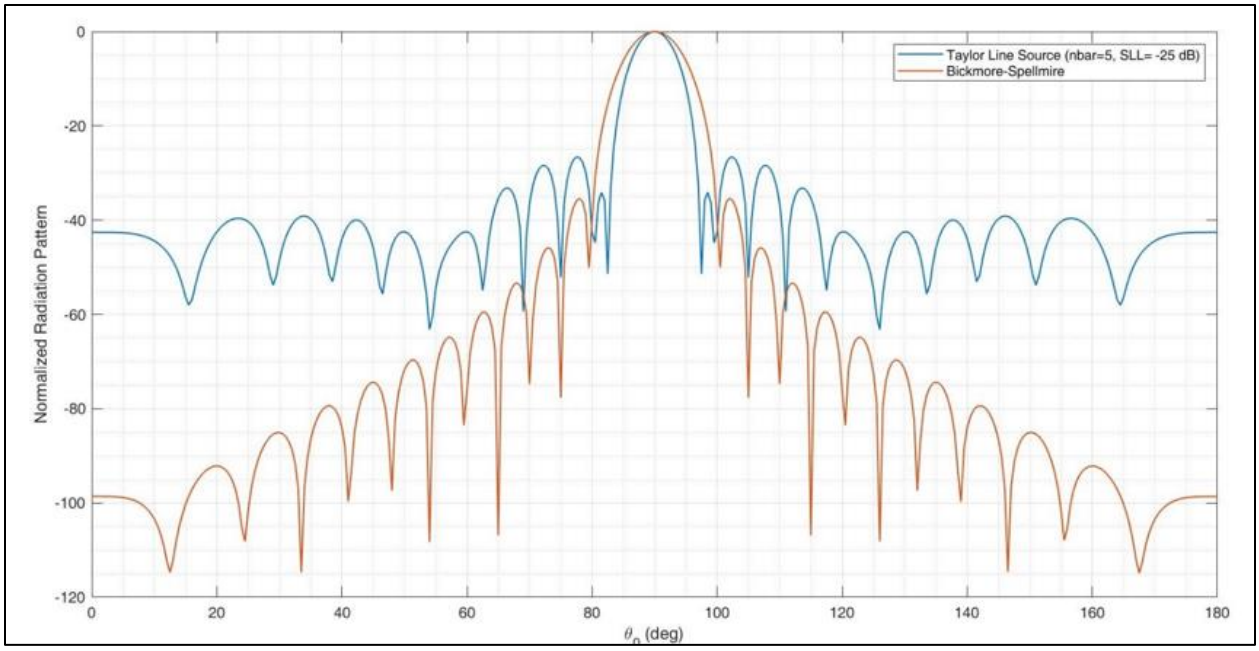


***Figure G4**. Comparisons between Taylor and Bickmore-Spellmire radiation patters for no scan. Both the results include mutual coupling effect that are contained in-situ via FEKO.*

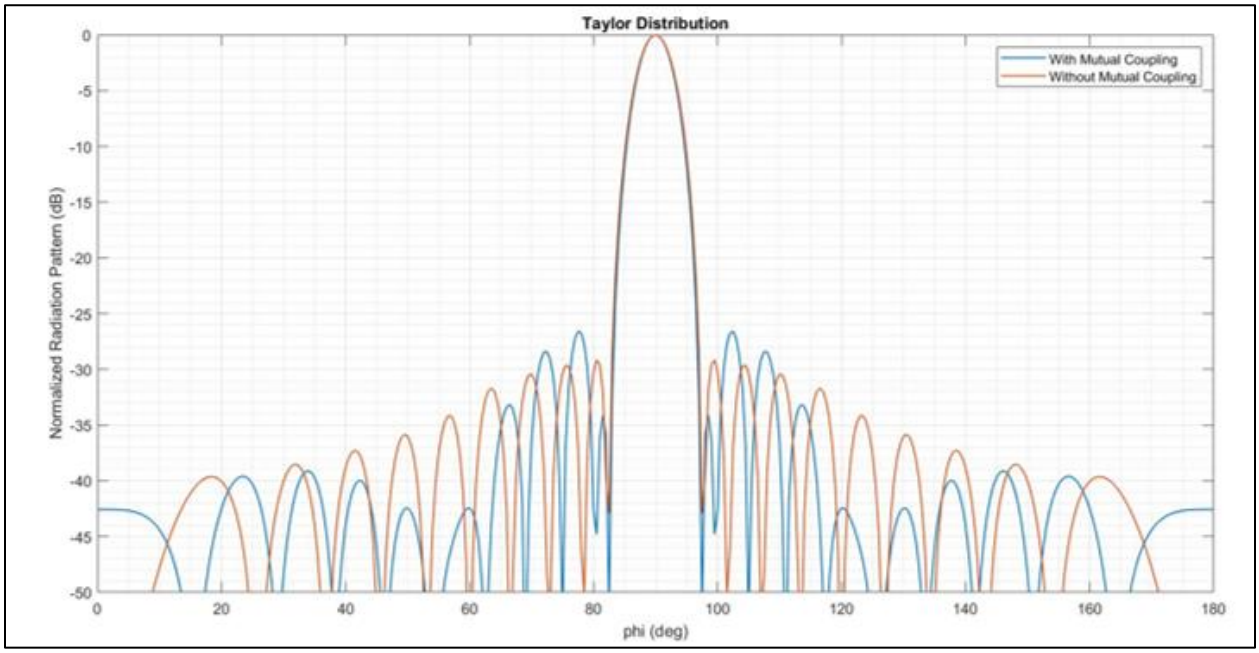


***Figure G5**. Effects of Mutual coupling on radiation patterns for no scan (boresight). Notice that the mutual coupling raises the near in sidelobe levels. This result is for Taylor distribution with $\bar{n} = 5$ and $\frac{\lambda}{2}$ spacing for 25 element linear array with a -25 dB sidelobe level.*

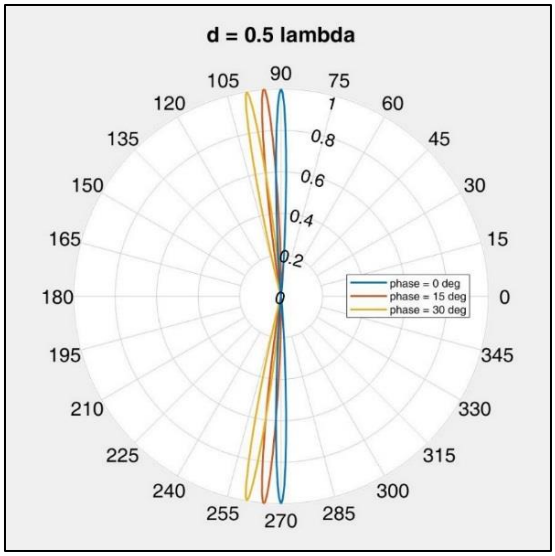


Figure G6. *Beam steering/scanning for the Taylor case including mutual coupling effects.*

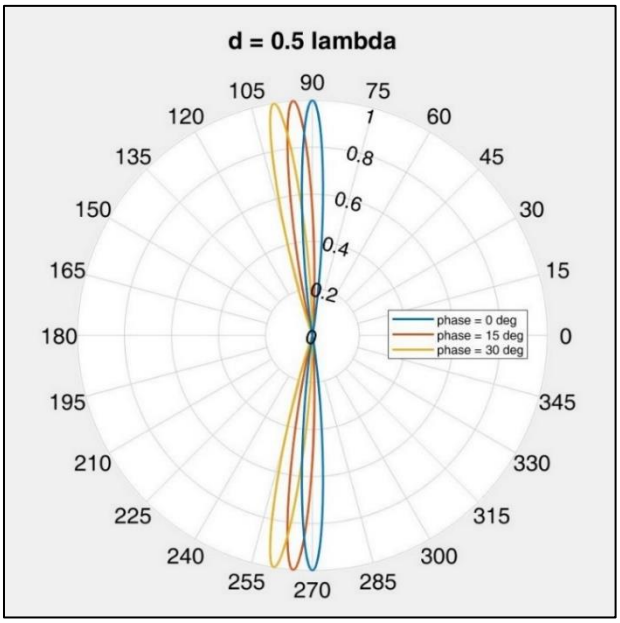


Figure G7. *Beam steering/scanning for the Bickmore-Spellmire case including mutual coupling effects*.

The four tables following Figures G6 and G7 show the change in beamwidth for Bickmore-Spellmire and Taylor distributions for interelement spacings of $\frac{\lambda}{2}$ and $\frac{\lambda}{4}$ respectively. One can see that as the interelement decreases the beamwidth increases. The beamwidth increases with increase in scan angle off the boresight consistent with the predictions from equation (6). Interestingly the FEKO results, that contain effects of mutual coupling, show graceful degradation in beamwidth at large scan angles compared to the predicted ones from (6). This could most likely imply that equation (6) is grossly invalid near large scan angles.

***Tables G1 and G2**. Bickmore-Spellmire Distribution*

θ_o (deg)	HPBW using eq. (6) (deg)	HPBW using FEKO (deg)
0	7.119	7.119
5	7.1462	7.136
10	7.2288	7.136
15	7.3701	7.147
20	7.5759	7.169
25	7.8549	7.186
30	8.2203	7.236
35	8.6907	7.261
40	9.2932	7.299
45	10.0678	7.357
50	11.0752	7.387
55	12.4116	7.471
60	14.2380	7.551

θ_o (deg)	HPBW using eq. (6) (deg)	HPBW using FEKO (deg)
0	14.14	14.14
5	14.1940	14.16
10	14.3581	14.22
15	14.6388	14.31
20	15.0475	14.46
25	15.6018	14.67
30	16.3275	14.92
35	17.2618	15.25
40	18.4585	15.63
45	19.9970	16.11
50	21.9979	16.69
55	24.6523	17.47
60	28.28	18.33

$$\boldsymbol{d = \frac{\lambda}{2}}$$

$$\boldsymbol{d = \frac{\lambda}{4}}$$

3-dB Beamwidth change with scan angle θ_o

Tables G3 and G4. *Taylor Distribution*

θ_0(deg)	HPBW using eq. (6) (deg)	HPBW using FEKO (deg)
0	10.20	10.20
5	10.2390	10.81
10	10.3574	10.91
15	10.5598	10.9
20	10.8546	11
25	11.2545	11.16
30	11.7779	11.46
35	12.4519	11.66
40	13.3152	11.98
45	14.4250	12.39
50	15.8684	12.86
55	17.7832	13.51
60	20.4	14.18

$d = \frac{\lambda}{4}$

θ_o (deg)	HPBW using eq. (6) (deg)	HPBW using FEKO (deg)
0	5.40	5.40
5	5.4206	5.42
10	5.4833	5.436
15	5.5905	5.43
20	5.7466	5.43
25	5.9582	5.459
30	6.2354	5.48
35	6.5922	5.56
40	7.0492	5.56
45	7.6368	5.575
50	8.4009	5.649
55	9.4146	5.668
60	10.8	5.714

$d = \frac{\lambda}{2}$

Summary

In this preliminary investigation on array trade space analysis, two types of amplitude distributions (Taylor & Bickmore-Spellmire) were used to synthesize the low-sidelobe, narrow main beam behavior of a 25 element linear array of dipoles. The general conclusions remain similar, *i.e.*, the beamwidth broadens as the scan angle moves away from the boresight. Interestingly it was found that the degradation in beamwidth, and

hence the directive gain, degrades gracefully in presence of mutual coupling. However the major difference was found to be in the radiation patterns. Bickmore-Spellmire radiation pattern is in some ways much superior to the Taylor pattern. The far out sidelobes in the former decay significantly, hence Bickmore-Spellmire appears to be far better suited for high-power applications than the Taylor amplitude excitation.

Future/Continuing Investigations

The following are continuing investigations of immediate importance:

i. The linear array was characterized for simple symmetrically driven dipoles; a very important case in down selection would be to replace the simple dipoles by an electrically small antenna (ESA) and repeat all the analysis and simulations for a comparative assessment
ii. The mutual coupling effects on element gain patterns [1],[2] need to be examined for possible pattern nulls corresponding to specific scan angles
iii. The sidelobe levels and mutual coupling effects due to non-uniform element spacing needs attention;
iv. The array factor calculation for Bickmore-Spellmire and other amplitude tapers/distributions using Schelkunoff's array polynomial approach
v. Floquet analysis of periodic structure of the array is necessary to validate any other approach
vi. Extension of the trade space analysis to planar arrays

References

[1] N. Amitay, V. Galindo and C. P. Wu, *Theory and Application of Phased Arrays*. NY, USA: Wiley-InterScience, 1972.

[2] A. A. Oliner and G. H. Knittel (eds.), *Phased Array Antennas*. Dedham, Mass., USA: Artech House 1972.

[3] A. K. Bhattacharyya, *Phased Array Antennas: Floquet Analysis, Synthesis, BFNs, and Active Array Systems*. NJ, USA: Wiley-InterScience, 2006.

[4] R. J. Mailloux, *Phased Array Antenna Handbook* (3rd ed.). Norwood, MA, USA: Artech-House, 2018.

[5] Randy L. Haupt, *Antenna Arrays: A Computational Approach*. Hoboken, NJ, USA: John-Wiley & Sons, Inc., 2010.

[6] S. P. Skobelev, *Phased Array Antennas with Optimized Element Patterns*. Boston, MA, USA: Artech House, 2011.

[7] A. J. Fenn, *Adaptive Antennas and Phased Arrays for Radar and Communications*. Boston, MA, USA: Artech House, 2008.

[8] A. J. Fenn and P. T. Hurst, *Ultrawideband Phased Array Antenna Technology for Sensing and Communications Systems*. Cambridge, Mass., USA: The MIT Press, 2015.

[9] A. W. Rudge, K. Milne, A. D. Olver and P. Knight (eds.), *The Handbook of Antenna Design* (vol. 2). London, UK: Peter Peregrinus, 1983.

[10] W. L. Stutzman and G. A. Thiele, *Antenna Theory and Design* (3rd ed.) Hoboken, NJ, USA: John-Wiley & Sons, Inc., 2013.

Appendix I: Bickmore-Spellmire Distribution

In this appendix, a simpler form of Bickmore-Spellmire distribution is derived that was used to generate the weights for calculating the array radiation pattern using the FEKO software. Bickmore-Spellmire taper is given by the relation [5] :

$$w_n = \left[1 - \left(\frac{r_n}{r_{max}}\right)^2\right]^q \Lambda_q\left(j\pi A\sqrt{1 - \left(\frac{r_n}{r_{max}}\right)^2}\right) \tag{1}$$

where, $$\Lambda_q(x) = \Gamma(q+1)\left(\frac{2}{x}\right)^2 J_q(x) \tag{2}$$

$q = \nu - 1$ (For a circular aperture)

and, $q = \nu - \frac{1}{2}$ (For a line source)

Two special cases occur for $\nu = 1$ (Hansen's One Parameter) and $\nu = \frac{1}{2}$ (Taylor's One Parameter).

Now, Bessel Function of first kind can be given by (Abramowitz & Stegun, *op. cit.*),

$$J_q(x) = \left(\frac{1}{2}x\right)^q \sum_{k=0}^{\infty} \frac{\left(-\frac{1}{4}x^2\right)^k}{k!\Gamma(q+k+1)} \tag{3}$$

Putting $\left(-\frac{1}{4}x^2\right)^k = (-1)^k\left(\frac{x}{2}\right)^{2k} = cos(\pi k)\left(\frac{x}{2}\right)^2$ and by replacing, $k! = \Gamma(k+1)$, eq. (3) is modified as:

$$J_q(x) = \left(\frac{1}{2}x\right)^q \sum_{k=0}^{\infty} \frac{cos(\pi k)\left(\frac{x}{2}\right)^{2k}}{\Gamma(k+1)\Gamma(q+k+1)} \tag{4}$$

Also, modified Bessel Function of first kind can be written in terms of Bessel Function of first kind as:

$$I_q(z) = e^{-\frac{1}{2}q\pi j} J_q\left(ze^{\frac{1}{2}\pi j}\right), \qquad -\pi < \arg(z) \leq \frac{1}{2}\pi \tag{5}$$

or, $$J_q\left(ze^{\frac{1}{2}\pi j}\right) = e^{\frac{1}{2}q\pi j} I_q(z) \tag{6}$$

We know,

$$I_q(y_n) = \left(\frac{1}{2}y_n\right)^q \sum_{k=0}^{\infty} \frac{\left(\frac{1}{4}{y_n}^2\right)^k}{k!\Gamma(q+k+1)} \tag{7}$$

Multiplying both sides of eq. (7) by $\left(\frac{2}{jy_n}\right)^q$,

$$\left(\frac{2}{jy_n}\right)^q I_q(y_n) = \left(\frac{1}{j}\right)^q \sum_{k=0}^{\infty} \frac{\left(\frac{1}{4}{y_n}^2\right)^k}{k!\,\Gamma(q+k+1)}$$

$$\left(\frac{2}{jy_n}\right)^q I_q(y_n) = e^{-j\frac{\pi q}{2}} \sum_{k=0}^{\infty} \frac{\left(\frac{y_n}{2}\right)^{2k}}{\Gamma(k+1)\Gamma(q+k+1)} \quad (8)$$

Now, let us replace, $\pi A\sqrt{1-\left(\frac{r_n}{r_{max}}\right)^2} = y_n$ in eq. (1), such that:

$$w_n = \left[1-\left(\frac{r_n}{r_{max}}\right)^2\right]^q \Lambda_q(jy_n) \quad (9)$$

Thus, from eq. (2) we have,

$$\Lambda_q(jy_n) = \Gamma(q+1)\left(\frac{2}{jy_n}\right)^q J_q(jy_n)$$

or,

$$\Lambda_q(jy_n) = \Gamma(q+1)\left(\frac{2}{jy_n}\right)^q I_q(y_n)e^{j\frac{\pi q}{2}} \quad (10)$$

From eq. (8), we put the expression for $\left(\frac{2}{jy_n}\right)^q I_q(y_n)$ into eq. (10)

$$\Lambda_q(jy_n) = \Gamma(q+1)\sum_{k=0}^{\infty} \frac{\left(\frac{y_n}{2}\right)^{2k}}{\Gamma(k+1)\Gamma(k+q+1)} \quad (11)$$

The Bickmore-Spellmire taper expression can therefore be simplified as:

$$w_n = \left[1-\left(\frac{r_n}{r_{max}}\right)^2\right]^q \Gamma(q+1)\sum_{k=0}^{\infty} \frac{\left(\frac{y_n}{2}\right)^{2k}}{\Gamma(k+1)\Gamma(k+q+1)} \quad (12)$$

[1] M. Abramowitz, and I. A. Stegun, *Handbook of Mathematical Functions with Formulas, Graphs, and Mathematical Tables*. New York, USA: Dover Publications, 1972.

Electrically Small Antenna (ESA) (James C. Kovarik and Deb Chatterjee)

Electrically small antennas have low gain, low bandwidth and poor radiation efficiency, in general. However, they are attractive choices because they have low form factor [1]. At 400 MHz the antenna size reduction becomes an important consideration and often is a deciding factor. This leads to examine tradeoff studies [2],[3] for antenna choices at low frequencies. Several approaches have been pursued [4],[5] for electrically small antennas.

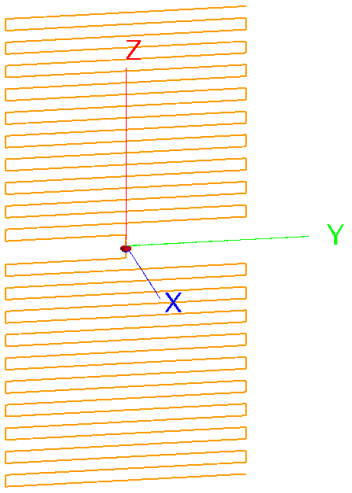
In this preliminary study a typical topology of the electrically small antenna – the meandering dipole – has been investigated. The geometry is shown in Figure G8. The radiation pattern, determined from FEKO, is shown. This is the topology of a planar antenna that is suitable for array applications. The typical gain of an ESA can be

determined from the Harrington's limit for antenna physical size and bandwidth. If the Chu sphere encloses an antenna of size *ka*, then the Harrington limit may be graphically understood by the following:

$$G = 10.0 \times \log_{10}[(ka)^2 + 2ka]$$

..... (1)

The result from (1) is plotted and shown here in Figure G9. The corresponding quality factor is shown in Figure G10. The percent bandwidth for various VSWR values are shown in Figure G11. The Figures G9 to G11 are generic results for any electrically small antenna. Preliminary investigation with the meandering dipole in Figure G8(a) was aimed at finding out the resonant frequency to be close to 400 MHz. To that end, the meandering dipole was shortened in length and the reflection coefficient magnitude was plotted. This result is shown in Figure G12. Notice that the reflection coefficient reaches a minimum at about 330 MHz. This suggests that one needs to reduce the dipole size further to slightly raise the resonant frequency.



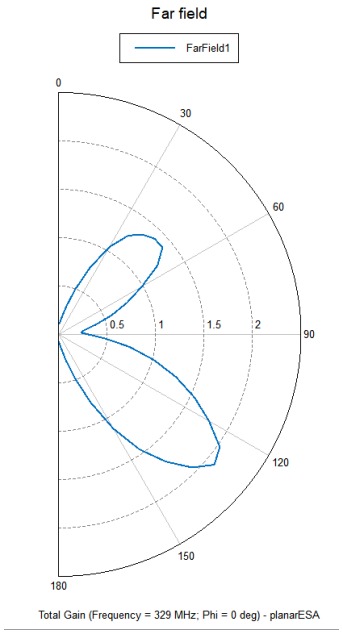


Figure G8*. (a) Meandering dipole* $ka = 0.67$ *(b) radiation pattern*

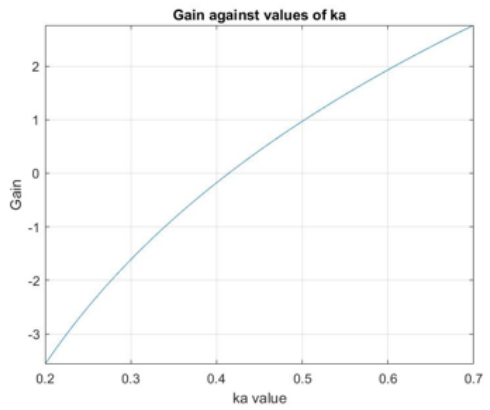


***Figure G9**. Harrington gain limits*

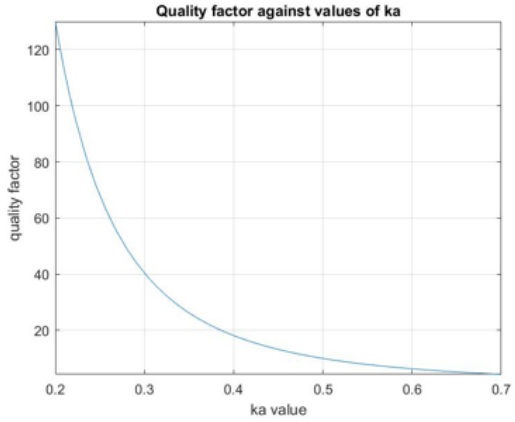


***Figure G10**. Quality factor*

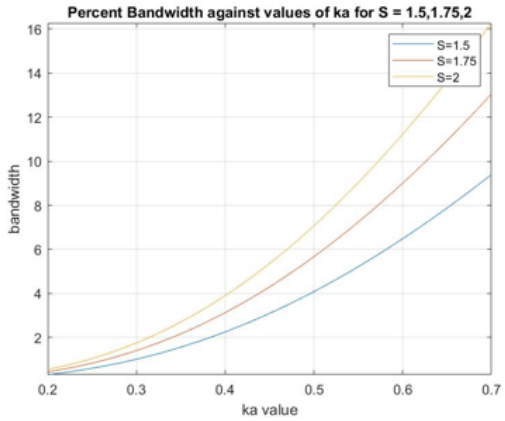


***Figure G11**. Percent bandwidth for various VSWR.*

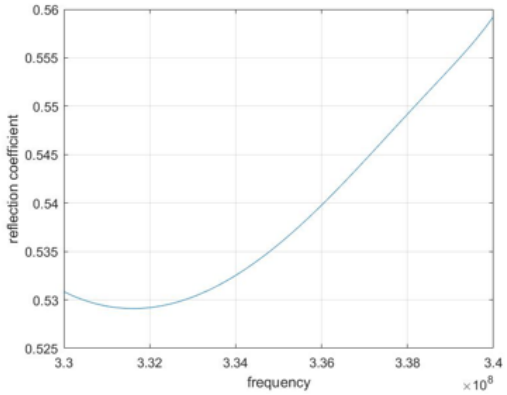


***Figure G12**. Reflection coefficient of the meandering dipole.*

(Figure G12 is untuned reflection coefficient.)

The result in Figure G12 is then “tuned” so that the dipole frequency is raised. The tuned result is shown below in Figure G13.

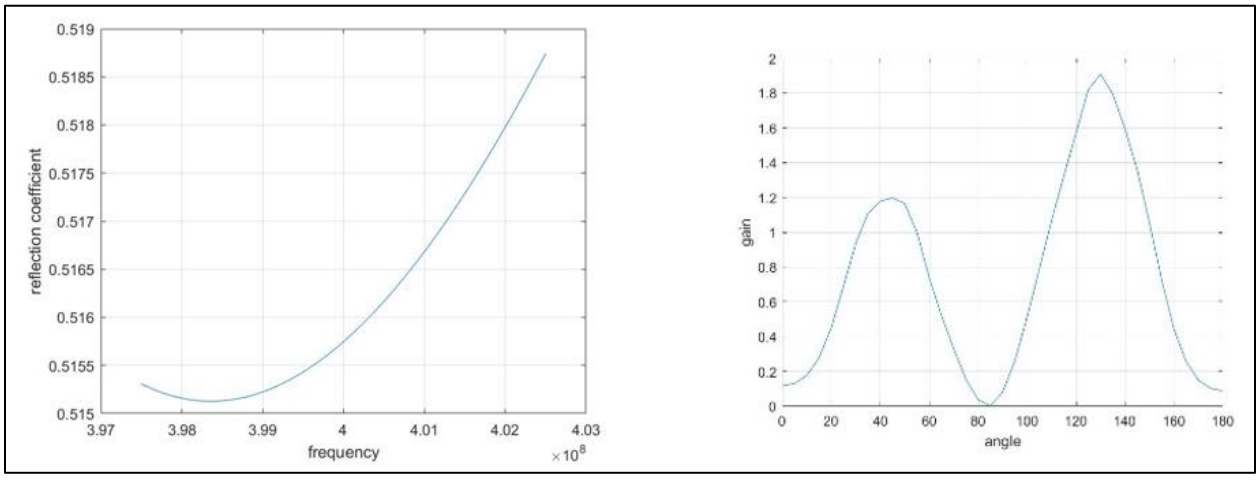


***Figure G13**. Tuned reflection coefficient@399 MHz.*

***Figure G14**. Gain at 332 MHz of the untuned dipole.*

The gain of the untuned meandering dipole antenna is maximum at 1.9 and this is for $ka = 0.67$ which is predicted by Harrington's limit conditions. Upon tuning, the antenna now resonates at $ka = 0.6$ which gives a predicted gain of 1.8. The corresponding tuned reflection coefficient and gain are shown below in Figure G15. This corresponds to the result in Figure G13 which shows that the tuned meandering dipole now resonates at 399 MHz.

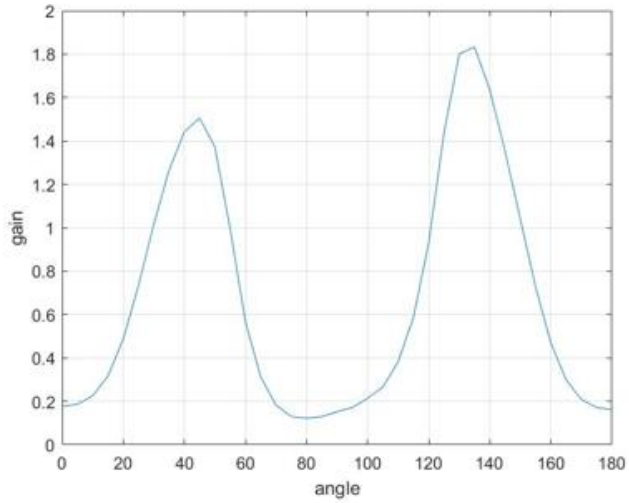


Figure G15*. Gain of a tuned meandering dipole.*

The preliminary results vindicates the application of the Harrington's formulas for estimating the gain and bandwidth. This is because we obtained agreement between the Harington's formulas and FEKO.

Further investigations on the other types of ESA and the application of the Gustafsson limits [7] for better agreement with experimental data shall continue with the ESA. Optimization studies using the Theory of Characteristic Modes [8]-[10] is also planned as a parallel investigation.

References

[1] J. L. Volakis, C.-C. Chen and K. Fujimoto, *Small Antennas: Miniaturization Techniques & Applications*. NY, USA: McGraw-Hill, 2010.

[2] S. R. Best, "Electrically Small Resonant Planar Antennas: Optimizing the Quality Factor and Bandwidth," *IEEE Antennas and Propagation Magazine*, pp. 38-47, June 2015.

[3] S. R. Best and D. L. Hanna, "A Performance Comparison of Fundamental Small Antenna Designs," *IEEE Antennas and Propagation Magazine*, pp. 47-70, February 2010.

[4] C. Pfeiffer and A. Grbic, "A Circuit Model for Electrically Small Antennas," *IEEE Transactions on Antennas and Propagation*, vol. 60, no. 4, pp. 1671-1683, April 2012.

[5] B. A. Kramer, C.-C. Chen, M. Lewis and J. L. Volakis, “Fundamental Limits and Design Guidelines for Miniaturizing Ultrawideband Antennas,” *IEEE Antennas and Propagation Magazine*, vol. 51, no. 4, pp. 57-69, August 2009.
[6] C. Pfeiffer, “Fundamental Efficiency Limits for Small Metallic Antennas,” *IEEE Transactions on Antennas and Propagation*, vol. 65, no. 4, pp. 1642-1650, April 2017.
[7] M. Shahpari, D. V. Thiel and A. Lewis, “An Investigation into the Gustafsson Limit for Small Planar Antennas using Optimization,” *IEEE Transactions on Antennas and Propagation*, vol. 62, no. 2, pp. 950-955, February 2014.
[8] J. J. Adams and J. T. Bernhardt, “A Modal Approach to Tuning and Bandwidth Enhancement of a Electrically Small Antenna,” *IEEE Transactions on Antennas and Propagation*, vol. 59, no. 4, pp. 1085-1092, April 2011.
[9] R. Li, D. McNamara and G. Wei, “Characteristic Modes Evaluation of Metallic Small Antennas with Unidirectional Pattern,” *IEEE Antennas and Wireless Propagation Letters*, vol. 16, pp. 3026-3029, 2017.
[10] R. Ma, T.-Y. Shih, R. Lian and N. Behdad, “Design of Bandwidth-Enhanced, Platform-Mounted Electrically Small VHF Antennas Using Characteristic Mode Theory,”*IEEE Antennas and Wireless Propagation Letters*, vol. 17, no. 12, pp. 2384-2388, December 2018.

I.H Cost Estimates and Engineering (Doynov)

i. No report submitted

II. <u>Issues</u>:

None

III. <u>Interactions with Others</u>:

IV. <u>Major Procurement Actions</u>:

None

V. <u>Travel</u>:

Travel Plans

Please note that all papers or presentations on any aspect of the ONR HPM program must be reviewed by the ONR Program Officer (or in some cases ONR Public Release Process) regardless of classification level or audience.

Planned Travel Details	Purpose	Attendees	Estimated Costs
DEPS	Conference	Multiple	Not established yet
2019 IEEE	Antenna Conference	Chatterjee group	Not established yet
cUAV Review Meeting	Semi-annual review	Multiple	Not established yet

VI. <u>Pending or Upcoming Public Release Requests</u>:

i. M. Z. M. Hamdalla, A. N. Caruso, Ahmed M. Hassan, "Characteristic Mode Analysis of the Effect of the UAV Frame Material on Coupling and Interference," *Submitted to the IEEE International Symposium on Antennas and Propagation and USNC-URSI Radio Science Meeting at Atlanta, Georgia*, USA, 7-12 July 2019.

ii. M. Z. M. Hamdalla*, Ahmed M. Hassan, A. N. Caruso, J. D. Hunter, Y. Liu, V. Khilkevich, D. G. Beetner, "Electromagnetic Interference of Unmanned Aerial Vehicles: A Characteristic Mode Analysis Approach," *Submitted to the IEEE International Symposium on Antennas and Propagation and USNC-URSI Radio Science Meeting at Atlanta*, Georgia, USA, 7-12 July 2019.

VII. <u>Selected Highlights (text and/or images)</u>:

None

ONR HPM 2019 Program - Monthly Status Report (MSR) – MARCH2019
Anthony Caruso – Univ. Missouri – Kansas City
N00014-17-1-3016 [OSPRES Grant]
ONR Short Pulse Research, Evaluation and non-SWaP Demonstration for C-sUAV Study

4/13/2019

Distribution Statement ~A: Distribution authorized to all OSPRES Grant and Contract Participants, and any uncompensated collaborators. Further dissemination per Ryan Hoffman (ryan.hoffman@navy.mil).

OSPRES Project Description: Develop tunable High Power Microwave (HPM) sources and electronically steerable radiators whose waveform(s) enable control over all levels-of-lethality on cUAV and similar targets, with the least power density.

Contents

Overview: 3
I. Current Month Progress: 4
II. Issues: 7
III. Interactions with Others: 7
IV. Major Procurement Actions: 7
V. Travel: 7
VI. Pending or upcoming public release requests: 7
vii. Selected highlights (text and/or images): 7

Executive Summary

Overview:

In March, UMKC hosted the OSPRES Spring 2019 technical interchange/review meeting. A major outcome of this review was to refocus some of the technical efforts to better align with program priorities. On the grant side of the OSPRES program, the PF-NLTL efforts were redirected due to the lack of amplifier sources that can meet program requirements within the program PoP. Statements of work for BAE and EHT have been reworked to include more support for UMKC in design, testing and integration. BAE will continue to work on Si PCSS development; additionally, they will support laser and optical systems on the contract side of the OSPRES program. EHT will continue development of the 2nd generation RCC, but will now support triggering and a paper study on ultrafast current drivers for laser diodes on the contract side of the OSPRES program related to the scaled demonstration.

UMKC continues to expand their staff and student support to facilitate development. An RF Engineer, Mechanical Engineer, and an OSPRES dedicated machinist are being sourced.

I. Current Month Progress:

I.A Photoconductive Solid-State Switches (Myers)

i. PCSS Modeling – We are currently transitioning the modeling effort for SiPCSS to new personnel and have made no major progress on this area. Progress on modeling SiPCSS will be reported in the next report.
ii. Lasers – We have received and installed the new Wedge laser system for Si- and GaN-PCSS testing. Testing with the new laser system has shown increased rise-time in the SiPCSS (~1ns), and we are currently measuring the laser pulse width to determine if the laser meets the specifications provided. For GaN, we are having issues with the THG system which we believe to be either due to an ineffective combination of 532- and 1064-nm light, or the temperature of the THG crystal due to heater failure.

I.B GaN:C Subgroup (Rulis)

i. Further debugging of the script development that was described in the previous month's report. (A particular library [called BLT] appears to have demanding version requirements regarding its interface with other libraries. We are debugging that now.)
ii. The FLOOXS TCAD software will be able to perform a range of different 1D and 2D device models, but it will require certain information about electron and hole drift velocities for GaN. That information can be obtained from Full Band Monte Carlo simulations. In the past month we have found and started working with a 1D FBMC code called Simple Monte Carlo Simulations which has been shown to work successfully for Si, GaAs, and InGaP. We are still mastering this software and will begin developing the necessary input files for GaN during the upcoming month. Based upon preliminary results, it looks like it will be a promising approach to connect our ab initio calculations to the FLOOX TCAD simulations.

I.C Small Unmanned Aerial Vehicle Diagnostics and Design-of-Experiments (Fields)

i. Refined the LabVIEW software to improve efficiency, repeatability and ease of use for both source and UAV control/data acquisition.
ii. Constructed the first prototype fixed-wing aircraft instrumented with a Pixhawk autopilot. Refinements are being made to the platform, and development is ongoing in the automated data analysis of the Pixhawk-based flight data.

I.D Positive Feedback Non-Linear Transmission Line (Khan)

i. A 2.1 kW positive feedback NLTL system has been built and tested with 3 ns rise time.

ii. We are fabricating an in-house pulse generator with optimized PCB layout to damp parasitic L-C network induced ringing and overshoot in a GaN switch based design.
iii. We are designing an NLTL with stacked high voltage schottky diodes and air core inductors to increase the breakdown voltage of the NLTL and increase the Bragg frequency limit of the NLTL.
iv. The overall PF-NLTL effort will be closed and resources direct to the prime power used for PCSS and DSRD-based drivers.

I.E Applied RF Coupling Simulation and Modelling to/for sUAV (Hassan)

i. We performed a detailed statistical analysis of the effect of wire length and orientation above both dielectric and perfect electric conductor (PEC) frames to estimate the maximum/minimum current that can couple to an unterminated wire above these frames.
ii. We studied the effect of coupling to multiple wires above a PEC UAV frame starting by considering two straight wires of variable separation. The coupling current was found to be highly dependent on the shape and size of the arms of the UAV and to vary significantly from the case of two wires in free space or two wires above an infinite PEC ground plane.
iii. In all of our previous analysis, the wires were located above the UAV frame similar to the UAV model developed by Caruso's group. However, in many commercial UAVs, the wires and PCBs are encapsulated in a casing composed of a thin dielectric shell. We are currently studying the effect of casings with simple shapes on the current coupled to the enclosed wires, and we are showing considerable differences from the coupling in free-space even for casings composed of low permittivity dielectrics.

I.F UMKC Diode Network Based NLTL (Doynov)

i. A second low-voltage Diode-based Non-Linear Transmission Line (D-NLTL) was designed with stacked diodes. The simulation results prove the theoretical understanding of the D-NLTL. The results from the simulations and testing of the implemented design were presented during the OSPRES review meeting, April 11-13, 2019.
ii. A high-voltage D-NLTL has been designed and is in the implementation process.
iii. The efficiency evaluation of D-NLTL topologies have been developed.

I.G Electrically Small Antennas (Chatterjee)

In this month's effort, significant progress was achieved in identifying a synthesis procedure (Bickmore-Spellmire) that is particularly suitable for high power applications.

Another milestone achieved was to optimize the electrically small antenna, a meandering dipole, with $(ka \leq 0.5)$ that appeared promising. While further studies are warranted for both cases, the preliminary results look promising.

i. Identified and obtained results from Bickmore-Spellmire distribution for a low-sidelobe phased array. It was also found that Bickmore-Spellmire was the most suitable for High Power applications.
ii. Analyzed an electrically small antenna to examine its suitability as a phased array element.

Electrically Small Antennas Meandering Dipole (James C. Kovarik)

i. A meandering dipole was characterized for its performance in terms of gain and bandwidth. The characterization was carried out using the full-wave EM simulator FEKO, and also examined against the Harrington's limits for upper bound on the Quality Factor.

Studies on Linear and Planar Phased Arrays (Bidisha Barman)

i. The initial study involved a linear phased array with 25 elements. Trade space data is currently being generated for examining the various options that exist between sidelobe levels, gain, 3-dB beamwidth.

I.G.1 Critical Tasks of the Antenna Subgroup

i. Completion of trade space data for a linear phased array.
ii. Completion of characterization of a meandering dipole.

I.G.2 Expected Products of Antenna Subgroup

i. Using a meandering dipole as a phased array element.
ii. Linear and Planar phased Arrays operating at the UHF regions.

I.H Cost Estimates and Engineering (Doynov)

i. The initial results from developing a cost estimation and cost management process were presented during the OSPRES review meeting, April 11 – 13, 2019.
ii. We are reviewing several tools which are used by DoD and DoD contractors in order to select and use one (preferably free source).

II. Issues:

None

III. Interactions with Others:

None

IV. Major Procurement Actions:

V. Travel:

Travel Plans

Please note that all papers or presentations on any aspect of the ONR HPM program must be reviewed by the ONR Program Officer (or in some cases ONR Public Release Process) regardless of classification level or audience.

Planned Travel Details	Purpose	Attendees	Estimated Costs
DEPS	Conference	Multiple	Not established yet
2019 IEEE	Antenna Conference	Chatterjee group	Not established yet

VI. Pending or upcoming public release requests:

i. M. Z. M. Hamdalla, A. N. Caruso, Ahmed M. Hassan, "Characteristic Mode Analysis of the Effect of the UAV Frame Material on Coupling and Interference," *Submitted to the IEEE International Symposium on Antennas and Propagation and USNC-URSI Radio Science Meeting at Atlanta, Georgia*, USA, 7-12 July 2019.

ii. M. Z. M. Hamdalla*, Ahmed M. Hassan, A. N. Caruso, J. D. Hunter, Y. Liu, V. Khilkevich, D. G. Beetner, "Electromagnetic Interference of Unmanned Aerial Vehicles: A Characteristic Mode Analysis Approach," *Submitted to the IEEE International Symposium on Antennas and Propagation and USNC-URSI Radio Science Meeting at Atlanta*, Georgia, USA, 7-12 July 2019.

VII. Selected highlights (text and/or images):

None

ONR HPM 2019 Program - Monthly Status Report (MSR) – APRIL2019
Anthony Caruso – Univ. Missouri – Kansas City
N00014-17-1-3016 [OSPRES Grant]
ONR Short Pulse Research, Evaluation and non-SWaP Demonstration for C-sUAV Study

5/13/2019

Distribution Statement ~A: Distribution authorized to all OSPRES Grant and Contract Participants, and any uncompensated collaborators. Further dissemination per Ryan Hoffman (ryan.hoffman@navy.mil).

OSPRES Project Description: Develop tunable High Power Microwave (HPM) sources and electronically steerable radiators whose waveform(s) enable control over all levels-of-lethality on cUAV and similar targets, with the least power density.

Executive Summary

Overview:

During April, the OSPRES group attended the DEPS conference and met with the majority subcontractors/collaborators. They continued the discussions on paths forward and program critical decisions about resources and delegation of efforts across subcontractors and collaborators. Eliot Myers developed charters for the source/driver and non-linear transmission line subgroups. The charters dictate responsible parties, short term, and long term goals for the subgroups. This will improve coordination and redistribute resources to facilitate technology down selection over the next few months. UMKC has hired a new post-doctoral researcher, Jay Eifler, to perform/lead simulations of switches, pulse forming networks, and other fundamental modeling. Jay has already added laser triggering and transmission line simulation to the TCAD models for SiPCSS. UMKC is also looking into other software packages for integration of all source/driver modeling. Since the culling of the positive feedback non-linear transmission line effort, Dr. Khan at UMKC has been redirected to support other efforts including power supply development and integration.

I. Current Month Progress:

I.A Photoconductive Solid-State Switches (Myers – OSPRES Technical Lead)

The following table outlines the efforts of UMKC for fundamental PCSS development.

Table A1. *Progress tracker for identified critical tasks and status. Color indicates the criticality of each task with respect to its current status and the objectives of the program: (GREEN) low-risk and/or no major delays, (YELLOW) medium risk and/or minor delays, (RED) major risk and/or delays.*

Critical Effort		Critical Task		Status
Simulation and Modeling	Si-PCSS	TCAD Simulation		We have conducted preliminary transient optical simulations of SiPCSS devices, and are currently refining the model to more accurately represent real devices and for improved data extraction.
Thermal Testing	Si-PCSS	Cooling System Test Fixture		We are improving our test fixturing for validating cooling system designs by adding flow, temperature, and pressure sensors on both the inlet and outlet.
Device Characterization	Si	Electroluminescence Studies		UMKC has designed and is building a vacuum chamber for HV device testing in an SF^6 environment.
Ultrafast Switching	TBD	Switch FOM		UMKC continues to work on developing a clear FOM for electrically and optically triggered ultra-fast rise, high power switches.
Device Characterization	GaN:C	GaN pulsing demonstration		We believe the SHG system for converting 1064-nm light is not operating correctly causing minimal photo-response of the THG system. We are exploring COTs solutions as well as conducting tests of the SHG/THG system.

Summary (Myers – OSPES Technical Lead)

During the last two months we have made progress on Si-PCSS modeling and characterization, however challenges continue with GaN:C-PCSS testing and developing a clear FOM for electrically and optically triggered ultrafast switches.

For SiPCSS, we have (1) achieved our objective of generating a transient, optically triggered pulse simulation, (2) made improvements to our cooling system test fixture, and (3) improved our electroluminescence system for breakdown characterization.

Our efforts to demonstrate pulsed power with GaN:C have been delayed due to issues

with the SHG and THG system using the newly purchased Wedge laser system, and believe either the SHG or THG system for converting the 1064-nm light to 355-nm has been damaged, or is not compatible with the Wedge laser characteristics. We are conducting tests on the SHG and THG system, as well as looking into alternative COTs solutions to generating the 355-nm light, including a laser-diode and compatible driving circuit. We will be reaching out to collaborators for assistance on this effort.

Our primary challenge in generating a figure of merit (FOM) for ultrafast, high power switches (both optically and electrically triggered) has been narrowing the large parameter space including device properties without losing the salient features of each device topology and mechanism. This effort will likely require a series of FOM for each topology, and we are beginning that effort by focusing on devices with which we have the most experience–PCSS.

SiPCSS Modeling (Eifler – Postdoc)

Up to now, we have focused on simulating static hold-off voltage and transient recovery time processes within Si-PCSS devices. Over the last two months, we have added a transient optical (laser) pulse and transmission line components to the TCAD model. Two preliminary simulations using these additions were performed in Silvaco TCAD on a 3D and 2D device.

The 3D PCSS model is comprised of 1×1×1.3-mm Si-PCSS with light incident on the anode. This device has a smaller cross sectional area in the plane of incidence than real devices to reduce computational cost. The incident laser is simulated by a transient square pulse of 1064-nm photons with a peak intensity of 1×10^6 W/cm^2. The electrical pulse is a square wave with a peak voltage of 1000 V. The optical and transient pulses are timed to arrive at the SiPCSS at the same time, although in experiment, the transmission line would be fully charged when the laser is incident on the Si-PCSS. Initially, the illumination intensity was chosen to avoid convergence that occurred when simulating intense light sources. The PCSS test circuit is shown in Figure A1 including two transmission lines (TL) connecting the source to reverse-biased PCSS and to resistive load (illumination source not shown).

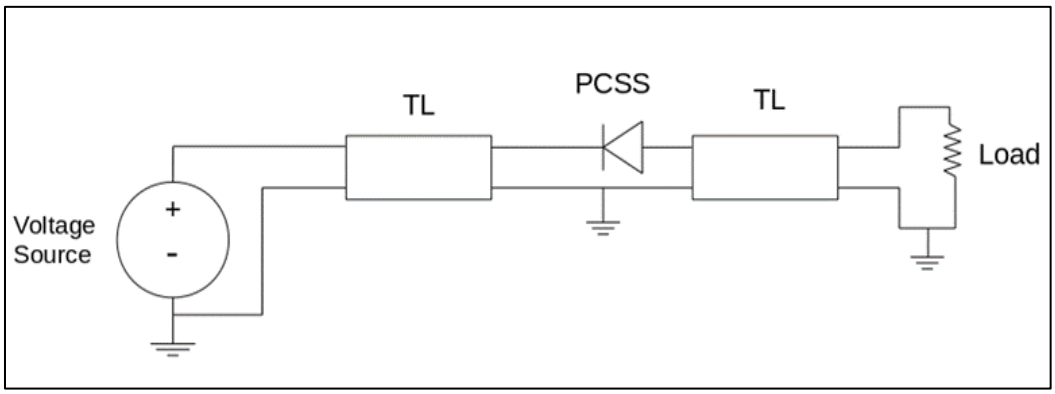


Figure A1. *Schematic of simulated Si-PCSS circuit.*

The low optical power density intensity does not generate enough photocarriers within the PCSS, per Figure A2**,** and the peak output voltage at the load vs transient simulation time is seen to be only 9 V. The simulation duration was 9 ns. The 4.8-ns delay of the output pulse is due to the two TLs used which have a Z_0 = 4.4 ohms and a propagation time of 2.4 ns as modeled in Atlas' mixed mode.

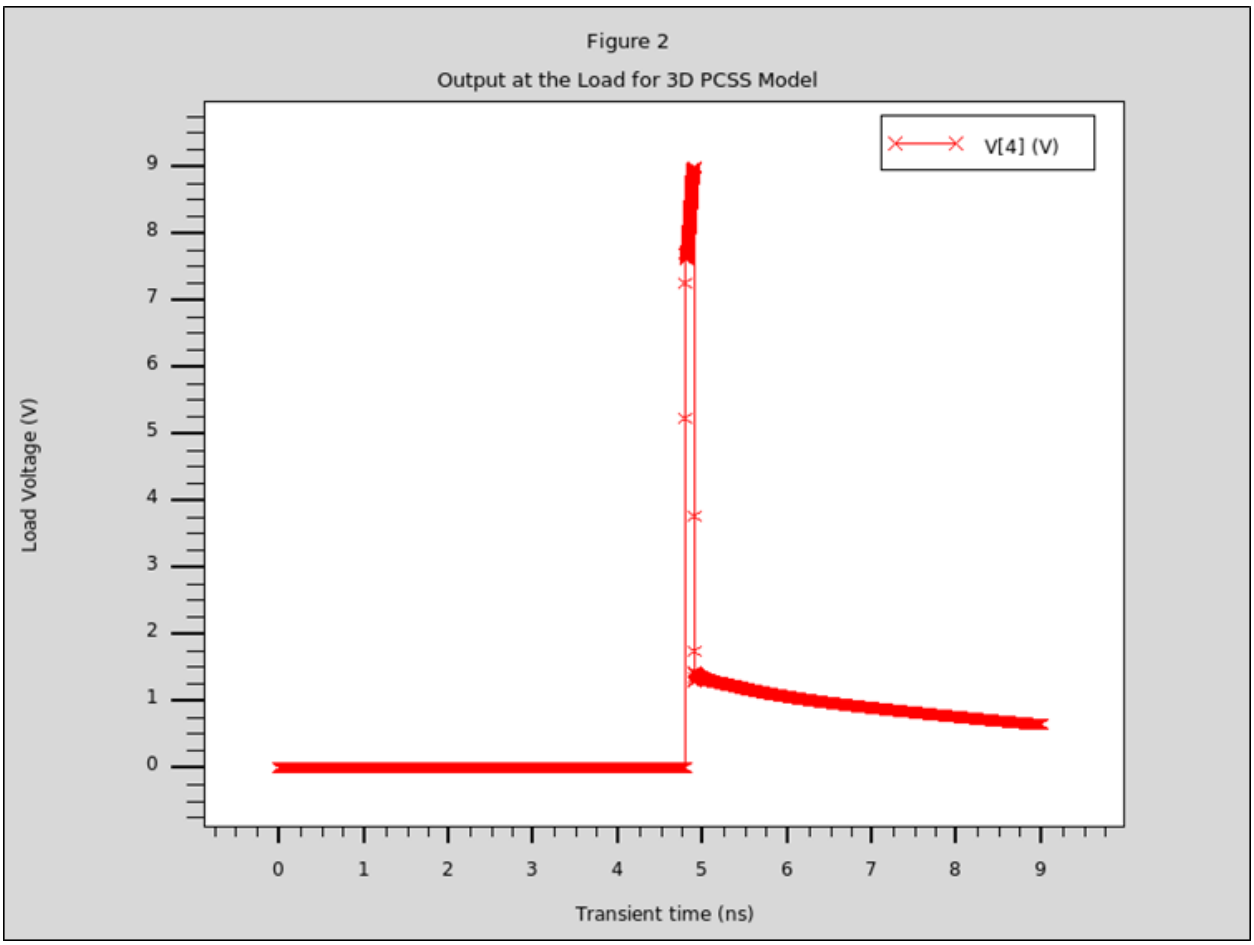


Figure A2. *Pulse output waveform from 3D Si-PCSS transient optical simulation via TCAD.*

To (1) reduce the overall computation time and (2) remove challenges in conversion allowing for greater optical power densities, a second simulation was conducted using a smaller cross sectional area (0.5 x 0.5 mm) and a 2D model. The model included a multiplicative width of 0.5 mm, incident laser intensity of 30×10^6 W/cm^2, and all other parameters were unchanged. Per Figure A3, the 2D simulation resulted in a pulse voltage of approximately 400 V with a charge voltage of 1 kV, corresponding to an on-state resistance of 1.1 Ω, per Figure A3. Although the minimum resistance achieved is only 1.1 Ω, the resistance quickly rises as the switch recovers much more quickly than measured in experiment, resulting in an exponential decay of the pulse. This further indicates that the Si model used in TCAD is not representative of the actual carrier recombination and generation rates.

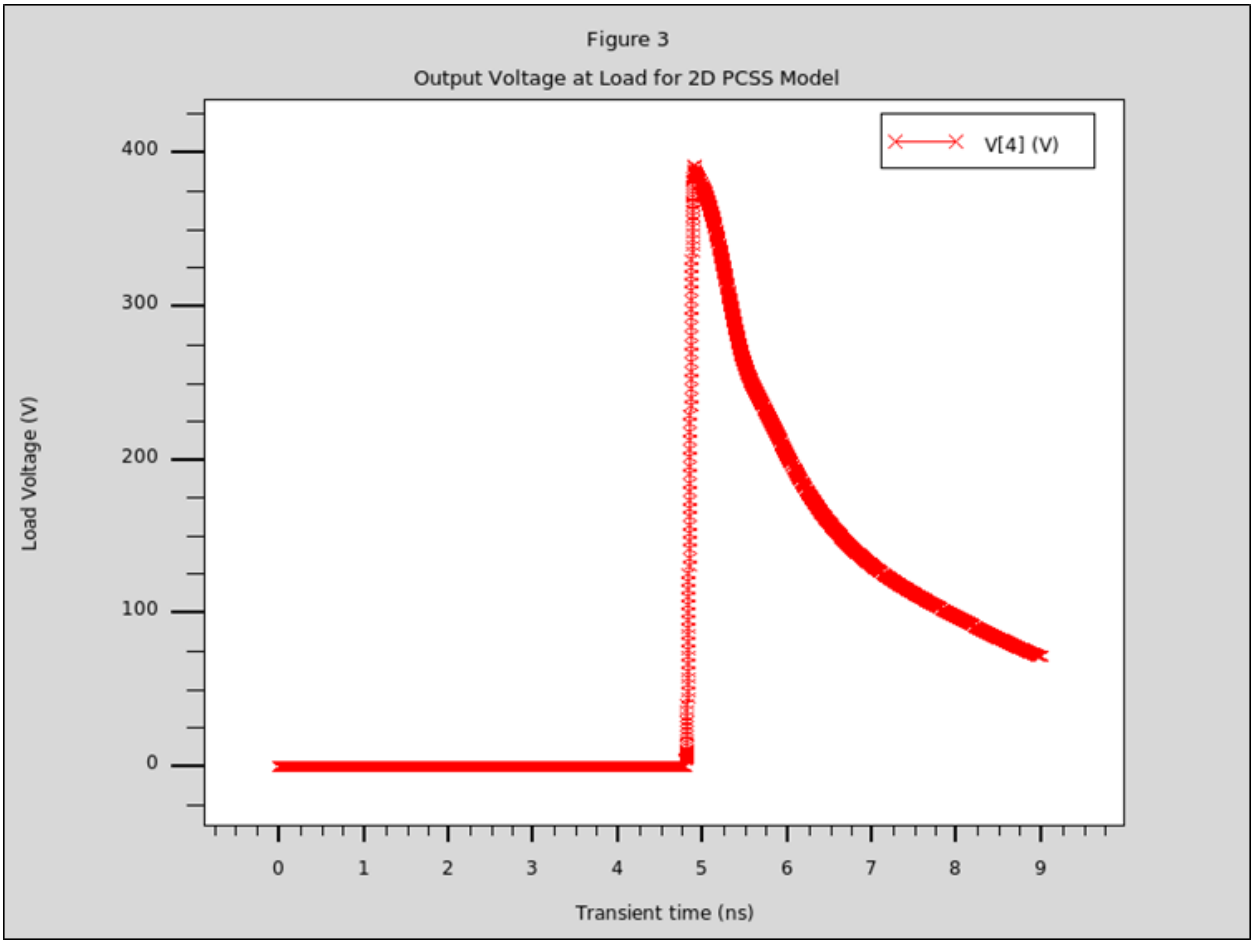
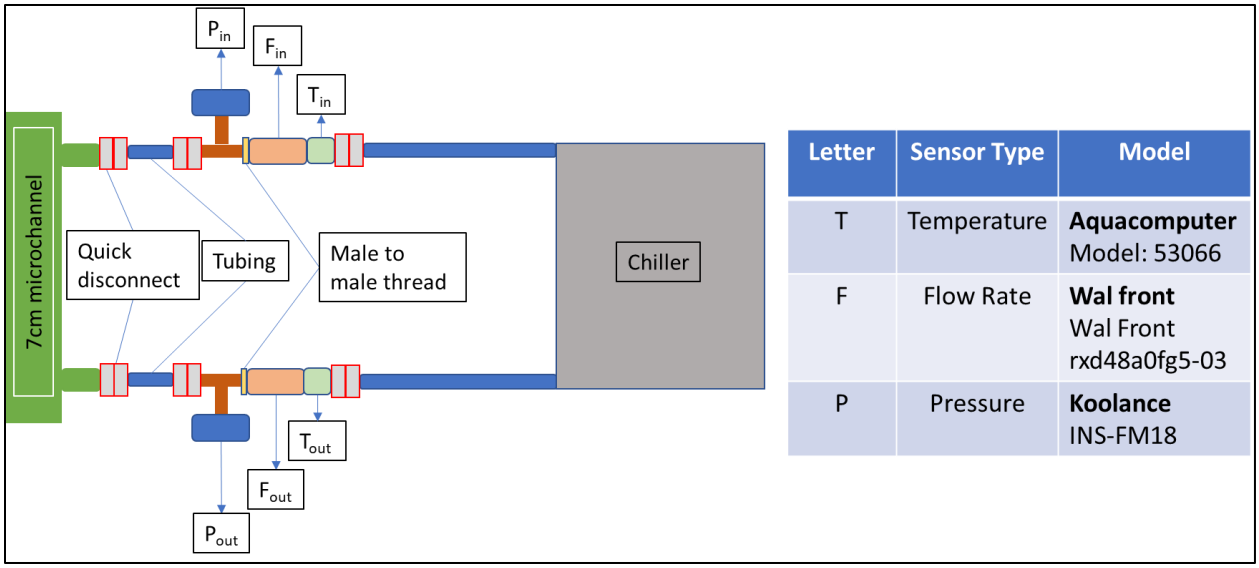


Figure A3. *Pulse output waveform from 2D Si-PCSS transient optical simulation via TCAD. The simulated recovery time is much shorter than experiment, resulting in an exponential decay following illumination.*

Moving forward, we will (1) continue to explore the mechanisms for decreasing carrier recombination rates within the device to better represent real device, (2) focus on 2D models for decreased computation time, starting with a section of a 1.2×1.2 cm device with an optical window pattern per the SiPCSS device design and (3) rather than start the electrical charge from 0 V at time zero, the transmission line will be fully charged prior to the laser pulse, and a source impedance will be added to isolate the power supply from the switch following the pulse.

Thermal Testing (Landwehr – Undergraduate Research Assistant)

To support design feedback on the cooling system designs for 7 cm SiPCSS, we are improving the fixture for cooling system validation. This will be done by adding sensors at the inlet and outlet of the microchannel to measure the coolant flow rate, temperature, and pressure of the coolant, per Figure A4. The modularity of the test design will allow for the testing of future microchannel designs using the same components.



Letter	Sensor Type	Model
T	Temperature	**Aquacomputer** Model: 53066
F	Flow Rate	**Wal front** Wal Front rxd48a0fg5-03
P	Pressure	**Koolance** INS-FM18

Figure A4. *Cooling system with generic microchannel. 6 sensors in total, 2 pressure, 2 flow rate, and 2 temperature, one of each on either side.*

The major improvement will be the pressure sensor at the inlet and outlet, allowing us to accurately correlate experiment to CFD simulation in which a fixed pressure is set at the inlet to the cooling system.

In addition, we will be using the FLIR camera to accurately measure the emissivity of the SiPCSS as a function of temperature so we can accurately measure surface temperature during pulse testing with the laser.

Electroluminescence (Landwehr - UGRA)

Progress in electroluminescence investigations of the 7cm SiPCSS has focused on the design and development of a vacuum chamber testing system. The chamber will allow for greater luminosity of EL by improving hold off voltages with a partial vacuum. We have also installed an SF_6 supply to enable testing at increased voltages and thus luminescence while decreasing the likelihood of air breakdown. EL images will be captured from above the chamber through a glass window, per Figure A5.



Figure A5. *Shows a plate and probe arm for reverse bias testing. The photo angle is representative of the EL event capture perspective*.

Our initial sealant for the feedthroughs was insufficient to seal the chamber during vacuum; we are currently reworking this feedthrough and will begin validating the chamber in the coming weeks. Moving forward, we are considering adding a thermoelectric heater/cooler to control the device temperature allowing temperature dependent electroluminescence.

GaN:C-PCSS Pulse Testing (Thompson – Graduate Research Assistant)

Recent efforts with GaN:C-PCSS have been focused on increasing the pulses generated by the GaN:C-PCSS above the mV range, by using the THG setup with the 1-ns pulse width Wedge laser. Figure A6 shows the THG setup used to convert the 1064-nm beam to a 355 nm beam. Initially, we believed the low voltage output (< 20 mV) was due to the carrier mobility and lifetime of GaN:C and the gap length of the devices in combination with the 70-ps pulse width of the NeoLASE laser. However, the output was still in the mV range when stimulated by the 1-ns pulse width of the Wedge laser.

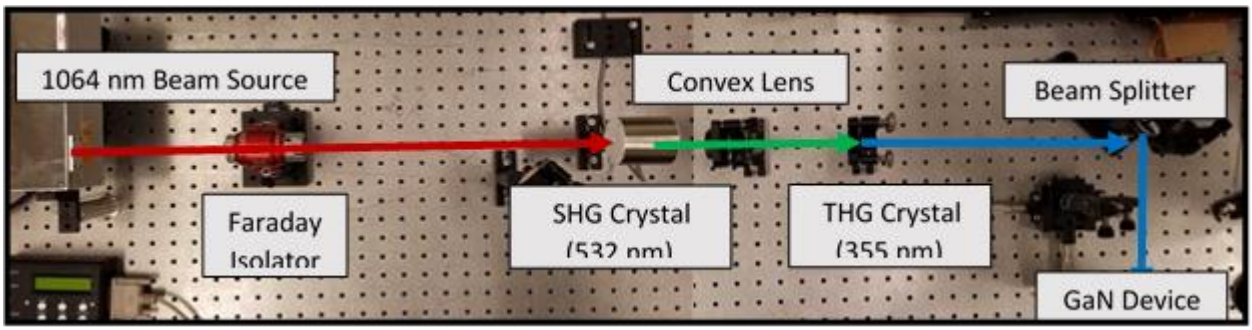


Figure A6. *Experimental setup with Wedge laser and THG system.*

The tests were repeated while removing each non-linear crystal to see if there was a change in the PCSS pulse. The pulses remained the same with the THG crystal removed (what should be 1064+532 nm) and with both the SHG and THG crystals removed (1064-nm only), indicating that at least the SHG crystal is not working properly. The output pulses are below in Figure A7 with these two configurations. In both cases, the output pulse width was measured using the oscilloscope to be 1.5 ns.

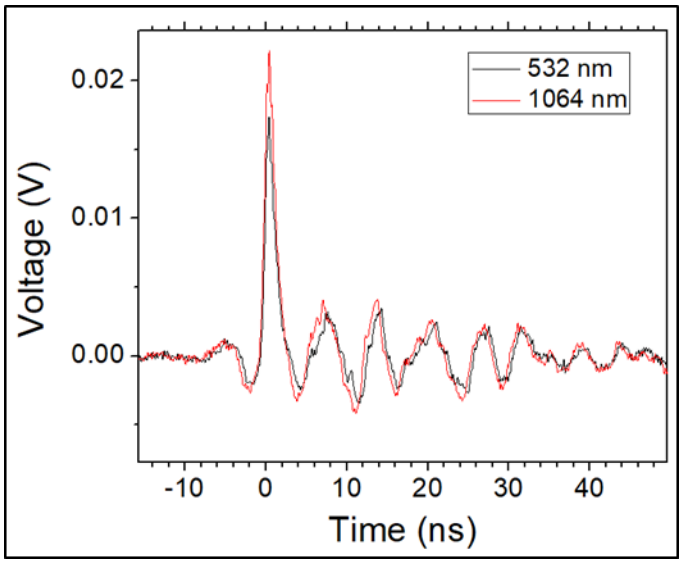


Figure A7. *GaN pulse waveforms showing similar response with and without the SHG system.*

Moving forward we will run diagnostic testing on the THG system to determine the cause of the SHG crystal failure and explore COTs lasers as an alternative to THG using a 1064-nm laser. In parallel to pinning down a solution for a laser source, testing for photo-carrier generation will be performed on the monochromator to compare carrier generation in 4-µm devices with the previous 1-µm devices that were tested. Once a viable solution is found for the laser, pulse testing using epoxies and a vacuum chamber will be done to allow for testing at higher voltages.

High Power Ultrafast Switch Fundamentals (Bhamidipati - GRA)

We have continued our survey of additional novel switching technologies for fast rise pulsed power applications, and downselected the material based on the characteristics including the material's breakdown field, saturation velocity, e-h mobility and thermal conductivity and the device topology based on the on-state resistance and noise level (often due to impact ionization). A diagram of the downselection status is shown in Figure A7, where downselected technologies are shown in green. We have selected one two terminal and three terminal devices for special consideration, highlighted in yellow in Figure A7:

- Two terminal device topology – GaN Gunn Diodes (electrically triggered)
- Three terminal device topology – AlGaN/GaN HEMTs (electrostatically gated 2DEG)

Transistors like MOSFETs and thyristors have been eliminated from the consideration due to their high on-state resistance and low repetition rate capability, respectively. Diamond PCSS is another technology under consideration, but its fabrication maturity and high carrier recombination rate, 9.0×10^{5}, is a possible limitation. For comparison, the recombination rate in GaN is 1.10×10^{-8}.

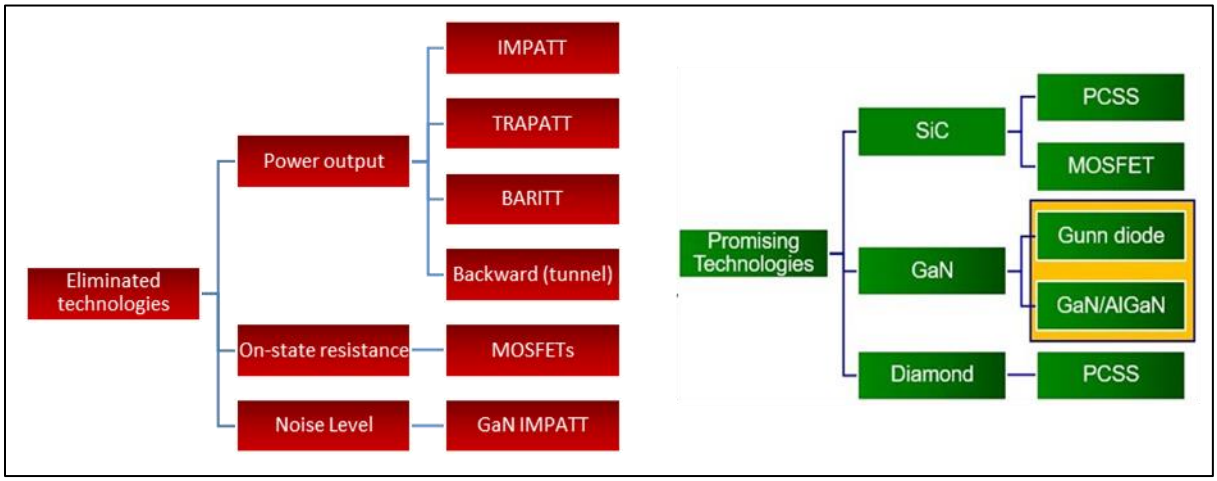


Figure A8. *Technology downselection diagram: (Red) eliminated technologies and (green) technologies for continued evaluation.*

In addition to another downselect, we have reviewed existing figures of merit (FOM) proposed by Baliga, Huang, Ohmi and Takeuchi, Johnson, Keyes and Shigekane to understand their basis at the material, device topology, and packaging level. While most of the FOM are derived from the power loss factor for MOSFETs, they do not emphasize on the fundamental Physics of the devices. Ohmi's and Takeuchi's FOM can be modified to fit the requirement for PCSS, which will provide us an electrical performance merit.

Using existing FOM as a starting point, our present focus is on generation of a new FOM for materials and devices emphasizing parameters influencing performance of all PCSS technologies. We have split our effort into generating two new FOMs: (1) a FOM based on the heat dissipation during recovery as a function of the recombination, surface effects and fabrication techniques for device treatment and (2) a FOM for the optical performance based on the excitation, photoconductivity. Using (1) we will be able to The purpose of (1) is to quantify performance at the device and packaging level, while the purpose of (2) is to quantify the optimal material for photo-excitation including phenomena involving interband transitions of indirect and direct bandgap materials. We are currently studying one-photon and two-photon absorption and its effect on optical properties including band edge absorption and density of states.

I.A.1 Immediate Tasks of Fundamental PCSS Subgroup

i. Complete build and validation of SF^{6} vacuum chamber and conduct initial electroluminescence tests at increased voltage.

ii. Improve model of SiPCSS transient, optically stimulated pulsing in TCAD for agreement experimentally measured recovery time.
iii. Narrow down the exploration to a specific material and switching technology.

I.A.2 Expected Products of Fundamental PCSS Subgroup

i. Improved fixture for cooling system validation testing.
ii. 355-nm illumination source for GaN:C-PCSS testing.
iii. Optically triggered transient simulation of Si-PCSS in good agreement with empirical results from pulse testing.

I.B GaN:C Subgroup (Rulis - Faculty)

The Simple Monte Carlo (SMC) program can compute material properties such as electron/hole drift velocity and ionization coefficients relevant for avalanche breakdown. In the past month we fixed a few small operational (machine dependent) bugs that the program had in it. The bugs had no impact on computed results but they prevented the code from working on the machines that we had accessible to us. That has been resolved now. We have run the program to reproduce Si and other material results as published in the paper of record for the method (Zhou X, Ng JS, Tan CH, "A simple Monte Carlo model for prediction of avalanche multiplication process in Silicon" J Inst, 2012 7(08), P08006–P08006 (2012). Available from: https://doi.org/10.1088/1748-0221/7/08/P08006). Preliminary results are shown in Figure B1 below.

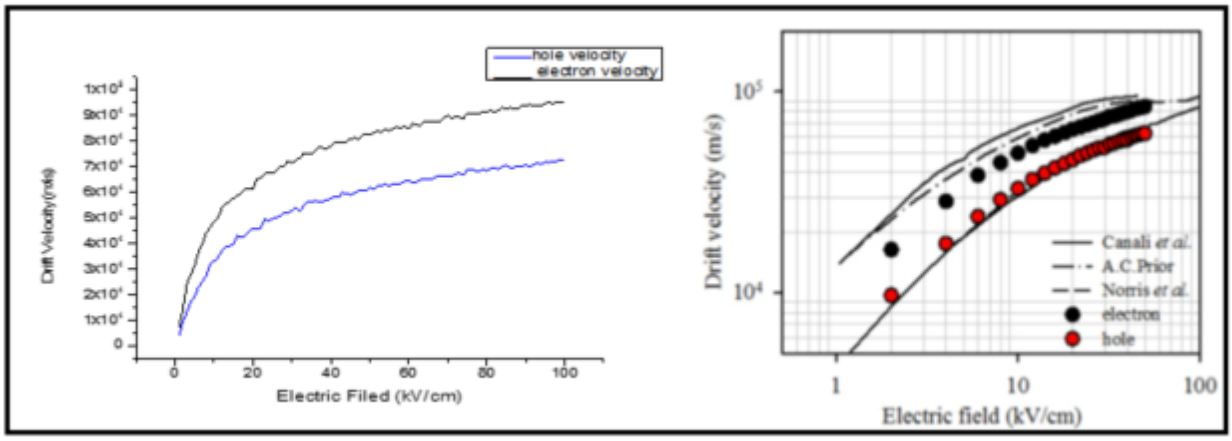


Figure B1*. Computed (left) vs. previously published Si drift velocities from SMC (right). Publication source is the same as above.*

We have also begun work to evaluate the Archimedes Monte Carlo code for 2D device simulation.

Finally, as shown in Figure B2, we are nearing establishment of a basic, to good, to strong understanding of all the computational concepts and explicit program codes that will be needed in the long tool chain for computing high level engineering quantities (breakdown

voltages, thermal conductivities, macroscopic optical response) from basic ab initio methods.

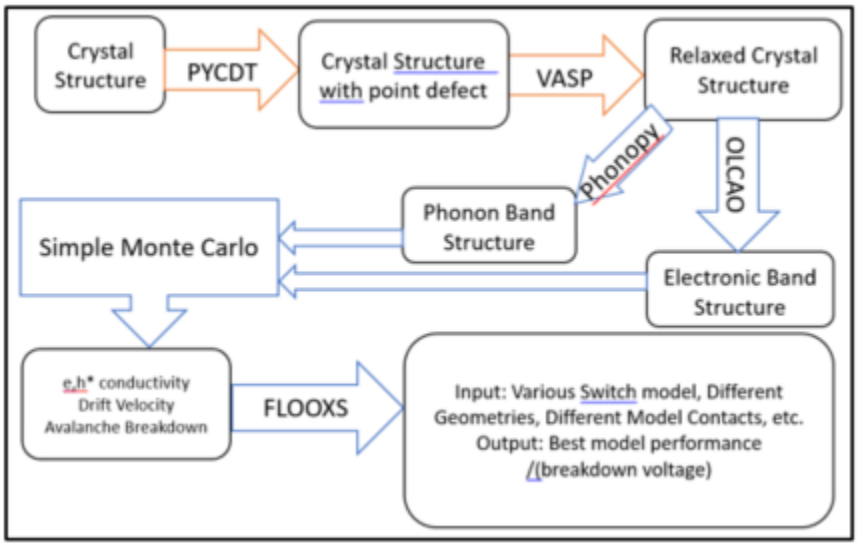


Figure B2. *Basic outline of code and data to be used to produce engineering predictors.*

I.C Small Unmanned Aerial Vehicle Diagnostics and Design-of-Experiments (Fields - Faculty)

Hardware/Software

UAS Manufactured/Purchased

PX4 ZOHD Nano Talon (3): T-001 T-002 T-003
PX4 Bixler 2.0 (2): B-001 B-002
PX4 F-450 Quadrotor (2): Q-001 Q-002
DJI Phantom 4 (5): P4.1-1 P4.1-2 P4.2-1 P4.2-2 P4.2-3

Quadcopter Developments

Free flight testing of a PX4-based quadcopter system has been ongoing in preparation for a free flight HPM test. Initial checks were done to insure the controller was tuned properly and flew robustly. In addition to this, a stamina test was done to assess what the maximum flight time is, given the weight and battery size. It is somewhere between 8 and 9 minutes. Tests were also conducted to verify the various flight modes are working properly (waypoint navigation, loiter, etc.).

Improvements were made to the automated data collection using the Navio2 Platform. A new Tektronix oscilloscope with more channels was integrated to allow verification of field levels using both a v-dot and d-dot. In addition to this, a variable illumination time was incorporated into the testing to begin to answer the question of burst length. On the hardware side of the test setup, a GPS repeater was installed in order to get GPS signal

into the GTEM. There has been an ongoing effort to incorporate a laser tachometer to pick up RPM from the motors during testing. A stand-alone Labview VI has been made to accomplish this and is awaiting integration into the automated test apparatus.

Fixed Wing Developments

Initially two fixed wing platforms were candidates for live-fire testing: H-King Bixler 2 and the ZOHD Nano Talon. The advantages/disadvantages were considered for each platform. Originally the Bixler 2 was the more attractive airframe due to its low price point and large payload capacity. However, once assembly of the Bixler 2 began, it became obvious that due to required modifications time of assembly would be very high. It is estimated that assembly requires eight hours per Bixler 2 aircraft. Compared to the Bixler 2, the ZOHD Nano's assembly time is approximately two hours per aircraft. Although the Nano's airframe and payload capacity is smaller than the Bixler 2, the Nano's payload capacity is sufficient for the project needs. The Nano also has the advantage of having modular control surfaces allowing quicker assembly/disassembly for transportation purposes.

As far as hardware is concerned, both aircraft run PX4 autopilot in their respective airframe configurations. Both planes are able to autonomously fly pre-programmed flight paths with GPS and upload new flight paths while in air. In the event of hard crashes, neither airframe survives, but interior data logging devices and spare parts have routinely been salvageable. Airframe selection was narrowed down to the ZOHD Nano Talon for its minimal assembly time, ease of interior access, modular and deconstructable design, and ease of transportation. For live fire testing, the ZOHD Nano is the airframe of choice.

Data Analysis Developments

Thanks to recent software development at DJI, they now allow users to pull the flight data off. Recent efforts have been put into using these data files to integrate DJI platforms into our test campaigns. For the time being, the platform that has been looked at is the DJI Phantom 4 pro V1/V2. When extracting the flight logs, you first need to install a program called DJI assistant 2, for the given Phantom variation. This program can be found on the DJI website under Phantom 4 pro downloads. The DJI assistant will pull log files from the drone in a ".dat" format, which is not incredibly useful. To overcome this, there is a converter that can be found at datfile.net, that will allow the use to convert the ".dat" file to a ".csv", while also resampling the data to a variety of different data rates (10Hz, 30Hz, 100Hz, 200Hz). It should be noted that the drone records a flight log every time it is powered on. This includes powering it on to plug into the computer to pull the log files. After the log files have been pulled from the drone over USB and converted to a csv, they are sent to a Matlab Data parser script that is still in development. Currently the parser pulls in the data, separates it out into the variables of interest, such as accelerometer, motor commands, etc. and creates plots of the flight data to visually inspect. Work is ongoing to fully integrate the data with the diagnostic analyzer.

I.C.1 Immediate Tasks for Diagnostics/DoE Subgroup

i. Analyze data from DOE 0 testing at all locations;
ii. Investigate individual sensor component propagation through a feedback control system;
iii. Demonstrate feasibility in adaptive experimental design for improved effects results confidence with minimal experiments;
iv. Integrate Pixhawk 2.1 into cUAV architecture.
v. Integrate DJI Phantom 4, v1 and v2 into cUAV architecture

I.C.2 Expected Products of Diagnostics/DoE Subgroup

i. Evaluation of adaptive DOE technique using NIRF amps and GTEM;
ii. Multiple fixed wing platforms for both GTEM and live-fire testing
iii. More powerful and cost-effective UAV platform for cUAV applications.
iv. Data parser for DJI based platforms.
v. Data parser for PX4 based platforms.

I.D Positive Feedback Non-Linear Transmission Line (Khan - Faculty)

PCSS Power Supply

During April 2019, we have shifted our focus from positive feedback NLTL design to Si-based photoconductive semiconductor switch (PCSS) design and associated circuits, which includes tail current minimization. We are conducting extensive literature study on the modeling of PCSS and its charging and discharging operations. PCSSs have been widely used for high power microwave (HPM) generation for their fast switching time, low trigger jitter, optical isolation of the trigger, high thermal capacity and thermal conductivity. Si, SiC, GaAs are the most widely used materials used for fabricating PCSSs. At UMKC, Si-based PCSS is being used as a part of HPM generation setup.

The PCSS acts as a closing switch when properly illuminated by an optical source (e.g., Laser). Upon the removal of illumination, the resistance of the PCSS increases significantly, thereby acting as an opening switch. However, slow recombination of the excess carriers in the Si substrate gives rise to the long tail current. This phenomenon translates into a switch which is not fully open even after the removal of the optical trigger. Therefore, if the PCSS is always connected to a power supply through a microstrip-based charging transmission line, it will draw current (tail current) even after the removal of optical pulse resulting in unwanted heat dissipation and lower efficiency for hundreds of nanoseconds to ones of microseconds yielding unwanted heating and efficiency losss.

We are planning to incorporate a solid state switch in series with the charging transmission line and the PCSS, and this transistor is M1 as shown in Figure D1. The transmission line will be charged through this switch, and it will be deactivated before the laser hits the PCSS, thereby disconnecting the PCSS from the power supply during the

active period. The charged transmission line will release energy through the PCSS to a load connected to a discharging transmission line.

During our LTSpice simulations, the PCSS has been represented as a time varying resistor for a recombination time of 5µs.

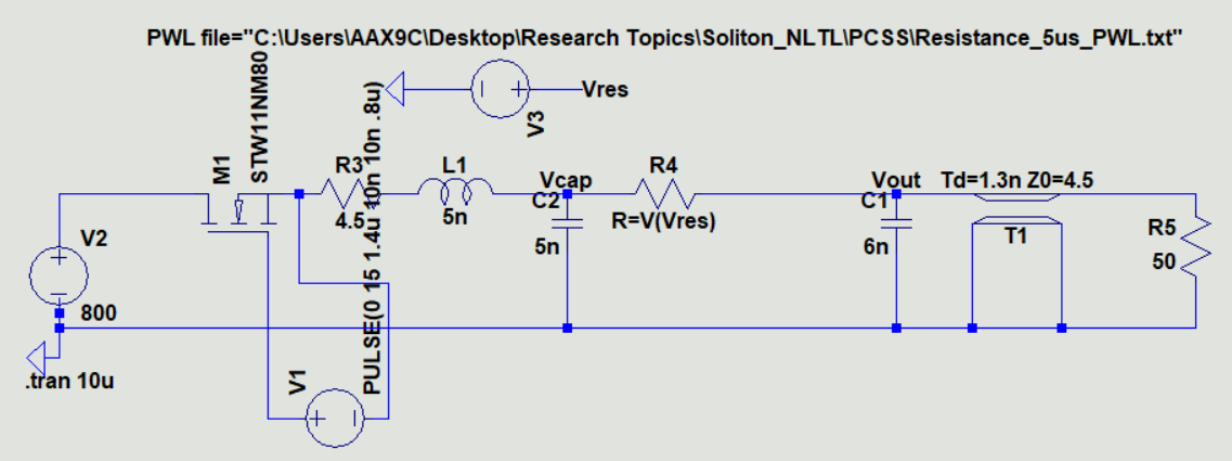


***Figure D1**. Schematic of series solid state switch (MOSFET) connected PCSS and power supply.*

The charging section is represented by a lumped RLC equivalent as shown in Figure D1. The discharging section is represented by a lossless transmission line model (T1) of LTSpice and shunt capacitance (C1) of the transmission line. The PCSS is represented by the time varying resistor (R4). The voltage across the 50 ohm load and the shunt capacitance (C1) of the discharging line are shown in Figure D2.

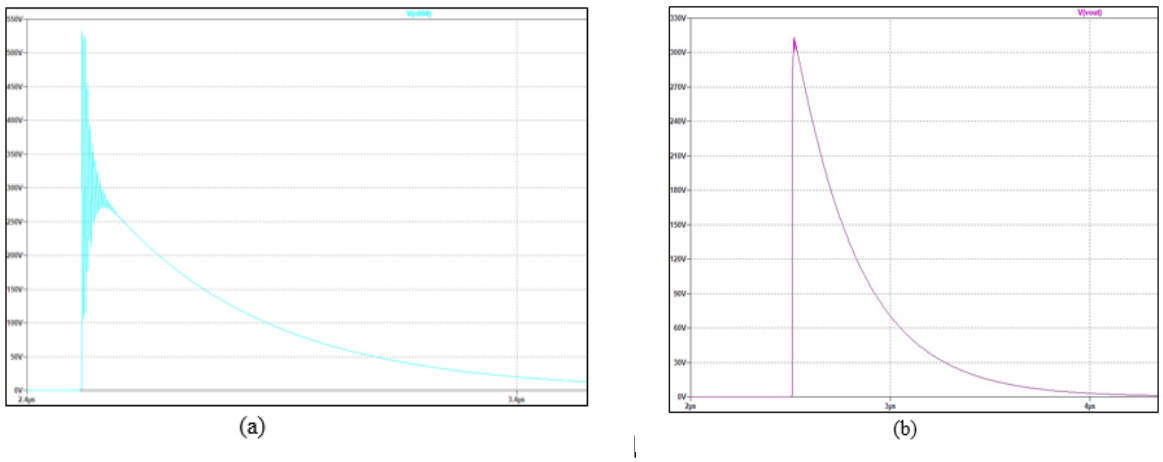


***Figure D2**. (a) Voltage across the 50Ω load (b) voltage across the shunt capacitance (C1) of the discharging transmission line.*

Another unique approach would be modeling the PCSS as an opto-isolator, although an opto-isolator is not designed to carry any meaningful current. An initial LTSpice schematic

based on this concept is illustrated in Figure D3. At present, we are working on the improvement of the PCSS model in LTSpice by incorporating the proposed solid state switches coupled with lossy transmission line to closely approximate the real time scenario. In addition, we are working on introducing a three-state switching pattern to sequentially trigger the series switch, PCSS emulating switch and shunt switch without overlapping. We are looking at fast high breakdown voltage (up to 18 kVDC) solid-state switches from BEHLKE as probable options to use as the series and shunt switches.

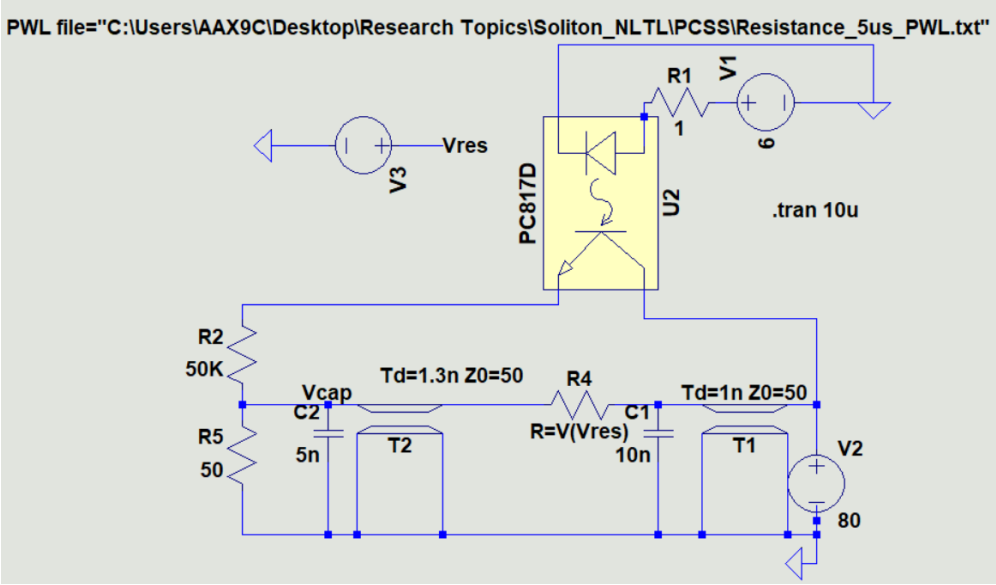


***Figure D3**. Schematic of optocoupler based PCSS circuit.*

I.D.1 Immediate Tasks for the Positive Feedback NLTL Subgroup

i. Simulating lossy transmission line model based PCSS circuit simulation.
ii. Designing three-state switching circuit to implement series and shunt solid state switches in PCSS circuit to simulate the tail current behavior.

I.D.2 Expected Products of Positive Feedback NLTL Subgroup

i. Designing a solid state switch based power supply circuit for PCSS to minimize tail current and increase system efficiency.

I.E Applied RF Coupling Simulation and Modelling to/for sUAV (Hassan - Faculty)

Effect of Wire Length and Orientation

In this MSR, we study how the orientation of the wire, relative to the UAV's frame, affects the electromagnetic coupling. Three identical wires are mounted above the dielectric

frame at different locations as shown in Figure E1a. The three wires have identical dimensions (Length = 65 mm, Radius = 0.25 mm). Figure E1b shows the current distribution of the first mode of the frame assuming that its relative dielectric permittivity ε_r = 3.3. This mode has a maximum or a hotspot at the center of the frame and, therefore, we hypothesized that Wire 2 will exhibit the highest coupling current because it is the closest wire to the hotspot of Mode 1. Figure E2 shows the current coupled to each of the three wires for the wire orientation shown in Figure E1a and it confirms that Wire 2 exhibits a higher coupled current at 1.5 GHz than Wire 1 and Wire 3. The other peaks of wire 1 and 3 at 2 GHz correspond to the inherent first resonance frequency of the wires themselves, as determined by their length, when they are located far from the UAV's frame. That is Wire 1 and Wire 3 are not significantly affected by the presence of the dielectric frame.

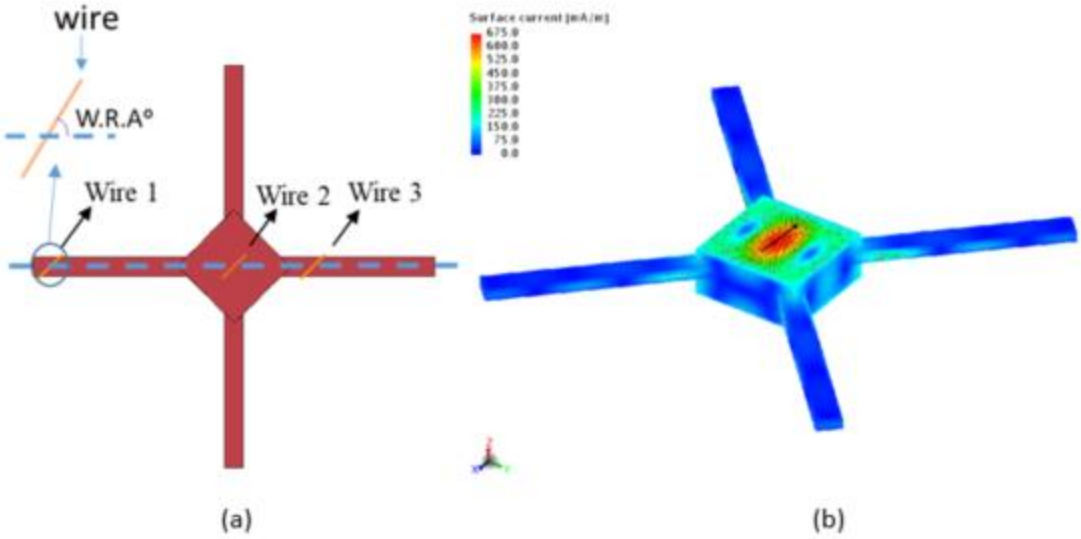


Figure E1. *(a) Frame model of the dielectric UAV and wire distribution, (b) Mode 2 current distribution of the dielectric UAV.*

In Figure E3, we show a comparison between the coupled currents of the 3 wires at different orientations. The coupled current plotted in Figure E3 is calculated at 1.5 GHz which is the resonance frequency of Wire 2 as shown in Figure E2. In Figure E3, the x-axis corresponds to the Wire's Relative Angle (WRA) as defined in Figure E1a. At WRA = 45°, Wire 2 is perfectly aligned with the current direction of Mode 1 of the frame as shown in Figure E2 and, therefore, Wire 2 exhibits maximum coupling current at this orientation. In comparison, Wires 1 and 3, do not exhibit a maximum at WRA = 45° because they are located far from the hot spot of Mode 1 of the frame. So the results in Figure E3 show that, depending on the location of the wire, its orientation can cause the coupled current to increase by more than 200%.

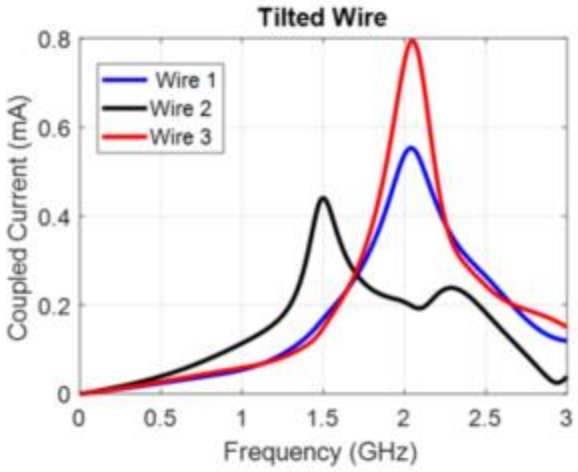


Figure E2. *Total coupled current to a 65 mm wires above the dielectric frames with different wire location.*

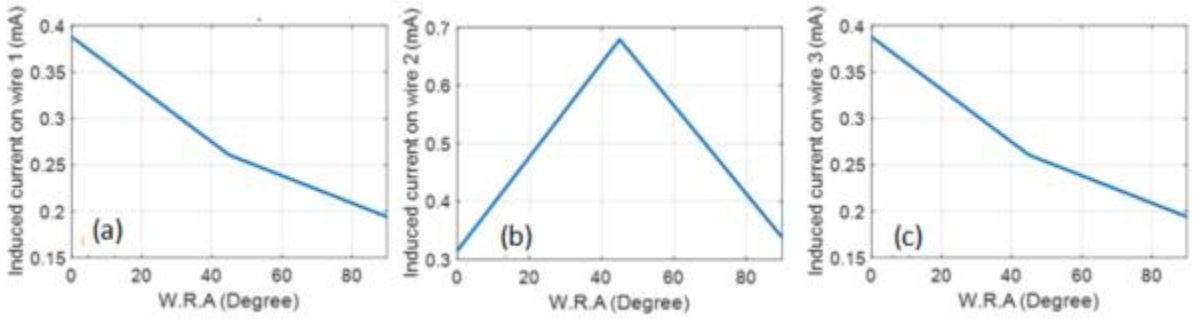


Figure E3. *Induced currents on the wires for different orientation (a) Wire 1 (b) Wire 2 (c) Wire 3.*

Effect of Wire Shape

We also studied the effect of wire shape on the coupling. The goal of this study is to define the average as well as the maximum coupled current to the UAV's wires with random shapes. Two identical wires are placed at two different locations above the drone as shown in Figure E4. Both wires have the same dimensions (length = 0.25 m, radius = 0.3 mm, height above the frame = 1 mm).The goal of this study is to combine two factors, the shape of the wire and its relative location with respect to the frame, and study the effect of the combined two factors on the electromagnetic coupling. This is a step forward towards modeling a realistic UAV wire distribution where the wires will exhibit both shape and location variations.

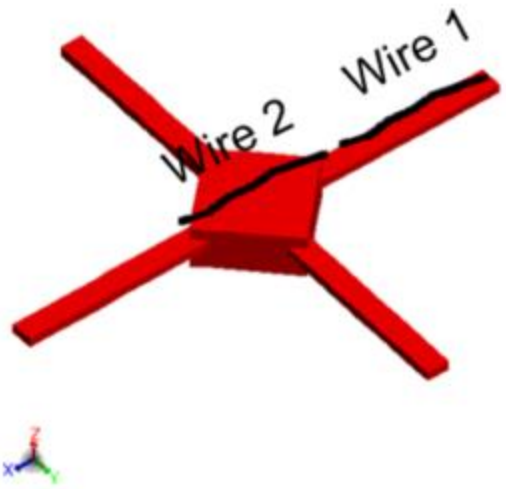


Figure E4. *Frame model of the UAV and wire distribution.*

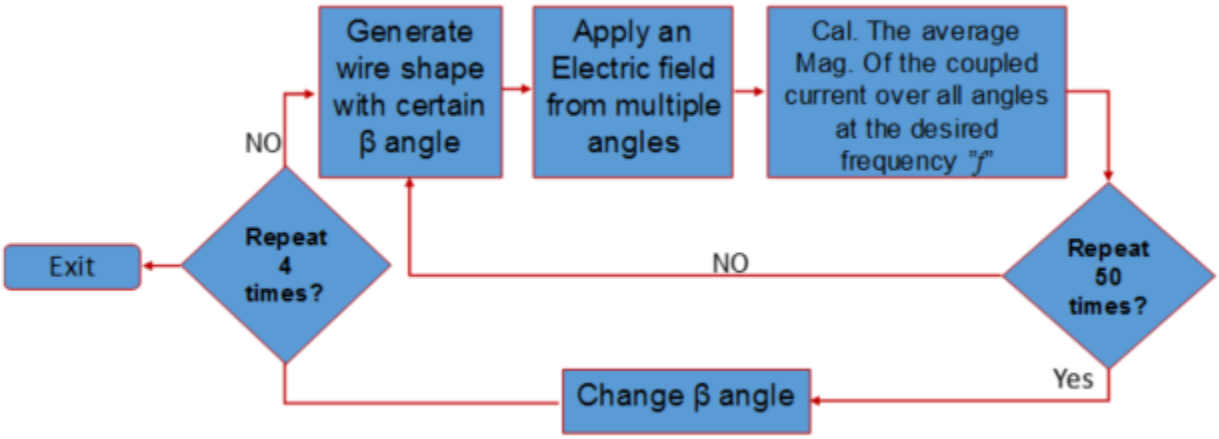


Figure E5. *Flowchart of the process used to calculate the results in Figure E6.*

Using the Random Walk Chain (RWC) model, we generated wires with four levels of waviness as described by the random angle (β) described in previous MSRs. Higher β values correspond to wires with higher levels of waviness. Each wire shape was exposed to electric field from 40 different incident angles and the average coupled current on each wire is calculated. For each waviness level, we repeated the same calculation 50 times for 50 different wire shapes and calculated the average coupled current. The flow chart in Figure E5 summarizes the process.

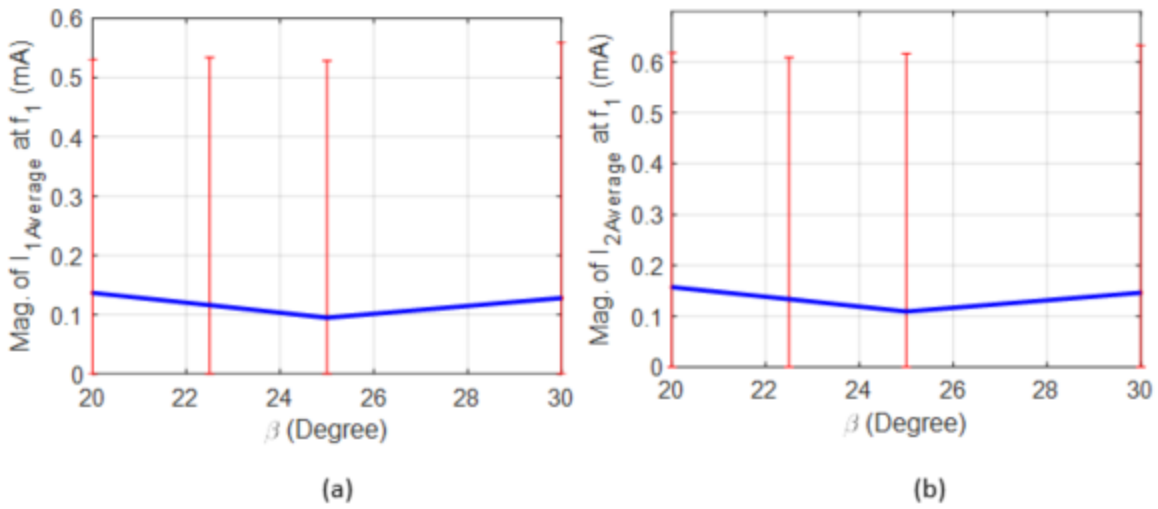


Figure E6. *Average induced currents on the wire for arbitrary wire shapes (a) Wire 1 (b) Wire 2.*

Figure E6 shows the average and the limits of the current coupled to the two wire configurations shown in Figure E4. Figure E6 illustrates the difference between the coupling to Wire 1 and Wire 2. The current coupled to Wire 2 is slightly higher than that of Wire 1. However, combining the two factors, wire shape and wire location, led to a significant increase in the range of the coupled current and we are increasing the number of incident angles and the number of different wire shapes to elucidate the trend in the coupling current accurately.



Figure E7. *A commercial drone showing the wires embedded in a dielectric enclosure.*

I.E.1 Immediate Tasks for RF Coupling Subgroup

I. Extended the statistical analysis of the wire shape effect on coupling for the dielectric frames using more wire shapes and more incident angles to have an accurate estimate of the trends in the coupling current.
II. Estimate how the coupling variations due to two factors, e.g. shape and location, correlate to the coupling variations due to each factor individually.
III. Study the coupling to terminated/loaded wires above the frames.
IV. So far we studied wires above a dielectric frame. Next we plan to study coupling to wires embedded inside a dielectric enclosure similar to Figure E7.

I.F UMKC Diode Network Based NLTL (Doynov – Research Faculty)

For an introduction to the scope of work on Diode-based Non-linear Networks (D-NLN), please see previous reports. For an updated reference, Figure F1 displays a copy of the poster presented at the Annual, Directed Energy Science and Technology Symposium, which was held from 8-12 April, 2019, in Destin, Florida. The poster summarized the results from the Diode-NLTL explorations to characterize the lumped elements networks in order to optimize their design and performance using PCSS as excitation sources.

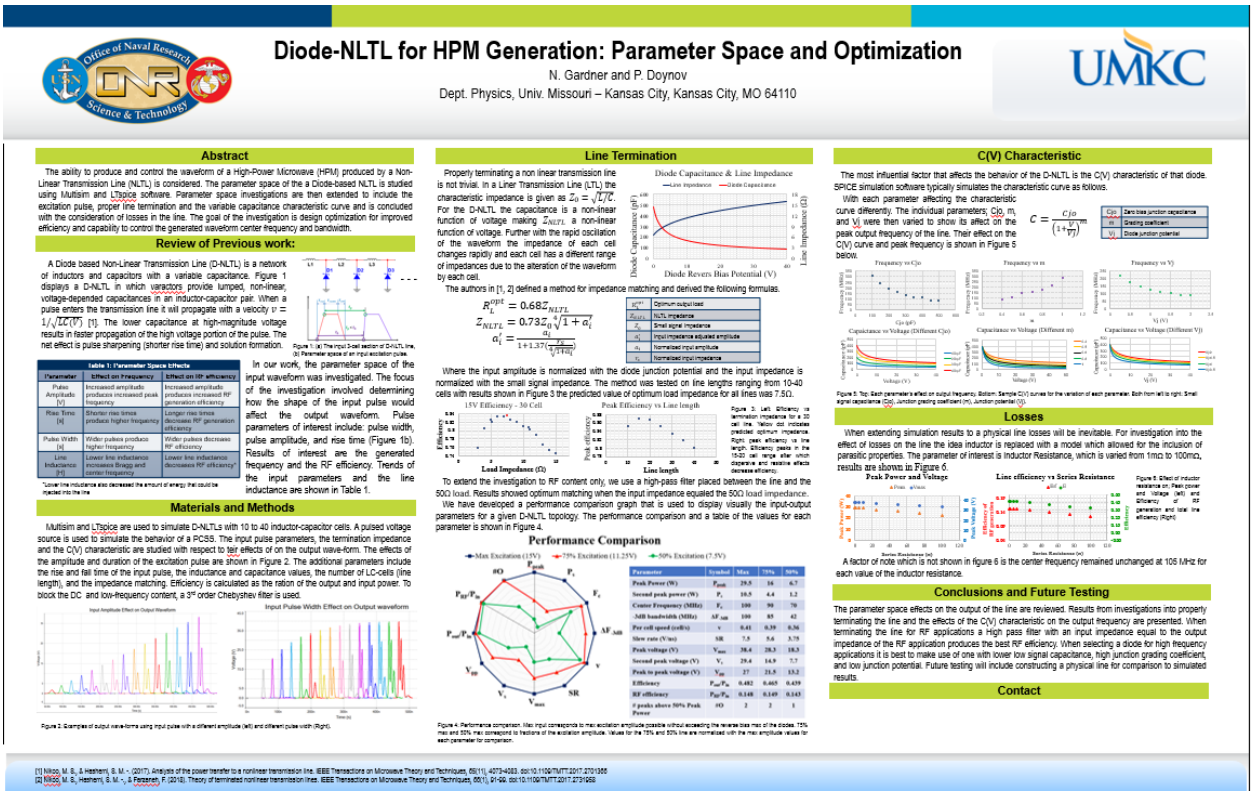


Figure F1*. Copy of the Diode-NLTL poster presented at the Annual, Directed Energy Science and Technology Symposium, which was held from 8-12 April, 2019, in Destin, Florida.*

Based on the parameters space exploration, we continue the optimization of Diode-NLTL design with the following objectives:

- Ability to generate waveforms that will produce frequency in the desired bandwidth;
- Efficiency of the D-NLTL;
- Excitation with currently available pulse sources.

Figure F2 displays the summary of a three-step design process with considerations for the lumped elements NLTL. The steps are:

1. Select a variable capacitance element with a low in series resistance and a large elastance swing that provides a high diode cutoff frequency.
2. Select the inductance value and verify that it provides a high value Bragg frequency and a characteristic impedance value within the desired working range.
3. Consider the number of L-C pair elements that will provide the desired depth of oscillations and the targeted number of solitons generation.

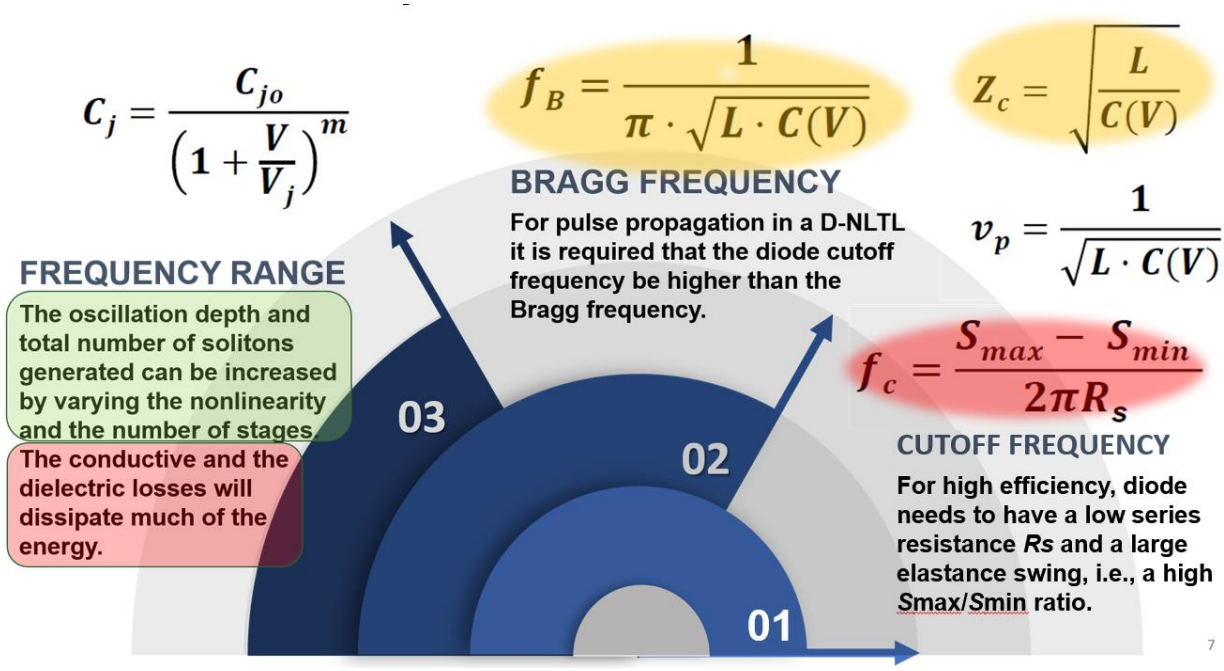


Figure F2. *Summary of a three-step design approach of Diode-NLTL.*

We use Multisim and LTspice to simulate multiple D-NLTLs topologies with different number (10 to 40) inductor-capacitor cells. A pulsed voltage source is used to simulate the behavior of a PCSS. The input pulse parameters, the termination impedance and the C(V) characteristic are studied to establish their effects on the output waveform generation. The effects of multiple parameters, including the amplitude and the duration

of the excitation pulse, were presented at the OSPRES semi-annual meeting at UMKC in March 2019.

Currently, we are in the process of repeating the initial simulations of lossless circuits with simulations that include parasitic parameters and frequency dependent losses. We continue the Diode-NLTL design optimization for generation efficiency defined as the ability to convert the input energy (power) to radiated energy (power). We express the ratio of the radiated cumulative power to the total power of the input excitation pulse in percent value and have named this the RF conversion efficiency. This is different from that commonly used ratio of the total power at the load of the NLTL and the input power. In the latter case, the power at the load includes the DC and low-frequency content. We focus on the RF efficiency which represents the real life performance of the D-NLTL HPM source.

At the OSPRES semi-annual meeting in March 2019, we presented a design concept that used a low-pass filter and delay line to redirect the reflected (non-transmitted) energy back to the input of the NLTL. Based on the simulation results, the calculated RF efficiency exceeded 40%. We further developed the concept for re-utilization and conversion of the reflected energy with a new design concept that provides an intentional reflection backward in the NLTL. During the reverse pass, the soliton formation process changes the reflected signal and the process continues after a secondary reflection at the input of the NLTL. Figure F3 presents the block-diagram of the new design with the wave-form transformation at different points of the NLTL.

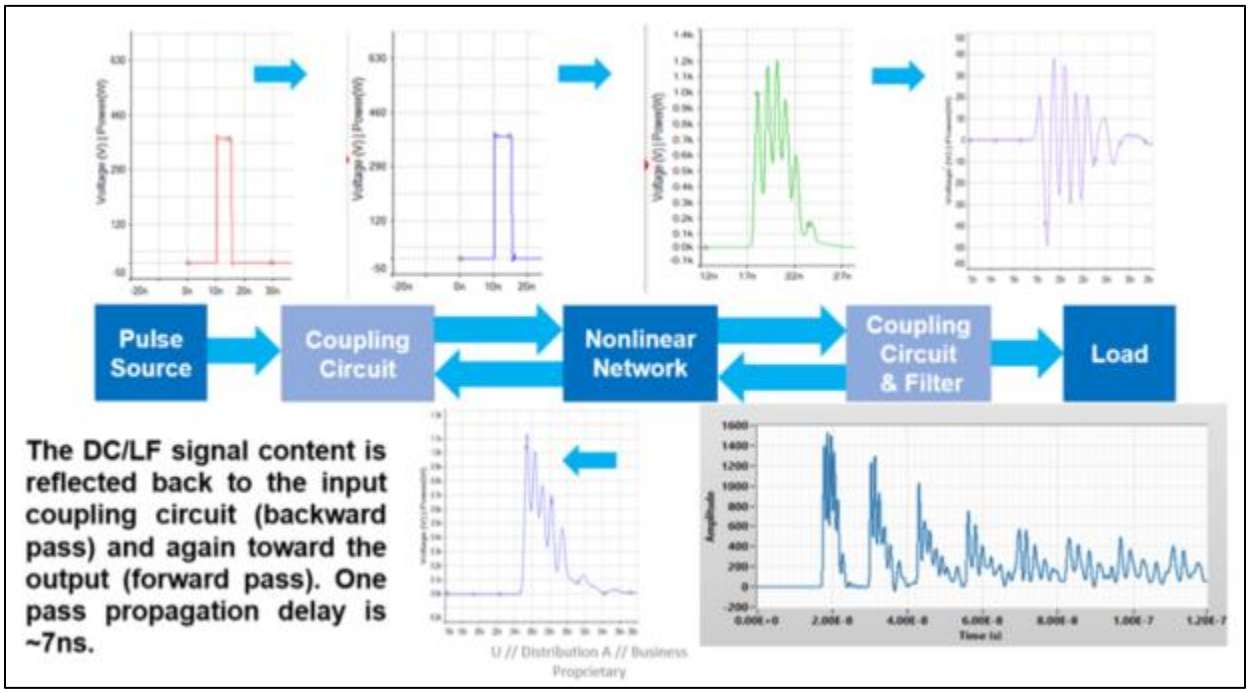


Figure F3. *Block-diagram and waveforms of the new NLN design.*

The double pass of the NLTL transforms the signal to higher frequency content which can be radiated. The net effect of this multi-pass NLTL design is an increased RF efficiency that exceeds 70% for simulated, lossless line. The design concept and results from the simulations of the design were included in an oral presentation at the DEPS Symposium. Figure F4 presents an example of the generated multiple bursts with a single excitation pulse (four waveforms in the top right graph captured in time domain). The magnitude of the cumulative power spectrum is presented on the botom left graph. The spectrogram in the botom right plot is calculated using the Short-time Fourier Transform and illustrates the time-frequency characteristics of the generated waveforms.

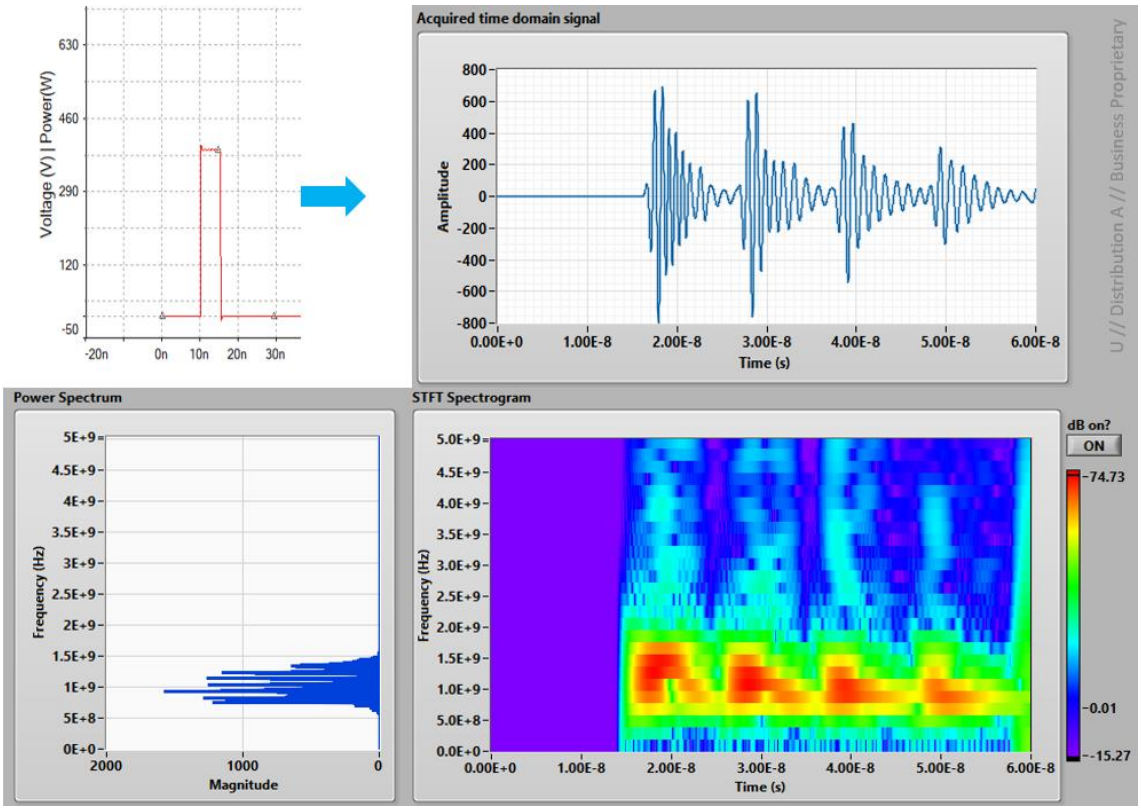


Figure F4*. The single excitation pulse (top, left) generates multiple waveforms in time domain (top, right) with multiple spectral lines. The cumulative spectral power and the spectrogram are also presented (bottom, left and right, respectively).*

The design of the D-NLTL can be optimized for peak power and for frequency content distribution. Figure F5 presents the input and RF output power and the calculated efficiency based on the number of bursts included in the calculation

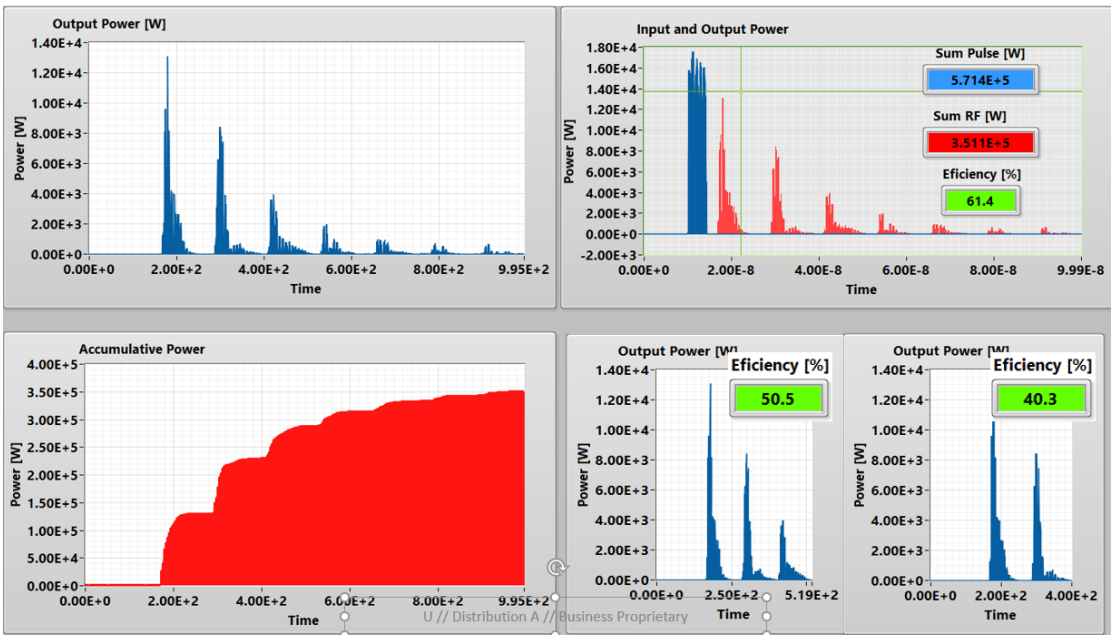


Figure F5. *The calculated power and RF efficiency (green background).*

The results in Figure F5 are for a D-NLTL optimized to generate multiple spectral lines at 75 MHz distances. The peak center frequency is at 670 MHz as can be seen in Figure F6.

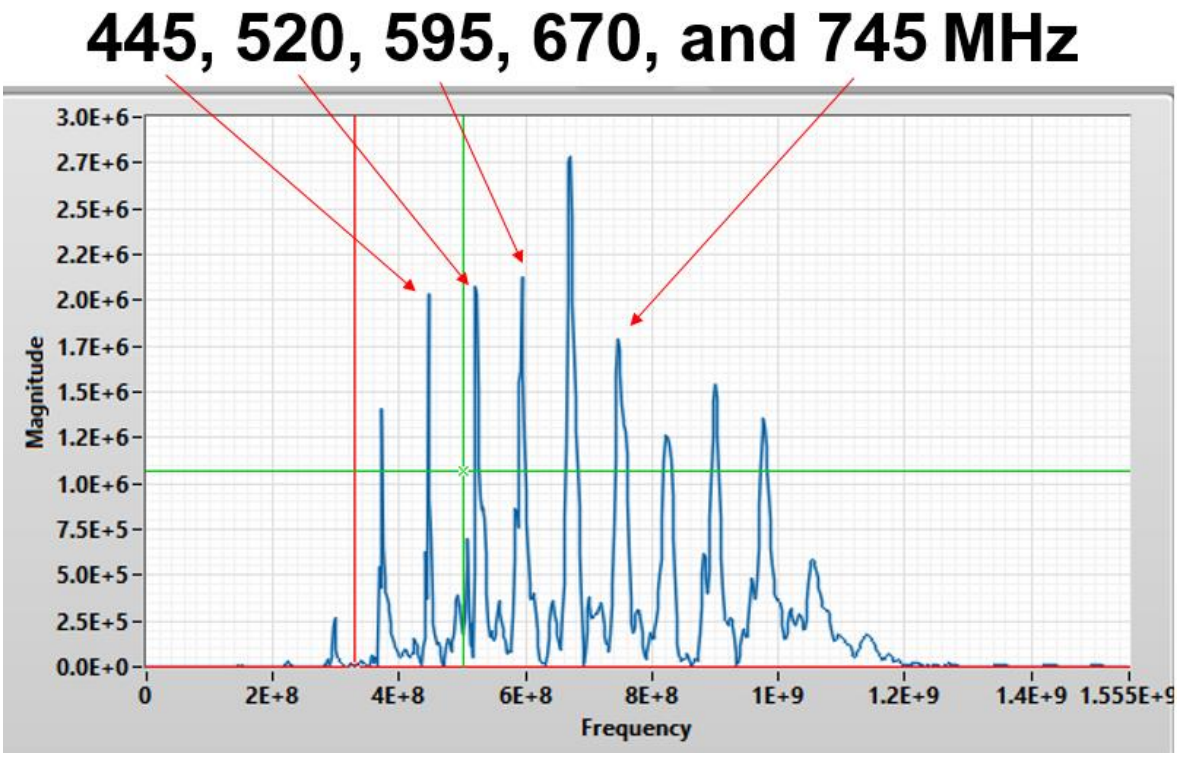


Figure F6. *An example of a multi-pass D-NLTL, a single excitation pulse generates multiple spectral lines.*

In some applications, a high peak power at a high repetition rate is important. The multi-pass D-NLTL can be optimized for high peak power and it is an inherently a high repetition rate operating source. The plots in Figure F7 display that the peak power of the first and second burst are comparable to the input peak power.

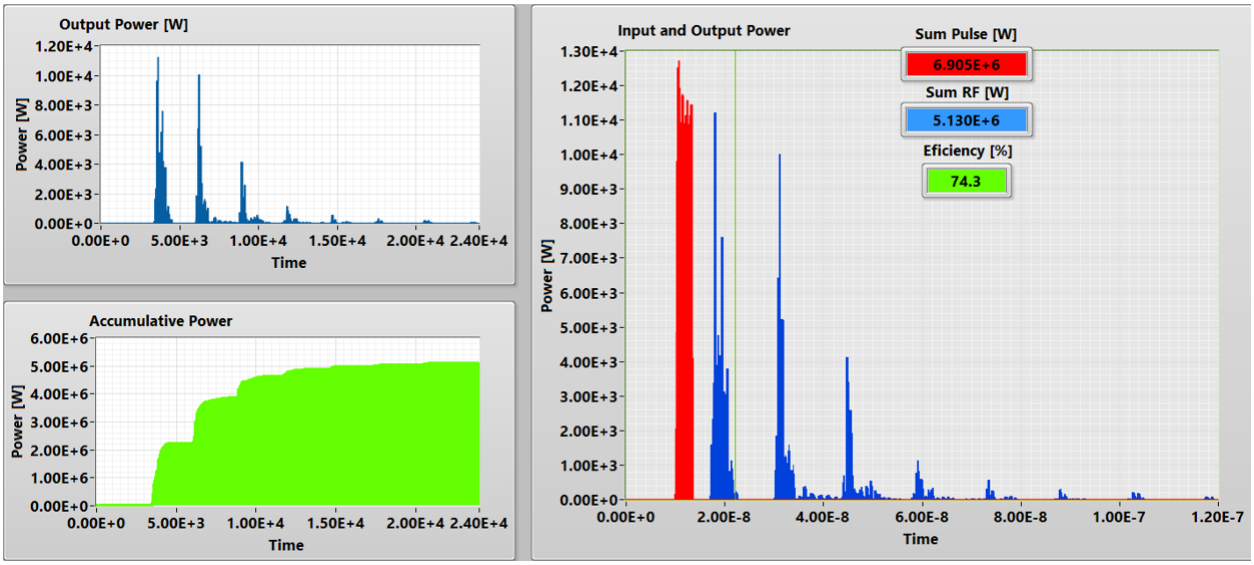


Figure F7. *Demonstration of high peak power, high repetition rate and high efficiency using multi-pass D-NLTL.*

Please note that the calculated cumulative RF efficiency is 74.3%. Obviously, the power in the bursts after the first three waveforms is very low and therefore not usable. The propagation delay of the D-NLTL is ~7ns, which results in an innate bursts repetition frequency of ~70 MHz.

I.G Electrically Small Antennas (Chatterjee - Faculty)

Overview

The ultimate aim to obtain a planar array of electrically small antennas (ESAs) has been divided into two distinct studies: (1) trade space/parametric analysis of a phased array antenna and (2) investigations into ESAs. In this report the trade space analysis of a linear array is presented. Important parameters such as Directivity, Beam-broadening factor, Half-power beamwidth and Fractional Bandwidth of a linear array with different amplitude distributions have been looked into. The future course of work has been outline in each section and also in the conclusion.

Trade-Space Analysis of Linear Array (Barman and Chatterjee)

One of the important purposes of antenna arrays is to obtain directive patterns for radar applications and direction finding. To obtain highly directive patterns, it is necessary to

have narrow main beam and low sidelobe levels. Lower sidelobe levels reduce unwanted signals in directions other than the main beam [1]. For the simple case of a uniformly excited array, the first sidelobe level is only 13.46 dB below the main lobe level which is not desirable for many directive applications. Several methods to reduce sidelobe levels of an array have been investigated in the past. Some of them include the use of tapered amplitude excitation [2-3], non-uniform element spacing [4-6], etc. The report focuses on the use of uniform as well as non-uniform amplitude excitations such as Dolph-Chebyshev and Taylor Line Source methods for sidelobe reduction. A general expression to obtain directivity of a linear array has also been derived. Comparison of directivity and fractional bandwidths for all the above types of amplitude distributions are presented.

It is well-known, the decrease in sidelobe levels on using amplitude tapers leads to main beam broadening and reduction in directivity [1]. However, for high power applications it is mostly important to concentrate on the reduction of sidelobe levels to reduce undesired raditaions. Before calculating the array parameters, it is necessary to compute the array factors for the different amplitude distributions. In this report, all calculations have been performed for a linear array placed along the x-axis where each of the elements are oriented along z-axis. Figure 1 portrays the array geometry. In the figure, $P(r,\theta,\phi)$ is the observation point. θ_s and ϕ_s are the scan angles from the z- and x-axis respectively

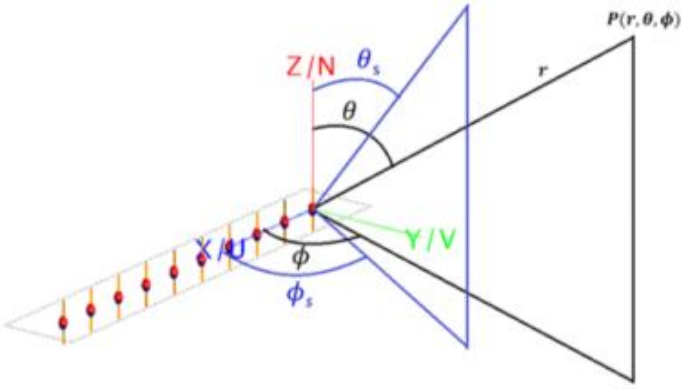


Figure G1. *Geometry of the linear array.*

Array Factor

The general expression to calculate the array factor of a linear array is obtained from Schelkunoff polynomial method [7]:

$$\mathrm{AF} = \sum_{\mathrm{n}=1}^{\mathrm{N}} \mathrm{w_n z^{n-1}} \qquad (1)$$

where, w_n are the excitation weights on each element of the array, N is the total no. of elements and

$$\mathrm{z} = \mathrm{e^{j\psi}} \qquad (2)$$

Along the x-axis, ψ is given as [8]:

$$\psi = \mathrm{kd}\cos\phi \ \text{ or } \mathrm{kd}\sin\theta \qquad (3)$$

where, $\mathrm{k} = \frac{2\pi}{\lambda}$ is the wave number and d is the inter-element spacing.

Therefore, for a linear array placed along the x-axis, the array factor can be re-written from eq. (1) as:

$$\mathrm{AF} = \sum_{\mathrm{n}=1}^{\mathrm{N}} \mathrm{w_n} \mathrm{e}^{\mathrm{jkd(n-1)}\cos\phi} \qquad (4)$$

An example of Array factor calculation is shown here. Taylor Line Source distribution for $\mathrm{N} = 25$, $\bar{\mathrm{n}} = 5$ and sidelobe level, $\mathrm{SLL} = -25\ \mathrm{dB}$ has been considered. The excitation currents calculated using the formulas given in [1] are enlisted in the table below:

$w_1 = w_{25}$	$w_2 = w_{24}$	$w_3 = w_{23}$	$w_4 = w_{22}$	$w_5 = w_{21}$	$w_6 = w_{20}$	$w_7 = w_{19}$	$w_8 = w_{18}$	$w_9 = w_{17}$	$w_{10} = w_{16}$	$w_{11} = w_{15}$	$w_{12} = w_{14}$	w_{13}
0.0474	0.0481	0.0505	0.0556	0.0638	0.0742	0.0850	0.0949	0.1029	0.1094	0.1144	0.1178	0.1191

For an inter-element spacing of $\mathrm{d} = \lambda/2$, $\mathrm{z} = \mathrm{e}^{\mathrm{j}\pi(\mathrm{n}-1)\cos\phi}$ (5)

Therefore, the Array Factor is,

$$\mathrm{AF} = 0.0474 + 0.0481\mathrm{e}^{\mathrm{j}(\pi\cos\phi)} + 0.0505\mathrm{e}^{\mathrm{j}2(\pi\cos\phi)} + 0.0556\mathrm{e}^{\mathrm{j}3(\pi\cos\phi)} + 0.0638\mathrm{e}^{\mathrm{j}4(\pi\cos\phi)} + 0.0742\mathrm{e}^{\mathrm{j}5(\pi\cos\phi)} + 0.0850\mathrm{e}^{\mathrm{j}6(\pi\cos\phi)} + 0.0949\mathrm{e}^{\mathrm{j}7(\pi\cos\phi)} + 0.1029\mathrm{e}^{\mathrm{j}8(\pi\cos\phi)} + 0.1094\mathrm{e}^{\mathrm{j}9(\pi\cos\phi)} + 0.1144\mathrm{e}^{\mathrm{j}10(\pi\cos\phi)} + 0.1178\mathrm{e}^{\mathrm{j}11(\pi\cos\phi)} + 0.1191\mathrm{e}^{\mathrm{j}12(\pi\cos\phi)} + 0.1178\mathrm{e}^{\mathrm{j}13(\pi\cos\phi)} + 0.1144\mathrm{e}^{\mathrm{j}14(\pi\cos\phi)} + 0.1094\mathrm{e}^{\mathrm{j}15(\pi\cos\phi)} + 0.1029\mathrm{e}^{\mathrm{j}16(\pi\cos\phi)} + 0.0949\mathrm{e}^{\mathrm{j}17(\pi\cos\phi)} + 0.0850\mathrm{e}^{\mathrm{j}18(\pi\cos\phi)} + 0.0742\mathrm{e}^{\mathrm{j}19(\pi\cos\phi)} + 0.0638\mathrm{e}^{\mathrm{j}20(\pi\cos\phi)} + 0.0556\mathrm{e}^{\mathrm{j}21(\pi\cos\phi)} + 0.0505\mathrm{e}^{\mathrm{j}22(\pi\cos\phi)} + 0.0481\mathrm{e}^{\mathrm{j}23(\pi\cos\phi)} + 0.0474\mathrm{e}^{\mathrm{j}24(\pi\cos\phi)} \qquad (6)$$

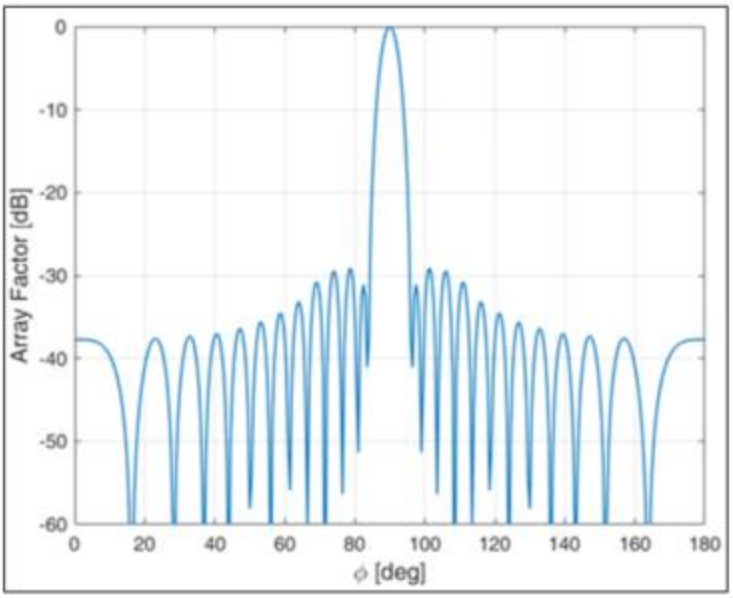


Figure G2. *Array Factor of Taylor Line Source distribution for* $N = 25, \bar{n} = 5, SLL = -25\ dB, {}^{d}/_{\lambda} =$ 0.5

Similarly, array factor for Uniform and Dolph-Chebyshev distributions are also calculated. Around 13 dB decrease in the sidelobe levels from Uniform to Taylor Line Source excitation has been achieved.

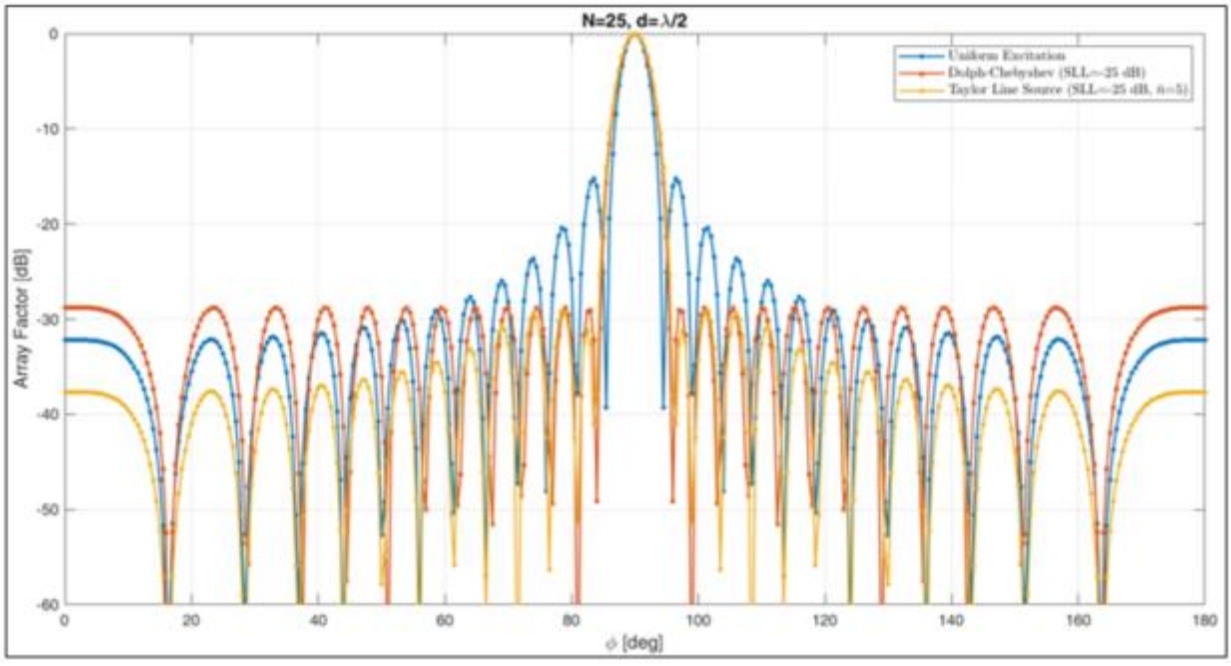


Figure G3. *Array Factors of 25 element linear array with different amplitude distributions and fixed inter-element spacing d/λ=0.5.*

Dilation Factor

A uniformly excited array has the narrowest beamwidth. The amount by which the main beam broadens with respect to the beamwidth of a uniformly excited array (on using an amplitude taper) is known as the dilation or beam-broadening factor. The dilation factor of a Dolph-Chebyshev distribution is [8]:

$$\sigma = 1 + 0.636\left\{\frac{2}{R}\cosh\left[\sqrt{(\cosh^{-1}R)^2 - \pi^2}\right]\right\}^2 \qquad (7)$$

where, R is the sidelobe level ratio, given by:

$$R = 10^{(-SLL/20)} \qquad (8)$$

Figure 4 shows the variation in dilation factor as a function of sidelobe level. As expected, σ increases with decrease in sidelobe levels. For Taylor Line Source method, the dilation factor is given by [1]:

$$\sigma = \frac{\bar{n}}{\sqrt{A^2 + \left(\bar{n} - \frac{1}{2}\right)^2}} \qquad (9)$$

where,

$$A = \frac{1}{\pi}\cosh^{-1} R \qquad (10)$$

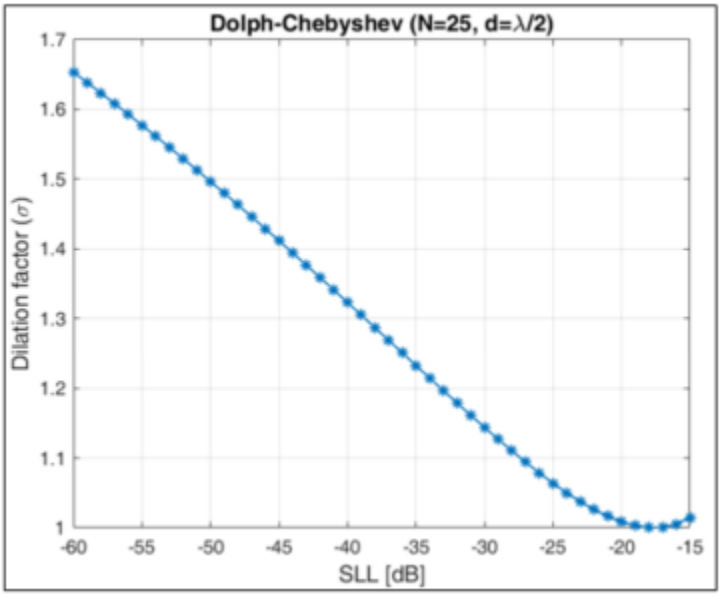


Figure G4. *Dilation factor of Dolph-Chebyshev array as a function of sidelobe level.*

Unlike Dolph-Chebyshev distribution the Taylor dilation factor decreases as the sidelobe level is decreased. Through computations using eq. (9), it has been observed that the dilation factor goes below 1 for some combinations of $\bar{n}$ and sidelobe levels. This is a physical impossibility as it implies narrower beamwidth compared to a uniformly excited array. It is therefore concluded from this observation that the input parameters, i.e., the sidelobe level and $\bar{n}$ cannot be chosen arbitrarily for a Taylor Line Source distribution.

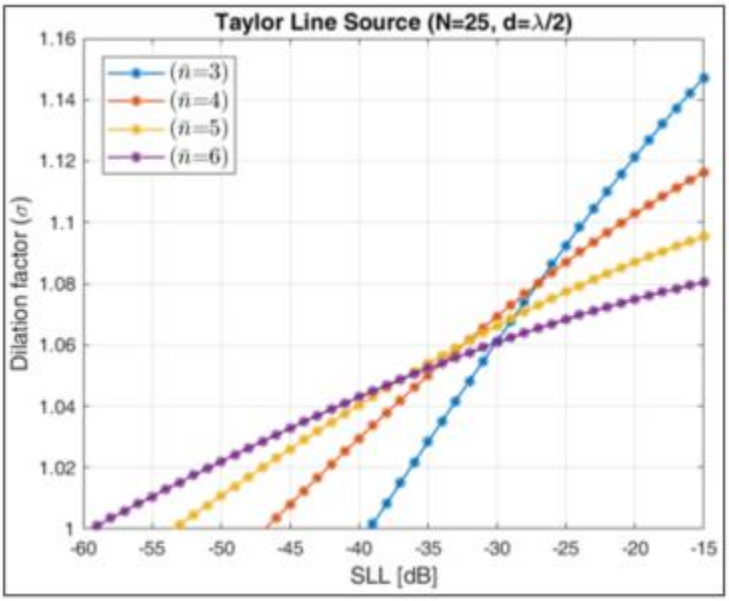


Figure G5. *Dilation factor vs. sidelobe level of a 25 element linear array with Taylor Line Source distribution.*

Directivity

The primary study is focused on the investigation of two important parameters: (a) Directivity and (b) Bandwidth of a linear array. The directivity of a linear array can be calculated using the expression [8]:

$$\mathrm{D} = \frac{4\pi|\mathrm{AF}_{\max}|^2}{\int_0^{2\pi}\int_0^{\pi}|\mathrm{AF}|^2 \sin\theta \, \mathrm{d}\theta\mathrm{d}\phi} \qquad (11)$$

For a linear array placed along the x-axis with the elements oriented along z-axis, a closed form expression for directivity has been derived as follows:
Putting the expression for Array Factor (AF) from eq. (4) into eq. (11):

$$\mathrm{D} = \frac{4\pi\left|\sum_{n=1}^{N} w_n\right|^2}{\int_0^{2\pi}\int_0^{\pi}\left[\sum_{n=1}^{N} w_n e^{j(n-1)kd\cos\phi}\right]\left[\sum_{m=1}^{N} w_m^* e^{j(m-1)kd\cos\phi}\right]\sin\theta \, \mathrm{d}\theta\mathrm{d}\phi} \qquad (12)$$

$$\text{or, } D = \frac{4\pi\left|\sum_{n=1}^{N} w_n\right|^2}{\sum_{n=1}^{N}\sum_{m=1}^{N} w_n w_m^* \int_0^{2\pi}\int_0^{\pi} e^{j(n-m)kd\cos\phi}\sin\theta\, d\theta d\phi} \quad (13)$$

$$\text{or, } D = \frac{4\pi\left|\sum_{n=1}^{N} w_n\right|^2}{\sum_{n=1}^{N}\sum_{m=1}^{N} w_n w_m^* \int_0^{2\pi} e^{j(n-m)kd\cos\phi} d\phi \int_0^{\pi}\sin\theta\, d\theta} \quad (14)$$

Now, $\int_0^{\pi}\sin\theta\, d\theta = 2$. So, eq. (14) reduces to,

$$D = \frac{2\pi\left|\sum_{n=1}^{N} w_n\right|^2}{\sum_{n=1}^{N}\sum_{m=1}^{N} w_n w_m^* \int_0^{2\pi} e^{j(n-m)kd\cos\phi} d\phi} \quad (15)$$

The integrand in the denominator can have a closed form solution [1]:

$$\int_0^{2\pi} e^{jx\cos\phi} = 2\pi J_0(x) \quad (16)$$

In eq. (15) we put $\int_0^{2\pi} e^{jkd(n-m)\cos\phi} = 2\pi J_0[kd(n-m)]$

$$D = \frac{2\pi\left|\sum_{n=1}^{N} w_n\right|^2}{\sum_{n=1}^{N}\sum_{m=1}^{N} w_n w_m^* \{2\pi\, J_0[kd(n-m)]\}}$$

$$\text{or, } D = \frac{\left|\sum_{n=1}^{N} w_n\right|^2}{\sum_{n=1}^{N}\sum_{m=1}^{N} w_n w_m^*\, J_0[kd(n-m)]} \quad (17)$$

Eq. (17) is the final expression for directivity of an array where the array elements are placed along the x-axis and oriented in the z-direction.
Using eq. (17), the directivity of a uniformly excited array is calculated for three values of N (N= 10, 25 and 50). Full-wave simulations have been used to obtain the directivity using commercial electromagnetic solver FEKO. Figure G6 shows the directivity of a linear array as a function of inter-element spacing.

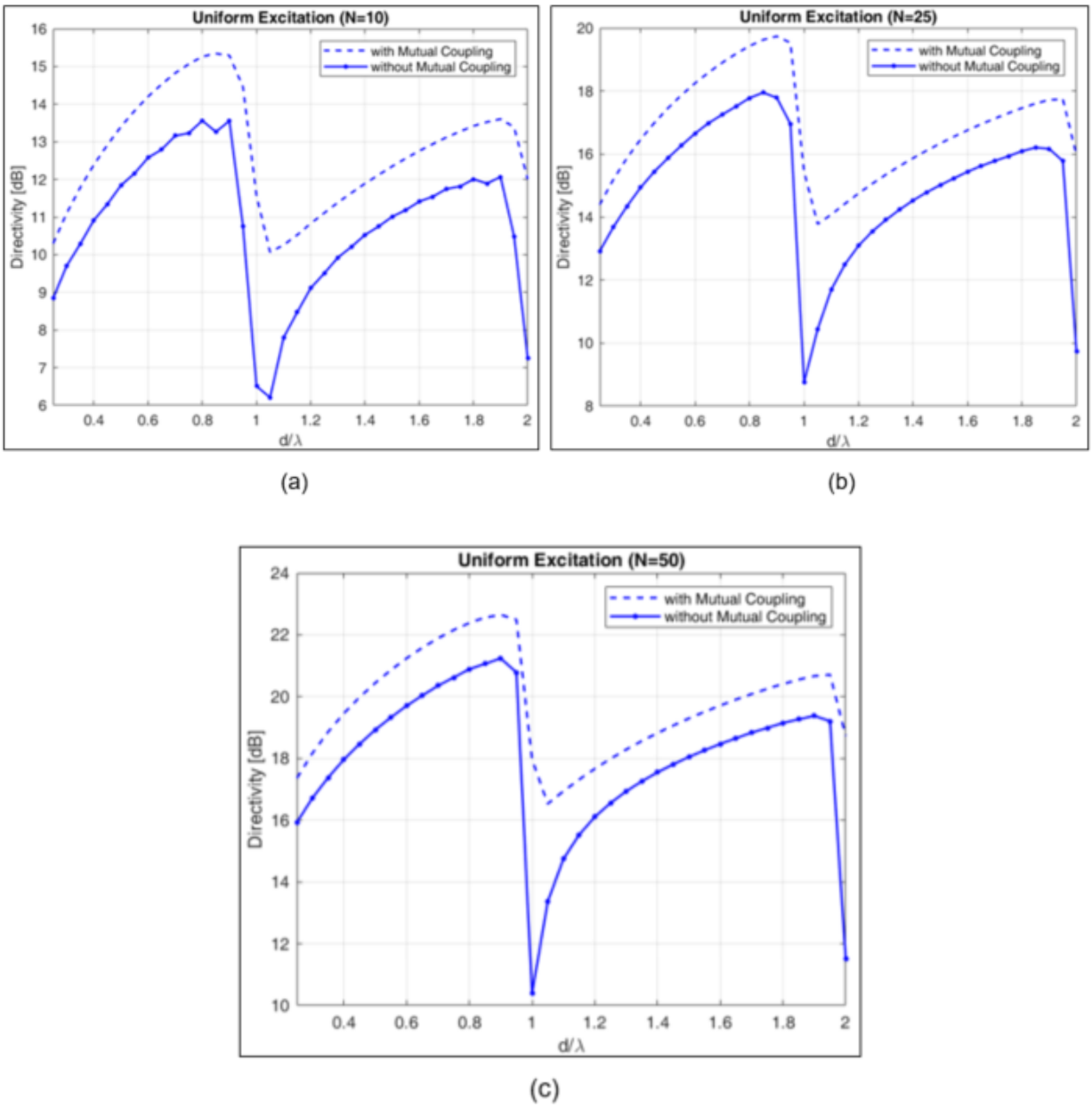


Figure G6. *Directivity of a uniformly excited array as a function of inter-element spacing d/λ for array lengths: (a) N=10, (b) N=25 and (c) N=50.*

An approximate difference of 2 dB between the calculated and simulated values is due to the consideration of individual element patterns along with the array factor in the full-wave simulations. The general expression calculates the directivity only from the array factor. The directivity of the array increases with increase in the number of array elements from N=10 to 50. However, the difference between the calculated and simulated values remain almost the same even on increasing N. Although the directivity increases with increase in inter-element spacing up to a certain value of d/λ, it drops at around d/λ=1. This happens even if the number of elements are increased. The reason of this plunge in directivity

might be attributed to the appearance of grating lobes on increasing the element spacing. A detailed investigation of it will be a future course of study.

An approximate formula for Dolph-Chebyshev directivity is given in [9]:

$$D = \frac{2R^2}{1 + (R^2 - 1)\sigma \frac{\lambda}{(L + d)}} \qquad (18)$$

Comparative analysis of Dolph-Chebyshev directivity with the results obtained using the approximate formula [eq. (18)], the derived general expression [eq. (17)] and FEKO has been performed. Figure 7 shows this comparison for a 25 element Dolph-Chebyshev array. It is observed that the derived general expression has better resemblance with the full-wave simulated results compared to the approximated expression. Also, the drop in the directivity at an inter-element spacing d/λ=1 is not reflected in the approximate calculation. The Taylor Line Source Directivity is computed using the general expression given by eq. (17) and compared with the FEKO generated results.

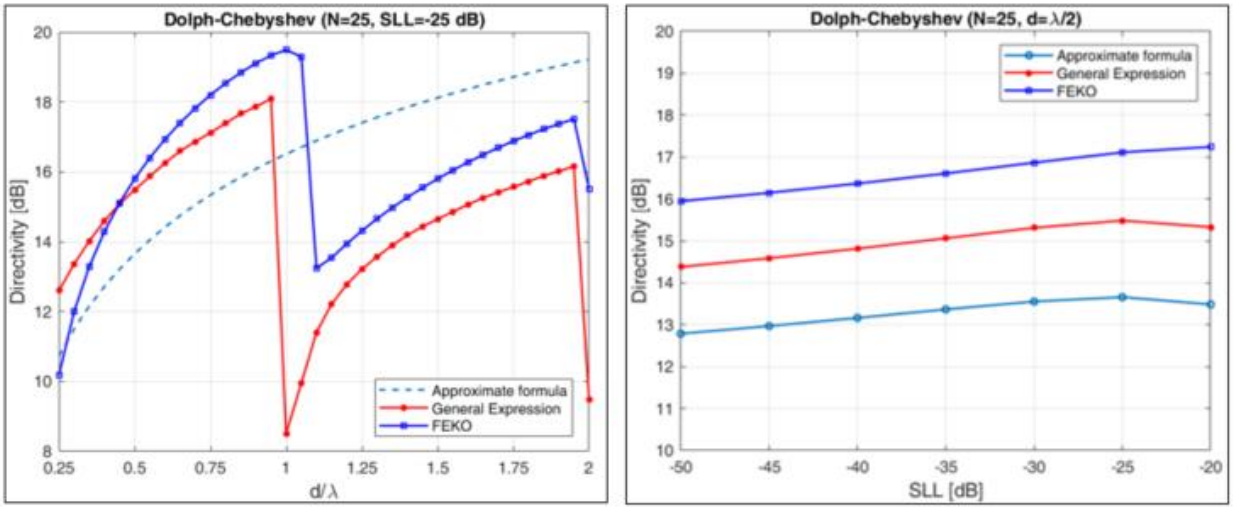


Figure G7. *Directivity of a 25 element Dolph-Chebyshev array as a function of (a) inter-element spacing d/λ and (b) sidelobe level.*

Half-Power Beamwidth and Fractional Bandwidth

Half-power beamwidth of an array is inversely proportional to its directivity. For a uniformly excited array the half-power beamwidth (in degrees) is given by [10]:

$$\theta_{3\mathrm{dB}} = \frac{101.5}{\mathrm{D}} \qquad (19)$$

For a Dolph-Chebyshev array, the half-power beamwidth can be related to the calculated directivity as [10]:

$$D = \frac{1.77}{\theta_{3dB}}\left[\frac{\sigma}{\sum_{p=-P}^{P}\left(a_p/a_0\right)^2}\right] \qquad (20)$$

For Taylor Line Source method, the half-power beamwidth is [1]:

$$\theta_{3dB} \approx 2\sin^{-1}\left\{\frac{\lambda\sigma}{L\pi}\left[\left(\cosh^{-1}R\right)^2 - \left(\cosh^{-1}\frac{R}{\sqrt{2}}\right)^2\right]^{\frac{1}{2}}\right\} \qquad (21)$$

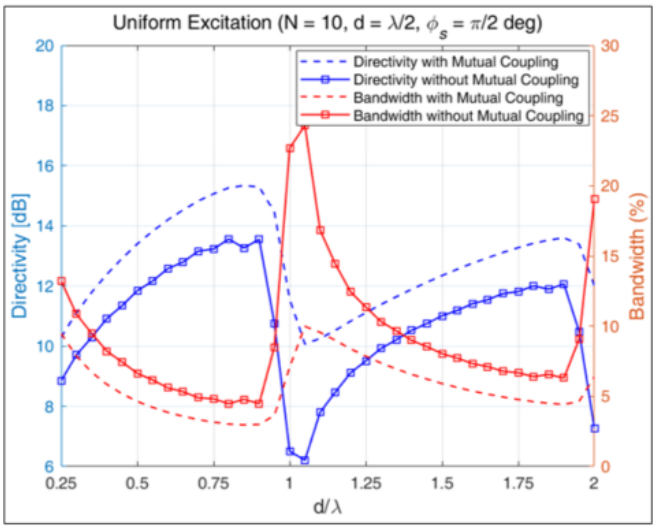
One of the important parameters of an array is fractional bandwidth. It is defined by the frequency limits at which the gain is reduced to half power. Fractional bandwidth of a linear array can be related to the half-power beamwidth as [11]:

$$\frac{\Delta f}{f} = \frac{\theta_{3dB}}{\sin\phi_S} \qquad (22)$$

where, ϕ_S is the scan angle. There is another commonly used relation between the half-power beamwidth and percentage bandwidth of a linear array:

$$\text{bandwidth (percent)} = 2 \cdot \text{beamwidth (degrees)} \qquad (23)$$

Using eq. (19-21) half-power beamwidth is calculated for three amplitude distributions followed by the bandwidth calculation through eq. (22). Two array lengths have been considered in each case, N=10 and 25. Figures (8-11) show the directivity and fractional bandwidth of the three amplitude excitations as a function of inter-element spacing or sidelobe level.



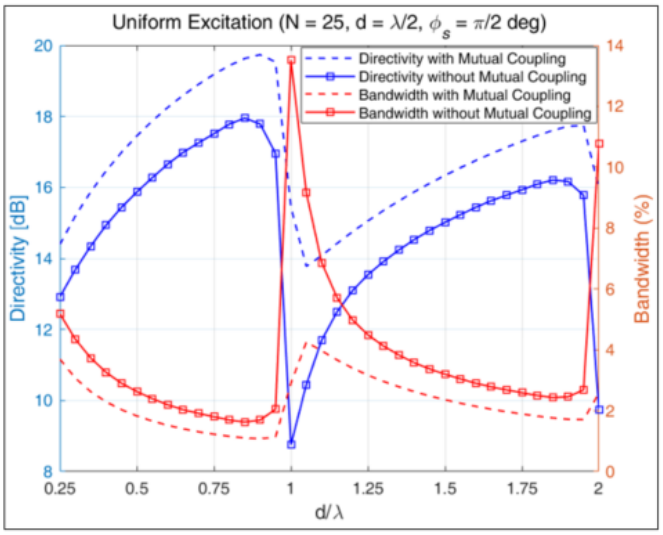
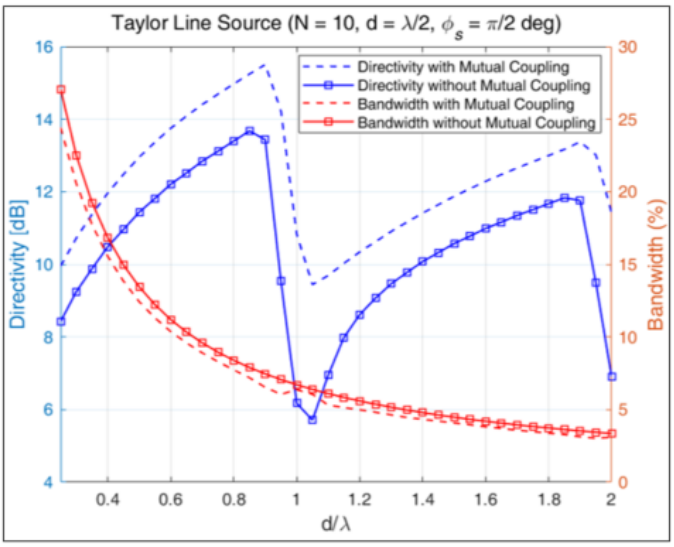


Figure G8. *Directivity and Percentage bandwidth of a uniformly excited array as a function of inter-element spacing d/λ for array lengths: (a) N=10 and (b) N=25.*



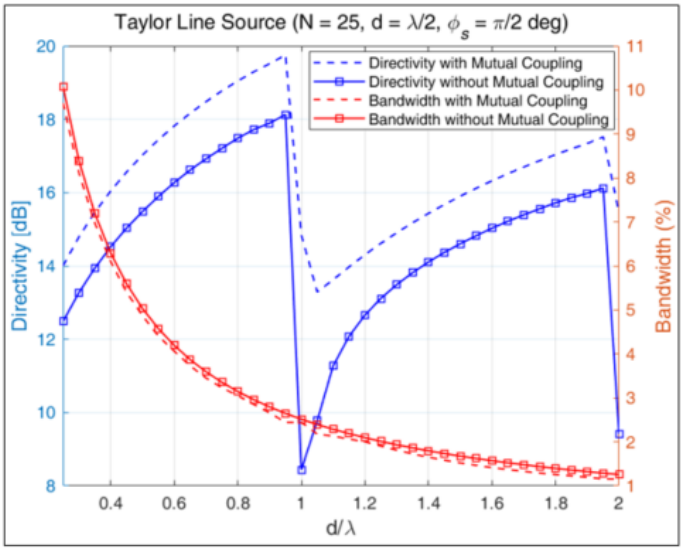
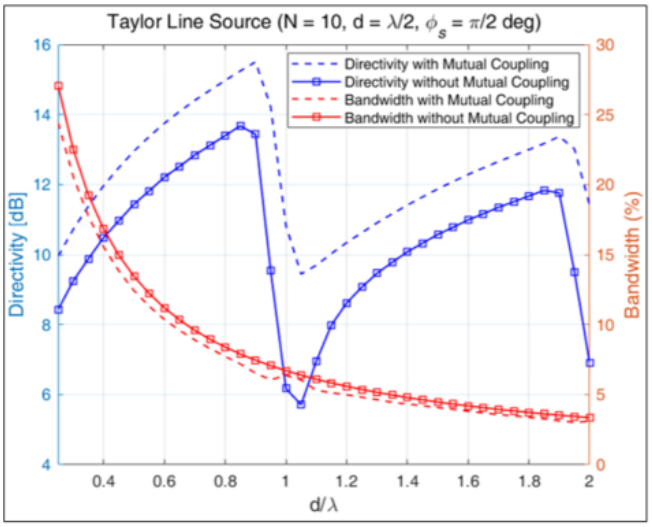


Figure 9. *Directivity and Percentage bandwidth of a Dolph-Chebyshev array as a function of sidelobe level for array lengths: (a) N=10 and (b) N=25.*



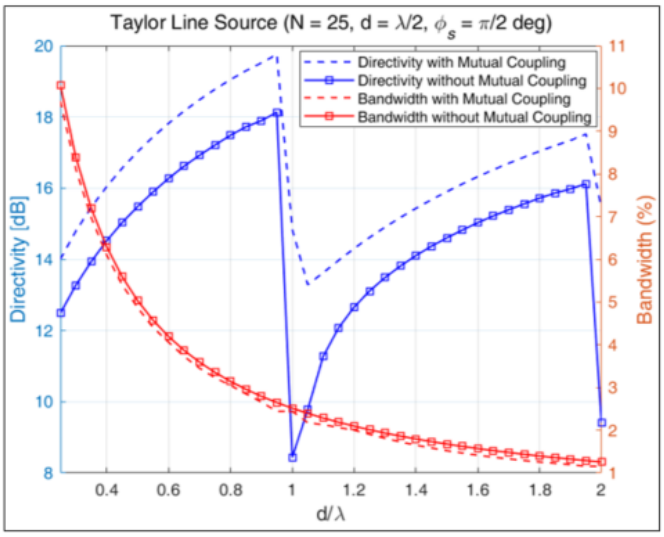


Figure G10. *Directivity and Percentage bandwidth vs. inter-element spacing d/λ of a linear array with Taylor Line Source distribution for array lengths: (a) N=10 and (b) N=25*

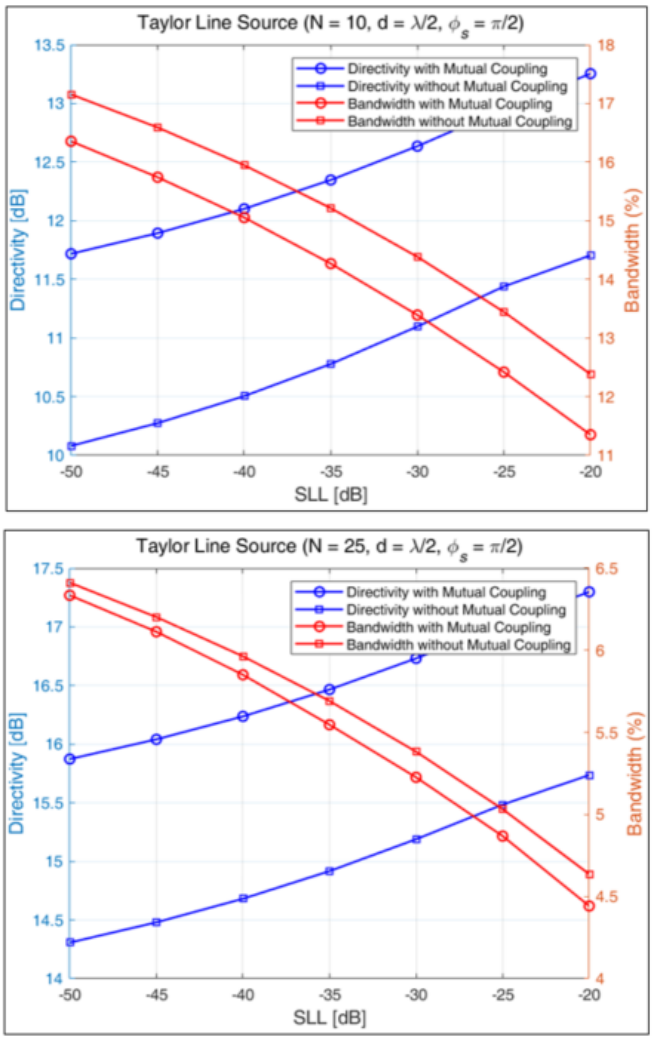


Figure G11. *Directivity and Percentage bandwidth vs. sidelobe level of a linear array with Taylor Line Source distribution for array lengths: (a) N=10 and (b) N=25.*

Conclusion

Three types of amplitude distributions have been studied so far: Uniform, Dolph-Chebyshev and Taylor Line Source. Among the three, the lowest sidelobe levels are obtained using Taylor distribution but at the cost of increased beamwidth and reduced directivity. Amplitude distributions which can further reduce the sidelobe levels and have extremely low amplitude excitations at the edge elements can dramatically reduce the input power consumption. This will be investigated in the future.

A general expression has been derived to calculate the directivity of an arbitrarily excited linear array of equispaced elements. The results are shown to agree favorably with the full-wave simulated results obtained through FEKO. Fractional bandwidth which is an important parameter has also been looked into. Non-uniform element spacing for sidelobe reduction will be investigated in the future.

References

[1] W.L. Stutzman and G. A. Thiele, *Antenna Theory and Design,* 3rd ed. New York, NY, USA: John Wiley & Sons, 2012.
[2] C. L. Dolph, “A Current Distribution for Broadside Arrays Which Optimizes the Relationship between Beam Width and Side-lobe Level,” Proc. IRE, Vol. 34, pp. 335–348, June 1946.
[3] T. T. Taylor, “Design of Line-Source Antennas for Narrow Beamwidth and Low Sidelobes,” IRE Trans. Ant. & Prop., Vol. AP-3, pp. 16–28, Jan. 1955.
[4] H. Unz, “Linear arrays with arbitrarily distributed elements,” IRE Trans. on Antennas and Propagation, Vol. AP- 8, pp-222-223; March, 1960.
[5] R. F. Harrington, “Sidelobe Reduction by nonuniform element spacing,” IRE Trans. On Antennas and Propagation, Vol. AP-9, pp-187-192, March, 1961.
[6] A. Ishimaru, “Theory of unequally spaced arrays,” IRE Trans. On Antennas and Propagation, Vol. AP-10, pp-691-702, November, 1962.
[7] S. A. Schelkunoff, “A Mathematical Theory of Linear Arrays,” Bell System Tech. J., Vol. 22, pp. 80–107, Jan. 1943.
[8] R.L. Haupt, *Antenna Array A Computational Approach*. New Jersey, USA: John Wiley & Sons, 2010.
[9] R. S. Elliott, “Beamwidth and Directivity of Large Scanning Arrays,” Microwave J., Part 1, Vol. 6, pp. 53–60, Dec. 1963.
[10] R. S. Elliott, *Antenna Theory and Design*. John Wiley & Sons, 2003.
[11] R. J. Mailloux, *Phased Array Antenna Handbook,* 3rd ed. Boston, USA: Artech House, 2018.

I.G.1 Electrically Small Antennas, Meandering Dipole Research-Effect of Arm Density Manipulation (Kovarik – UGRA Transitioning to Graduate Research Asst.)

Introduction

This investigation concerns the comparison of different wire geometries of electrically small planar meandering antennas. We need to provide an antenna that has good gain, bandwidth, modal significance, and VSWR. The primary focus is in optimizing these qualities through manipulation of arm density within the geometry of the design.

Methodology

All research is done through the use of simulation in CADFEKO software. For simplicity, electrically perfect materials are simulated and all wires are assumed to be infinitesimally thin.

The antenna is designed as a rectangular meandering dipole. The basic concept is to make a design that has the low frequency resonance of a longer dipole while also making

the structure compact enough to be electrically small. Figure G12 shows the original design [1,2].

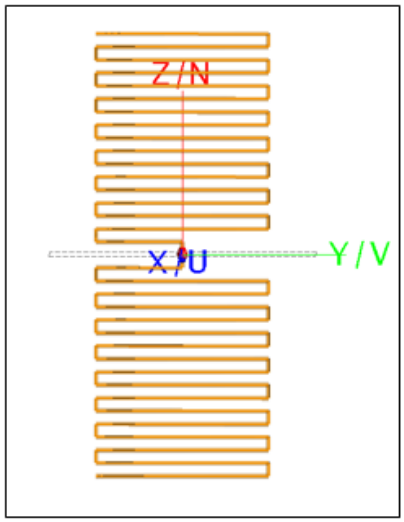


Figure G12. *20 arm geometry*

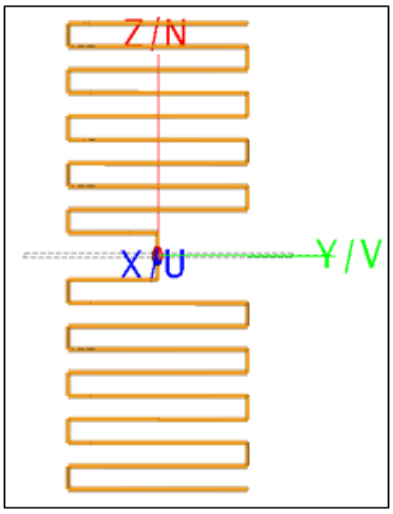


Figure G13. *10 arm geometry*

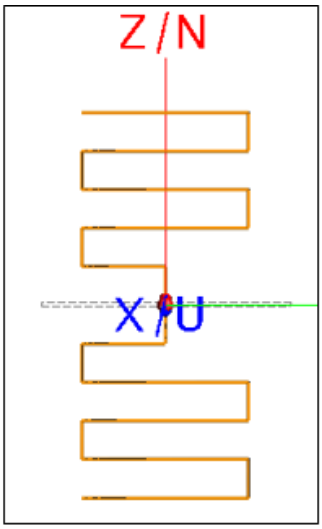


Figure G14. *5 arm geometry*

This form allows the antenna to obtain a *ka* of less than .5, with *k* being the length of the antenna and *a* being the radius of the Chu's sphere. *ka* being less than .5 is the prerequisite for an electrically small antenna [3]. The length from the center to the furthest point is held constant while the width of the arms is manipulated to ensure resonance at the intended frequency. The symmetric rectangular geometry is used to ensure a symmetric far field radiation pattern.

The main concern of investigation is in how differing arm densities affects the performance of the antenna [4]. Figure G13 and Figure G14 show antennas with equal *ka* values but less arms than the original design. Figure G12 has 20 arms on each side, Figure G13 has 10, and Figure G14 has 5.

The analysis on performance will be on several criteria. Gain, bandwidth, modal significance, and voltage standing wave ratio will all be investigated to determine what geometry has better performance [5].

Gain, modal significance, and VSWR can be obtained through POSTFEKO. However, the bandwidth needs to be found analytically. The bandwidth can be found through this equation:

$$B_{v,ub} = \frac{(ka)^3}{1+(ka)^2}\frac{VSWR-1}{\sqrt{VSWR}}$$

To use this equation, the *ka* must be found at every distinct point in the graph. Because *ka* is dependent on frequency, the *ka* changes over the graph even when the geometry of the antenna remains constant. Applying this changing *ka* to the VSWR is necessary to properly calculate the bandwidth [6].

Data and Results

Gain and Bandwidth

The Harrington limit shows the absolute maximum gain an electrically small antenna of certain *ka* can produce. Figure G15 shows the gain of each geometry in decibels. It additionally shows the bandwidth resultant from the antenna. This comparison is important because these two factors are primary in determining what the ideal *ka* and arm density is.

The gain is consistently about 1.5 dB below the maximum established by the Harrington limit. This is a fairly good result and shows the antenna geometry is relatively efficient in terms of gain. Additionally, less dense arms are marginally better for gain, with the 5 arm geometry being having a gain .4 dB higher than the 20 arm. We want as high a gain as possible, so longer *ka* is good for gain. The bandwidth reaches a minimum around .5 *ka,* which is to be expected.

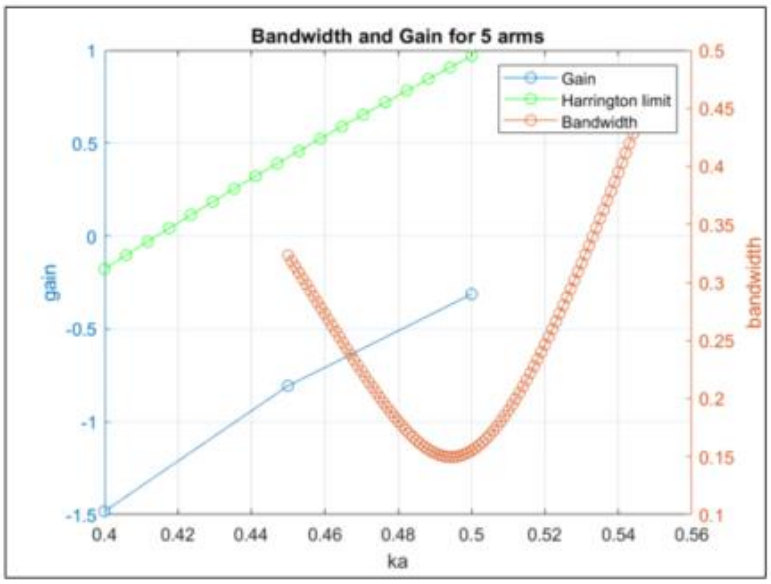


Figure G15. *Gain (dB) and bandwidth for differing ka compared to the Harrington limit, 5 arms (10, 20 arms found in appendix A).*

We need to bring this bandwidth as high as we can, so shortening the *ka* is optimal for the bandwidth. Finding a good medium for gain and bandwidth is the key to finding the best *ka*. It seems that ~.46 *ka* is ideal in this investigation.

Modal Significance

The modal significance shows the viability of the design through characteristic mode analysis. All modal analysis is done through the first mode. Figure G16 demonstrates that all geometries are optimal, reaching a modal significance of 1.

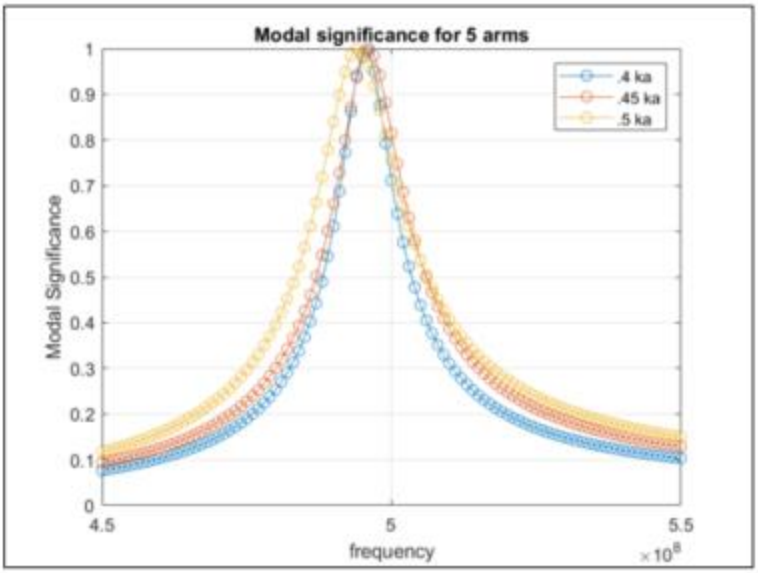


Figure G16. *Modal significance graphs for varying ka, 5 arms (10, 20 arms found in appendix B)*

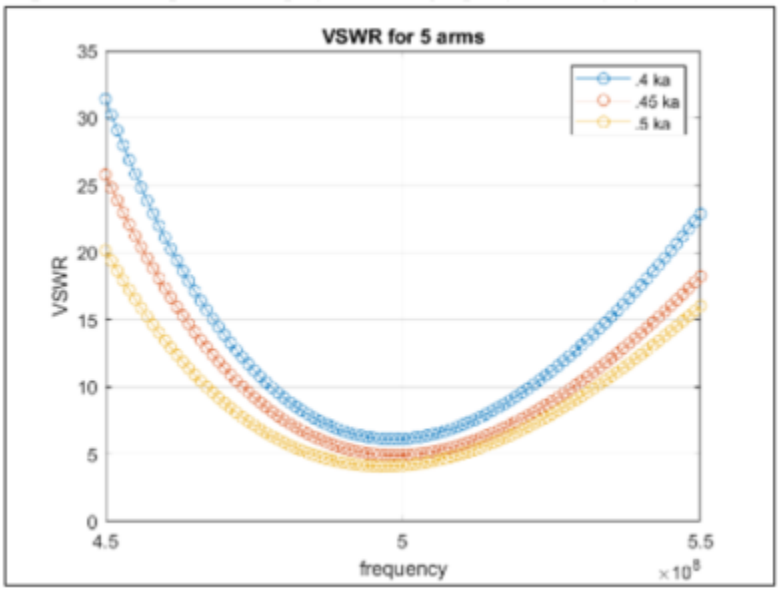


Figure G17. *VSWR values for varying ka, 5 arms (10, 20 arm found in Appendix C).*

Voltage Standing Wave Ratio

The VSWR of the antenna measures the feedback that the antenna produces at a given frequency. Ideally, this VSWR is as low as possible around the resonant frequency, at least lower than 2. Figure G17 features the VSWR of each antenna geometry. Unfortunately, none of the geometries reach an ideal minimum. Much effort was put into trying to lower these values as much as possible, and lowering this value further will be a primary part of investigation going forward.

Conclusion

The meandering rectangular geometry is useful in making an electrically small antenna. The modal significance and gain are promising qualities of this design. Additionally, the 5 arm geometry is better in most aspects (especially gain), and will be used for future work. Bandwidth and gain investigation reveal that an optimal length of ~.46 is ideal However, the VSWR values are not ideal. Future investigation is needed to optimize these qualities. Research suggests that a trapezoidal geometry will provide much better bandwidth and VSWR results [7].

Appendix A

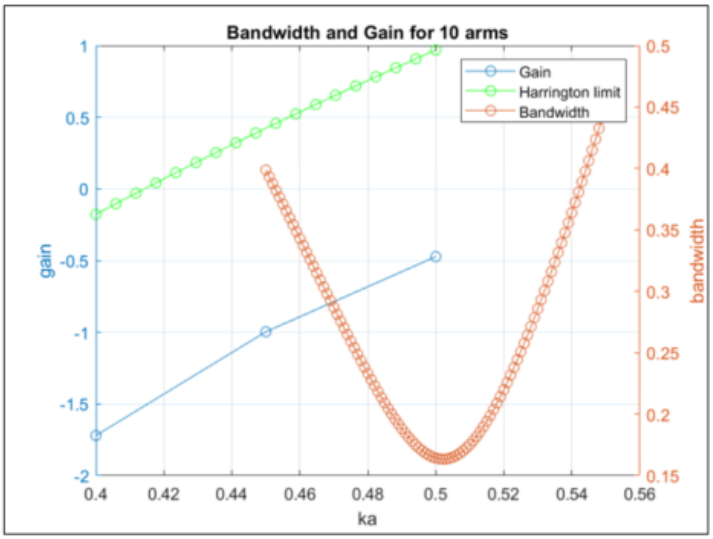


Figure G15a. *Gain (dB) and bandwidth for differing ka compared to the Harrington limit, 10 arms.*

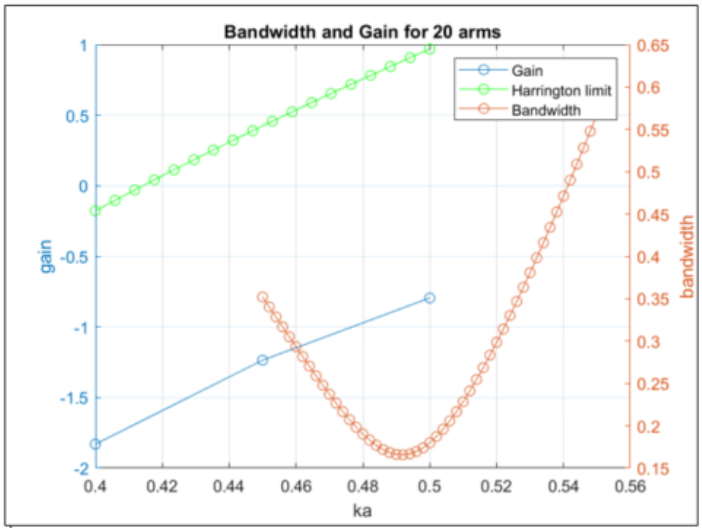


Figure G15b. *Gain (dB) and bandwidth for differing ka compared to the Harrington Limit, 20 arms.*

Appendix B

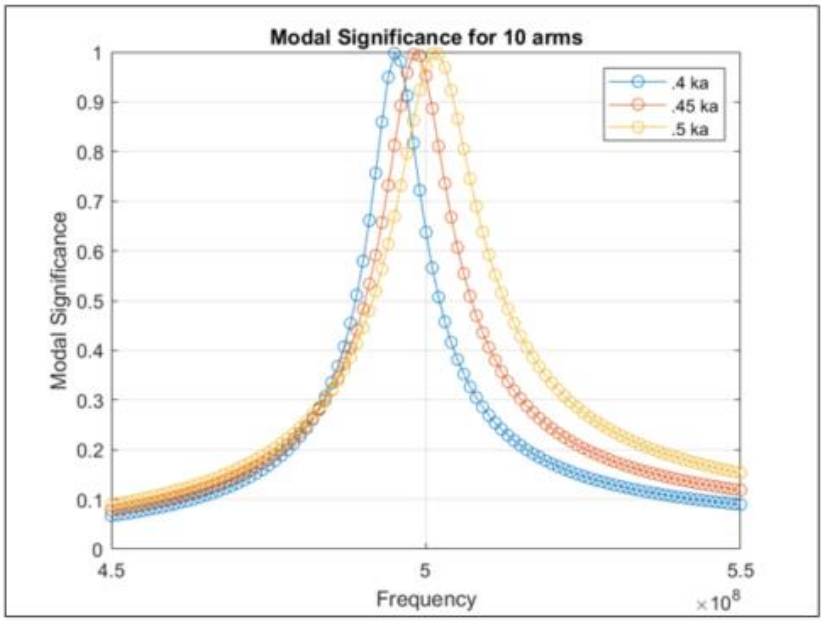


Figure G16a. *Modal significance graph for varying ka, 10 arms.*

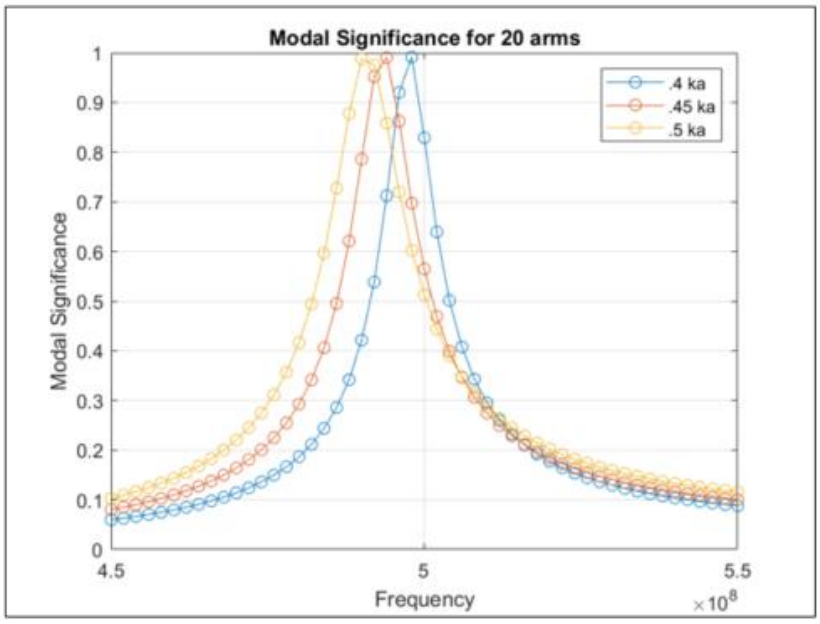


Figure G16b. *Modal significance graph for varying ka, 20 arms.*

Appendix C

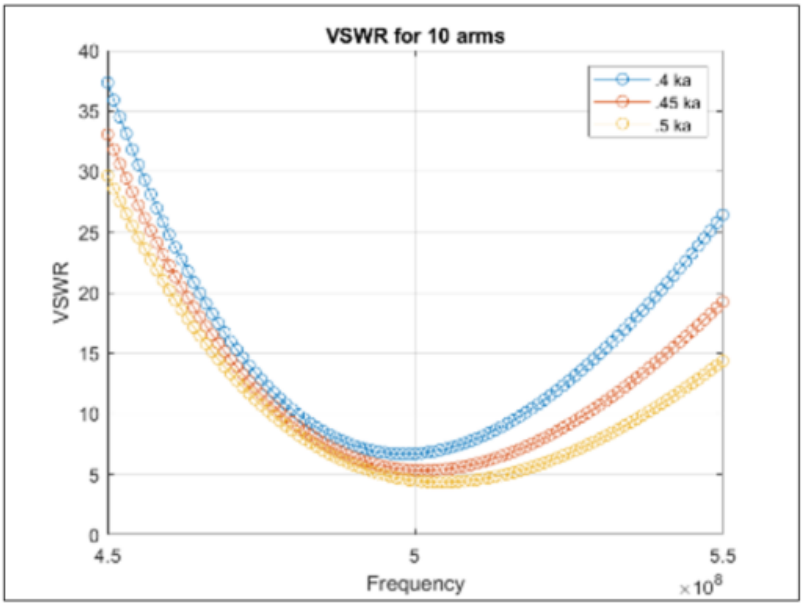


Figure G17a. *VSWR for varying ka, 10 arms.*

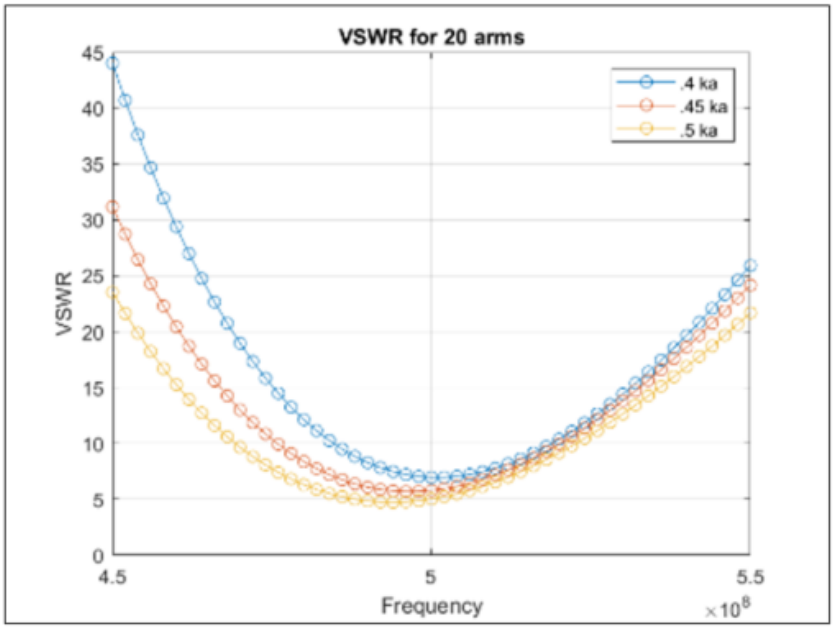


Figure G17b. *VSWR for varying ka, 20 arms.*

References

[1] S. R. Best, “Electrically small resonant planar antennas,” *IEEE Antennas Propag. Mag.*, vol. 57, no. 3, pp. 38–47, June 2015.
[2] Rashed , J. Tai, C.-T. “A New Class of Resonant Antennas” *Trans IEEE,* Vol. AP -39, September 1991, pp. 1428-1430.
[3] Volakis, Chen, Fujimoto, “Small Antennas: Miniaturization techniques and Applications” *McGraw-Hill publishing.* 2010.
[4] Best, S.R. and Morrow, J.D. “On the Significant of Current Vector Alignment in Establishing the Resonant Frequency of Small Space Filling Wire Antennas.” *IEEE Antenn. Wireless Propag. Lett.,* Vol. 2, 2003 pp 201-204.
[5] Garg, Bharita, Bahl, Ittipiboon, “Microstrip antenna design handbook” *Artech House INC,* 2001.
[6] Uzunoglu, N.K, N. G. Alexopoulos and J. G. Fikioris, :Radiation Properties of Microstrip Dipoles” *IEEE Trans. On Antennas and Propogation,* Vol. AP-27, 1979, pp.853-858.
[7] Stutzman, Thiele, “Antenna Theory and Design 2nd edition” *Jensen Books,* pp. 246-256

I.H Cost Estimates and Engineering (Doynov)

I. No report submitted.

II. Issues:

III. Interactions with Others:

None

IV. Major Procurement Actions:

Tektronix, Arbitrary Waveform Generator and an Oscilloscope

V. Travel:

Travel Plans

Please note that all papers or presentations on any aspect of the ONR HPM program must be reviewed by the ONR Program Officer (or in some cases ONR Public Release Process) regardless of classification level or audience.

Planned Travel Details	Purpose	Attendees	Estimated Costs
2019 IEEE	Antenna Conference	Chatterjee group	Not established yet

VI. Pending or Upcoming Public Release Requests:

i. M. Z. M. Hamdalla, A. N. Caruso, Ahmed M. Hassan, “Characteristic Mode Analysis of the Effect of the UAV Frame Material on Coupling and Interference,” *Submitted to the IEEE International Symposium on Antennas and Propagation and USNC-URSI Radio Science Meeting at Atlanta, Georgia*, USA, 7-12 July 2019.

ii. M. Z. M. Hamdalla*, Ahmed M. Hassan, A. N. Caruso, J. D. Hunter, Y. Liu, V. Khilkevich, D. G. Beetner, “Electromagnetic Interference of Unmanned Aerial Vehicles: A Characteristic Mode Analysis Approach,” *Submitted to the IEEE International Symposium on Antennas and Propagation and USNC-URSI Radio Science Meeting at Atlanta*, Georgia, USA, 7-12 July 2019.

VII. Selected Highlights (text and/or images):

None

ONR HPM 2019 Program - Monthly Status Report (MSR) – MAY2019
Anthony Caruso – Univ. Missouri – Kansas City
N00014-17-1-3016 [OSPRES Grant]
ONR Short Pulse Research, Evaluation and non-SWaP Demonstration for C-sUAV Study

6/14/2019

Distribution Statement ~A: Distribution authorized to all OSPRES Grant and Contract Participants, and any uncompensated collaborators. Further dissemination per Ryan Hoffman (ryan.hoffman@navy.mil).

OSPRES Project Description: Develop tunable High Power Microwave (HPM) sources and electronically steerable radiators whose waveform(s) enable control over all levels-of-lethality on cUAV and similar targets, with the least power density.

Executive Summary

Overview:

The master coordination document developed by Eliot Myers during April and May saw the formation of working groups to improve coordination and planning. This document can be found as an appendix to the May 2019 OSPRES contract report. Charters for the subgroups have been or are in the process of being drafted with leads for the subgroups identified. June and July will see the start of the new subgroups and coordination meetings. Sean Ahern officially started with the UMKC group in May. It is expected that his expertise and experience will drive decisions for the scaled demonstration next year. Previous failure of the triple harmonic generator to produce a 355nm laser line from a 1064nm seed for GaN testing has been resolved and preliminary results have shown peak pulse voltages equivalent to the charge voltage of the setup at low voltages for GaN devices. SiPCSS team members continue to explore alternative/novel avenues for thermal management through simulation. One of more recent methods is jet impingement, which is typically used in high cooling capacity requirements such as processors. This method should theoretically be capable of creating a high heat transfer equation. Data acquired on UAV's has been analyzed by James Currie, some of the results are shown in the May 2019 OSPRES contract report. The RF coupling subgroup, headed by Ahmed Hassan, has shown that RF coupling current induced wire inside of a UAV can be up to 50% higher than similar wires in free space. Plamen Doynov has designed a diode nonlinear transmission line for high voltage with a mono-polar pulse conversion to RF without DC content.

I. Current Month Progress:

I.A Photoconductive Solid-State Switches (Myers)

i. GaN PCSS testing – poor 355nm beam intensity from the triple harmonic generator for GaN testing was resolved after determining that the polarization into the THG system was incorrect, resulting in reduced conversion from 1064-nm to 355-nm. Initial testing after correcting this issue has demonstrated pulses with a peak voltage equal to the charge voltage (tested up to 150 V). Now that the GaN system is operational, we are beginning parameter tests with pulse forming networks for the GaN pulse forming capability

ii. Thermal management - We have enlisted a new team member for executing thermal simulations on novel cooling systems including but not limited to jet impingement. Reports from this effort will be included in subsequent reporting periods.

iii. HPM FOM – We are working with LLNL to improve upon the figure of merit (FOM) work by including three different switching circuit topologies. The goal is to understand where the performance of materials and circuit topologies intersect, and generate FOMs based on the strengths of materials tailored to the circuit.

iv. SiPCSS modeling – we continue to make major progress on modeling the transient behavior of the SiPCSS system. We are currently trying to extend the model time to capture the recovery time beyond a few hundred nanoseconds. Our most recent simulation of SiPCSS recovery required 11 days to process, which must be reduced by adjusting the time resolution following the initial excitation.

I.B GaN:C Subgroup (Rulis)

i. We performed some basic tests with the Monte Carlo code “Monte”, but determined that it would not be appropriate for large band gap materials.

ii. Continued testing with the Simple Monte Carlo (SMC) code and ran a basic simulation for GaN. Results are shown in Figure B1.

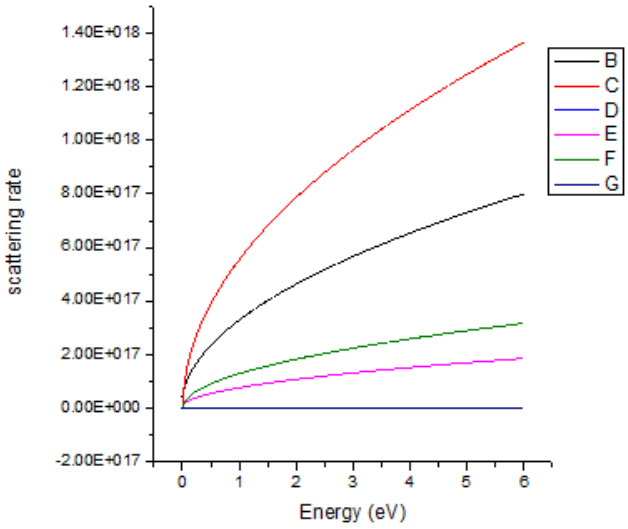


Figure B1*. Scattering rates computed using SMC for different electric field strengths B-G ranging from 0 to 10000 kV/cm.*

iii. We will continue to gather and tabulate all parameters and sources for the tool chain as applicable specifically for doped GaN. This includes determination of exactly what can and cannot be calculated using tools and packages from *ab initio* up through FLOOXS device scale calculations.

I.C Small Unmanned Aerial Vehicle Diagnostics and Design-of-Experiments (Fields)

i. Ongoing work to refine the data parsing software for all aircraft platforms to expedite on-site quick-look data analysis.
ii. Incorporation and testing of a UMKC designed and built onboard RF sensor package on UMKC UAVs.
iii. Began the large effort of creating platforms for outdoor, live-fire testing event (fixed wing and multirotor).

I.D Switch Development and Pulsed Power Support (Khan)

i. Programmed the laser pulse generator circuit to activate the IGBT
ii. Wrote a test protocol to conduct this high voltage (HV) test
iii. Outlined the test setup with necessary schematics and conducted initial tests to check the operation of the sequence circuit.
iv. We are in the process of conducting the complete HV test within a day or two.

I.E Applied RF Coupling Simulation and Modelling to/for sUAV (Hassan)

i. In the previous reports, we investigated coupling to wires mounted on the top of UAV frames. However, in many UAVs, the wires are not only mounted on top of

the frame but they can also be placed inside a dielectric enclosure as shown in Figure E1.

ii. Investigated the configuration where the wires are placed inside a dielectric shell cuboidal in shape approximating one of the four arms of the UAV and found
   - a straight wire near the inside corners will couple ~50% higher currents than the wires in free space.
   - wires at the center of the cuboidal cavity will couple more than the wires in free space but less than the wires near the corners. Over the next month, we will expand the analysis by simulating wires at multiple locations inside a realistic frame similar to the one shown in Figure E1. We will also continue studying the effect of the wire's shape on the coupling to the wires above and inside a dielectric frame.



Figure E1*. Wires and PCB distribution inside a plastic drone frame.*

iii. Conducted a literature review to identify antennas that are compact, ultra-wideband, and can handle moderately high levels of power.

iv. Identified the ring coupled log periodic antenna published in [1]. The antenna is quasi frequency independent, meaning that its radiation characteristics can be uniform across frequency, and it was re-configured to achieve a 2.3 miniaturization factor by adding a coupled ring radiator [1].

v. We also plan to review and propose different approaches for the use of metamaterials and Frequency Selective Surfaces (FSS) to enhance performance of the developed antennas.

References

[1] R. Sammeta and D. S. Filipovic, "Quasi frequency-independent increased bandwidth planar log-periodic antenna," *IEEE Trans. Antennas Propag.*, vol. 62, no. 4, pp. 1937–1944, Apr. 2014.

I.F UMKC Diode Network Based NLTL (Doynov)

i. The design of a multi-pass NLTL was optimized for efficiency and two criteria: peak power and center frequency/bandwidth.
ii. A new high-voltage D-NLTL has been designed with a mono-polar pulse conversion to RF without DC content and respectively eliminating the need for a high-pass filter.
iii. The manuscript of a paper "Diode-based NLTL: Parameter Space" has been drafted and is under internal review.

I.G Electrically Small Antennas (Chatterjee, Barman, Kovarik)

In this month's effort progress was achieved by examining the tradeoffs between: directivity, beamwidth, array bandwidth, vs, interelement spacing ($\frac{d}{\lambda}$), sidelobe levels and scan angle (measured from boresight). These initial studies were restricted to a 25-element linear array.

Another milestone to achieve is to optimize the design of an electrically small antenna (ESA) to operate in the UHF frequency range.

The description of the above are included here, as below.

i. The trade space studies for the 25-element linear array were carried out with and without mutual coupling. The mutual coupling was calculated using the full-wave EM solver FEKO. Results were examined for several types of array excitations: (a) uniform, (b) Dolph-Chebyshev and (c) Taylor distributions. Closed-form formula for directivity using the array factor of a linear array was derived to facilitate the calculations. Results showed good corroboration between with and without mutual coupling cases. It was concluded that the array factor had a dominant effect on the directivity. (*Bidisha Barman*)

ii. Optimization studies with the ESA involved the meandering dipole, but the results were not favorable. TCM analysis was used to optimize the dipole size, but it was not very successful. This will be revisited again. (*James Kovarik*)

iii. An L-Probe excited rectangular patch was designed to yield a 2:1 VSWR (-10 dB return loss) bandwidth from 350 MHz to 630 MHz. The patch overall dimensions turned out to be $ka \cong 0.5$ at the center frequency. However the maximum gain of the patch antenna was – 3 dB which is unacceptable since the Harrington limit for the gain is 1 dB. The optimization procedure was extremely tedious because there are no design equations/methodologies that could be used to obtain the initial geometry. However continued progress is expected. (Bidisha Barman)

I.G.1 Critical Tasks of the Antenna Subgroup

i. Continue of trade space analysis for linear and planar phased array.
ii. Continue optimization studies of ESA to operate in the L-band.

I.G.2 Expected Products of Antenna Subgroup

i. ESA as phased array elements that meet the requirements.
ii. Plans for experimental validation of ESA performance.

I.H Cost Estimates and Engineering (Doynov)

i. The initial cost estimate was completed for the mono-polar pulse generation channel. Cost estimates for a single channel system, 4 x 4 and 16 x 16 channel systems have been drafted and are in a review process.
ii. We have developed an interactive tool for cost estimation based on three-point cost estimation techniques using the triangular and beta-distribution.

II. Issues:

None

III. Interactions with Others:

None

IV. Major Procurement Actions:

V. Travel:

Travel Plans

Please note that all papers or presentations on any aspect of the ONR HPM program must be reviewed by the ONR Program Officer (or in some cases ONR Public Release Process) regardless of classification level or audience.

Planned Travel Details	Purpose	Attendees	Estimated Costs
2019 IEEE	Antenna Conference	Chatterjee group	Not established yet

VI. Pending or Upcoming Public Release Requests:

i. M. Z. M. Hamdalla, A. N. Caruso, Ahmed M. Hassan, “Characteristic Mode Analysis of the Effect of the UAV Frame Material on Coupling and Interference,” *Submitted to the IEEE International Symposium on Antennas and Propagation and USNC-URSI Radio Science Meeting at Atlanta, Georgia*, USA, 7-12 July 2019.

ii. M. Z. M. Hamdalla*, Ahmed M. Hassan, A. N. Caruso, J. D. Hunter, Y. Liu, V. Khilkevich, D. G. Beetner, “Electromagnetic Interference of Unmanned Aerial Vehicles: A Characteristic Mode Analysis Approach,” *Submitted to the IEEE International Symposium on Antennas and Propagation and USNC-URSI Radio Science Meeting at Atlanta*, Georgia, USA, 7-12 July 2019.

VII. Selected Highlights (text and/or images):

None

ONR HPM 2019 Program - Monthly Status Report (MSR) – JUNE2019
Anthony Caruso – Univ. Missouri – Kansas City
N00014-17-1-3016 [OSPRES Grant]
ONR Short Pulse Research, Evaluation and non-SWaP Demonstration for C-sUAV Study

7/14/2019

Distribution Statement ~A: Distribution authorized to all OSPRES Grant and Contract Participants, and any uncompensated collaborators. Further dissemination per Ryan Hoffman (ryan.hoffman@navy.mil).

OSPRES Project Description: Develop tunable High Power Microwave (HPM) sources and electronically steerable radiators whose waveform(s) enable control over all levels-of-lethality on cUAV and similar targets, with the least power density.

Executive Summary

Overview:

During the month of June the switch development group simulated silicon PCSS devices using 3 different circuit topologies to investigate fundamental switching behavior of SiPCSS devices and electronic characteristics including recovery time and carrier concentration during switch operation. Once optimized, the models developed will be transitioned to GaN and SiC PCSS devices. The group is also incorporating thermal, optical coupling/triggering, and pulse formation into computational models moving towards the goal of full simulations for completed source/driver configurations. GaN:C testing at low voltage resumed after multiple issues with the second and triple harmonic generators (detailed in previous MSR's) have been resolved. Results of low voltage testing are found in the body of this report. Additionally, a new pulse forming network suitable for GaN:C devices has been fabricated and is currently being tested with the devices. Device power losses has been incorporated into the figure of merit for high power PCSS'. By focusing on the device losses and operational efficiency a figure of merit that can be generalized to different switch technologies with highly variant material characteristics can be generated. The UAV development and testing group at UMKC performed multiple tests on the RF sensor data logger in shielded and unshielded configurations and determined that the shielding configuration was suitable in preventing errors during testing. Diode non-linear transmission line (NLTL) simulations have shown upwards of 49% transmission efficiency, at low voltage, when load impedance is matched to that of the NLTL. Simulations also showed that the center frequency generated by the NLTL is dependent on the capacitance and voltage characteristics of a reverse biased diode indicating that the transmission line can be designed to specific frequencies. Chatterjee's group has investigated 3 possible substrates for electrically small micro-strip patch antennas and performed characteristic mode analysis to investigate bandwidth and gain of each design individually and in an array. Bandwidth upwards of 46% in the UHF range have been predicted and are guiding further antenna designs. They have decided to move forward with a micro-strip patch antenna design on a TMM-4 (thermoset laminate material) substrate for fabrication of a prototype for testing. They also investigated balun style and two tapered (Chebychev and gradual) impedance transformer designs for feeding a planar transmission line from SiPCSS/Pulse forming networks to the coaxial input of a GTEM test chamber. FEKO simulations showed that the Chebychev tapered transformer was unsuitable for fabrication and testing due to large reflections that could not be mitigated through any changes in geometry. The balun and gradual tapered designs will continue to be simulated and move into fabrication once the ideal geometries are determined.

I. Current Month Progress:

I.A Photoconductive Solid-State Switches (Myers)

The following table outlines the efforts of UMKC for fundamental PCSS development.

Table A1. *Progress tracker for identified critical tasks and statuses. Color indicates the criticality of each task with respect to its current status and the objectives of the program: (GREEN) low-risk and/or no major delays, (YELLOW) medium risk and/or minor delays, (RED) major risk and/or delays.*

Critical Effort		Critical Task		Status
Simulation and Modeling	Si-PCSS	TCAD Simulation		We have conducted a large set of SIPCSS transport physics simulations in various configurations and are currently conducting more in-depth analysis on the results, and improving the models and simulation efficiency.
Thermal Testing	Si-PCSS	Cooling System Test Fixture		Validation of the cooling system test fixture has been conducted and initial results are being collected. These results are outside the scope of this report.
Device Characterization	Si	Electroluminescence Studies		Nothing to report this period.
Fundamental High Power Switches	n/a	High Power Figure of Merit		We have expanded the scope of the FOM to include the circuit topologies of significance for high power switches. Initial models of class E amplifiers have been generated, which will be expanded to include additional pulse forming networks and transmission lines.
Device Characterization	GaN:C	GaN pulsing demonstration		We are currently conducting testing at reduced optical energy density until a new THG crystal arrived. We have also designed and tested a new GaN pulse forming network with results detailed in the report

Summary (Myers)

Over the reporting period we have made progress in three major areas: (1) Si-PCSS modeling of pulse formation including optical stimulation and transmission lines via Silvaco TCAD, (2) fixing the THG system for GaN:C PCSS testing and a new PCB-based pulse forming network for more efficient testing, and (3) extending the high power switch

figure of merit development effort to incorporate circuits topologies of significance for pulse power switches.

We have made a major leap in modeling SiPCSS via Silvaco TCAD, and have generated a substantial data set to be analyzed further. Ultimately, our goal of having a transient SiPCSS model including optical, thermal, and pulse formation have been achieved, and now the challenging work of optimizing the results to highlight switching behavior dynamics and analysis are underway. Moreover, the progress made with Si PCSS modeling will be extended to aid students and other researchers at UMKC in their respective modeling needs.

GaN PCSS testing, although delayed by equipment malfunctions, is back on track and we are pushing to collect the datasets to characterize the switches as a function of incident laser energy and switch geometry. We have improved the circuit used for testing by switching to a PCB-based design which, once optimized, should improve the ease-of-testing and generate more consistent results.

Regarding developing a figure-of-merit for high power, fast switches (HP FOM), we have committed to including the circuit topologies of importance for these devices because we believe the switch performance is inherently linked to the driving/driven circuit. Various switch types (e.g., fast recovery SiC and GaN vs. slow recovery Si) fundamentally require different circuits for optimal performance, thus a material based FOM is inadequate for capturing the merit of a given material or switch type. Because of our familiarity with pulse-forming networks with slow-recombination switches, we have begun modeling class-E amplifiers to improve our expertise in the circuits more suitable for fast-recombination switches to better position the team for generating an accurate and meaningful FOM.

SiPCSS Simulation and Modeling – SiPCSS Recovery (Eifler)

Three types of circuit models for the SiPCSS (Silicon Photoconductive Semiconductor Switch) have been used in Silvaco TCAD simulations as shown in Figure A1. These are: (a) zero-bias, (b) capacitive and (c) transmission line (TL). A source impedance of 100 kΩ and capacitance of 1 μF was used in the respective circuits. The load for the capacitive circuit was 50 Ω and the load in the TL circuit was 4.4 Ω, matching the characteristic impedance of the TLs. The propagation delay of the TLs was 2.4 ns. The simulations were performed to calculate the recovery time of the SiPCSS in terms of the electrode characteristics and carrier concentrations within the device. In all simulations laser illumination was used to turn on the switch and will be detailed later in the report.

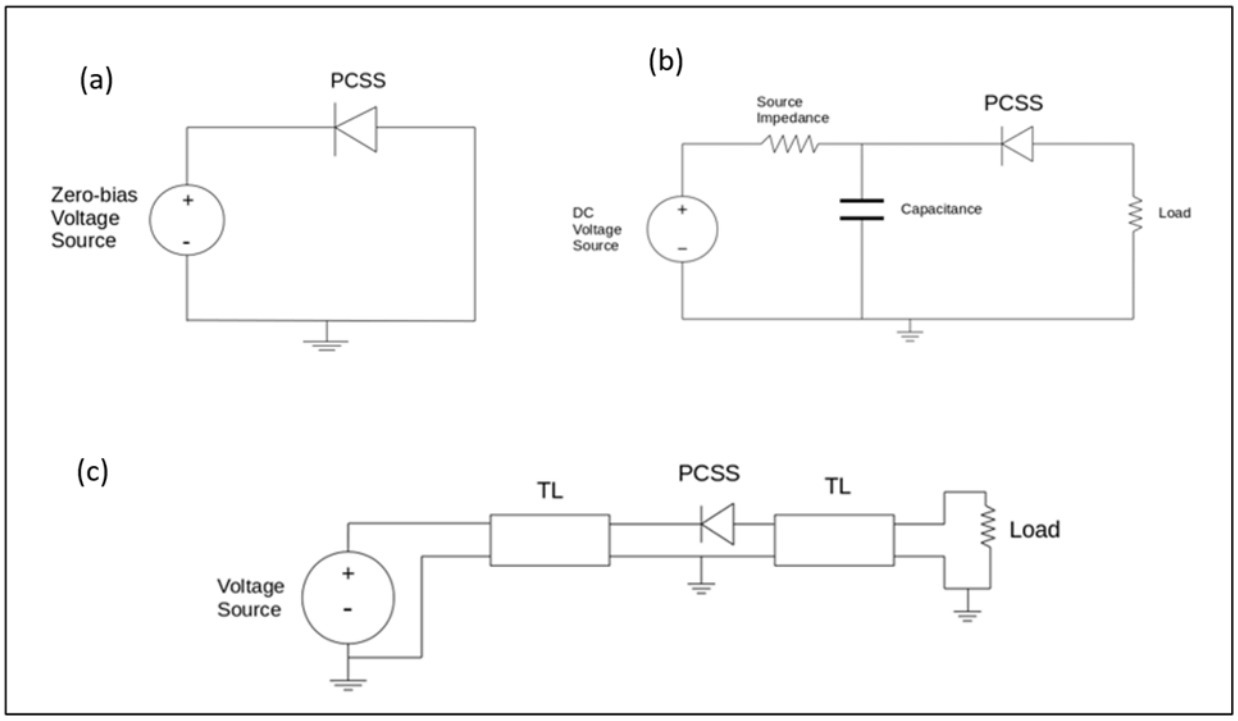


Figure A1*. The three circuits for the SiPCSS. (a) The zero-bias circuit. (b) The capacitive circuit. (c) The transmission line circuit (source impedance not shown).*

Zero-bias Simulation

The circuit model for the “zero-bias simulation” uses a DC voltage source with zero voltage applied to the cathode of the reverse-biased Si-PCSS and has the anode grounded (as opposed to an open-circuited switch). This is done to observe the recovery of the Si-PCSS without an applied non-zero voltage. The recovery of the Si-PCSS is assessed with carrier concentrations defined in the various regions of the device which is essentially a PIN diode: the P+-region, the Intrinsic (n-)-region, and the N+-region. This allows majority and minority carriers to be defined as well as charge-adrift in the intrinsic region. The initial simulation(s) results are shown in Figure A2 consisting of transport quantities Si-PCSS with 1064-nm light and sampling various parameters related to recovery.

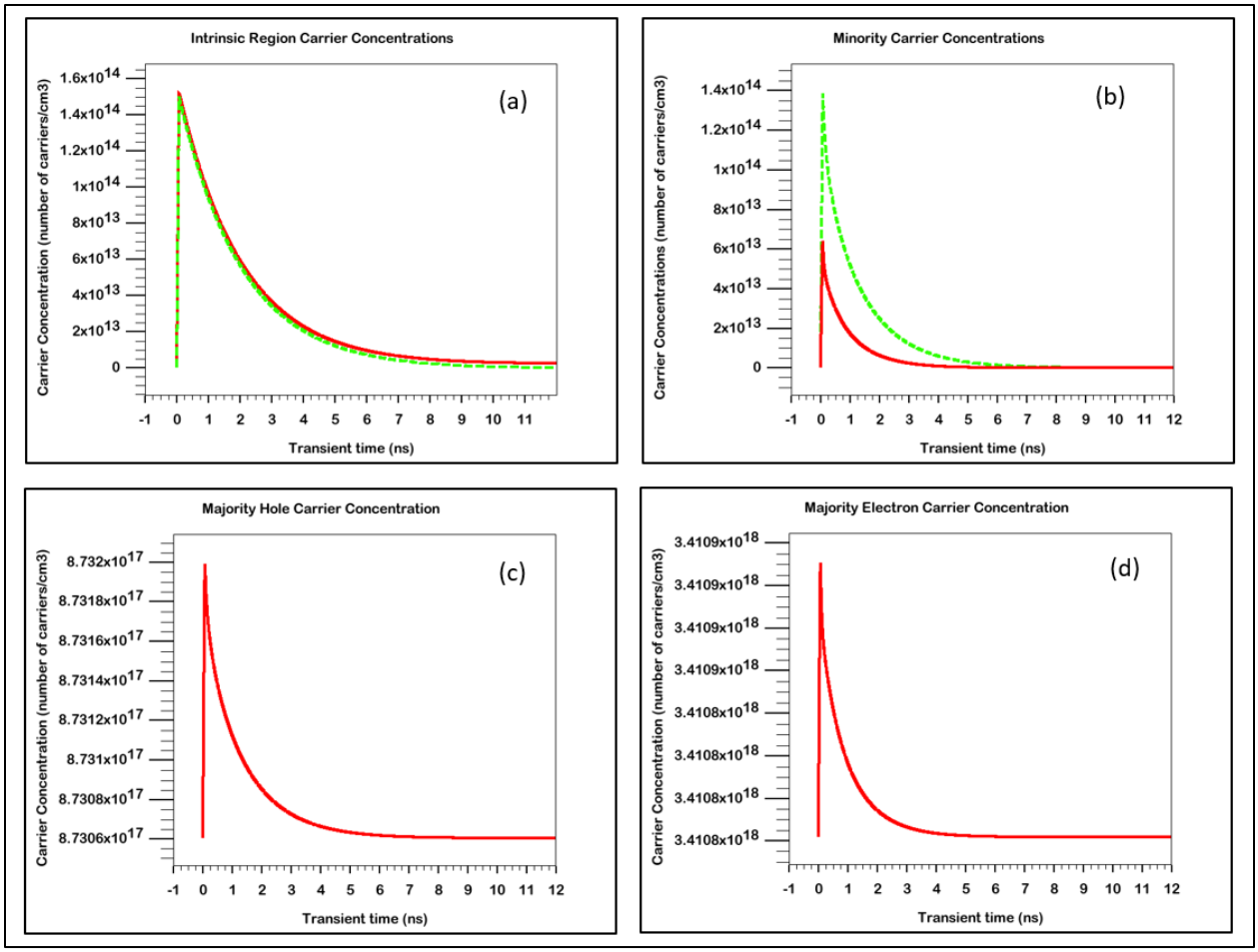


***Figure A2**. Recovery time of switch by carrier concentrations. (a) Electron (red-solid) and hole (green-dash) concentrations of the Intrinsic region. (b) Minority carrier concentrations with electrons (red-solid) and holes (green-dash). (c) Majority hole concentration. (d) Majority electron concentration.*

The intensity of the illuminating laser was set to 100 kW/cm^2 and the lifetime of both electrons and holes was set to 1 ns to speed the recovery of the PCSS. The simulation was performed to 980 ns and took 56 hours to calculate on four processors. To keep explanation shorter and simpler, a large number of details in the models and methods used have not been described.

Per Figure A2, the carrier concentrations decayed over time as expected. For (a)-(d), the time-scale was set for 12 ns of the 980-ns simulation, and the carrier concentrations were put on different concentration scales. Note, (a) refers to carriers in the Intrinsic(n-)-region, (b) refers to electrons (green-dash) in the P+-region and holes (red-solid) in the N+-region (these are the minority carriers), (c) holes in the P+-region (majority carrier), and (d) electrons in the N+-region (majority carrier). The rapid increase seen in carrier concentrations were due to the photo-generation via laser and the decrease was due to recombination, primarily Shockley-Read-Hall and to a much lesser extent Auger recombination. All the carrier concentrations returned to their initial values, however the hole concentration in the intrinsic region and the minority electrons in the P+-region did

not equilibrate for any reasonable length of time and trended slightly downward and upward in carrier concentration, respectively. At 980 ns, all carrier concentrations returned to initial values.

Although various measures may be used to quantitatively assess recovery time, we initially took a general approach focusing on carrier concentrations without setting a cutoff for recovery. This resulted in long simulation times to allow sufficient time for the device to return to its initials state. Unlike our zero-bias simulations, standard reverse recovery tests for diodes use the output voltage and current through the switch at 10% of their maximum reverse voltage and current. However, this is a crude measure of the output pulse duration and not necessarily reflective of the recovery process, nor a consistently definable measure between devices and/or materials. Moreover, the 10% approach does not accurately differentiate between differing device parameters that result in the same or similar recovery time. Although the 10% rule is functional for simple analysis, we will continue to develop and refine a metric for recovery in the context of PCSS that is both computationally efficient and representative of the carrier transport physics we aim to optimize.

Capacitive Circuit Simulation

The second set of simulations used a circuit model for the capacitive circuit derived from experimental setups but which smoothed the power input in simulation producing more efficient convergence. This enabled the use of a larger time-step (1 ps) being used than in the zero bias and TL circuit. A 100 kΩ resistor was used to limit current with a 50-Ω load and 1 μF shunt capacitor. The laser intensity was 40 MW/cm^2, resulting in a minimum on-resistance of 57 mΩ. The electron and hole lifetimes used were 10 ns to lessen the recovery time and thus simulation time (test simulations were conducted with increased lifetime which produce increased recovery time, as expected). The simulation was performed to 451 ns using 1ps time-step and took roughly two days to simulate.

The voltage output, switch resistance, and carrier concentrations in the p, i, n regions of the diode were recorded. In Figure A3, the voltage output pulse and switch resistance are shown. The output pulse had a maximum value of 97.506 V at 91 ps, which is close to the DC input voltage and is a measure of the rise-time of the switch. The main output pulse had a ~90 ns width at 10% of the maximum voltage. The output voltage returned to the initial value (0.00119 V) at ~380 ns, which we used as a measure of full recovery. The switch resistance rapidly decreased to the target on-value, remained low (sub-ohm) for less than 100 ns before rapidly increasing toward its initial value of approximately 4 MΩ. Although the final value was slightly below the initial value (by less than 0.07%), the difference is likely due to the recharging time of the capacitor through the source resistance. Ultimately, the concern with recovery time arises from heating in the switch due to the large reverse bias (kilovolts) and medium-to-high resistance (ones to thousands of Ohms) throughout the recovery process. The best way to measure recovery time would be with multiple closing and openings of the switch to evaluate the quality of the output pulses. However, this is more computationally expensive and has not yet been modeled in detail.

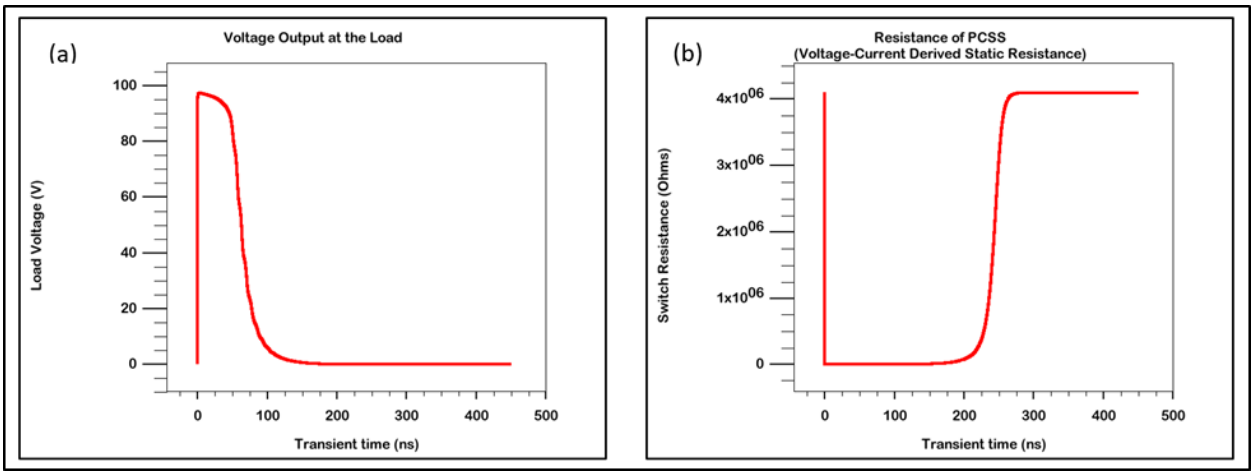


Figure A3*. (a) The voltage output pulse using the capacitive power source. (b) The voltage-current derived static resistance of the switch.*

We now examine the recovery in terms of carrier concentrations as with the zero-bias case. In Figures A4 and A5, the electron and hole concentrations for the p, i, n regions are shown in full and zoomed view showing the shape of the final equilibration of carrier concentration vs simulation time. The bottom zoomed (d–f) views are the same as the top views (a–c) but with magnified scale for visualization. The electron concentration in the intrinsic region is the only carrier-type not to equilibrate for a substantial time within the total simulation time. The other carriers equilibrate in range from ~270 ns to ~400 ns. As seen in the magnified plots, some carrier-types decrease to a minimum concentration below the initial concentration before recovering to their initial state. Other carrier-types equilibrate to a slightly higher, lower final, or the same value as the initial concentration. The details of the carrier concentrations in their recovery reveal the operation of the device and are dependent on both the external circuit and device parameters. These results require further analysis and simulations to reveal connections between device parameters, external circuits, and desirable properties such as reduced recovery time of the PCSS.

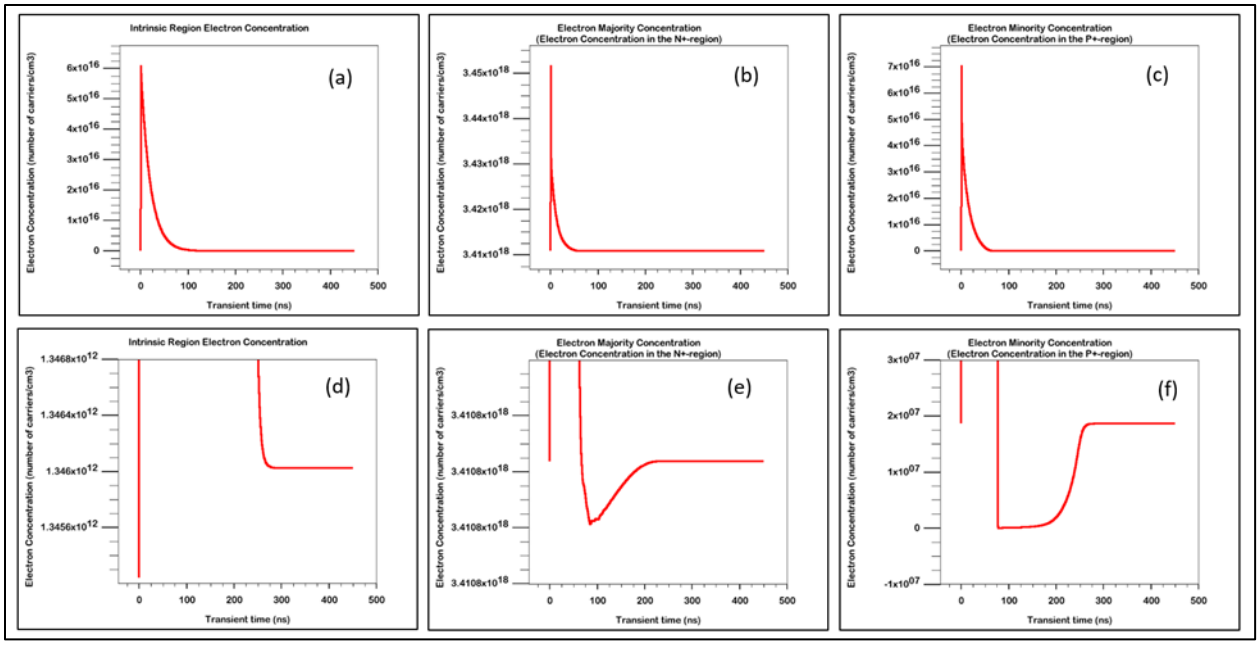


Figure A4. *(a) and (d) Electron concentration in the Intrinsic region full and zoomed views. (b) and (e) Majority electron concentration. (c) and (f) Minority electron concentration.*

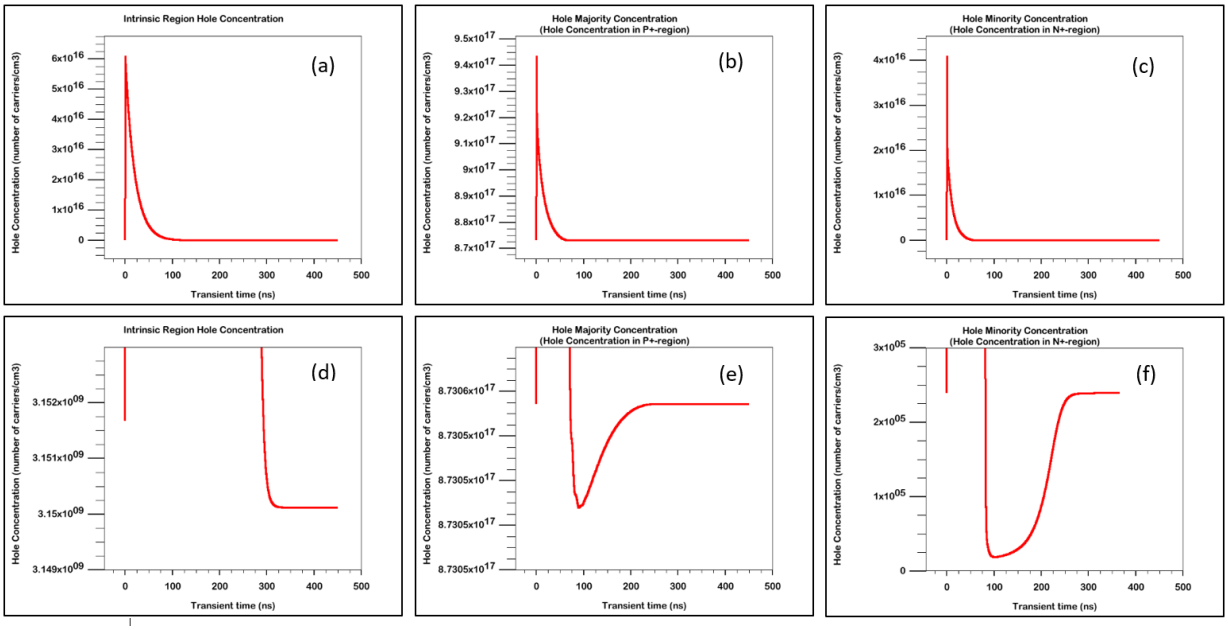


Figure A5*. (a) and (d) Hole concentration in the Intrinsic region full and zoomed views. (b) and (e) Majority hole concentration. (c) and (f) Minority hole concentration.*

Transmission-line Circuit Simulation

The circuit model used for the TL-setup for the PCSS included a source impedance of 100 kΩ for a 100 V DC voltage source. The TLs had a characteristic impedance (Z_0) of 4.4 Ω and a propagation delay of 2.4 ns, corresponding to the transmission lines

configuration used in empirical SiPCSS characterization. The load was matched to Z_0. First the TLs were allowed to charge fully before the laser closed the switch. The laser intensity was set to a large value of 140 MW/cm^2 and was flat-topped. This provided an initial on-state resistance of 0.123 Ω which was low enough for the diode to act as a short when closed. The electron and hole lifetimes were set to 10 ns. The simulation was performed to 680 ns but unfortunately required ~12 days to complete due to the 0.1-ps time step used to eliminate convergence problems caused by transmission line reflections when too large a time step was used. Moreover, parallelization has negligible impact on simulation time for mixed mode simulation (i.e., transient simulations) in Silvaco TCAD.

The voltage output at the PCSS is shown in Figure A6. Full (a) and zoomed (b) views are provided again for visualization. The output pulse amplitude is slightly less than half the DC input voltage and is 4.8 ns in duration as expected from the single pulse-forming TL. Both the main pulse and after-pulse are slightly sloped, however in opposite directions.

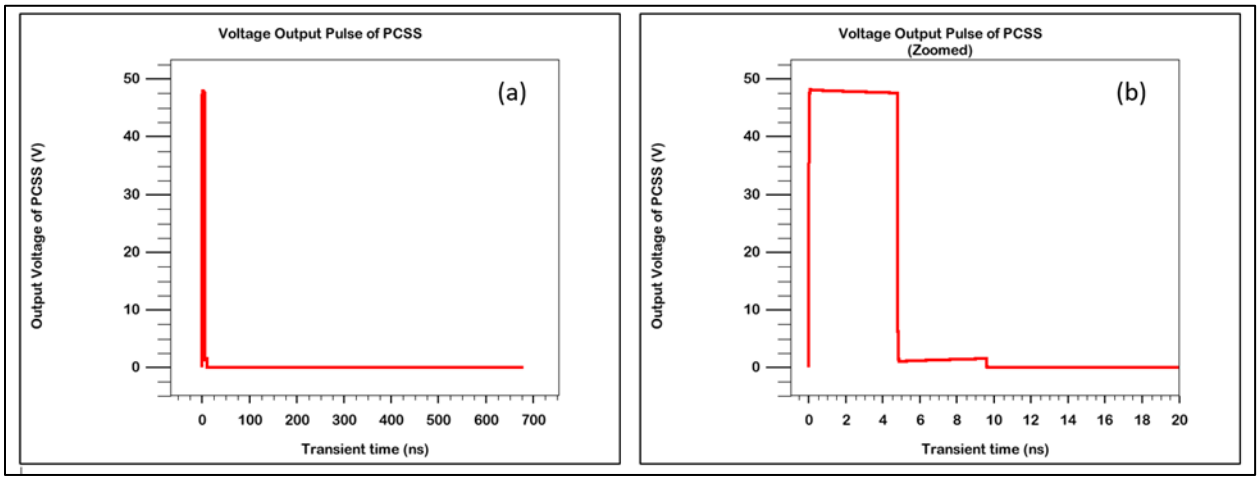


Figure A6*. (a) Full view of the voltage output at the PCSS. (b) Zoomed view showing detail of the output pulse and after-pulse.*

The voltage-derived static resistance for the switch resistance is shown in Figure A7, providing insight into the combined voltage and current characteristics of the PCSS during and after pulse formation. The sub-plots shown include: (a) two large resistance spikes correlating to current crossing zero (i.e., current changing direction due to TL reflections), (b) the beginning of the recovery process during the pulse, (c) the recovery of the switch resistance to ~110 kΩ, and (d) the recovery of the switch to ~65 kΩ. It should be noted that reflections result in the current and voltage changing signs and thus negative derived resistance between (b) and (c), and between the (c) and (d). These negative resistance values are not shown in the figure. The effect of these reflections is that the simulated device never fully recovers even at 680-ns, nearly twice the recovery time in previous simulations. This was due to the long time to run such a simulation. In conclusion, the switch resistance was not yet fully recovered due to TL reflections, which are covered in more detail below.

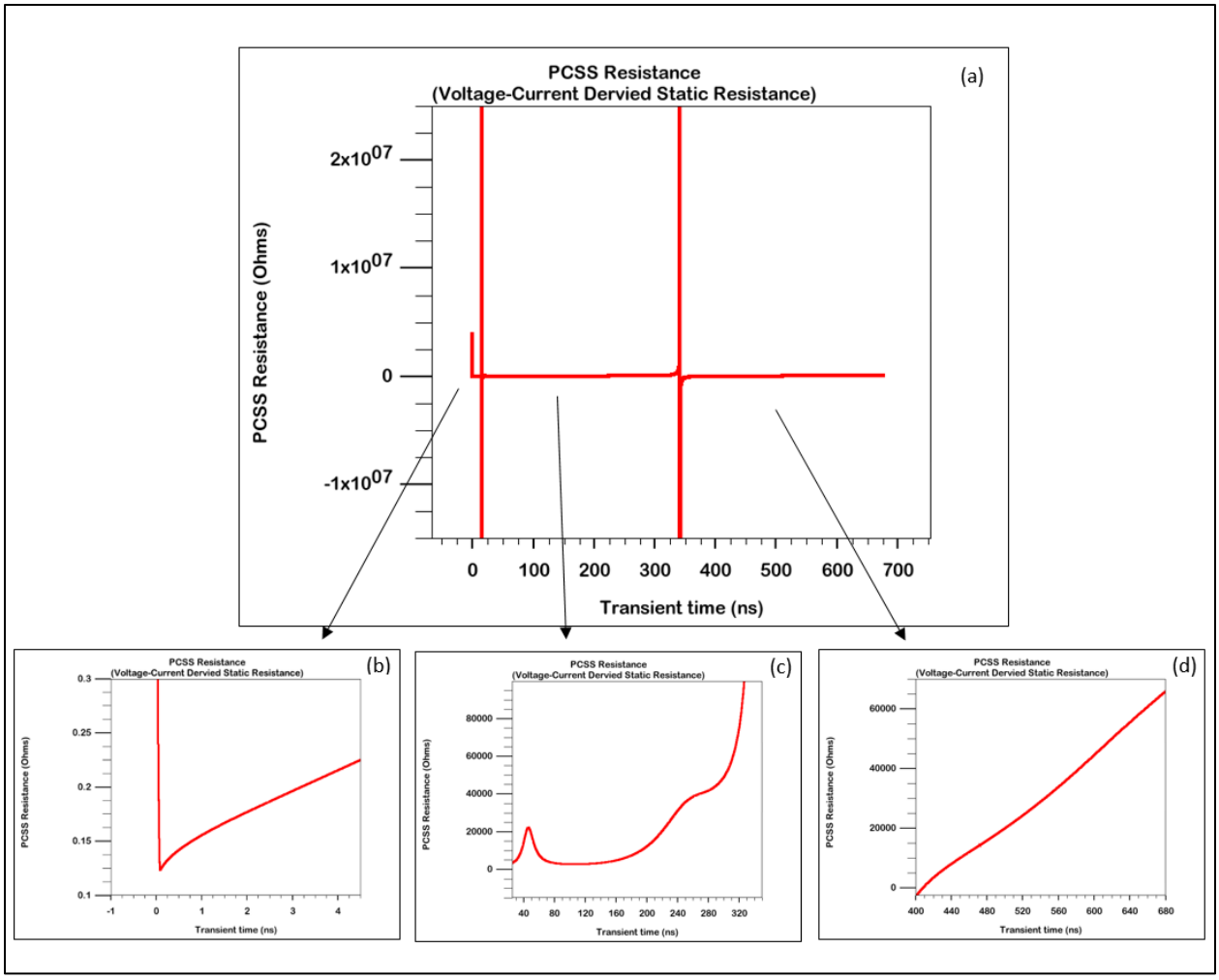


Figure A7*. (a) Full view of switch resistance recovery. (b) Zoom of beginning portion of switch resistance recovery showing closing of switch. (c) Zoom of middle portion of switch resistance showing recovery. (d) Zoom of ending portion of switch resistance showing recovery.*

To clarify the effect of reflections on the device, Figure A8 shows (a) the voltage output of the switch (green-dot) and voltage input (red-solid) and (b) the cathode current (red-solid) and anode current (green-dot) crossing zero due to these reflections. The output voltage at the switch was a small, positive value and input voltage (red-solid) was from the charge-side TL charging and passed from a negative value to a positive value. This caused the voltage across the switch to change signs and was the second occurrence of such an event. The cathode and anode currents (equal and opposite) both crossed zero which caused the second large spike in switch resistance, and was the second occurrence of this event. Put simply, the voltage and current changed signs twice, returning to their initial direction. This was due to the pulse reflections from the slight mismatch in impedance due to the non-zero resistance/impedance of the switch.

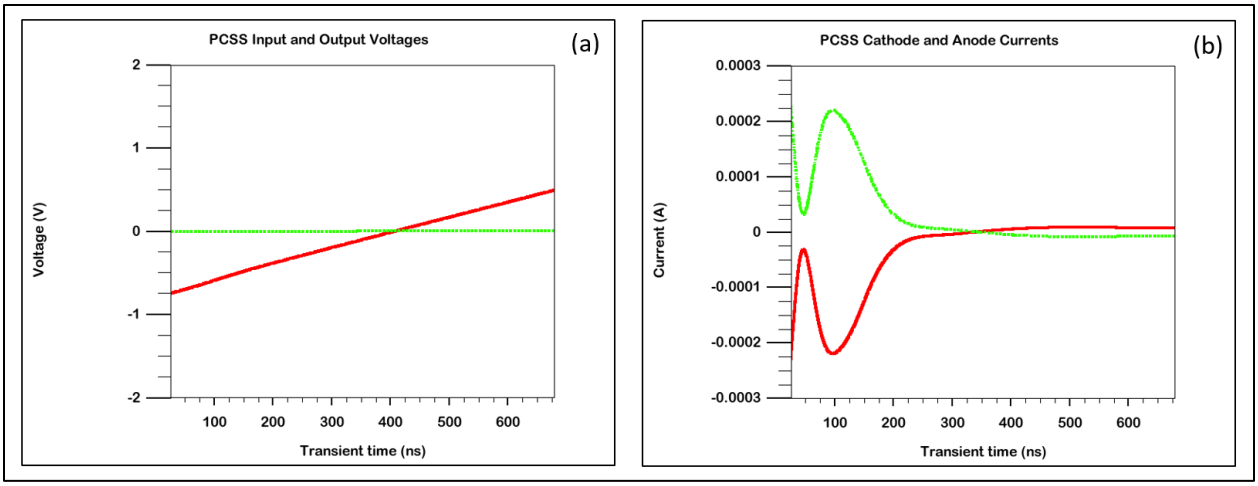


***Figure A8**. (a) Output voltage at switch (green-dot) and input voltage at switch (red-solid). (b) Current of cathode (red-solid) and current of anode (green-dot) seen crossing zero.*

Carrier concentrations for recovery are shown in Figure A9. The concentrations here are somewhat quantitatively in error due to the manner of their collection, however the relative quantitative amounts are still accurate. The concentration values are an order of magnitude below the correct value. The electron (a) and hole (b) concentrations that are shown have rapidly increased due to photo-generation and then have decreased due to recombination. (c) The amounts of electrons (red-solid) and holes (green-dot) can be compared showing that the number of electrons was much larger than holes in the device due to doping. While the dopant concentration of the (P+)-region than the (N+)-region, the combined donor doping of the (N+)- and (n-)-region exceeded the P acceptor doping level.

Interestingly, the switch resistance had not appeared to be fully recovered, yet the carrier concentrations indicated recovery. This points to the difficulty of assessing full recovery in terms of just one device characteristic. Often, recovery is assessed as some percentage of the maximum attained voltage or current, say 10%, despite this providing an ideal measure for comparing devices for optimal recovery. In the TL-setup we saw that reflections were sweeping charge in and out of the device extending the recovery time of the device. In addition, the on-state resistance for this TL-setup necessitated a much larger laser intensity which also increased the recovery time. There are many variables affecting the determination and comparison of device recovery for which careful, considerate simulations must be designed to clarify.

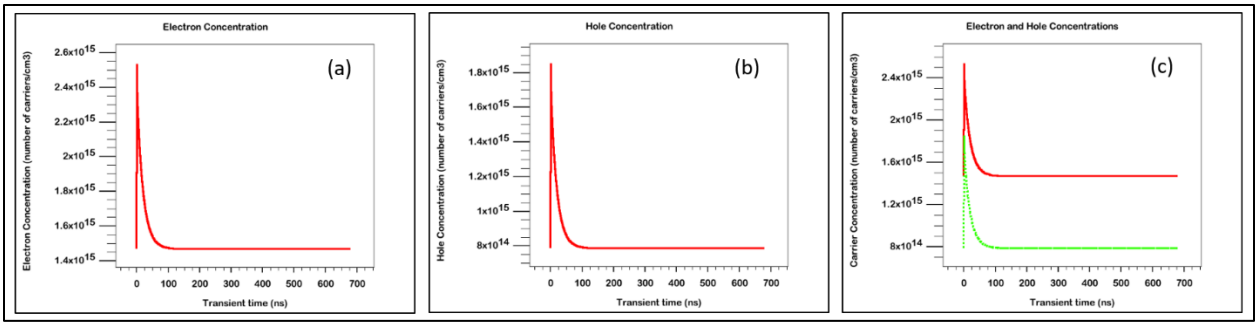


***Figure A9**. (a) Electron concentration. (b) Hole concentration. (c) Electron (red-solid) and Hole concentration (green-dot) clearly showing magnitude of difference.*

Future simulations will include currents (including recombination currents) within the device and 2D structure plots quantitatively compared to the electrode characteristics of the device. These will be used to compare devices varied in geometry/size, electrode sizes, doping variations and carrier lifetimes for an optimal PCSS which minimizes the recovery time and therefore potential heat generated during the switch operation and increased pulse rate frequency (PRF) of the laser illuminating and closing the switch. Additionally, circuit-based dampening of the reflections to make them more representative of physical circuits will be explored in simulation. A number of challenges remain in terms of numerical accuracy, computational cost, and the models and methods used in the simulation. The inclusion of realistic-sized devices, thermal calculations and 3D models of the device have all been tentatively performed but can add substantial computational cost. As well, the PCSS can be tested in a number of external circuits as shown in this report.

GaN:C Test and Development (Thompson)

Gan:C testing has been held up the past few months due to issues with the triple harmonic generation (THG) system that is being used to convert the 1064-nm laser to a 355-nm laser (see previous reporting periods). The THG system is now functioning and we have resumed pulse testing to characterize the devices. The first cause of this delay was issues with the temperature control of the THG oven not reaching the required temperature of 35°C. This has been remedied temporarily by refitting the oven with a heating element (resistor) and temperature sensor, and controlling temperature via an Arduino. The second issue was with polarization which was only realized by using band-pass filters to find the optimal rotational angles of the SHG and THG crystals. The 532-nm band-pass filter was only used in setting up the SHG crystal to ensure the correct orientation of the crystal. The 355-nm band-pass filter was used to find the optimal orientation for the THG crystal. Once the orientation was corrected, the 355-nm band pass filter was left in the setup to attenuate any residual 1064-nm and 532-nm light before the beam is incident on the GaN:C device. A photo of the final setup is shown in Figure A10.

In the process of fixing the THG oven, the crystal was damaged which causes an approximate 60% reduction in beam intensity through the THG. To correct this, a new

oven and crystal have been ordered and will arrive around August 8th. Meanwhile testing continues with the "custom" oven and crystal until replacements arrive. Along with the band-pass filter, an engineered diffuser has also been added to provide a more uniform, top-hat energy distribution. The uniform distribution will allow us to more accurately measure the optical power density within the top-hat distribution, reducing the sensitivity of positioning the GaN:C device for more consistent results. A square shape was chosen to allow for the different sizes of devices and gap lengths to be used with the same energy density.

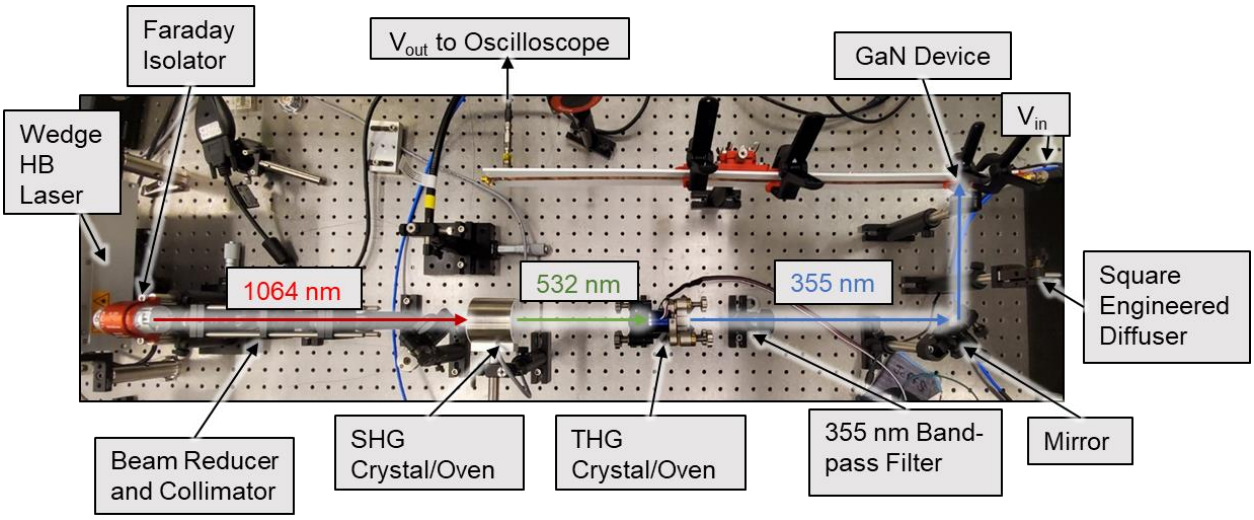


Figure A10. *Pulse testing setup for GAN:C PCSS with the addition of the 355 NM Band-Pass filter and square engineered diffuser.*

With the corrected THG system, initial pulse tests were conducted on GaN:C devices with gaps lengths of 50–1000 µm and a charge voltage of 100-150 V. The waveforms resulting from a 50-µm gap device with a 10 µJ/cm^2 energy density are shown in Figure A11. For the 50-µm gap, the peak output voltage was approximately equal to the input voltage resulting in on-state resistance of less than 1 Ω. For devices with longer gap lengths, the on-state resistance increased approximately linearly with gap length, per Figure A12. Selected individual waveforms for these test on the 50-µm gap length at a charge voltage of 50-V are shown in Figure A13. However, the results in Figure 12 were collected with an optical energy density of ~4 µJ/cm^2 (conducted after damage to the THG crystal) instead of ~10 µJ/cm^2 used previously. It appears that with lower incident energy density, there is an increase in on-state resistance in the devices. We expect lower on-state resistance when the new crystal arrives and testing can resume at higher incident energy densities.

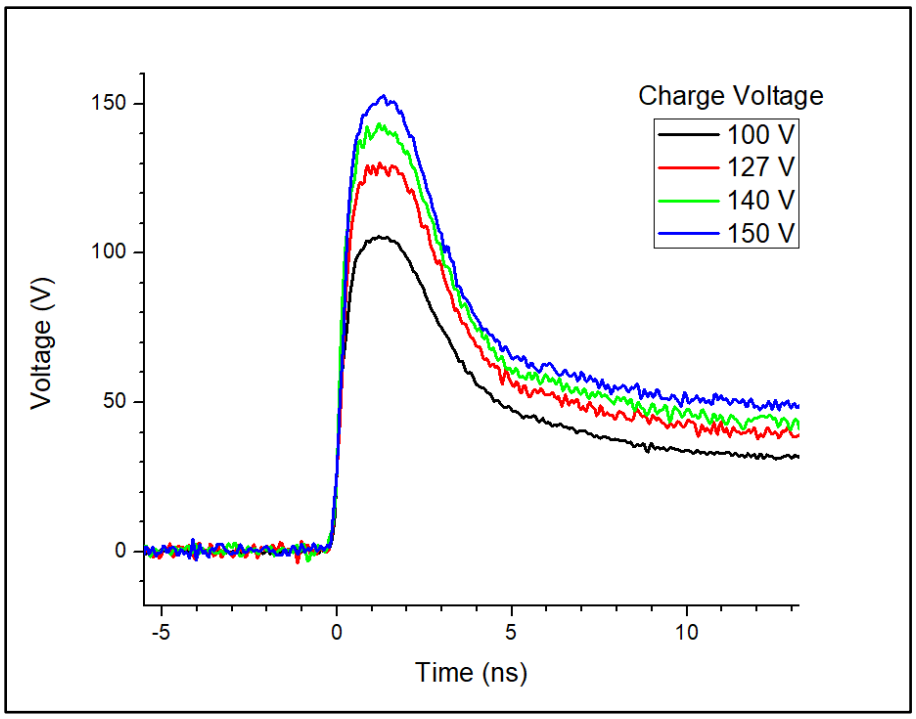


***Figure A11**. Initial waveforms of a GaN:C device with a gap length of 50 µm.*

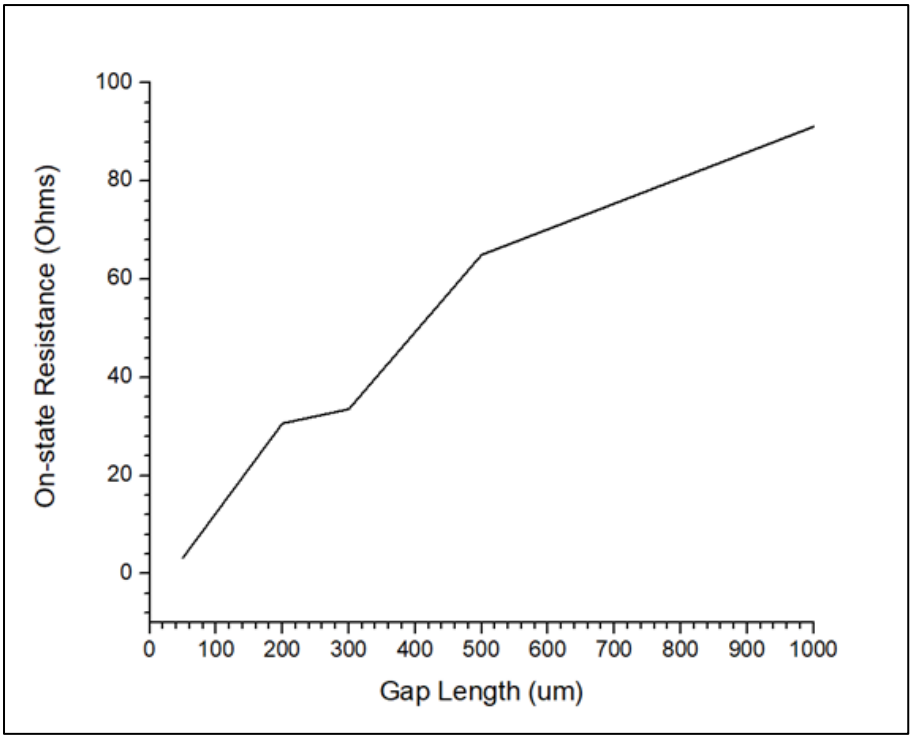


***Figure A12.** On-state resistance as a function of gap length at 150 V charge voltage*

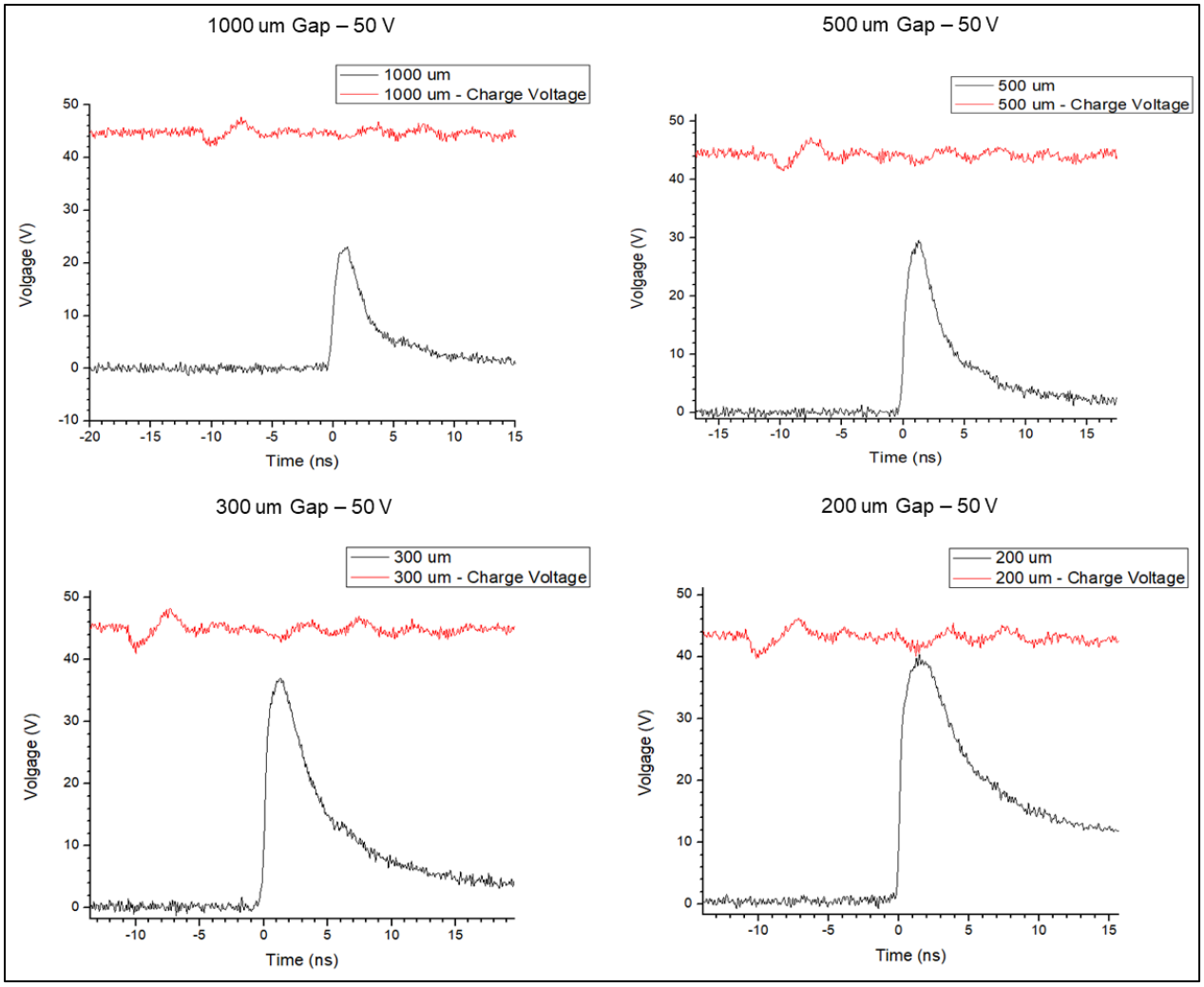


***Figure A13**. Waveforms with charge voltage for various gap lengths of GaN:C at 50 V charge voltage.*

In addition to testing polystyrene transmission line, a new, more compact PCB-based pulse transmission line was designed, fabricated, and tested. A photo of the first iteration of the PCB design is shown in Figure A14. Figure A15 shows the waveform measured with the PCB transmission line with a 50-µm GaN:C device at 50 V charge voltage, and Figure 16 shows a zoomed out image of multiple waveforms with this configuration to show how the charge voltage is dropping due to the circuit not being optimized. In the zoomed out image, the yellow represents the charge voltage and the blue the output pulse. The intricacies (capacitors, resistors, and layout) of the circuit are still being modified, and LTSpice is being used to simulate the equivalent circuit and find the optimal design.

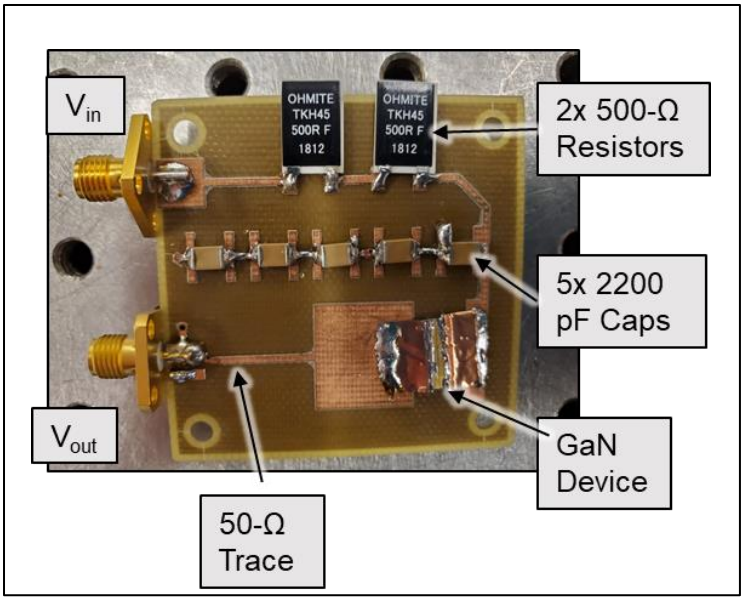


Figure A14*. New transmission line for GAN pulse testing.*

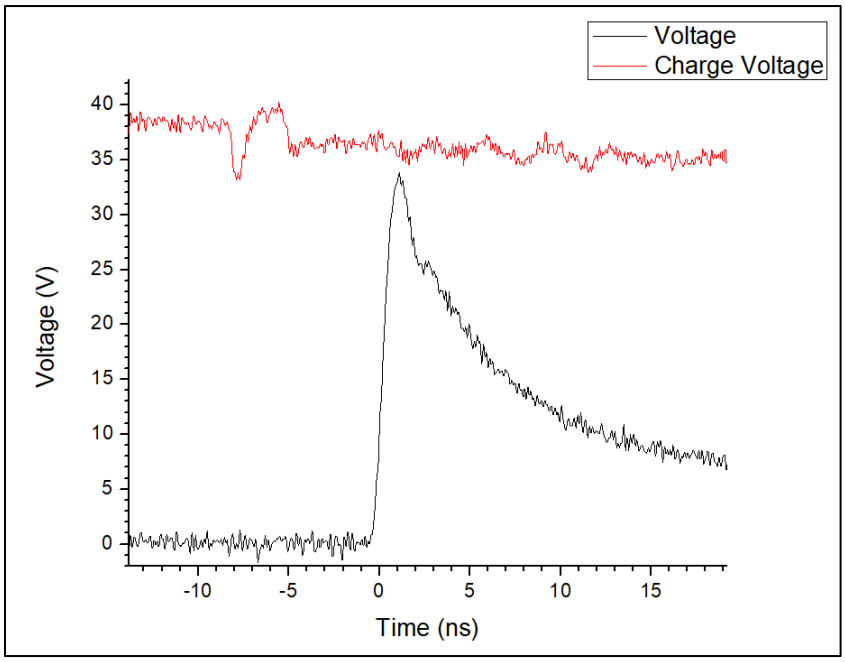


Figure A15. *Initial waveform using the PCB TL with a 50 μm GaN:C device at 50 V charge voltage.*

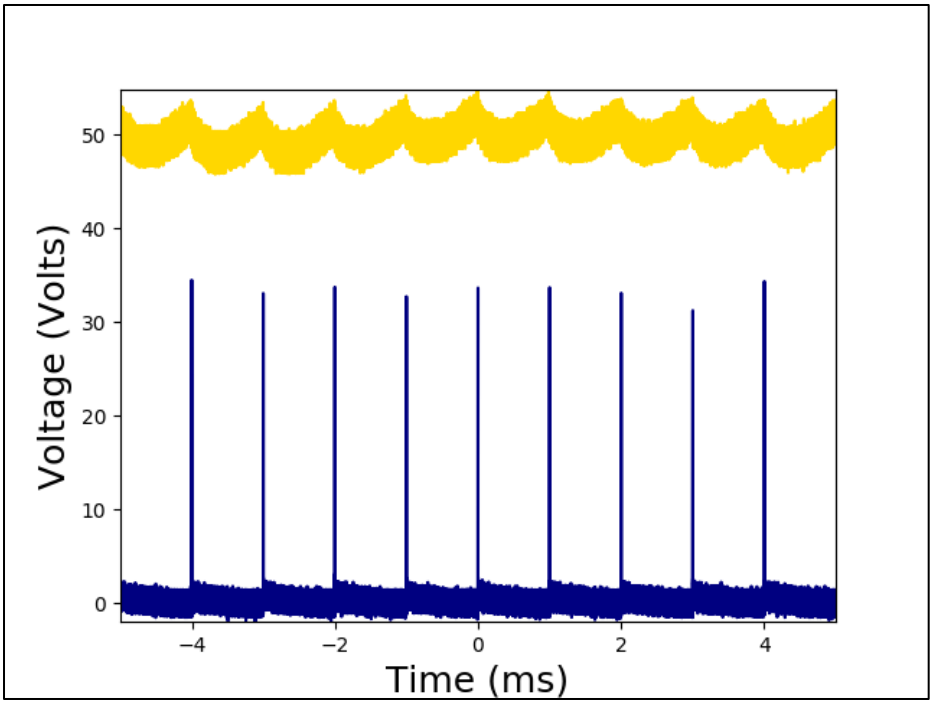


Figure A16. *Zoomed out image of the waveforms using the PCB TL with a 50 μm device at 50 V charge voltage.*

Moving forward, the charge voltage will be increased with the goal of hitting 1 kV by the next report. The breakdown voltage in open air will be found along with the breakdown voltage using a clear epoxy and encapsulating material as well. Testing will also be performed varying the voltage to keep the electric field constant for each of the gap lengths in order to better compare the on-state resistance and recovery. Modifications to the new design of the transmission line will also be made as guided by simulations of the circuit.

High Power FOM (Bhamidipati)

In our continued efforts to derive a *figure of merit* that would effectively summarize the performance of different materials, we have coordinated our efforts with Lawrence Livermore National Laboratory and are taking an approach from the device power loss stand point to propose an expression that would effectively incorporate power losses at every stage of switch operation. The device losses are mainly characterized by the power dissipated in the device in all the three states (on, off and switching) as shown in Figure A17. When operated at high repetition rates, switching losses may become the dominant cause of thermal runaway and/or fatigue in the device. These switching losses exist during the transition from the off-state to the on-state, and vice versa due to the dynamic change in switch voltage, current, and resistance during these transitions. This transition stage is critical when generating a figure of merit (FOM) considering the fundamental differences in Si, GaN, and SiC.

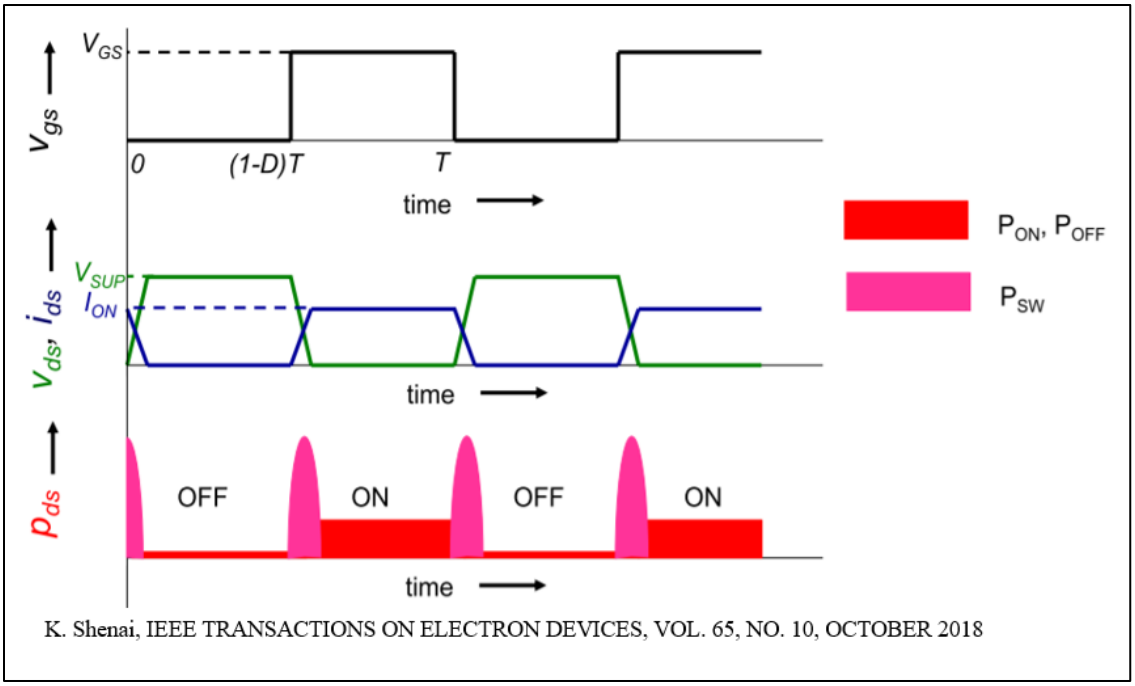


Figure A17. *Optical trigger with duty cycle 'D', the current and voltage transients and power dissipated in the device during each phase of the switch operation, (P_{ON} - On state loss, P_{OFF}- off state loss and P_{SW}-switching loss) [1].*

For an effective FOM, it is important to look beyond fundamental material properties and toward the dependence of the switching performance in the context of switching circuits (e.g., pulse forming transmission lines and switching amplifiers). To analyze at circuit level, we have begun focusing on ideal circuit topologies, beginning with class-E amplifiers. An initial model is shown in Figure A18 to use as the driving circuit for source driver operation. The model was implemented using an ideal voltage-controlled switch. At this moment, the models use a sinusoidal voltage source for excitation, but the goal is to change to representative models of R_{on} in future simulations to more accurately represent real devices. Our first objective is to model the ideal amplifier to utilize the source driver and implement zero voltage switching as shown in Figure A20 to minimize the power losses during turn-on by manipulating the circuital elements and categorize the switches based on their losses during turn-off, as predicted by material properties.

The class E amplifier is a switching mode amplifier (ideally with a 50% duty cycle as shown in figure A20 where the device is driven to saturation in order to act as a switch with two discrete states, ON and OFF. The idea behind class E is to reduce or eliminate the effects that device parasitics may have on efficiency and operation at high frequencies. The major operational condition is that the device is only switched on when there is little to no voltage across the device. This eliminates switching losses - a major loss component of most RF amplifiers.

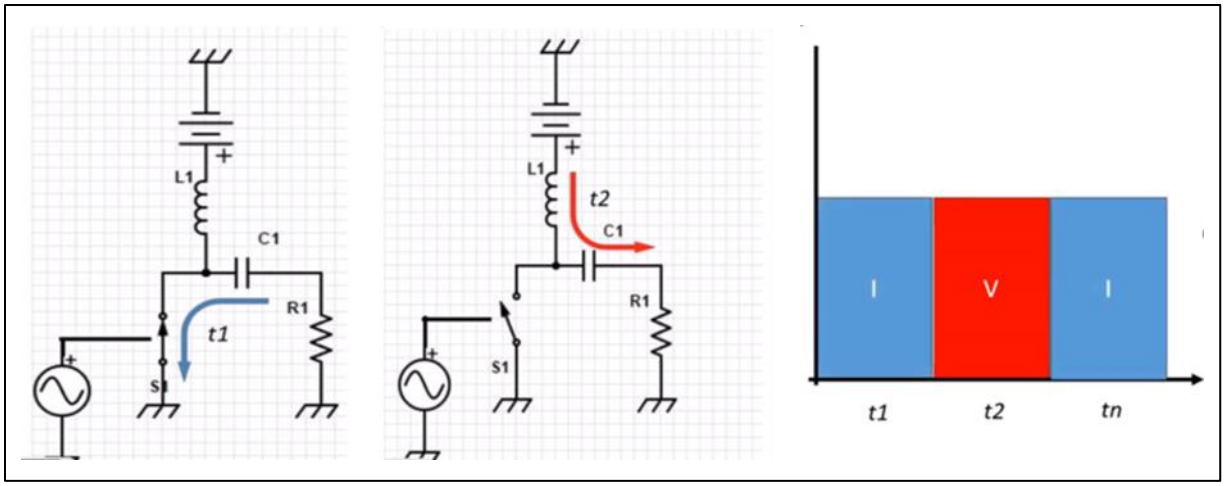


Figure A18. *Ideal operation of Class E amplifier – Zero Voltage Switching. The plot on the right shows the non-overlap of voltage and current in the device. When the device is closed, current flows through it (blue shaded region) and when it is open current flows through the capacitor and the device remains open at high voltage.*

Theoretical efficiency of the amplifier with an ideal switch approaches 100%, but in reality, the best we can achieve is 81% in spite of fine tuning the circuit components. Most of the power is lost during the intermodulation of harmonic frequencies. To control the harmonics, the resonator at the output is added as shown in Figure A19.

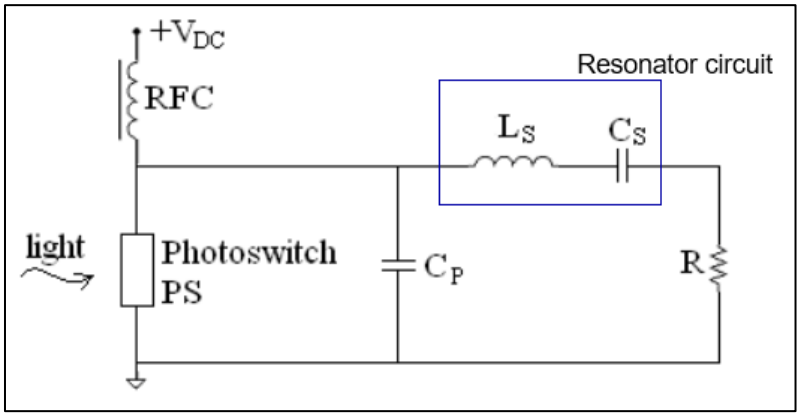


Figure A19. *Ideal class E amplifier model with photo activated switch.*

This resonator creates a condition where the circuit is shorted at fundamental frequencies and open to harmonics. The effects of the capacitances within the device can be reduced by making them part of resonant circuits and by controlling the timing of the switching of the device such that the device is switched on only when the output capacitor is discharged.

Our initial efforts in modeling class E amplifiers (Figure A20) showed the need to fine tune the circuit per the device characteristics as shown in Figure A21. Because the circuit was

not tuned for optimal performance and the device's on state resistance used is more than expected, the class E amplifier output did not reflect Zero Voltage Switching.

If designed correctly, the switch would open and close with a perfect 50% duty cycle, avoiding any overlap between the voltage and current which would eliminate the power losses in the device.

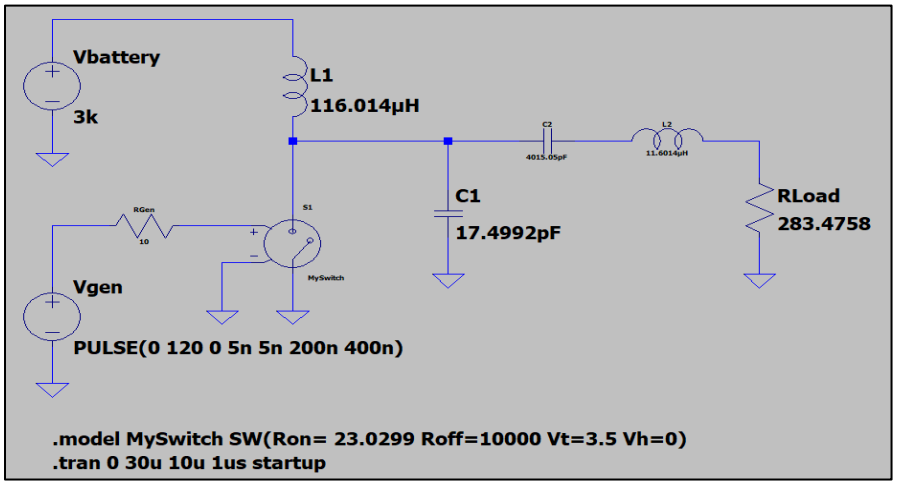


Figure A20. *Initial model of Class E circuit with shunt capacitance and resonant circuit*

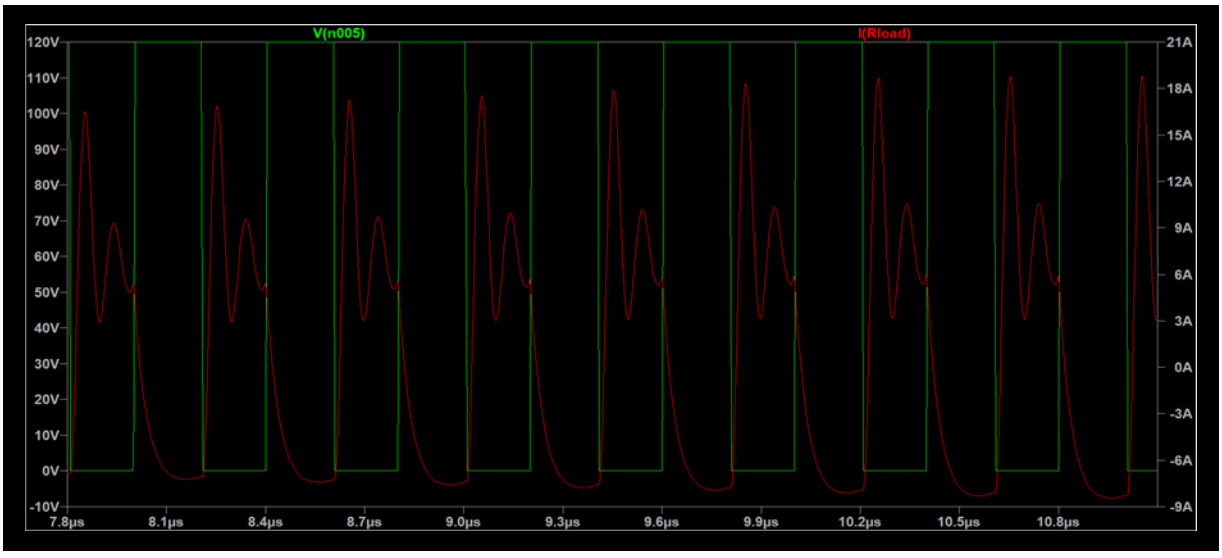


Figure A21. *Initial simulation results of Class E amplifier – Input excitation pulse (Green) output current (Red). Zero Voltage switching not achieved in the model.*

In our recent efforts, the circuit we have modeled is excited with 1.2kV peak to peak pulse input with 1 ns rise and fall times, 0.5us duty cycle and on-resistance on the order of mOhms at 3-kV DC bias (shown in Figure A22). We continue to work on refining the model with multiple iterations by varying the circuital components and duty ratio on the model to obtain a tunable circuit for devices made of different materials to implement zero voltage switching.

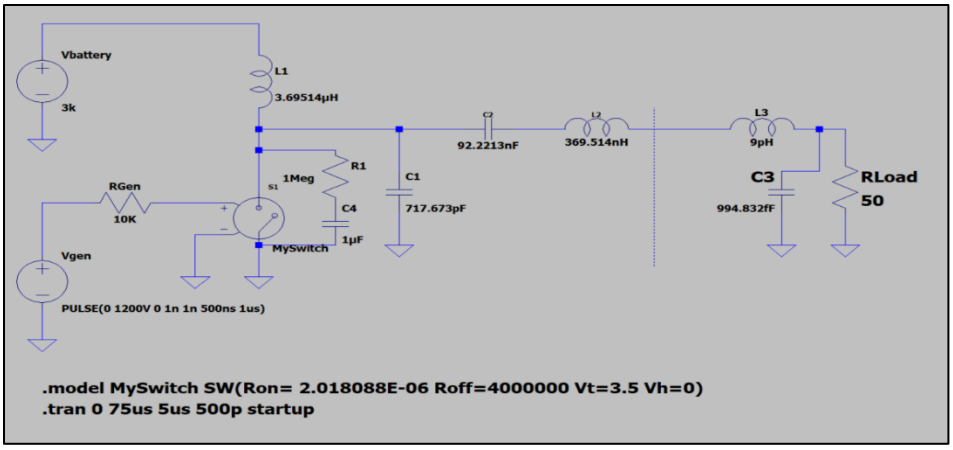


***Figure A22**. Modeled class E amplifier with 50% duty ratio, tuned to operate at 10MHz.*

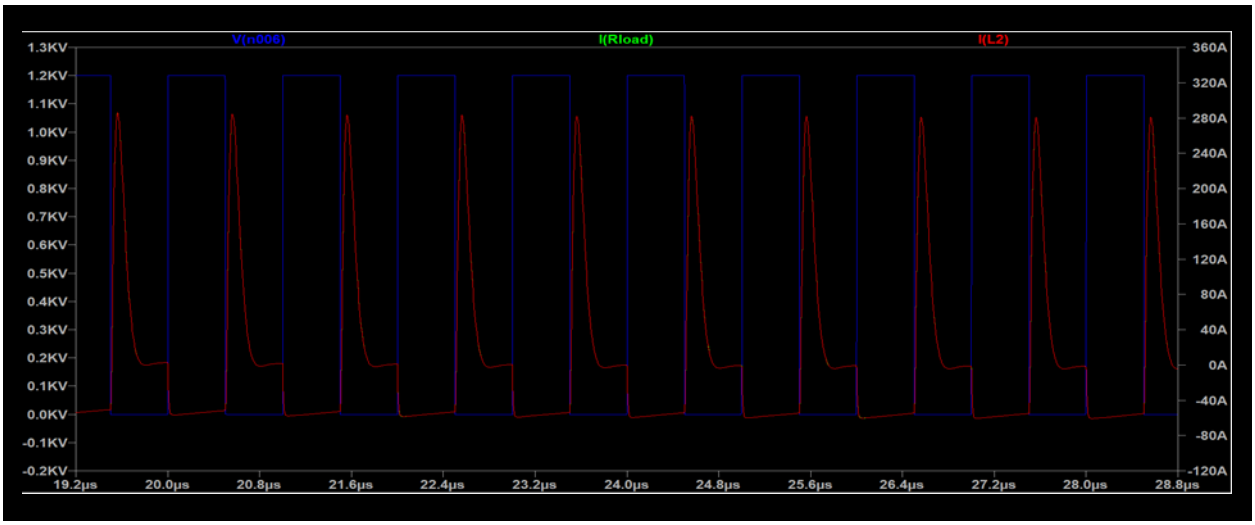


***Figure A23.** The excitation pulse (blue) of 50% duty cycle and the output current (red) waveform across the load. Plot shows the non-overlap of voltage and current.*

In addition to modeling circuit topologies, we are also revisiting models of the carrier generation and change of device resistance as a function of light intensity, geometry and recombination times for Si, GaN and SiC so we can determine the suitable device material, geometry and dimensions for the driver. The results from this effort will be used to provide approximate switch resistance during the transitions between the on and off state.

The approach has been divided into two steps: (1) Using MATLAB to plot Nunnaly's equations for the materials (Si, SiC and GaN) varying geometry and the light intensity and (2) implement the devices in Class E amplifier to minimize turn-on losses and characterize the devices based on their power dissipation during turn-off. The initial simulations for the carrier generation and the device resistance have been done and a sample of it is shown in Figure A24. For this model, all three materials have been illuminated with the light intensity of 600 mJ on a 500-µm device (500 µm thickness for Si and SiC, and 500-µm

switch gap for GaN device) with an assumed recombination time of 1 µs. This long recombination time represents a worst case, and is likely only applicable to Si since both SiC and GaN recovery times are much less than 1 µs. To resolve this, more accurate models of recovery and recovery time based on the material will be required. The end goal is to obtain the optimal operation geometry, operation and topology of each device by studying the power losses in each of them under different conditions.

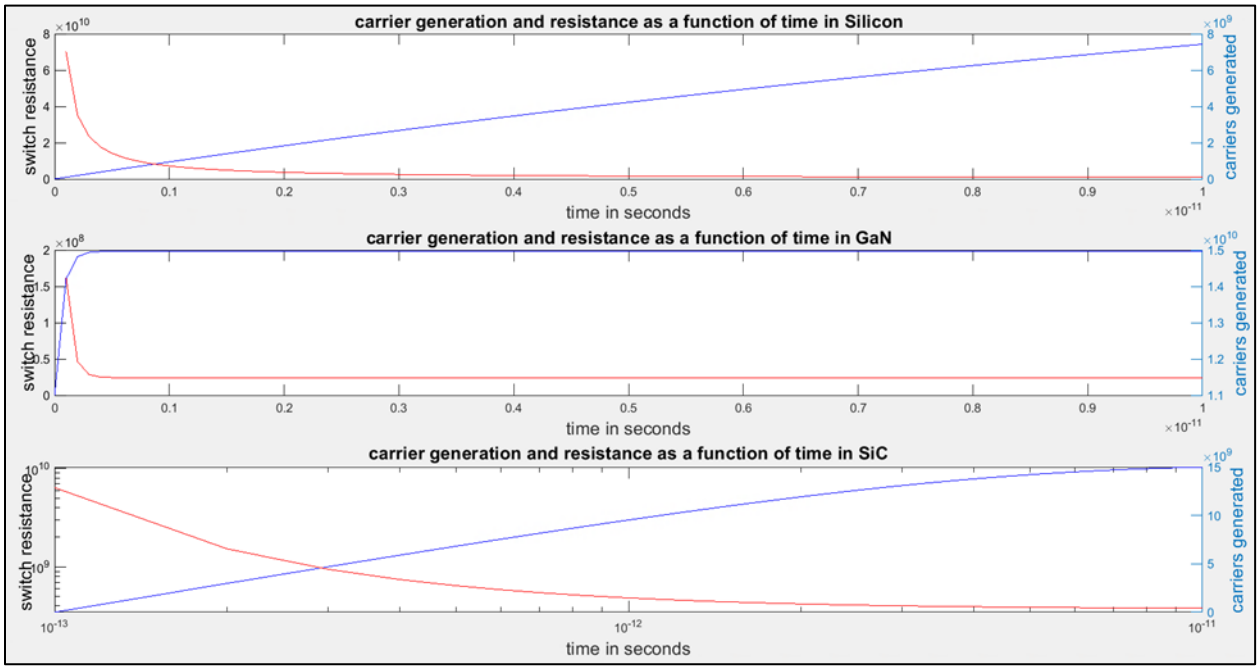


Figure A24. *Carrier generation (blue) and switch resistance (red) as a function of time for Si, GaN and SiC.*

References

[1] K. Shenai, "The Figure of Merit of a Semiconductor Power Electronics Switch", IEEE Transactions on Electron Devices, Vol. 65, No. 10, October 2018

I.A.1 Immediate Tasks of Fundamental PCSS Subgroup

i. Further analysis of SiPCSS TCAD models and extension to higher power switching dynamics, including the effect of reflections on switch recovery and performance.
ii. Continued testing of GaN:C PCSS with the new THG crystal once delivered.
iii. Complete initial models of class-E amplifiers and incorporate realistic switch resistance profiles into models. Extend to pulse forming transmission lines.

I.A.2 Expected Products of Fundamental PCSS Subgroup

i. Results from GaN:C PCSS testing showing dependence of Ron as a function of gap length and incident light.
ii. Demonstrate ≥1 kV pulses with GaN:C PCSS

I.B GaN:C Subgroup (Rulis)

i. No report submitted.

I.C Small Unmanned Aerial Vehicle Diagnostics and Design-of-Experiments (Fields)

Ground Station Developments

In order to operate a PX4-based UAV in fully autonomous mode it is necessary to have both a laptop ground station running one of a couple of ground station GUI's (Mission Planner, Q-Ground Control, etc.), as well as a wireless transmitter. There has been a recent development called the Herelink that combines the ground station and the transmitter into a single unit, allowing for more mobile UAV operations. This system also has fully integrated telemetry and onboard camera streaming. The Herelink has been integrated into both our quadcopter and fixed wing PX4 systems. Flight testing was conducted in order to verify the efficacy of these systems and ensure that all flight modes are accessible to the user.

RF Sensor Developments

Testing was done to ensure that the data logger portion of the RF sensor (Raspberry Pi Zero W), is adequately shielded from RF. The Raspberry Pi Zero was encased in an aluminum box and subjected to RF at varying frequencies. It was then tested again without the aluminum box. These tests showed that the aluminum box was effective at shielding the Raspberry Pi Zero W from RF. Testing will continue at higher power levels to verify that this is a viable solution.

Further field testing was conducted with the PX4-based quadcopter paired with the RF sensor. A total of 4 test flights were done, under varying conditions, in order to verify that the log files from the RF sensor and the flight logs from the quadcopter can be time synced based on the IMU data.

DJI Phantom 4 Developments

Field testing was conducted with several DJI Phantom 4's in order to verify their airworthiness as well as assess our ability to detect anomalies in the flight data. A variety of tests were done, each with a different kind of physical disturbance. The most severe of which was completely stopping a motor mid-flight. The purpose of this was to verify that it is possible to identify specific motor failures from the flight data.

In-Field Quick-Look Developments

All existing quick-look scripts for plotting data and identifying extreme points has been ported over from Matlab to a python script. Matlab requires the use of a license and is

limited based on the specific computer being used. Python can be used on any machine and is extremely versatile.

UAS Manufactured/Purchased

A total of 6 new PX4-based quadcopters and 2 PX4-based fixed wings were developed. A flight ready checklist was created in order to have a degree of quality assurance and work is still being done to flight test all of them and verify that all autonomy modes are functioning.

I.C.1 Immediate Tasks for Diagnostics/DoE Subgroup

i. Incorporate Skywalker X8 platform into diagnostic architecture;
ii. Evaluate which methodology for time syncing RF sensor to flight data is most robust;
iii. Flight test UAV's with added RF sensor payload;
iv. Finish live-fire test plan;
v. Develop methodology for identifying anomalies in free-flight data;
vi. Attend live-fire test event in Albuquerque NM, with AFRL;
vii. Attend GTEM test event at Johns Hopkins University.

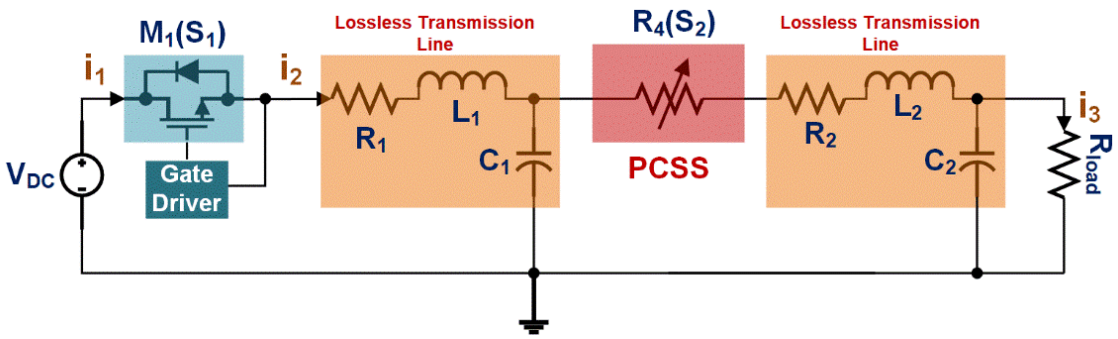
I.C.2 Expected Products of Diagnostics/DoE Subgroup

i. Field tested fixed-wing and quad-copter platforms outfitted with a custom RF sensor;
ii. Quick-look scripts for in-field evaluation of flight logs for both PX4 and DJI products;
iii. Field data from live fire test event;
iv. GTEM data from Johns Hopkins event.

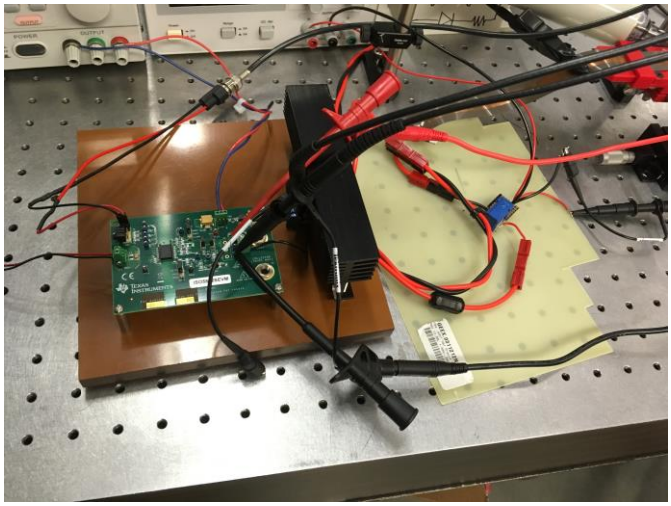
I.D Switch Development and Pulsed Power Support (Khan)

During June 2019, we conducted charging of a transmission line through a series connected IGBT switch followed by subsequent discharging of the line through a Si PCSS. Different configurations of the charging section of the transmission line have been used in the experiments for comparative performance evaluation.

We have assembled the IGBT attached to a heat sink, and the gate driver module of the IGBT in a compact single phenolic board to efficiently interface with the transmission line. Two 30 V programmable DC power supplies have been used to power the input side and output side of the gate driver. The series connected IGBT switch-based PCSS circuit schematic is illustrated in Figure D1(a) and the setup is shown in Figure D1(b).



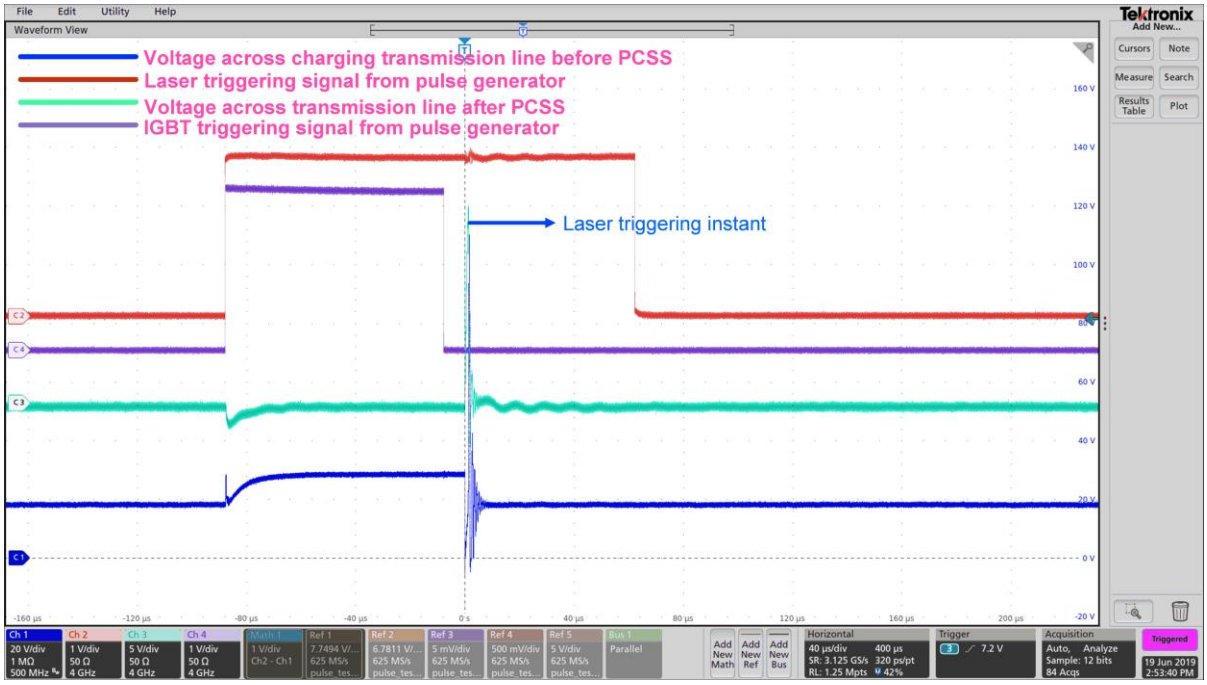
(a)



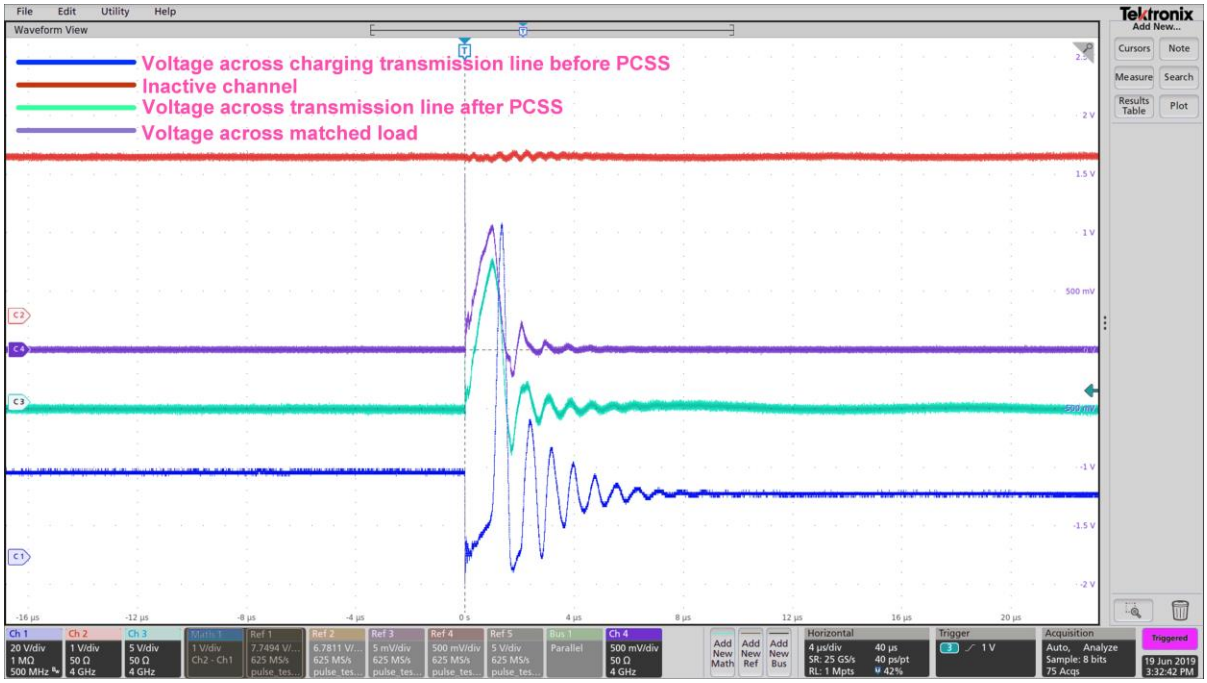
(b)

***Figure D1**. (a) Schematic of series IGBT connected PCSS and power supply, (b) photograph of the actual prototype.*

Using a series pulse generator (Emerald 9250) we can control the triggering of the IGBT and the laser. We have turned the IGBT ON for 80 µs. The dead time (the time when neither the IGBT nor the laser is activated) was set to 15 µs. The transmission line was charged by the supply voltage during the time the IGBT remained ON. The transmission line holds the charge and initiates rapid discharging once the PCSS is turned ON by the incident laser. The initial experimental results are illustrated in Figure D2.



(a)



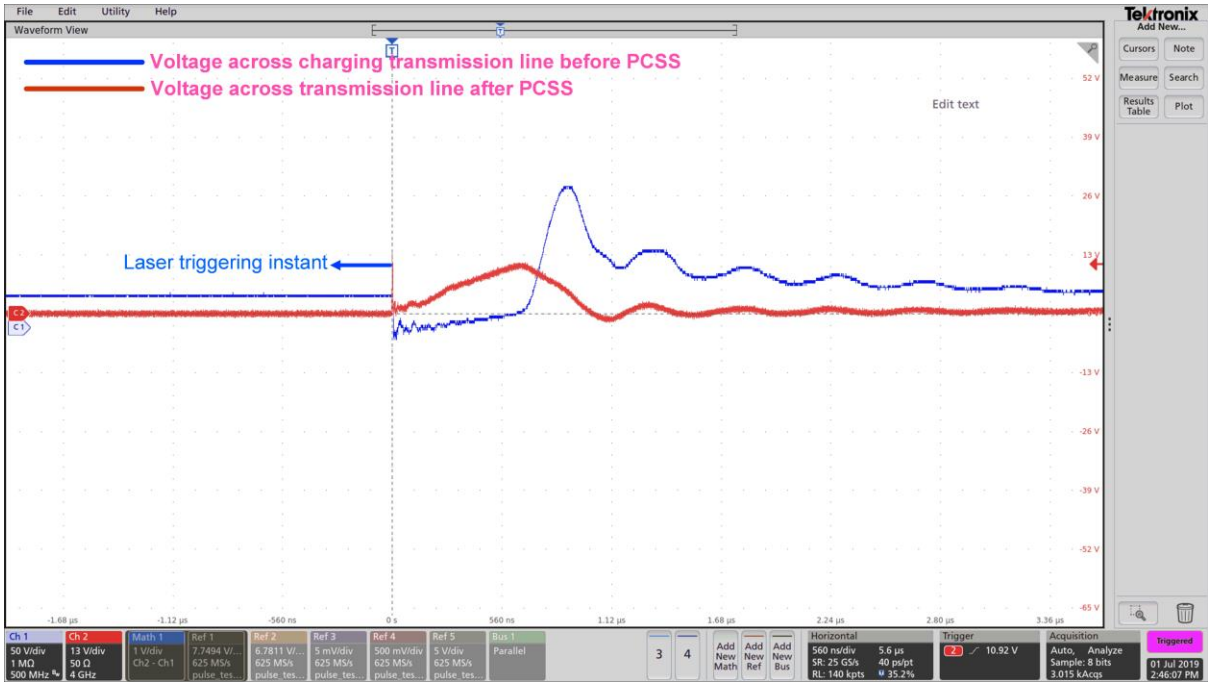
(b)

***Figure D2**. (a) Measured voltages at different points of the transmission line; (b) Zoomed version of measured voltages across different points of the transmission line.*

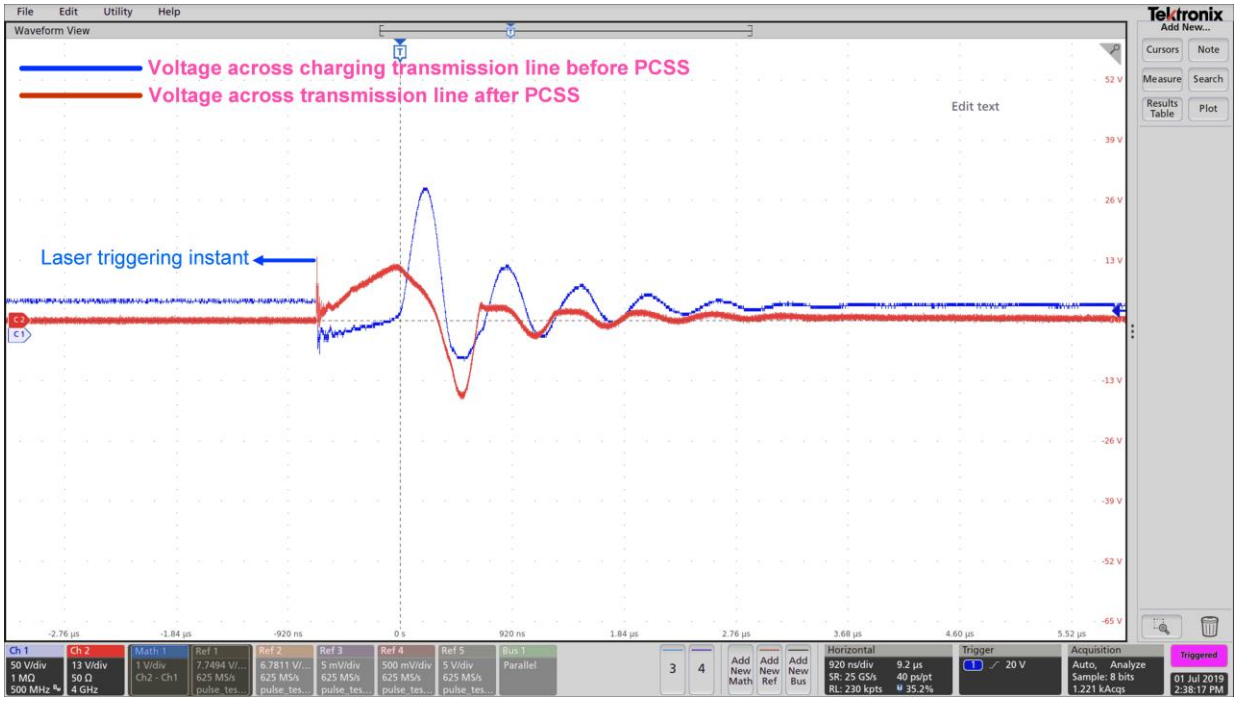
Figure D2 shows that the transmission line has charged up to a supply voltage of 35 V within 20 µs after the IGBT has been turned ON. After the IGBT was turned OFF, the line

continued to hold the charge until the PCSS was switched ON by the incident laser. The time interval between the instances of switching off the IGBT and turning on the PCSS has been set to a value of approximately 15 µs. The voltage across the charging section of the transmission line before the PCSS sharply falls to zero transferring the stored energy to the load after the PCSS is switched ON. At the matched load, we have observed a pulse having a width close to 15 ns whose peak amplitude reached a maximum value of 17 V (half of the supply voltage). These observations from the experiments match with theoretical expectation. However, shortly (≈1 µs) after being discharged, the charging section of the transmission line before the PCSS experienced significant ringing causing the line to be charged up to two-third of the supply voltage in the absence of the IGBT triggering signal. In addition, the output section of the line has shown similar pattern of ringing until the PCSS has fully recovered.

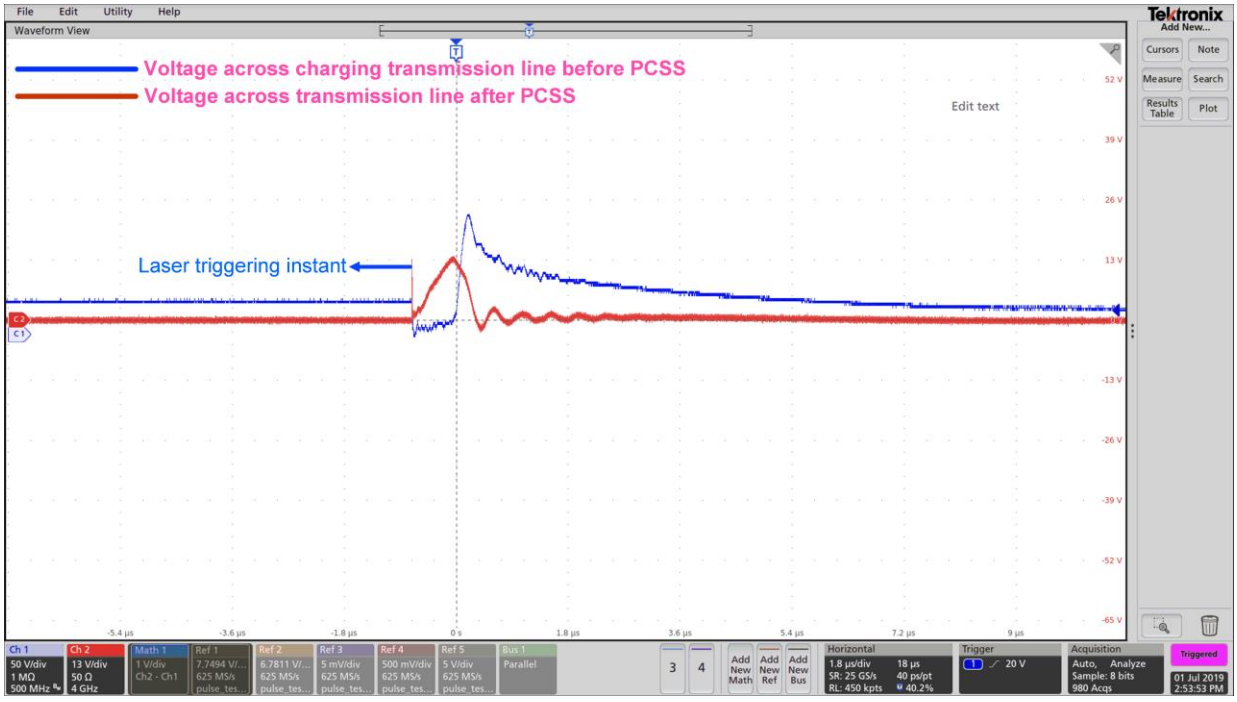
We have placed a Schottky diode between the IGBT and the transmission line to observe its effect on the unwanted ringing in the charging transmission line. Another Schottky diode has been placed across the charging transmission line before the PCSS to act as a freewheeling diode in another setup. In addition, we conducted experiments placing the diode after the PCSS to understand if reflections coming back from the load end are contributing to the ringing in the charging transmission line. These results are shown in Figure D3.



(a)



(b)



(c)

Figure D3*. (a) Series diode placed between the IGBT and the PCSS (b) Series diode placed after the PCSS (c) Series diode placed between the IGBT and the PCSS and parallel diode placed across the charging transmission line after the IGBT.*

Figure D3 shows that the series diode placed between the IGBT and the PCSS has rectified the ringing in the charging transmission line. However, the peak ringing amplitude has not changed significantly. The series diode placed after the PCSS has not impacted the experimental result referring to the insignificant impact of the reflection coming back from the load end on the ringing in the charging line.

We have decided to use current sensor to measure current through the charging transmission line at various instances of the charging and discharging cycle. We have chosen LEM-CKSR-25P as the current sensor to be used in the experiments. We have designed a PCB using ExpressPCB to assemble the current sensor and the IGBT together. The PCB and the gate driver of the IGBT will be placed together in the same phenolic board used in the previous experiments. The schematic of the PCB layout is shown in Figure D4.

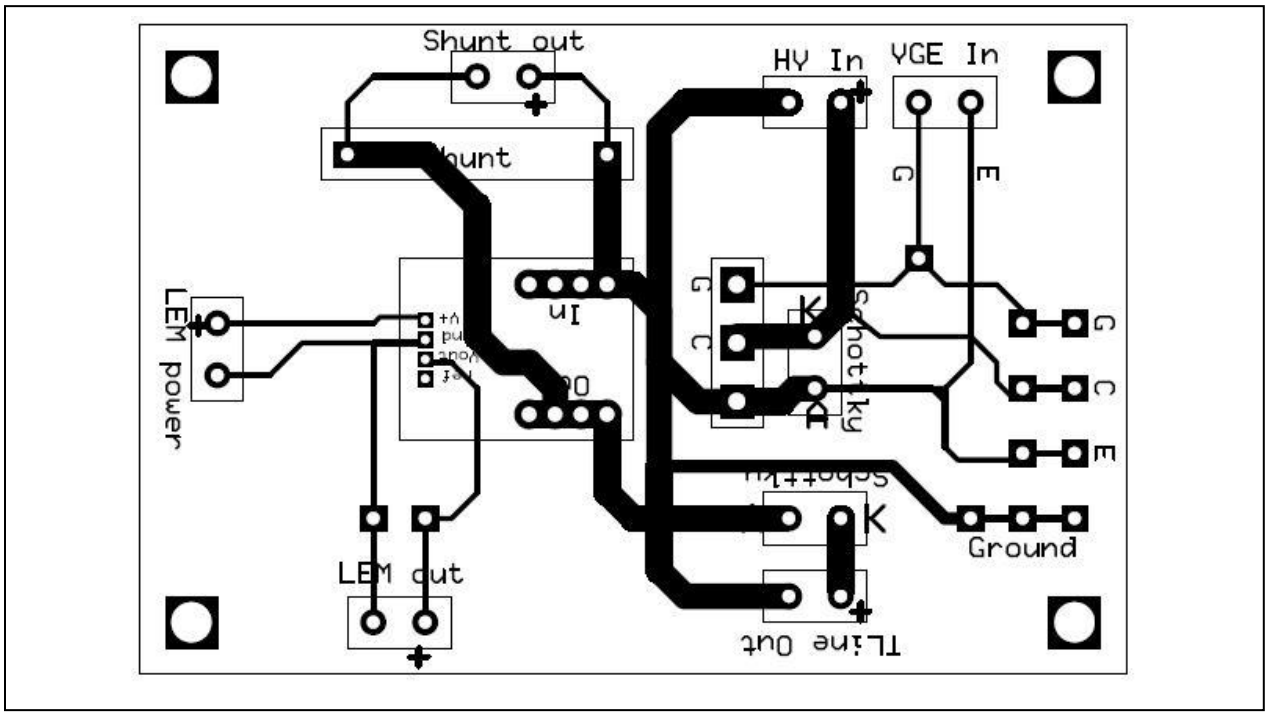


***Figure D4**. PCB layout of the current sensor and IGBT assembly.*

At present, we are developing a detailed simulation model of the test setup to emulate the real-time experimental behavior in the simulation as closely as possible. We will include the probe loading effect, probable parasitic reactance in the simulation along with improved models of the IGBT and the PCSS. We will measure the current through the charging transmission line and voltage across the terminals of the IGBT during a full cycle of charging and discharging to further investigate the ringing issue in the line.

I.D.1 Immediate Tasks for the Switch Development and Pulsed Power Support Subgroup

i. Integrating the PCB containing the current sensor and the IGBT with the existing setup.
ii. Investigating any irregularity in the switching of the IGBT in terms of measured voltages across its terminals and current through it.
iii. Developing a detailed simulation model of the test setup to emulate the experimental results as closely as possible.

I.D.2 Expected Products of the Switch Development and Pulsed Power Support Subgroup

i. Designing a solid state switch based power supply circuit for PCSS to minimize tail current and increase system efficiency.

I.E Applied RF Coupling Simulation and Modelling to/for sUAV (Hassan)

i. No report submitted.

I.F UMKC Diode Network Based NLTL (Doynov)

Based on the parameters space exploration, we continue the optimization of Diode-NLTL design with the following objectives:

- Ability to generate waveforms that will produce frequency in the desired bandwidth
- Effect of lumped elements on the efficiency of the D-NLTL
- Optimal load impedance matching

Following the design steps outlined in the report for April 2019, we conducted studies on the lumped inductance influence on D-NLTL performance by monitoring the first peak amplitude, center frequency, and efficiency of RF generation. In the simulations, excitation pulses with 15 V amplitude are used to avoid exceeding the reverse-bias rating of the diodes. The resulting voltage wave forms are displayed in Figure F1a and the peak output amplitudes in Figure F1b for inductance values from 10 nH to 100 nH. The results for the center frequency and RF efficiency are shown in Figure F1c. Inductance was found to have a significant effect on the center frequency which changes from 191 MHz to 7 MHz for inductance changes of 10 nH to 80 nH and is consistent with the well-known equation:

$$f_c = \frac{1}{\pi\sqrt{LC_0}}$$

The increased efficiency of RF generation from 6% to 49% should be viewed as the result of improved load impedance matching as the characteristic impedance of the line increases with the higher value inductance.

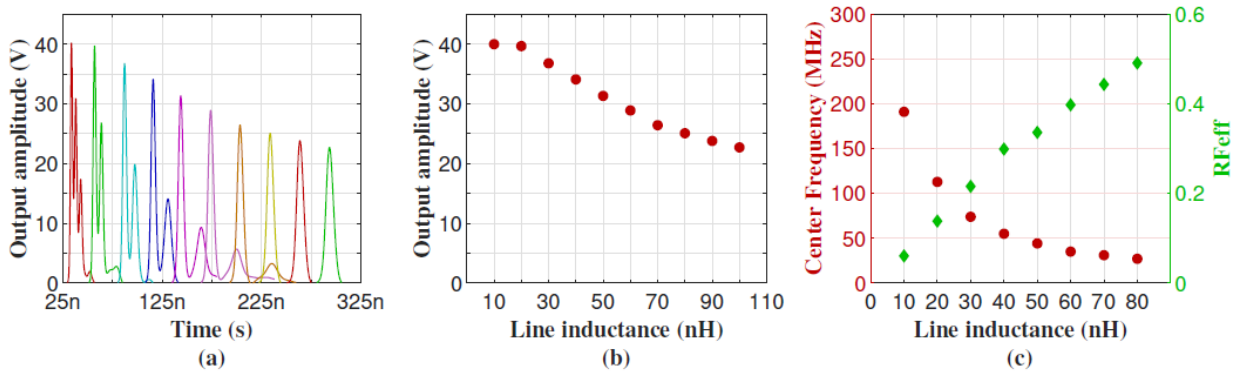


Figure F1. *Results for the effect of lumped inductance on the output waveform. (a) Output wave forms, (b) First peak amplitude results, (c) Center frequency (red dots) and RF generation efficiency (green diamonds).*

The non-linear capacitance curve of the diode is studied for the effect on the center frequency of the output waveform. Several factors in the SPICE modeling of a diode were investigated. To test different C(V) curves, the non-linear function is integrated with respect to voltage and a Q(V) curve is obtained. In LTpice, the value of the capacitor is then set as:

$$Q = \int C(V)dV$$

in LTspice. An example of simulation results using a custom C(V) curve for the output waveform is shown in Figure F2, left. The FFT of the signal after the high-pass filter is shown in Figure F2, right.

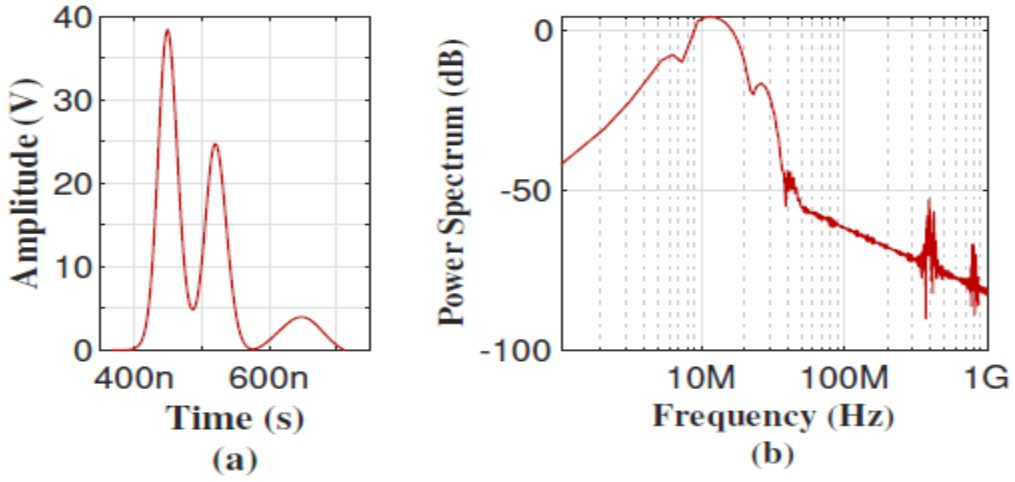


Figure F2. *Waveform generated with a custom C(V) curve (left) and its FFT after the high-pass filter (right).*

We performed multiple simulation tests to explore the effects of different parameters describing the C(V) curve of the diode. The P-N junction of a reverse-biased diode has a voltage dependent capacitance modeled as:

$$C(V) = \frac{C_{jo}}{\left(1 - V/V_j\right)^m}$$

The C_{jo}, V_j , and m values in the above equation are tested by altering the characteristic capacitance curve. For comparison, the parameters are swept in a range corresponding to the specifications of a 1N5822 diode. The results are shown in Figure F3.

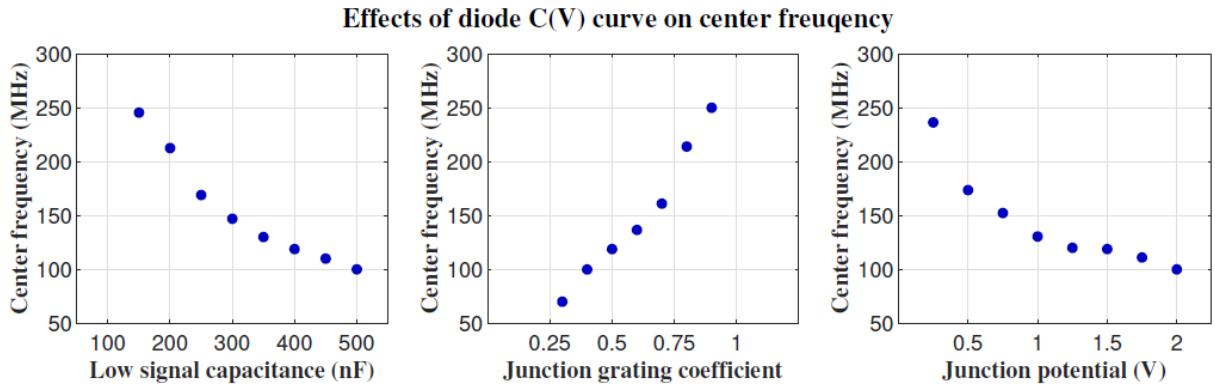


Figure F3. *Results for the effect each parameter of the C(V) curve has on center frequency.*

The plots indicate that to generate the highest center frequency possible, the diode should have a low Cjo, a low Vj , and a high m characteristic values. Note that these results are purely related to the shape of the C(V) curve. In general, a diode with these optimal values could have other issues such as a low maximum reverse bias potential or a high parasitic resistance thereby limiting the performance of the D-NLTL.

I.G Electrically Small Antennas (Chatterjee, Barman, Kovarik)

In this report we are focusing mostly on the electrically small antenna design. Our main target is to design an electrically small antenna with reasonable 2:1 VSWR bandwidth and gain. This electrically small antenna will be used in a linear array and later in a planar array to achieve the desired performance. Nearly electrically small antennas (having greater than 30% bandwidth) have been characterized so far using simple microstrip patches. Bandwidth improvement is attained using proximity coupled feed (discussed below). A linear array has been modelled using the electrically small antenna. Gain of the embedded elements and the array have been studied using full wave simulations in FEKO. Furthermore, the effect of different types of amplitude distributions such as uniform, Dolph-Chebyshev, Taylor Line Source and Bickmore-Spellmire on the array radiation patterns have been investigated.

Electrically Small Antenna Design

Electrically small antennas (ESAs) can be classified as those which satisfy the condition $\mathrm{ka} \leq 0.5$, where k and a are the wavenumber and minimum radius of the circumscribing sphere of antenna, Figure G1 (also known as Chu's Sphere) [1].

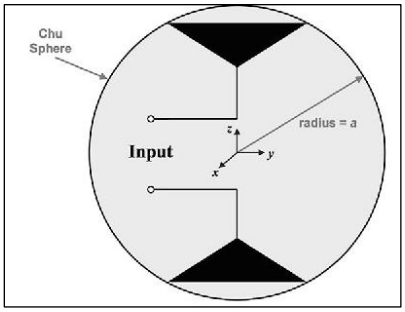


***Figure G1**. An antenna enclosed in Chu's Sphere.*

The aim is to design an electrically small antenna which operates in the ultrahigh frequency (UHF) region and ultimately to integrate it as an element in a phased array for realizing a desired performance.

We have approached the problem by first analyzing a simple microstrip patch antenna. Three different substrates have been considered to design the microstrip patch, viz., RT/duroid ($\varepsilon_r = 2.2, \tan\delta = 0.0009$), TMM-4 ($\varepsilon_r = 4.5, \tan\delta = 0.0020$), and TMM-10i ($\varepsilon_r = 9.8, \tan\delta = 0.0020$). The antenna dimensions in each case are obtained through the following set of formulas:

1. SUBSTRATE THICKNESS:

The thickness of the dielectric substrate is chosen such that the ratio $\frac{h\sqrt{\varepsilon_r}}{\lambda} = 0.175$, λ being the wavelength of the operating frequency.

2. PATCH LENGTH:

Length of the patch is related to the resonant frequency as [2]:

$$f_r = \frac{c}{2\sqrt{\varepsilon_r}}\left(\frac{1}{L_e}\right) \qquad (1)$$

where, L_e is the effective length of the patch and is given by:

$$L_e = L + 2\Delta L \qquad (2)$$

ΔL being the fringing length extension. For quick estimation of ΔL, a good rule of thumb is $\Delta L \approx 0.5h$.

The patch length is therefore calculated as:

$$L = L_e - 2\Delta L \approx L_e - h \quad (3)$$

3. PATCH WIDTH:

Width of a rectangular patch should be less than twice its length, i.e.,$W < 2L$.

Antenna dimensions, corresponding to the design frequency of 575 MHz, are calculated using the above relations, followed by microstrip patch modeling in FEKO. In each of the three cases, the probe location and the radius of the probe have been varied to obtain the best bandwidth and gain values. After extensive parametric analysis it has been observed that the best bandwidth is obtained when the probe is located along the diagonal of the rectangular patch at 2/3rd distance from the center (indicated in Figure G2). The results obtained using different substrates are summarized in Table G1. Figure G3 shows the bandwidth and gain vs. frequency plots for all the three cases. The ka value is calculated with $k = \frac{2\pi}{\lambda}$, where λ corresponds to 575 MHz. Diameter of the Chu's sphere is considered equal to the diagonal length of the patch, i.e. $2a = \sqrt{L^2 + W^2}$. It can be seen that as the electric permittivity increases the antenna tends to become electrically small.

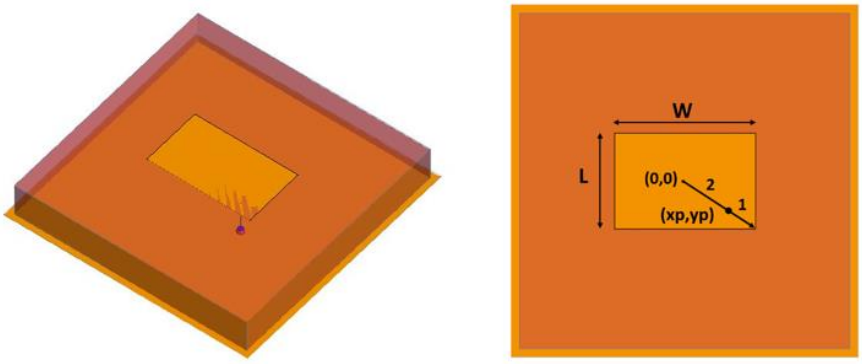


Figure G2. *Geometry of the patch.*

***Table G1**. Microstrip patches with different substrates.*

Parameters	Substrates		
	RT/duroid 5880	**TMM-4**	**TMM-10i**
ε_r	2.2	4.5	9.8
$\tan\delta$	0.0009	0.0020	0.0020
h (mm)	61.5148	43.0115	29.1459
$h\sqrt{\varepsilon_r}/\lambda$	0.175	0.175	0.175
L (mm)	114.2417	79.8785	54.1281
W/L	1.7	1.7	1.6
W (mm)	194.2108	135.7934	86.6050
r (mm)	14	7	3.5
(x_p, y_p)	(38.0806, 64.7369)	(26.6262, 45.2644)	(18.0427, 28.8683)
f_L(MHz)	483.1	497.5	562.3
f_c(MHz)	579.1	609.75	668.65
f_U(MHz)	675.1	722	775
%BW	33.1549	36.7989	31.8104
Max. Gain (dB)	6.5983	4.60662	3.38158
ka	1.3577	0.9493	0.6154

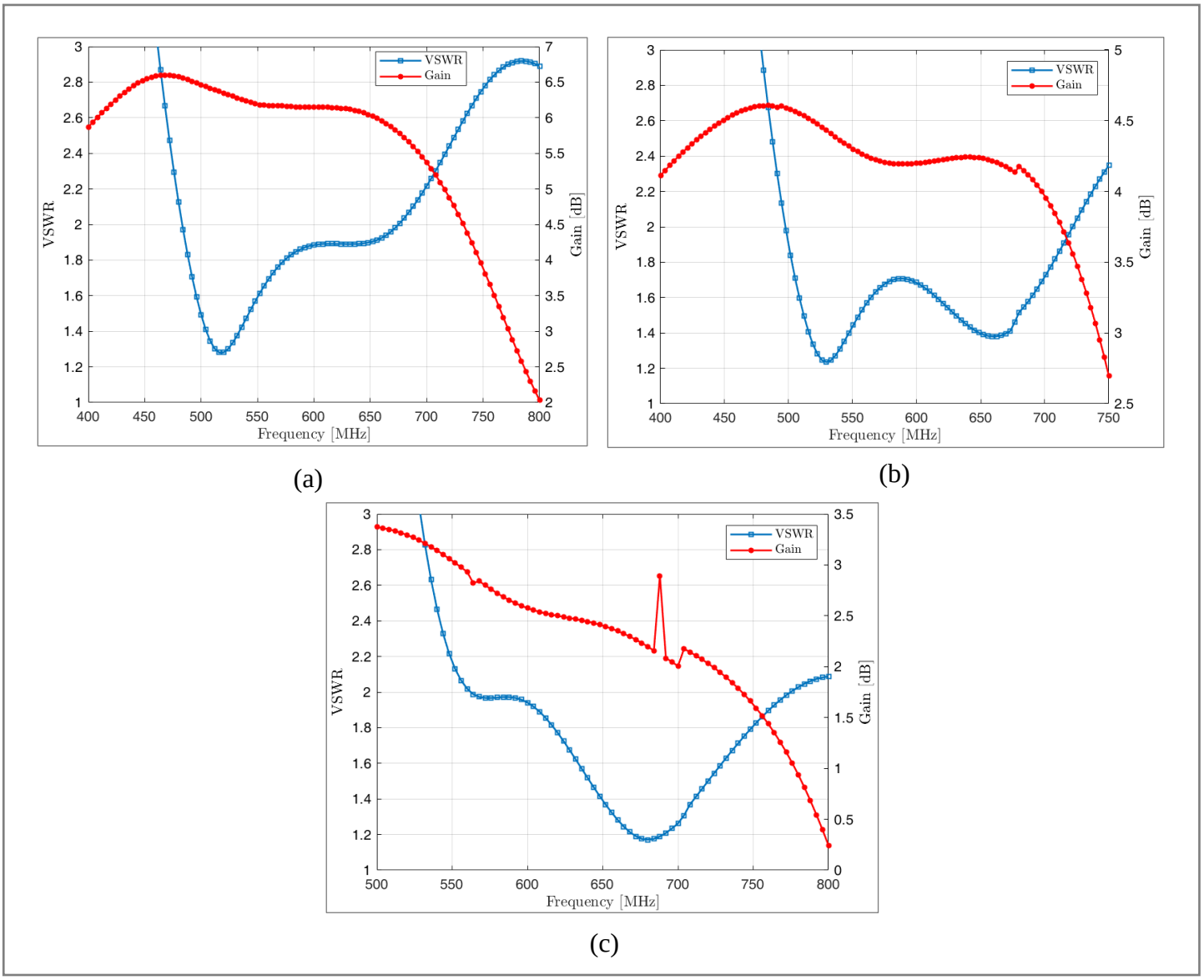


***Figure G3**. VSWR and Gain as a frequency for (a) RT/duroid (b) TMM-4 and (c) TMM-10i substrates.*

Among the three designs, maximum bandwidth of 36.79% is obtained with TMM-4 substrate. Characteristic Mode Analysis of this design is performed to analyze the modal contributions to the VSWR bandwidth.

Characteristic Mode Analysis (CMA) of Simple Rectangular Patch

CMA for the microstrip patch on TMM-4 substrate is carried out using the TCM solver available in FEKO. For understanding the different modes that contribute towards the patch behavior we have performed parametric analysis of the design. Figure G4 shows that as the probe radius is increased the bandwidth increases and the modes J1 and J3 have the maximum contribution.

***Table G2**. Effects of variation in probe radius in a simple microstrip patch.*

r_p (mm)	f_L (MHz)	f_c (MHz)	f_U (MHz)	%BW	Max. Gain (dB)
5	492.6	594	695.4	34.14	4.58982
6	494.1	599.25	704.4	35.09	4.5902
7	497.6	609.75	722	36.79	4.60662
8	500.8	620.15	739.5	38.49	4.62268

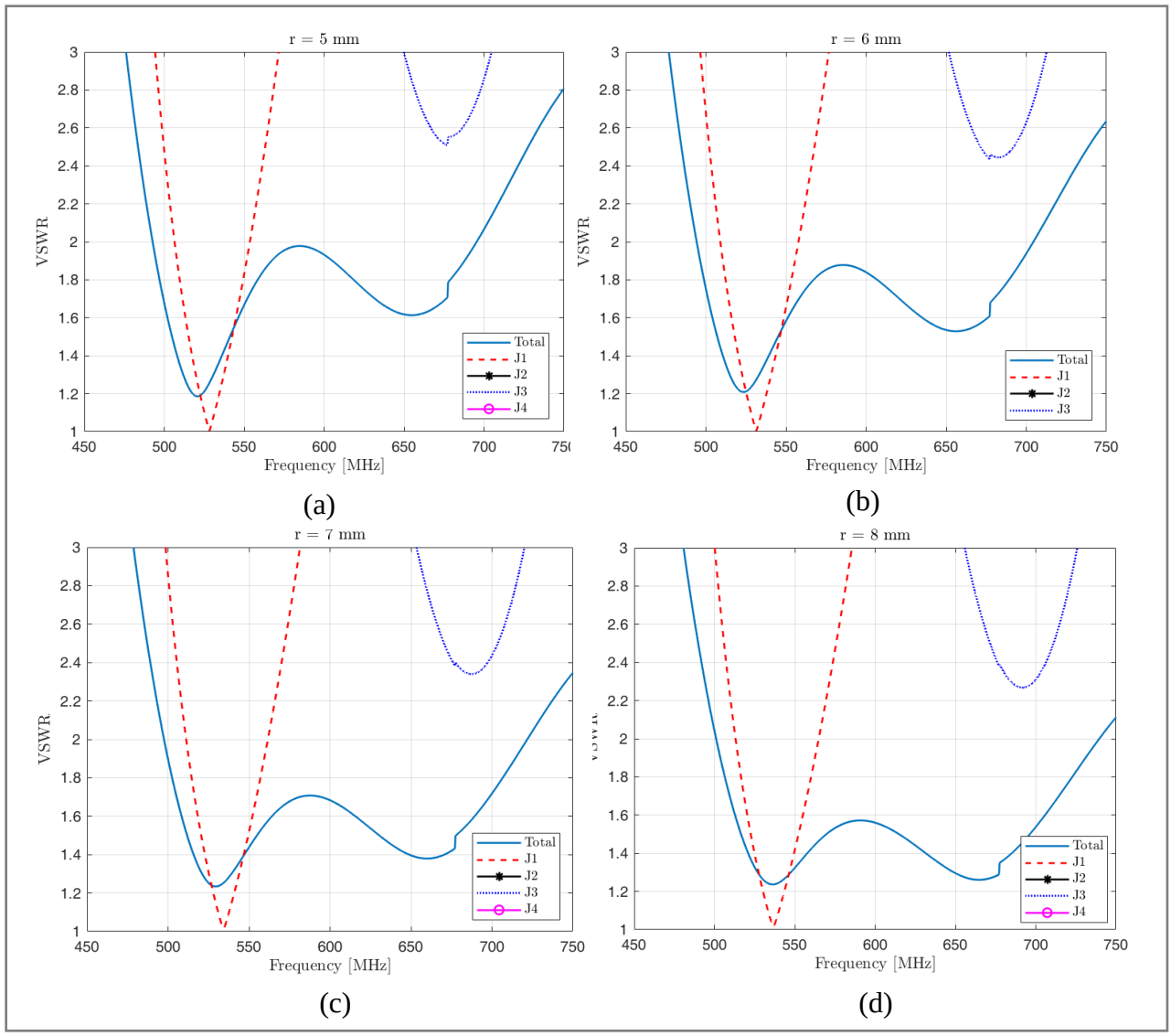


***Figure G4**. VSWR for various characteristic modes of the probe fed rectangular patch at (a) r_p =5 mm (b) r_p =6 mm (c) r_p =7 mm and (d) r_p =9 mm.*

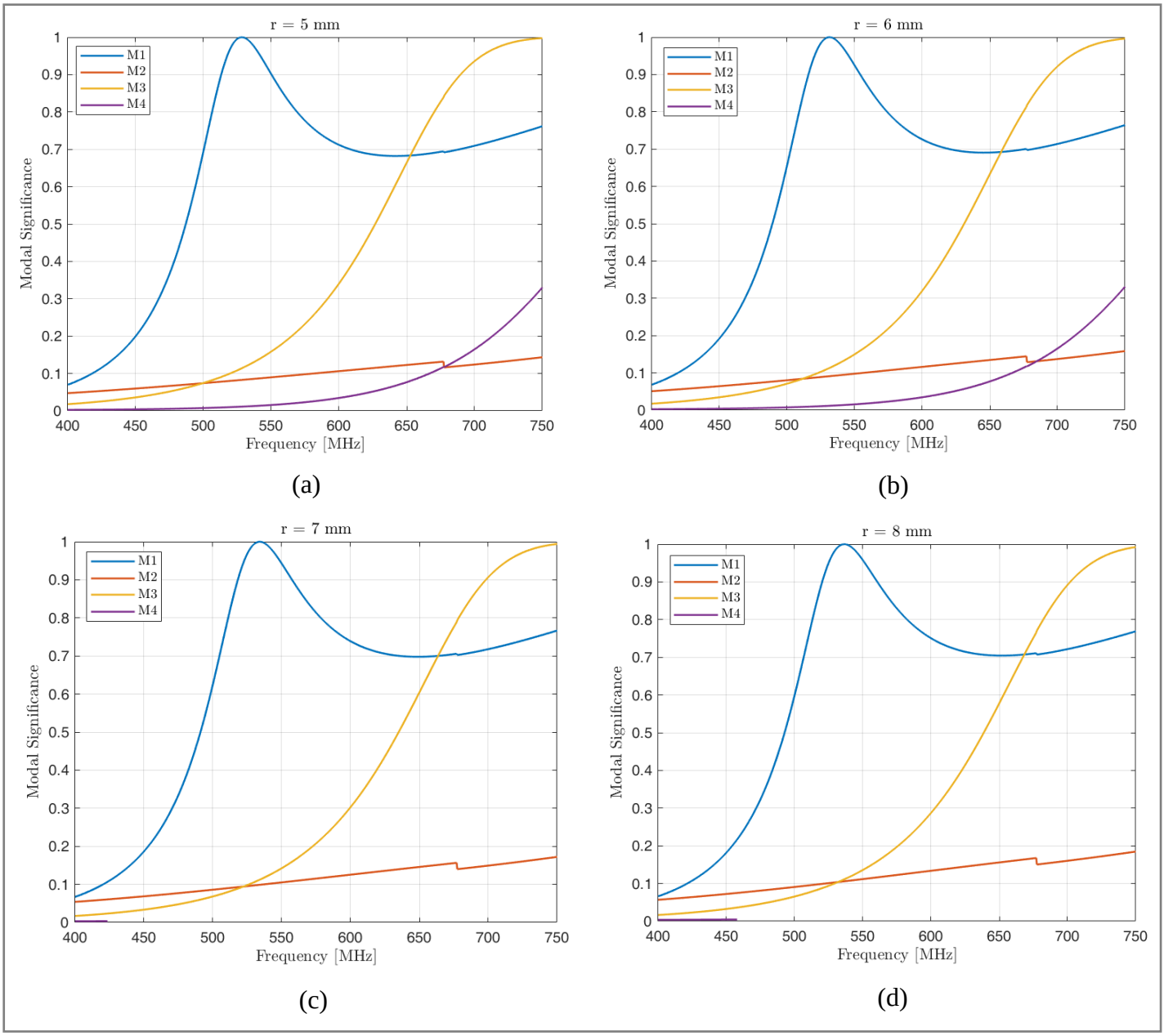


***Figure G5**. Modal Significance for different probe radius (a) r_p =5 mm (b) r_p =6 mm (c) r_p =7 mm and (d) r_p =9 mm.*

To study the behavior of this nearly electrically small antenna element in an array, we have formed a 25 element linear array, with all the elements placed along the X-axis on the X-Y plane. Figure G6 shows the linear array geometry.

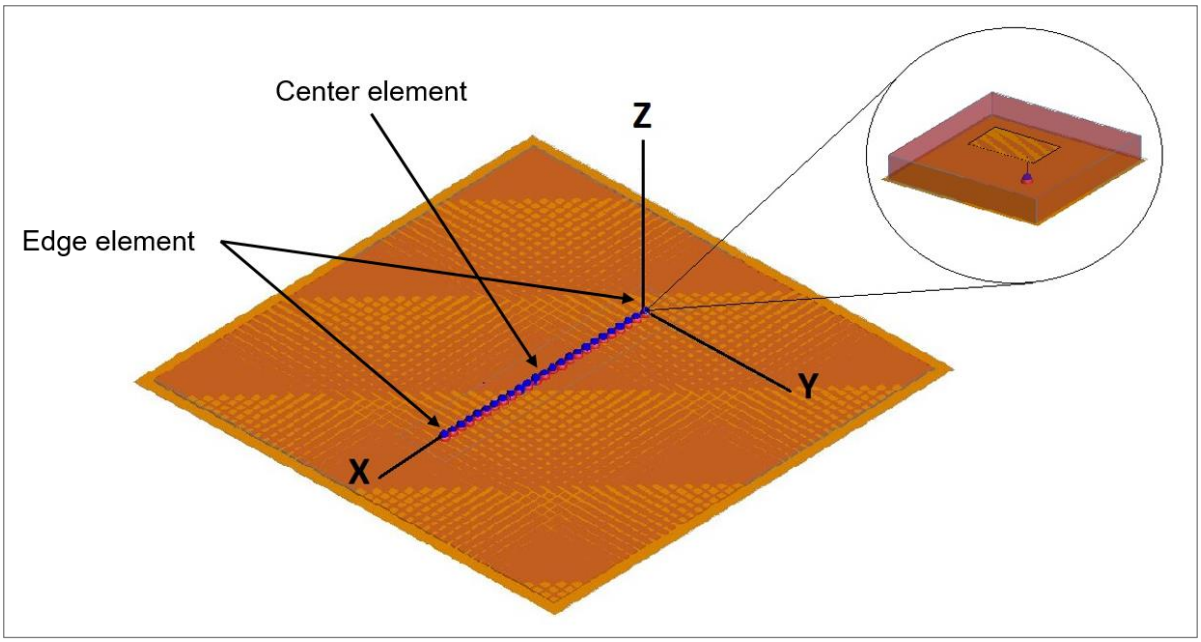


***Figure G6**. Geometry of the linear array.*

We have considered the active element patterns of the edge (25th) and center (13th) elements. Active element patterns can be obtained when a single element is excited in an array, with all other array elements terminated in matched load [3]. Figure G7 shows the boresight gain vs. frequency curves for isolated, edge and center elements. It can be clearly observed that the embedded elements have better gain compared to the isolated element at higher frequencies. However, no significant change in 2:1 VSWR bandwidth is observed between the isolated and embedded elements (Figure G8).

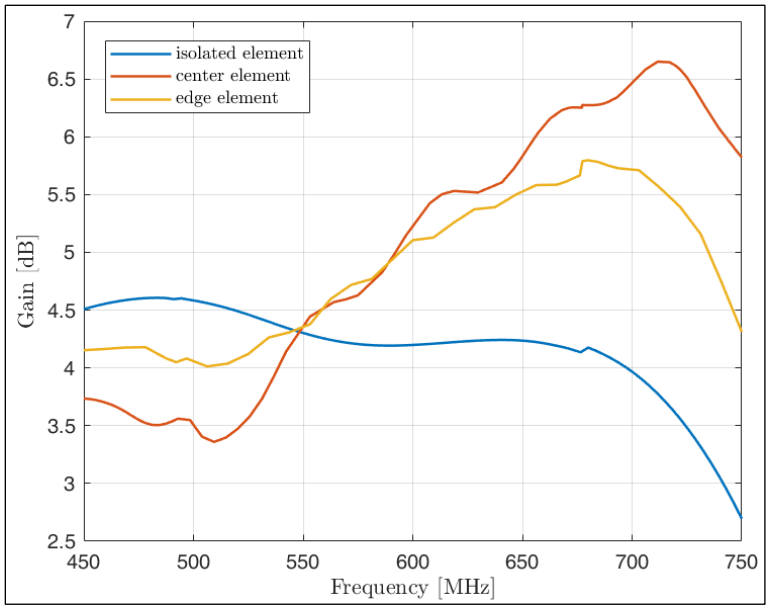


***Figure G7**. Gain as a function of frequency for isolated, center and edge elements.*

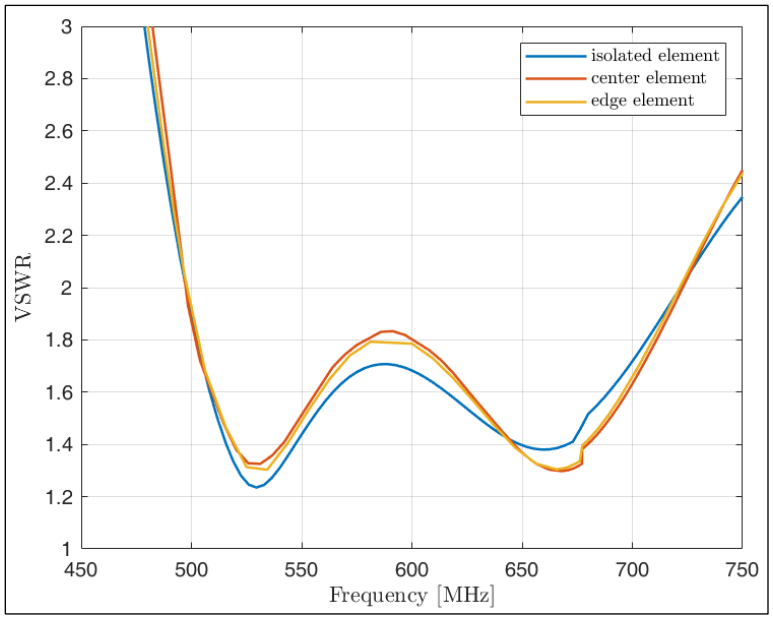


***Figure G8**. VSWR of the embedded and isolated elements (2:1 VSWR bandwidth is 36.79%).*

We have also obtained the radiation patterns of an isolated element and embedded elements (i.e., edge and center) in the Z-X plane ($\phi = 0$). It has been observed that mutual coupling has disastrous effect on the embedded element patterns. This can be clearly seen in Figure G9 which compares the radiation pattern of embedded and isolated elements at 592.2 MHz. The maximum gain of the isolated element is 4.24 dB, whereas for the edge and center elements it is 3.25 dB and 2.73 dB respectively.

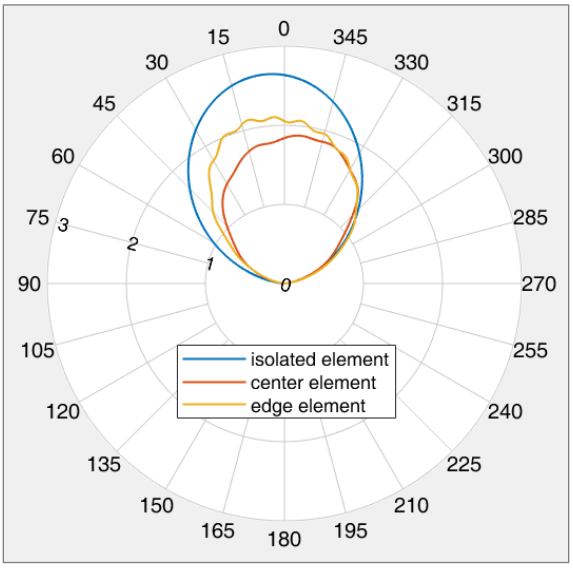


***Figure G9**. Radiation pattern of an isolated microstrip patch antenna and its radiation pattern in the array environment in the Z-X plane ($\phi = 0$).*

The radiation pattern of a fully excited linear array has been investigated. Apart from uniform excitations we have considered non-uniform amplitude distributions such as Dolph-Chebyshev, Taylor Line Source and Bickmore-Spellmire. Radiation patterns in the Z-X plane ($\phi = 0$) at the two edge frequencies (497.5 MHz and 722 MHz) and at the center frequency (609.75 MHz) of the 2:1 VSWR bandwidth are plotted in Figures G10-12.

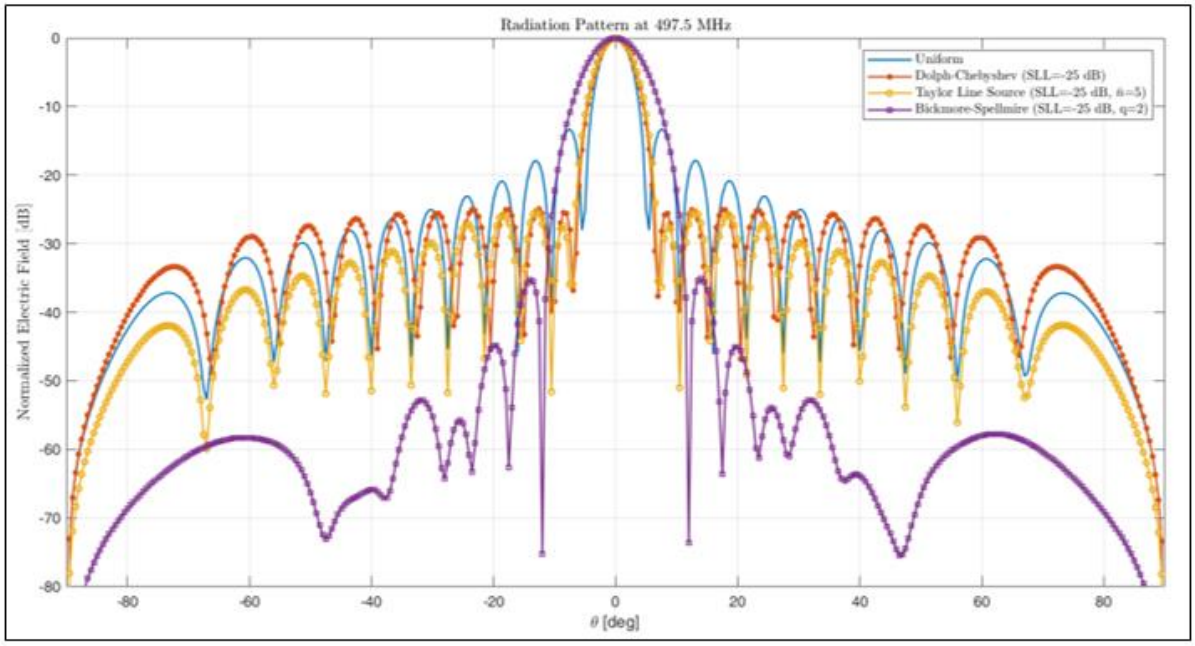


***Figure G10**. Radiation Pattern of the linear array at 497.5 MHz in the Z-X plane ($\phi = 0$).*

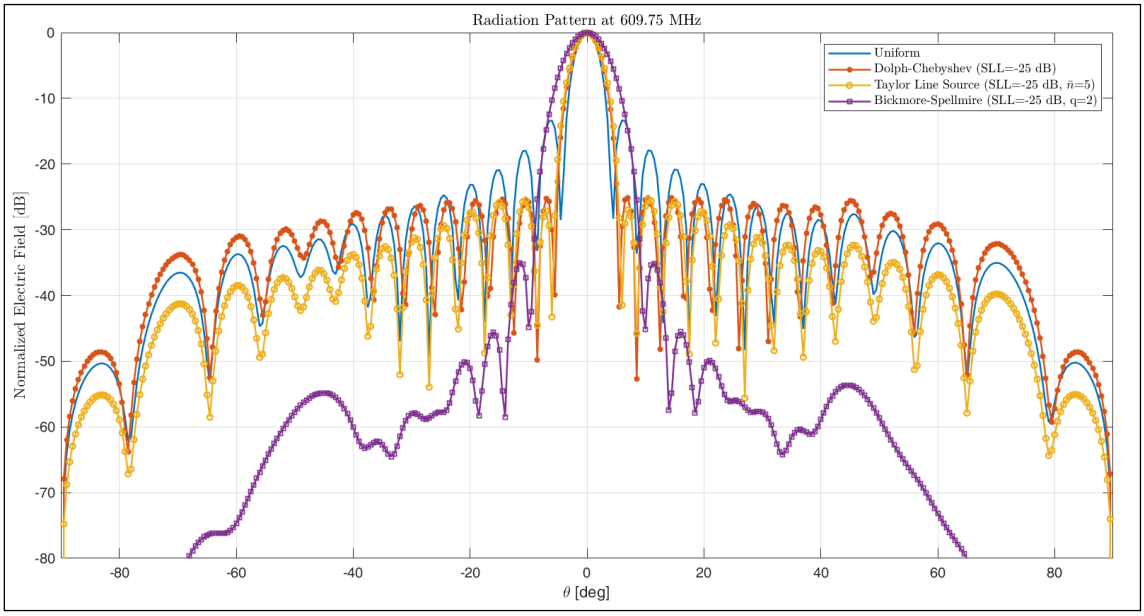


***Figure G11**. Radiation Pattern of the linear array at 609.75 MHz in the Z-X plane ($\phi = 0$).*

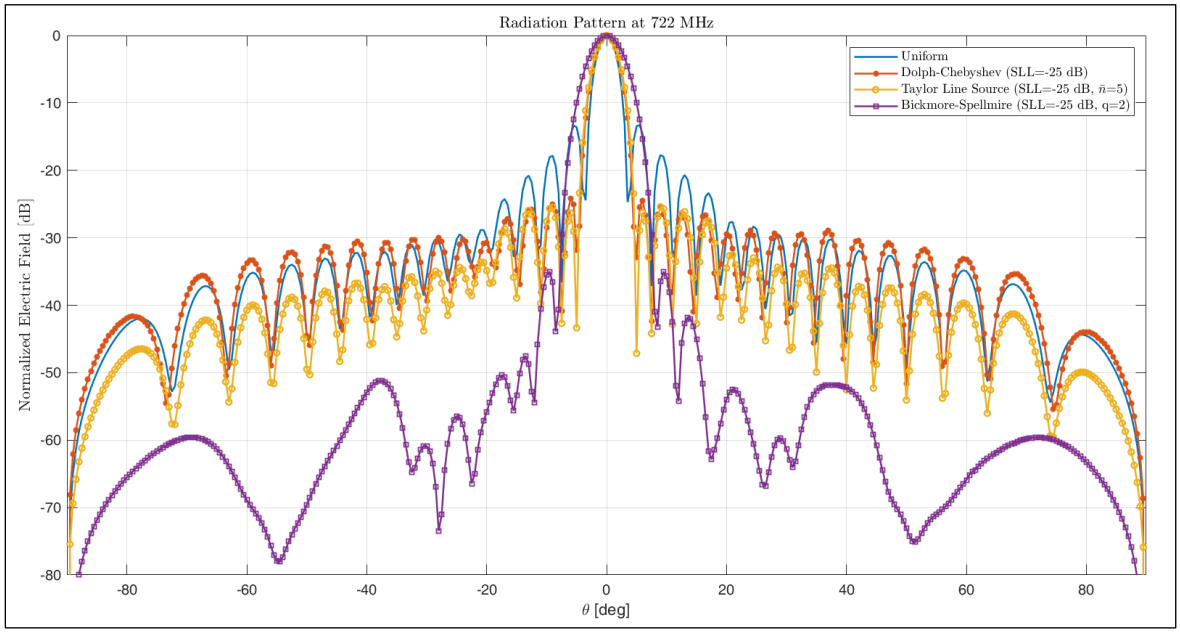


***Figure G12**. Radiation Pattern of the linear array at 722 MHz in the Z-X plane ($\phi = 0$).*

Bickmore-Spellmire distribution has minimum sidelobe levels but maximum half-power beamwidth. This reduces the array gain for Bickmore-Spellmire distribution. Boresight gains of the linear array for uniform, Taylor and Bickmore-Spellmire distributions are shown in Figure G13. As expected, the uniformly excited array records the maximum gain compared to non-uniform excitations. For Taylor Line Source method, maximum gain of 19.84 dB is obtained at 690.62 MHz, whereas in case of Bickmore-Spellmire it is 18.17 dB at 689.84 MHz.

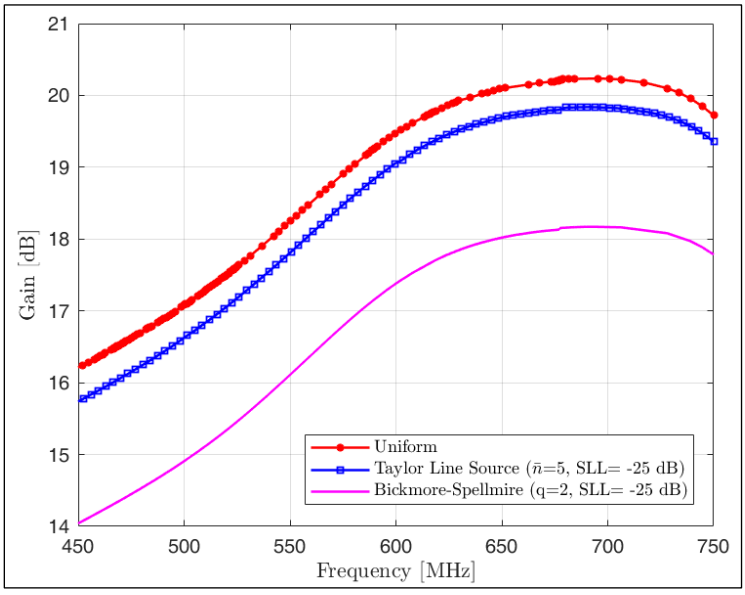


***Figure G13**. Boresight gain vs. frequency for different amplitude distributions.*

After preliminary investigations of array characteristics, we get back to improving the element design. Our next target is to improve the bandwidth without changing the element dimensions. According to the literature, bandwidth can be improved by using proximity coupled feed such as L-probe [4]. In L-probe feed the probe does not touch the patch but is bent horizontally from a certain height. Capacitances are developed between the horizontal length of the probe and the ground plane and also between the horizontal length and patch. These capacitances cancel out the inductance of the vertical section of the probe resulting in wider bandwidth.

For our computations, we have taken the same microstrip patch antenna with TMM-4 substrate and replaced the straight probe with an L-probe feed. Figure G14 shows the geometry of the L-probe fed patch. TCM and parametric analysis have been done to find out the effects of the contributing modes.

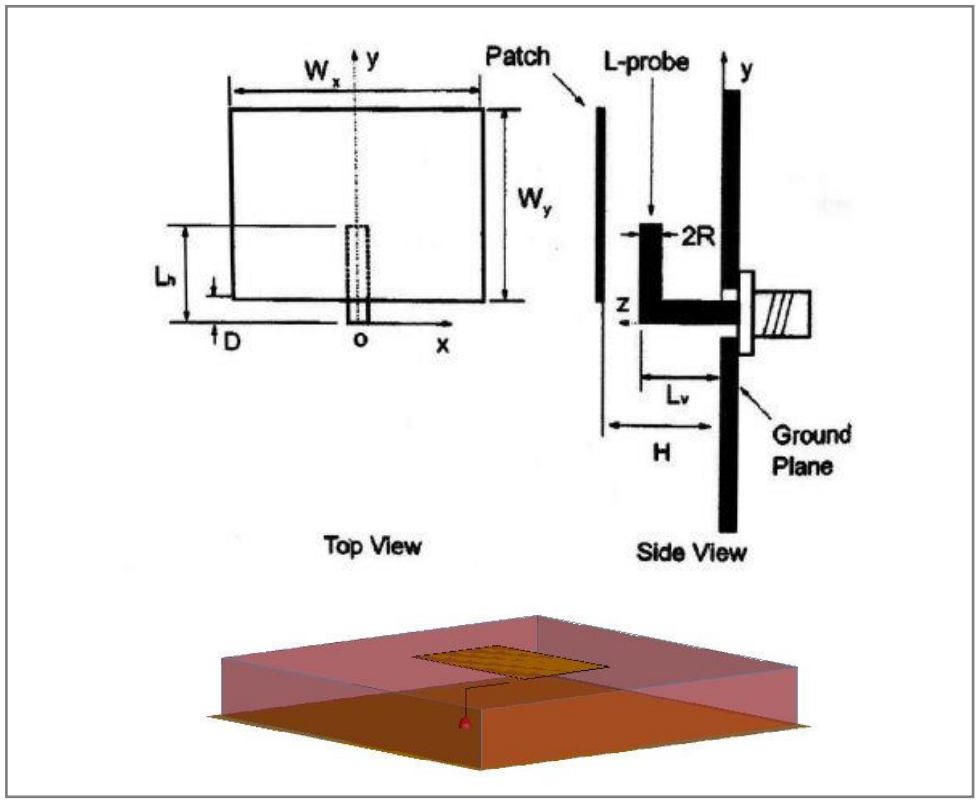


***Figure G14**. Geometry of the L-probe fed microstrip patch.*

Variation in Probe Radius

The radius is kept uniform throughout the vertical and horizontal sections of the probe. Improvement in the bandwidth with increasing probe radius is summarized in the table below. It can be observed in Figure G15 that mode J3 has the maximum contribution for the VSWR bandwidth.

***Table G3**. Effects of changing probe radius on percentage bandwidth.*

L_V=25 mm, L_H = 40 mm					
r_p (mm)	f_L (MHz)	f_c (MHz)	f_U (MHz)	%BW	Max. Gain (dB)
5	596.3	644.1	691.9	14.84	3.80225
6	594.6	646.3	698	15.99	3.80686
7	592.5	648.15	703.8	17.17	3.80988
8	591.1	650.4	709.7	18.23	3.81109

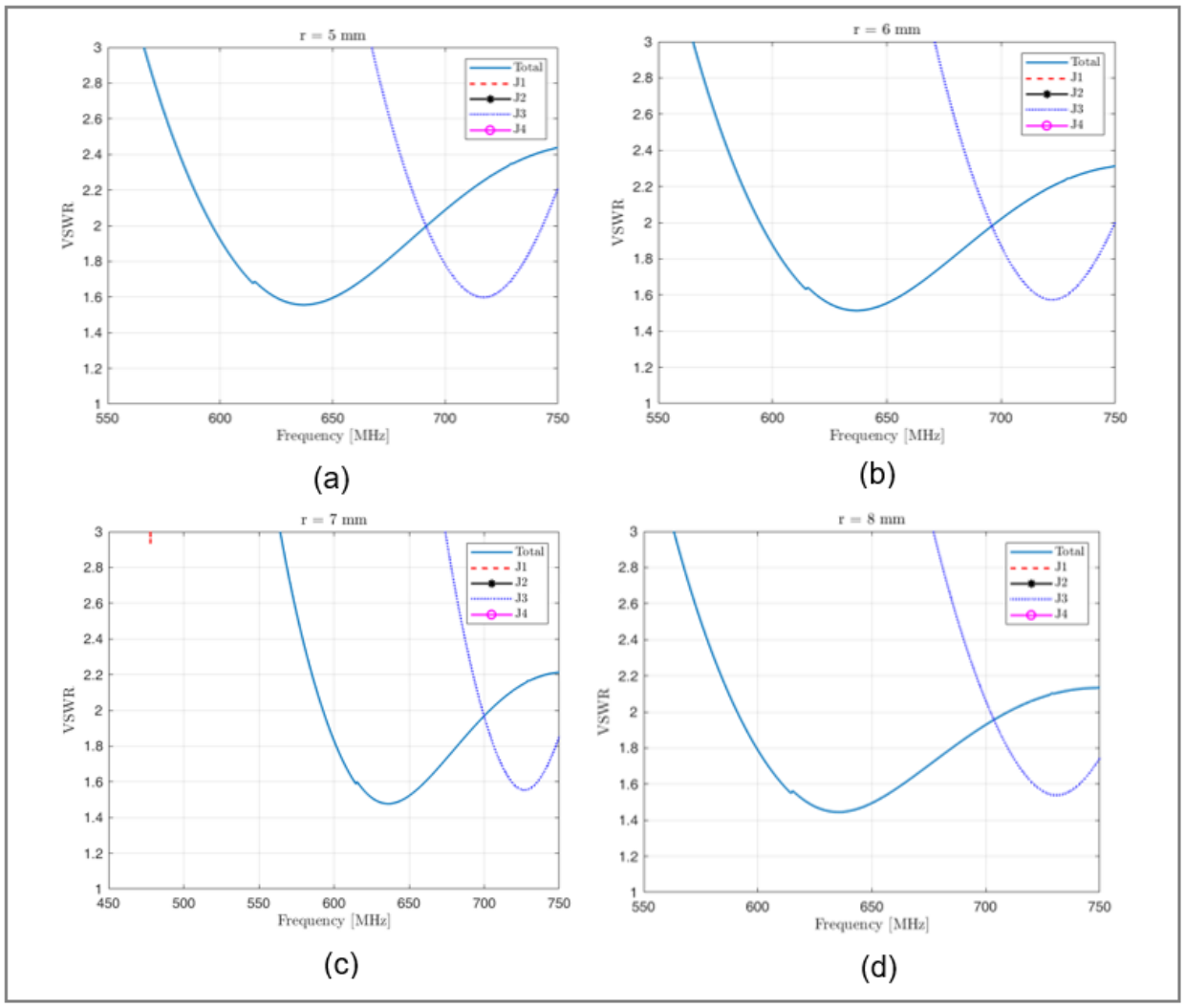


***Figure G15**. TCM analysis of VSWR for different probe radius at $\varepsilon_r = 4.5$, h=43.0115 mm, W=135.7934 mm, L=79.8785 mm, L_V=25 mm, and L_H=40 mm.*

Variation in the Vertical Length of the p\Probe (L_V)

Keeping the radius of the probe constant at 8 mm, we have varied the vertical height of the probe. A drastic increase in the bandwidth is noted at L_V=29 mm. Figure G16 shows the VSWR for different values of L_V.

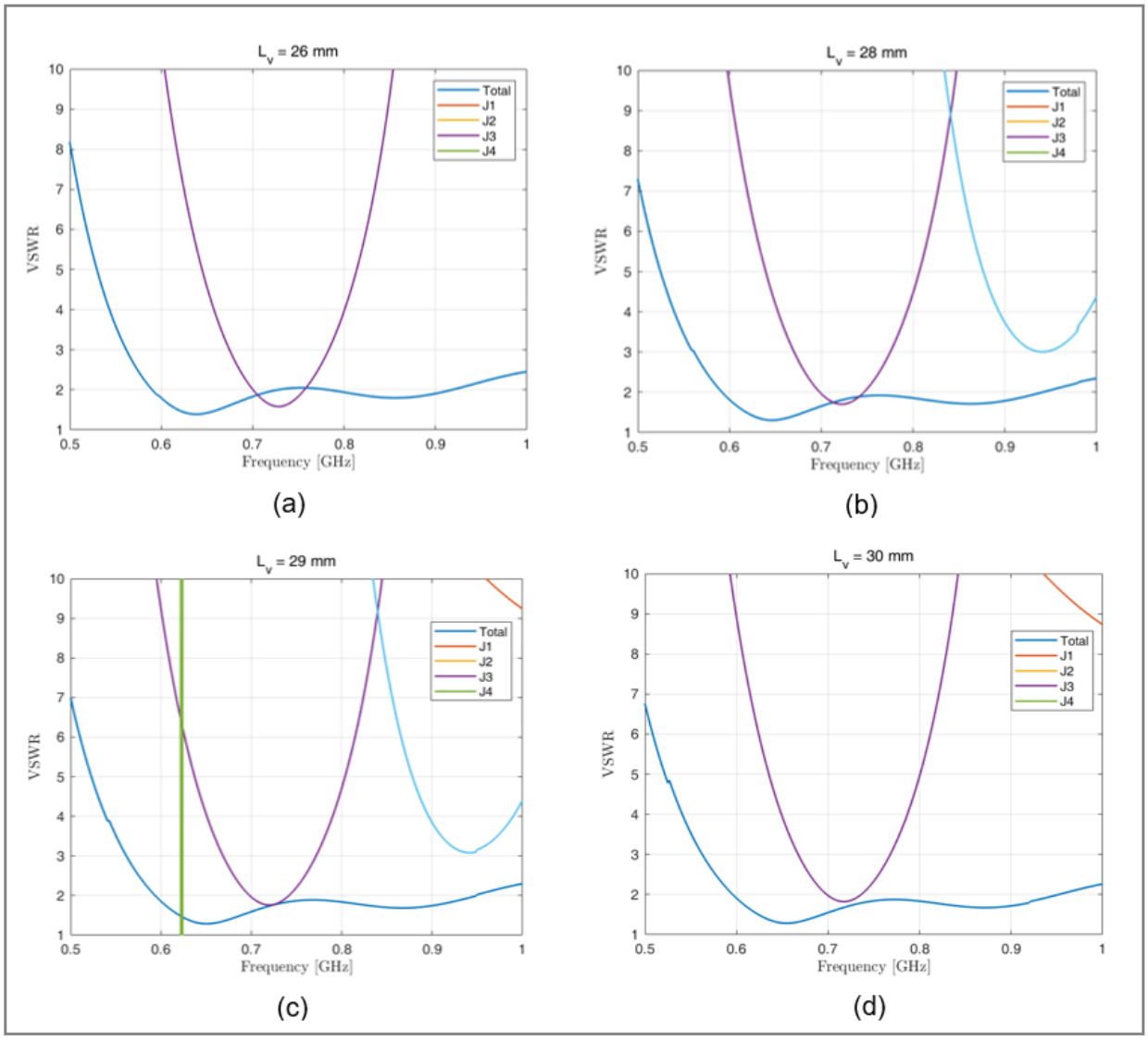


***Figure G16**. TCM analysis of VSWR for different L_V at $\varepsilon_r = 4.5$, h=43.0115 mm, W=135.7934 mm, L=79.8785 mm, L_H=40 mm, and $r_p = 8\ mm$.*

The increase in bandwidth can be attributed to the excitation of higher order modes. From Figure G16 it can be seen that other than mode J3, mode J5 contributes for the bandwidth increment too. Antenna gain, which changes very little with increasing L_V, is plotted as a function of frequency in Figure G17. The maximum gain in each case is around 3.8 dB.

***Table G4**. Effect of increasing L_V the gain and bandwidth of the antenna.*

r_p = 8 mm					
L_V (mm)	f_L (MHz)	f_c (MHz)	f_U (MHz)	%BW	Max. Gain (dB)
26	590	659	728	20.94	3.78601
28	592	766.5	941	45.53	3.81483
29	593	771	949	46.17	3.80688
30	596	774	952	45.99	3.80128

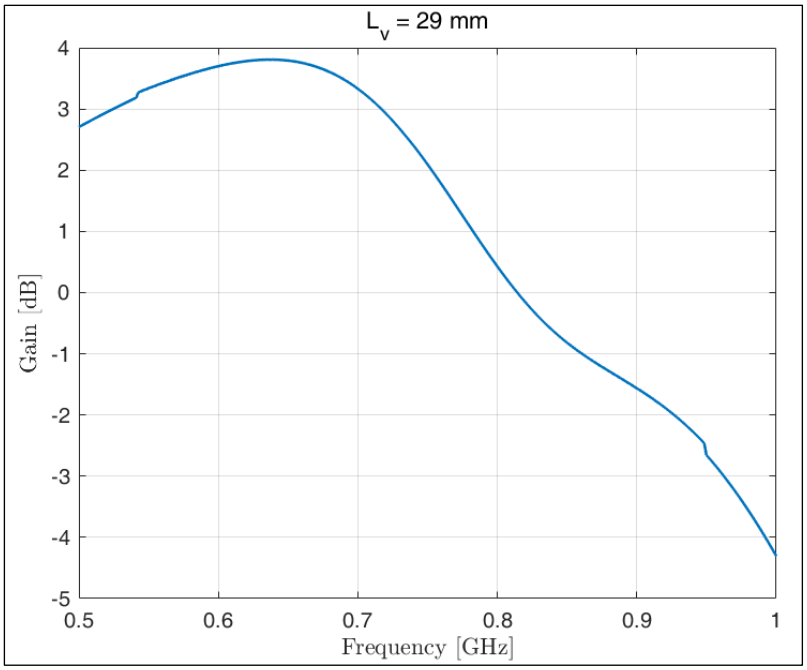


***Figure G17.** Boresight gain vs. frequency for $\varepsilon_r = 4.5$, h=43.0115 mm, W=135.7934 mm, L=79.8785 mm, L_H=40 mm, L_V = 29 mm, and $r_p = 8\ mm$.*

Similar analysis has been performed by varying the horizontal length of the probe and also by changing the probe location. Maximum bandwidth obtained is 46.17% for r_p = 8 mm, L_V = 29 mm and L_H = 40 mm.

The next aim is to use this element in an array and perform trade space analysis. This will be pursued next. So far we have used a nearly electrically small antenna for which $ka \approx 0.95$. We need to reduce the element size, using various miniaturization techniques available in the literature, to obtain an array of electrically small antennas.

Future Work

Antenna Miniaturization

As has been mentioned earlier, the size of the individual antenna elements must be reduced such that $\mathrm{ka} \leq 0.5$. To achieve that, we can use shorting wall or shorting pin with smaller patch dimensions. Preliminary investigations into L-probe fed microstrip patches with shorting wall has shown improvement in bandwidth but at the cost of tremendous reduction in gain. Ways to reduce the antenna size without having much impact on the gain and bandwidth will be looked into.

Element Design Optimization

Since the array pattern is a product of array factor and element pattern, designing an electrically small antenna efficiently is an important task. Each antenna element should have reasonable gain and bandwidth to meet design requirements. Hence, optimization of the antenna design forms one of our main goals. For optimization of electrically small antennas we are adopting two techniques:

i. Characteristic Mode Analysis (CMA): This has already been explored to some extent in this report and will be utilized more efficiently for optimizing the antenna performance.

ii. D/Q Ratio: This is a multi-parameter optimization technique first hypothesized by Gustafsson [5], [6] and later investigated by Shahpari *et al.* [7]. Here D is the directivity of the antenna which is a far-field parameter whereas Q is the quality factor, a near-field parameter. After preliminary optimization of an antenna (using CMA) with respect to its bandwidth and gain, we can obtain the D/Q ratio for that specific design. This would give an insight into the values of D/Q that usually result in the best gain and bandwidth combination in an ESA. Optimization of a design using parametric analysis is cumbersome and extremely time consuming (even using FEKO). A knowledge of D/Q ratio will help us to expedite the optimizations. In house code will be developed to derive the D/Q ratio of an electrically small antenna. The following steps will be used for writing the code:

   (a) Directivity (D): Directivity of an antenna can be derived using the general expression [8]:

$$\mathrm{D} = \frac{4\pi}{\lambda^2} \frac{\left| \iint_{\mathrm{Sa}} \mathrm{E_a} \mathrm{dS}' \right|^2}{\iint_{\mathrm{Sa}} |\mathrm{E_a}|^2 \mathrm{dS}'} \qquad (4)$$

However, as a start we can import the directivity values of a design from FEKO.

The results can later be verified against the values obtained through the general expression (eq. 4).

(b) Quality Factor (Q): Quality factor is given by [9]:

$$Q = \frac{w_r W_T}{\text{Associated power loss}} \qquad (5)$$

where, w_r is the resonant frequency (in radian) and W_T is the energy stored at resonance. The total quality factor can, therefore, be expressed in terms of the quality factors associated with various types of losses as [9]:

$$\frac{1}{Q_T} = \frac{1}{Q_d} + \frac{1}{Q_C} + \frac{1}{Q_r} + \frac{1}{Q_{sur}} \qquad (6)$$

where, Q_d, Q_c, Q_r, Q_{sur} are the quality factors associated with dielectric, conduction, space wave radiation and surface wave losses respectively and are given as:

$$Q_d = 1/\tan\delta \qquad (7)$$

$\tan\delta$ being the loss tangent of the dielectric substrate.

$$Q_c = h\sqrt{\pi f \mu_0 \sigma} \qquad (8)$$

$$Q_r = \omega_T W_T / P_r \qquad (9)$$

where, $$W_T = \frac{1}{4}\epsilon_0 \epsilon_r hLW \qquad (10)$$

Q_{sur} can be derived from the surface wave power through:

$$P_{sur} = -\frac{1}{2}\text{Re}\int_0^{\infty}\int_0^{2\pi} E_z H_\phi^* \rho \, d\phi \, dz \qquad (11)$$

FEKO does not have the option to directly import the quality factor of a design. Hence, we need to use the above relations (eq. 4-11) to derive it.

Another definition of minimum quality factor for electrically small antennas first derived by Chu and later by Collin and Mclean is [7], [10]:

$$Q_{TE+TM} = \frac{1}{2(ka)^3} + \frac{1}{ka} \qquad (12)$$

This equation, however, does not account for any other parameters of the patch other than its electrical length and operating frequency. We need to investigate which of these two quality factor expressions is more accurate for this technique. Interestingly, preliminary investigations have shown that different antennas with same ka value have different gain and bandwidth, thus, rendering eq. (11) insufficient for our considerations. Figures G18 shows the gain and bandwidth of a simple rectangular patch and a rectangular patch loaded with U-slot respectively. The U-slot loaded rectangular patch

has been designed using the Dimensional Invariance Method [11]. In both the antennas ka=0.67, yet they have different characteristics in terms of gain and bandwidth. The dimensions, percentage bandwidth and gain of these two antennas have been enlisted in Table G5.

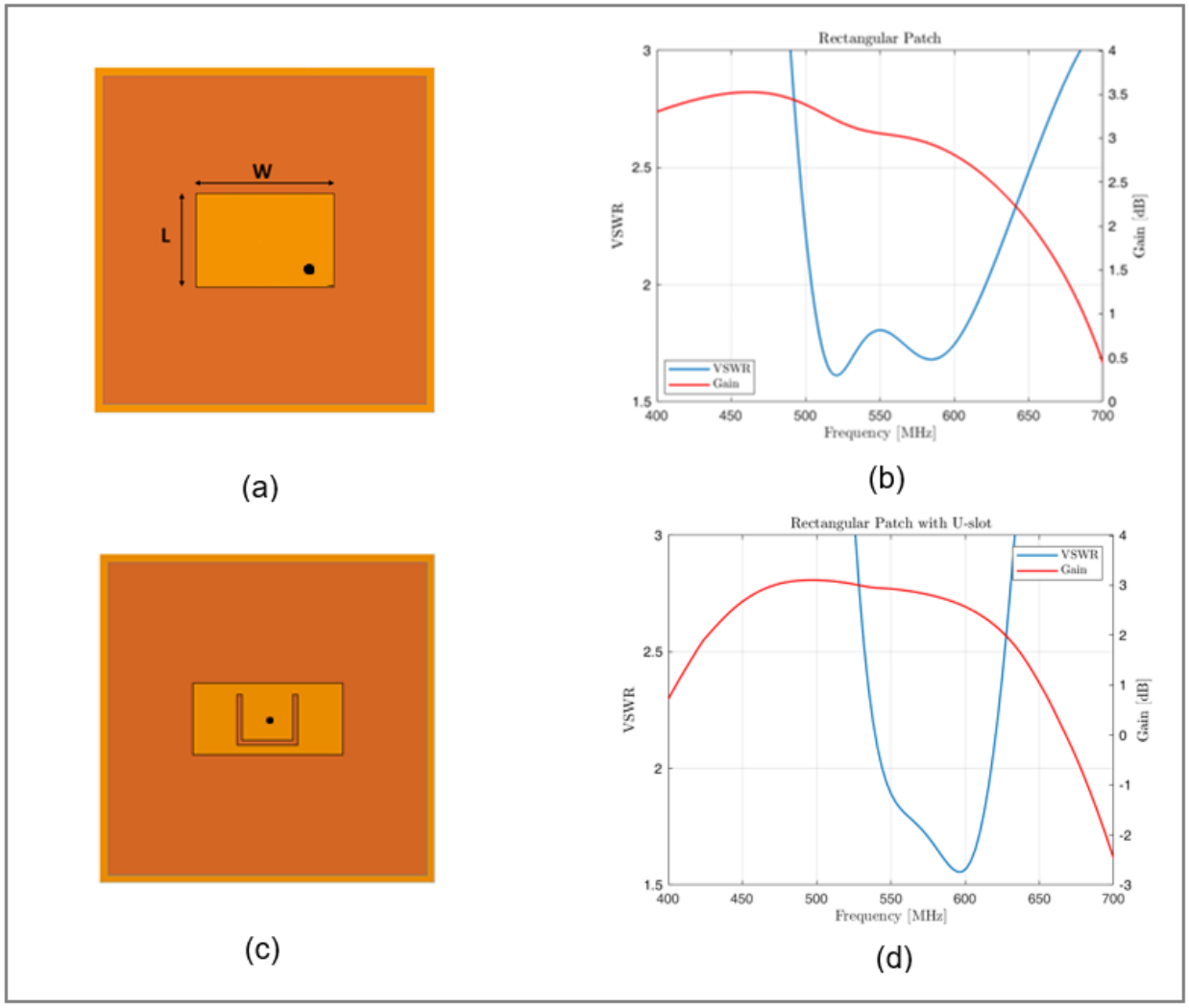


***Figure G18**. (a) Rectangular patch (b) gain and bandwidth of the rectangular patch (c) U-slot loaded rectangular patch (d) gain and bandwidth of the u-slot loaded patch.*

***Table G5**. Summary of the simple patch and U-slot loaded rectangular patch with same ka value.*

Parameters	Rectangular Patch	U-Slot loaded Patch
ε_r	9.8	9.8
$\tan\delta$	0.0020	0.0020
h (mm)	29.1459	29.1459
$h\sqrt{\varepsilon_r}/\lambda$	0.175	0.175
L (mm)	65.3561	65.3561
W (mm)	90.3524	90.3524
L_s (mm)	-	45.2465
W_s (mm)	-	35.1566
r (mm)	3.5	1
(x_p, y_p)	(21.7853, 30.1174)	(-5,0)
f_L(MHz)	504.2	544.2
f_c(MHz)	562.8	580.95
f_U(MHz)	621.4	617.7
%BW	20.82	12.65
Max. Gain (dB)	3.52555	3.10337
ka	0.6719	0.6719

Developing In-house Code for Analyzing ESAs

Full wave simulations of linear arrays require 6-7 hours of computations using the Supercomputer available with the University. Therefore, codes should be developed for speedy computations. Applicability of the D/Q ratio for array optimizations should also be looked into in the future.

Fabrication and Experimentation

After performing all the trade space analysis of the linear array with microstrip patches our next aim is to validate the results through experiments. We are planning on fabricating a linear array of microstrip patches (ka=0.95) at University of Missouri-Rolla campus. Measurement of different parameters such as, embedded element gain vs. frequency, array gain vs. frequency, and radiation pattern for different types of amplitude distributions will be performed. Comparison of the simulated results with the measured ones would give us an insight regarding the validity of our approach. The fundamental limitations that will be looked into are:

i. Beam Steering: Scanning the main beam when the inter-element spacing is too large can result in peaks other than the main beam within the visible region. These are called grating lobes. Techniques to reduce these undesired grating lobes will be investigated in the future.
ii. Mutual coupling, which has disastrous effects on the element pattern and hence on the entire array, must be reduced.

Conclusion

A simple probe fed microstrip patch antenna (ka=0.95), having 36.79% bandwidth in the UHF region, has been designed. CMA of the patch has been performed to understand the contribution of the various modes in its behavior. A linear array is modeled using this antenna as the array element. Gain of the edge and center elements (when all the other elements are terminated in matched loads) are compared to the isolated element gain. It is observed that the embedded elements have better gain at higher frequencies compared to that of the isolated element. Embedded element gain characteristics are similar to the full array gain which increase with rising frequency.

Effect of different amplitude distributions on the sidelobe levels of the array radiation pattern has been observed. Bickmore-Spellmire distribution has the lowest sidelobe level at the cost of increased half-power beamwidth (or reduced gain).

Efforts have been made to increase the bandwidth of the nearly electrically small antenna using L-probe feed. Optimization of the structure using CMA has resulted in an antenna with 46.17% bandwidth for the same ka=0.95. Further investigations to reduce the size of the antenna using shorting wall will be done in future.

References

[1] J. L. Volakis, C. C. Chen, and K. Fujimoto, *Small Antenna Miniaturization Techniques and Applications*. New York, NY, USA: McGraw-Hill, 2010.
[2] D. R. Jackson, *Introduction to Microstrip Patches,* IEEE International Symposium on Antennas and Propagation and USNC-URSI National Radio Science Meeting. Jul. 2013.
[3] D. M. Pozar, "The active element pattern," *IEEE Trans. Antennas and Propag.*, vol. 42, no. 8, pp. 1176-1178, Aug. 1994.
[4] K. F. Lee, K. M. Luk, and H. W. Lai, *Microstrip Patch Antennas*. 2nd Ed. New Jersey, USA: World Scientific, 2018.
[5] M. Gustafsson, C. Sohl, and G. Kristensson, “Illustrations of new physical bounds on linearly polarized antennas,” *IEEE Trans. Antennas Propag*., vol. 57, no. 5, pp. 1319-1327, May 2009.
[6] M. Gustafsson, C. Sohl, and G. Kristensson, “Physical limitations on antennas of arbitrary shape,” Proc. R. Soc. A, vol. 463, no. 2086, pp. 2589-2607, 2007.

[7] M. Shahpari, D. V. Thiel, A. Lewis, “An Investigation Into the Gustafsson Limit for Small Planar Antennas Using Optimization,” *IEEE Trans. Antennas and Propag.*, vol. 62, no. 2, pp. 950-955, Feb. 2014.

[8] W. L. Stutzman, and G. A. Thiele, *Antenna Theory and Design*. USA: John Wiley & Sons, 2012.

[9] R. Garg, P. Bhartia, I. Bahl, and A. Ittipiboon, *Microstrip Antenna Design Handbook*, Boston, USA: Artech House, 2000.

[10] R. C. Hansen, and R. E. Collin, *Small Antenna Handbook*, New Jersey, USA: John Wiley & Sons, 2011.

[11] M. Khan, and D. Chatterjee, "Characteristic Mode Analysis of a Class of Empirical Design Techniques for Probe-Fed, U-Slot Microstrip Patch Antennas," *IEEE Trans. Antennas and Propag.,* vol. 64, no. 7, pp. 2758-2770, July 2016.

[12] R. F. Harrington, *Time Harmonic Electromagnetic Fields*, New York, USA: McGraw-Hill,1961

[13] R. S. Elliott, *Antenna Theory and Design*. John Wiley & Sons, 2003.

[14] R. J. Mailloux, *Phased Array Antenna Handbook,* 3rd ed. Boston, USA: Artech House, 2018.

Studies on Balun Style Impedance Transformer Design (James Kovarik)

A component is needed to transfer an EM wave from a parallel plate transmitter input into a coaxial cable output. The parallel plate transmitter has dimensions of 1.4 cm by 8 cm, and the coaxial cable is to be 2.5 cm thick. The primary goal is to maximize scattering parameters between the ports using frequencies from 500MHz to 1.5 GHz.

Much of the research is based on research into balun transformers [1], as well as work looking into transition from coaxial cables to rectangular waveguides using a horn design [2]. The balun transformer from Duncan’s work does not properly match the transformer as we want it, so the initial design incorporates the horn design to compensate for that.

The design currently under investigation is a tapered balun that primarily operates by gradually tapering the positive plate into the center of the coaxial output, while the ground plane curls into the coax shield through a conical shape. This design is beneficial as it provides for a lot of variation in design to optimize the component and allow good transmission.

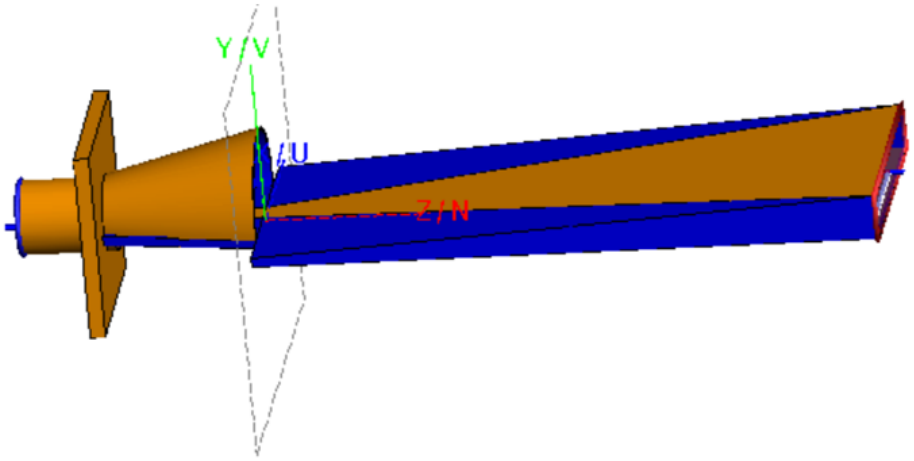


***Figure G19**. Initial design.*

The primary trouble in the simulation is properly simulating the incoming and outgoing transmissions. Using standard waveguide ports gives unexpected results, and we suspect it is because FEKO is not properly differentiating between a regular rectangular waveguide and the parallel plate waveguide that is in the component. We are concerned that the S12 parameters are showing gain at certain frequencies where there should be none (Figure G22). This is supported by power transmission through the component (Figure G21). We are currently looking into using Finite Element Method ports or edge ports instead and see if it gives better results. We can, however, glean some good things from the waveguide results. When tested at 600MHz, the scattering parameters are very high (>.9) and increases with length, which is to be expected (Figure G20).

We expect to see verifiable results in the coming weeks, and consequently an initial design that can be built and tested. Our current goals are to ensure proper port simulation in FEKO and to further optimize the component into a good adapter.

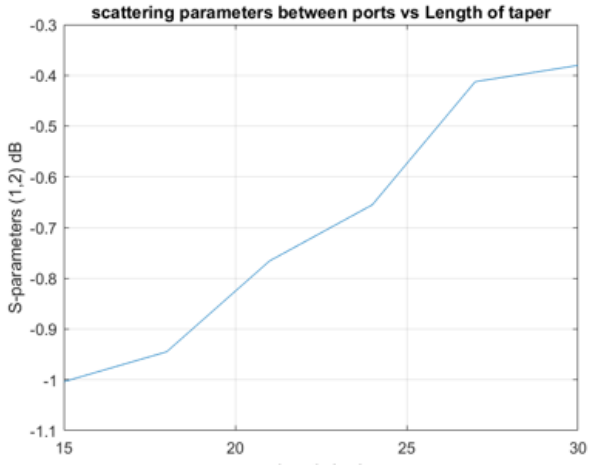


***Figure G20**. Transmission is less lossy with increased length.*

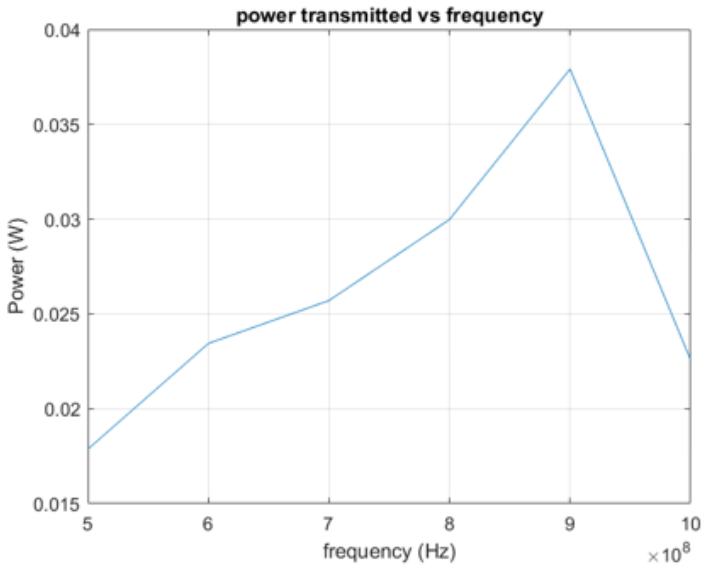


Figure G21. *Power transmitted hits a maximum at 900 MHz, where the unaccounted for gain is.*

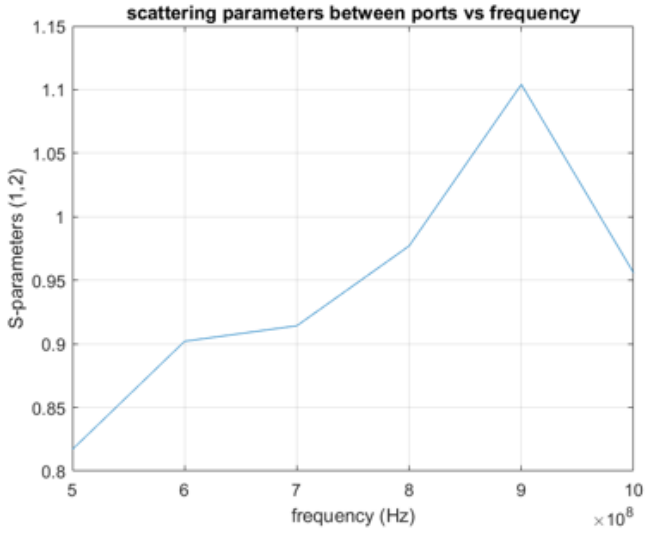


Figure G22. *Scattering parameters. Unaccounted for gain is found at around 900 MHz, as shown by S(1,2) rising above 1.*

References

[1] J. W. Duncan and V. P. Minerva, “100:l bandwidth balum transformer,” Proc. IRE, vol. 48, no. 2, pp. 156-164, Feb. 1960.

[2] Louis N. Ridenour, *Microwave Transmission Circuits,* first edition, pp. 314-361, Office of Scientific Research and Development, McGraw-Hill Book Company, 1948

Studies on Tapered Impedance Transformer Designs (William Spaeth)

Simulations on the Tchebycheff taper and alternate impedance transformer designs (Figure G23) provided by Eliot have been performed. These simulations of the Tchebycheff taper showed high amounts of reflection that could not be decreased through alteration of any dimensions. Increasing the length of the taper decreased reflection slightly, but an S1-1 parameter lower than 0.45 could not be achieved. Coupled with the difficulty in fabricating this design effort was focused on the second taper design provided.

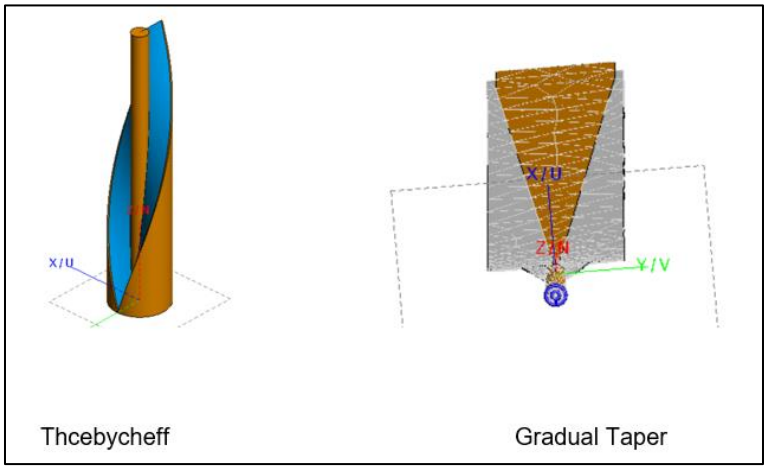


Figure G23: *Models of the Tchbycheff and gradual taper design impedance transformers.*

The gradual taper design presents its own issues, but overall looks much more promising than the Tchebyceff. After running several simulations and optimizing the design, FEKO was returning incorrect S-parameters that were greater than 1. Simulations were run on each individual section of the taper to try to identify the problem. The coax section behaved almost ideally, it is believed that the issue is caused by the parallel plate waveguide port. Simulations using the rectangular waveguide port as it matches the geometry were run but this option in FEKO only supports 4-wall rectangular waveguides and were not suitable for the gradual tape design. Currently, simulations with alternative types of ports are being run. Using an edge port design, S-parameters that were more realistic were achieved (Figure G24).

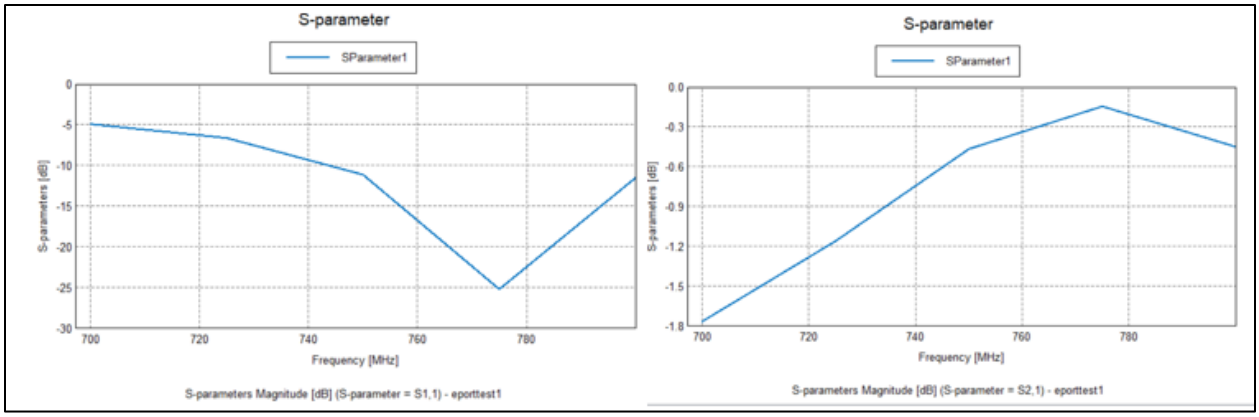


Figure G24: *S-parameters for the gradual taper design*

This taper was designed for 800MHz. Transmission peaks around 775MHz. The S1-1 parameter shows reflection of -25dB at this frequency. The VSWR plot is as follows in figure G25:

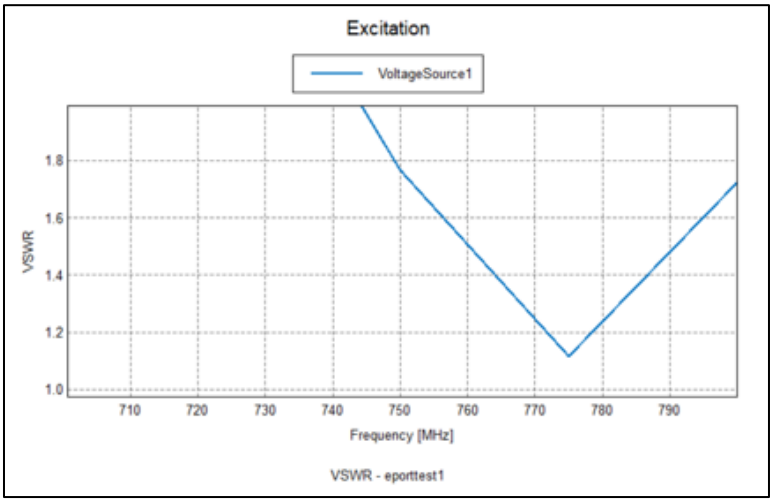


***Figure G25**: VSWR for the gradual taper design shows -25dB S11 at 775MHz*

In figure G25 the graph goes below 1.2 at 775MHz. This value also corresponds to minimum power loss:

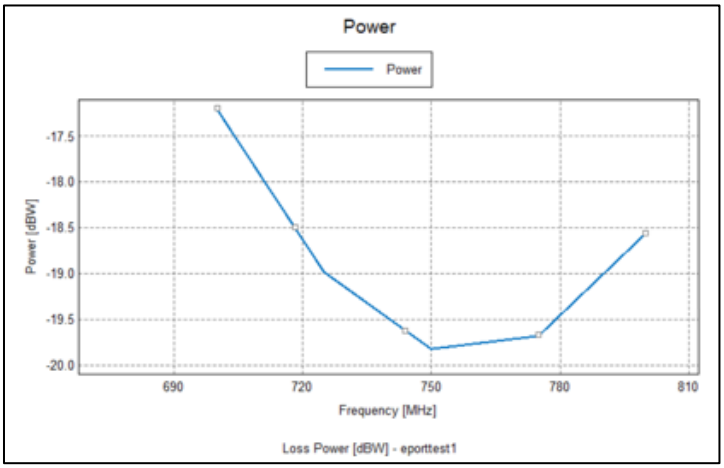


***Figure G26:** Power as a function of frequency for the gradual taper design*

The design has several parameters that can be altered to optimize the design. The above results are from a taper of length 30cm. Depending on the design constraints the taper can be lengthened to increase transmission further. Adding a cone to the outer layer of the coaxial cable can also be experimented with to improve results.

I.H Cost Estimates and Engineering (Doynov)

Moved to Contract Report.

II. Issues:

None

III. Interactions with Others:

IV. Major Procurement Actions:

V. Travel:

Travel Plans

Please note that all papers or presentations on any aspect of the ONR HPM program must be reviewed by the ONR Program Officer (or in some cases ONR Public Release Process) regardless of classification level or audience.

Planned Travel Details	Purpose	Attendees	Estimated Costs
2019 IEEE	Antenna Conference	Chatterjee group	Not established yet

VI. Pending or Upcoming Public Release Requests:

i. M. Z. M. Hamdalla, A. N. Caruso, Ahmed M. Hassan, "Characteristic Mode Analysis of the Effect of the UAV Frame Material on Coupling and Interference," *Submitted to the IEEE International Symposium on Antennas and Propagation and USNC-URSI Radio Science Meeting at Atlanta, Georgia*, USA, 7-12 July 2019.

ii. M. Z. M. Hamdalla*, Ahmed M. Hassan, A. N. Caruso, J. D. Hunter, Y. Liu, V. Khilkevich, D. G. Beetner, "Electromagnetic Interference of Unmanned Aerial Vehicles: A Characteristic Mode Analysis Approach," *Submitted to the IEEE International Symposium on Antennas and Propagation and USNC-URSI Radio Science Meeting at Atlanta*, Georgia, USA, 7-12 July 2019.

VII. Selected Highlights (text and/or images):

None

ONR HPM 2019 Program - Monthly Status Report (MSR) – JULY2019
Anthony Caruso – Univ. Missouri – Kansas City
N00014-17-1-3016 [OSPRES Grant]
ONR Short Pulse Research, Evaluation and non-SWaP Demonstration for C-sUAV Study

8/10/2019

Distribution Statement ~A: Distribution authorized to all OSPRES Grant and Contract Participants, and any uncompensated collaborators. Further dissemination per Ryan Hoffman (ryan.hoffman@navy.mil).

OSPRES Project Description: Develop tunable High Power Microwave (HPM) sources and electronically steerable radiators whose waveform(s) enable control over all levels-of-lethality on cUAV and similar targets, with the least power density.

Contents

Executive Summary: 3
Current Month Progress: 4
I. Source Development (Myers) 4
A. *Power Conditioning – IGBT (Khan)* 4
B. *Switches - GaN:C (Thompson/Myers)* 4
C. *Switches - Figure of Merit (Bhamidipati)* 4
II. Effects, Coupling and UAS Developments (Lancaster) 5
D. *RF Coupling (Hassan)* 5
E. *UAS Developments (Fields)* 5
III. Antenna Development (Ahern) 5
F. *Antennas* - Electrically Small Antennas (Chatterjee/Barman) 5
G. *Antennas* - Log Periodic (Hassan) 8
IV. Research and Development Support (Smith) 8
H. *Mechanical Designs (Smith)* 8
I. *Device and Materials Modelling (Eifler)* 8
J. *GaN:C Simulations (Rulis)* 8
V. Miscellaneous (Crow) 9
Issues: 9
Interactions with Others: 9
Major Procurement Actions: 9
Travel: 9
Pending or Upcoming Public Release Requests: 10
Selected Highlights (text and/or images): 10

Executive Summary:

Highlights from the grant performers in JUL2019 include: (A) driver efficiency improvement through addition of RC elements; (B) demonstrated GaN:Fe linear mode PCSS on-state resistance competitive with SiPCSS devices within the same order of energy per laser pulse; (C) finer temporal mechanisms are being included in carrier transport and circuit level simulations, showing an increase in maturity in understanding of the pulsed power operation of the PCSS; (D) clever implementation of Numerical Green's Function have allowed for a tenfold increase in the number of UAV wire simulation permutations that can be run; (D) the RF Coupling impact of neighboring macroscopic inductive elements on secondary UAV components are showing systematic trends, but still many studies to go to reach sweeping conclusions…stay tuned; (E) average E-field sensor boards have been built, calibrated and tested for free-flight free-space effects testing; (F) the patch-based electrically small antenna elements show element level promise, with individual gain of 1.5x that of the antipodal counterparts, but with a tradeoff in bandwidth…stay tuned on all radiator property comparisons; (F) PCSS modelling had incremental improvements, but, formed the foundation to work toward contact pattern optimization…should be interesting output in the coming months from this subgroup.

Current Month Progress:

I. Source Development (Myers)

A. *Power Conditioning – IGBT (Khan)*

i. A PCB accommodating a solid state switching device and a current sensor has been fabricated to test the PCSS performance.
ii. We have tested a commercial 14 kV rated HV switch connected in series with the PCSS switch in our experimental setup. We have conducted experiments for a supply voltage up to 1000 V. Intriguingly, even at this high voltage, the output pulse holds its expected shape, and almost reaches the theoretical peak amplitude limit of 500 V.
iii. Our proposed solution has proven effective in reducing voltage and current ringing associated with the PCSS device, thereby reducing power dissipation substantially.

B. *Switches – GaN:C (Thompson/Myers)*

i. A new THG crystal has enabled much greater laser pulse energies (ones to tens of μJ) and we are able to consistently achieve a V_{pulse}/V_{charge} ratio of 1 at V_{charge} of 150 V or more.
ii. The next steps are to begin applying the passivation provided by NRL to the device and testing at higher voltages at low repetition rates.
iii. We are using spice models to improve the PCB pulsing circuit and combining with experimental results to predict the thermal requirements of a GaN PCSS at higher power.

C. *Switches – Figure of Merit (Bhamidipati)*

i. We are currently working on a figure of merit manuscript for PCSS to include the losses due to transient turn-on and turn-off states.
ii. SPICE models of a class-E amplifier circuit have been conducted, but we need additional tuning to achieve efficient switching operation.
iii. We are beginning initial modeling of simple pulse-forming networks to compare to slow-recovery (on the order of microseconds) PCSSs such as Si.

II. Effects, Coupling and UAS Developments (Lancaster)

D. *RF Coupling (Hassan)*

i. As the number of different combinations of UAV's component increases, the computational time required for the statistical analysis significantly increases. Therefore, we are currently adapting the Numerical Green's Function (NGF) approach in FEKO to reduce the computational time. That is, we can simulate the UAV frame, typically the largest component, one time and store its NGF. Then we can run hundreds of simulations where we vary the parameters of the UAV's wires/PCBs. Each time we would change any parameter of the wires/PCBs whilst keeping the frame unchanged, we don't need to re-simulate the frame but we can simply load its saved NGF. The new technique reduces the computational time by one order of magnitude while maintaining exactly the same accuracy.

ii. We studied how a conducting UAV frame affects the coupling to adjacent wires. We proved that conducting frames with a quadcopter shape totally changes the coupling behavior to wires. For example, some incident angles will lead to minimal coupling to a wire in free space, but once the wire is placed on a conducting frame the same angles will lead to maximum coupling. We will investigate how this change in coupling behavior will affect the probability of effect.

E. *UAS Developments (Fields)*

i. Manufactured unmanned aircraft (fixed wing and multirotor) for indoor and outdoor testing (nearly 30 assets manufactured).

ii. Manufactured and calibrated RF sensor packages for use in outdoor testing.

iii. Refreshing the sensor-level direct inject software for use in outdoor non-HPM testing.

III. Antenna Development (Ahern)

F. *Antennas* - Electrically Small Antennas (Chatterjee/Barman)

i. The goal is to design electrically small antennas (electrical length, $\mathrm{ka} \leq 0.5$) having $\approx$ 1 GHz bandwidth at three different center frequencies: 600 MHz, 800 MHz, and 1 GHz.

ii. So far, the behaviors of simple microstrip patches with different types of feed such as straight probe and L-probe, have been studied through full wave simulations in FEKO at 600 MHz.

iii. At 600 MHz center frequency, the simple probe fed rectangular patch on TMM-4 substrate ($\varepsilon_r = 4.5, \tan\delta = 0.0020$) yields a maximum

bandwidth of 42.6949% whereas, with L-probe the maximum bandwidth obtained is 51.0986%.

iv. However, the maximum gain obtained using the straight and L-probe feed are 4.6776 dB and 3.81 dB respectively. Unlike a simple probe fed patch, in L-probe feed, the gain is unstable and drops suddenly within the desired frequency range. Hence, we are only considering straight probe fed patches for the preliminary trade space analysis of the array.

v. Optimization of the antennas at 800 MHz and 1GHz center frequencies are being carried out at the moment. This will be followed by fabrication of the antennas along with experimental validations of the simulated results.

Impedance Transformer for GTEM (Kovarik/Myers/Chatterjee)

i. We were able to come to the conclusion that the faulty simulations were because of FEKO calculating the parallel plate port as a rectangular waveguide. The geometry did not match the calculations and this was the cause of the unpredictable results. To solve this, we had to construct the port manually, using edge port parameters, instead of using the waveguide port function. The resultant port did work as it should.

ii. After the simulation worked, we were able to further optimize the transformer, until we reached a good design. The final design contains low reflection parameters (<20%) (Figure F1), high transmission parameters (>90%) (Figure F2), and a wide bandwidth (Figure F3).

iii. After design was completed, we decided on material (copper for the conducting plates, tapered polystyrene for the taper, and ABD for the cone), and built step files and instructions for fabrication. Two transformers will be fabricated and tested end-to-end so that we can measure with both coax-in and coax-out.

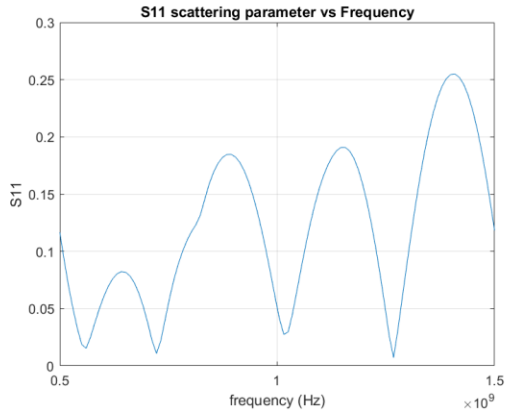


***Figure F1**. Scattering parameters for S11.*

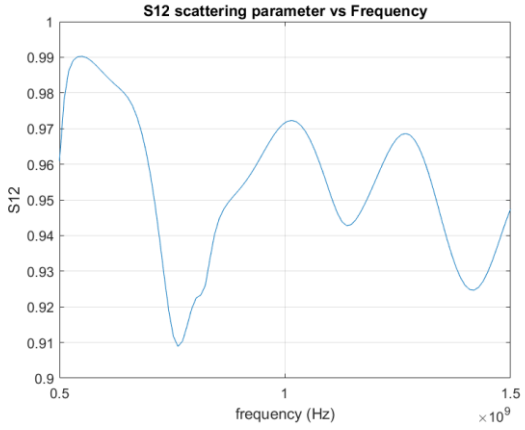


***Figure F2**. Scattering parameters for S12.*

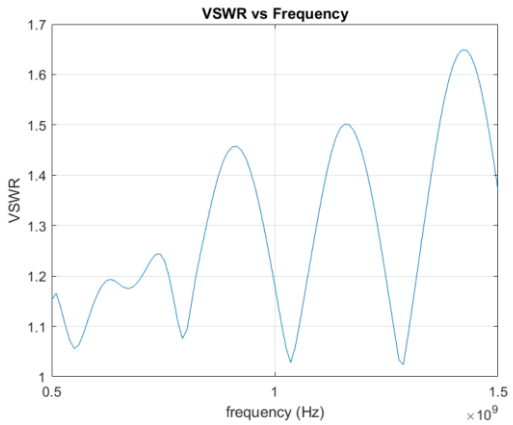
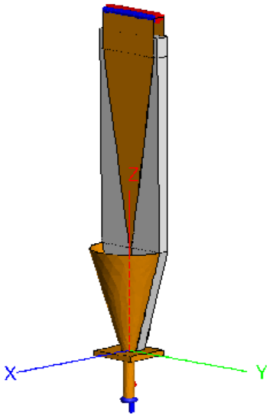
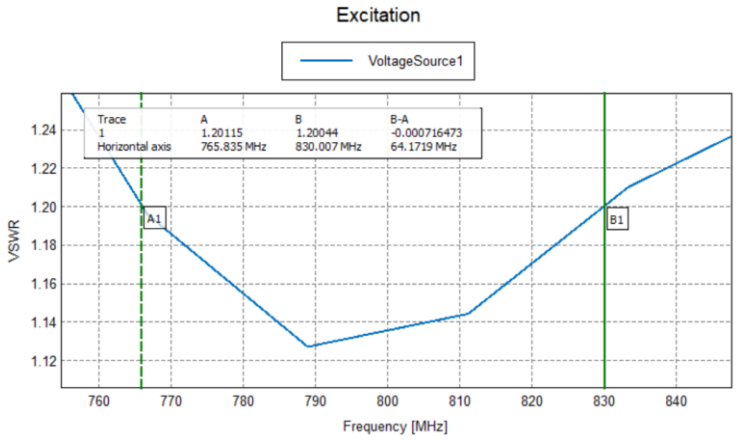


***Figure F3**. VSWR, bandwidth is high considering a VSWR<1.5.*

Impedance Transformer for GTEM (Spaeth/Myers/Chatterjee)

i. Work simulating the gradual taper design was completed, and we are now shifting focus to the Tchebycheff/Zipper design. A parametric model of the 800MHz gradual taper was made in FEKO and several parameter sweeps were run to optimize the final design. The final design and its simulation results are as follows:





ii. A VSWR under 1.2 was achieved for a bandwidth of approximately 65MHz. The most determinant variables were the length of the overall taper and the length of the cone. The section including the cone represents size increase in y-z plane from the width of the coax to the width of the parallel plates, by far the most drastic change. The rest of the taper is a much more gradual shift from the spacing between the inner and outer conductors of the coax to the spacing between the plates. The simulations showed that increases to length in both cases yielded quasi-periodical results; ever 10cm increase has a corresponding rise and fall in terms of reflection. Parameters such as the cone angle and dimensions of the base plate were used to tune the design to the desired frequency, although the spacing of

the plates more or less kept it centered around 800MHz. The best results were achieved with a cone length of 10cm (the first dip in reflection), and an overall length of 30 cm.

G. *Antennas* - Log Periodic (Hassan)

i. We are working on adjusting the Log Periodic antennas design to reflect the recent changes in the design parameters of the antenna.

IV. Research and Development Support (Smith)

H. *Mechanical Designs (Smith)*

i. No mechanical designs were required for this reporting period.

I. *Device and Materials Modelling (Eifler)*

i. Current simulations of SiPCSS show increasing recovery time with increasing length or thickness of device. They also show that the metal grid reduces laser energy needed for Ron of ~0.057ohms compared to split anode, so recovery time will be reduced with less laser energy as well.
ii. The simulations using an experimental doping profile, with higher concentration and thickness of doping, produced decreased recovery time.
iii. Simulation using analytical Gaussian profiles show separately:
   a) Increasing concentration of doping profile decreases recovery time
   b) Increasing thickness of doping profile p and n regions decreases recovery time
iv. Results were analyzed in terms of total energy efficiency and show an increased length and efficiency, but the max efficiency for 800um thickness is from 500um to 1000um.

J. *GaN:C Simulations (Rulis)*

i. We attempted to get a program called PyCDT (Python Charge Defects Toolkit) to work for GaN:C defect simulations. One of the students was able to get the program installed on the Lewis computer cluster and to set up some test runs. There is some tweaking that needs to be done in order to produce some nice figures of the optimized defect configurations, but we should be able to produce that during the next month. Our student is in contact with the program author and is working out the bugs with him.
ii. We will be initiating discussions with Jay Eifler regarding the use of Silvaco TCAD for performing the 3D full-band Monte Carlo

simulations that will be needed. The next step is to determine the exact form of the input and parameters required by TCAD.

V. Miscellaneous (Crow)

Issues:

[1] ***Scope*** *–*

[2] ***Budget*** *–*

[3] ***Schedule*** *–*

Interactions with Others:

Agency/Org	Performer	Project Name	Purpose of Research/ Collaboration

Major Procurement Actions:

Travel:

Travel Plans

Please note that all papers or presentations on any aspect of the ONR HPM program must be reviewed by the ONR Program Officer (or in some cases ONR Public Release Process) regardless of classification level or audience*.*

Planned Travel Details	Purpose	Attendees	Estimated Costs

Pending or Upcoming Public Release Requests:

Selected Highlights (text and/or images):

ONR HPM 2019 Program - Monthly Status Report (MSR) – AUGUST2019
Anthony Caruso – Univ. Missouri – Kansas City
N00014-17-1-3016 [OSPRES Grant]
ONR Short Pulse Research, Evaluation and non-SWaP Demonstration for C-sUAV Study

9/15/2019

Distribution Statement ~A: Distribution authorized to all OSPRES Grant and Contract Participants, and any uncompensated collaborators. Further dissemination per Ryan Hoffman (ryan.hoffman@navy.mil).

OSPRES Project Description: Develop tunable High Power Microwave (HPM) sources and electronically steerable radiators whose waveform(s) enable control over all levels-of-lethality on cUAV and similar targets, with the least power density.

Contents:

Executive Summary: **3**
Current Month Progress: **4**
I. Source Development (Myers) **4**
A. *PCSS Power Conditioning – IGBT (Khan)* 4
B. *Switches - GaN:C (Thompson)* 13
C. *Switches - Figure of Merit (Bhamidipati)* 17
II. Effects, Coupling and UAS Developments (Currie) **21**
D. *RF Coupling (Hassan)* 21
E. *UAS Developments (Fields)* 23
III. Antenna Development (Ahern) **24**
F. *Antennas* - Electrically Small Antennas (Chatterjee/Barman) 24
G. *Antennas* - Log Periodic (Hassan) 33
IV. Research and Development Support (Smith) **33**
H. *Device and Materials Modelling (Eifler)* 33
I. *GaN:C Calculation (Rulis)* 38
V. Miscellaneous (Crow) **40**
Issues: **40**
Interactions with Others: **40**
Major Procurement Actions: **41**
Travel: **41**
Pending or Upcoming Public Release Requests: **41**
Selected Highlights (text and/or images): **41**

Executive Summary:

In August, Faisal Khan's group investigated multiple power conditioning topologies to improve/mitigate charge-discharge inefficiencies with an effective SiPCSS load. In simulation they were successful in reducing losses across the PCSS using BEHLKE- and SiC-MOSFET-based designs/devices by 50% and 73% respectively. The switch development group has designed and fabricated a new GaN PCB based pulser that has improved testing efficiency by a factor of X, by making individual components easily swappable and interchangeable as well as pulser reconfiguration(s). Pulse testing of GaN is now moving forward with the replaced triple harmonic generator for the Wedge 1064nm laser, which also has improved the transmission efficiency of the THG and increased the peak pulse energy incident on the GaN devices. Quick analysis of preliminary on-state resistance data as a function of gap width shows a near linear rise in on-state resistance with increasing gap width. Estimates put on-state resistance at ~0.5Ω for every 10-μm of gap width. It has also been observed that smaller gap widths require less laser energy to facilitate lower on-state resistance values (figure B1). Decreased laser energy requirements may potentially drive laser cost down as lower peak energy lasers tend to cost less. In previous months Hassan's RF coupling group predicted, for a simplistic model of a UAV, that there would be a maximum in RF coupling (i.e., eigencurrent maxima) at 250MHz. Working with the UAV testing groups, a surrogate model, similar to that used in simulations, was constructed and tested; the tests successfully verified the CMA prediction. Other CMA predictions of coupling minima between 0.6 and 0.9GHz were anticipated for some UAV/current probe configurations and were also verified empirically. Antenna developments from the Chatterjee research group includes simulation/modeling of rectangular versus circular ground planes for the microstrip patch antenna designs. They continue to optimize the bandwidth, gain, and VSWR for the antenna designs through variations in geometry of the radiator and ground planes. Bandwidths of up to 300-MHz for lower center frequencies have been predicted in the models. In further studies, they will need to begin looking at the full trade-space to include beam steering capabilities of the microstrip patch designs to make valid comparisons to the non-electrically small or classical antenna designs. The electrically small antenna research group has also began to source materials to prototype some of the antenna designs/geometries for testing and characterization to validate the models.

<u>Current Month Progress</u>:

I. Source Development (Myers)

Over the reporting period, the source development efforts have focused on (1) improving the power conditioning circuit for charging the SiPCSS system, (2) evaluation of GaN:C PCSS at voltages above 1 kV, improving the GaN:C PCB pulse forming network (PFN), and continued effort to define a FOM for linear PCSS. The following table outlines the efforts of the source development subgroup under this grant:

Table I*. Progress tracker for critical tasks and status: (GREEN) low risk and/or no major delays, (YELLOW) medium risk and/or minor delays, (RED) major risk and or delays.*

Critical Effort	Critical Task		Status
Power Conditioning	Charging method evaluation & development		Various charge switching methods have been evaluated for increasing the efficiency of charging the SiPCSS transmission lines. So far, the BEHLKE based pulse charger has shown the least losses resulting in less heat in the PCSS. Moving forward, an improved BEHLKE-based system will be designed and fabricated to further increase charging efficiency.
Switches – GaN:C	High Power Figure of Merit		The GaN:C has been pulsed at 1.8 kV, demonstrating 20 kW peak power pulses. Passivation continues to be challenging, but recent success shows promise for further increasing the hold-off and thus pulse voltage. So far, no correlation between R_{on} and charge voltage has been detected with 1-mm gap devices.
Switches – Figure of merit	Power loss FOM		Efforts continue to accurately define a FOM for linear PCSS. Calculations of on-state losses for Si, SiC, and GaN have been approximated.

A. *PCSS Power Conditioning – IGBT (Khan)*

During the months of July and August in 2019, we have tested different mechanisms of charging a transmission line connected to a PCSS. MOSFET with low input capacitance and an IGBT have been alternatively used as the charge controller of the transmission line. Both series and shunt configurations of the switches have been interchangeably tested to evaluate their impact on the charging and discharging profiles. An LEM current sensor and the switch were assembled in a PCB to make the experimental setup compact, and this arrangement was used to measure the current through the transmission line. High di/dt associated with the rapid triggering of the PCSS switch induces unwanted ringing in the charging transmission line. RC snubber, negative gate

bias, external gate resistor, decoupling capacitors etc. have been used in the experimental setup to suppress the unwanted ringing after PCSS triggering. A commercial high-voltage (HV) switch (MOSFETs stacked in series and parallel) coupled with the transmission line and connected to PCSS has been tested. *We have been able to generate a ringing free output pulse* while maintaining an extra low steady input voltage across the PCSS (after firing) resulting in significant reduction in power losses across the PCSS. This has significantly increased the system efficiency. The HV switch has been successfully tested with a negative power supply from Magnum Power. The schematic of the series-connected switch-based PCSS circuit is shown in Figure A1.

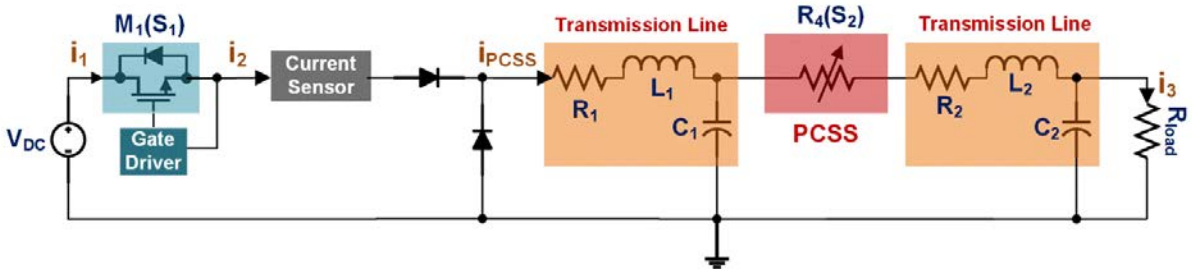


Figure A1. *Schematic of series switch connected PCSS power conditioning circuit*

LEM current sensor has been used to measure the current through the transmission line. Differential probes have been used to measure the gate to source voltage (V_{GS}), and drain to source voltage (V_{DS}) of the series connected MOSFET switch using test points in the PCB. The PCB prototype of the current sensor and the switch assembly is shown in Figure A2.

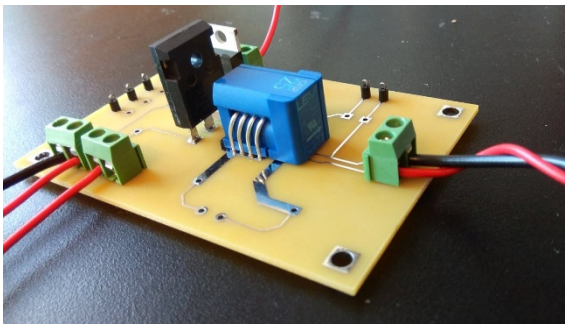
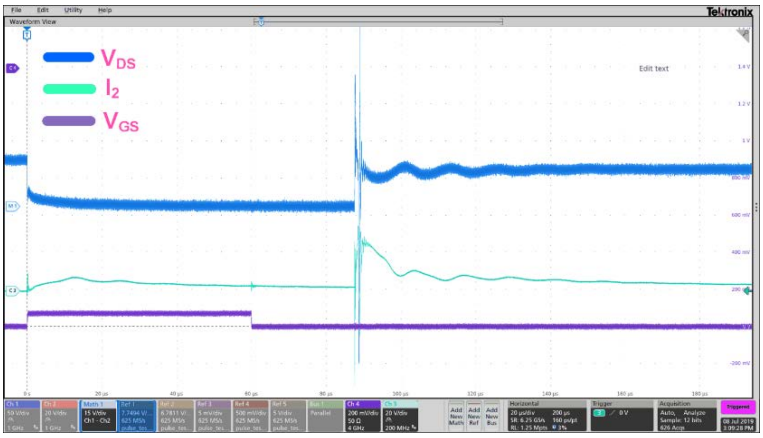


Figure A2. *Current sensor and switch assembly in a PCB*

A 35 V DC supply has been used to charge the transmission line through the series connected switch. A low input capacitance (150 pF) MOSFET from CREE has been used as the series switch to charge the transmission line connected to the PCSS. The experimental results are shown in Figure A3.



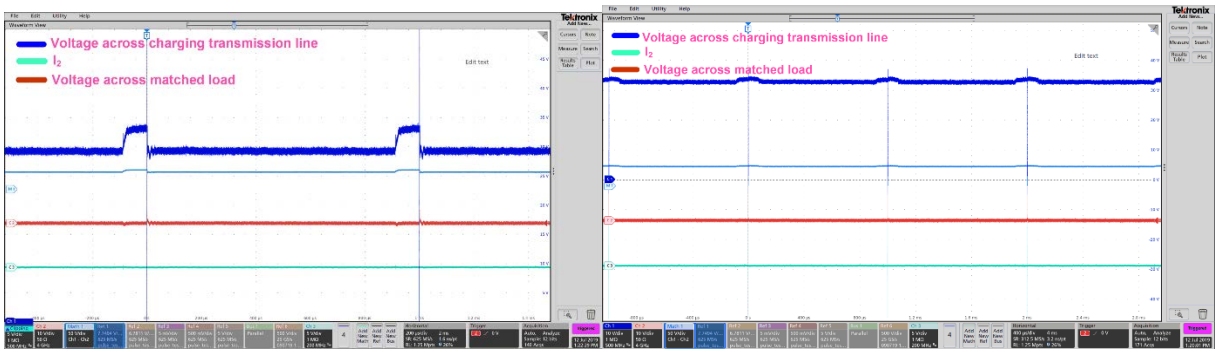
(a)



(b)

Figure A3. *(a) Voltage across drain-source (V_{DS}), gate-source (V_{GS}) and current (I_2) through the charging transmission line (b) voltage across charging transmission line and matched load during switching transitions*

As shown in Figure A3(b), ringing was observed in the charging transmission line after the triggering, which has settled down to a voltage of 18 V (while using a CREE MOSFET) or 21 V (IGBT from IXYS). The peak ringing voltage was 80 V while using the MOSFET, and it was 96 V while the IGBT was used. If the transmission line is charged by either a direct DC power supply or through a low-pass filter (LPF), the voltage across the charging line connected to the PCSS rises, and a few microseconds later, it settles down to a voltage (32 V) close to the supply voltage (35 V). These observations are illustrated in Figure A4. *Therefore, the use of series connected switches significantly reduced the settling voltage and thereby the power dissipation*.

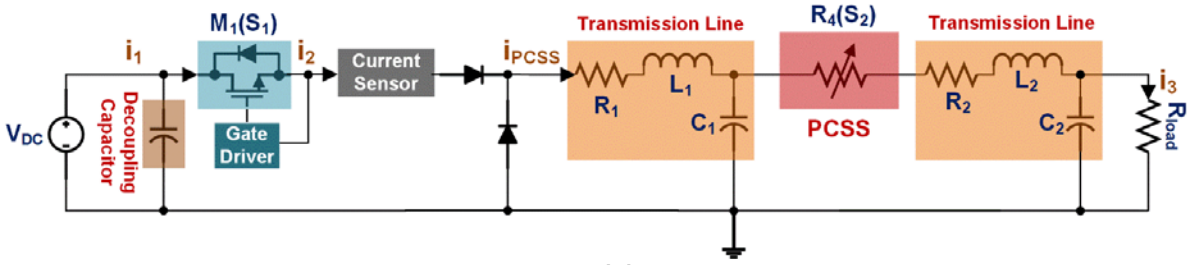


(a) *(b)*

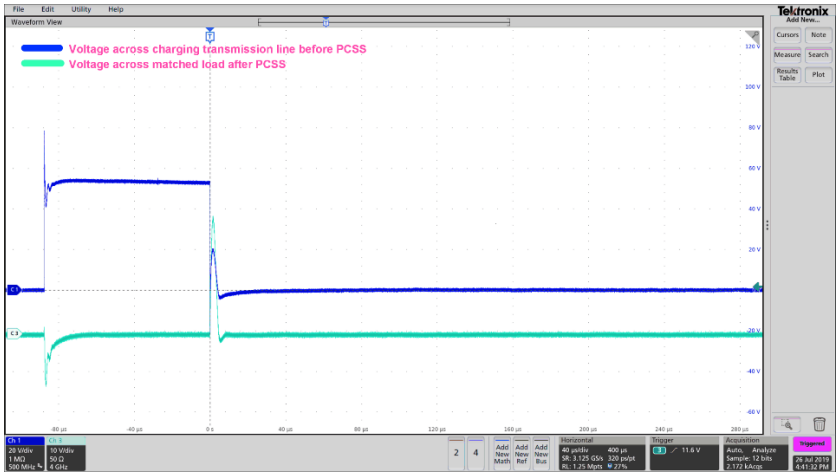
Figure A4. *Measured voltages at different points of the setup when (a) CREE MOSFET is used (b) LPF is used for charging the transmission line*

The power losses across the PCSS over a single cycle corresponding to 35 V DC supply and 1 kHz repetition rate are close to 18 mJ, 23 mJ, 40 mJ, 101 mJ for CREE MOSFET, IXYS IGBT, LPF charging, and direct DC charging based experimental setups respectively.

After the PCSS is triggered, high *di/dt* occurring from the rapid switching of the PCSS (<10 ns) interacting with the stray inductance of the circuit causes significant ringing in the transmission line. One of the classical ways to mitigate the impact of the high di/dt induced ringing is to employ a series connected resistor and a capacitor across the switching node known as a RC snubber circuit. The snubber resistor value is selected to have an impedance similar in magnitude to the impedance of the power circuit parasitic components to be damped. The snubber capacitor value is selected to have a value slightly larger than the parasitic capacitance in the power circuit but constrained in value by practical limits related to power loss and component size requirements. In practical circuits, the snubber components are evaluated empirically. We have used a series RC snubber circuit (R=12 Ω, C= 18 pF) across the series MOSFET switch. The component values have been derived empirically. A 3 kV rated 22 nF decoupling capacitor has been added between the drain terminal and the DC power supply ground. The capacitor has been placed close to the drain terminal to minimize the path for inrush current during switching transients. This modified configuration has resulted in a significantly damped oscillation in the charging transmission line after the PCSS is triggered. The modified configuration and experimental results are shown Figure A5.



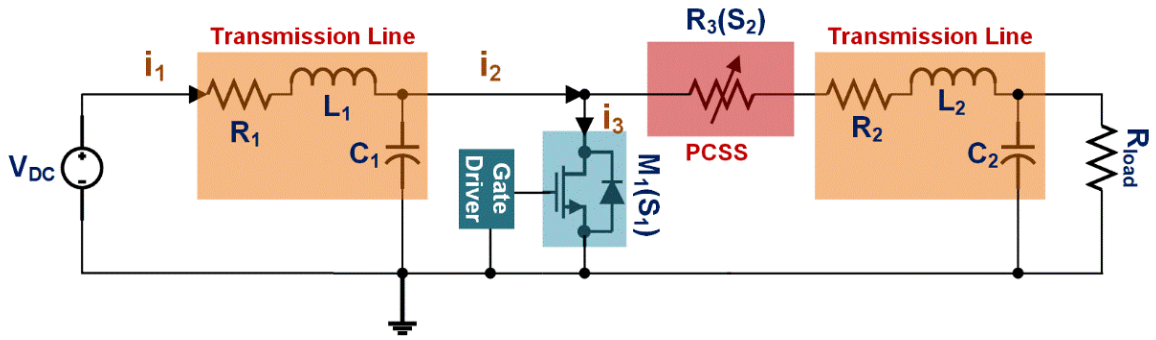
(a)



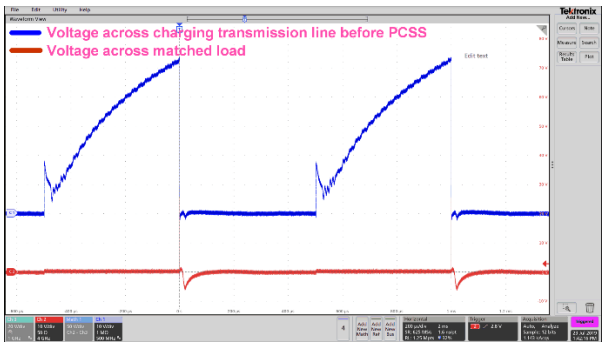
(b)

Figure A5. *(a) Schematic of series switch connected PCSS power conditioning circuit with decoupling capacitor (b) Measured voltages at different points of the experimental setup*

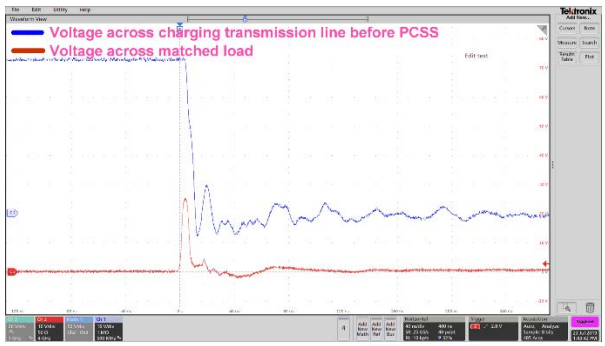
As shown in Figure A5(b), the slight ringing in the transmission line after the PCSS triggering results in a secondary pulse at the output. We are planning to include an inductive clamp circuit between the MOSFET and the PCSS to damp the oscillation in the charging line furthermore and subsequently minimize the secondary output pulse.
Another approach that can minimize the power loss across the PCSS and increase the overall efficiency of the circuit is the use of a solid-state switch in shunt configuration before the PCSS. This switch is activated immediately after the PCSS is turned OFF. This scheme creates a path to the ground for the residual charge in the transmission line once the PCSS triggering is completed. We have conducted experiments connecting the MOSFET as a shunt before the PCSS, and triggered it 2 µs after the PCSS was triggered ON. The PCSS triggering laser signal remains active for less than 15 ns, thereby eliminating any chance for these two switches (PCSS and MOSFET) to remain ON simultaneously. This described alternative configuration and the experimental results are shown in Figure A6.



(a)



(b)



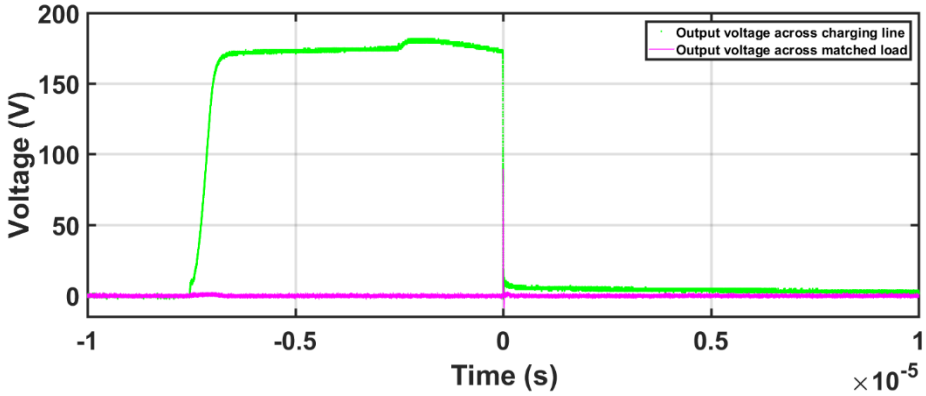
(c)

Figure A6. *(a) Schematic of PCSS power conditioning circuit with shunt connected switch across charging transmission line (b) Measured voltages at different points of the setup with shunt-connected switch (b) Zoomed version of (a) during PCSS triggering transient*

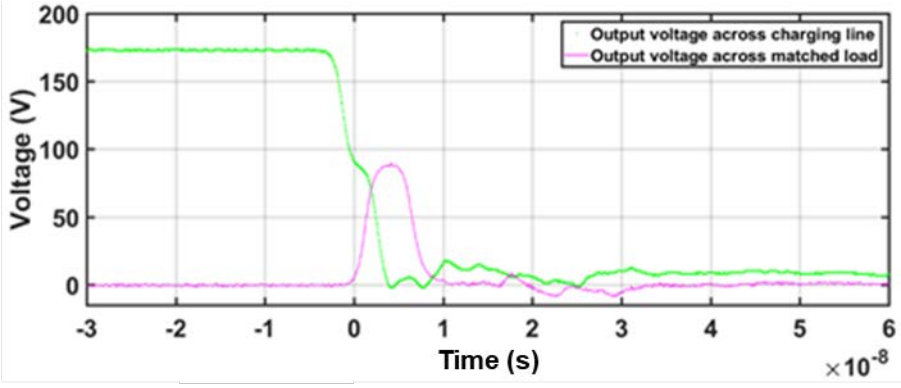
As shown in Figure A6(b), the settling voltage across charging transmission line remains at zero as long as the shunt switch remains ON, and we can control the charging period of the transmission line by changing the ON-time of the shunt switch. This can control the residual charge in the charging transmission line connected to the PCSS and further minimize the power loss across the PCSS. We can dampen stray inductance induced additional voltage buildup ($V_L = L * {di}/{dt}$) across the charging transmission line by inserting a parallel combination of a freewheeling diode and an inductor in series with the PCSS.

We have tested a commercial 14 kV rated Si HV switch from BEHLKE connected in series with the PCSS in our experimental setup. The switch ON-time is controlled by a TTL signal provided by a pulse generator. The switch is constructed from a series and parallel combination of MOSFETs to increase its voltage and current ratings. At this moment the internal construction and the schematic diagram of the series-parallel combination is unknown. A decoupling capacitor (13 nF) has been used before the HV switch, and an inductor coupled with a freewheeling diode has been used after the switch to ensure adequate immunity from the high slew rate caused by the rapid triggering of the PCSS. Using this HV switch, we have been able to generate output

pulses with a peak amplitude close to the theoretical value (half of the supply voltage) and minimal ringing in the charging transmission line after PCSS triggering. The experimental results are shown in Figure A7.



(a)



(b)

Figure A7. *(a) Experimental results using HV switch for a supply voltage of 200 V (b) Zoomed in switching transients in (a)*

We have used an ON-time of 5 µs for the HV switch and were able to generate a ringing-free output pulse with a width close to 7 ns at full width at half maximum (FWHM). As shown in the figure, the ringing in the charging transmission line is minimized to a great extent. We have conducted experiments using this HV switch for a supply voltage up to 1000 V. Even at this high voltage, the output holds its expected shape, and almost reaches the theoretical peak amplitude limit of 500 V at this supply voltage. The voltage drop across the ON-resistance of the switch, diode and other resistive elements in the circuit contributes to this reduction of the peak output pulse amplitude. The experimental results at 1000 V are shown in Figure A8.

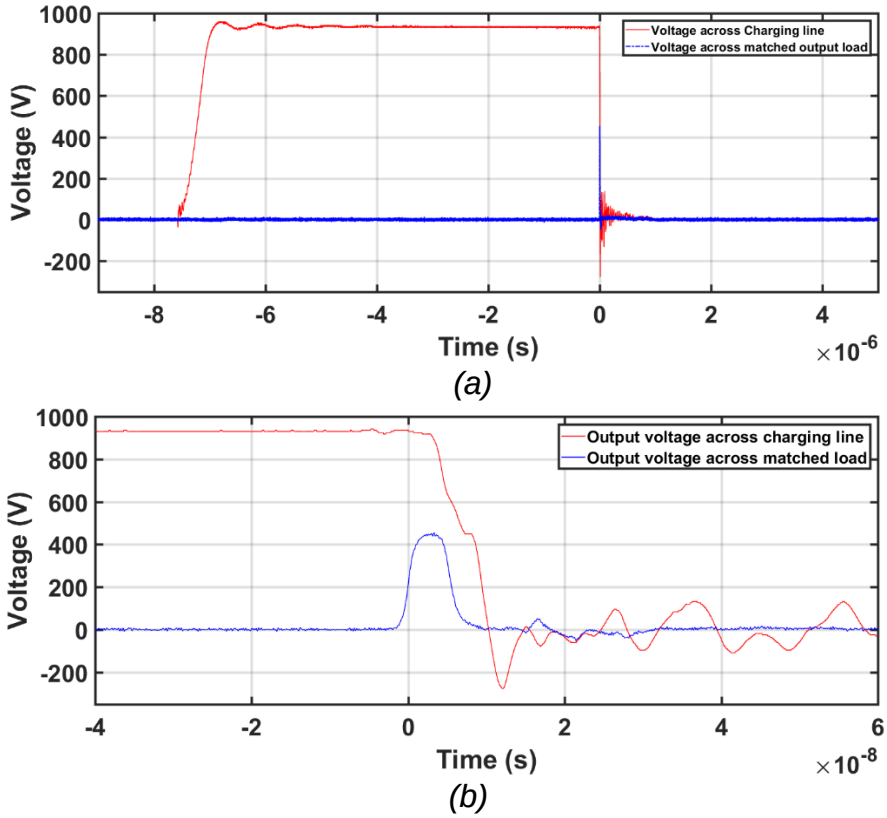
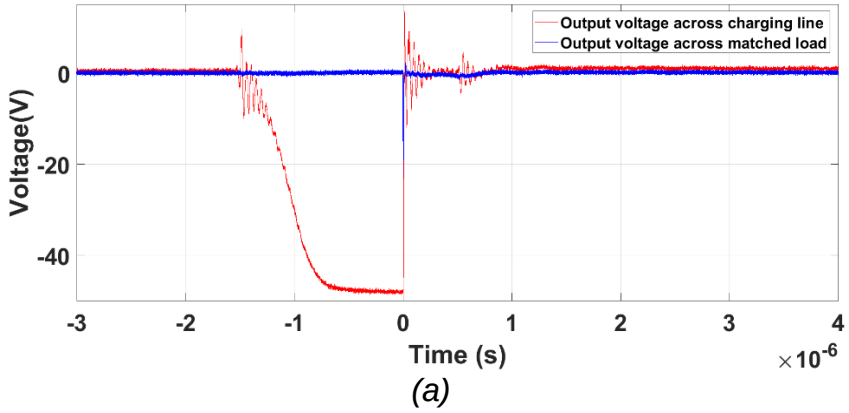
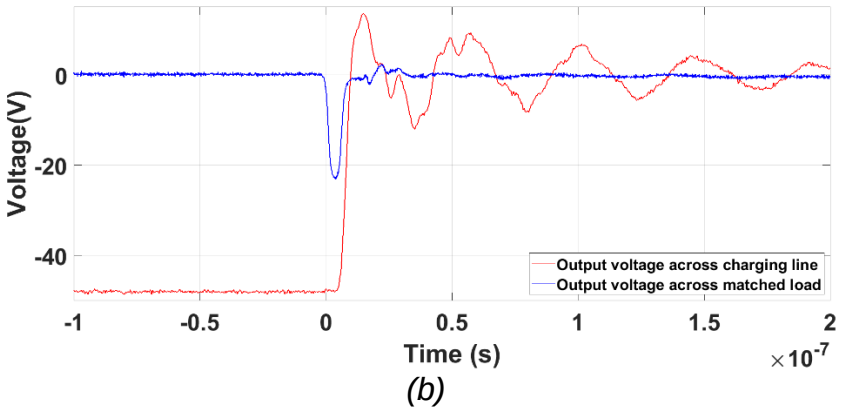


Figure A8. *(a) Experimental results using HV switch for a supply voltage of 1000 V (b) Zoomed in switching transients in (a)*

This experimental setup will help us to minimize the power loss across the switch by a great margin.

We have tested the HV switch with a negative power supply from Magnum Power. We have used an ON-time of 2 µs for the HV switch and a negative supply voltage of 50 V for the power conditioning circuit. The experimental results are shown in Fig A9.





(b)

Figure A9. *(a) Experimental results using HV switch for a negative supply voltage of 50 V (b) Zoomed in switching transients in (a)*

A comparative analysis of energy loss across the PCSS and energy input into the circuit in a single cycle is presented in Table A1.

Table A1*. Comparison of different methods of power conditioning*

Method	Input voltage (V)	Energy input into the circuit	Energy lost across PCSS	Measurement technique
Direct DC charging	40	117.2 mJ	101 mJ	Experimental
DC charging with low-pass filter	40	57 mJ	40 mJ	Experimental
CREE SiC MOSFET	40	**36.7 mJ**	**18 mJ**	Experimental
Si IGBT	40	42.4 mJ	23 mJ	Experimental
BEHLKE Si MOSFET	40	**36 mJ**	**9.5 mJ**	Experimental

The BEHLKE switch-based power conditioning circuit has substantially reduced the energy loss across the PCSS. However, total energy input in a single cycle in the BEHLKE switch-based power conditioning circuit is similar to SiC MOSFET based circuit. The damping elements of the BEHLKE switch-based circuit has contributed to the losses to some extent. We believe that the SiC based circuit can also be fine-tuned to minimize loss across the PCSS.

At present, we are working on the optimization of the HV switch-based pulse forming circuit to reduce the input energy in the power conditioning circuit. The ON-resistance of the HV switch is approximately 30 Ω at 10% of the rated maximum peak current and 90 Ω at the rated maximum peak current of the switch. Therefore, some loss is incurred during the ON-time of the switch. The forward voltage drop of a series connected diode slightly reduces the output voltage.

We are developing an in-house power conditioning circuit PCB based on the HV switch-based reference prototype. We will examine the impact of different damping elements (R, L) of the power conditioning circuit on the overall system efficiency. We will

implement a current measurement technique in the conditioning circuit to measure losses across various elements of the circuit and energy input into the circuit. Rogowski coil, shunt resistor, current transformer based current measuring techniques are being compared in terms of bandwidth, accuracy, cost. We will explore different power conditioning circuit topologies using the HV switch to further reduce the power loss in the circuit.

We will eventually use a high-end, low ON-resistance SiC BEHLKE switch in the power conditioning circuit to further improve the efficiency of the overall system. At higher operating voltage, thermal management of the power conditioning circuit is critical for efficient operation. We will devise an efficient thermal management system for the power conditioning circuit.

Immediate Tasks for the Power Conditioning Subgroup

i. Designing and fabricating an in-house power conditioning circuit based on Si BEHLKE switch.
ii. Optimizing HV switch based power conditioning circuit to minimize the power losses across the resistive elements of the circuit.
iii. Choosing and implementing current measurement technique in the power conditioning circuit.

Expected Products of Power Conditioning Subgroup

i. Designing HV SiC BEHLKE switch-based power conditioning circuit to increase system efficiency.
ii. Ensuring robust thermal management of the power conditioning circuit.
iii. Exploring different power conditioning circuit topologies to find out the most suitable one for the intended application.

B. *Switches - GaN:C (Thompson)*

To further understand how much incident laser energy is necessary to reach minimum on-state resistance for GaN:C, measurements were made at varying energy settings of the 1-ns Wedge HB laser with the THG setup. The incident beam was passed through a square engineered diffuser so that the entire active area was covered and the energy density could more accurately be measured. Previously, a cylindrical lens was used that shaped the beam to a line covering the active area of the switch. This setup provided less losses in the optical energy incident on the switch, but made accurately measuring the incident energy more challenging. The minimum on-state resistance measured for gap lengths of 20 um, 300 um, 500 um, and 1000 um lengths were 0.5 Ohms, 6.5 Ohms, 30.6 Ohms, and 50 Ohms, respectively, and are shown in Figure B1.

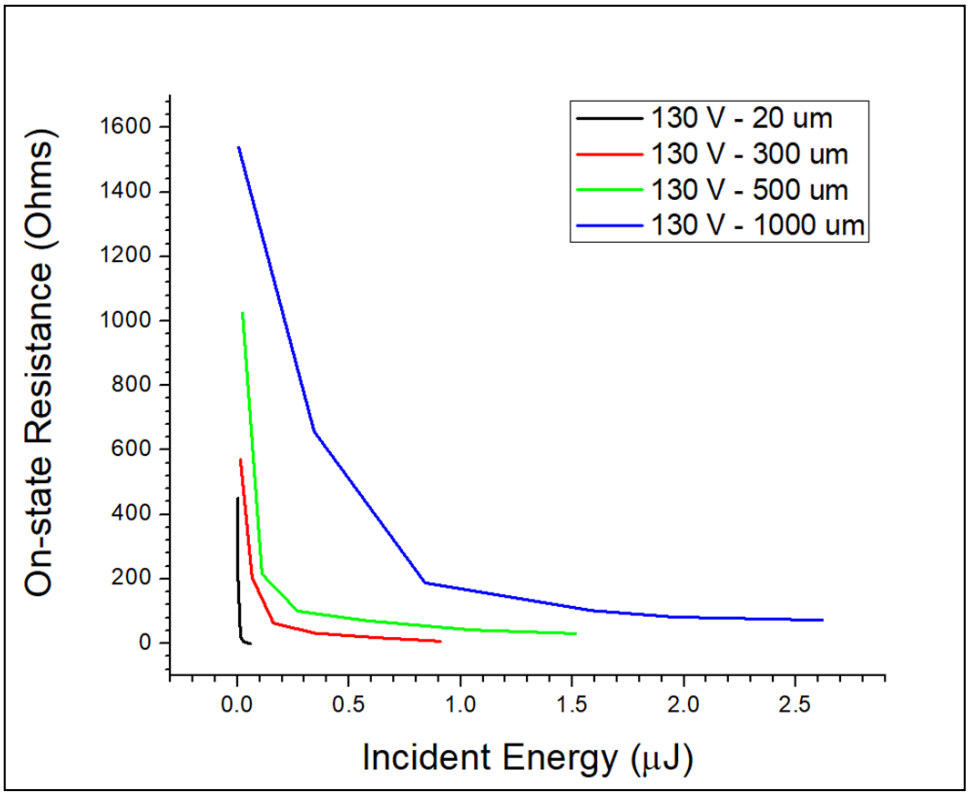


***Figure B1**. On-state resistance as a function of incident energy for various gap lengths of GaN:C devices*

Along with GaN testing at various laser energies, high voltage pulse testing was performed using a 1-mm gap length device mounted on the PCB from last month's report. The device was covered in Sylgard 184 Silicone Elastomer (provided by NRL) to prevent arcing between the contacts. Tests, at a PRF of 1 Hz, began at charge voltage of 400 V and was increased in 100 V increments until the switch failed at 1900 V. As seen in Figure B2 the device was damaged on the edge where the copper was soldered onto the switch. The damage was caused from arcing between the switch and the copper. For future testing, a mount of FR4 is being made to allow for epoxy to completely encapsulate the switch and be cured in a vacuum oven without damaging the PCB.



***Figure B2**. Damaged 1mm gap length GaN:C device*

The on-state resistance for the 1-mm gap length device was approximately 40 Ohms and did not decrease as voltage increased; raw waveforms are shown in Figure B3. The peak voltage as a function of charge voltage increased approximately linearly per Figure B4 with a slope of 0.57, showing that the output was about 57% of the charge voltage. The slope of this line will be steeper for shorter gap length devices, due to a drop in on-state resistance, and the slope will also change with changing the incident energy. For future testing devices of varying gap lengths will be sent to NRL, with FR4 mounts, for encapsulation using a vacuum oven to prevent failure from air bubbles in the encapsulation material.

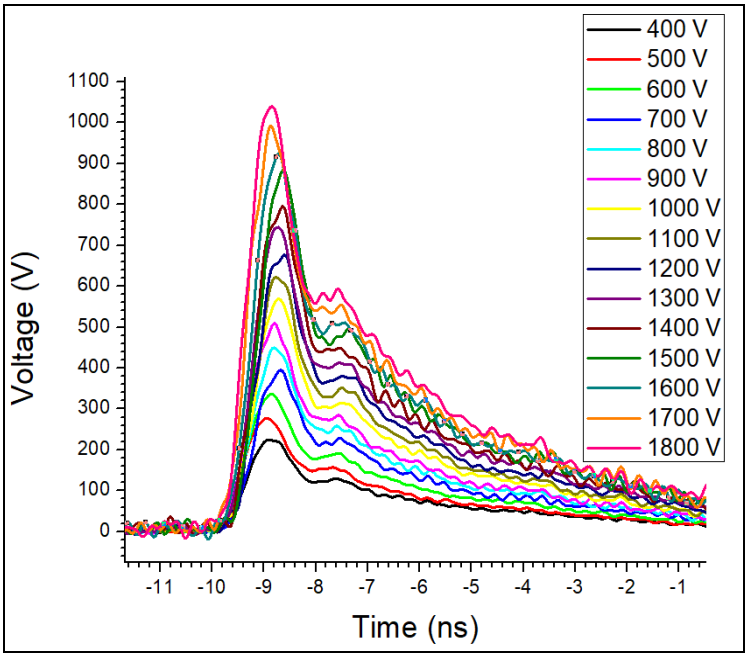


***Figure B3**. Output waveforms from HV testing*

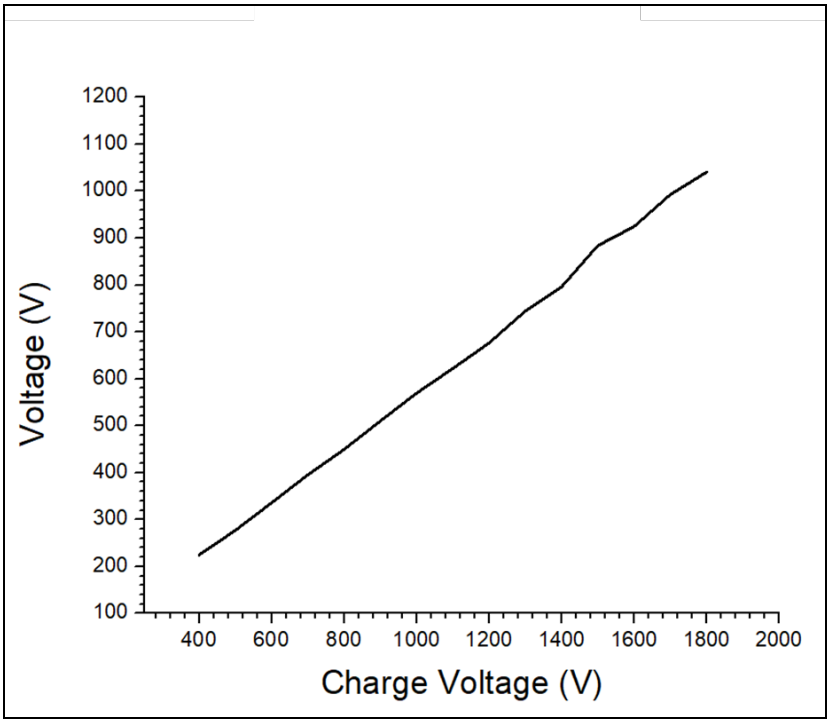


***Figure B5**. Peak voltage as a function of charge voltage for a 1 mm gap length GaN:C device*

GaN:C Pulse PCB (Labrada)

In addition to testing GaN, improvements were made in the pulser PCB. This new more compact pulse forming network (PFN) increased testing efficiency through its robust modular design. With swappable components - resistors and capacitors – as well as switches, quick changes are more easily made. Meaning quicker data collection, with varying parameters, without sacrificing circuit integrity thus improving confidence in data accuracy.

The PCB was designed in a microstrip configuration (Fig B6) with a characteristic impedance (Z_0) of 50 Ω to match a load impedance at the coaxial input/output terminals. It is a two-sided PCB, with 20 mils of FR4 dielectric separating the 1-oz Cu plates. Optimal trace thickness was calculated to 40 mils across for the stated Z_0. The four large drill holes are for affixing the PCB to the mount to be normal with the incident laser. The geometry of the top layer was rearranged to a linear composition to minimize parasitic capacitances and inductances from the prior iteration.

A large gap is present between the GaN:C PCSS pads to accommodate an FR4 holder slide that houses the switch under epoxy resin. This allows testing at much higher voltages without damaging the PCSS. As testing continues and different values/models become of interest we will continue to iterate on this design. Having an already compact and convenient form-factor, this PCB can quickly be adjusted and packaged for prototyping if desired.

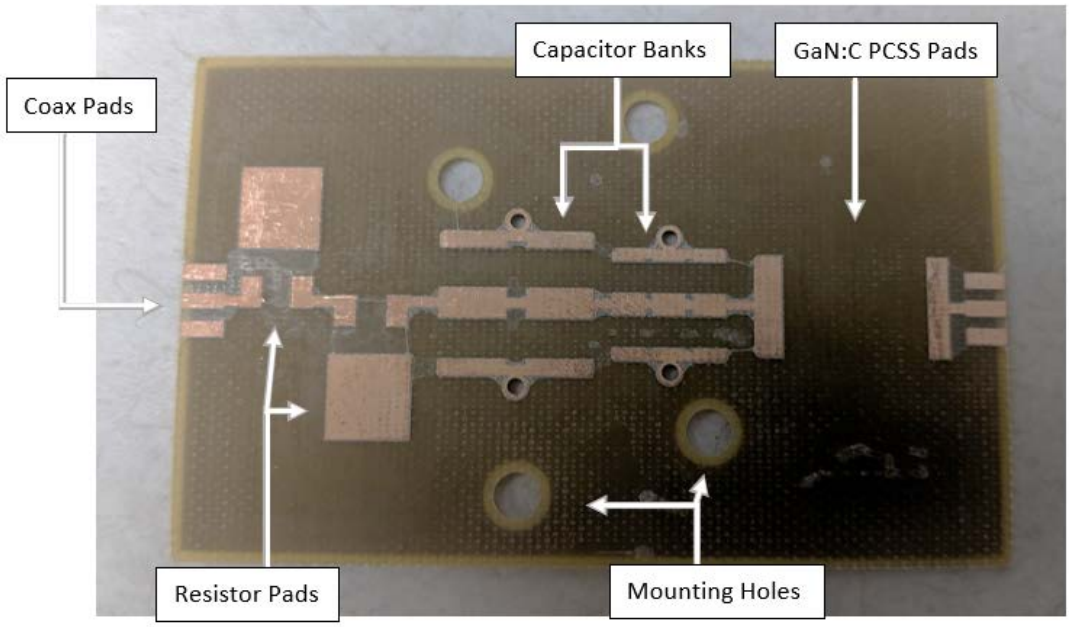


Figure B6*. Upgraded and unpopulated GaN PCB pulse forming network.*

Immediate Tasks of Fundamental GaN:C PCSS Subgroup

i. Continued testing of GaN:C PCSS at higher voltages to find the Ron dependence as a function of incident energy and gap length at 150 V to 1000 V.
ii. Mount vacuum oven passified devices and components to linear PCB for pulse testing.

Expected Products of Fundamental GaN:C PCSS Subgroup

i. Results from GaN:C testing showing dependence of incident energy and gap length on Ron at higher voltages (150 V–1000 V).
ii. Demonstrate ≥ 2 kV pulses with GaN:C device with gap length of 1 mm and ≥ 1 kv with GaN:C with gap length of 500 µm
iii. Results from new GaN:C PCB design

C. *Switches - Figure of Merit (Bhamidipati)*

Recent efforts to derive a figure of merit for linear mode PCSS were on analytically calculating the power losses incurred within the device during the full cycle of operation constituting on-state, off-state and switching (turn-on and turn-off) states of a linear mode PCSS. To accomplish this, we've used the Nunnaly [1] carrier generation model to derive equations for the device resistance and current as a function of time and can be used to calculate losses in the time domain. The device's geometry, band gap, electron and hole mobilities, conductivity, recombination time, and transit time were included in the power loss calculations given by:

$$P_{on}=E_c^2\ L^4\ h\upsilon/[(R_{on}+R_{Load})^2\ q\ \mu_T t_r I_0] \quad (1)$$

During the switching stages the temporal change in device resistance and is characterized by:

$$R_{device}(t) = L^2\ h\upsilon/[qIT_{net}\mu_T(1-e^{-t/Tnet})] \quad (2)$$

And temporal change in the device current is characterized by:

$$i(t)=E_cLdwq\ \mu_T n(t)/[R_L dwq\mu_T n(t)+L] \quad (3)$$

$$n(t)=I/\ (h\upsilon\ dwL)\ *\ T_{net}\ *[1-exp(-t/T_{net}) \quad (4)$$

Where:
n(t) – carriers generated;
E_c – critical field
L – thickness of the device (switch gap)
d,w – length and width of the device
hυ – Energy carried in each photon
R_{on} – On state resistance
R_{Load} – load resistance
q – Charge of the electron
μ_T – Mobility of holes and electrons
t_r – inherent device recombination time
t_T – transit time of carriers
T_{net} – $t_r*t_T/(t_r+t_T)$
I_0 – peak optical intensity
I – $I_0*exp(-2.77(t/T_{FWHM})^2)$ - temporal Gaussian light pulse with peak optical intensity I_0

The device is considered to be illuminated by a temporal Gaussian pulse with FWHM of 2 ns and wavelength of the light equal to the material's bandgap. Power losses in the switch are primarily due the temporal overlap of voltage and current while switch resistance is non-zero. The on-state losses were calculated in Si, SiC, and GaN while varying switch geometry (i.e. gap length or thickness) and the intensity of incident optical energy, as shown in Figure C1, C2 and C3, respectively. These plots show the on-state power loss by taking mobility of the generated carriers and the recombination time into account as shown in Equation (1). The recombination time used was held constant for all materials. The analytical power loss equations during the switching stages have also been derived and will be used with the thermal conductivity of the respective materials to calculate the temperature rise in the material to determine their figure of merit. By comparing the plots for Si, GaN and SiC, we notice that SiC has relatively higher on-state losses.

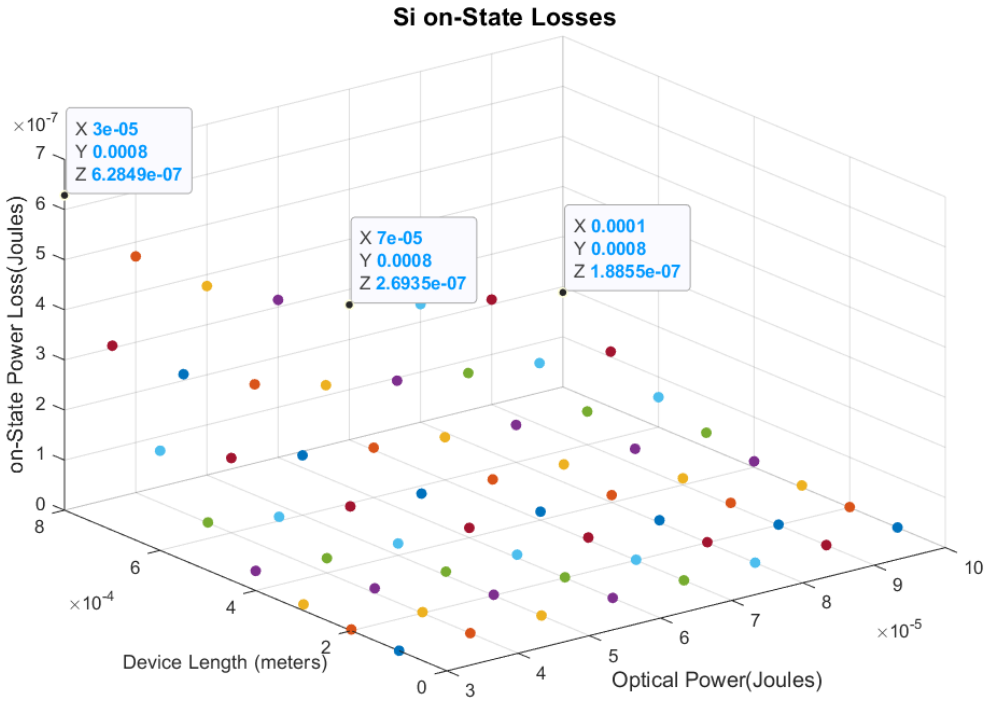


Figure C1: *Si on-state losses as a function of varied path length and incident optical power*

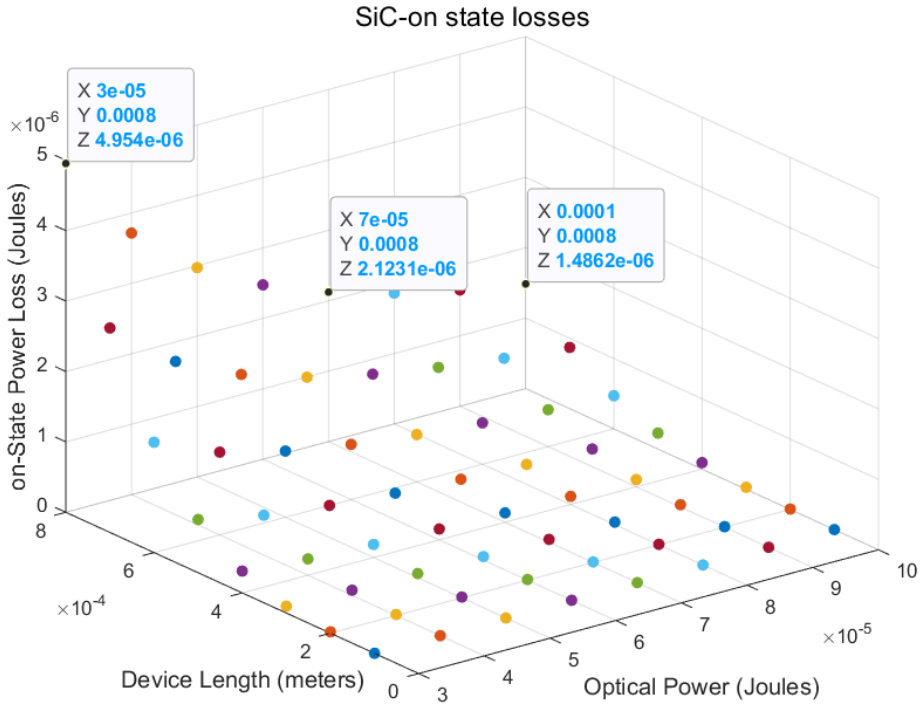


Figure C2: *SiC on-state losses as a function of varied path length and incident optical power*

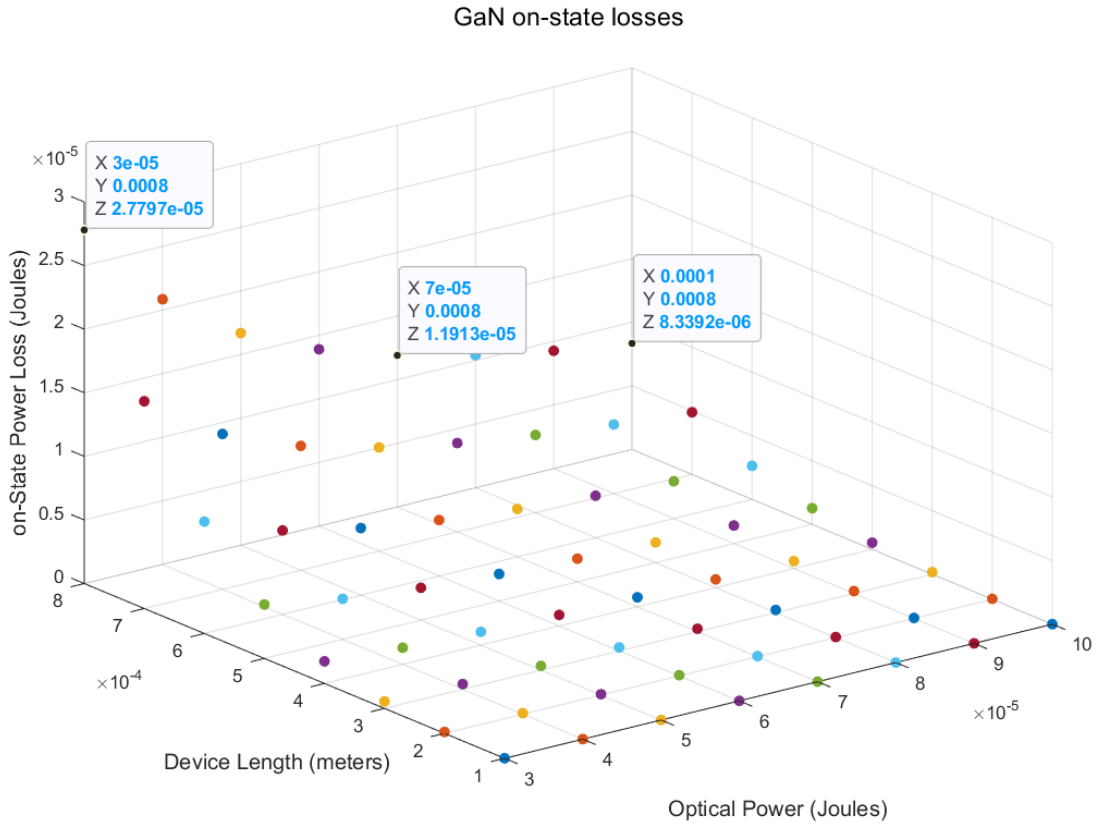


Figure C3: *GaN on-state losses as a function of varied path length and incident optical power*

While this approach of calculating power losses and lattice temperature rise to propose a figure of merit can be used to classify the materials for the linear PCSS, the approach does not serve as a general classification tool for all applications. For a more application specific FOM, an ideal application-specific figure of merit for a material should take power requirements, bandwidth, operational mode (pulsed/CW), PRF, manufacturing maturity, cost and cooling requirements into consideration. To achieve this we are focusing on extending the figure of merit to include wide range of PCSS applications that have different sets of requirements in the linear mode.

Immediate Tasks for the Figure of Merit Subgroup

i. Quantitatively analyze the derived power loss equations for switching stages of the devices for Si, SiC, GaN and diamond with varied geometry and illumination conditions as next step to defining figure of merit for PCSS without PFN.
ii. Work on defining the FoM to be application specific depending on the power and the PRF requirements.

[1] William C. Nunnally, Robert B. Hammond, "*Optoelectronic Switch for Pulsed Power*", Chapter 12 in book edited by Chi H. Lee, "Picosecond Optoelectronic Devices", Academic Press, Inc., 1984

II. Effects, Coupling and UAS Developments (Currie)

D. *RF Coupling (Hassan)*

Over the last month, we built a small UAV model that consisted of a 220 mm × 220 mm square metallic plate at the center with four identical wires attached to its corners, as shown in Fig. D1. The wires' lengths and radii are 380 mm and 0.5 mm, respectively. The model is designed to be a first-order approximation of a quadcopter UAV where the square metallic plate represents the PCBs and controllers, typically located at the center of the UAV, and the 4 wires approximate the interconnects and harnesses that connect the controllers and batteries to the motors. This model is similar in shape to the UAV model used in experimental measurements performed by the group of Daryl Beetner at Missouri University of Science and Technology that we discussed in previous MSRs. However, we improved the uniformity of the fabricated model and we also doubled its size to shift its response to lower frequencies which are more accurate to measure and are also compatible with the measurement facilities at UMKC. The simplicity of the model permits the experimental measurement of the coupled currents and performing quantitative comparisons with the simulations and Characteristic Mode Analysis (CMA) predictions. However, the model is sophisticated enough to generate general coupling conclusions to practical UAVs especially how coupling varies with the orientation of the UAV.

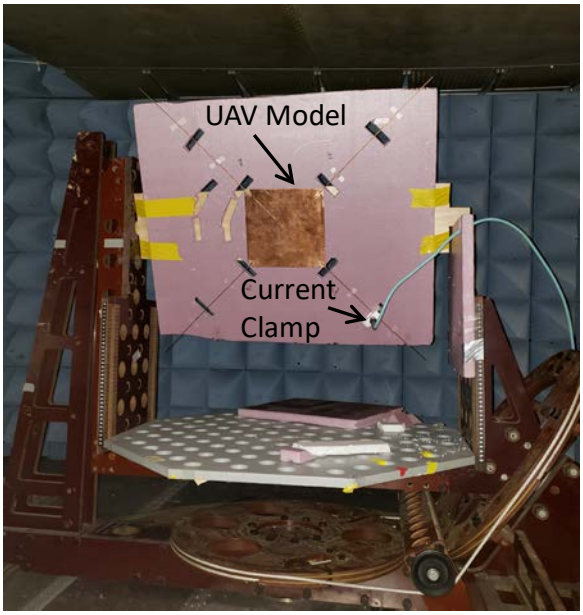


Figure D1. *Picture of the model UAV fabricated*

The fabricated UAV model was placed inside the GTEM cell at UMKC to expose it to a uniform transverse electromagnetic excitation. The GTEM cell can accommodate targets up to 1100 mm in height and frequencies that range from DC - 20 GHz. At the small side, the GTEM cell has coaxial input that was connected to the HP 5753 series

vector network analyzer (VNA) to generate the incident power. A picture of the setup inside the GTEM cell is shown in Fig. D2. A BCP-512 Broadband Current Probe that can measure currents in the frequency range of 1 MHz – 1 GHz was placed at the beginning of one of the four wires, at the corner of the metal plate, and at the middle of the wire. Moreover, the UAV was mounted on a platform that can be rotated to study how the coupled current varies with the angle of incidence. The knowledge of the modal behavior, as calculated by the CMA, allows us to easily predict the coupled current at the different locations and for different orientations of the UAV. The measurements described in this report were conducted to confirm these predictions.

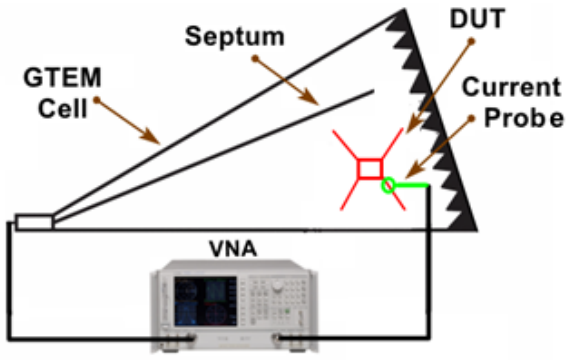


Fig. D2: *A sketch of the experimental setup showing the UAV model inside the GTEM*

The measured current at the beginning of one of the 4 wires, near the corner of the plate, is shown in Fig. D3a due to normal incidence. Both the measurements and simulations show a peak at 0.15 GHz and a minimum in the 0.6 GHz to 0.9 GHz range. In previous MSRs, we predicted using CMA, that this minimum in the coupled current will be removed by placing the current probe away from the beginning of the wire near the middle or by using oblique incidence. Fig. D3b and Fig. D3c confirm these predictions for the case when the current is measured at the middle of the wire and for the case of oblique incidence (θ_i = 45°), respectively. For the case of oblique incidence in Fig. D3c, the new current coupling peak near 0.25 GHz was also predicted by the CMA in previous MSRs. The excellent agreement between the CMA predictions and the experimental measurements adds validity to the CMA approach facilitating its applications for more complex UAV models.

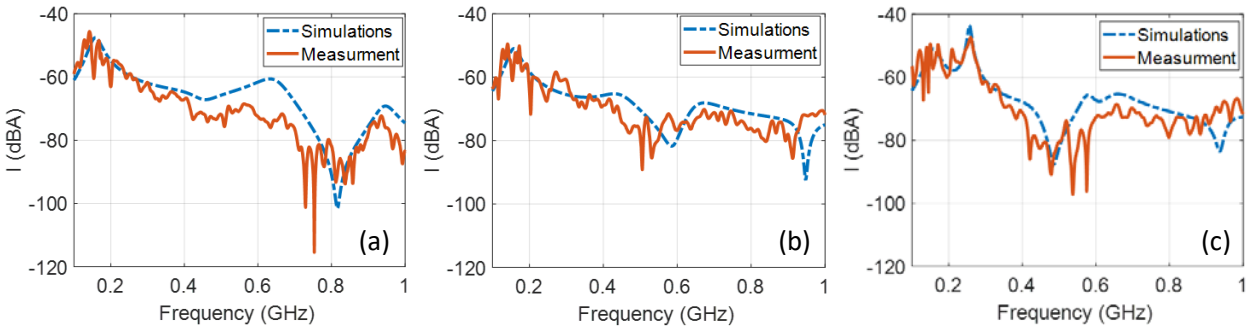


Figure D3: *Coupled current at (a) start of Wire 1 of the UAV due to normal incidence, (b) middle of Wire 1 of the UAV due to normal incidence, (c) start of Wire 1 of the UAV due to oblique incidence ($\theta_i = 45^\circ$)*

E. *UAS Developments (Fields)*

Table E1*. Progress tracker for identified critical tasks and statuses. Color indicates the criticality of each task with respect to its current status and the objectives of the program: (green) low-risk and/or no major delays, (yellow) medium risk and/or minor delays, (red) major risk and/or delays.*

Effort / Area	Critical Task		Status
Target Systems and Development	RF Sensor and Calibration		Exploration of continuous frequency susceptibility as an additional source of information to be used for down-select. The testing will occur during the two week testing at JHUAPL. Low risk is attributed to this being additional data that should help for down-select, but not necessary.
Target Systems and Development			Phone call with Tom & Chip regarding Coupling Study, and outlined next steps for Effects Testing Methodology meeting expected to happen mid-June. Template for Effects Testing Methodology meeting to be finished end of May.
Target Systems and Development			Continued refinement and analysis of RCS measurements for targets of interest. Risk associated due to RCS measurements use of similar equipment as Effects Testing, but much lower priority.

Data Collection and Measurement (Lancaster & Fields)

For data collection, 2048 tests were collected using randomized input RF parameters generated from a Sobol distribution based on the power, pulse width, pulse rate frequency, and S-band center frequency boundaries of the 5kW IFI PT42-5KW Traveling Wave Tube Pulse Amplifier. Smaller distributions were produced to test other target platforms to determine susceptibility and comparability. Equipment was prepared for L-Band testing to be completed in September.

Target System and Development (Fields)

The first version of an RF sensor designed for free-flight testing has been made, with 15 boards populated and calibrated. The calibration process is to use well calibrated RF generators connected to the RF sensor board, and measuring the digital output for frequencies of interest. The gain of the antenna (Taoglass Maximum FXUB66) is used to relate the field strength incident on the antenna to power at the input of the sensor.

Experimental Design (Fields)

The radiated susceptibility of several target platforms has been tested using a GTEM. The relative homogeneity of the GTEM's electric field enables cost effective testing of DUT orientation and higher field strengths. A signal generator feeds into an amplifier of some frequency band. Traveling wave tube amplifiers require an arbitrary waveform generator for triggering and pulse formation. An oscilloscope collects VPP from a V-dot probe positioned before the tip of the GTEM. The DUT is positioned as far forward in the GTEM as the septum permits at the desired orientation. For manual data collection, an RC arms and disarms the device before and after illumination if possible, and then data is downloaded after each test for analysis. Automated tests collect data via ethernet (process validated in previous MSR).

Data Analysis Refinement (Fields & Currie)

The automatic data analysis script is currently undergoing improvements that will improve the reliability of categorizing the data as well as investigating additional sensor data within the data files. Thresholding is used to determine if, and how severe, an effect is in each of the autopilot sensor subsystems (attitude, command and control, flight control module, etc.). Thresholds utilized the initial 10 seconds for mean quantification; however, in some cases the data fusion levels are not at steady state. This can lead to false positives and false negatives. The code is being reworked to additional metrics for pre, during, and post illumination assessment. Additionally, the secondary inertial measurement unit data is being incorporated (along with the data fusion algorithms) into the data analysis script.

III. Antenna Development (Ahern)

F. *Antennas - Electrically Small Antennas (Chatterjee/Barman)*

To cover the target frequency range of 0.4 GHz to 1.2 GHz, three separate microstrip patch antennas have been designed. These antennas have center frequencies at 600 MHz, 800 MHz and 1 GHz. A fourth antenna has been designed at the upper L-band with a center frequency of 1.74 GHz. In each case $\geq$30% 2:1 VSWR bandwidth with $\approx$ 5 dB maximum gain has been achieved by proper positioning of the probe. Different EM solvers like FEKO and HFSS have been used to verify the simulated results.

Electrically Small Antenna (ESA) Design

A simple rectangular patch can yield greater than 30% 2:1 VSWR bandwidth and a reasonable gain if the probe is placed along the diagonal at 2/3rd distance from the center. The geometry of the patch is shown below in Figure F1.

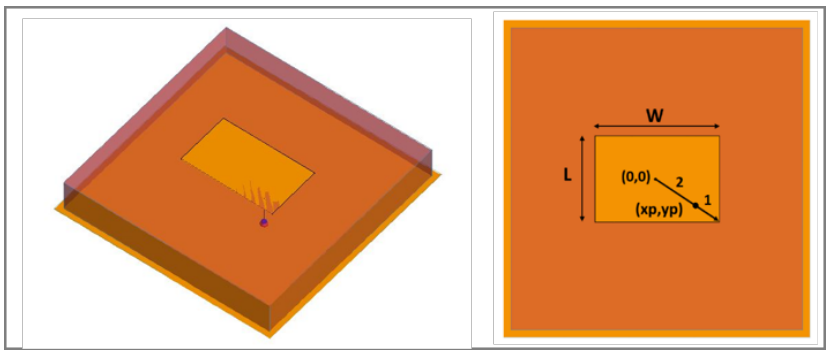


***Figure F1**: Geometry of the rectangular microstrip patch along with the probe location (x_p, y_p)*

This idea has been employed to design a microstrip patch antenna which can operate from 0.4 GHz to 1.2 GHz (i.e., 800 MHz). However, at ultrahigh frequency (UHF) region, a single microstrip antenna cannot cover more than 300 MHz of bandwidth. Therefore, three separate antennas with center frequencies at 600 MHz (Antenna 1), 800 MHz (Antenna 2) and 1 GHz (Antenna 3) have been designed to cover the entire frequency range. It has been observed that as the center frequency increases, a single antenna, with center frequency above 1.0GHz is predicted to have more than 700 MHz of bandwidth is observed. For example, a fourth antenna (Antenna 4) has been designed at a center frequency of 1.74 GHz and it covers the frequency range from 1.38 GHz to 2.1 GHz (720 MHz).

Initially, the antennas have been simulated on infinitely grounded substrates using the EM Solver FEKO. TMM 10i ($\varepsilon_r = 9.8, \tan\delta = 0.0020$) has been used as the substrate material. A more realistic study is done by replacing the infinitely grounded substrates with the finite ones. Two types of finitely grounded substrates of the same area of cross section have been considered viz. rectangular and circular. Figure F2 shows the different types of finitely grounded substrates that have been investigated.

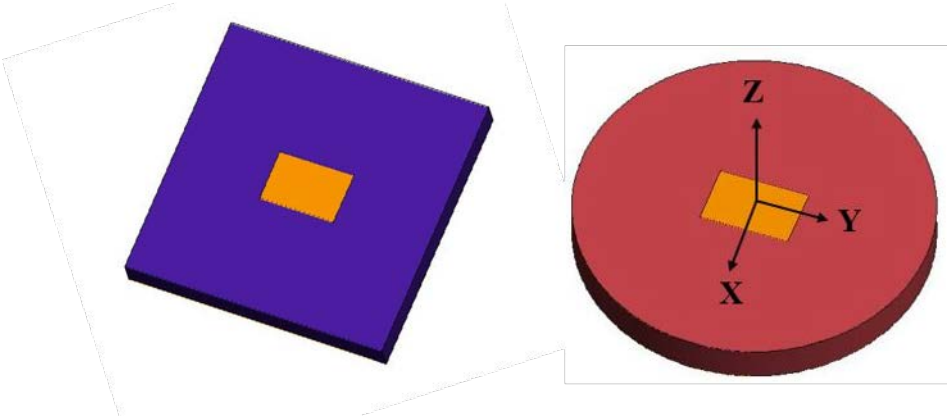


Figure F2*. Microstrip patches on rectangular and circular finitely grounded substrates*

The optimized dimensions for all the four antennas have been summarized in Table F1. At the center frequency fr, L and W represent the length and width of the patch respectively while h is the substrate thickness. The probe radius and location are denoted by rp and (xp,yp) respectively.

Antenna #	f_r (GHz)	h (mm)	$h\sqrt{\varepsilon_r}/\lambda$	L (mm)	W (mm)	r_p (mm)	(x_p,y_p)
1	0.6	38.1	0.1989	57.6652	86.4978	3	(19.5, 28.8326)
2	0.8	25.4	0.1989	38.4434	57.6651	1	(13.5, 19.2217)
3	1	19.05	0.1930	30.3135	45.4702	1	(10.5, 15.15675)
4	1.5	12.70	0.1989	19.2217	28.8326	1	(6.4072, 9.61085)

Table F1: *Optimized Antenna Dimensions*

Results:

The antenna characteristics have been summarized in the tables below. Figures F3 to F6 show the VSWR and gain of each of the antennas.

Antenna 1						
Ground Plane	f_L (GHz)	f_C (GHz)	f_U (GHz)	% BW	Max. Gain (dB)	ka
Infinite	0.478	0.601	0.724	40.93	2.86	0.6547
Finite (Rectangular)	0.466	0.5535	0.641	31.62	5.6	0.6030
Finite (Circular)	0.462	0.5825	0.703	41.37	5.61	0.6346

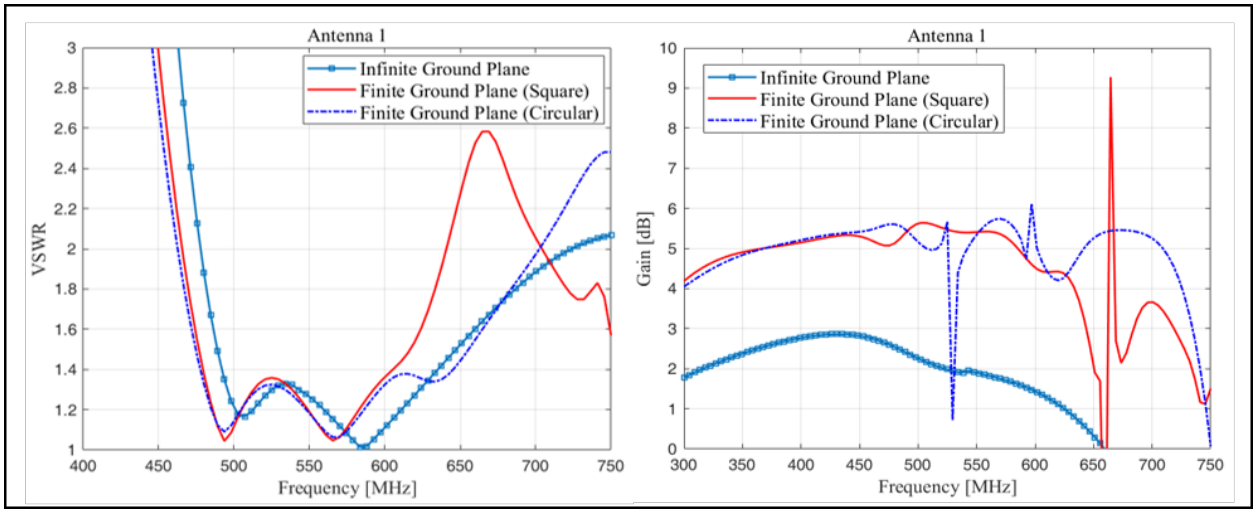


***Figure F3**: VSWR and Gain of Antenna 1*

Antenna 2						
Ground Plane	f_L (GHz)	f_C (GHz)	f_U (GHz)	% BW	Max. Gain (dB)	ka
Infinite	0.712	0.832	0.951	28.80	2.835	0.6043
Finite (Rectangular)	0.697	0.810	0.923	27.81	(Unstable)	0.5886
Finite (Circular)	0.695	0.827	0.960	32.05	5.89418	0.6013

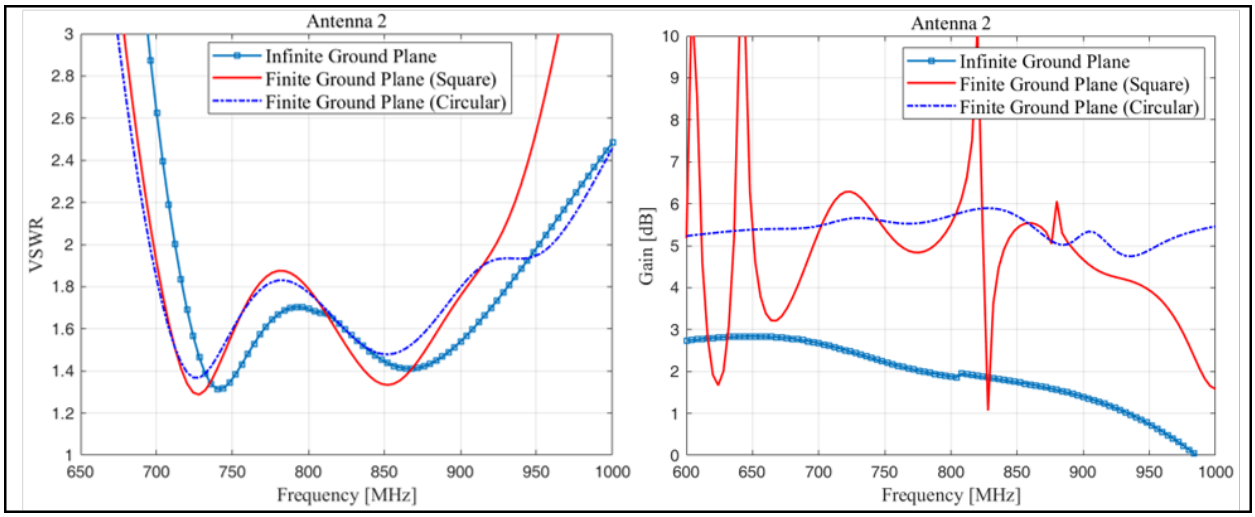


***Figure F4:** VSWR and Gain of Antenna 2*

Antenna 3						
Ground Plane	f_L (GHz)	f_C (GHz)	f_U (GHz)	% BW	Max. Gain (dB)	ka
Infinite	0.919	1.0935	1.268	31.9159	2.98746	0.6262
Finite (Rectangular)	0.894	1.0530	1.212	30.1994	5.80832	0.6030
Finite (Circular)	0.892	1.0815	1.271	35.0439	7.87	0.6193

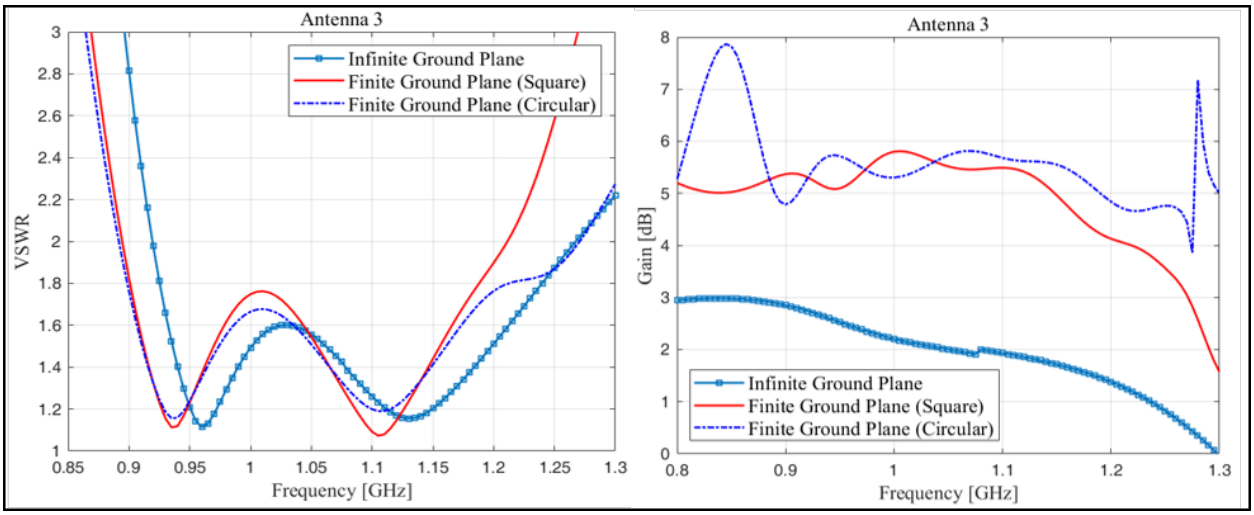


Figure F5: *VSWR and Gain of Antenna 3*

Antenna 4						
Ground Plane	f_L (GHz)	f_C (GHz)	f_U (GHz)	% BW	Max. Gain (dB)	ka
Infinite	1.434	1.7995	2.165	40.6224	2.8539	0.6531
Finite (Rectangular)	1.397	1.659	1.921	31.5853	5.46662	0.6024
Finite (Circular)	1.388	1.7445	2.101	40.8713	5.76802	0.6335

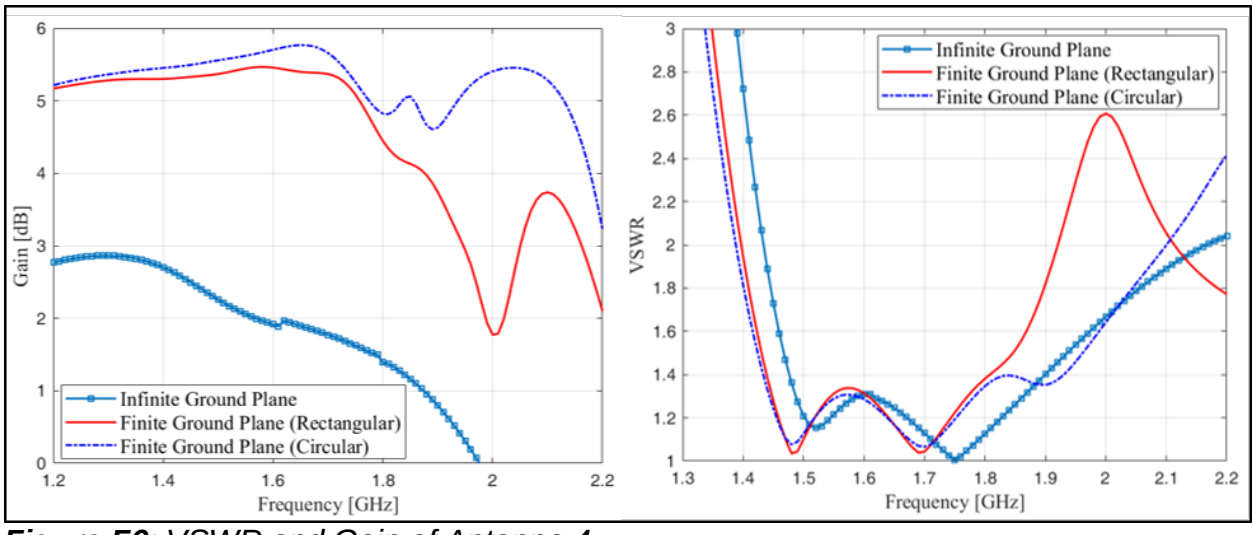


Figure F6*: VSWR and Gain of Antenna 4*

It can be observed that better bandwidth and stable gain is obtained with the circular ground planes compared to the rectangular ones. (Figure F7) This may be attributed to the effect of diffraction from the edge of the substrates. For an antenna to qualify as electrically small, its electrical length must be ka≤0.5, where k and a are the wavenumber and minimum radius of the circumscribing sphere of antenna respectively. In all the above cases, the ka value is in the range of 0.6 to 0.65. Thus, nearly electrically small antennas which can cover the frequency range from 0.4 to 2.1 GHz have been designed; tradeoffs with other array parameters are ongoing and will be reported.

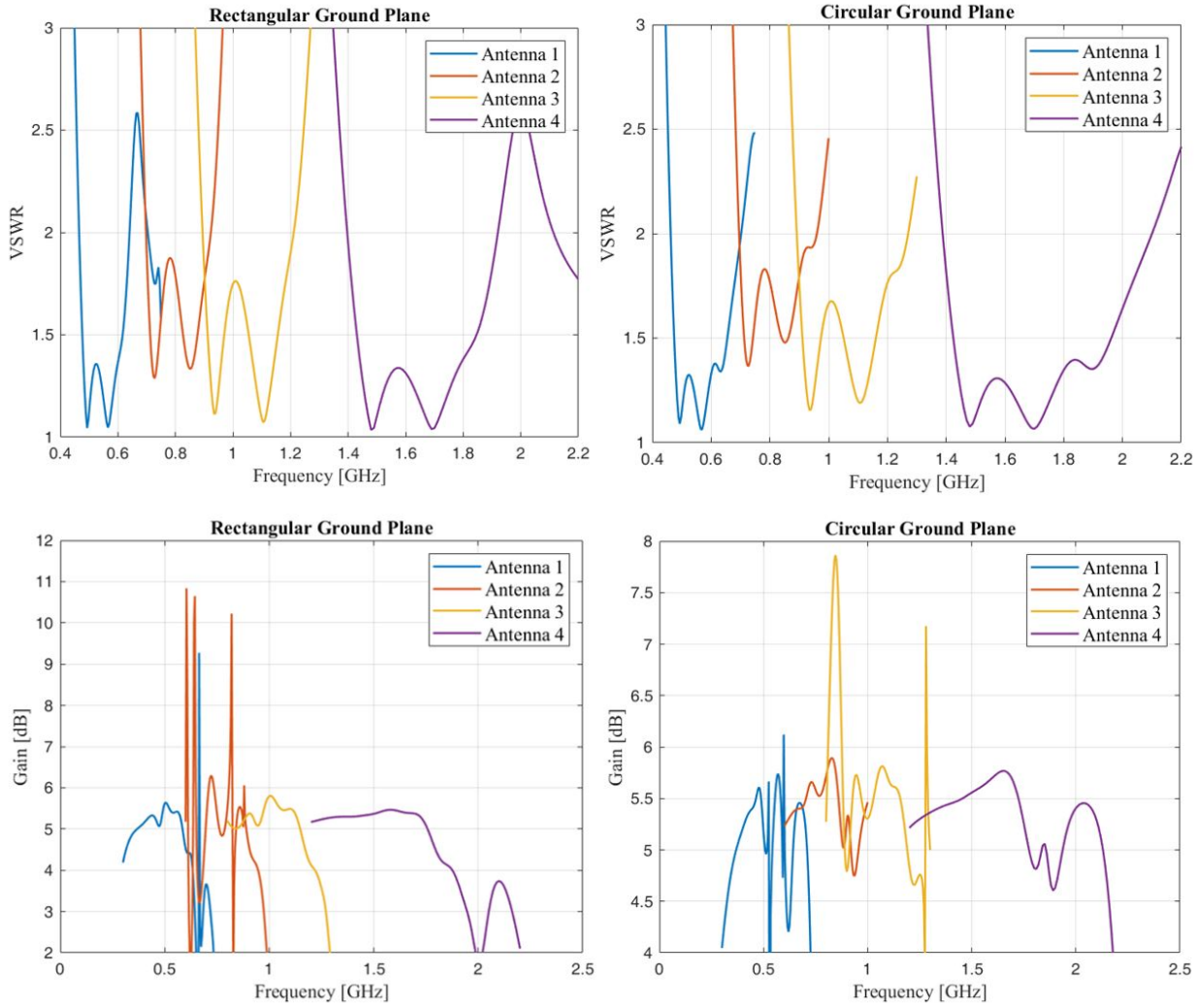


***Figure F7**: VSWR and Gain of Antenna 4*

Validation of FEKO Results

Due to the lack of analytical models, the results obtained for the circular ground plane using FEKO are compared to that of HFSS. Both the results show reasonable agreement which validates the designs to some extent. Figure F7 shows the comparison of the VSWR for all the four antennas.

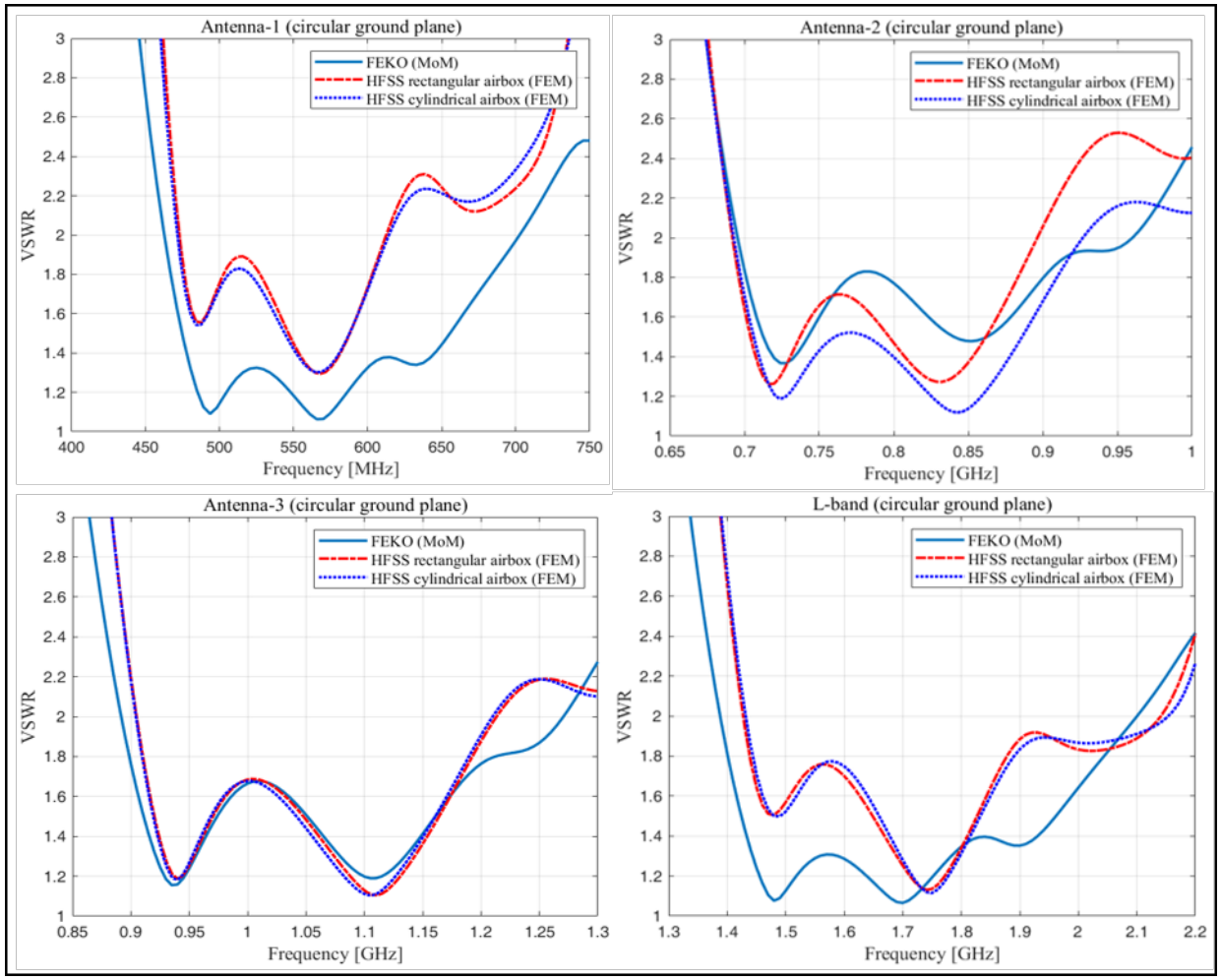


Figure F8: *Comparison of VSWR results obtained through FEKO and HFSS for all the four cases*

Antenna #	Software	f_L (GHz)	f_c (GHz)	f_U (GHz)	%BW	ka
1	FEKO	0.462	0.582	0.703	41.3734	0.6346
	HFSS (rect airbox)	0.471	0.542	0.613	26.2426	0.5908
	HFSS (cyl airbox)	0.472	0.542	0.612	25.7669	0.5909
2	FEKO	0.6952	0.8279	0.9609	32.0570	0.6013
	HFSS (rect airbox)	0.6926	0.809	0.9263	28.8715	0.5879
	HFSS (cyl airbox)	0.691	0.793	0.8957	25.7451	0.5763
3	FEKO	0.892	1.081	1.271	35.043	0.6193
	HFSS (rect airbox)	0.9039	1.057	1.2106	29.00	0.6055

	HFSS (cyl airbox)	0.9048	1.058	1.2121	29.03	0.6062
4	FEKO	1.388	1.744	2.101	40.871	0.6335
	HFSS (rect airbox)	1.4316	1.79	2.15	40.116	0.6503
	HFSS (cyl airbox)	1.4270	1.784	2.1414	40.040	0.6479

Conclusion and Future Work:

Four nearly electrically small (ka=0.6) microstrip patch antennas have been designed which can cover the desired frequency range from 0.4 GHz to 1.2 GHz and beyond. All the antennas have more than 5 dB of maximum gain. The results obtained from different EM solvers have good agreements against each other which validates the approach.
Future work includes fabrication of the antennas and hence validation of the simulated and measured results. Once the single antennas are characterized, a linear array composed of these microstrip patches will be investigated followed by a planar array.

GTEM Impedance Transformer (Taper) Design (Chatterjee/Myers/Spaeth)

We have been addressing design constraints that arise when fabricating the taper-based impedance transformers (figure F8) and incorporating them into the simulations. The mounting plate was removed in favor of soldering the coax directly to the taper. Simulations showed removing the plate had no significant impact on the results. The previously metallic cone was replaced with a dielectric cone coated in metallic material, which also had little effect on the final results. The taper is simulated mirrored (i.e., balanced) as it would be during testing. Testing the tapers end to end can achieve more precise measurements when the input and output are both coaxial (impedance matched to the measurement device and with respect to one another). However, this means that all transmission goes through not one but two tapers, and any interference or reflection due to the taper is doubled. In fact, the effect is squared: 90% transmission on one taper should result in 81% transmission through the other. Likewise, if when testing we see 64% transmission on the receiving taper or second taper, we know the input signal had a transmission of approximately 80% through the first tapered transformer.

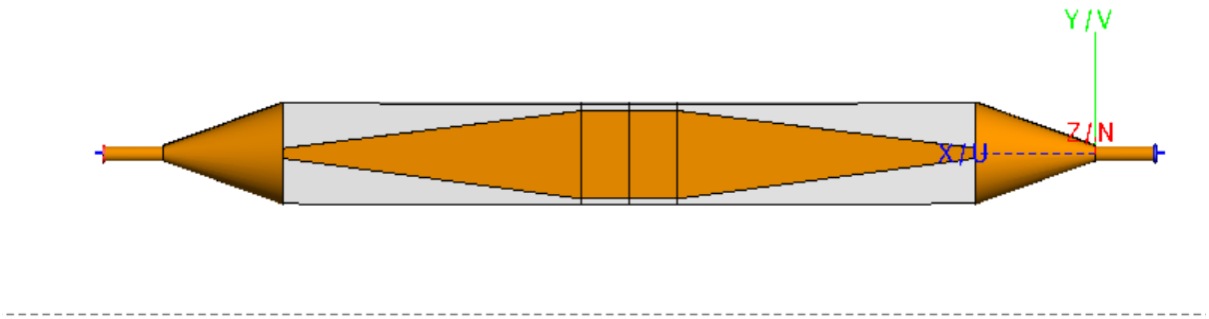


Figure F9: *Computer representation of the back to back tapered impedance transformer**.***

Various methods of tuning the taper to specific frequency ranges have been identified. Decreasing the slope of the ramp increases transmission at higher frequencies (800MHZ to 1100MHz), but decreases transmission at lower frequencies (500Mhz to 700Mhz). Below (figure F10) is an example of a design favoring the higher frequencies (left), and the lower frequencies (right):

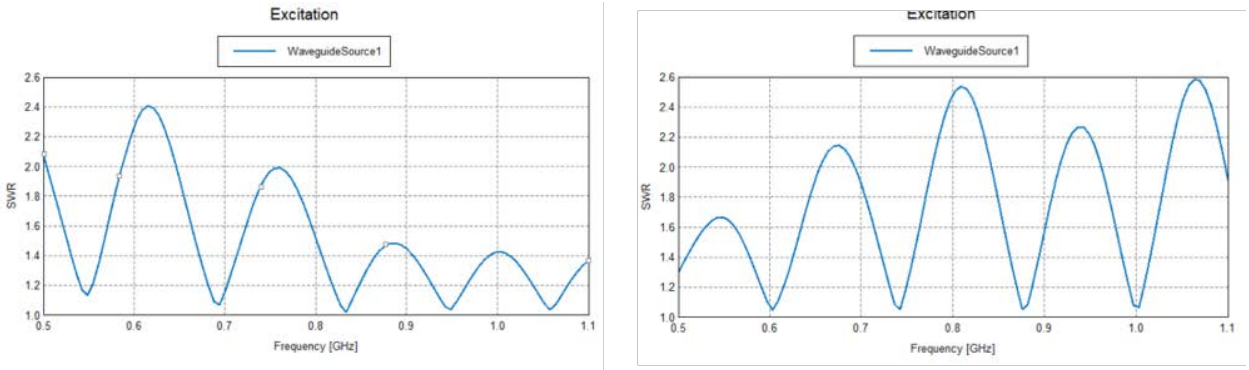


Figure F10: *Comparison of tapered impedance transforms favoring lower frequencies (left) and higher frequencies (right).*

We are testing the tapers end to end because we can achieve more precise measurements when the input and output are both coaxial. However, this means that all transmission goes through not one but two tapers, and any interference or reflection due to the taper occurs doubly. In fact, the effect is squared: 90% transmission on one taper should result in 81% transmission through 2. Likewise, if when testing we see 64% transmission, we know the transmission through one taper is 80%.

The design can also be tuned by increasing and decreasing the total length, which will shift the peaks and troughs of the SWR to wherever it needs to be. In the higher frequency example above, the local peak at 1GHz can be easily advanced by a centimeter increase in taper length so that a trough now exists at that frequency. In this way nearly total transmission can be achieved at an exact frequency.

Antenna Fabrication and Measurements (Chatterjee/Durbhakula)

We are gathering required materials to fabricate and test 4 electrically small antennas (ESA) which showed decent bandwidth covering from 0.4 GHz to 2 GHz. The initial task is to obtain the VSWR from measurement and then compare it with the results seen from the simulation. Moreover, antenna characteristics such as beam width, gain, side lobe levels can only be measured using the anechoic chamber, which is available at Missouri Science and Technology campus. In addition, we are planning on carrying out time-variant pulsed antenna measurements using PNA series Microwave Network Analyzer. This requires the use of external pulse generators, RF mixer in conjunction with PNA. Some output parameters under pulsed measurements include beam formation, distortions and power output (gain) as a function of time within a single pulse or over a pulse burst. Fitting choice of pulse width, pulse repetition frequency (PRF), duty factor (DF), IF bandwidth, and wideband/narrowband approach is essential in achieving an optimum result.

One of the key factors when deciding to use either wideband/narrowband approach is the rise-time of antenna under test. If the rise-time is significantly fast (≥ ⟦10⟧ ^(-12)secs), then it is ideal to use wideband approach, which provides good dynamic range and greater ability to measure single pulse without any distortion. On the other hand, if having pulsed RF signal with constant PRF is the case, the narrowband approach is more suitable. This increases the sensitivity of any receiver.

G. *Antennas - Log Periodic (Hassan)*

Antenna efforts for this reporting period can be found in reporting for ONR Contract N6833519C0255 under the supervision of ASR.

IV. Research and Development Support (Smith)

H. *Device and Materials Modelling (Eifler)*

This computational study is an examination of varying device parameters for SiPCSS and observing device operation for changes in recovery time. The device width and thickness and the doping depth and doping concentration were individually varied and the load voltage observed from which the recovery time was estimated. Decreased recovery time reduces switching losses and the goal of this study was to determine what changes in device parameters produced decreased recovery time.

The same circuit for the SiPCSS was used in the simulations. The same experimentally determined doping profiles were used for all simulations varying width and thickness. For simulations varying the doping profile, a Gaussian doping profile was used for

simple quantitative comparisons. In Figure H1, the circuit used is shown in (H1a). In (H1b), a mockup device is shown giving designations for the length, width and thickness of the Si-PCSS to help orient the reader. The simulated device was a 2D device model where the length is a multiplicative constant. In (H1c) is shown an example Gaussian doping profile with the P, I and N regions labeled. The PCSS on-state resistance (R_{on}) was set to 0.057 Ω by adjusting and holding constant the laser energy to reduce the number of simulations and computational cost, however this complicates whether recovery time was due to the laser energy or the device parameter that was varied.

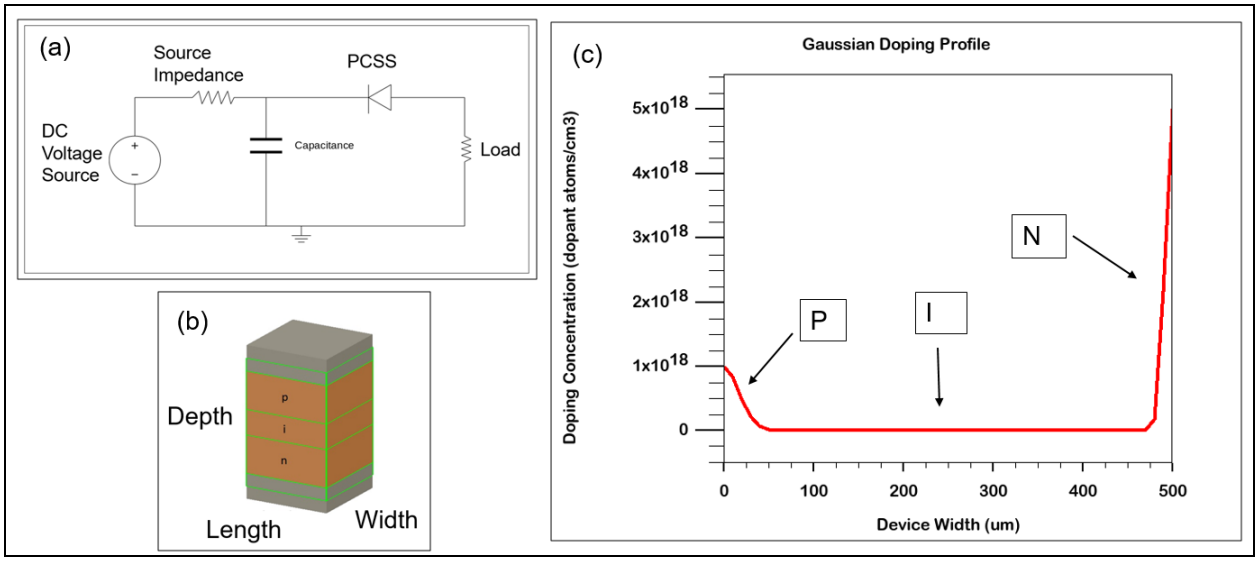


Figure H1*. (a) Circuit for Si-PCSS. (b) Mock-up of Si-PCSS showing the length, width and thickness designations. (c) Gaussian doping profile used in doping profile variations.*

Increments in Device Width

A series of simulations were performed with incremented widths to observe changes in recovery time. Widths of 1 mm, 2 mm, 3 mm and 4 mm were chosen to mimic the 1 cm to 7 cm widths of actual devices but on a smaller scale to save computational cost. In Figure H2, the load voltage (H2a) and switch resistance (H2c) are shown on log scales. The capacitor voltage is shown in (H2b) but on a linear scale.

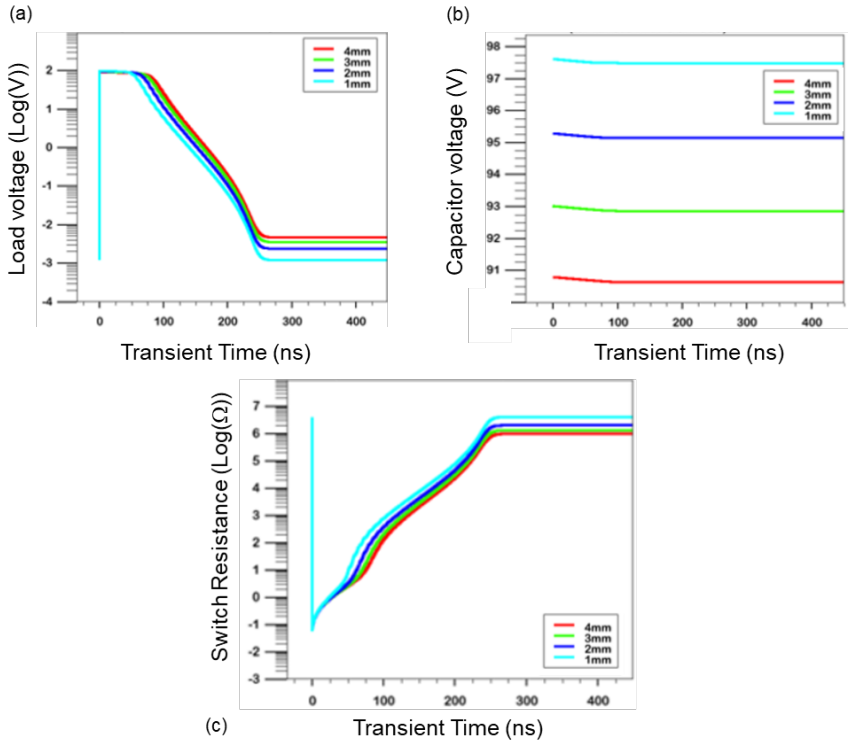


***Figure H2**. (a) Load Voltage, (b) Capacitor Voltage, (c) Switch Resistance.*

In (H2a) the load voltage had decreased recovery time for decreased widths. The switch resistance in (H2c) had a decreased recovery time for decreased widths. However, setting R_{on} to the same value obscured how much width affects recovery time. The increasing laser energy used to produce the same R_{on} for increased widths is what increased recovery time by producing increased amounts of excess carriers. In (H2c), the capacitor voltage stayed roughly constant. In practice, the width is set to fit the switch to the transmission lines and for thermal dissipation.

Increments in Device Thickness

Device thickness was incremented to observe the effect on recovery time. Thicknesses of 500 µm, 800 µm, 1000 µm and 1300 µm were chosen based on devices fabricated. In Figure H3, the load voltage (H3a) and switch resistance (H3c) are shown on log scales. The capacitor voltage is shown in (H3b) but on a linear scale. The recovery time decreased for decreased thickness. Limits on the thickness of the device are chosen based on hold-off voltage requirements which limit the amount of power generated by the switch.

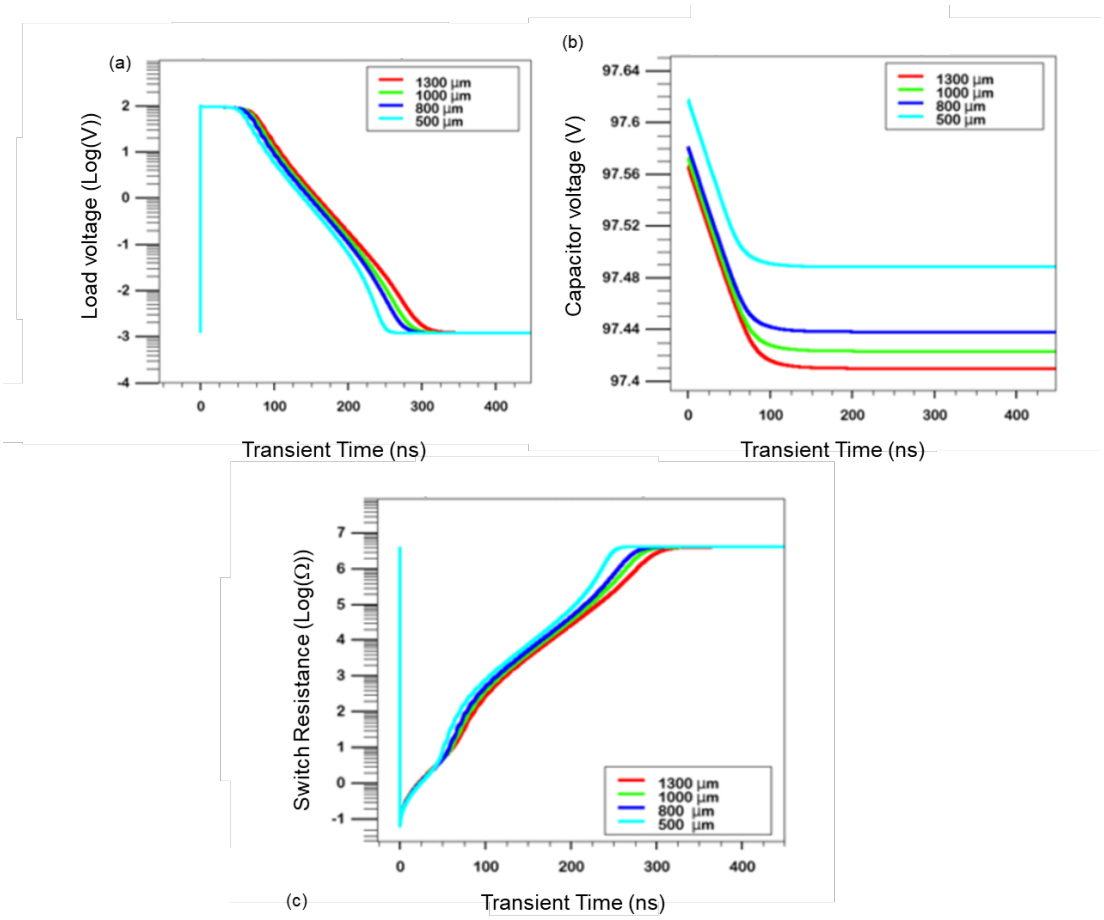


***Figure H3**. (a) Load Voltage, (b) Capacitor Voltage, (c) Switch Resistance.*

Increments in Doping Depth

The doping profile can be described as a doping concentration (peak doping concentration) and a doping depth. The doping depth was varied to observe recovery time. Doping depths for the P and N regions were set as pairs: p 90 µm, n 43 µm; p 120 µm, n 60 µm; and p 150 µm, n 120 µm. The doping depths were chosen based on spreading resistance profiling (SRP) for actual devices. The doping concentration used was p:1e18 dopant atoms/cm^3, n:5e18 dopant atoms/cm^3. The doping concentration in the I-region was set to 1e12 dopant atoms/cm^3. In Figure H4, the load voltage (H4a) and switch resistance (H4c) are shown on log scales. The capacitor voltage is shown in (H4b) but on a linear scale. The load voltage (H4a) and switch resistance (H4c) recovery times decreased with increased doping depths.

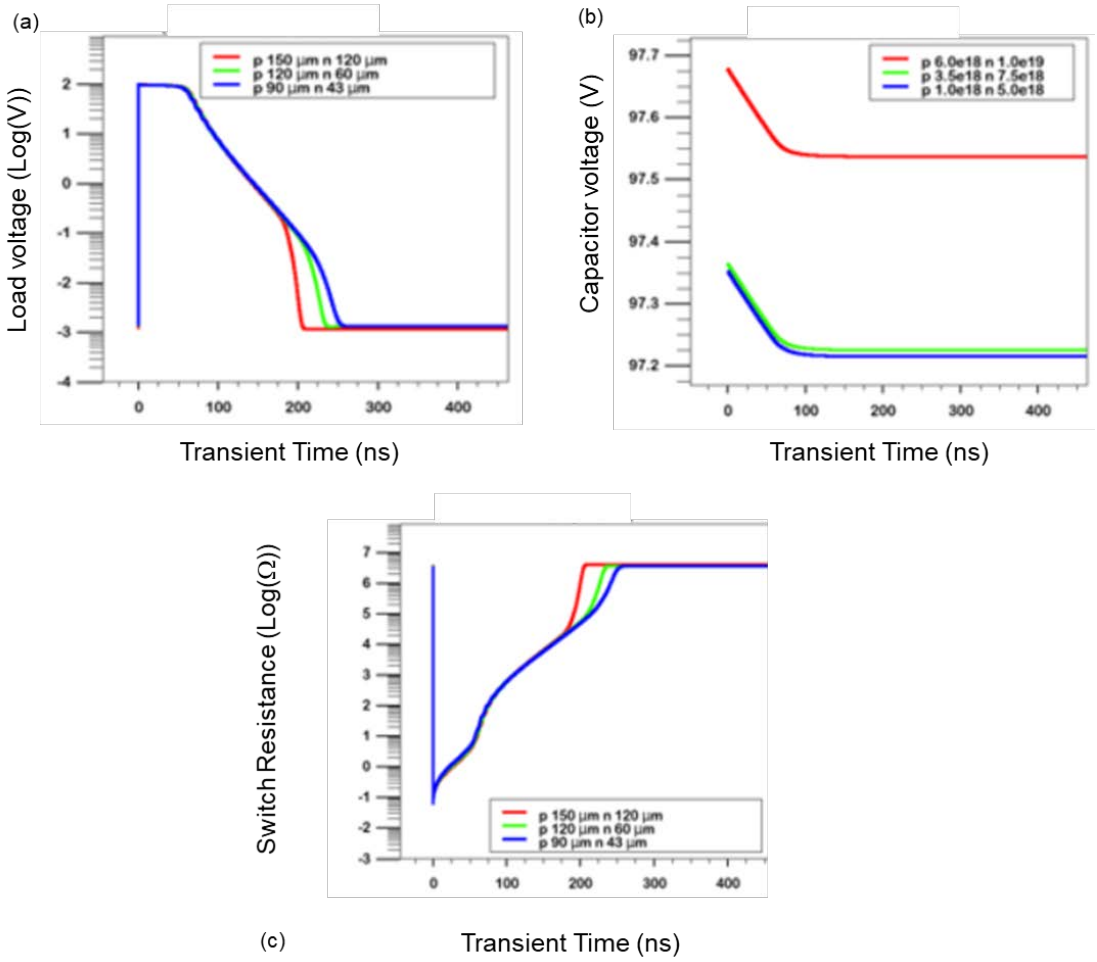


Figure H4*. (a) Load Voltage, (b) Capacitor Voltage, (c) Switch Resistance. Increments in Doping Concentration*

The doping concentration was incremented with fixed doping depths of p:90 µm and n:43 µm. The doping concentrations used were in dopant atoms/cm^3, p:1e18, n:5e18; p:3.5e18, n:7.5e18; p:6e18, n:1e19. The background doping is 1e12 dopant atoms/cm^3. These doping concentrations are based on SRP of actual devices. In Figure H5, the load voltage (H5a) and switch resistance (H5c) are shown on log scales. The capacitor voltage is shown in (H5b) but on a linear scale. With the increased doping concentration, the recovery time decreased for load voltage (H5a) and switch resistance (H5c).

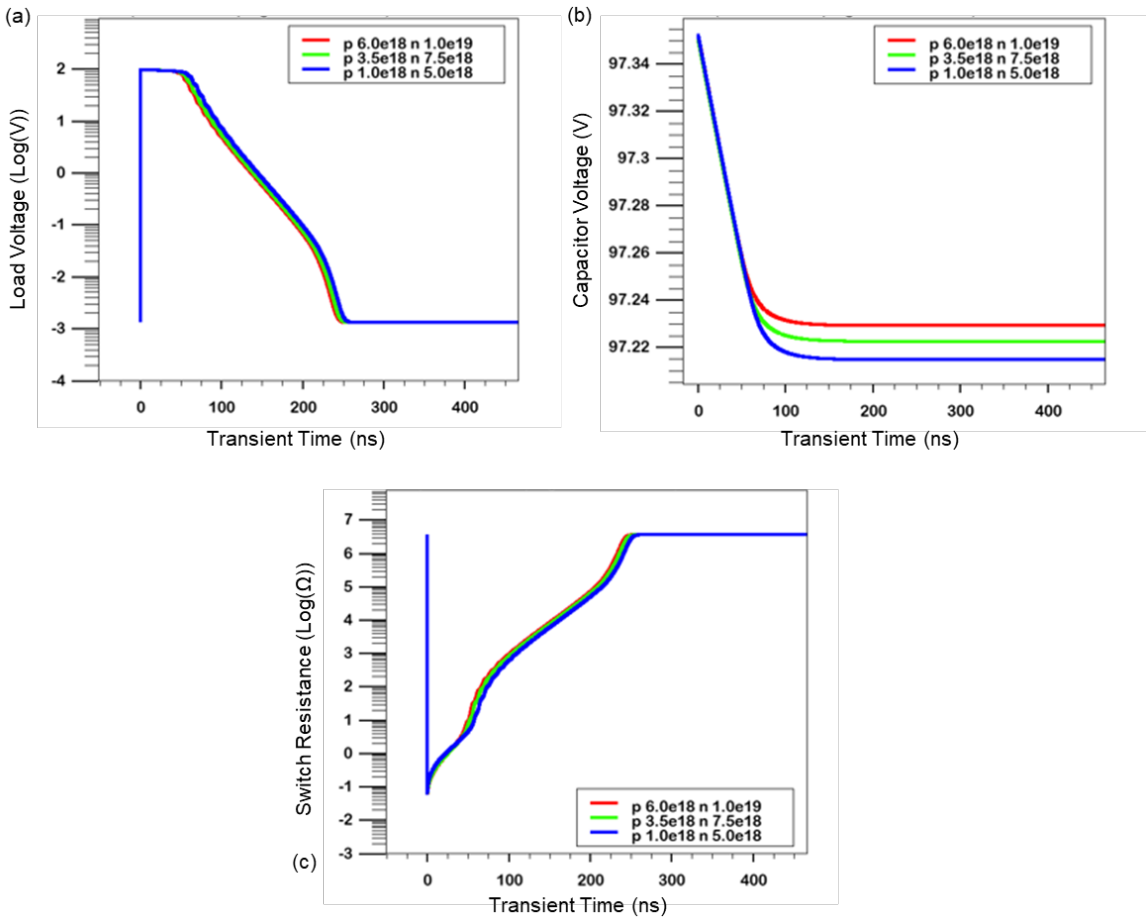


***Figure H5**. (a) Load Voltage, (b) Capacitor Voltage, (c) Switch Resistance.*

I. *GaN:C Calculation (Rulis)*

The main activity to report over the past month is the further development of our tool-chain in concert with discussion with Jay Eifler and his work on Silvaco TCAD. We have identified appropriate areas to focus our efforts. Of key interest is the determination of certain material dependent parameters for Monte Carlo simulation. In the Simple Monte Carlo code the parameters needed are given in Table I1. The list of parameters needed in Silvaco TCAD is being compared to this list.

***Table I1:** SMC scripts of GaN required parameters for both electrons and Holes.*

Our capability / Parameters	Can	Cannot
Phonon energy (meV)	Yes (Phonopy)	
Threshold energy Eth (eV)	Full band Monte Carlo (FBMC)	----------

Impact ionization rate coefficient Cii (s^{-1})	Simple Monte Carlo Device Simulator (SMCS)	Required Full Band Monte Carlo
Softness factor γ	Required Experiment	----------
Effective mass m ∗ (kg)	Yes (VASP), OLCAO	
Free path length λ (A)	Yes (Phonopy-vasp)	
X-ray spectroscopy	Possible	
XANES/ELNES calculation	Yes (OLCAO)	

The PyCDT and PyMatGen codes were installed on Lewis (UM Supercomputer) and made operational there. The PyCDT code will be crucial for helping establish working models of carbon doped GaN. We do not yet know where in the lattice that the carbon goes and we are planning to predict sites using PyCDT. This is ongoing. We have also spent time this past month identifying user facilities that can assist with XANES or ELNES based core-level spectral measurements of samples so that we could compare modeled results with experimental data to confirm any predictions from PyCDT.

The graduate student is starting with XANES calculations (Figures I1, I2), but still needs to learn more to produce accurate spectra.

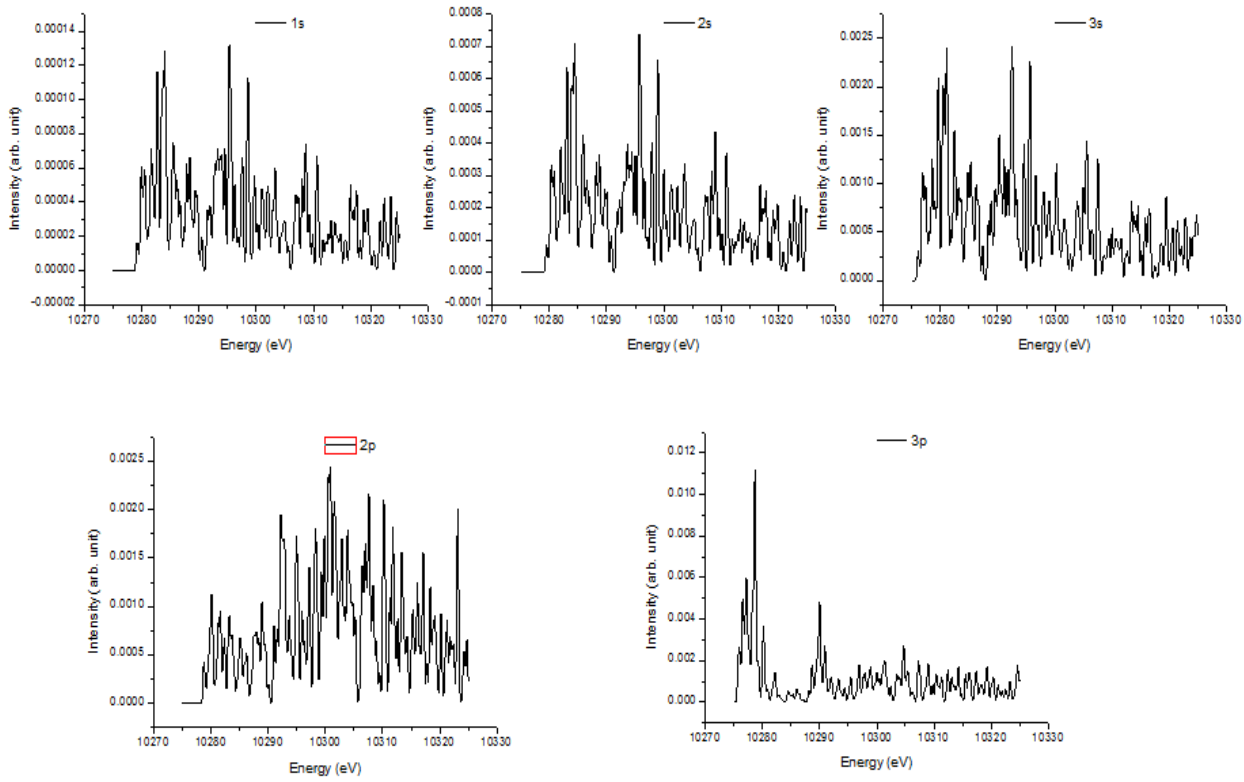


Figure I1*: Above is the XANES spectra for Ga orbitals (1s,2s,3s,2p,and 3p) using OLCAO methods*

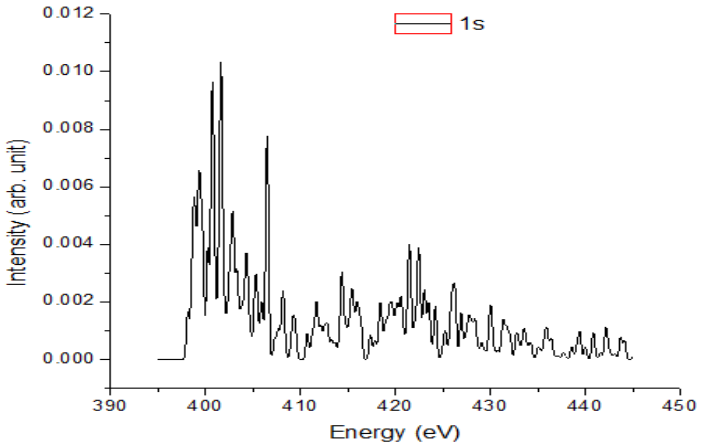


***Figure I2**: XANES spectra for 1s orbital of N*

V. Miscellaneous (Crow)

Nothing to report this period.

Issues:

[1] ***Scope*** *–*

[2] ***Budget*** *–*

[3] ***Schedule*** *–*

Interactions with Others:

Agency/Org	Performer	Project Name	Purpose of Research/ Collaboration

Major Procurement Actions:

Travel:

Travel Plans

Please note that all papers or presentations on any aspect of the ONR HPM program must be reviewed by the ONR Program Officer (or in some cases ONR Public Release Process) regardless of classification level or audience.

Planned Travel Details	Purpose	Attendees	Estimated Costs

Pending or Upcoming Public Release Requests:

None at this time.

ONR HPM 2019 Program - Monthly Status Report (MSR) – SEPTEMBER2019
Anthony Caruso – Univ. Missouri – Kansas City
N00014-17-1-3016 [OSPRES Grant]
ONR Short Pulse Research, Evaluation and non-SWaP Demonstration for C-sUAV Study

10/15/2019

Distribution Statement ~A: Distribution authorized to all OSPRES Grant and Contract Participants, and any uncompensated collaborators. Further dissemination per Ryan Hoffman (ryan.hoffman@navy.mil).

OSPRES Project Description: Develop tunable High Power Microwave (HPM) sources and electronically steerable radiators whose waveform(s) enable control over all levels-of-lethality on cUAV and similar targets, with the least power density.

Contents:

Executive Summary: **3**
Current Month Progress: **4**
I. Source Development (Myers) **4**
A. *PCSS Power Conditioning –– IGBT (Khan)* 4
B. *Switches - GaN:C (Thompson)* 4
C. *Switches - Figure of Merit (Bhamidipati)* 4
II. Effects, Coupling and UAS Developments (Currie) **4**
D. *RF Coupling (Hassan)* 4
E. *UAS Developments (Fields)* 5
III. Antenna Development (Ahern) **5**
F. *Antennas* - Electrically Small Antennas (Chatterjee/Barman) 5
G. *Antennas* - Log Periodic (Hassan) 6
IV. Research and Development Support (Smith) **7**
H. *Device and Materials Modelling (Eifler)* 7
I. *GaN:C Calculation (Rulis)* 7
V. Miscellaneous (Crow) **7**
Issues: **7**
Interactions with Others: **8**
Major Procurement Actions: **8**
Travel: **8**
Pending or Upcoming Public Release Requests: **8**
Selected Highlights (text and/or images): **8**

Executive Summary:

- Three variations of the nearly electrically small microstrip patch antennas were simulated in a linear array of 25 elements. Power, as a function of the scan angle, was reported between 0 and 60 degrees. At 1km distance, approximately 50% power loss between 25 and 30 degrees scan angle has been documented. With a program goal of 30 degrees minimum steerable angle, redesign/reconfiguration of the antenna/array must be performed to maintain power levels in the far-field at 30 degrees scan angle.

- GaN:C pulse testing has been performed on devices with varying contact gap widths at varying incident energy. On-state resistance as a function of gap width and incident energy, as determined through further testing, will inform the optimum geometry of GaN PCSS and help to define the specifications for a laser dedicated to GaN PCSS development.

- The RF coupling group is working to simulate short pulse excitations into CMA models. Once implemented, conditions of the CMA simulations will more closely match experimental parameters.

- The IGBT team has fabricated a MOSFET based PCSS driver circuit that will be able to limit the flow of current during the OFF state, making it possible to significantly minimize the power loss across the PCSS while increasing the system efficiency and device lifetime. This system is currently being tested.

Current Month Progress:

I. Source Development (Myers)

A. PCSS Power Conditioning - IGBT (Khan)

- We have fabricated a MOSFET based PCSS driver circuit and are presently testing it. This circuit has EMI related difficulty at voltages more than 1200 V DC.
- We are designing an EMI shield to isolate the power conditioning circuit from the radiated EMI caused by the rapid triggering of the PCSS.
- During October, we will operate the power conditioning circuit at a higher voltage (> 2 kV) and at a repetition frequency of 2 kHz.
- During October, we will test the power conditioning circuit at a lower voltage (<1 kV) and at a higher repetition frequency (>50 kHz).

B. Switches - GaN:C (Thompson)

- Started pulse testing using the encapsulation material (Sylgard-184) provided by NRL to allow higher voltage testing without arcing between the contacts and the copper on the PCB.
- Performed pulse testing to find the on-state resistance and gain as a function of incident energy from the laser. Testing for a device with a 500 μm gap length was completed. Further testing will be done on the remaining gap lengths to find how gap length affects the necessary incident energy to reach maximum gain.
- 900 V on the 500 μm gap length device was achieved, but was limited by the resistors on the PCB. Will add more resistors or resistance to the circuit to allow for higher voltages to be achieved.

C. Switches - Figure of Merit (Bhamidipati)

- Trends in power losses and temperature rise during switch operation at varied light intensities and device geometries have been studied for different materials.
- In the effort of making the figure of merit application specific, and to be applied for wide PCSS trade space, application specific requirements have been laid out.
- Numerical correlation between the application requirements and the cost-effective optimal material needs to implement them are being studied.

II. Effects, Coupling and UAS Developments (Currie)

D. RF Coupling (Hassan)

- We studied coupling to common UAV electronic components, such as the speed controller. We measured the input impedance to the different ports of the speed controller and developed simple models of the wires feeding these ports. We studied RF coupling to the speed controller when it was placed above UAV

frames of different material and we quantified the coupling at different angles of incidence.

- We started to study RF study coupling to UAVs due to excitation composed of short-time pulses. We are currently extracting the frequency-domain Characteristic Mode Analysis conclusions that apply to the coupling due to short-time pulsed excitation.

E. UAS Developments (Fields)

- Identified limitations in open-source autopilot logging, and are currently attempting to remedy the log file problems prior to additional testing.
- Developed a test plan for additional GTEM HPM evaluations with a myriad of platforms.

III. Antenna Development (Ahern)

F. Antennas - Electrically Small Antennas (Chatterjee/Barman)

- Three separate rectangular patch antennas have been designed on finite circularly grounded substrates to cover the target frequency range: 0.4 - 1.2 GHz.

TABLE 1. *Summary of antenna characterization.*

Antenna #	f_L (GHz)	f_c (GHz)	f_U (GHz)	% BW	Max. Gain (dB)	ka
1	0.462	0.5825	0.703	41.3734	5.61	0.6346
2	0.6952	0.8279	0.9609	32.0570	5.89	0.6013
3	0.892	1.0815	1.271	35.0439	7.87	0.6193

- Linear arrays composed of antennas 1, 2 and 3 (with the elements placed along the X-axis at an inter-element spacing d=λ/2) have been modelled in FEKO.
- Power densities of the linear arrays are computed at a distance of 1 km for different scan angles (Figure F1).
- To enhance the power density, a planar array of electrically small antennas has been investigated. Figure F2 shows the power density at a distance of 1 km vs. scan angle plot of a uniformly excited 10×10 planar array (of Antenna 1).
- Future Work:
    - Full wave simulations of planar arrays using commercial EM solver are a computational bottleneck. For speedier analysis, new formulations are being looked into.
    - Fabrication and measurement of the designs to validate the simulated results will be carried out in the near future.

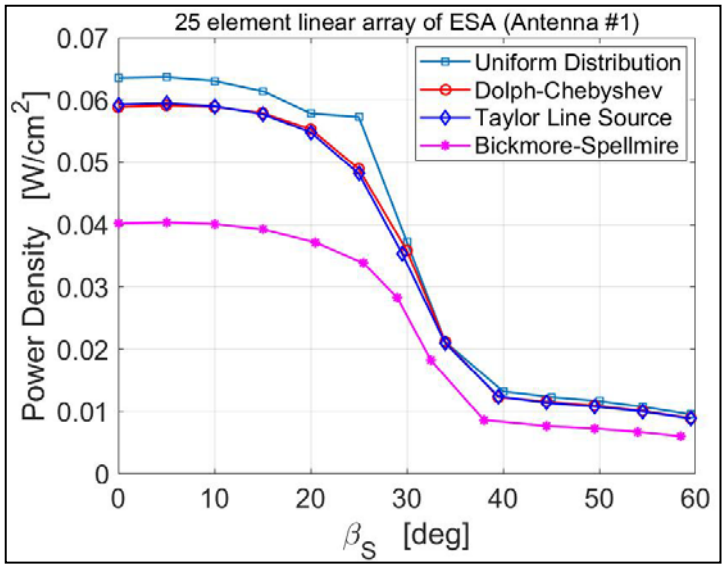


Figure F1. *Power Density of a Linear Array of Antenna 1.*

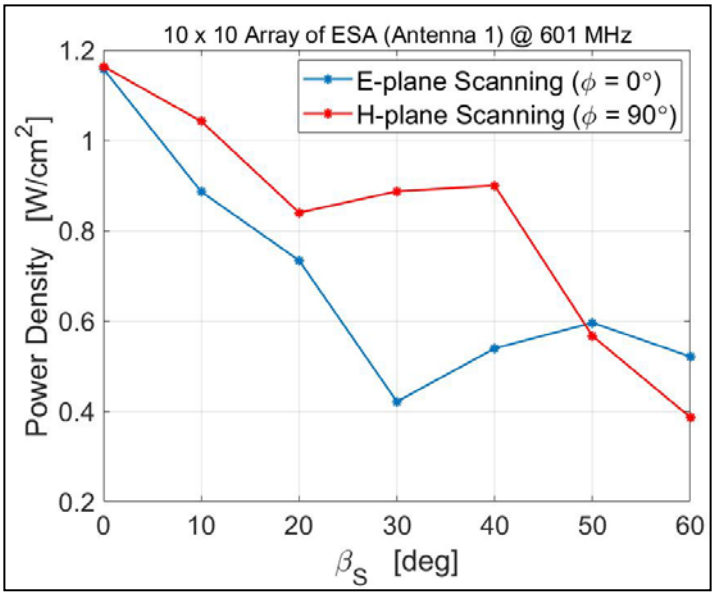


Figure F2. *Power Density of the Planar Array of Antenna 1.*

G. Antennas - Log Periodic (Hassan)

- In addition to the log periodic, we are also investigating the helical antennas as another alternative to meet the program requirements. We studied the theory behind helical antennas, started to explore the parameter space for the design of helical antennas, and will continue to optimize the design to meet the program requirements

IV. Research and Development Support (Smith)

H. Device and Materials Modelling (Eifler)

- Compared Experimental and Simulation results for Si-PCSS on PCB showing reasonably close Load Voltage and Switch Resistance with some differences due to contact inductances in lab experiments and device differences: doping profile, carrier lifetimes, metal electrode spacing, accounting for shape of laser window, and reflectivity of front surface (anti-reflective coating).
- Simulated in-line TL-setup to reduce simulation time by adding resistor to dissipate reflections which successfully reduced necessary timestep from 0.1 ps to 1ps.
- Incorporated an open-circuiting switch to disconnect charge-side TL from Si-PCSS to improve recovery and simulation time; inconclusive and under testing.
- Set maximum voltage steps to simulate high power simulation for TL-setup successfully up to 5.6 MW but required smaller timestep and more testing for high power simulations.
- Added backside/sidewall reflections for laser and set front reflections for Silicon which increased available photocurrent/source photocurrent ratio (external quantum efficiency) from 0.31 to 0.47. More testing needed to properly set reflectivity to match with experiment and account for free-carrier absorption.

I. GaN:C Calculation (Rulis)

- Students were able to use VASP+PyCDT to produce a range of GaN:C defect models (substitutions, interstitials, different charge states, and vacancies in standard hexagonal and also cubic GaN).
- Students were able to compute core level spectra (ELNES spectra) on several models, while evaluating the suitability of existing samples for use in ELNES experimental measurements that could be conducted by a collaborator. The students now have a much better understanding of how to compute accurate spectra.

V. Miscellaneous (Crow)

Nothing to report this period.

Issues:

[1] ***Scope*** *– N/A*

[2] ***Budget*** *– N/A*

[3] ***Schedule*** *– N/A*

Interactions with Others:

Agency/Org	Performer	Project Name	Purpose of Research/ Collaboration

Major Procurement Actions: N/A

Travel:

Travel Plans

Please note that all papers or presentations on any aspect of the ONR HPM program must be reviewed by the ONR Program Officer (or in some cases ONR Public Release Process) regardless of classification level or audience.

Planned Travel Details	Purpose	Attendees	Estimated Costs
2019 IEEE International Symposium on Phased Array Systems and Technology, Boston MA (14-16 Oct)	Present paper on mutual coupling analysis in linear arrays	Dr. Deb Chaterjee Bidisha Barman	$900

Pending or Upcoming Public Release Requests:

N/A